BULGARIAN CHEMICAL COMMUNICATIONS

Journal of the Chemical Institutes
of the Bulgarian Academy of Sciences
and of the Union of Chemists in Bulgaria

Editor-in-Chief:
V. Beschkov

Visiting editor:

Abdol Ghaffar Ebadi

EDITORIAL BOARD

Screening of an attenuated strain of *Fusarium oxysporum* f. sp. cucumerinum using rhizosphere soil treated with ethanol extract of parsley (*Apium graveolens*)

Q. Lijin [1, 2], S. Zhiyong[1], G. Cheng[1], Q. Cheng[1], Y. Xingfu[2]

[1] *College of Life Science, Chifeng University, Chifeng 024000, China;*
[2] *College of Agronomy, Inner Mongolia Agricultural University, Hohhot 010019, China*

In the present study, an ethanol extract of parsley (*Apium graveolens*) fresh rhizosphere soil was supplemented to PDA plates for successive culturing of *Fusarium oxysporum* f. sp. cucumerinum, to screen an attenuated strain of *F. oxysporum* f. sp. *cucumerinum*. The results revealed that 50 mg·mL^{-1} ethanol extract of parsley fresh rhizosphere soil had allelopathic inhibitory effect on the first to fifth generation of *F. oxysporum* f. sp. *cucumerinum*. The diameter of colonies displayed significant difference between ethanol extract-treated and control 48 and 144 h after inoculation ($P < 0.05$). *F. oxysporum* f. sp. *cucumerinum* from the first to fifth generation was attenuated in virulence by the ethanol extract of parsley rhizosphere soil, and the virulence of *F. oxysporum* f. sp. *cucumerinum* decreased with the increase in generation number. As a result, an attenuated strain of *F. oxysporum* f. sp. *cucumerinum* with only 6.7% virulence was screened out from the fifth generation.

Key words：Parsley (*Apium graveolens*), Rhizosphere soil, Ethanol extract, Fusarium wilt of cucumber, Attenuated strain

INTRODUCTION

Fusarium wilt is an important disease in cucumber and melons, which generally causes 10% to 30% loss in cucumber yield, even up to 80% to 90% in some cases, leading to huge economic losses. In recent years, Fusarium wilt has become increasingly prevalent in cucumber due to the intensive and continuous cropping system, and thus has caused great economic losses to farmers. Fusarium wilt as a common vascular wilt fungal disease, is difficult to control with chemicals in the field. Although large amounts of agricultural chemicals have been used to control the disease, Fusarium wilt remains a serious threat to cucumber, and the abuse of agricultural chemicals has resulted in serious pollution to cucumber products and environment [1]

Currently, grafting between cucumber and pumpkin is the most effective way to prevent Fusarium wilt in cucumber. However, due to the difficulties in grafting technology and the cumbersome management procedures after grafting, the survival rate of grafted seedlings is very low, and the cucumber quality is also obviously declined by grafting, so this technology cannot be popularized widely. As Fusarium wilt is still a major problem in the production of cucumber, it is urgent to screen attenuated strains (biological "vaccine") of *Fusarium oxysporum* f. sp. *cucumerinum* to control Fusarium wilt in rhizosphere soil containing ethanol extract of parsley for several generations, to induce abnormal division, growth and development of this pathogen, which was then inoculated into cucumber seedlings to detect the virulence of every generation, till an attenuated strain of *F. oxysporum* f. sp. *cucumerinum* was screened out. It is expected that the attenuated strain can be used instead of agricultural chemicals to control Fusarium wilt in cucumber. The results may provide a theoretical basis for the production and development of pollution-free, green and safe vegetables.

EXPERIMENTAL

Materials

American four-season parsley was provided by Chunfeng Vegetable Breeding Farm in Qing County of Hebei Province. The cucumber variety Jinchun No. 4 was developed by Tianjin Kerun Agricultural Science and Technology Co., Ltd. *F. oxysporium* f. sp. *cucumerinum* strain was purchased from the Laboratory of Plant Pathology, Institute of Vegetables and Flowers, Chinese Academy of Agricultural Sciences.

Parsley seeds were germinated by soaking in water before they were sown in a greenhouse on January 24, 2016. Then, 60-day seedlings were transplanted into a greenhouse at the Scientific Research Base of Inner Mongolia Agricultural University on March 24, 2016, under conventional field managements.

Fresh parsley roots were excavated from 10 random sites, and 20 g of soil was collected from every site. The soil samples were bulked and packed in a plastic bag. In laboratory, 60 g of the soil was weighed, divided into three portions of

---

*To whom all correspondence should be sent:
E-mail: yxf5807@163.com

equal weight in brown jars. After absolute ethanol (analytical grade) was added, the jars were placed on a reciprocating shaker at 25ºC and 240 r·min^{-1} for 24 h [1]. Then, the raw ethanol extract was filtered first with qualitative filter paper, and then with 0.22 µm bacterial filter. The resulting mother liquid of the ethanol extract of parsley rhizosphere soil was 200 mg·mL^{-1}.

Methods

Measurement of the allelopathic effects of the ethanol extract of parsley rhizosphere soil on F. oxysporum f. sp. cucumerinum.

The mother liquid of the ethanol extract of parsley rhizosphere soil was diluted 4 times to the working concentration of 50 mg·mL^{-1}. Then, 2 mL of the diluted ethanol extract was added into 18 mL molten PDA medium to make plates (ethanol extract treatment), while in ethanol control (CK) the diluted ethanol extract was replaced by 2 ml of 25% ethanol, and nothing was added to normal PDA plates in negative control.

F. oxysporium f. sp. *cucumerinum* discs (0.6 cm diameter) were made using a hole puncher, and inoculated into the center of the agar plates prepared as described above, with the mycelium side facing down and one disc in each plate. Plates were cultured at 25 °C. The colony diameter in each treatment was measured once every 24 h, from 48 to 144 h after inoculation (when the fungal mycelia of the control covered the whole plate). Five replicates were set for each treatment, and the mean colony diameter of the five replicates was used to measure allelopathic effects [1]. Actual colony diameter (cm) = mean colony diameter measured -0.6.

Measurement of the virulence of F. oxysporum f. sp. cucumerinum treated by the ethanol extract of parsley rhizosphere soil

The conidia were washed with sterile water off the plates that had been cultured for 144 h and collected. The cell concentration of the suspension was calculated using a hemocytometer under a microscope, and diluted to 1.0×10^6 cells·mL^{-1} before inoculation. After disinfection and germination, the cucumber seeds with radicles of 1 cm long were soaked in the above conidia suspension for 20 min, and then sown into plastic pots filled with high-pressure sterilized soil, covered with small sheds and plastic films to maintain heat and moisture. When 60% of the seedlings emerged, the plastic films were removed. Three replicates were prepared for each treatment, with 20 seedlings in each replicate.

The disease index of each treatment was surveyed once every other day from disease occurrence till the disease incidence in control

6

stabilized. The disease classification and identification were performed by referring to Weng [2], as follows:

Level 0: no obvious wilt symptoms; level 1: cotyledons turned yellow but did not wilt; level 2: cotyledons completely wilted or the seedlings slightly wilted; level 3: seedlings obviously wilted or dwarfed; level 4: seedlings wilted and died (or did not emerge). Disease index = Σ (disease level × the number of seedlings at this level) /the highest disease level × total number of seedlings × 100%.

Screening of attenuated strains of F. oxysporum f. sp. cucumerinum during successive subculturing

The colonies that had been cultured for 144 h according to "*Measurement of the allelopathic effects of the ethanol extract of parsley rhizosphere soil on F. oxysporum f. sp. cucumerinum*" were considered as the first generation. The discs of the first-generation colonies of ethanol extract treatment, ethanol control and negative control were made using a hole puncher, inoculated into the center of fresh PDA plates, respectively, cultured in dark in an incubator for 144 h to yield the second-generation colonies. By the same way, further generations of colonies were cultured. Attenuated strains of *F. oxysporum* f. sp. *cucumerinum* in each generation were screened following the steps described in "*Measurement of the allelopathic effects of the ethanol extract of parsley rhizosphere soil on F. oxysporum f. sp. cucumerinum*" and "*Measurement of the virulence of F. oxysporum f. sp. cucumerinum treated by the ethanol extract of parsley rhizosphere soil*".

Data processing and plotting were performed with Excel 2007, data analysis and Duncan's multiple comparison were carried out with SPSS 17.0.

RESULTS AND DISCUSSION

The allelopathic effects of the ethanol extract of parsley rhizosphere soil on the first to the fifth generation of *F. oxysporum* f. sp. *cucumerinum* are shown in Figures 1, 2. 48 h after inoculation, the colony diameter of the first to fifth generation in ethanol extract treatment was respectively by 76.7%, 66.5%, 72.5%, 67.1% and 67.2% less than that in ethanol control, indicating that the colony growth was inhibited by the allelopathic effect of the ethanol extract of parsley rhizosphere soil. 144 h after inoculation, the colony diameter in ethanol extract treatment was respectively by 40.5%, 22.0%, 47.0%, 38.0%, and 13.8% less than that in ethanol control, and the colony growth was still inhibited by the allelopathic effect of the ethanol extract. There was significant difference in colony diameter between ethanol extract treatment and ethanol control from 48 to 144 h after inoculation ($P < 0.05$).

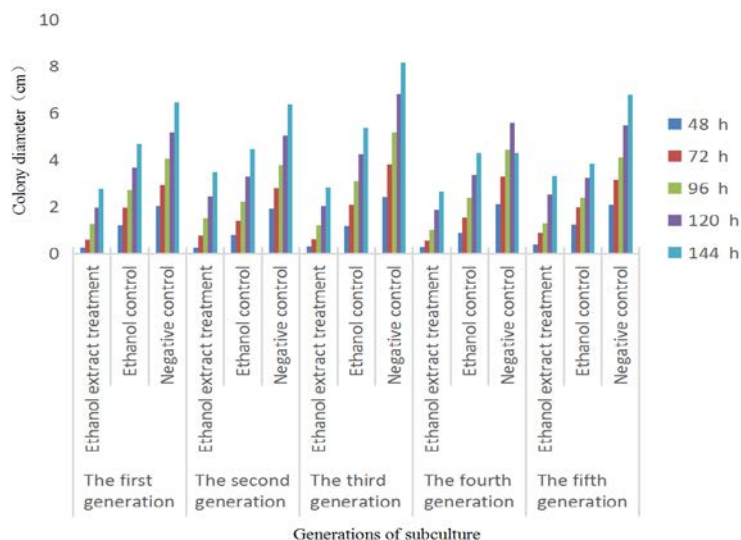**Fig. 1**. Allelopathic effect of the ethanol extract of parsley rhizosphere soil on the five generations of *F. oxysporum* f. sp. *cucumerinum* during successive subculturing
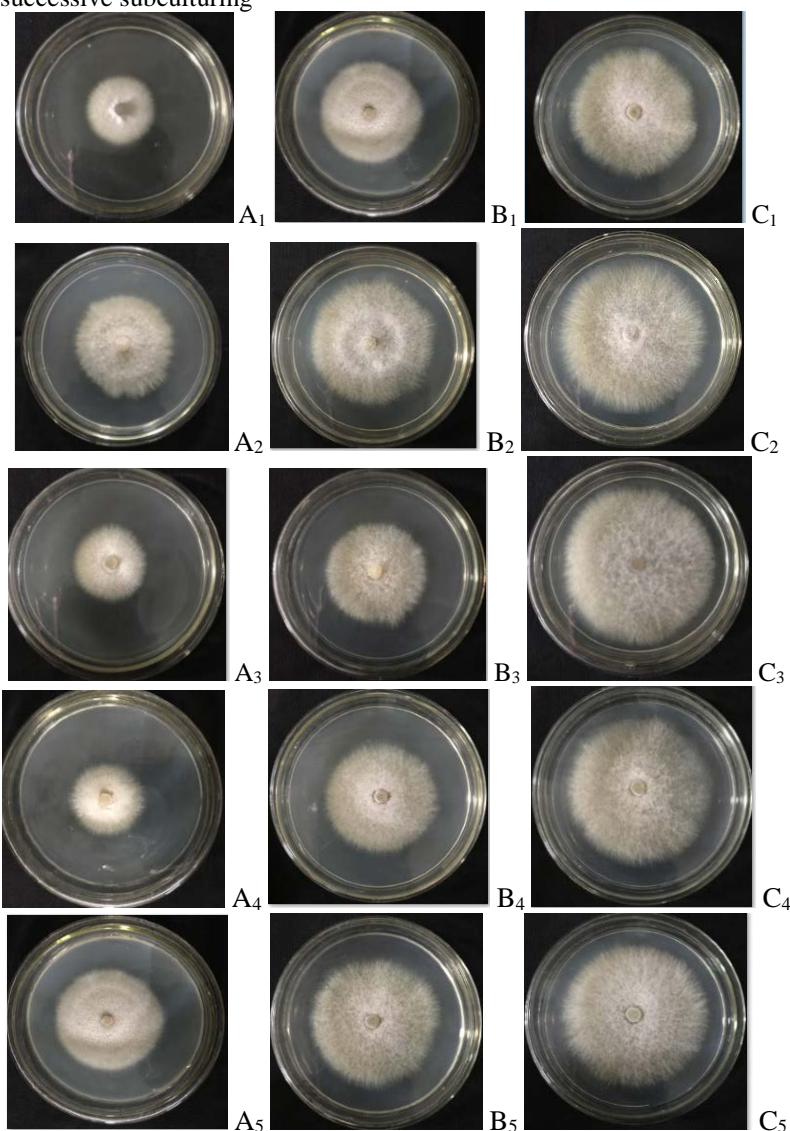

Fig. 2. Colony growth of the first to the fifth generation of *F. oxysporum* f. sp. *cucumerinum* 144 h after inoculation. A$_{1-5}$, Ethanol extract treatment; B$_{1-5}$, Ethanol control; C$_{1-5}$, Negative control

Changes in the virulence of *F. oxysporum* f. sp. *cucumerinum* treated by the ethanol extract of parsley rhizosphere soil during successive subculturing.

The virulence of first-generation *F. oxysporum* f. sp. *cucumerinum* was different between the treatments (Fig. 3). Seven days after inoculation, the disease index in ethanol extract treatment was 11.7, which was by 33.1% lower than that in ethanol control (17.5). Fifteen days after inoculation, the disease index in ethanol extract treatment was 23.3, which was by 22.3% lower than that in ethanol control (30). The fact that the virulence of *F. oxysporum* f. sp. *cucumerinum* was lowered by the ethanol extract suggested that the ethanol extract of parsley rhizosphere soil was capable of attenuating the virulence of *F. oxysporum* f. sp. *cucumerinum*. There was significant difference in the virulence of *F. oxysporum* f. sp. *cucumerinum* between ethanol extract treatment and ethanol control 7, 11, 13, and 15 days after inoculation (P <0.05).

As shown in Fig. 3, 7 days after inoculation, the disease index in ethanol extract treatment was 6.7, which was by 33% lower than that in ethanol control (10), indicating that the virulence of *F. oxysporum* f. sp. *cucumerinum* was attenuated by ethanol extract. Fifteen days after inoculation, the disease index in ethanol extract treatment was 17.5, which was 30% lower than that in ethanol control (25.0), suggesting that the virulence of *F. oxysporum* f. sp. *cucumerinum* was still attenuated by he ethanol extract. The second generation of *F. oxysporum* f. sp. *cucumerinum* showed lower virulence than the first generation 15 days after inoculation, indicating that the attenuating effect of the ethanol extract on the pathogen increased from the first generation to the second generation. There was significant difference in the virulence of *F. oxysporum* f. sp. *cucumerinum* between ethanol extract treatment and ethanol control 13 and 15 days after inoculation (*P* <0.05).

As shown in Fig. 3, 7 days after inoculation, the disease index in ethanol extract treatment was 0, while that in ethanol control was 10, indicating that the virulence of *F. oxysporum* f. sp. *cucumerinum* was attenuated by the ethanol extract from the third generation to the fifth generation. Fifteen days after inoculation, the disease index in ethanol extract treatment was 15, which was by 35.6% lower than that in ethanol control (23.3), indicating that the virulence of *F. oxysporum* f. sp. *cucumerinum* was still attenuated by ethanol extract. The third generation of *F. oxysporum* f. sp. *cucumerinum* had smaller disease index than the second generation, suggesting that the attenuating effect of the ethanol extract increased from the second generation to the third generation.

As shown in Fig. 3, fifteen days after inoculation, the disease index in ethanol extract treatment was 11.7, which was by 41.5% lower than that in ethanol control (20), indicating that the virulence of *F. oxysporum* f. sp. *cucumerinum* was continuously attenuated by the ethanol extract. Compared with the third generation, the disease index of fourth-generation *F. oxysporum* f. sp. *cucumerinum* treated by ethanol extract decreased to 11.7, so an attenuated strain of *F. oxysporum* f. sp. *cucumerinum* could be screened out by further treatment.

As shown in Fig. 3, fifteen days after inoculation, the disease index in the ethanol extract treatment was 6.7, which was by 66.5% lower than that in ethanol control (20), indicating that the virulence of *F. oxysporum* f. sp. *cucumerinum* was continuously attenuated by the ethanol extract. Inaddition, the disease index of the fifth generation decreased from 11.7 in the fourth generation, to 6.7 indicating that the virulence of *F. oxysporum* f. sp. *cucumerinum* was gradually attenuated by ethanol extract treatment during successive subculturing. An attenuated strain with a disease index of 6.7 was screened out in the fifth generation.
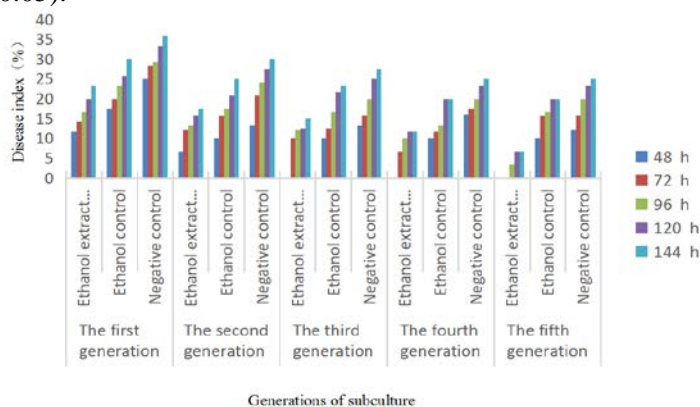

Fig. 3. Changes in the virulence of the five generations of *F. oxysporum* f. sp. *cucumerinum* during successive subculturing
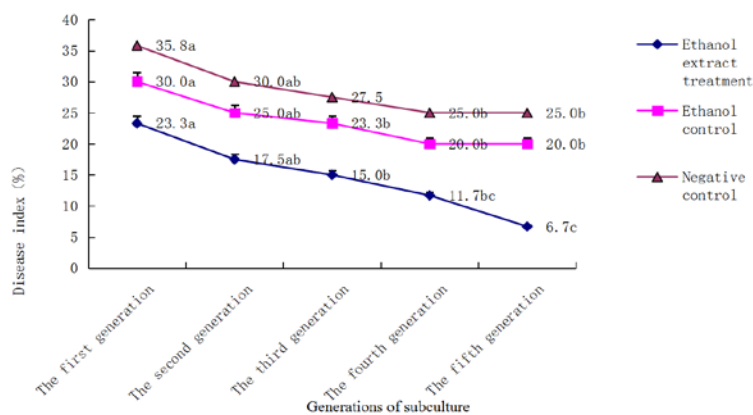
Fig.4. Intergenerational changes of the virulence of *F. oxysporum* f. sp. *cucumerinum* during successive subculturing

Intergenerational changes of the virulence of F. oxysporum f. sp. cucumerinum

In general, the virulence of *F. oxysporum* f. sp. *cucumerinum* gradually decreased from the first to the fifth generation during successive subculturing. In ethanol extract treatment, the maximum disease index (23.3) appeared in the first generation, and was lower than that in the controls of the same generation. The minimum disease index (6.7) appeared in the fifth generation, which was lower than that in the controls of the same generation. The virulence of *F. oxysporum* f. sp. *cucumerinum* in all treatments gradually increased from the first to the fifth generation. But the range of intergenerational decrease was different, indicating different attenuating effects between these treatments. In ethanol extract treatment, there was no significant difference in the disease index between two adjacent generations, but significant difference between skipped generations ($P < 0.05$). In addition, the virulence of the negative control decreased at first and then became stable with the increase in generation number, indicating that the virulence of *F. oxysporum* f. sp. *cucumerinum* was gradually attenuated during successive subculturing (Fig. 4).

CONCLUSIONS

Allelopathy refers to the beneficial or detrimental effects of the metabolic exudates of one plant or microorganism on another plant or microorganism in the environment. The existing studies of allelopathy are mainly focused on the effects of allelopathic plants on the receptor plants, the allelopathic autotoxicity of plants, the separation of allelopathic components, the identification of allelopathic plants and their action mechanism on microorganisms [3-5].The allelopathic effect of plant extracts on pathogens is a hot issue in recent studies, which not only reveals the mechanism of continuous cropping obstacles of vegetable crops,

but also opens up a new way to prevent and control crop diseases.

The allelopathic effects of the extracts of parsley fresh roots, rotten roots and seeds on *F. oxysporum* f. sp. *cucumerinum* and related mechanisms have been studied in our earlier works Reference 6-8. Based on this, *F. oxysporum* f. sp. *Cucumerinum* was treated with 50 mg·mL^{-1} ethanol extract of parsley fresh rhizosphere soil for five successive generations in the present study to explore the allelopathic effect of the ethanol extract on the first to fifth generations of *F. oxysporum* f. sp. *cucumerinum*. The results showed that 50 mg·mL^{-1} ethanol extract inhibited the growth of all five generations of *F. oxysporum* f. sp. *cucumerinum*, which validated that the ethanol extract of parsley rhizosphere soil contained active allelopathic substances that inhibited the growth of microorganisms.

F. oxysporum has formae specialis (f. sp.) that infect a variety of hosts causing various diseases, physiological races, and several non-pathogenic strains. Such strains can be obtained by natural screening or artificial mutagenesis, and are used to control wilt in crops. Wu and Wang isolated two attenuated strains with 4.35% and 7.14 virulence from disease cucumber seedlings, and proved that attenuated strains of *F. oxysporum* f. sp. *cucumerinum* could induce resistance of cucumber to wilt [9]. In the study of Gu *et al.*, a non-pathogenic mutant of *F. oxysporum* f. sp. *cucumerinum* was isolated by UV mutagenesis and proved to be positive in wilt prevention by artificial inoculation [10]. A non-pathogenic *F. oxysporum* strain was isolated by UV mutagenesis from cucumber and melon by Yang *et al*. All the results suggested that attenuated strains of *F. oxysporum* were mostly isolated by physical methods, but rarely using the allelopathic effects of plants on microorganisms.

The results of the present study showed that the ethanol extract from parsley rhizosphere soil had allelopathic inhibitory effects on all the five

9

generations of *F. oxysporum* f. sp. *cucumerinum* during successive subculturing, and the virulence of *F. oxysporum* f. sp. *cucumerinum* was gradually attenuated from the first to the fifth generation in all treatments. An attenuated strain of *F. oxysporum* f. sp. *cucumerinum* with 6.7% virulence was screened out by ethanol extract treatment from the fifth generation.

REFERENCES

1. C. Qian, X.F. Yun, X.M. Gao, Y.Y. Bao, D.D. Zhang, J. Li, Y.Wang, *Chinese Journal of Eco-Agriculture*, **21**(05), 606 (2013).
2. Z.X. Weng, X.X. Jiang, X.W. Xiao, *China Vegetables*, **2**, 30 (1985).
3. H. Molish, *Fischer*, 13, 1937.
4. B.S. Singh *New Bot.,* **9**, 13 (1982).
5. E.L. Rice, Allelopathy (2nd ed.), New York: Academic Press, 1, 1984.
6. Y. Cao, The study on the allelopathy of extracts of the rotten root and the rhizosphere zone rot soil of parsley on *Fusarium oxysporum* sp. *Cucumeris,* Inner Mongolia Agricultural University, Hohhot, 2009.
7. J.Y. Jia, Study of allelopathy mechanism of extracts of parsley seed on *Fusarium oxysporium* f. sp. *Cucumeris,* Hohhot: Inner Mongolia Agricultural University, 2011.
8. X.M. Gao, Study on the isolating and identifying allelochemicals in the extract solution of parsley and its' induced resistance on the cucumber wilt, Inner Mongolia Agricultural University, Hohhot, 2015.
9. Y.C. Wu, S.Z. Wang, *Journal of Henan Agricultural University*, **4**, 433 (1991).
10. Z.M Gu, J. Chen, Z.G. Gao, J.H. Zhuang, *World Pesticides*, **2**, 46 (2007).

Impact of nitrogen addition on plant litter decomposition in a sheepgrass meadow steppe

C. Shang[1,2], Q. Zhang[2], H.L. Zhang[2], J.K. Li[2], H.Y. Liu[2], J.L. Liu[2], R.F. Zhu[2], X.L. Kong[2], J.S. Chen[2*]

[1] Heilongjiang Academy of Agricultural Science Postdoctoral Programme, Harbin, China
[2] Institute of Pratacultural Science, Heilongjiang Academy of Agricultural Science, Harbin, China

In order to examine the effect of species (S) and nitrogen (N) on litter decomposition rate and the cumulative CO_2 emissions, litter from three species and soil samples subjected to different N-addition treatments (CK, LD, MD, HD) were collected from a sheepgrass (*Leymus chinensis* Tzvel) meadow steppe. We found litter of *L. chinensis* had higher initial nitrogen content and lower carbon to nitrogen ratios and decomposed faster than that of *A. hirta* while each species decomposing in isolation. Moreover, N addition significantly enhanced litter decomposition rate of each species. Estimated litter decay rate constant (k) under N-free treatments was significantly lower than expected based on N-added soils results, while the k was affected by nitrogen addition and increased by amount of nitrogen addition, indicating exogenous N additions could positive effects, and the positive effects of N additions on litter decomposition could influence litter decomposition and, therefore, Carbon as well as nutrient cycling in sheepgrass meadow steppe.

INTRODUCTION

Litter decomposition is very important process in most land ecosystems. The procedure offers soil nutrients for vegetative cover development and affects land net primary production [1-2]. A lot of carbon (C) may go down into belowground for soil organic matter [3]. Besides, litter decomposition often affects the fluxes of soil C [4,5]. This means a key function in the carbon budget of land ecosystems [8]. Litter decomposition processes relate to C shift between plant litter and the soil ecosystem at the litter-soil interface [9]. A lot of studies have been done to *in situ* examine what soil CO_2 emissions are affected by litter form [10], especially N-deficient grasslands in China. To research this issue in Songnen grassland with nitrogen limitation, the present study selected three plant species in Songnen grassland of China and studied its litter decomposition in a sheepgrass steppe ecosystem. We addressed the issues as follows: 1) to examine the effect of species (S) and nitrogen (N) on litter decomposition rate; 2) to examine the inference of S and N, and their interactions on the cumulative CO_2 emissions.

EXPERIMENTAL

Experimental site

The experiments were carried out in Lanxi County in Northeast China, which is run by the Heilongjiang Academy of Agricultural Sciences (HASS). The station has longitude of 125°58' E and latitude of 46°32' N. The climate is classified as a typically steppe environment.

Experimental design and sampling

There were 4 nitrogen addition treatments with four replicates at four levels: CK, LD, MD, HD; the area of each block was 10×10 m with a 2 m buffer between plots. Nitrogen was added as urea from 2010 to 2013. Then the soil samples were sieved and segmented into two parts. One part was used to monitor soil ammonium-nitrogen (ANsoil) and nitrate-nitrogen (NNsoil) concentrations and to do incubation experiments; the rest part was used to monitor soil pH, Csoil (soil organic C), Nsoil (soil N), Psoil (soil P), APsoil (soil available P) in the laboratory. The chemical properties were analyzed by a CNS elemental analyzer.

Soil CO_2 emission measurements

We calculated the CO_2 that was evolved from the plant litter by incubating soils without litter. We performed an incubation experiment using the first-order kinetic model following equation (1) [11]:

$$C_m = C_0 (1 - e^{-kt}) \tag{1}$$

where C_m refers to the cumulative CO_2-C emissions; C_0 is the potentially mineralizable C (mg g^{-1}); k is the decomposition rate constant (day^{-1}), and t is the time of incubation (days).

*To whom all correspondence should be sent:
E-mail: cyszps@163.com

All data were assessed by ANOVA with LSD using SPSS 20.0 (SPSS Inc., Chicago, USA). The decomposition kinetics was fitted by OriginPro 7.5 (OriginLab Corporation, USA).

RESULTS AND DISCUSSION

Litter chemical properties

The litter from each species had a different initial chemical composition. *Arundinella hirta* litter had the lowest N_{litter} and P_{litter} concentrations and the highest C_{litter} to N_{litter} ratio, while the opposite was found for *Leymus chinensis* litter. Although no significant differences were found between the N concentrations and C_{litter} to N_{litter} ratios for *L. chinensis* litter and *Carex duriuscula* litter, the initial N concentrations in *Carex duriuscula* litter were lower than those in *Leymus chinensis* litter but larger than those in *Arundinella hirta* litter. No significant differences in initial C_{litter} concentrations were found between the three species (Table 1). *Soil physicochemical property*

When soils from N addition treatments were tested before the incubation, soil total C_{soil}, N_{soil}, P_{soil} and AP_{soil} were not remarkably affected by the N-addition treatment (Table 2). However, N-addition treatment increased NN_{soil} and AN_{soil} concentrations (Table 2). It is seen from Table 2 that soil pH with N-addition treatment is significantly lower than that without N-addition treatment, and the highest pH value is for soil with

HD treatment, while the lowest pH is registered in the soil without N-addition after N addition treatment ($P < 0.05$).

Effect of species and N addition on litter decomposition rate

Taking into consideration the total litter decomposition during incubation presented in Table 3, it follows that litter decomposition rate and nitrogen addition are significantly different for the four incubation periods (all $P < 0.001$). For each species, the decay rate constant (k) estimated by the first-order exponential model varied from 0.017 day^{-1} for litter of *A. hirta* in no N-added soils to 0.068 day^{-1} for litter of *C. duriuscula* in HD soils. Among the three species, *A. hirta* had the minimum attenuation rate (k) under all N-added conditions ($P < 0.001$), while k was affected by nitrogen addition and increased with the amount of nitrogen addition to soils mixed with the same litter type.

Cumulative CO2 emissions

The cumulative amount of CO_2 from N-added (MD) soil with *C. duriuscula* litter was generally the highest one compared to all treatments, and *A. hirta* litter without N addition was the lowest among all treatments. Based on the time of incubation (days), the cumulative amount of CO_2 from different N-added soils with different litter was generally estimated by 12 models (equations) included in Table 4.

Table 1. Mean initial C_{litter}, N_{litter}, P_{litter}, C_{litter} to N_{litter} ratio, and N_{litter} to P_{litter} ratio of litter from the three species

Species	C_{litter} (mg g^{-1})	N_{litter} (mg g^{-1})	P_{litter} (mg g^{-1})	C_{litter} to N_{litter} ratio	N_{litter} to P_{litter} ratio
Arundinella hirta	460.3±3.6[a]	12.5±1.3[c]	1.0±0.05[b]	36.8±2.7[a]	12.5±1.1[b]
Carex duriuscula	464.3±3.5[a]	15.6±1.4[b]	1.4±0.04[a]	29.8±2.6[b]	11.1±0.9[b]
Leymus chinensis	465.3±3.8[a]	16.3±1.3[a]	1.1±0.06[b]	28.5±2.9[c]	14.8±1.3[a]

Table 2. Chemical properties of soils with different treatments before the incubation.

T	Csoil	Nsoil	Psoil	APsoil	NNsoil	ANsoil	pH
CK	3.59±1.0a	0.32±0.02a	0.11±0.01a	10.22±0.3a	3.20±0.26d	4.22±0.06d	8.1±0.20a
LD	3.56±1.2a	0.31±0.01a	0.12±0.02a	11.38±0.4a	7.14±0.22c	10.63±0.04c	7.8±0.10b
MD	3.60±1.3a	0.33±0.02a	0.15±0.01a	12.32±0.2a	8.36±0.24b	12.50±0.09b	7.6±0.05c
HD	3.58±1.1a	0.28±0.03a	0.10±0.02a	11.46±0.4a	8.92±0.19a	13.31±0.03a	7.2±0.20d

Table 3. Two-way ANOVA of the effect of species (S) and nitrogen (N) addition on rate of litter decomposition in six incubation periods (Ⅰ, Ⅱ, Ⅲ, Ⅳ, Ⅴ and Ⅵ).

V	Incubation periods					
	I (5 days)	II (10 days)	III (15 days)	IV (20 days)	V (25 days)	VI (30 days)
S	<0.001	<0.001	<0.001	<0.001	<0.001	<0.001
N	<0.001	<0.001	<0.001	<0.001	0.376	0.054
S *N	<0.001	<0.001	<0.001	0.169	0.461	0.039

Table 4. Models (equations) of cumulative CO2 emissions of soils with different litter types and N addition.

Treatment	Models	R^2
Litter of A. hirta + CK	C m= 896.2 (1 – e-0.017t)	0.978
Litter of A. hirta + LD	C m= 764.5 (1 – e-0.028t)	0.991
Litter of A. hirta + MD	C m= 548.3 (1 – e-0.035t)	0.992
Litter of A. hirta + HD	C m= 468.7 (1 – e-0.039t)	0.990
Litter of C. duriuscula + CK	C m= 546.5 (1 – e-0.055t)	0.991
Litter of C. duriuscula + LD	C m= 522.3 (1 – e-0.059t)	0.988
Litter of C. duriuscula + MD	C m= 508.7 (1 – e-0.062t)	0.982
Litter of C. duriuscula + HD	C m= 448.0 (1 – e-0.068t)	0.998
Litter of L. chinensis + CK	C m= 646.9 (1 – e-0.045t)	0.998
Litter of L. chinensis + LD	C m= 528.5 (1 – e-0.049t)	0.998
Litter of L. chinensis + MD	C m= 510.3 (1 – e-0.052t)	0.998
Litter of L. chinensis + HD	C m= 496.1 (1 – e-0.059t)	0.998

In our study, the mixtures of litter powder and soil samples were fixed to similar glass jars. As a result, litter contact area may be least different from soil. A well-known fact is that litter decay depends on the soil nutrient status [12, 13]. This outcome was consistent with previous research [14, 15]. However, others have shown that litter decomposition may decrease [16], or not change [1, 18] under N addition conditions. Our findings on the cumulative relationship between CO_2 emissions and soil characteristics showed that cumulative CO_2 emissions increased in response to three different soil nutrient supply responses. The addition of inorganic nitrogen can change the nutritional status of soil microorganisms, thereby affecting the growth and activity of microorganisms, thereby affecting the decomposition of carbon and nutrient release from litter decomposition.

CONCLUSIONS

Our study revealed that litter of *L. chinensis* had higher initial nitrogen content and lower carbon-to-nitrogen ratios and showed a marked increase over that of *A. hirta*. Estimated litter decay rate constant (k) under N-free treatments was significantly lower than expected based on the results for N-added soils, while k was affected by nitrogen addition and increased with the amount of nitrogen addition, indicating that exogenous N additions could have positive effects, and the positive effects of N additions on litter decomposition could influence litter decomposition and, therefore, carbon, as well as nutrient cycling in a sheepgrass meadow steppe.

REFERENCES

1. J.C. Moore, E.L. Berlow, D.C. Coleman, *Ecology Letters*, **7**, 584 (2004)
2. M. Almagro, M. Martínez-Mena, *Plant and Soil*, **358**, 323 (2012)
3. Y.F. Jiang, X.Q. Yin, F.B. Wang, *European Journal of Soil Biology*, **55**, 28 (2013).
4. D.A. Wardle, M.C. Nilsson, O. Zackrisson, *Soil Biology and Biochemistry*, **35**, 827 (2003).
5. C.E. Prescott, *Forest Ecology and Management*, **220**, 66 (2005).
6. B. Berg, C. McClaugherty, *Springer Verlag*. 2008
7. M.M. Coûteaux, P. Bottner, B. Berg, *Trends in Ecology and Evolution*, **10**, 63 (1995).
8. R. Amundson, *Annual Review of Earth and Planetary Sciences*, **29**, 535 (2001).
9. R. Aerts, R.S.P. van Logtestijn, P.S. Karlsson, *Oecologia*, **146**, 652 (2006).
10. Y. Kuzyakov, J.K. Friedel, K. Stahr, *Soil Biol Biochem.*, **32**, 1485 (2000).
11. Q.Y. Shang, X.X. Yang, C.M. Gao, P.P. Wu, J.J. Liu, *Global Change Biol.*, **17**, 2196 (2011)
12. K. Fog, *Biological Reviews*, **63**, 433 (1988).
13. M.J. Swift, O.W. Heal, J.M. Anderson, *University of California Press*, 1979
14. L.P. Liao, H. Gao, S.L. Wang, *Acta Phytoecologica Sinica*, **24**, 34 (2000).
15. P. Micks, J.D. Aber, R.D. Boone, E.A. Davidson, *Forest Ecology and Management*, **196**, 57 (2004)
16. R.D. Bowden, E. Davidson, K. Savage, C. Arabia, P. Steudler, *Forest Ecology and Management*, **196**, 43 (2004)
17. W.H. McDowell, A.H. Magill, J.A. Aitkenhead-Peterson, J.D. Aber, J.L. Merriam, S.S. Kaushal, *Forest Ecology and Management*, **196**, 29 (2004).
18. K.A. Whittinghill, W.S. Currie, D.R. Zak, *Ecosystems*, **15**, 450 (2012).

Simultaneous saccharification and co-fermentation of steam-exploded poplar wood to ethanol with *Escherichia coli* KO11

B. L. Ai[1], Z. W. Sheng[1], Q. Y.Wang[2], L. L. Zheng[1], X. Y. Zheng[1], Y. Q.Wang[2]*

[1] *Haikou Experimental Station, Chinese Academy of Tropical Agricultural Sciences, Haikou, China*
[2] *Key Lab of Non-wood Forest Nurturing and Protection of the National Ministry of Education, Central South University of Forestry and Technology, Changsha, China*

Steam explosion pretreatment is a promising method for the preparation of lignocellulosic biomass for biofuels production. Steam explosion was performed to assess the effectiveness of pretreating poplar wood for ethanol production. Maintaining steam pressure at 4 MPa for 10 min, 66.8% of hemicellulose and 5.3% of cellulose were hydrolyzed. The scanning electron microscopy observation, FT-IR spectroscopy analysis and X-ray diffraction analysis showed that hydrolysis of hemicellulose and modification of cellulose and lignin structures improved the accessibility of cellulose to hydrolytic enzymes. Cellulase production by *Trichoderma reesei* RUT C-30 was initiated with inocula prepared by different methods. It was found that the composition of pre-culture medium and inoculum age have minimal or no impact on cellulase production. Using the steam-exploded poplar wood as feedstock with cellulase loading of 20 FPIU g^{-1} substrate, ethanol production by gene-engineered *Escherichia coli* KO11 reached 3.6 g L^{-1}, corresponding to 51.4% of the maximum theoretical yield based on glucan remaining in the input substrate. The ethanol yield was limited by the low solid content of steam-exploded residue, and inhibited by the inhibitors released in the pretreatment process. So the steam explosion process needs to be improved for lower water content and less inhibitors, and detoxification is necessary to achieve a good fermentability of pretreated poplar wood to ethanol.

Key words: Steam explosion pretreatment, Simultaneous saccharification and co-fermentation, Poplar wood, Ethanol.

INTRODUCTION

With the rising tightness of the world's energy supply, growing attention has been devoted to ethanol fuel, but the real cause was the inevitable depletion of fossil fuels. However, nearly all bioethanol fuel is produced by fermentation of sugar from food crops, corn and sugarcane [1]. On the other hand, the utilization of cellulosic materials with relatively low cost and plentiful supply is very limited. The central technological impediment to bioconversion of lignocellulosic biomass to ethanol is the general absence of low-cost and efficient technology for delignification to liberate cellulose and hemicellulose from their complex with lignin, depolymerization of cellulose and hemicellulose to monose, and fermentation of mixed hexose and pentose to ethanol [2-3].

Steam explosion pretreatment is a promising method for the preparation of lignocellulosic biomass for biofuels production. The utilization of lignocellulosic biomass is limited by the hard-textured structure existing among the three main components of the plant cell wall - cellulose, hemicellulose and lignin [4]. Steam explosion as a pretreatment method is used to overcome the physical and chemical barriers of lignocellulosic materials quickly and efficiently. Steam explosion can be carried out to pretreat a great variety of lignocellulosic feedstocks including forestal and agricultural residues [5]. One of the central economic impediments to the bioconversion of lignocelluloses was the cost of cellulolytic enzymes [6-7]. Many efforts have been made in cost reduction of cellulolytic enzyme usage for the commercialization of cellulosic ethanol [8-9]. Fermentable sugars from the hydrolysis of cellulose and hemicellulose by pretreatment with cellulolytic enzymes include hexose and pentose. However, most microbes consume the mixed sugars sequentially because of the carbon catabolite repression existing in most microbes [10]. To overcome this barrier, specific strains of *Escherichia coli*, *Saccharomyces cerevisiae*, and *Zymomonas mobilis* have been engineered for simultaneous fermentation of hexose and pentose to improve the efficacy of the overall process [11]. In this study, cellulase fermentation was carried out with *Trichoderma reesei* RUT C-30. The preparation methods of the inoculum were tested to find out the effect of pre-culture medium composition and inoculum age on cellulase production. Pretreatment of poplar wood was performed in a custom-made steam explosion device, trying to evaluate the steam explosion process for preparing poplar wood as feedstock for

---

*To whom all correspondence should be sent:
E-mail: wangyiqiang12@163.com

ethanol production. The steam-exploded poplar wood was converted to ethanol in a process termed SSCF (simultaneous saccharification and co-fermentation) using *T. reesei* cellulase and *E. coli* KO11 as genetically engineered ethanol-producing bacteria efficiently converting both hexose and pentose sugars to ethanol [12]. The SSCF process integrates the enzymatic hydrolysis of cellulose with the simultaneous fermentation of hexose and pentose to ethanol. Furthermore, scanning electron microscopy (SEM), FT-IR spectroscopy and X-ray diffraction analysis were carried out to evaluate the physical/chemical changes of poplar wood.

EXPERIMENTAL

Steam explosion pretreatment of poplar wood

Poplar wood was cut into chips of 5 cm × 3 cm × 0.2 cm. Steam explosion pretreatment was carried out in a custom-made device produced by Haian Huada Petroleum Instrument Corporation, Jiangsu Province, China. This device is mainly composed of two parts, an electrical heating high pressure steam generator and a steam explosion reactor with a working volume of 3 L. The maximum operating pressure and temperature are 10 MPa and 220°C, respectively. The steam explosion process involves first filling a vertical cylinder with poplar wood chips, and then inletting saturated steam. Maintaining the pressure at 4 MPa for 10 min, with a sharp release of pressure steam explosion pretreatment was accomplished, and the steam-exploded residue was collected and used as feedstock for ethanol production. The steam-exploded residue contained 34.4 g L^{-1} of poplar wood.

Preparation of inoculum for cellulase production

Trichoderma reesei RUT C-30 used as cellulase producer was obtained from the CCICC (China Center of Industrial Culture Collection). The culture was maintained on potato dextrose agar slants for 7 days at 28°C and then stored at 4°C. Conidia were harvested by washing the slant with 3 mL of sterile distilled water. The spore concentration in the conidial suspension was determined by counting with a blood cell counting chamber. 1 mL of spore suspension (10^7 spores mL^{-1}) was inoculated into a 250 mL Erlenmeyer flask containing 50 mL of pre-culture medium and placed on an orbital shaker at 200 rpm and 28°C for 2 days.

Cellulase production

A 5 % (v/v) inoculum concentration was used to initiate the cellulase production. Cellulase fermentation was carried out in 250 mL Erlenmeyer flasks containing 50 mL of fermentation medium at 200 rpm and 28°C for 5 days with initial pH of 4.8. The cellulase fermentation medium was composed of 12 g cellulose, 24 g bran, 10 g tryptone, 100 mL Mandels nutrient salts solution, 1 mL Mandels trace elements solution, and 50 mL 1 mol L^{-1} citrate buffer per liter [13]. The cellulase was collected from the fermentation broth by centrifugation (5000 *g*, 10 min), and concentrated by ultrafiltration.

Preparation of inoculum for ethanol fermentation

Escherichia coli KO11 was used as ethanol producer. The *Zymomonas mobilis* genes for pyruvate decarboxylase (*pdc*) and alcohol dehydrogenase II (*adh*B) were integrated into the chromosome of *E. coli* within or near the pyruvate formate-lyase gene (*plf*), so that the gene-engineered *E. coli* KO11 can efficiently convert both hexose and pentose sugars to ethanol [12]. *E. coli* KO11 was grown on plates containing solid LB medium supplemented with 20.0 g L^{-1} glucose and 0.6 g L^{-1} chloramphenicol [12], and incubated at 30°C for 24 h. Seed cultures were grown on liquid LB medium supplemented with 20.0 g L^{-1} glucose at 30°C for 24 h with agitation of 100 rpm. Cells were harvested by centrifugation (5000 *g*, 5 min) and used as an inoculum to provide an initial concentration of 33 μg/ml dry weight (about 0.1 OD_{550}).

Simultaneous saccharification and co-fermentation (SSCF)

The SSCF runs were performed in a 3 L fermentor (BioFlo 110, New Brunswick, United States) with a working volume of 2 L at 38°C with agitation of 150 rpm and pH control at 5.5. Steam-exploded poplar wood was introduced in the fermentor with cellulase loading of 20 FPIU g^{-1} substrate. The ethanol fermentation medium was composed of 27.3 g steam-exploded poplar wood, 10 g tryptone, 1 g KH_2PO_4, 0.5 g K_2HPO_4, 3 g/l $(NH_4)_2SO_4$, 0.4 g $MgCl_2 \cdot 6H_2O$ and 0.02 g $FeCl_3 \cdot 6H_2O$ per liter. A 4 mol L^{-1} KOH solution and a 6 mol L^{-1} HCl solution were used for pH control.

Analytical methods

Cellulase activity was measured as filter paper activity according to the method recommended by Ghose [14]. One international unit of cellulase activity is the amount of enzyme that forms 1 μmol glucose per min during the hydrolysis reaction. The cellulose, hemicellulose and lignin were measured using a method described previously [15]. Ethanol was determined by using gas chromatography (Clarus 500 GC, PerkinElmer, United States) with

1-propanol as internal standard, as described earlier [16]. A scanning electron microscope (JSM-6380LV, JEOL, Japan) was used to take images of treated and untreated samples at 10 kV acceleration voltage after gold coating. The FT-IR spectra were obtained on an FT-IR spectrophotometer (FTIR-8400S, Shimadzu, Japan) using a KBr disc. Infrared transmittance between 400 cm^{-1} and 4000 cm^{-1} was measured. X-ray diffraction analysis was done by X-ray powder diffractometry (D8-Advance, Bruker, Germany) to determine the crystallinity of samples. The sample was scanned in the 2θ values from 10° to 30°, and the resultant graphs were printed out using the software OriginPro 8.0, and the crystallinity index was calculated by using the software MDI JADE 5.0. Statistical analysis was performed using the software SPSS 19.0.

RESULTS AND DISCUSSION

Cellulase production by Trichoderma reesei RUT C-30

Many methods of inoculum preparation, including different carbon sources in pre-culture medium and different ages of inocula, have been reported for cellulase production [17-21]. The preparation method could be a contributory factor in improving cellulase production. In this study, nine preparation methods were selected and compared to investigate the effect on cellulase production (Table 1). With the same inoculum concentration of 5 % (v/v), cellulase production was initiated and the cellulase yield calculated by filter paper activity measured after 5 days of culture. According to the fermentation results shown in Fig.1, the composition of pre-culture medium and inoculum age have minimal or no impact on cellulase production.

From the time course of ethanol production in Fig. 2, it is seen that these remaining fermentable sugars are difficult to be converted to ethanol. The unhydrolyzed poplar wood implies that inhibitors

have formed in the steam explosion pretreatment and inhibited cellulase activity. The unutilized reducing sugars imply that the growth and activity of the ethanol-producing strain *E. coli* KO11 were
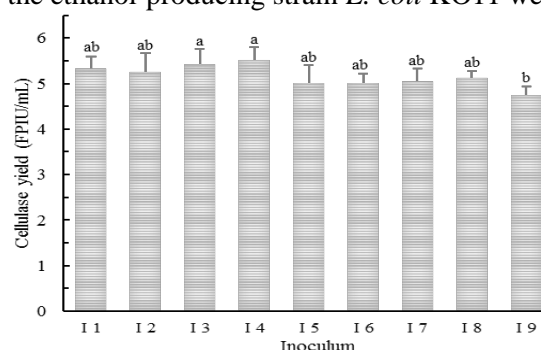

Fig. 1. Cellulase yield with different methods of inoculum preparation. Clusters followed by the same letter are not significantly different at P=0.001, according to least significant difference test.

inhibited. In this study, the ethanol yield was low, caused by the low concentration of pretreated poplar wood loaded in the fermentation medium. The steam-exploded residue with a water content as high as 96.5% was further diluted by loading the crude cellulase solution, which ultimately led to a substrate concentration of 27.3 g L^{-1}. Another cause is that inhibitors are released during the pretreatment process. So detoxification is necessary to achieve efficient fermentability of steam-exploded feedstock to ethanol.

SSCF of steam-exploded poplar wood with E. coli KO11

The SSCF of steam-exploded poplar wood was carried out with cellulase loading of 20 FPIU/g substrate (Fig. 2). The maximum ethanol yield reached 3.6 g L^{-1}, corresponding to 51.4% of the maximum theoretical yield based on glucan remaining in the input steam-exploded poplar wood. It was observed that 16.7 g L^{-1} of solid substrate and 2.7 g L^{-1} of reducing sugars remained.

Table 1. Preparation methods of inoculum of *T. reesei* RUT C-30 for cellulase production

Inoculum	Pre-culture medium composition					Culture time (days)
	Basic nutrients [a]	Glucose (g L^{-1})	Cellulose (g L^{-1})	Lactose (g L^{-1})	Tween 80 (mL L^{-1})	
I 1	√	20				2
I 2	√	20	10			2
I 3	√		7.5			4
I 4	√		10			4
I 5	√		10		0.5	4
I 6	√	30				2
I 7	√	20			0.5	2
I 8	√			30		2
I 9	Spore suspension (10^7 spores)					

[a] The basic nutrients contain 1 g L^{-1} peptone, 100 mL L^{-1} Mandels nutrient salts solution, 1 mL L^{-1} Mandels trace elements solution, and 50 mL L^{-1} 1 M citrate buffer.
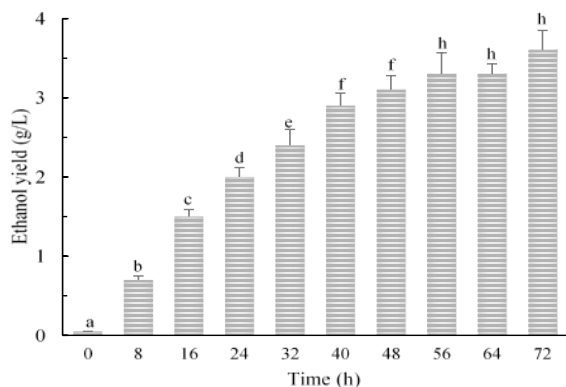
Fig. 2. Time course of ethanol production from steam-exploded poplar wood. Clusters followed by the same letter are not significantly different at P=0.001, according to least significant difference test

Compositional analysis

The compositional changes of the poplar wood during the steam explosion pretreatment and SSCF are presented in Table 2. In the steam explosion pretreatment process, 16.3% of the dry weight of poplar wood were lost, including 66.8% of hemicellulose and 5.3% of cellulose. During the SSCF process, 62.2% of cellulose and 76.2% of hemicellulose were hydrolyzed and utilized. From this analysis results, no significant changes in lignin content were observed. The high-pressure steam chemically modified lignin structure improved the accessibility of cellulose to hydrolytic enzymes [4]. Due to condensation and re-polymerization reactions, the lignin content remained almost unchanged during steam explosion pretreatment [4, 22].

Scanning electron microscopy analysis

Poplar wood samples were observed using SEM to establish what occurred to the physical structure of poplar wood after steam explosion and enzymatic hydrolysis.

Fig. 3 (b) clearly presents that unorganized and loose structure of the poplar wood fiber bundles was generated by the steam explosion compared to the untreated one shown in Fig. 3 (a). The picture of residual solids after enzymatic hydrolysis in the SSCF process (Fig. 3 (c)) suggests that steam explosion pretreatment significantly improved the biodigestibility of poplar wood. The irregular fiber bundles (Fig. 3 (b)) were hydrolyzed into small fragments (Fig. 3 (c)). It can be speculated that the improvement in biodigestibility by steam explosion pretreatment was due to the modification of the compact structure of cellulose and lignin and the increase in the accessible surface area.

Fig. 4 presents the FT-IR spectra of raw poplar wood, steam-exploded poplar wood and fermentation residue. The sharp peak at 1736 cm^{-1} in the spectrum of raw poplar represents the carboxyl groups, which are the main constituents of hemicellulose [23]. As shown in Fig. 4, this characteristic hemicellulose peak almost disappeared in the pretreatment process, which is consistent with the compositional analysis result that steam explosion pretreatment has led to the hydrolysis of the major part of the hemicellulose. The changes observed in the peak at 898 cm^{-1} are due to absorption of cellulose [24]. The decrease in intensity of this characteristic peak indicates the hydrolysis of cellulose during pretreatment and fermentation processes.

X-ray diffraction analysis

The poplar wood samples were analyzed by X-ray diffraction to characterize their crystallinity and the diffraction patterns are shown in Fig. 5. The diffraction peaks at 2θ angles of 16.5° and 22.5° correspond to crystalline cellulose [25]. These two characteristic peaks markedly weakened.
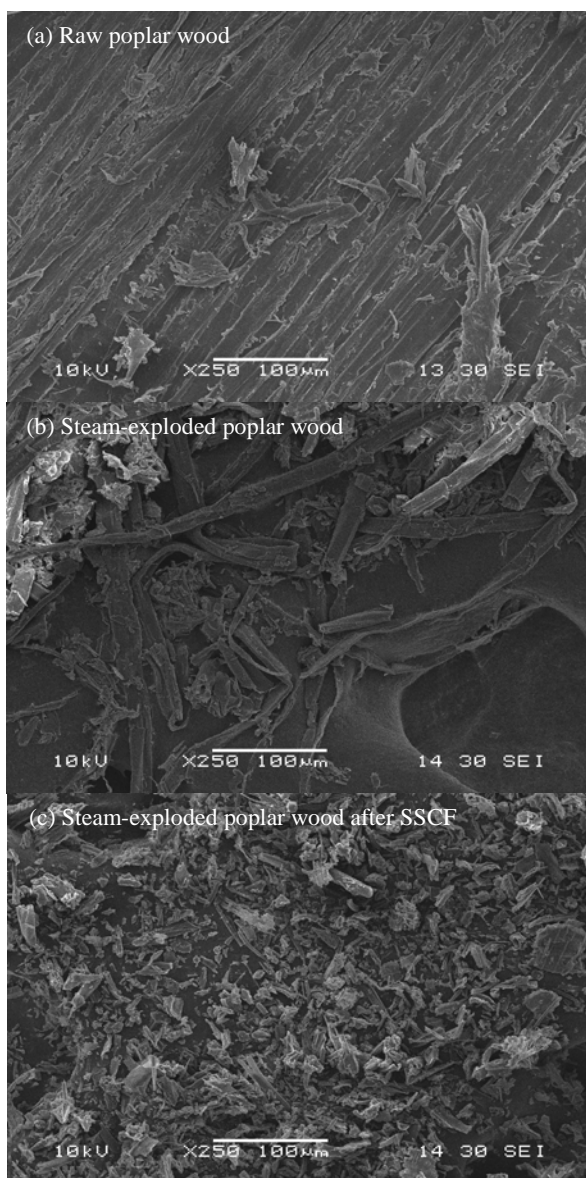
Table 2. Composition of poplar wood samples

	Dry weight loss (%)	Cellulose (%)	Hemicellulose (%)	Lignin and ash (%)	Cellulose removal (%)	Hemicellulose removal (%)
Raw poplar wood	0	45.0±3.7 A [a]	22.3±1.6 A	20.5±1.4 A	0	0
Pretreated poplar wood	16.3±0.7 A	42.6±3.9 B [b]	7.4±0.6 B	20.4±0.8 A	5.3±0.8 A	66.8±6.4 A
Pretreated poplar wood after SSCF	48.2±5.1 B	17.0±2.3 C	5.3±0.6 C	19.4±1.3 A	62.2±6.8 B	76.2±4.7 B

[a] Values are expressed as mean±SEM (n=3). Values in the same column followed by different capital letters are significantly different at P=0.05, according to least significant difference test. [b] The data in the rows are based on the oven dry untreated poplar wood. For example, 42.6 doesn't mean that the oven dry solid residue contains 42.6% cellulose, but infers that the residue (84.7% of untreated biomass) contains 50.3% cellulose.

Fig. 3. SEM pictures of poplar wood samples.

SSCF of steam-exploded poplar wood with E. coli KO11
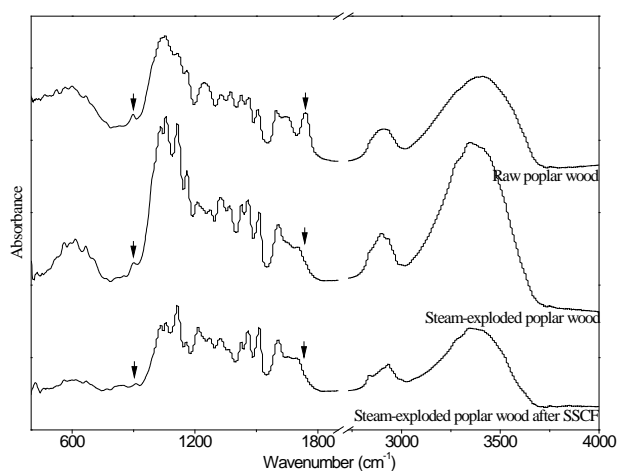

Fig. 4. FT-IR spectra of poplar wood samples.

The steam-exploded poplar wood had a decreased relative crystallinity index due to the

phase change in the crystal structure from cellulose I to cellulose III [26-27]. With the degradation of cellulose by cellulase enzymes in the SSCF process, the relative crystallinity further decreased. These results are consistent with the observations from compositional analysis and FT-IR spectroscopy analysis.
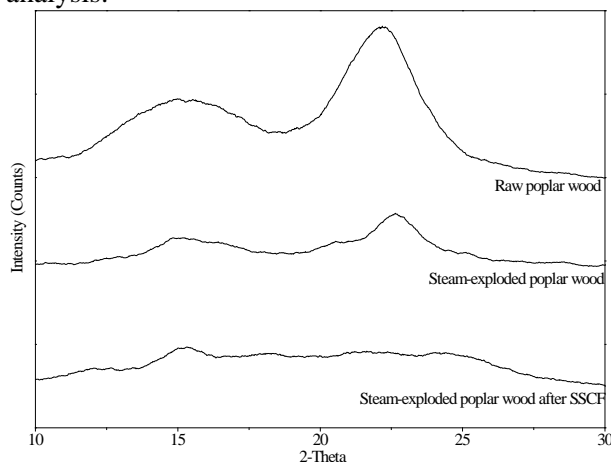

Fig. 5. X-ray diffraction intensity curves of poplar wood samples.

CONCLUSION

Steam explosion is shown to be a practicable method for quickly and efficiently pretreating poplar wood for ethanol production. By steam-explosion at 4 MPa for 10 min, 66.8% of hemicellulose and 5.3% of cellulose were hydrolyzed. Using the steam-exploded poplar wood as feedstock with cellulase loading of 20 FPIU g^{-1} substrate, ethanol yield reached 3.6 g L^{-1}, corresponding to 51.4% of the maximum theoretical yield based on glucan remaining in the input substrate. The ethanol yield was limited by the low solid content of steam-exploded residue, and inhibited by the inhibitors released in the pretreatment process. So the steam explosion process needs to be improved for lower water content and less inhibitors, and detoxification is necessary to achieve a good fermentability of pretreated poplar wood to ethanol.

REFERENCES

1. H. L. Chum, E. Warner, J. E. A. Seabra, I. C. Macedo, *Biofuel. Bioprod. Bior.*, **8**, 205 (2014).
2. J. S. Kim, Y. Lee, T. H. Kim, *Bioresour. Technol.*, 199, **42** (2016).
3. R. C. Kuhad, D. Deswal, S. Sharma, A. Bhattacharya, K. K. Jain, A. Kaur, B. I. Pletschke, A. Singh, M. Karp, *Renew. Sust. Energ. Rev.*, **55**, 249 (2016).
4. L. P. Ramos, *Quim. Nova*, **26**, 863 (2003).
5. T. Auxenfans, D. Crônier, B. Chabbert, G. Paës, *Biotechnol. Biofuel.*, **10**, 36 (2017).
6. A. Amore, O. Pepe, V. Ventorino, L. Birolo, C. Giangrande, V. Faraco, *FEMS Microbiol. Lett.*, **339**, 93 (2013).
7. T. R. Dutra, V. M. Guimarães, E. M. Varela, L. da Silva Fialho, A. M. F. Milagres, D. L. Falkoski, J. C. Zanuncio, S. T. de Rezende, *Sci. Rep.*, **7**, 3893, (2017).
8. G. Liu, J. Zhang, J. Bao, *Bioproc. Biosyst. Eng.*, **39**, 133 (2016).
9. D. Cannella, H. Jørgensen, *Biotechnol. Bioeng.*, **111**, 59 (2014).
10. J. H. Kim, D. E. Block, D. A. Mills, *Appl. Microbiol. Biotechnol.*, **88**, 1077 (2010).
11. M. W. Lau, C. Gunawan, V. Balan, B. E. Dale, *Biotechnol. Biofuel.*, **3**, 1 (2010).
12. K. Ohta, D. Beall, J. Mejia, K. Shanmugam, L. Ingram, *Appl. Environ. Microbiol.*, **57**, 893 (1991).
13. H. Fang, C. Zhao, X. Y. Song, *Bioresour. Technol.*, **101**, 4111 (2010).
14. T. Ghose, *Pure Appl. Chem.*, **59**, 257 (1987).
15. P. v. Van Soest, J. Robertson, B. Lewis, *J. Dairy Sci.*, **74**, 3583 (1991).
16. B. B. Deng, H. Q. Fang, C. Xue, H. L. Zhao, Z. M. Liu, *Ind. Microbiol.*, **2**, 8 (2001).
17. N. Szijarto, Z. Faigl, K. Reczey, M. Mezes, A. Bersenyi, *Ind. Crop. Prod.*, **20**, 49 (2004).
18. H. Fang, L. Xia, *Fuel*, **143**, 211 (2015).
19. L. Olsson, T. M. I. E. Christensen, K. P. Hansen, E. A. Palmqvist, *Enzyme Microb. Tech.*, **33**, 612 (2003).
20. A. Ahamed, P. Vermette, *Biochem. Eng. J.*, **40**, 399 (2008).
21. F. C. Domingues, J. A. Queiroz, J. M. S. Cabral, L. P. Fonseca, *Enzyme Microb. Tech.*, **26**, 394 (2000).
22. A. K. Biswas, K. Umeki, W. Yang, W. Blasiak, *Fuel Process. Technol.*, **92**, 1849 (2011).
23. C. U. Maheswari, K. O. Reddy, E. Muzenda, B. Guduri, A. V. Rajulu, *Biomass Bioenerg.*, **46**, 555 (2012).
24. M. Rosa, E. Medeiros, J. Malmonge, K. Gregorski, D. Wood, L. Mattoso, G. Glenn, W. Orts, S. Imam, *Carbohydr. Polym.*, **81**, 83 (2010).
25. U. T. M. Sampath, Y. C. Ching, C. H. Chuah, R. Singh, P. C. Lin, *Cellulose*, **24**, 2215 (2017).
26. C. Zhao, W. Ding, F. Chen, C. Cheng, Q. Shao, *Bioresour. Technol.*, **155**, 349 (2014).
27. Y. Horikawa, N. Konakahara, T. Imai, A. Kentaro, Y. Kobayashi, J. Sugiyama, *Polym. Degradation Stab.*, **98**, 2351 (2013).

Hydraulic design and numerical investigation of twin-screw hydraulic turbine for high pressure power recovery

Q. Li[1], S. H. Liu[2], X. P. Jiang[3]*, L. Zhou[3]*, W. Li[3]

[1] *School of Environment and Safety Engineering, Jiangsu University, Zhenjiang, China*
[2] *The Institute of Seawater Desalination and Multipurpose Utilization, SOA, Tianjin, China*
[3] *National Research Center of Pumps, Jiangsu University, Zhenjiang, China*

As a novel type of energy recovery device based on the reverse operation principle of screw pump, the twin-screw turbines (TSHT) are widely used in high-efficiency sea water reverse osmosis systems. It is important to investigate the performance and internal flow patterns of TSHT. The research presents the hydraulic design of TSHT and analyzes the general characteristics of the internal flow field and the efficiency performance by numerical simulation and experimental methods. In order to solve the Navier-Stokes equations for three-dimensional unsteady flow, dynamic mesh technique was used in the commercial Computational Fluid Dynamics (CFD) software. Pressure distribution and velocity distribution, as well as efficiency performance of the flow field were studied by the numerical simulation method which was validated by the prototype experiment. The twin-screw hydraulic turbine (TSHT) can be widely used in sea water reverse osmosis systems for power recovery due to its stable performance.

Key words: Twin-screw turbines, Hydraulic design, CFD, Numerical simulation, Energy recovery

INTRODUCTION

The twin-screw hydraulic turbine (TSHT) is a novel type of energy recovery device based on the reverse operation principle of a screw pump. It can be widely used in petrochemical, electric power, metallurgy, environmental protection, ammonia synthesis, seawater desalination and other industrial processes. The recycling of pressure energy from the high-pressure wastewater in these processes can help reduce carbon emissions and environmental pollution [1-8].

At present, the research on hydraulic turbine is mainly concentrated on the reverse operation of the centrifugal pump used as a hydraulic turbine. Barbarelli *et al.* [9] used a predictive model to predict the performance of the centrifugal pumps used as turbines by a theoretical computation method. Sanjay *et al.* [10] carried out experimental investigations to improve the performance of the pumps as turbines by optimizing its geometric and operational parameters. Yang *et al.* [11,12] predicted the performance of the single-stage centrifugal pumps as turbines based on theories, simulations and experiments, and studied the influence of blade wrap angle and blade inlet angle on the centrifugal pump. Zhu *et al.* [13] also proposed an optimal design method to ensure high efficiency and steady operation of the pump-turbine runner. Despite the research on hydraulic turbines has attained many achievements, most of the pumps

as turbines are not suitable for the small flow rate, high head water and even ultrahigh head water inlet working conditions, except the multistage pump as turbine being able to run under conditions of high inlet pressure but with low efficiency [14,15].

For the screw-type energy recovery device, Tang *et al.* [16] have theoretically and experimentally studied the performance of a twin-screw expander. Kovacevic *et al.* [17] have used the numerical simulation method to study the combined screw compressor-expander machines for use in high pressure refrigeration systems. Papes *et al.* [18] have studied the flow inside a screw expander, which will help in optimization of the screw expander's performance by CFD calculations. In the field of single screw mechanical energy recovery, Waters [19] has put forward the use of Archimedes spiral pump as a turbine. Rohmer *et al.* [20] have analyzed the performance of this model by means of modeling design and experiment. In addition, Xia *et al.* [21] have investigated the performance of a single-screw expander of different inlet vapor dryness, but there are no reports on twin-screw pumps used as turbines.

Twin-screw hydraulic turbine (TSHT) has the advantages of stable medium transport, weak pressure pulsation, low mechanical vibration and noise, simple and compact structure, as well as long serving period. Most importantly, TSHT could handle a gas-liquid two-phase flow. As a volumetric liquid turbine, the efficiency is still an important indicator of its performance. The decrease in efficiency is mainly influenced by the

---

*To whom all correspondence should be sent:
E-mail: jxp2502@163.com

combination of various gaps in its structure. In this paper, the influence of the general characteristics of the internal flow field and the effect of the leakage on the efficiency of the internal flow field are analyzed by the CFD numerical simulation method.

MATERIALS AND METHODS

Hydraulic design

Twin-screw hydraulic turbine (TSHT) is based on the inverse operation principle of the twin-screw pump. Compared with other pumps as turbines (PAT), TSHT has a relatively compact structure. The entire turbine is split into inlet cavity and outlet cavity by two screws, as shown in Fig. 1. When the working medium flows from the inlet to the inlet cavity, the pressure inside the cavity would continue to rise. Then the working medium flows into the front bushing hole acting on the helicoid surfaces of screws under the inlet cavity pressure. After that, the medium flows through the back bushing hole and outlet cavity and finally flows out of the outlet. The differential pressure in the adjacent screw seal chamber produces a rotational torque to drive the twin screws. The sum of the torques of the main-follower screws can be transmitted by main screws to drive a generator or a power machinery connected with actuator shaft, thus conversing the fluid pressure energy to electricity or mechanical energy and achieving the purpose of energy recovery.

The transmission of the main-follower screws relies on a pair of meshing gears with the same transmission ratio for avoidance of the screw locking caused by small lead. Since the main screw bears the most torque and axial force in most cases, it is used as the actuator shaft. The main screw is also provided with a pair of positioning plates to ensure that it will not cause axial displacement under the action of axial force produced by medium pressure, thus playing a role of positioning and thrusting. The screw profile of type A can in theory divide the inlet cavity and outlet cavity into two connected parts, so as to greatly improve the volumetric efficiency of TSHT. Furthermore, the whole device has the advantages of simple structure and easy processing. The tooth curves of type A twin screw pumps contain four types of basic curves. They are arc, prolate epicycloid, involute, and curtate epicycloid, as shown in Fig. 2 and Table 1. The main size parameters on the main and follower screws are summarized in Table 2.
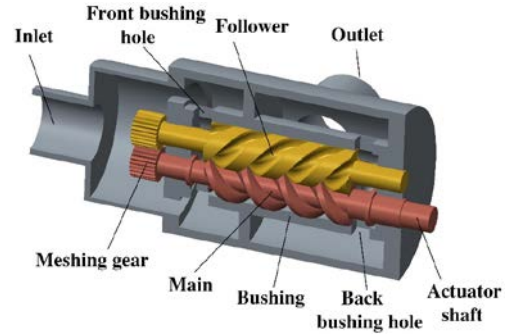

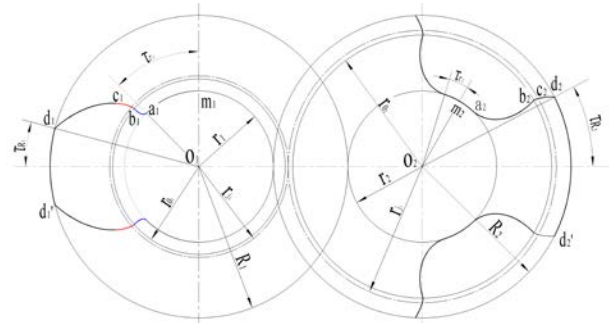**Fig. 1.** Structure of the twin-screw hydraulic turbine

Fig. 2. Tooth curves and basic dimension parameters

Table 1. Geometrical characteristics

Tooth profile curves	Main screw	Tooth profile curves	Follower screw
m_1a_1	Arc (radius=r_1)	m_2a_2	Arc (radius=r_2)
a_1b_1	Prolate epicycloid	a_2b_2	Prolate epicycloid
b_1c_1	Involute	b_2c_2	Involute
c_1d_1	Curtate epicycloid	c_2d_2	Curtate epicycloid
d_1d_1'	Arc (radius=R_1)	d_2d_2'	Arc (radius=R_2)

Table 2. Main size parameters of the main and follower screw

Parameter	Main screw		Follower screw	
	Symbol	Value	Symbol	Value
Gear number	n_1	2	n_2	3
Radius of addendum circle	R_1	31mm	R_2	31mm
Rated axial distance of screws	C	46.5mm	/	/
Meshing angle of involute	α	15°	α	15°
Central angle of addendum circle	τ_{R1}	14.7°	τ_{R2}	30°
Central angle of dedendum circle	τ_{r1}	45°	τ_{r2}	9.8°
Radius of pitch circle	r_{j1}	18.6mm	r_{j2}	27.9mm
Radius of base circle	r_{o1}	17.97mm	r_{o2}	26.95mm
Radius of dedendum circle	r_1	15.5mm	r_2	15.5mm
Coefficient of addendum height	H_1	2/3	H_2	1/9

Calculation domain and meshes

The calculation domain used in this paper is shown in Fig. 3. It is totally based on a real model. The interface is set between the fluid domain of inlet cavity and the fluid domain of screw. The CAD models of inlet and outlet fluid domain are imported into Pumplinx for generation of a cartesian grid. The dynamic mesh technique is used to simulate the flow field changing with time due to the boundary motion.
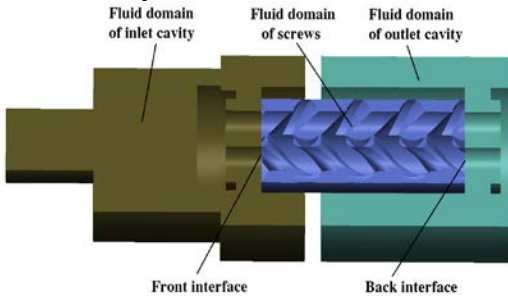

Fig. 3. Calculation domain and interfaces

The mesh of screw fluid domain can keep overall transformation as time step increases, which can be interpreted as a type of re-meshing of overall mesh. However, this type of re-meshing has no restriction on the initial mesh. In the process of pretreatment, a rotation period is divided into several meshing states, with each meshing state corresponding to a fluid domain model in each time step. Fig. 4 presents the overall mesh of the screws fluid domain and the mesh on screw surface.
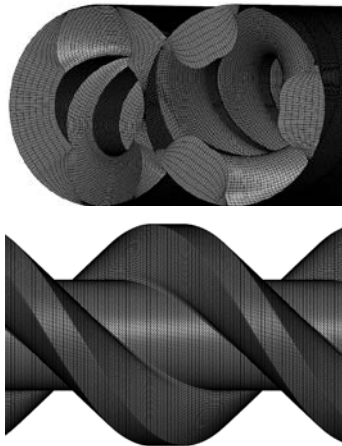

Fig. 4. **Mesh on screw domain and screws surface**

Grid sensitivity analysis

The number of radial grid tiers is one of the important factors that affect the total number of grids and the grid sensitivity. It can significantly affect the value of Y+ and directly relate to the first tier of the grid nodes near the boundary set in the region where the turbulence is fully developed, thus having an impact on simulation. The influence of different radial grid tiers on the simulation results in

the fluid domain of screw is studied as shown in Fig. 5. The TSHT with 4-7 radial grid tiers is numerically simulated. The torque, flow rate, and efficiency under the simulated conditions of 1.0MPa inlet pressure, 0.02MPa outlet pressure and the Y+ variation range of the whole flow field under the simulated condition of 0.2-1.0MPa inlet pressure are shown in Table 3.
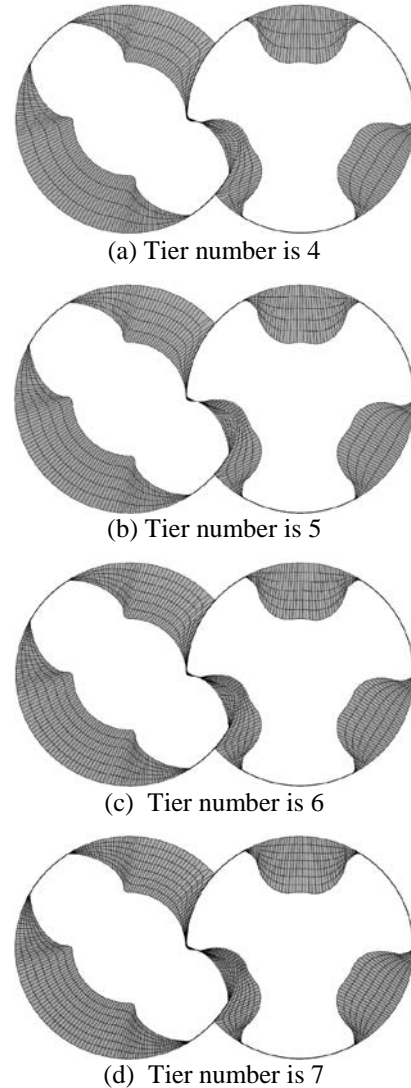

(a) Tier number is 4

(b) Tier number is 5

(c) Tier number is 6

(d) Tier number is 7

Fig. 5. Different tier numbers in radial direction

As shown in Table 3, the torque, flow rate and efficiency do not change significantly as the number of grid tiers increases, which indicates that the influence of the number of grid tiers on the above parameters can be ignored. But considering the rationality of the first tier grid nodes, when radial grid has a tier of 7, the value of Y+ is more reasonable thus making the simulation results more credible. Therefore, the number of radial grid tiers in the screw fluid domain was set to 7.

Table 3. Grid sensitively with different number of tiers

Number of tiers	Torque (N·m)	Flow rate (m³/h)	Efficiency (%)	Y^+
4	24.129	13.527	59.55	74.0~154.8
5	24.141	13.522	59.60	65.7~131.9
6	24.133	13.525	59.57	49.2~108.4
7	24.135	13.528	59.56	35.1~68.5

Turbulence model and boundary

In consideration of the specific conditions of the fluid flow and the flow field characteristics of TSHT, the following assumptions are used: (a) the fluid is incompressible, (b) the flow field is stable and isothermal, (c) the inertia force, and gravity are negligible, (d) the fluid is completely filled in the volume, and (c) the turbine is working at a stable rotating speed.

The flow through the model pump was simulated with the commercial code Pumplinx, which employs the finite volume method to solve the Reynolds averaged Navier-Stokes equations for the 3D incompressible unsteady flow. The CFD flow domain was divided into two types of subdomains. The outlet section belongs to the first type of subdomain, and the equations for this type of region are solved in a stationary framework. The second type of subdomain is the screw passage that simulates the rotating process of the screws by the dynamic mesh technique. The rotational speed was set to 900r/min according to the experimental value. The interfaces were formed between different subdomains. The boundary conditions were set to pressure inlet and pressure outlet by considering the coupling fluctuation with the flow rate. The inlet pressure ranged from 0.2 to 1.8MPa at an interval of 0.2MPa, and the outlet pressure was set to 0.02MPa, approximating the actual conditions.

RESULTS AND DISCUSSION

Experimental validation

The TSHT model used in this paper was established and tested. A high pressure energy recovery test rig was designed and established in the National Research Center of Pumps, China. The schematic arrangement of the test rig facility and test equipment are shown in Figs. 6 and 7, which have the identification from the technology department in Jiangsu province of China.

This test rig was based on an open-type system. A booster pump was driven by a motor with variable-frequency drive (VFD) to adjust the inlet pressure of different values. Pressure sensors were set in both the inlet and outlet of TSHT. A torque-speed sensor was installed on the output shaft to

measure the torque and rotation speed. The combination of generator and electrical load was used to consume the power generated by the turbine, and the rotating speed could be controlled by adjusting the electrical load that was placed in a circuit of the generator. In the experiment, both the flow meter and the torque-speed sensor had a precision of 0.5% FS, and the pressure had a precision of 0.1% FS. All sensors and instruments had electrical output signal of 4-20mA. PLC was used in this test rig to achieve automatic control, as illustrated in Figs. 6 and 7 presenting the test rig, including the connection of turbine, torque-speed sensor and generator.
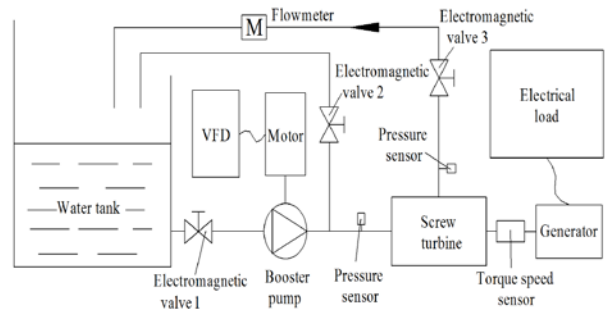

**Fig. 6.** System diagram of the test rig

Fig. 7. Shaft power load and dissipation module

Fig. 8 presents the comparison between simulation and experimental results. The flow rate and the efficiency obtained by the experiment had the similar varying tendency with that obtained by numerical simulation. However, as the pressure rose, the error between experiment and simulation had an obvious increasing trend. The changing trends were basically the same, indicating that the simulation was consistent with the actual condition. The main reason for the increasing error is that as the inlet pressure rose, the axial force actcng on the screws increased, thus leading to the rise of mechanical losses in the location of bearings, which cannot be predicted by the simulation method in this study. Overall, there was a good agreement between the experiment and simulation results, which could further prove the accuracy of the numerical methods used.
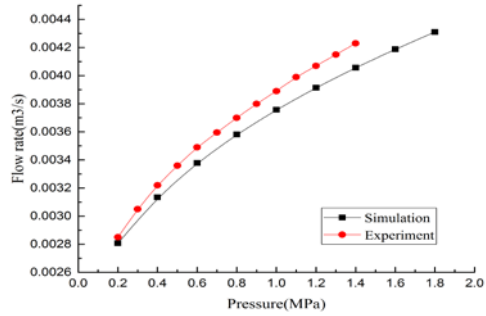
(a) Flow rate
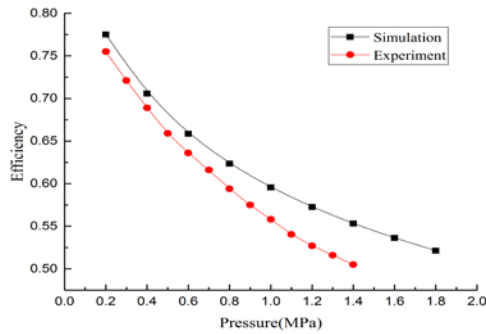
(b) Efficiency

Fig. 8. Comparison of flow rate and efficiency between simulation and experiment

Numerical analysis

In this paper, a CFD numerical simulation analysis was carried out to illustrate the common characteristics of the TSHT under the working conditions of 1.0MPa inlet pressure and 0.02MPa outlet pressure.

The screw surface pressure distribution at a rotating speed of 900r/min is shown in Fig. 9. The inlet cavity and outlet cavity maintained the high and low pressure distribution, respectively. The screw was divided into 5 sealing chambers with different pressure levels in its effective length under the influence of meshing curve sealing function and the third sealing rule. The inlet side of the screw had the highest pressure and the outlet side had the lowest pressure. The distribution of the meshing curve can be clearly seen from the pressure cloud diagram, and it had the same distribution characteristics as the pressure level boundary of the different sealing chambers. The sealing chambers at the same pressure level were connected under the current meshing condition. In addition, near the meshing curve there would be low pressure area or even negative pressure area relative to the sealing chamber on both sides of the meshing curve. The reason for this is that the medium in leakage clearance near the meshing curve has a higher leakage flow rate. Based on the principle of energy conservation, the pressure will be relatively lower.

Fig. 10 shows the velocity distribution of TSHT. First of all, for twin screws in a meshing state, the screw dedendum circle surface relative to the outer spiral tooth surface and addendum circle surface have a relatively low surface velocity distribution, especially for follower screw with a lower dedendum surface velocity. From the velocity vector diagram sectioned along the screw middle section we can see that the working medium that flows in or out of the screw fluid domain through the bushing hole maintains a relatively low flow velocity (kinetic energy). The flow velocity of the medium keeps rising as it gradually flows into the screw seal chamber till acting on the screw spiral surface. Then some of the medium flows into the radial clearance and produces jet-flow of higher velocity. Jet-flow in the first radial clearance from the inlet side of screw is not very obvious. While from the second radial clearance it maintains the basic characteristics of a high-speed jet-flow.

The flow velocity distribution in the central section of the screws is shown in Fig. 11, where the left is the inlet side of the screw and the right is the outlet side. It can be clearly seen that the leakage flow rate in the flank clearance has several rules of changing: high-speed flow occurs in the minimum flank clearance, and as the flow area in the clearance is reduced, the velocity has a trend of rapid rising. The site with the minimum flank clearance is the place where the meshing point is located. And because of the sealing effect of the meshing line, the two sides of the meshing point show different levels of pressure.
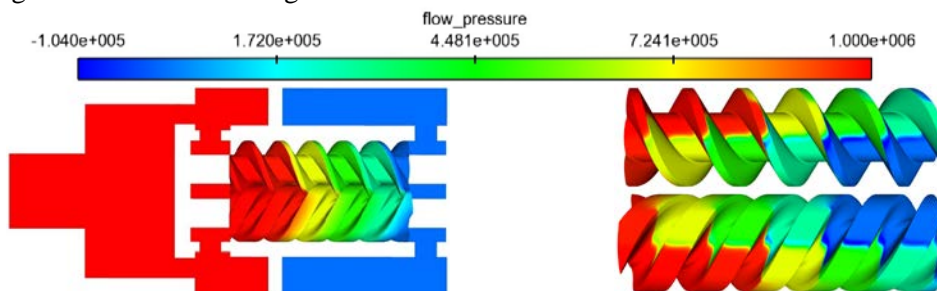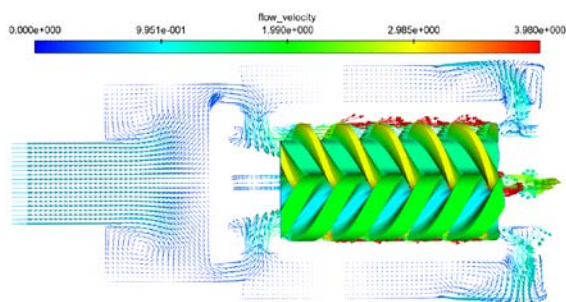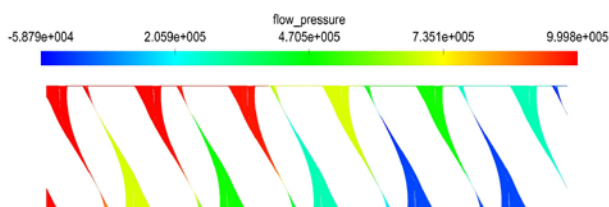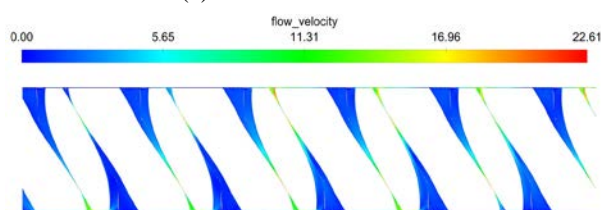

Fig. 9. Pressure distribution

Fig. 10. Velocity distribution diagram

(a) Pressure distribution

(b) Velocity distribution

Fig. 11. Gear side clearance leakage pressure and velocity distribution

CONCLUSIONS

(1) The adjacent screw teeth form a multistage seal cavity. Each stage seal cavity divided by meshing curve has different pressure levels while the sealing chambers in a connected state without the sealing action of meshing curve have the same pressure level. The pressure near the inlet of the sealing cavity is the highest one while the pressure near the outlet is the lowest one; the distribution of the meshing curve and the demarcation line of different pressure levels have the same distribution characteristics. In addition, in the leakage clearance near the meshing curve, low pressure area, or even the negative pressure area will appear relative to the sealing cavity on both sides of the meshing curve. This is the result of the transformation of pressure energy into kinetic energy.

(2) The twin-screw dedendum circle surface in a meshing state has a relatively low surface velocity distribution and the flow velocity gradually increases as the medium gradually enters the screw sealing cavity until it acts on the screw spiral surface. Due to the pressure difference between the adjacent sealing cavities, some medium will enter the radial clearance and produce a jet-flow with higher velocity. The inlet and outlet of the radial clearance have a certain length of convergence and jet segments. The velocity of flow shows a sharp rising trend with the decrease of flank clearance.

The interlobe clearance has a higher leakage velocity.

REFERENCES

1. W. Liu, L. Henrik, V.M. Brianet, X. Zhang, *Applied Energy*, **88**, 518 (2011).
2. L. Francis, *Energy Policy*, **35**, 2187 (2007).
3. X.H. Wang, J.H. Yang, F.X. Shi, *Journal of Drainage and Irrigation Machinery Engineering,* **09**, 742 (2014).
4. H.L. Huang, Z. Yan, *Renewable and Sustainable Energy Reviews*, **13**, 1652 (2009).
5. Varun, R. Prakash, I.K. Bhat, *Renewable and Sustainable Energy Reviews,* **13**, 2716 (2009).
6. B. Orchard, S. Klos, *World Pumps*, **8**, 22 (2009).
7. L. Yao, B. Liu, Z.X. Wu, *Nuclear Engineering and Design,* **237**, 1468 (2007).
8. W.A. Raja, R.W. Piazza, *Desalination*, **38**, 123 (1981).
9. S. Barbarelli, M. Amelio, G. Florio, *Energy*, **107**, 103(2016).
10. V. J. Sanjay, S. Abhishek, H. M. Karan, N. P. Rajesh, *Energy Conversion and Management*, **89**, 808 (2015).
11. S. S. Yang, D. Shahram, F. Y. Kong, *Renewable Energy,* **48**, 507 (2012).
12. S. S. Yang, F. Y. Kong, H. Chen, X. H. Su, *ASME Journal of Fluids Engineering*, **134**, 061102 (2012).
13. B.S. Zhu, X.H. Wang, L. Tan, D.Y. Zhou, Y. Zhao, S.L. Cao, *Renewable Energy*, **81**, 366 (2015).
14. P. Francesco, D.P. Francesco, F. Nicola, G. Maurizio, M. Gustavo, *Renewable Energy*, **99**, 180 (2016).
15. Z.G. Zuo, S.H. Liu, Y.K. Sun, Y.L. Wu, *Renewable and Sustainable Energy Reviews*, **41**, 965 (2015).
16. H. Tang, H.G. Wu, X.L. Wang, Z.W. Xing, *Energy*, **90**, 631 (2015).
17. *K. Ahmed, S. Nikola, I.K. Smith, Simulation Modelling Practice and Theory*, **14**, 1143 (2006).
18. I. Papes, J. Degroote, J. Vierendeels, *Applied Thermal Engineering*, **91**, 535 (2015).
19. S. Waters, G.A. Aggidis, *Renewable and Sustainable Energy Reviews,* **51**, 497 (2015).
20. J. Rohmer, D. Knittel, G. Sturtzer, D. Flieller, J. Renaud, *Renewable Energy*, **94**, 136 (2016).
21. G. D. Xia, Y. Q. Zhang, Y. T. Wu, C. F. Ma, W. N. Ji, S. W. Liu, H. Guo. *Applied Thermal Engineering*, **87**, 34 (2015).

Effect of environmental regulation on the manufacturing FDI in China: spatial econometric studies

W.H. Li[1*], C. Li[1], W.Ch. Huang[2], C.J. Dong[1]

[1]School of Economics and Management, Harbin Engineering University, Harbin, Heilongjiang, China
[2]Department of Economics, Western Michigan University, Kalamazoo, MI, USA

Previous studies on the relationship between foreign direct investment (FDI) and environmental regulation have generally not considered the spatial characteristics. This paper applies spatial econometrics to explore whether or not environmental regulation inhibits the inflow of manufacturing FDI to China. Using a dataset across China's 29 provinces over the period from 2010 to 2015, we examined the spatial autocorrelation pattern about manufacturing FDI. We then used an improved spatial econometric model to explore the effect of environmental regulation on manufacturing FDI, incorporating other determinants of FDI, including the level of economic development, the degree of industrialization and the manufacturing labor cost. Our study reveals that manufacturing FDI exhibits clear spatial autocorrelation and regional agglomeration characteristics. Furthermore, the inhibitory effect of environmental regulation on manufacturing FDI inflow is gradually increasing with the passage of two stages, which confirms the "pollution shelter" hypothesis in China. We also find positive effects of the level of economic development and the industrialization degree on the manufacturing FDI inflow while, as expected, the manufacturing labor cost is found to be negatively correlated with FDI inflow.

Keywords: Environmental regulation, FDI, Spatial econometric models

INTRODUCTION

Foreign direct investment (FDI) is no doubt one of the important contributing factors to China's rapid economic growth. Attracted by the traditional comparative advantages of the Chinese economy, a staggering amount of foreign capital has continuously flowed to China's manufacturing sector each year. However, while China's manufacturing sector has been benefitted from tremendous infusion of FDI, the inflows of foreign capital also transferred pollution manufacturing into China, which has profound negative impact on China's ecological environment [1].

In the 1980s, China didn't impose essential environmental regulation measures to FDI. Consequently, the so-called "bottom competition" phenomenon in capital attraction resulted in increasingly serious environmental pollution. To prevent the environment from further worsening, Chinese central government and local governments have issued a series of environmental regulations since the 1990s, including raising the access threshold of FDI to manufacturing, closing down heavy polluting enterprises and reducing pollution sources. Meanwhile, heated debates and serious questions have been raised among researchers and policy makers regarding the issues surrounding environmental regulation and FDI, such as, whether

or not the regional environmental regulation inhibits manufacturing FDI? Does the effect of environmental regulation on FDI exhibit regional differences?

In general, there are three views concerning the above questions. The first view states that environmental regulation has a negative effect on the inflow of manufacturing FDI [2-4]. The second view is that strict environmental regulation may not preclude the inflow of FDI or lead to regional industrial reset phenomenon, but could actually promote more inflow of FDI [5, 6]. The third middle-of-the-road view holds that the impact of environmental regulation on FDI inflows to various regions is uncertain [7, 8].

Despite the divergent views in the existing literatures concerning the effect of environmental regulation on FDI, we can still draw two common implications. First, environmental regulation can serve as a useful "filter" to screen out the "dirty" foreign capital, thereby improving the quality of FDI. So it is necessary to explore more deeply the broader statistical relationships among environmental regulation and FDI, as well as other determinants of FDI across regions and over years. Second, some spatial features that differ across regions may cause environmental regulations to exert different impacts on FDI. So it is necessary and more realistic to consider relevant spatial heterogeneity when exploring these variables' interrelationships [9]. Therefore, we apply a spatial

econometric model to examine whether or not environmental regulation inhibits the manufacturing FDI inflow to China, hoping to provide more insights to the issues related to environmental regulation and foreign investments, and contribute to the literature in this field.

EXPERIMENTAL

Methods for spatial autocorrelation

We began our research by conducting spatial autocorrelation tests of manufacturing FDI. Spatial autocorrelation can be analyzed by two different methods: global spatial autocorrelation and local spatial association-LISA [10].

Global spatial autocorrelation is most extensively measured by Moran's I, which is defined as [11]:

$$I = \frac{\sum_{i=1}^{n}\sum_{j=1}^{n} W_{ij}(Y_i - \overline{Y})(Y_j - \overline{Y})}{S^2 \sum_{i=1}^{n}\sum_{j=1}^{n} W_{ij}} \quad (i \neq j) \tag{1}$$

where, $S^2 = \frac{1}{n}\sum_i (Y_i - \overline{Y})^2$, $\overline{Y} = \frac{1}{n}\sum_{i=1}^{n} Y_i$, W_{ij} is a matrix of spatial weights with zeroes on the diagonal terms, Y_i are the observed values of unit i, and n is the number of spatial units. Possible values of Moran's I range between 1 and -1. A Moran's I with value approaching 1 represents a situation in which similar values are clustered together, and a value near -1 represents a situation in which similar values repel one another [12].

The method outlined above provides summaries of global spatial pattern. However, there have been various adaptations to the standard approaches to allow assessment of local variation in spatial autocorrelation. Anselin defined a body of local indicators of spatial association (LISA) [9]. This study used Moran scatter plots (often mapped by Geoda based on each local Moran's I) and LISA cluster maps as indicators of the local spatial association. Local Moran's I is given as:

$$I_i = \frac{(Y_i - \overline{Y})}{S^2}\sum_{j=1}^{n}[W_{ij}(Y_j - \overline{Y})] \tag{2}$$

where $I_i > 0$ indicates that unit i and its neighbors have strong positive spatial autocorrelation and agglomeration, while $I_i < 0$ indicates that they have a negative correlation and discretization.

Protocols of estimating a spatial econometric model

In the standard linear regression model, spatial dependence can be incorporated in two alternative ways: the spatial lag model (SLM) and the spatial error model (SEM) [13].

Spatial lag model (SLM) is employed when there is a reason to postulate a direct effect on the dependent variable from neighboring locations [14]. SLM is expressed as:

$$Y = \rho WY + X\beta + \varepsilon, \quad \varepsilon \sim N(0, \sigma^2 I) \tag{3}$$

where Y represents an $n \times 1$ vector of dependent variables, X is an $n \times k$ matrix of explanatory variables, ρ is a spatial autoregressive coefficient, β is a $k \times 1$ vector of the coefficients to be estimated, W is an $n \times n$ spatial weights matrix, and ε is an $n \times 1$ vector of error terms.

Spatial Error Model (SEM) is adopted from a practical application where spatial autocorrelation is detected in the residuals of the typical linear regression model. In such case, SEM is used to obtain unbiased and efficient estimates of the regression parameters, and is expressed as:

$$Y = X\beta + \varepsilon, \varepsilon = \lambda W\varepsilon + \mu, \mu \sim N(0, \sigma^2 I) \tag{4}$$

where, λ is a spatial parameter similar to ρ in Equation (3) and all other notations are as previously defined.

Conditional on the specification of the intercept term (and the error term), the panel data regression equation can be estimated by either a fixed effect or a random effect model [15].

Generally, the model choice of either SLM or SEM is determined by Moran's I test statistics, two Lagrange multipliers (LM (error) and LM (lag)), and robust R-LM (error) and R-LM (lag). Anselin (2004) [16] proposed the following criterion: if the LM (lag) is statistically more significant than LM (error), and R-LM (lag) is significant but R-LM (error) is not significant, then SLM is considered to be a more suitable estimation model. Conversely, if the LM (error) is more notable than LM (lag), and R-LM (error) is significant but R-LM (lag) is not significant, then SEM is more suitable than SLM.

In addition to the above criterion for specification selection, other model selection criteria commonly used by the researchers are: Log Likelihood (logL), Akaike Information Criterion (AIC) and Schwartz Criterion (SC). In those cases, the larger LogL, the smaller SC and AIC test statistics, the better fitting the model would be.

Implementation of a spatial panel data model

Following the lead of Jaffe and Palmer (1997) [17], we measured environmental regulation (*Eregulation*) by the ratio of "three industrial wastes" (waste water, waste gas and solid waste) abatement expenditures to the total value of industrial output. We also added three more

determinants of manufacturing FDI in our model: the level of economic development (*Elevel*, measured by *per capita* GDP in each province), the degree of industrialization (*Idegree*, measured by the province's total industrial output value) and the manufacturing labor cost (*Lcost*, measured by the average wage of manufacturing workers in this province). We then estimated the following improved spatial panel data model:

$$\ln FDI_{it} = \alpha_{it} + \beta_{1t}Eregulation_{it} + \beta_{2t}\ln Elevel_{it}$$
$$+ \beta_{3t}Idegree_{it} + \beta_{4t}\ln Lcost_{it} + \mu_{it} \quad (5)$$

In this equation, i denotes province i, t stands for the period or stage (1,2), $\ln FDI_{it}$, $Eregulation_{it}$, $\ln Elevel_{it}$, $Idegree_{it}$ and $\ln Lcost_{it}$ represent the manufacturing FDI, the extent of environmental regulation, the level of economic development, the degree of industrialization and the manufacturing labor cost of province i at t stage, respectively. β_{1t} to β_{4t} are the coefficients associated with the respective FDI determinants, α_{it} and μ_{it} are the constant term and random error term.

Raw data

This paper collected and used annual data from 29 provinces except Hainan, Tibet, Hong Kong, Taiwan, and Macao (due to the large amount of missing data) over the years from 2010 to 2015. The FDI in each province was measured by the actual amount of manufacturing FDI (unit: RMB'0000), and the data were collected from the 2011-2016 China Statistical Yearbook and the CEINET. In order to reflect the temporal and spatial characteristics of manufacturing FDI, we divided the studying years into two stages: the first stage (2010-2012) and the second stage (2013-2015). We took the average value of every observation in the sample in each stage in the empirical analysis.

RESULTS AND DISCUSSION

Global spatial autocorrelation of manufacturing FDI

We analyzed the global spatial correlation of FDI in China's provincial manufacturing by the matrix W based on binary Rook contiguity weight. The results are shown in Table 1.

Table 1. Global Moran's I indices of China's provincial manufacturing industry from 2010 to 2015

Stage	Moran's I	Average	SE	z	P
2010-2012	0.508	-0.035	0.119	4.578	0.001
2013-2015	0.526	-0.036	0.126	4.483	0.001

As can be seen from Table 1, the global Moran's I indices in the two stages are positive and the P-values are all significant at 1% level. So they indicate that the manufacturing FDI in these provinces have positive spatial correlation and exhibit agglomeration characteristics.

We further used the Monte Carlo simulation method to test the significance of Moran's I. The results of 999 times simulation arrangements calculations are shown in Figures 1 and 2.
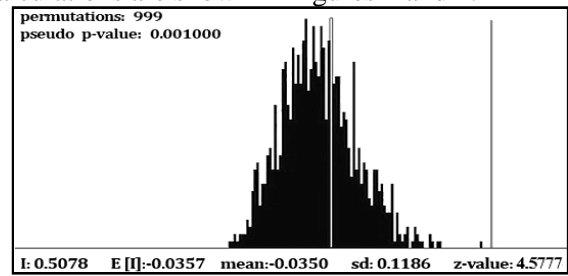
Fig. 1. Monte Carlo simulation results of China's provincial manufacturing FDI from 2010 to 2012
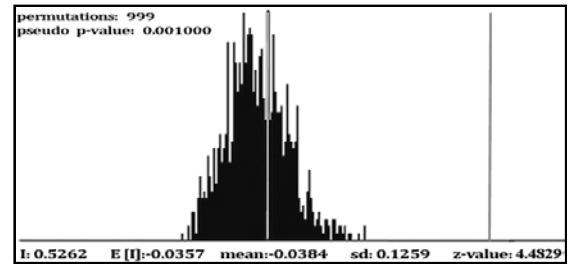
Fig. 2. Monte Carlo simulation results of China's provincial manufacturing FDI from 2013 to 2015

Local spatial association of manufacturing FDI by Moran scatter plots

Given that the local spatial correlation of provincial manufacturing FDI and the trend of local spatial agglomeration cannot be characterized by the global Moran's I indices, we applied the local index cluster analysis method, by the Moran scatter plots and LISA cluster maps, to further reveal the local spatial characteristics of manufacturing FDI. The Moran scatter plots analyses of the two stages are shown in Figures 3 and 4.

Fig. 3. Moran scatter plots of China's provincial manufacturing FDI from 2010 to 2012

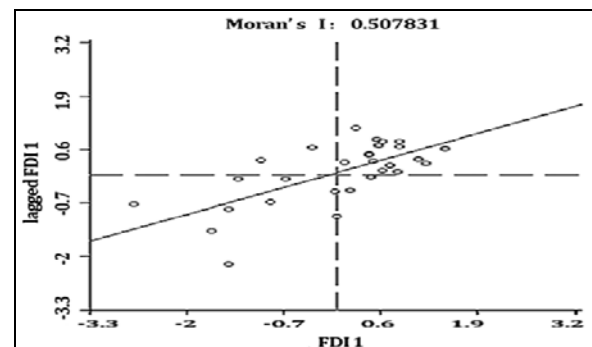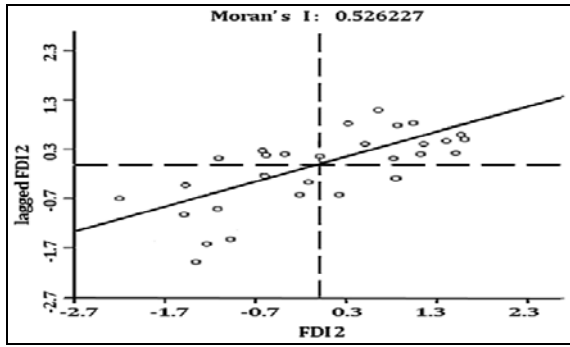**Fig. 4.** Moran scatter plots of China's provincial manufacturing FDI from 2013 to 2015

As can be seen from Figures 3 and 4, most provinces fall in the first and third quadrants, rejecting the assumption that manufacturing FDI is spatially distributed in a random fashion, and indicating that there is a positive correlation of FDI among different geographical or spatial units. That is, the amount of manufacturing FDI inflows tends to be close to other provinces with the similar FDI amounts. It is interesting to note that this local spatial pattern of FDI is the same as the results presented from the global spatial autocorrelation.

Local spatial association of manufacturing FDI by LISA cluster maps

LISA cluster maps were drawn to further illustrate the above local spatial characteristics, as shown in Figures 5 and 6.
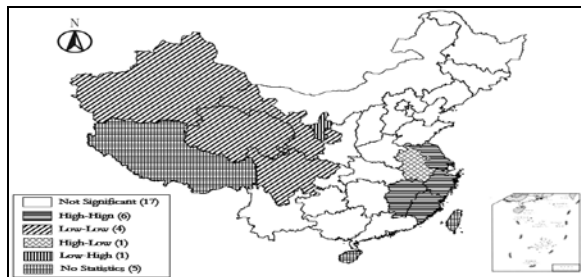

Fig. 5. LISA cluster map China's provincial manufacturing FDI from 2010 to 2012
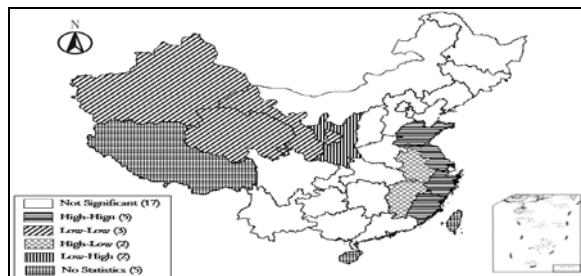

Fig. 6. LISA cluster map China's provincial manufacturing FDI from 2013 to 2015

We can see from the above figures that China's provincial FDI manufacturing is decreasing from the eastern to western regions. Specifically,

Shanghai, Fujian and Zhejiang are all located in the H-H cluster regions in two stages. Whereas the western provinces of Xinjiang, Qinghai and Gansu are in the L-L cluster regions, which indicates that the amount of manufacturing FDI flowed into these provinces and their neighbors is less than that of eastern provinces. These distinctively different spatial characteristics of FDI further confirmed that we need to use the spatial econometric model to investigate the relationship between manufacturing FDI and its influence factors.

Baseline estimation results from Ordinary Least Squares (OLS)

For comparison purpose, we first estimated Equation (5) based on OLS by software OpenGeoDa. The OLS baseline estimation results are displayed in Table 2. It shows that the OLS estimation model is significant at 1% level in both stages, with adjusted R square of 78.16% and 77.30%, and F value of 26.0462 and 30.0060, respectively. However, the spatial correlation test results in the preceding section already showed that manufacturing FDI clearly exhibits a spatial correlation pattern, which will cause the simple OLS estimators to be bias and inconsistent. Therefore, we need to further estimate the relationship between these variables by spatial econometric models.

Spatial econometric estimation based on SLM

As can be seen from Table 2, the Moran's I indices and the two Lagrangian multipliers are all significant at the 5% level in the two stages, indicating the presence of spatial autocorrelation and the need to estimate spatial econometric models. Then, the question arises: which spatial econometric model is more suitable for our purpose here? Applying the criteria mentioned above, we can answer that the statistical properties of the SLM model are relatively more appropriate in analyzing the relationship between these variables from Table 2. For the purpose of comparison, we estimated Equation (5) with both SLM and SEM specifications. The results are shown in Table 3. Comparing Tables 2 and 3, we can see that the goodness-of-fit statistics by SLM and SEM are higher than those by OLS. In addition, the logL values of SLM in the two stages are larger than the corresponding values of OLS and SEM. Thus, the classical linear regression model based on OLS is not suitable to analyze manufacturing FDI as it does not consider the spatial autocorrelation.

Table 2. OLS estimation results

Variable	2010-2012				Variable	2013-2015			
	Coefficient	SE	t	P		Coefficient	SE	t	P
constant	41.4198	12.8241	3.2298	0.0036	constant	32.0112	11.7263	4.0611	0.0021
E$regulation_1$	-6.3448	1.2507	-5.0728	0.0000	E$regulation_2$	-7.0609	2.3140	-6.8126	0.0000
ln$Elevel_1$	1.4186	0.6969	2.0357	0.0530	ln$Elevel_2$	3.5061	0.7211	2.0857	0.0482
$Idegree_1$	0.1613	0.0682	2.3647	0.0265	$Idegree_2$	1.1232	0.0968	3.2323	0.0031
ln$Lcost_1$	-3.1134	1.6496	-1.8874	0.0713	ln$Lcost_2$	-2.9266	1.2434	-2.1008	0.0496
R^2adj	0.7816				R^2adj	0.7730			
F-statistic	26.0462			1.9954e-0	F-statistic	30.0060			2.0432e-0
*Log*L	-34.3096				*Log*L	-36.4724			
AIC	78.6192				AIC	89.2938			
SC	85.4557				SC	97.5309			
Spatial test	MI/DF	Value	P		Spatial test	MI/DF	Value	P	
Moran's I (error)	0.1041	1.6159	0.0361		Moran's I	0.1982	2.6202	0.0059	
LM(lag)	1	4.8934	0.0270		LM(lag)	1	7.2964	0.0043	
R- LM (lag)	1	4.4409	0.0351		R- LM (lag)	1	6.5732	0.0169	
LM (error)	1	0.6257	0.4290		LM (error)	1	0.7181	0.3962	
R-LM (error)	1	0.1731	0.6773		R-LM (error)	1	0.2023	0.5781	

Table 3. SLM and SEM estimation results

Stage	Variable	SLM				SEM			
		Coefficient	SE	Z	P	Coefficient	SE	Z	P
2010-2012	Constant	35.5243	10.7869	3.2933	0.0010	36.1401	11.6301	3.1075	0.0019
	E$regulation_1$	-5.5910	1.0765	-5.1935	0.0000	-5.6231	1.1252	-4.9972	0.0000
	ln$Elevel_1$	1.1978	0.5879	2.0376	0.0416	1.3243	0.6539	2.0254	0.0428
	$Idegree_1$	0.1416	0.0582	2.4352	0.0149	0.1663	0.0609	2.7303	0.0063
	ln$Lcost_1$	-2.9103	1.3748	-2.1168	0.0343	-2.5353	1.4878	-1.7041	0.0884
	ρ/λ	0.2608	0.1215	2.1461	0.0319	0.3086	0.1345	1.3746	0.1693
	Statistical	DF	Value	P		DF	Value	P	
	R-squared		0.8429				0.8235		
	LogL		-32.0044				-33.8028		
	LR	1	4.6105	0.0008		1	1.0136	0.3140	
	AIC		76.0087				77.6056		
	SC		84.2125				84.4421		
2013-2015	Constant	42.3928	12.6731	4.0911	0.0007	37.3831	11.9029	3.9820	0.0009
	E$regulation_2$	-5.6256	1.9033	-3.5009	0.0012	-3.5476	1.5324	-4.7620	0.0001
	ln$Elevel_2$	1.0197	0.4709	2.5866	0.0173	1.9831	0.5839	2.9304	0.0078
	$Idegree_2$	0.1307	0.1223	3.1034	0.0038	0.1243	0.1128	2.6677	0.0120
	ln$Lcost_2$	-3.8671	1.6685	-1.1056	0.0264	-3.3229	1.4661	-1.6252	0.1082
	ρ/λ	0.3719	0.1469	3.1231	0.0025	0.4165	0.1672	3.5328	0.0014
	Statistical	DF	Value	P		DF	Value	P	
	R-squared		0.7834				0.7529		
	LogL		-37.0623				-39.2788		
	LR	1	4.9238	0.0018		1	2.6707	0.0105	
	AIC		79.4313				87.0269		
	SC		80.8226				89.5217		

Furthermore, comparing the values of logL, LR, AIC and SC statistics, SLM clearly performs better than SEM, hence most of the discussion and interpretation of the estimation results in the following section are based on SLM results.

We also obtained four empirical results based on SLM model as follows: First, environmental regulation has a significant negative impact on FDI in both two stages. From Table 3, we can see that the impacts in the two stages are statistically significant at a 1% level. Also, the values of the coefficient estimates for this variable imply that a 1% rise in environmental regulation intensity can inhibit FDI inflow by around 5.5910% and 5.6256%, respectively. The inhibitory effect of environmental regulation on the inflow of manufacturing FDI is increasing over the two stages. This could be because more stringent environmental regulations were implemented from 2012 to 2015 in China, especially those against foreign capital investments in some pollution intensive manufacturing industries. As a result, environmental regulation gradually became an important negative determinant (inhibitor) of FDI inflows. Meanwhile, compared with the results of OLS in Table 2, the inhibiting effects estimated by the SLM model are weakened. This suggests that when considering the spatial lag effect, the environmental regulation of neighboring provinces can dilute the inhibitory effects of environmental

regulation on manufacturing FDI in the provinces under study.

Second, the economic development level and industrialization degree variables have positive significant impacts on the manufacturing FDI inflow. From Table 3 we can see that the positive effect of economic development level on manufacturing FDI is statistically significant at 5% in two stages, and that a 1% increase in economic development level significantly promotes the FDI inflow by around 1.1978% and 1.0197%. The provincial degree of industrialization also has a positive effect at the 5% and 1% significance level respectively, and the FDI inflow increases by 0.1416% and 0.1307% following a 1% increase in industrialization level. Comparing the magnitude of the coefficient estimates for the two stages, we can also find that the impacts of these two factors on manufacturing FDI showed a downward trend, indicating that foreign investment in China's manufacturing is less and less impacted over time by the level of economic development and the degree of industrialization. This finding corroborates with the recent phenomenon that many foreign capitals are transferred (relocated) from the more developed and industrialized eastern provinces of China to the central and western provinces.

Finally, turning to the manufacturing labor cost variable, it appears that labor cost has a statistically significant negative impact on manufacturing FDI inflow at the 5% significance level in both stages. The value of the coefficient estimates indicates that a 1% increase in the labor cost significantly inhibits the FDI inflow by around 2.9103% and 3.8671% respectively. Evidently, China's main comparative advantage in attracting FDI still lies in the low labor cost in these two stages. As a result, most FDI is still concentrated in China's labor-intensive industries, which are at the lower end of the global industrial chain.

CONCLUSIONS

This study investigates the relationship between manufacturing FDI and environmental regulation, along with other relevant FDI determinants, using the spatial econometric models over the period from 2010 to 2015. Overall, we found that manufacturing FDI exhibits clear spatial autocorrelation and regional agglomeration characteristics. We also found a statistically significant negative relationship between environmental regulation and manufacturing FDI in China's 29 provinces. This finding implies that imposing more stringent environmental regulations would inhibit the

manufacturing FDI. It was also found that the inhibitory effect is gradually increasing during the 2010-2015 study period. Furthermore, the level of economic development and degree of industrialization in a province are positively related to the inflow of manufacturing FDI when we consider the spatial correlations. But the positive effect is decreasing in the two stages. Finally, there is a statistically significant negative correlation between labor costs and manufacturing FDI inflows.

In summary, the foreign direct investment is inhibited by the environmental regulation in China in this six-year period. Other factors, such as factor prices, regional climate, and available market, have also be proved to be key determinants in the foreign capital inflowing decisions[4]. So we anticipate inducing these factors into our further research about this issue.

REFERENCES

1. J. Yu, C.W.H. Lo, P.H.Y. Li, *Bus. Strateg. Environ*, **26**, 371 (2017).
2. B.R. Copeland, M.S. Taylor, *Q. J. Econ.*, **109**, 755 (1994).
3. H.N. Tian, X.M. Li, *Forum on Sci. Technol. China*, **10**, 53 (2015).
4. A. Dechezleprêtre, M. Sato, *Rev. Environ. Econ. Policy,* **11**, 183 (2017).
5. B.R. Dijkstra, A.J. Mathew, A. Mukherjee, *Rev. Int. Econ.,* **19**, 568 (2011).
6. R.J.R. Elliott, Y. Zhou, *Environ. Res. Econ.*, **55**, 141 (2013).
7. C.F. Zhou, Y.W. Du, A.P. Peng, *World Econ. Studies,* **1**, 110(2016).
8. F. Sanna-Randaccio, R. Sestini, *Rev. Int. Econ.,* **20**, 580 (2012).
9. L. Anselin, *Geographical. Analysis,* **27**, 93 (1995).
10. Z.N. Li, W.Q. Pan, Econometrics (Third ed.), Higher Education Press, Peking, 2010.
11. C.D. Lloyd. Local models for spatial analysis, CRC Press, New York, 2010.
12. F. A. Feltus, J. Wan, S. R. Schulze, J. C. Estill, N. Jiang, A.H. Paterson, *Genome Res.,* **14**, 1812 (2004).
13. L. Anselin, *Int. Reg. Sci. Rev.,* **26**, 153 (2003).
14. D.M. Lambert, J.P. Brown, R.J.G.M. Florax, *Reg. Sci. Urb. Econ.,* **40**, 241 (2010).
15. J. P. Elhorst, *Int. Reg. Sci. Rev.,* **26**, 244 (2003).
16. L. Anselin, R. Bongiovanni, J. Lowenberg-DeBoer, *Am. J. Agr. Econ.*, **86**, 675 (2004).
17. A.B. Jaffe, K. Palmer, *Rev. Econ. Stat.,* **79**, 610 (1997).

Study on the application of a self-regulating heater for pre-control of concrete curing temperature in winter

Liu Lin

School of Resources & Civil Engineering, Northeastern University, Shenyang 110819, China.
School of Civil Engineering, Shenyang Jianzhu University, Shenyang 110000, China

As a concentrated high-temperature exothermic material, a self-regulating heater is embedded in the concrete for heating and maintenance in winter, which can greatly improve the short concrete construction period in a severe-cold area. In order to achieve the expected temperature control, adjust the performance of concrete and optimize the design method of heating and curing, a pre-control method of concrete temperature history with the change of hydration degree is established based on the first law of thermodynamics, using the concept of equivalent age, considering the effect of temperature on the hydration reaction and thermal performance of concrete through the expected mechanical strength design. The method was verified by a temperature control test. The results show that the method can effectively control the heating rate of concrete. When the temperature at the design stable phase is 45°C, the temperature at the concrete phase is relatively stable due to the decrease of hydration reaction, slowly decreasing at a rate of 0.11 °C /h and 0.08 °C /h. The temperature at the actual stable phase is in the range of 39.69-45.63 °C, the variation range is 0.12%. The buried heat source can effectively accelerate the hydration reaction, and the hydration degree under the condition of 45 °C for 3 curing days equals to that at 20 °C for 7 curing days.

Keywords: Curing in winter; Equivalent age; Self-regulating heater; Pre-control

INTRODUCTION

The winter in severe cold areas can last for several months, resulting in a short effective construction period of many concrete projects. If the concrete is frozen and kept frozen below -10 °C with only a small extent of cement hydration, the concrete will lose its strength. Therefore, as an important early step of the construction method in winter, the temperature for heating and curing will affect the early performance of concrete, hence assessment and control countermeasures must be fully understood, so as to avoid the impact on concrete performance. Heating and curing mainly consists of steam curing, moist heat curing, electric heat curing, etc. However, with the development and application of high-rise and large-volume concrete structures, under the influence of site construction conditions and site space conversion, the engineering community began to adopt a new type of concentrated exothermic material - self-regulating heater to provide a heat source in concrete.

This method is flexible, safe, reliable and energy-saving, it can greatly improve the short duration of concrete in severe-cold areas. Self-regulating heater is a band-shaped electric heater with resistivity positive temperature coefficient (PTC) conductive polymer composite as a heating element. Compared with conventional constant-power exothermic materials which may easily cause local overheating, wire burning and other shortcomings [1], the automatical adjustment of the output power with the heated system permits to reach the temperature balance point and keeps the temperature constant without the need of other equipment.

As early as the 1980s, the Soviet engineering staff made a loop using a 1.2 mm-diameter galvanized wire as the heating wire and applied it in concrete heating and curing. In 2010, Ni [1] used an internally installed circulating electrical heating as the method of curing in the Polo Pearl project of St. Petersburg, Russia to achieve concrete heating by laying a resistance wire in the concrete. However, the heating wire is of constant power type and cannot be automatically adjusted, as this may easily lead to local overheating, wire burning and concrete cracks. In 2004, Lu [2] successfully adopted the self-regulating "ribbon heater method" in the construction of a 9 m reinforced concrete platform for the No.5 converter project in the winter construction of Bengang Steel Plates Co., Ltd. The method followed the principle of heat conservation, designed the laying plan and calculated the length of heater in the concrete, but did not consider the effect of the water spray heat release of the concrete on the temperature field. In 2013, through field measurements, Cao and Wu [3, 4] laid ribbon heaters along the forms of Hai river extra-large bridge pier and Yalu river bridge main tower for heat insulation and maintenance. In addition, in the construction of two pouring joint

*To whom all correspondence should be sent:
E-mail: sunxiaoyu520634@163.com

surfaces, electric tracing was used prior to pouring. These results were mostly combined with specific engineering research, by embedding pre-assumed temperature control points in temperature sensors for temperature control. Man-made blackout will be made in case of exceeding the specified temperature, resulting in outage of the local or the entire loop, and achieving passive intervention of the temperature field. Based on the theory of heat transfer, the influence of temperature on concrete hydration reaction was considered by the maturity of equivalent age, and the hydration degree was used to express the development of concrete thermal performance. According to the pre-set strength, the temperature history was set, the adjustment time and speed of the designed temperature were pre-controlled, and verified by experiment.

BASIC THEORY

Equivalent age

In 1951, Saul [5] pointed out that whatever the temperature history of concrete, as long as the maturity is equal, the strength must be equal, that is, the concept of concrete maturity. He also put forward the "Nurse-Saul" maturity equation that expresses the joint role of different curing conditions, age and temperature in the development of concrete strength, as shown in formula (1).

$$M = \int_0^t (T(t) - T_0) \mathrm{d}t \qquad (1)$$

where M is the maturity coefficient, t is the curing age, T is the temperature at age t, T_0 is the initial temperature parameter and is usually $-10\,^{\circ}\text{C}$.

According to the Nurse-Saul equation, the concrete age at different curing temperatures is transformed into an equivalent age under the same maturity, and it can be seen that the equivalent age is essentially the same as the maturity, and the expression is as follows:

$$t_e = \frac{\sum (T - T_0)\Delta t}{T_r - T_0} \qquad (2)$$

where T_r is $20\,^{\circ}\text{C}$.

Cement hydration in concrete is an exothermic reaction accelerated by temperature. Thus, Copeland *et al.* [6] pointed out that in chemical reactions, the effect of temperature on the hydration reaction rate follows the Arrhenius function, as shown in formula (3):

$$k(T) = A e^{\frac{E_a}{RT}} \qquad (3)$$

where k(T) is the chemical reaction rate; T is the reaction temperature, using adiabatic temperature. E_a is the activation energy of concrete. R is the gas constant, generally 8.314J/mol·K.

In 1977, Hansen and Pedersen [7] carried out a hydration heat test at different curing temperatures to calculate the activation energy of concrete, as shown in formula (4):

$$E_a = \begin{cases} 33.5 & T_c \geq 20\,^{\circ}\text{C} \\ 33.5 + 1.47(20 - T_c) & T_c < 20\,^{\circ}\text{C} \end{cases} \qquad (4)$$

The equivalent age maturity function based on Arrhenius function was proposed:

$$t_e = \sum_0^t exp\left[\frac{E_a}{R}\left[\frac{1}{273 + T_r} - \frac{1}{273 + T}\right]\right]\Delta t \qquad (5)$$

where t_e is the equivalent age. E_a is the activation energy of concrete.

According to formula (5), 1h of concrete curing at $45\,^{\circ}\text{C}$ is equivalent to 2.05 h at $20\,^{\circ}\text{C}$.

By means of maturity theory, the early compressive strength of concrete at any temperature history can be converted to the compressive strength equivalent at $20\,^{\circ}\text{C}$ using equivalent age conversion formula. Based on this idea, researchers at home and abroad have proposed some compressive strength formulas based on age spray degree, as shown in Table 1.

Table 1. Compressive strength formulas based on equivalent age

Compressive strength	Formula	Ref.
$\dfrac{f_c(t_e)}{f_{c,\,u}} = \dfrac{k_f(t_e - t_0)}{1 + k_f(t_e - t_0)}$	(6)	[8]
$\dfrac{f_c t_e}{f_{c672}} = exp\left[S \times \left(1 - \sqrt{\dfrac{672}{t_e - t_0}}\right)\right]$	(7)	[9]

where $f_c (t_e)$ is the concrete compressive strength at an equivalent age of t_e, h, MPa, f_{c672} is the concrete compressive strength at the curing condition of $20\,^{\circ}\text{C}$ for 672 h, MPa, $f_{c,\,u}$ is the compressive strength when cement reaches the ultimate hydration degree, MPa, S、k_f is the shape coefficient, t_0 is the time when concrete mechanical property starts developing, generally adopting the initial setting time of concrete, h.

If concrete strength is calculated by formula (7), then the compressive strength of C40 concrete at any time t is:

$$f_c t_e = 40 \times exp\left[0.271 \times \left(1 - \sqrt{\frac{672}{t_e - 12}}\right)\right] \qquad (8)$$

where S is 0.271 [9], t_0 is 12 h.

Hydration degree

Hydration degree reflects the hydration reaction degree of concrete gelling material at a certain age, since the hydration degree monotonously increases with the hydration reaction of cement [10], so the

exothermic heat of hydration was used to express the degree of hydration, see formula (9):

$$\alpha(t) = \frac{Q(t)}{Q_0} \qquad (9)$$

where $\alpha(t)$ is the hydration degree of age t, which monotonously increases with the hydration reaction of cement. $Q(t)$ is the exothermic heat of hydration of age t, kJ. Q_{max} is the exothermic heat under full hydration of cement, kJ.

On the basis of no test, the cumulative hydration heat can be expressed by formula (10):

$$Q(t) = Q_0(1 - e^{-mt}) \qquad (10)$$

where $Q(t)$ is the cumulative hydration heat when age is t, kJ/kg, Q_0 is total cement hydration heat, kJ/kg, it is 330 kJ/kg when is ordinary Portland cement 425, m is heating rate, see Table 2. Then,

$$\alpha(t) = \frac{Q(t)}{Q_0} = (1 - e^{-mt}) \qquad (11)$$

Table 2. Value of heating rate (m)

Pouring temperature (℃)	5	10	15	20	25
m (1/d)	0.295	0.318	0.340	0.362	0.384

Specific heat

The specific heat (C) of concrete refers to the absorbed (or released) heat when the temperature of a unit mass of concrete is increased (or reduced), and can be expressed as follows:

$$c = \frac{Q}{G(t_2 - t_1)} \qquad (12)$$

where Q is the absorbed (or released) heat, kJ, C is specific heat of concrete, kJ / (kg · ℃), G is the mass of concrete, kg, $t_2 - t_1$ is the temperature difference before or after the concrete temperature is increased (or reduced), ℃.

Since the specific heat of water is 5-6 times that of concrete and aggregate, the specific heat has a great effect on the concrete water content. In addition, the more the aggregate content, the smaller is the specific heat of the concrete. Van Breugel *et al.* [11] proposed a formula of concrete considering the temperature, mix ratio and the change of hydration degree, as shown below:

$$c = \frac{\rho_c \alpha c_{cef} + \rho_c(1-\alpha)c_c + \rho_a c_a + \rho_W c_W}{\rho} \qquad (13)$$

$$c_{cef} = 8.4T_d + 339 \qquad (14)$$

where C is the concrete specific heat, J · kg⁻¹ · ℃⁻¹, ρ is the concrete density, kg · m⁻³, W_c、W_a、W_W are the weights of each m³ of cement, aggregate and water,respectively, kg · m⁻³, C_c、C_a、C_W are the specific heats of cement, aggregate and

water, respectively, J · kg⁻¹ · ℃⁻¹, C_{cef} is the assumed specific heat of hydrated cement, J · kg⁻¹ · ℃⁻¹, α is the hydration degree, T_c is the current temperature.

Pre-control of temperature history of concrete with buried heat source based on the first law of heat transfer

For a period of time, the amount of thermal and mechanical energy increase stored in the control vessel must be equal to the difference between the entering and leaving thermal and mechanical energy plus the thermal energy generated in the control vessel. Therefore, for the concrete members with embedded heater as a heat source, we used the first law of thermodynamics considering the convection and radiant heat transfer of concrete surfaces, the chemical energy of concrete (hydration), the changes in thermal energy and its storage items generated by the heater. Therefore, for a concrete me9mber with a designed heater length of L, the formula of the control system is:

$$\Delta \dot{E}_{st} = \dot{E}_{in} + \dot{E}_{out} + \dot{E}_g \qquad (15)$$

where $\Delta \dot{E}_{in}$ is the rate at which the energy is generated by the heater, kJ, $\dot{E}_{out}$ is the rate at which the concrete energy dissipates, kJ, $\dot{E}_g$ is the rate at which the chemical energy of the concrete is generated, kJ, $\Delta \dot{E}_{st}$ is the rate at which the thermal energy storage items change, kJ.

$$\Delta \dot{E}_{in} = PL \qquad (16)$$

where P is the heater power, kW, L is the heater length, m.

$$\dot{E}_{out} = -(q_{conv} + q_{rad}) \qquad (17)$$
$$q_{conv} = \beta_s A(T - T_\infty)$$
$$q_{rad} = \varepsilon \sigma A(T^4 - T_\infty^4)$$
$$\beta_s = \frac{1}{R_s} = \frac{1}{(1/\beta) + \sum(h_i/\lambda_i)}$$

Where q_{conv} is convection heat transfer, kW, q_{rad} is net radiation, kW, β_s is the equivalent surface exothermic coefficient, kJ/ (m²·h· ℃), β is the solid surface exothermic coefficient, kJ/ (m²·h· ℃), λ_i is thermal insulation layer thermal conductivity, kJ/(m·h·℃), h_i is Insulation thickness, m, A is the concrete exothermic area, m², T is concrete surface temperature, ℃, T_∞ is ambient temperature, ℃, σ is Stephen-Boltzmann constant, 5.67×10⁻⁸W/(m²·K⁴), ε is emissivity, 0.9.

$$\dot{E}_g = \frac{d\left[WQ_0(1 - e^{-mt_e})\right]}{dt} \qquad (18)$$

where W is the amount of cement, kg.

$$\dot{E}_{st} = \rho c V \frac{dT}{dt} \qquad (19)$$

Substituting formulas (16) , (17) , (18) and (19) into formula (15), (20) can be obtained:

$$PL - \beta_s A\left(T - T_\infty\right) - \varepsilon\sigma A(T^4 - T_{sur}^4) + \frac{d\left[Q_0(1-e^{-mt_e})\right]}{dt} = 0$$

$$\frac{dT}{dt} = \frac{PL - \beta_s A\left(T - T_\infty\right) - \varepsilon\sigma A(T^4 - T_{sur}^4) + \frac{d\left[Q_0(1-e^{-mt_e})\right]}{dt}}{\rho c V}$$

(20)

The temperature change of the concrete along with time can be obtained by means of numerical integration. When the temperature is basically no longer changed and is relatively stable, $\frac{dT}{dt} = 0$, the temperature of the concrete can be obtained by the following formula:

$$PL - \beta_s A\left(T - T_\infty\right) - \varepsilon\sigma A(T^4 - T_{sur}^4) + \frac{d\left[Q_0(1-e^{-mt_e})\right]}{dt} = 0$$

(21)

STUDY OF METHOD APPLICATION

Raw materials and mix ratio

Shenyang Dunshi 42.5 ordinary Portland cement was adopted. Coarse aggregate was gravel with a particle size of 5-20 mm and apparent density of 2650 kg/m^3. Fine aggregate was natural sand with an apparent density of 2630 kg/m^3. Water-reducing agent was polycarboxylate high- performance water-reducing agent. Water was tap water. According to compressive strength design, C40 was adopted, the match ratio is shown in Table 3.

Method

Winter temperature is -15°C, casting length×width×height are 0.8×0.8×1.5m concrete columns, temperature of casting concrete is 10°C, the target stability temperature is 45 °C and is expected to reach in 20h, that is, the temperature change is subject to formula (22), formula (23) can be derived from formula (5) and (22). We can see that 20h of temperature rise and 72 hours (3 days) of heating at a stable temperature of 45°C is equivalent to 120h of equivalent age.

$$T = \begin{cases} V_s t + T_m & t < t_s \\ T_h & t_s \leq t \leq t_s + t_h \\ T_h - V_d t & t > t_h \end{cases}$$

(22)

Where V_s is heating rate, 2°C/h, V_d is cooling rate, 0.5°C/h, T_m is concrete pouring temperature, 5°C, T_h is target temperature, 45°C, t_s is target temperature arrival time, 20h, t_h is stable phase time, 52h.

$$t_e = \begin{cases} \sum_0^t exp\left[\frac{E_a}{R}\left[\frac{1}{273+T_r} - \frac{1}{278+2t}\right]\right]\Delta t & t < 20h \\ \sum_0^t exp\left[\frac{E_a}{R}\left[\frac{1}{273+T_r} - \frac{1}{318}\right]\right]\Delta t & 20h \leq t \leq 72h \\ \sum_0^t exp\left[\frac{E_a}{R}\left[\frac{1}{273+T_r} - \frac{1}{318-0.5t}\right]\right]\Delta t & t > 72h \end{cases}$$

(23)

According to formula (8), concrete compressive strength $f_c(120h) = 26.85\text{MPa} > 0.81\,f_{c672}$, after the outage of heater power and concrete cooling, cooling rate is less than 0.5°C /h, then according to formula (20)

$$\frac{dT}{dt} = \frac{PL - \beta_s A\left(T - T_\infty\right) - \varepsilon\sigma A(T^4 - T_{sur}^4) + \frac{d\left[Q_0(1-e^{-mt_e})\right]}{dt}}{\rho c V} < 0.5$$

where c is calculated according to formula (13), take the beginning of the cooling phase. The parameters of each component are shown in Table 3, so $\beta_s > 10 kJ/m^2 \cdot h \cdot °C$. In this case, if there is a protective layer of plastic blanket and quilt, then, $\beta_s = 14.15\beta_s > 10 kJ/m^2 \cdot h \cdot °C$. According to formula (21), L=14 m.

A 15DXW low-temperature limit (self-control temperature of 70°C) ribbon heater was arranged in the steel skeleton, and the layout is shown in Fig 1. FS-NM15 embedded temperature strain sensor manufactured by Jiangxi Fashion Technology Co., Ltd. was adopted. Temperature measurement error is 0.5°C, test range: -20 -80°C, test collecting devices were composed by the TFL-F-10xx series of vibrating wire collector, microcomputer and other devices.

Table 3 Concrete mix ratio and thermal performance of material

Component	Cement	Sand	Pebble	Water	Water-reducing agent (polycarboxylate dry powder)
Weight/kg	390	673	1222	165	0.2%
Specific heat	0.456	0.699	0.716	4.18	7

Fig. 1. Layout of temperature measuring points

Results and discussion

(1) The test results are shown in Fig. 2, where T1 was the temperature of the column center, the heating rate was 1.58℃ /h in temperature rise period and the maximum temperature was 45.63℃, reached after 22.5 h. T2 was the temperature of the same temperature level 5 cm from the surface, more obviously affected by the ambient temperature E than T2. The heating rate was 2℃ /h in temperature rise period and the maximum temperature was 43.38℃, reached after 17h. T1 and T2 trends were basically the same, the maximum temperature difference was 2℃, the temperature field of concrete columns was basically uniform and the temperature change was consistent.
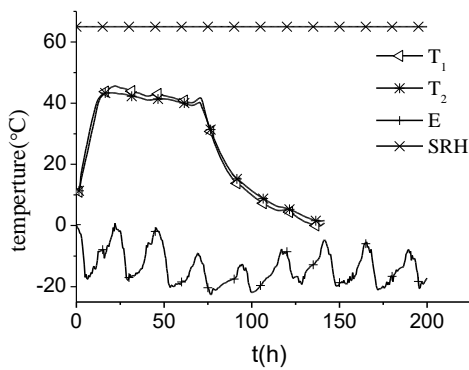

Fig. 2. Test results

(2) The comparison of design temperature history and measurement results is shown in Table 4. T1 and

T2 phases have relatively stable temperatures, but are actually slowly declining at 0.11℃ /h and 0.08℃ /h, this is because of the cement hydration reduction in concrete and hydration heat continues to decrease, see Fig. 3. Especially that in the hydration degree under buried heat source after 3 days reaches that of 7 days under 20℃.
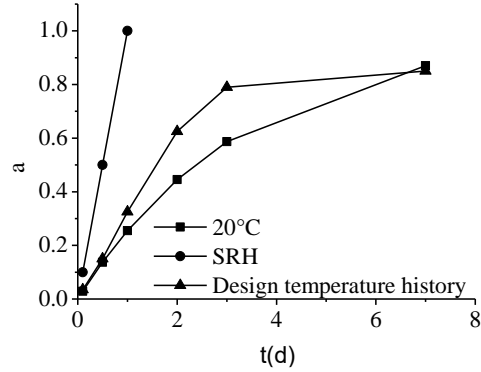

Fig. 3. Design temperature history and hydration degree at 20℃

(3) When T1 and T2 coincide with the ambient temperature E, that is, when the overall temperature of concrete dropped completely to the ambient temperature on the 7th day, form was removed. Concrete column strength test was conducted using core-drilling method, including the contact area with SRT, the results are shown in Fig. 4. The strength of the concrete is higher than that of the design time, but the strength of the 28d concrete is less than 20℃ and 65℃.
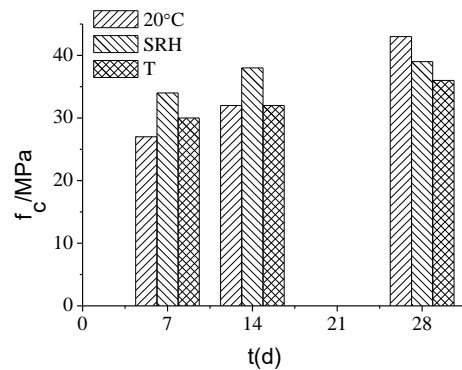

Fig. 4. Concrete strength development (4) SRH is the temperature of the self-regulating heater, which quickly reaches the rated temperature of 65℃ after connecting power, and keeps the temperature unchanged, see Fig. 2. There is a large temperature difference between SRT, T1 and T2.

Table 4 Comparison of test results

	V_s (℃ /h)	t_s (h)	T_h (℃)	t_h (h)	V_d (℃ /h)
T	2	20	45	52	0.5
T1	1.58	22.5	45.63-40.25	49.5	0.56
T2	1.96	17	43.38-39.69	55	0.53

CONCLUSIONS

1) Based on the equivalent age hydration degree theory, the pre-control method of the concrete temperature of buried heat source using the first law of thermodynamics is accurate. When the temperature at design stable phase is 45℃, the temperature at the actual stable phase is in the range of 39.69-45.63℃, the variation range is 0.12%.

2) Due to the decrease of the hydration reaction, the temperature at the concrete stable phase is relatively stable, slowly decreasing at a rate of 0.11℃ /h and 0.08℃ /h.

3) The buried heat source can effectively accelerate the hydration reaction and hydration degree, 1h of concrete curing at 45℃ is equivalent to 2.05 h under 20℃, and the hydration degree under the condition of 45℃ for 3 curing days equals to that under 20℃ for 7 curing days.

REFERENCES

1. F. Ni, *Building construction*, **32**(7), 687 (2010).
2. Y. Lu, *Construction Technology*, **35**(8), 60 (2006).
3. W. Chao, Z. Chao, *High Way*, **8**, 59 (2013).
4. Ch. Wu, The Ya Lu, *High Way*, **8**, 59 (2013).
5. A.G.A. Saul, *Magazine of Concrete Research*, **2**(6), 127 (1951).
6. L.E. Copeland, D.L. Kantro, G. Verbeck, Chemistry of Hydration of Portland Cement. Energetics of the Hydration of Portland Cement Part III., *Washington DC, NBS Monograph*,453(1962).
7. P.F. Hansen, E.J. Pedersen, *Nordisk Betong*, **1**(19), 21(1977).
8. N.J. Carino, R.C. Tank, *ACI Materials Journal*, **89**(2), 188 (1992).
9. Comité Euro: CEB-FIP model code 1990: Design code. London, Tomas Telford Ltd, 1993, 102.
10. P.W. Brown, J. Pommersheim, G. Frohnsdorff, *Cement & Concrete Research*, **15** (1), 35 (1985).
11. K. Van Breugel, *Computers and Structures*, **80**, 2035(2002).
12. G. De Schhutter, L. Taerwe, *Cement & Concrete Research*, **25** (3), 593 (1995)

Influence of hydraulic flow and clay hydration on pore pressure and collapse pressure of swelling shale

H.B. Liu[*], F. Zhang, Y.F. Meng, G. Li, G.D. Zhang

Laboratory of Oil and Gas Reservoir Geology and Exploration, Southwest Petroleum University, Xindu, Chengdu, 610500 China

A modified model for wellbore instability of shale formations is developed by considering the coupled flows of water and ions, crystal hydration and osmotic hydration of clay minerals. Based on the thermodynamic theory, we proposed new models to describe the hydraulic flow of water solutions and chemical diffusion of ions, taking into account the permeability and porosity of formation. Simultaneously, we deduced a new expression for the total stress controlling the clay crystal swelling and osmotic swelling with the energy balance between adjacent clay crystals and the diffuse double layer theory. Theoretical simulation indicates that the effects of clay hydration swelling are related to formation water, drilling fluid and ion salinity, as well as the spacing between adjacent clay crystals, and clay crystal swelling stress is far higher than the osmotic swelling stress between clay particles when the spacing is shorter than 4 nm. Ultimately, based on the modified effective stress laws, considering the mineral distribution in shale formation, pore size and clay hydration, the borehole stability model of physico-chemical coupling effects in shale was developed.

Key words: swelling shale; coupled flow; clay platelet hydration; osmotic hydration; modified effective stress, pore pressure, equivalent density of collapse pressure.y

INTRODUCTION

Over the past few decades, many researchers have extensively studied the physical and chemical coupling wellbore instability, and several methods have been proposed to analyze wellbore instability mechanics. Monte Carlo molecular modeling simulations were performed to investigate the swelling and shrinking behavior of hydrated Wyoming-type montmorillonites including different counterions [1]. Shi [2] studied the intercalating behavior of positively charged counterions in montmorillonites with Si^{4+}/Al^{3+} substitution in their first internal layer. The driving forces for the hydration of montmorillonites saturated with alkaline-earth cations were investigated by Fabrice [3]. The welling pressure of compact bentonite was estimated by Tom [4] using Gouy-Chapman diffuse layer theory. The wellbore stability of coal formation was studied by Zhao with discrete elements [5]. The wellbore stability in fractured rock formation with considering mud infiltration was studied by Chen [6]. Huang [7] believed that the pore pressure change and swelling pressure development are two main relevant factors in shale wellbore instability issue. Tao [8] believed that the *in-situ* stress state and rock strength were key parameters in evaluating the wellbore instability and studied the poro-thermoelastic effects on wellbore stability. Ghassemi [9] believed

mud filtrate invasion due to thermal and chemical effects to be several times larger than hydraulic flow. Tao and Ghassemi [10] studied the poro-thermoelastic effects on *in situ* stresses and rock strength, and found that neglecting heating and cooling effects will underestimate/ overestimate wellbore instability. AL-Bazali [11] evaluated the interaction between drilling fluid and shale and its effect on pore pressure and alterations of mechanical properties around the wellbore. Gelet [12] investigated the influence of diffusion and mass transfer on the pore pressure distribution in dual porous media: porous blocks and fissure network. Wang [13] developed a fluid-solid chemistry model considering fluid flow and ion transmission. The results showed that the pore pressure and stress are lower without consideration of the diffusion potential, and the linear model overestimates the pore pressure and stress around the wellbore. Hang [14] established a chemo-mechanical coupling model of borehole stability in hard brittle shale considering structure characteristics and targeted hydration. Zeynali Roshan [15] developed a coupled chemo-poroplastic model to investigate the change in ion transfer and its effect on pore pressure and effective stresses in chemically active fractured media. Liang [16] studied the wellbore stability of fracture formation considering weakness planes and porous flow. Zhang [17] improved the evaluating model for borehole stability considering bedding planes and rock anisotropy.

*To whom all correspondence should be sent:
E-mail: sunxiaoyu520634@163.com

In this paper, we try to develop a new model for describing the controlling forces between adjacent clay crystals, and the force equation for osmotic hydration swelling with the diffuse double layer theory. Simultaneously, the coupled flow of water and ions induced by gradients in hydraulic pressure and chemical potential is described with the irreversible thermodynamic theory. Finally, the effective stresses and wellbore instability are investigated with the modified effective stress theory.

THEORIES AND MODELS

The coupled flows of water and ions in shale formation can be conveniently described with a nonequilibrium or irreversible thermodynamic theory, and the relationship between flux J_i and driving forces X_j [18-20] can be expressed as follows:

$$J_i = \sum_j L_{ij} X_j \qquad (1)$$

The mass flux of the total solution J_V can be expressed as:

$$J_V = -L_{11}\nabla p - RT\sum_{i=1}^{n} L_{1,i+1}\nabla C_i \qquad (2)$$

The ion i molar flux J_i can be written as:

$$J_i = -L_{i+1,1}\nabla p - RTL_{i+1,2}\nabla C_i \qquad (3)$$

With the continuity equation for the solute and the solvent:

$$\frac{\partial C_i}{\partial t} + \nabla J_i = 0 \qquad (4)$$

$$\frac{\partial \rho}{\partial t} + \nabla(\rho J_V) = 0 \qquad (5)$$

And the relationship between the density and the pressure:

$$\rho = \rho_0 \exp\left[c_t(p - p_0)\right] \qquad (6)$$

Substituting Eq. 3 into Eq. 4, the equation is obtained for the transport of ion i:

$$\frac{\partial C_i}{\partial t} = L_{i+1,1}\nabla^2 p + RTL_{i+1,2}\nabla^2 C_i \qquad (7)$$

Substituting Eqs. 2 and 6 into Eq. 5, the equation is obtained for the transport of hydraulic pressure transmission:

$$\frac{\partial p}{\partial t} = \left(L_{11}\nabla p + RT\sum_{i=1}^{n} L_{1,i+1}\nabla C_i\right)\nabla p \qquad (8)$$
$$+ \frac{1}{c_t}\nabla\left(L_{11}\nabla p + RT\sum_{i=1}^{n} L_{1,i+1}\nabla C_i\right)$$

Assuming $(\nabla p)^2 \ll 1$, $\nabla p \nabla C_i \ll 1$, $L_{11} = k/\mu$, $RTL_{i+1,2} = D_i$, and in Eq. 7 the coefficient $L_{i+1,1}$ that multiplies the derivative of pressure is proven to be about three orders of magnitude smaller than the other coefficients. Therefore, Eqs. 7 and 8 can be simplified to:

$$\frac{\partial C_i}{\partial t} = D_i\nabla^2 C_i \qquad (9)$$

$$\frac{\partial p}{\partial t} = \frac{1}{c_t}\frac{k}{\mu}\nabla^2 p + \frac{1}{c_t}RT\sum_{i=1}^{n} L_{1,i+1}\nabla^2 C_i \qquad (10)$$

where, p is the hydraulic pressure, C_i is the ion i concentration, k is the permeability, μ is the fluid viscosity, ρ_0 is the fluid density, R is the universal gas constant, T is temperature in Kelvin, $L_{i,j}$ are the coefficients, c_t is the fluid compressibility, D_i is the ion i diffusivity M_i is the molar mass of ion i, ϕ_0 is the porosity, p_0 is the original pore pressure.

Norrish [21], Parker [22] and Laird [23] have developed a model for describing the clay crystal swelling with the potential energy balance. Here, we want to deduce a new model to describe the forces controlling the clay crystal swelling.

The potential energies of repulsion G_{rp}, attraction G_{at}, resistance G_{rs} between two adjacent clay crystals are [23]:

$$G_{rp} = G_{at} + G_{rs} \qquad (11)$$

The potential energy of attraction can be expressed as:

$$G_{at} = \frac{f_i\sigma e}{2\beta_I(D+r_s)} \qquad (12)$$
$$+ \frac{H}{12\pi}\left(\frac{1}{(2D)^2} + \frac{1}{(2D+2Th)^2} + \frac{2}{(2D+Th)^2}\right)$$

And the interlayer diabattivity β_I is defined as:

$$\beta_I = 4\pi\varepsilon_0\left[\left(1+\tanh\left(\frac{2D-C1}{C2}\right)\right)\left(\frac{\varepsilon_B-\varepsilon_C}{2}\right)+\varepsilon_C\right] \qquad (13)$$

The potential energy of repulsion can also be written as:

$$G_{rp} = \left(\frac{\sigma z_i e}{2r_i} + \frac{\sigma e}{2r_s}\right)\left(\frac{1}{\beta_I}-\frac{1}{\beta_B}\right) + \frac{L_B}{(2D)^{12}} \qquad 14)$$

where, e is the unit charge on a proton; f_i is the valence of the interlayer cations; r_s is the effective anionic radius of the negative charge sites; σ is the surface charge density; H is the Hamaker constant; L_B is a constant; Th is the thickness of the crystalline plate; D is one half of the layer separation; β_I is the interlayer diabattivity related to layer separation $2D$; ε_0 is the permittivity of vacuum, and $C1$, $C2$, ε_B and ε_C are empirical constants.

Based on Eq. (12), a model for attractive forces between adjacent crystals can be obtained deriving the potential models with respect to the variable D:

$$p_{ats} = \frac{f_i\sigma e}{2\left[\beta_I(D+r_s)\right]^2}\left[\beta_I'(D+r_s)+\beta_I\right] \qquad (15)$$
$$+ \frac{H}{3\pi}\left[\frac{1}{8D^3} + \frac{1}{8(D+Th)^3} - \frac{2}{(2D+Th)^3}\right]$$

and β_I' is as follows:

$$\beta_I^{'} = 4\pi\varepsilon_0\left(\varepsilon_B - \varepsilon_C\right)\frac{1 - \tanh\left(\frac{2D - C1}{C2}\right)^2}{C2} \quad (16)$$

With Eq. (14), a model for describing the repulsive forces can be derived:

$$p_{rps} = \left(\frac{\sigma z_i e}{2r_i} + \frac{\sigma e}{2r_s}\right)\frac{1}{\beta_I^{'2}}\beta_I^{'} + \frac{24L_B}{(2D)^{13}} \quad (17)$$

So, with Eqs. 14 17, assuming that the repulsive force is positive, and the attractive forces are negative, a model for the clay crystal swelling force can be expressed as:

$$p_{totals} = \left(\frac{\sigma z_i e}{2r_i} + \frac{\sigma e}{2r_s}\right)\frac{1}{\beta_I}\beta_I^{'} + \frac{24L_B}{(2D)^{13}}$$
$$- \frac{f_i\sigma e}{2\left[\beta_I\left(D + r_s\right)\right]}\left[\beta_I^{'}\left(D + r_s\right) + \beta_I\right] \quad (18)$$
$$- \frac{H}{3\pi}\left[\frac{1}{8D^3} + \frac{1}{8(D + T)^3} - \frac{2}{(2D + T)^3}\right]$$

Besides the model for clay crystal swelling, we adopt the diffuse double layer theory to model the osmotic swelling force between clay particles [24]. The repulsive force controlling osmotic swelling can be written as:

$$p_{rpo} = 64nkT\kappa^2 \exp\left[-2\left(\frac{2ne^2z^2}{\varepsilon_r\varepsilon_0 kT}\right)^{1/2}D\right] \quad (19)$$

$$\kappa = \frac{\exp(Z/2) - 1}{\exp(Z/2) + 1} \quad (20)$$

$$Z = ze\psi_0 / kT \quad (21)$$

$$\psi_0 = (2kT/ze)\sinh^{-1}\left(\sigma_{su} / \left(8n\varepsilon_r\varepsilon_0 kT\right)^{1/2}\right) \quad (22)$$

$$\sigma_{su} = \left(e \cdot CEC \cdot Na\right) / S \times 10^{-5} \quad (23)$$

where, n is the bulk solution electrolyte concentration, k is the Boltzmann constant, T is the temperature in Kelvin, z is the valence of the compensating cations, e is the proton charge, ψ_0 is the surface potential, ε_r is the relative permittivity of the medium, ε_0 is the permittivity of vacuum, σ_{su} is the surface charge density, CEC is the cation exchange capacity, S is the specific surface area, and Na is the Avogadro constant.

Assuming that the thickness of the clay particle is T and the spacing of adjacent clay particles is $2D$, the attractive force can be obtained by:

$$p_{ato} = \frac{H}{3\pi}\left(\frac{1}{(2D)^3} + \frac{1}{(2D + 2T)^3} - \frac{2}{(2D + T)^3}\right) \quad (24)$$

where, H is the Hamaker constant.

The osmotic swelling force can be expressed as:

$$p_{totalo} = p_{rpo} - p_{ato} = 64nKT\gamma^2\,e^{-2\kappa D}$$
$$- \frac{H}{3\pi}\left[\frac{1}{(2D)^3} + \frac{1}{(2D + 2T)^3} - \frac{2}{(2D + T)^3}\right] \quad (25)$$

The clay-water system in shale formation is simplified as a series of single clay platelets connected to a pore [25-29], and presented in Fig. 1.
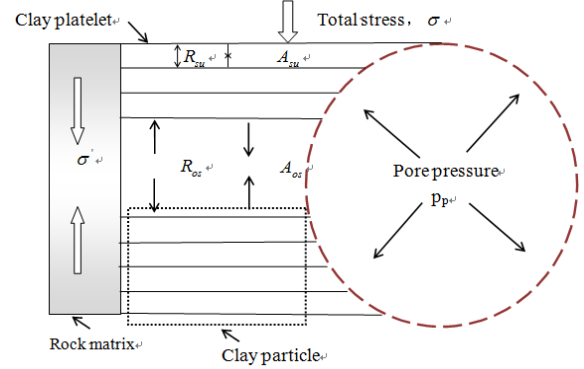

Fig. 1. Simplified structure of the clay-water system in shale formation

According to Fig. 1, the effective stress acting on the rock matrix can be written as:

$$\sigma_{i,j}^{eff} = \sigma_{total i,j} - \alpha p_p^{all}\delta_{i,j}$$
$$= \sigma_{total i,j} - \alpha(p_p + p_{swell})\delta_{i,j} \quad (26)$$

where, $\sigma_{i,j}^{eff}$ is the effective stress; $\sigma_{total_{i,j}}$ is the total stress; α is Biot's constant; p_p is pore pressure; p_{swell} is the clay swelling stress; p_{totals} is the clay crystal swelling stress; and p_{totalo} is the osmotic swelling stress.

The stresses around the wellbore in a deviated well can be obtained with the Cartesian coordinate conversion, and expressed as:

$$\begin{bmatrix} \sigma_x & \tau_{xy} & \tau_{xz} \\ \tau_{xy} & \sigma_y & \tau_{yz} \\ \tau_{xz} & \tau_{yz} & \sigma_z \end{bmatrix} = T\begin{bmatrix} \sigma_H & 0 & 0 \\ 0 & \sigma_h & 0 \\ 0 & 0 & \sigma_v \end{bmatrix}T^T \quad (27)$$

and

$$T = \begin{bmatrix} \cos\beta\cos\alpha & \cos\beta\sin\alpha & -\sin\alpha \\ -\sin\alpha & \cos\alpha & 0 \\ \sin\beta\cos\alpha & \sin\beta\sin\alpha & -\cos\beta \end{bmatrix} \quad (28)$$

where, α is the azimuth angle; β is the inclination angle.

So, the stresses around the wellbore can be written as:

$$\sigma_x = \cos^2\gamma\left(\sigma_H\cos^2\beta + \sigma_h\sin^2\beta\right) + \sigma_V\sin^2\beta$$
$$\sigma_y = \sigma_H\sin^2\beta + \sigma_h\cos^2\beta$$
$$\sigma_z = \sin^2\gamma\left(\sigma_H\cos^2\beta + \sigma_h\sin^2\beta\right) + \sigma_V\cos^2\gamma \quad (29)$$
$$\tau_{xy} = \cos\gamma\sin\beta\cos\beta\left(\sigma_h - \sigma_H\right)$$
$$\tau_{xz} = \cos\gamma\sin\gamma\left(\sigma_H\cos^2\beta + \sigma_h\sin^2\beta - \sigma_V\right)$$
$$\tau_{yz} = \sin\gamma\cos\beta\sin\beta\left(\sigma_h - \sigma_H\right)$$

Based on the Drunker-prager criterion, the minimum drilling fluid density maintaining wellbore stability can be obtained as follows:

$$\rho_m = \frac{-B - \sqrt{B^2 - 4b}}{2H} \times 100 \qquad (30)$$

where

$$B = -3\sigma_H + \sigma_h$$

$$b = \frac{1}{6}\left[(3\sigma_H - \sigma_h)^2 + (3\sigma_H - \sigma_h - \sigma_v)^2 + \sigma_v^2\right]$$

$$-\left[\frac{\sqrt{3}\sin\varphi}{3\sqrt{3+\sin\varphi^2}}(3\sigma_H - \sigma_h - \sigma_v - 3\alpha(p_p + p_{swell}))\right]^2$$

$$-\frac{\sin 2\varphi}{2\sqrt{3+\sin\varphi^2}}(3\sigma_H - \sigma_h - \sigma_v - 3\alpha(p_p + p_{swell})) - \frac{3C^2\cos\varphi^2}{3+\sin\varphi^2}$$

where, σ_H and σ_h are the maximum and minimum principal stresses; C is the cohesion; φ is the internal friction angle; and H is the depth.

RESULTS AND DISCUSSION

The input data used to calculate the coupled flow of water and ions are presented in Table 1. The coefficient L describes the chemical effect on the hydraulic flow, and it is negative in Lomba's paper [30]. Applying the experimental data in Table 1, the pore pressure and ion concentration distribution of fluid in the near wellbore zone are calculated, and are shown in Figs. 2 and 3.

Table 1. Input data

Parameters	Value
p_0	30MPa
p_w	45MPa
C_0	2000mol.m^{-3}
C_{df}	1000 mol.m^{-3}
k	3×10^{-19}m^2
c_t	4.35×10^{-4}MPa^{-1}
D	10^{-10}m^{2}s^{-1}
μ	10^{-9}MPa.s
R	8.314J.mol^{-1}K^{-1}
T	300K
L	-4.38×10^{-17}MPa.m.s

As shown in Figs. 2 and 3, when the shale formation is opened, water-based drilling fluid quickly flows into the shale formation under the pressure gradient and the chemical potential gradient, the pore pressure in the wellbore surface increases to the bottom pressure in a short time, and the increasing rate depends on the pressure difference between the original pore pressure and bottom pressure.
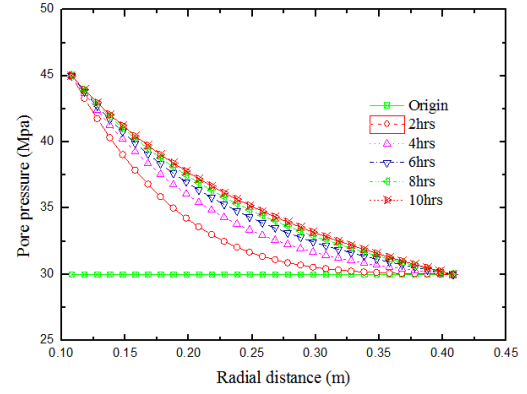

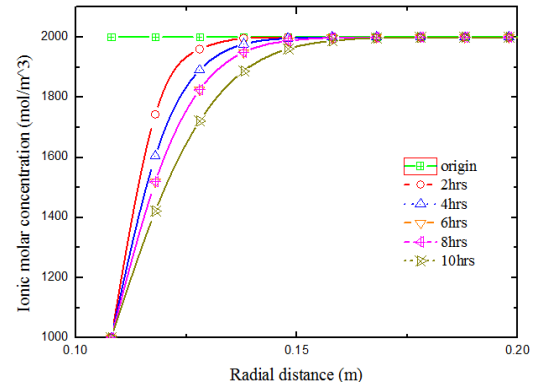**Fig.2.** Pore pressure profiles as a function of time

Fig.3. Solute concentration profiles as a function of time

We calculated the clay crystal swelling and osmotic swelling with the basic data in Table 2.

Table 2. Basic input data

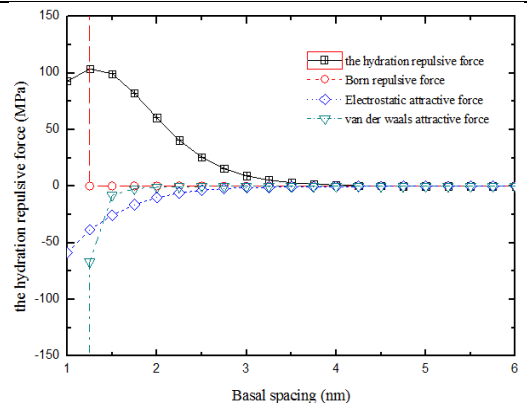| Parameters	Value
σ	0.193C.m^{-2}
e	1.602×10^{-19}C
D	7.5×10^{-10}m
H	10^{-20}J
T	9.6×10^{-10}m
r_s	4.7×10^{-10}m
r_i	3.58×10^{-10}m
β_B	8.695×10^{-9}C^{-2}N^{-1}m^{-2}
ε_B	78
ε_C	6
L_B	1.4627×10^{-124}J.m^{10}

Fig. 4. Relationship between interlayer forces and basal spacing
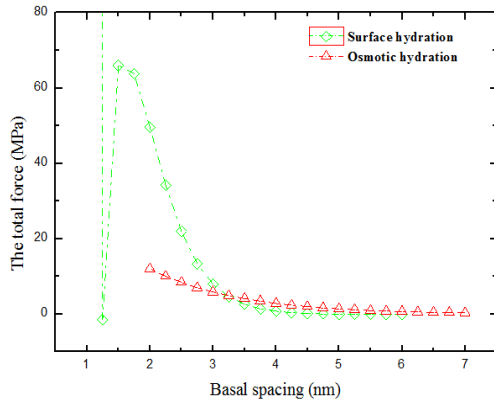
41

Fig. 5. Comparison of the total forces for surface hydration and osmotic hydration

Fig. 4 compares all forces of interlayer and their relationship with basal spacing. When the basal spacing is very small, born repulsive force and Van der Waals attractive force are super high. Once one layer of water molecules is adsorbed, born repulsive force and Van der Waals attractive force would rapidly decrease. Born repulsive force decreases to 0 and Van der Waals decreases to 0 for a spacing of 2 nm. Relatively, the hydration repulsive forces and the electrostatic attractive force decrease more slowly, the electrostatic attractive force drops to 0 when the basal spacing is about 3 nm, and the hydration repulsive forces drop to 0 for a spacing about 4 nm.

Fig. 5 shows that there are significant differences between surface hydration swelling force and osmotic hydration swelling force. The total force of surface hydration is super high for a basal spacing of 1 nm, and then drops to about 0 for a basal spacing of 1.25 nm.

The pore pressure, effective stresses and collapse force are evaluated with the modified effective stress law.

As shown in Fig. 6, the original formation pressure is 30 MPa, and the coupled flows and the clay swelling cause pore pressure on the wellbore wall to increase to 55.65 MPa.
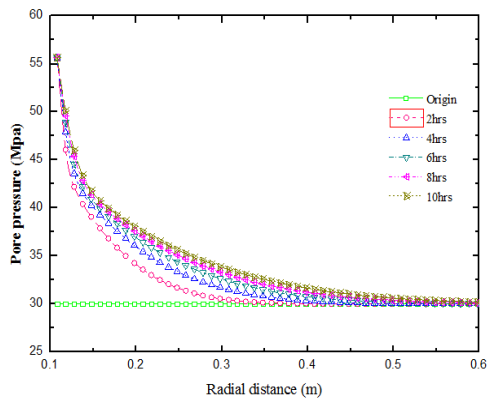

Fig. 6. Pore pressure distributions by considering coupled flows and clay hydration swelling

Fig. 7 shows that the increase in the pore pressure in the near wellbore zone leads to a

42

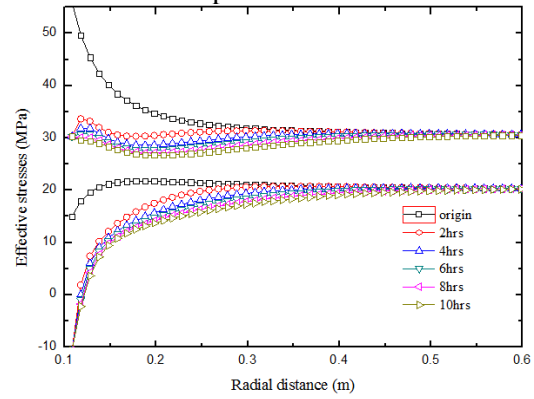continuous reduction of the effective radial stress and the effective hoop stress on the rocks.

Fig. 7. Effective stresses distribution around wellbore
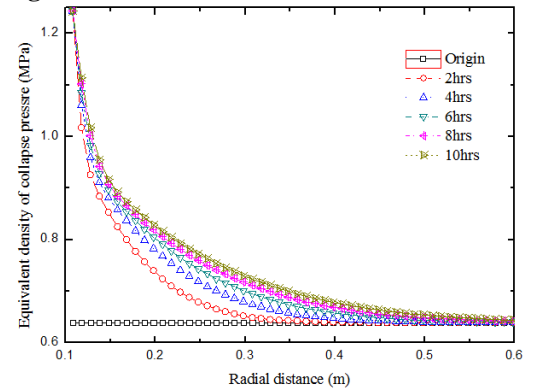

Fig. 8. Distribution of the equivalent density of collapse pressure

Fig. 8 indicates that both the penetration of the drilling fluid into the formation and the clay hydration swelling lead to a sharp increase of the collapse pressure in the near wellbore zone. The increasing amount on the rock surface is approximately 100% for the equivalent density to increase from 0.639 g/cm^3 to 1.244 g/cm^3. This is the reason why the borehole is unstable using conventional water-based drilling fluid but stable in gas drilling.

CONCLUSION

This paper deduces the coupled flow of the water solution and its components on the basis of the irreversible thermodynamic theory. The results indicate that the effect of clay permeable membrane on the pore fluid flow is not significant. Combining with the potential equilibrium equation controlling the clay crystal swelling potential, the equilibrium equation for forces controlling the clay crystal swelling was developed. Ultimately, based on the modified effective stress laws, considering the physical-chemical coupled flow of the pore fluid in the shale formation and the clay hydration swelling effect, as well as the calculation models for the pore pressure, the effective stresses and the equivalent density of collapse pressure in shale formation were developed. The calculation results indicated that the

coupled flow of the drilling fluid in the formation, the clay crystal swelling and the clay osmotic swelling have a significant effect on the borehole stability, and also showed that the effect of the clay crystal swelling is more significant than that of osmotic swelling.

REFERENCES

1. Y. Zheng，A. Zaoui，I. Shahrour, *Applied Clay Science*, **51**(1), 177 (2011).
2. J. Shi，H. Liu，Z. Lou，Y. Zhang，Y. Meng, Q. Zeng, M. Yang, et al., *Computational Materials Scienc*e, **69**, 95 (2013).
3. F. Salles ，J.M. Douillard ，O. Bildstein ，C. Gaudin，B. Prelot, J. Zajac, H. Van Damme, *Journal of colloid and interface scienc*e, **395**, 269 (2013).
4. T. Schanz，M.I. Khan，Y. Al-Badran, Applied Clay Science, **8**3, 383 (2013).
5. H. Zhao，M. Chen，Y. Li，W. Zhang, *International Journal of Rock Mechanics and Mining Sciences*, **5**4, 43 (2012).
6. X. Chen ，C.P. Tan ，C. Detournay, *Journal of Petroleum Science and Engineerin*g, **38**(3), 145 (2003).
7. H. Huang，J.J. Azar，A. Hale, Numerical simulation and experimental studies of shale interaction with water-base drilling fluid. 1998.
8. Q. Tao，A. Ghassemi, *Geothermics*, **39**(3), 250 (2010).
9. A. Ghassemi，A. Diek, *Journal of Petroleum Science and Engineering*, 2002. **34**(1): p. 123-135.
10. R. Gelet ，B. Loret ，N. Khalili, *International Journal of Rock Mechanics and Mining Science*s, **50**, 65 (2012).
11. Q. Wang，Y. Zhou，G. Wang，H. Jiang，Y. Liu, *Petroleum Exploration and Development*, **39**(4), 508 (2012).
12. S. He ，W. Wang ，M. Tang ，B. Hu ，W. Xue, Journal of Natural Gas Science and Engineering, **21**, 338 (2014).
13. H. Wen ，M. Chen ，Y. Jin, K. Wang, Y. Xia, G. Dong, Ch. Niu, *Petroleum Exploration and Development*, **41**(6), 817 (2014).
14. M.E. Zeynali, *Journal of Petroleum Science and Engineering*, **82**, 120 (2012).
15. H. Roshan，M. Fahad, *International Journal of Rock Mechanics and Mining Sciences*, **52**, 82 (2012).
16. E.V. Oort，A.H. Hale，F.K. Mody，S. Roy, *SPE Drilling & Completion*, **11**(03), 137 (1996).
17. R.F.T. Lomba ，M.E. Chenevert ，M.M. Sharma, Chenevert, M.M. Sharma, *Journal of Petroleum Science and Engineering*, **25**(1–2), 25 (2000).
18. G. Chen，R.T. Ewy，M. Yu, J*ournal of Petroleum Science and Engineering*, **72**(1), 158 (2010).
19. K. Norrish, *Discuss. Faraday Soc*., **18**, 120 (1954).
20. J.C. Parker, *Clays Clay Miner.*, **28**(2), 135 (1980).
21. D. A. Laird, *Clays Clay Miner.*, **44**(4), 553 (1996).
22. N. Alcantar，J. Israelachvili，J. Boles, *Geochimica et Cosmochimica Acta*, **67**(7), 1289 (2003).
23. S.L. Barbour, D.G Fredlund, *Canadian Geotechnical Journa*l, **26**(4), 551 (1989).
24. P.K. Chatterji, N.R. Morgenstern, K.B. Hoddinott，R.O. Lamb, In *Physico-chemical aspects of soils and related materials*, ASTM International, 1095, 118 1990.
25. L. Ge, P. Hu, X.H. Xie, Z. Hu, Q. Zeng, J.B. Liao, *Oxid Commun,* **39**(1), 317 (2016).
26. L. Ge, Z. Hu, P. Chen, L. Shi, Q.Yang, J.B. Liao, *Mathematical Problems in Eng.*, Volume 2014, 1 (2014).
27. L. Ge, Z.Y. Wang, K. Deng, Q. Zeng, X. Wang, X.S. Chen, J.B. Liao, *Journal of the Balkan Tribological Association*, **21**(4), 897 (2015).
28. L. Ge, G.H. Wei, Q. Wang, Z. Hu, J.L.Li, *IEEE Sensors Journa*, **17**(18), 5831 (2017).
29. L. Ge, Q. Zeng, Z.Y. Wang, X.H. Xie, J.B. Liao, J.L. Li, *Oxid Commun*, **39**(1), 240 (2016).
30. R.F.T. Lomba ，M.E. Chenevert ，M.M. Sharma, *Journal of Petroleum Science and Engineering*, 25(1-2), (2000).

Mechanical properties and microstructure of hot rolled NM360/Q345R composite interface analysis

J. Li[1,3], L. Ma[1,2,3*], G. Zhao[1,2,3], Q. Huang[2,3], X. Yang[1,2,3], M. Cheng[1,2,3]

[1]Taiyuan University of Science and Technology, Taiyuan 030024,Shanxi,China
[2]Shanxi Provincial Key Laboratory of Metallurgical Device Design Theory and Technology,
[3].The Coordinative Innovation Center of Taiyuan Heavy Machinery Equipment

The rolling reduction rate is one of the important factors that affect the bonded reduction rates. The NM360/Q345R composite plates were analyzed by a universal tensile testing machine, OM, SEM and EDS. As the rolling reduction rate increased, both the tensile strength and the elongation increased. When the reduction rates were 30% and 50%, the bonding interface was poor and apparent cracks could be observed after the tensile tests. When the reduction rate reached 70%, no voids or cracks existed, the breaking interface was smooth and neat and the bonding interface formed a common structure. Significant decarbonization of NM360 occurred at the bonding interface. When the reduction rates were 30% and 50%, long strips or black dots of particles appeared near the interface. The black particles were Mn and Si oxides, which could have a negative effect on the bonding interface.

Key words: NM360/Q345R, Mechanical properties, Bonded interface, Microstructure.

INTRODUCTION

The wear-resistant composite steel plate is a new anti-wear composite material manufactured by a cladding technology, which could not only fully utilize the advantage of anti-wear alloys and base materials, but it could also make up for the corresponding shortcomings. Owing to their perfect performance not displayed by other single metals or alloys, the wear-resistant composite steel plates are widely utilized in various industrial fields [1-8].

The wear-resistant composite steel plates are often fabricated by an overlaying technology [9]. During overlaying, the base steel plate is unevenly heated; therefore the gradient of temperature fields is high. This could easily lead to high welding residual stress and deformation. Moreover, the overlaying leads to significant roughness of the overlaying surface, which could cause issues to further machining.

In hot roll bonding [10-12] rolling mills are utilized in the production of composite plates. As a result of the strong force of the rolling mill in combination with the thermal effect, two surfaces of compound metals are pressed together and plastic deformation occurs over the entire metallic cross-section [13].

Until recently, there have been only a few studies on wear-resistant hot rolled bonding plates has been significantly rare. Qiu (2017) studied the effects of rolling and heat-treatment on the structure and properties of the NM450D/ Q235B clad plate [14]. Gong studied the cladding rolling technology of the wear-resistant steel/carbon steel [15].

In this paper, the mechanical properties, the metallographic structure and microstructure of the wear-resistant steel 360 (NM360) - carbon steel Q345R composite plate after vacuum hot rolling were analyzed.

EXPERIMENTAL PROCEDURE

Fabrication of hot-rolled two-layered NM360/Q345R composite

In this study, the two-layered NM360/Q345R composite was roll-bonded, Q345R, being the base layer and NM360 the cladding layer. The chemical composition of Q345R and NM360 is presented in Table 1.

Firstly, the NM360 and Q345R steels were prepared and underwent surface treatment. The composite surface had to be cleaned and smoothly ground, which allowed the two types of metal atoms to mutually diffuse and reach a metallurgical bonding.

Table 1. Main chemical composition of NM360 and Q345R materials (mass fraction %)

	C	Si	Mn	P	S	Cr	Ni	Mo	B
NM360	≤0.25	≤0.70	≤1.30	≤0.025	≤0.010	≤1.40	≤1.00	≤0.50	≤0.004
Q345R	0.15	0.35	1.40	0.013	0.004	—	—	—	—

*To whom all correspondence should be sent:
E-mail: mlf060913@163.com

By a wire brush machine the surfaces were polished until the "sand surface" effect was observed, though the surface roughness surface roughness increase led to the subsequent rolled bonding of the composite.

Subsequently, the polished surfaces were cleaned with absolute ethanol for surface adhesion and oil removal. The surfaces were blown-dried. Secondly, the NM360 and Q345R steels were batched and welded with the clean surfaces facing each other. The composite slab was sealed by argon arc welding and the vacuum evacuating nozzle was welded. Finally, a two-stage diffusion vacuum pump was utilized for the slab to be pumped to the high vacuum state of 1.0×10^{-3}Pa and the suction nozzle was sealed at a high temperature by hot pressure.

The NM360 thickness was 3 mm and the Q345R thickness was 10 mm. The NM360/Q345R composite slabs were preheated at 1200°C and held at this temperature for 10 min. Consequently, hot rolling experiments were performed at 0.2 m/s, the stacks were roll bonded with reduction rates of 30%, 50% and 70%, respectively and cooled down in the air, subsequently to rolling. The sizes of the stacks and the rolling conditions of hot rolled composite are presented in Table 2.

Microstructure analysis and mechanical tests

In order to evaluate the rolling reduction effects of the NM360/Q345R composites on the tensile strength, the rolled composites were prepared according to the Chinese Standard GB/T 6396-2008, along the rolling direction. For the tensile fracture type study, the tensile fracture surfaces were observed by a scanning electron microscope (SEM).

The NM360/Q345R composites were polished and etched in a solution of 4% nitric acid and 96% ethyl alcohol. The RD-ND plane microstructure was observed by ultra-deep microscope (OM), scanning electron microscope (SEM) (ZEISS SIGMA FE-SEM) and EDS.

RESULTS AND DISCUSSION

Mechanical properties of NM360/Q345R composite plate

Fig.1 demonstrates the tensile strength data of the NM360/Q345R composites with various rolling reduction rates. The yield and tensile strength increased along with the elongation, as the rolling reduction rate increased. Regarding the NM360/Q345R composite at 70% rolling reduction rate, the yield and tensile strength reached the maximum of 396.12 MPa and 514.84 MPa respectively, whereas the elongation was the longest, 39.95%. The tensile strength revealed that

coherent and well-bonded layers could support each other; this had a direct effect on both the tensile strength and the elongation [16]. The best performance was observed when the reduction rate was 70%.
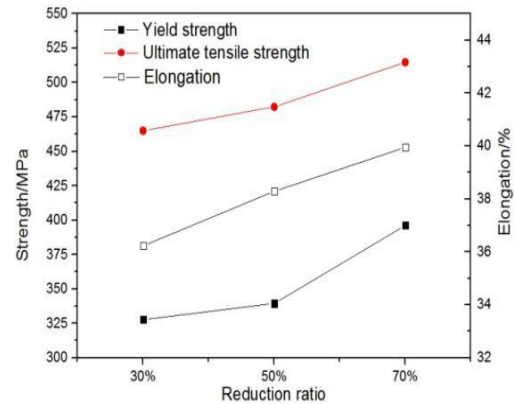

Fig. 1. Comparison of mechanical properties of NM360/Q345R composite

Tensile fractography

Fig. 2 a/b presents the fractography at 30% and 50% reduction rate, respectively. Subsequently to tensile failure, an apparent delamination could be observed from the low-magnification picture (100×) in these two conditions, which could be attributed to low bonded strength and poor compatibility of deformation. In NM360 and Q345R a high number of dimples existed, therefore it could be proved that the fracture type of the substrates was ductile. As the reduction rate increased, an increasing number of dimples on the substrates occurred and became increasingly low-sized. It could be observed that the toughness of every single layer was improved as the reduction rate increased, which could also be proved from the tensile mechanical properties.

Fig. 3 presents the tensile fracture morphology at 70% reduction rate. The bonding interface was quite straight and neat, no visible cracks and high-sized pores appeared which proved that the bonding performance was good, as shown in Fig. 3a/b. When the reduction rate increased to 70%, the interface was well-bonded and no delamination could be observed at the interface. Therefore, the bonding strength was high. Through further observation of the fracture morphology (Fig. 3b/c), it could be seen that the substrates near the interface displayed a number of dimples that were the typical ductile fracture feature, demonstrating that a ductile fracture occurred on the substrate. Compared to Q345R or te NM360, the dimples on the interface were quite close and the overall interface was well combined. From the aforementioned discussion, only at a reduction rate of 70%, good bonding between NM360 and Q345R could be obtained under the tested conditions.

Table 2. Various base layer thicknesses of rolling compound crafts

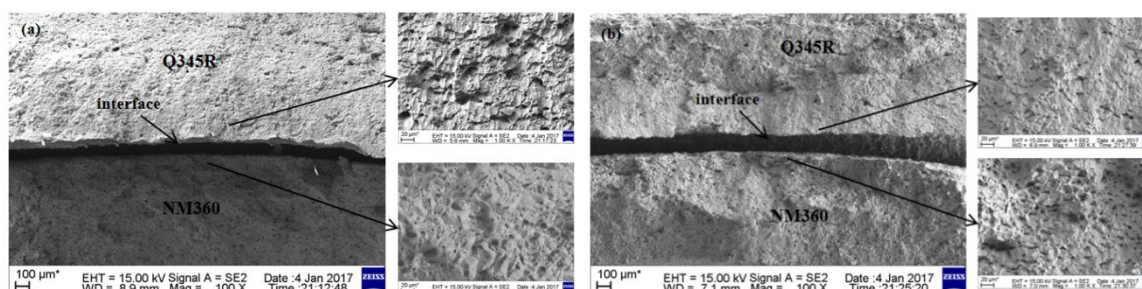|	Plate length+width	NM360	Q345	Rolling temperature	Rolling reduction rate
1	200×100	3mm	9mm	1150°C	30%
2	200×100	3mm	9mm	1150°C	50%
3	200×100	3mm	9mm	1150°C	70%

Figure. 2. Interface and fracture morphology of NM360/Q345R composite: (a) 30% reduction rate; (b) 50% reduction rate

CONCLUSION

This paper deduces the coupled flow of the water solution and its components on the basis of the irreversible thermodynamic theory. The results indicate that the effect of clay permeable membrane on the pore fluid flow is not significant. Combining with the potential equilibrium equation controlling the clay crystal swelling potential, the equilibrium equation for forces controlling the clay crystal swelling was developed. Ultimately, based on the modified effective stress laws, considering the physical-chemical coupled flow of the pore fluid in the shale formation and the clay hydration swelling effect, as well as the calculation models for the pore pressure, the effective stresses and the equivalent density of collapse pressure in shale formation were developed. The calculation results indicated that the coupled flow of the drilling fluid in the formation, the clay crystal swelling and the clay osmotic swelling have a significant effect on the borehole stability, and also showed that the effect of the clay crystal swelling is more significant than that of osmotic swelling.

REFERENCES

1. Y. Zheng，A. Zaoui，I. Shahrour, *Applied Clay Science*, **51**(1), 177 (2011).
2. J. Shi，H. Liu，Z. Lou，Y. Zhang，Y. Meng, Q. Zeng, M. Yang, et al., *Computational Materials Science*, **69**, 95 (2013).
3. F. Salles，J.M. Douillard，O. Bildstein，C. Gaudin，B. Prelot, J. Zajac, H. Van Damme, *Journal of colloid and interface science*, **395**, 269 (2013).
4. T. Schanz，M.I. Khan，Y. Al-Badran, Applied Clay Science, **83**, 383 (2013).
5. H. Zhao，M. Chen，Y. Li，W. Zhang, *International Journal of Rock Mechanics and Mining Sciences*, **54**, 43 (2012).
6. X. Chen，C.P. Tan，C. Detournay, *Journal of Petroleum Science and Engineering*, **38**(3), 145 (2003).
7. H. Huang，J.J. Azar，A. Hale, Numerical simulation and experimental studies of shale interaction with water-base drilling fluid. 1998.
8. Q. Tao，A. Ghassemi, *Geothermics*, **39**(3), 250 (2010).
9. A. Ghassemi，A. Diek, *Journal of Petroleum Science and Engineering*, 2002. **34**(1): p. 123-135.
10. R. Gelet，B. Loret，N. Khalili, *International Journal of Rock Mechanics and Mining Sciences*, **50**, 65 (2012).
11. Q. Wang，Y. Zhou，G. Wang，H. Jiang，Y. Liu, *Petroleum Exploration and Development*, **39**(4), 508 (2012).
12. S. He，W. Wang，M. Tang，B. Hu，W. Xue, Journal of Natural Gas Science and Engineering, **21**, 338 (2014).
13. H. Wen，M. Chen，Y. Jin, K. Wang, Y. Xia, G. Dong, Ch. Niu, *Petroleum Exploration and Development*, **41**(6), 817 (2014).
14. M.E. Zeynali, *Journal of Petroleum Science and Engineering*, **82**, 120 (2012).
15. H. Roshan，M. Fahad, *International Journal of Rock Mechanics and Mining Sciences*, **52**, 82 (2012).
16. E.V. Oort，A.H. Hale，F.K. Mody，S. Roy, *SPE Drilling & Completion*, **11**(03), 137 (1996).
17. R.F.T. Lomba，M.E. Chenevert，M.M. Sharma, Chenevert, M.M. Sharma, *Journal of Petroleum Science and Engineering*, **25**(1–2), 25 (2000).
18. G. Chen，R.T. Ewy，M. Yu, J*ournal of Petroleum Science and Engineering*, **72**(1), 158 (2010).
19. K. Norrish, *Discuss. Faraday Soc.*, **18**, 120 (1954).
20. J.C. Parker, *Clays Clay Miner.*, **28**(2), 135 (1980).
21. D. A. Laird, *Clays Clay Miner.*, **44**(4), 553 (1996).
22. N. Alcantar，J. Israelachvili，J. Boles, *Geochimica et Cosmochimica Acta*, **67**(7), 1289 (2003).
23. S.L. Barbour, D.G Fredlund, *Canadian Geotechnical Journal*, **26**(4), 551 (1989).
24. P.K. Chatterji, N.R. Morgenstern, K.B. Hoddinott，R.O. Lamb, In *Physico-chemical aspects of soils and related materials*, ASTM International, 1095, 118

1990.

25. L. Ge, P. Hu, X.H. Xie, Z. Hu, Q. Zeng, J.B. Liao, *Oxid Commun,* **39**(1), 317 (2016).
26. L. Ge, Z. Hu, P. Chen, L. Shi, Q.Yang, J.B. Liao, *Mathematical Problems in Eng.*, Volume 2014, 1 (2014).
27. L. Ge, Z.Y. Wang, K. Deng, Q. Zeng, X. Wang, X.S. Chen, J.B. Liao, *Journal of the Balkan Tribological Association*, **21**(4), 897 (2015).
28. L. Ge, G.H. Wei, Q. Wang, Z. Hu, J.L.Li, *IEEE Sensors Journa*, **17**(18), 5831 (2017).
29. L. Ge, Q. Zeng, Z.Y. Wang, X.H. Xie, J.B. Liao, J.L. Li, *Oxid Commun*, **39**(1), 240 (2016).
30. R.F.T. Lomba，M.E. Chenevert，M.M. Sharma, *Journal of Petroleum Science and Engineering*, 25(1-2), (2000).

Effect of additives on thiosulfate leaching of a gold ore

S.J. Dai, P.C. Li, Q.Q. Wang[*], D.W. Feng

University of Science and Technology, Liaoning, Anshan, China

The effect of additives on gold leaching was investigated using ammonium thiosulfate or calcium thiosulfate. Thiosulfate stability was evaluated with additive dosage and thiosulfate type, usage, and ageing. The study results showed that ethylene diaminetetraacetic acid (EDTA) at its optimum concentration of 2 mM enhanced gold leaching and slightly improved the stability of gold thiosulfate species in solution while carboxy methyl cellulose (CMC) improved gold leaching, but gold was not stable in solution. There was an optimum CMC dosage, and beyond this, further addition of CMC hindered gold leaching. The surfactant sodium dodecyl sulfate (SDS) had a similar effect to CMC. At an agitation speed of 250 r/min, 100% leach recovery of gold was achieved with 0.03 M fresh ammonium thiosulfate, 2 mM EDTA after 11 h leach. In a resin-in-leach system, full gold recovery was also achievable with sufficient resin after 24 h leach with 0.06 M fresh ammonium thiosulfate and 2 mM EDTA at an agitation speed of 250 r/min.

Key words: Gold leaching, Thiosulfate, Additives, Leaching kinetics, Thiosulfate stability

INTRODUCTION

In recent years extensive research has focused on thiosulfate as a potential alternative lixiviant for gold due to the growing environmental and public concerns over the use of cyanide [1-4]. From an economic point of view, it is required that the leaching should be carried out under low reagent concentrations over extended periods where reagent consumption is low. In order to achieve this, stabilization of thiosulfate and gold thiosulfate in solution and reduction of passivation to allow gold leaching over extended periods are among the key issues to be concerned [5-7]. From previous experience, ore mineralogy is known to affect thiosulfate leaching of gold and the stability of thiosulfate and gold thiosulfate species. Specifically, sulfide minerals retard gold leaching and catalyse the degradation of thiosulfate and gold thiosulfate. Other reductants, e.g. carbonaceous matter, have also been found to affect the stability of thiosulfate and gold thiosulfate. Semi-conductive iron minerals, especially newly formed iron mineral phases generated in the leach system, were also reported to influence the stability of thiosulfate. Silica is not usually viewed as problematic in gold hydrometallurgy, but previous tests have shown that newly formed silica generated *via* acid or alkaline processing of silicate minerals and/or during calcination has a high adsorption capability, and strong reducing power for both Au(I) and Au(III) [8-11].

Thus, at low reagent concentrations the stability of thiosulfate and gold thiosulfate is a problem in natural ores where amorphous silica and iron oxide are present. Because of this, the use of surfactants to manipulate the mineral particle surface properties to reduce the catalytic decomposition of thiosulfate and gold thiosulfate is necessary. In addition, the stabilization of thiosulfate and gold thiosulfate can be realised through manipulation of the solution chemistry using additives. Our previous studies have shown that the combination of solution and surface chemistry modification is able to stabilize the thiosulfate leaching system [12-15]. In this paper, the effect of selected additives on thiosulfate leaching of a gold ore, *i.e.* EDTA, carboxy methyl cellulose (CMC) and sodium dodecyl sulfate (SDS) was investigated.

EXPERIMENTAL

Materials

A milled gold ore sample with a solid content of 50% was provided by a gold mine and used in the leaching tests without further treatment. The gold ore sample was a refractory ore mainly containing 6 g Au/t, about 3% pyrite and 0.8% carbonaceous matter.

Laboratory reagent grade ammonium thiosulfate was purchased from Chem Supply (Australia). For comparison, an aged and consolidated ammonium thiosulfate from the same supplier was used as well. Calcium thiosulfate (30%) was used and the product has been stored in a sealed drum in the lab for over 6 years. Some precipitates appeared and some yellowish materials were present at the outlet. These materials, likely degradation products of calcium thiosulfate, may affect gold leaching. Hydrochloric and nitric acids were obtained from Merck. EDTA (disodium salt), CMC (sodium salt) and SDS were

---

*To whom all correspondence should be sent:
E-mail: wqq52526@126.com

provided by BDH Laboratory Supplies. MilliQ water was used in the tests. An anionic ion exchange resin was used in the resin-in-leach tests.

Analytical techniques

Elemental concentrations in solutions were determined by ICP-OES (Varian Instruments). Thiosulfate concentration was determined by the iodometric method. Fire assay was used to determine gold content in selected leach residues. Gold-loaded resins were ashed in a furnace at 640 °C for 1 h and the ash was digested in *aqua regia*. The elemental concentrations in the acidified solutions were determined by ICP-OES.

Leaching

Leaching of the ore samples was performed in 1.5 L baffled PVC reactors using overhead stirrers with flat-blade impellers. Slurry of 1.4 kg with a solid content of 35% was mixed with desired amounts of calcium or ammonium thiosulfate. All additives were mixed with the ore slurry and heated to 50 °C, followed by the addition of thiosulfate for leaching. A natural pH of about 8 was used in the leaching. Leaching was performed at $50 \pm 1°C$. Samples were taken regularly over 24 h. Samples were filtered, then immediately iodine titrated for thiosulfate determination and analysed by ICP-OES after dilution. Recovery of gold was defined as the percentage of dissolved gold in relation to the gold in the ore. Leach residues of 24 h were fire assayed for determination of gold contents. Mass balance calculations showed a good agreement.

RESULTS

Effect of additives on gold leaching with calcium thiosulfate

Fig. 1 shows the leaching results of the ore slurry with 0.03 M CaS_2O_3 at a stirring rate of 200 r/min. As shown in fig. 1, under the baseline condition, gold recovery reached its maximum at 7 h and dropped afterwards. However, the dissolved gold was not stable in solution, which is likely linked with the surface properties of the mineral particles in the ore. Thiosulfate and gold thiosulfate species interact with the mineral particles (especially sulfide minerals) as well as carbonaceous matter, causing instability of the gold thiosulfate species.

Addition of EDTA increased gold recovery but reduced the initial kinetics. This effect became more noticeable with increased EDTA concentration up to 2 mM. Gold recovery still decreased over time, but to a lesser extent in the presence of EDTA.
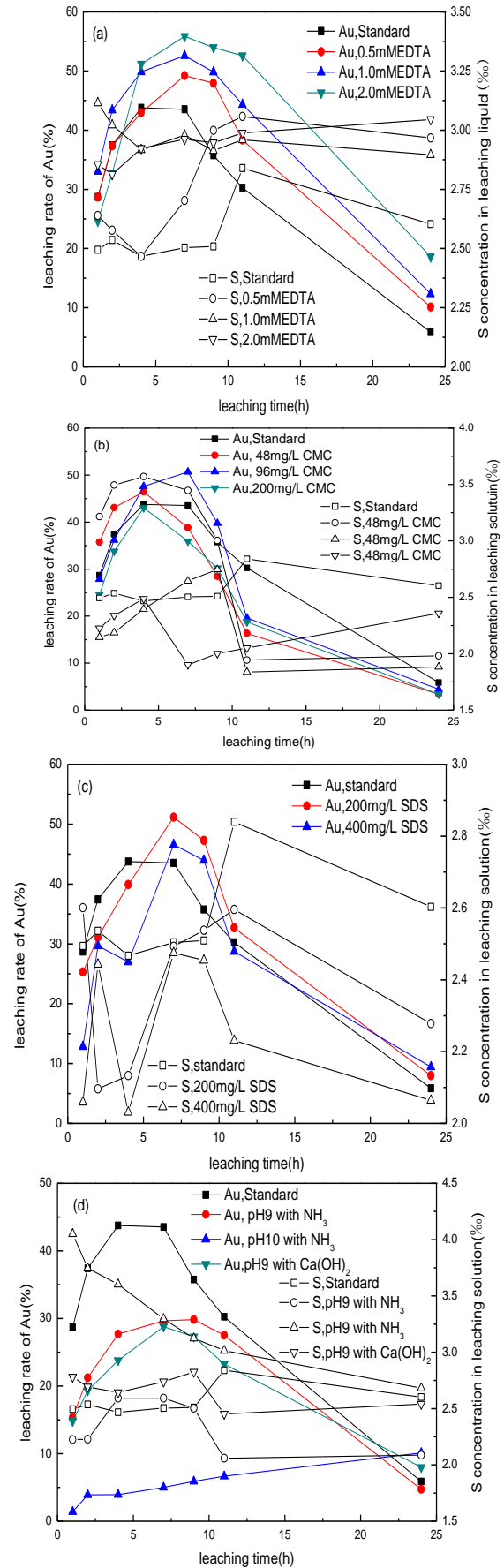

Fig. 1. Leaching results of the gold ore with different additives: (a) EDTA; (b) CMC; (c) SDS; (d) NH_3 and $Ca(OH)_2$

The leaching of sulfide minerals increased with the addition of EDTA, as reflected by the increased sulfur concentration in solution. CMC slightly increased gold recovery at low concentration but hindered gold leaching at a high concentration. At low CMC concentrations, the S concentration increased initially, but dropped substantially together with gold after prolonged leaching. The surfactant sodium dodecyl sulfate (SDS) slightly enhanced gold recovery at a lower concentration, but could not stabilise gold thiosulfate in solution. Gold recovery decreased at a higher pH with the addition of ammonia, despite the higher sulfide leaching. This is because the mixed solution potential substantially decreased at a higher pH level. At an elevated pH, ammonia was more beneficial for gold leaching than calcium hydroxide, due to the enhanced leaching of the sulfide minerals with ammonia.

Effect of stirring speed on gold leaching

Fig. 2 shows the leaching of the slurry feed with CaS_2O_3 and EDTA conducted at 200 and 250 r/min, respectively.
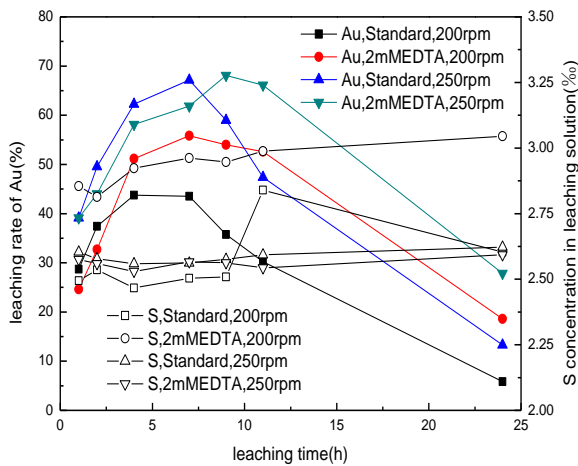

Fig. 2. Effect of stirring speed on gold leaching

In comparison with 200 r/min stirring speed, a higher stirring speed of 250 r/min gave a higher gold recovery at 0.03 M CaS_2O_3. A higher stirring speed may cause slightly higher attrition among mineral particles and hence clean surface for gold leaching. In addition, a high stirring speed may lead to the absorption of more O_2 from the air into the solution. The dissolved oxygen concentration should thus be higher at a higher stirring speed.

The trends observed at higher stirring rates were consistent with those obtained at 200 r/min; EDTA again decreased initial leaching kinetics but stabilized gold thiosulfate to some extent.

Effect of dosage of EDTA on gold leaching with calcium thiosulfate

Leaching of the slurry feed with 0.03M CaS_2O_3 was conducted at 250 r/min, and the results are shown in Fig. 3.
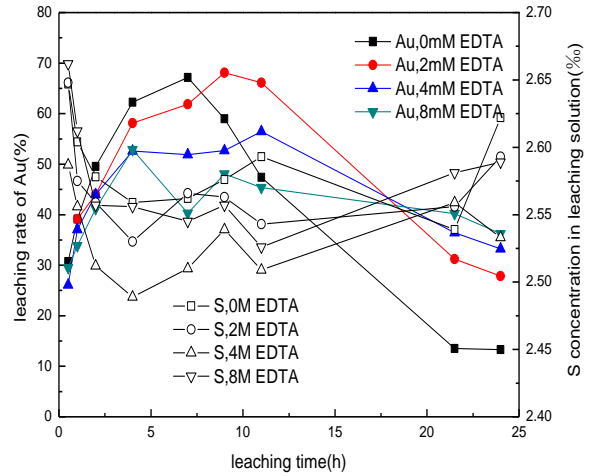

Fig. 3. Effect of dosage of EDTA on gold leaching

Fig. 3 shows that gold recovery reached its maximum at 7 h and dropped afterwards with no EDTA. The dissolved gold was not stable in solution, which is probably related to the surface properties of the mineral particles in the ore. Addition of EDTA increased gold recovery but reduced the initial kinetics. The gold recovery reached its maximum of 68.11% for 9 h and dropped afterwards with increased EDTA concentration up to 2 mM. A higher EDTA dosage caused a drop in gold recovery and reduced the initial kinetics with a concentration more than 2 mM. Gold recovery reached its maximum at 11 h and dropped afterwards with 4 or 8 mM EDTA. Gold recovery still decreased over time, but to a lesser extent in the presence of EDTA. The leaching of sulfide minerals increased with the addition of EDTA, as reflected by the increased sulfur concentration in solution. Thus, EDTA enhanced gold leaching and slightly improved the stability of gold thiosulfate species in solution, and its optimum concentration was 2 mM.

Effect of dosage of CaS_2O_3 and $(NH_4)_2S_2O_3$ on gold leaching

Fig. 4 shows the leaching of the slurry feed with CaS_2O_3 and $(NH_4)_2S_2O_3$ at 2 mM EDTA and 250 r/min.

Gold recovery increased at a higher thiosulfate concentration, and gold thiosulfate species became more stable in solution with time. When added at the same concentration, $(NH_4)_2S_2O_3$ gave a higher gold recovery than CaS_2O_3. This is because the sulfide minerals were leached to a greater extent in the

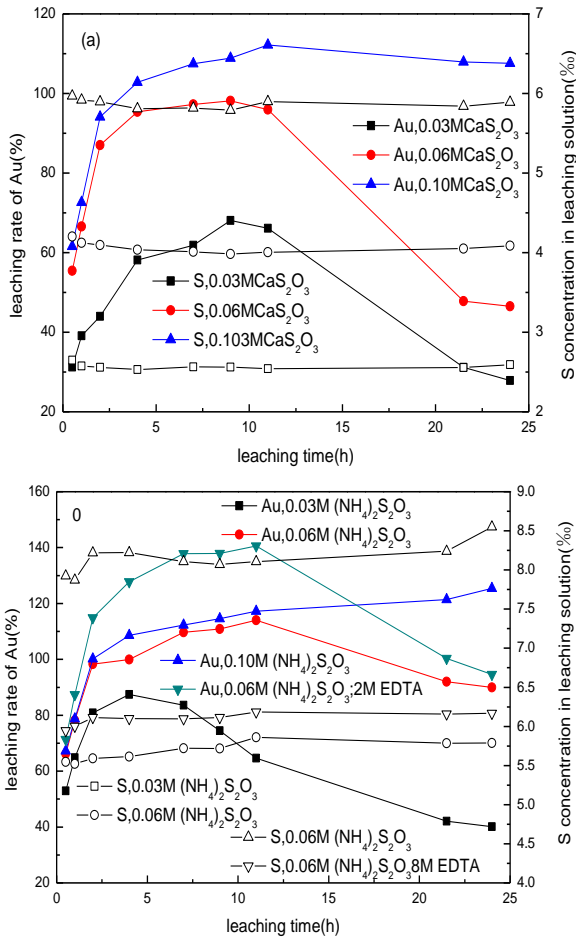presence of $(NH_4)_2S_2O_3$, as indicated by the higher sulfur content in solution. Leaching of the sulfide

Fig. 4. Effect of dosage of (a) CaS_2O_3 and (b) $(NH_4)_2S_2O_3$ on gold leaching

minerals mainly occurred at the particle surfaces. Thus, higher leaching of the sulfide minerals appears to have reduced the interactions between thiosulfate/gold thiosulfate species and the sulfide mineral surfaces. EDTA enhanced gold leaching and slightly improved the stability of gold thiosulfate species in solution. EDTA enhanced gold leaching and slightly improved the stability of gold thiosulfate species in solution by using $(NH_4)_2S_2O_3$ as leaching agent. In some cases, the gold recovery was over 100% according to the dissolved gold concentration determined by ICP-OES. Analytical discrepancies resulting from the interference of other elements such as Fe may cause this phenomenon. However, the results do show that almost full gold recovery was achieved using ≥0.06 M CaS_2O_3 with 2 mM EDTA or $(NH_4)_2S_2O_3$.

The variation in thiosulfate concentration in leaching is shown in Fig. 5.

Fig. 5 presents the variation in thiosulfate concentration in leaching the slurry sample with CaS_2O_3 and $(NH_4)_2S_2O_3$. In the CaS_2O_3 leaching systems, thiosulfate degraded, and this appeared to

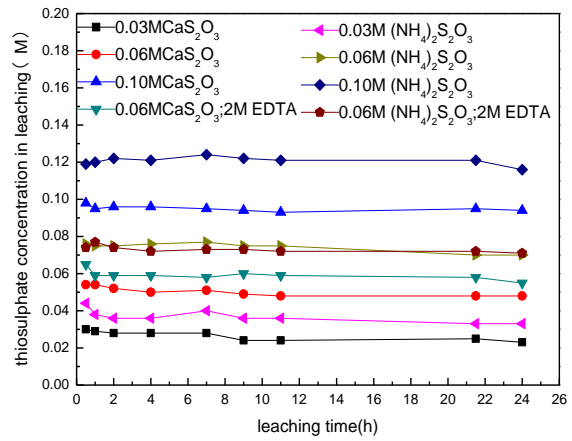**Fig. 5.** Variation of $S_2O_3^{2-}$ concentration in leaching slurry feed with CaS_2O_3 and $(NH_4)_2S_2O_3$. Stirring speed 250 r/min.

be more noticeable at a lower concentration. EDTA slightly enhanced the stability of thiosulfate. In contrast, thiosulfate degradation was limited in the $(NH_4)_2S_2O_3$ leaching system. The titrated thiosulfate concentrations after leaching were even higher than the initial thiosulfate concentrations. This is believed to be because some sulfide or oxysulfate species were generated in the leaching of the sulfide minerals due to ammonia. The formed intermediate sulfur species, e.g. S^{2-} and S_8, were found to cause the loss of gold to leach residues, even in trace concentrations. The presence of dissolved S^{2-} may result in gold precipitation, and S_8 has high affinity for gold species.

Resin-in-leach

For each resin-in-leach test, 5 ml of anionic resin was added into the leach slurries to enable sorption, and then separated from the slurries after 7 h or 24 h using a 300 μm sieve. The loaded resins were washed with deionised water, dried and ashed for acid digestion. To reduce the breakdown of resin in the leaching tanks, the stirring speed was reduced to 200 r/min. The resin-in-leach results are displayed in Table 1.

In the presence of 5 ml of resin, the gold recovery dropped slightly at 0.06 M CaS_2O_3 between 7 h and 24 h. In all other cases, the gold recovery increased from 7 h to 24 h.

There was still some gold remaining in solution with the addition of 5 mL of resin, which indicates either that the ion exchange capacity of 5 mL of resin was insufficient for uptake of all gold, or that other metal species present saturated the resin. EDTA showed no impact on gold adsorption on the resin, and gold recovery increased in the presence of EDTA with resin. At 0.06 M $(NH_4)_2S_2O_3$, the gold recovery approached 100% with the addition of 2 mM EDTA.

51

Table 1. Resin-in-leach tests. Stirring speed 200 r/min

Conditions	Solution	Resin	Overall	Residue
0.06 M CaS$_2$O$_3$,7 h	7.57	72.74	80.31	23.1
0.06 M CaS$_2$O$_3$, 24 h	3.93	74.56	78.49	14.2
0.06 M CaS$_2$O$_3$, 12 mM EDTA,7 h	7.94	69.57	77.51	24.6
0.06 M CaS$_2$O$_3$, 12 mM EDTA, 24 h	8.14	87.90	96.04	5.70
0.06 M (NH$_4$)$_2$S$_2$O$_3$,7 h	4.58	69.7	74.32	27.5
0.06 M (NH$_4$)$_2$S$_2$O$_3$, 24 h	12.81	78.55	91.36	10.1
0.06 M (NH$_4$)$_2$S$_2$O$_3$, 2 mM EDTA, 7 h	8.22	83.75	91.97	11.3
0.06 M (NH$_4$)$_2$S$_2$O$_3$, 2 mM EDTA, 24 h	12.94	89.36	102.3	3.2

Effect of ageing of (NH$_4$)$_2$S$_2$O$_3$ on gold leaching

Fig. 6 shows the leaching results with fresh and aged 0.06 M (NH$_4$)$_2$S$_2$O$_3$ at a stirring speed of 250 r/min.
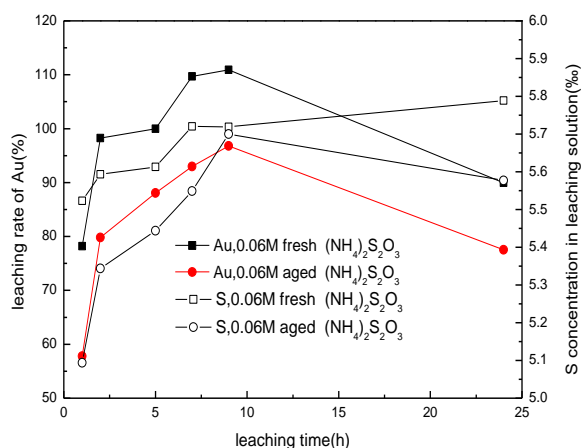
Fig. 6. Influence of ageing of (NH$_4$)$_2$S$_2$O$_3$ on gold leaching

The aged (NH$_4$)$_2$S$_2$O$_3$ was stored in the laboratory for over a couple of years, and the crystals were consolidated. Also, thiosulfate probably degraded to some extent after ageing. The aged (NH$_4$)$_2$S$_2$O$_3$ provided a relatively lower gold recovery. The degradation of thiosulfate may form intermediate sulfur species such as elemental sulfur, which may cause the loss of gold.

DISCUSSION AND CONCLUSIONS

Ammonium thiosulfate showed better leaching performance than calcium thiosulfate at the same concentration, at least in part because ammonium thiosulfate leached more sulfide minerals than calcium thiosulfate. This will reduce the galvanic interactions among sulfide minerals and the interactions between thiosulfate/gold thiosulfate species and the sulfide minerals, hence reducing leaching passivation, as well as precipitation of gold.

Gold recovery increased and gold became more stable in solution over time at a higher thiosulfate concentration. A higher stirring speed was beneficial for gold recovery and stability. At a relatively low solids content of 35%, the attrition among the mineral particles is expected to be low. At 50 °C, the dissolved oxygen content will be low in the leaching

solution. A higher oxygen intake at a higher stirring speed is assumed to be a significant factor in the observed higher gold recovery. In sulfide mineral-containing systems, intermediate sulfur-containing reaction products including S^{2-} and S$_8$ are present. S^{2-} and S$_8$ can cause gold loss when present even in trace amounts. In the presence of oxygen, S^{2-} can react with S$_2$O$_3$$^{2-}$ to form SO$_3$$^{2-}$ according to (1):

$$S_2O_3^{2-} + S^{2-} + 3O_2 + 2e^- \leftrightarrow 3SO_3^{2-} \qquad (1)$$
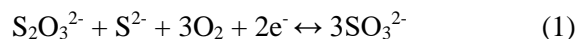
The S^{2-} concentration should remain lower at higher dissolved oxygen content, and S$_8$ should be also lower. However, this needs to be further investigated to be proven.

EDTA increased gold recovery and gold stability, and this beneficial effect became more pronounced at a higher concentration. Gold recovery from the slurry sample approached 100% after 24 h at 0.06 M calcium or ammonium thiosulfate with the addition of EDTA. CMC improved gold leaching, but gold was not stable in solution. There was an optimum CMC dosage, and beyond this, further addition of CMC hindered gold leaching. The surfactant SDS had a similar effect to CMC. EDTA has complexing abilities, which enhance the leaching of sulfide surfaces and reduce the interference of heavy metals. This will reduce the galvanic interactions among sulfides, as well as the catalytic interactions between thiosulfate/gold thiosulfate and the sulfide minerals. Surfactants such as SDS and CMC mainly act to modify particle surfaces, minimising the leaching passivation. In an ammonia-copper-thiosulfate system, S^{2-} and S$_8$ are unlikely to be present in solution, because Cu^{2+} ions could efficiently precipitate S^{2-}. The mixed solution potential is also higher, reducing the possibility of S$_8$ formation. Thus, additives should be used to remove the S^{2-} and S$_8$ species, and/or operating conditions should be changed to minimise the formation of S^{2-} and S$_8$ species. Therefore, a combination of various additives should be used to improve gold leaching and to keep gold stable in solution.

Aged thiosulfate gave a lower gold recovery than the freshly purchased batch. Polythionates and S$_8$

may be present in the aged thiosulfate. Polythionates cause lower gold leaching and S_8 adsorbs gold.

EDTA had little impact on adsorption of gold thiosulfate on resin. In the resin-in-leach process, almost full gold recovery was achieved at 0.06 M thiosulfate with the addition of EDTA. It should be noted that not all variables were optimised, e.g. resin usage, thiosulfate and EDTA concentrations. In the resin-in-leach process using ammonium thiosulfate and EDTA, gold recovery reached over 90% after 7 h. With process optimisation, it was expected that full gold recovery can be achieved in shorter time in resin-in-leach using ammonium thiosulfate and EDTA.

Thiosulfate consumption was higher for calcium thiosulfate at lower concentrations. In contrast, thiosulfate consumption was negligible for ammonium thiosulfate leaching. The titrated thiosulfate concentration after leaching was even higher than its original concentration in the case of ammonium thiosulfate. Ammonium thiosulfate enhanced the leaching of the sulfide minerals in the ore, generating various sulfur species to stabilise thiosulfate. Even for calcium thiosulfate, the thiosulfate consumption was relatively low. Thus, the stability of gold thiosulfate species was not directly linked to the stability of thiosulfate. This further indicates that traces of S^{2-} and S_8 should be blamed for gold drop with time.

REFERENCES

1. M.G. Aylmore, D.M. Muir, *Minerals Engineering*, **14**, 135 (2001).
2. C. Abbruzzese, Fomaria, R. Massidda, F. Vegli, S. Ubaldini, *Hydrometallurgy*, **39**, 265 (1995).
3. DAR. Murthy, P.M. Prasad, *Hydrometallurgy*, **42**, 27 (1996).
4. P. Navarro, C. Vargas, A. Villarroel, F.J. Alguacil, *Hydrometallurgy*, **65**, 37 (2002).
5. D.W. Feng, J.S.J. van Deventer, *Minerals Engineering*, **23**, 143 (2010).
6. G. Senanayake, *Hydrometallurgy*, **115-116**, 1 (2012).
7. D.W.Feng, J.S.J. van Deventer, *Minerals Engineering*, **24**, 115 (2010).
8. D.W. Feng, J.S.J. van Deventer, *Hydrometallurgy*, **82**, 126 (2006).
9. D.W.Feng, J.S.J. van Deventer, *International Journal of Mineral Processing*, **82**, 138 (2007).
10. D. W.Feng, J.S.J. van Deventer, *Minerals Engineering*, **20**, 273 (2007).
11. G. Senanayake, X.M. Zhan, *Hydrometallurgy*, **115-116**, 21 (2012).
12. H. Yu, F.T.Zi, X.Z.Hu, J. Zhong, Y.H. Nie, Pengzhi Xiang, *Hydrometallurgy*, **150**, 178 (2014).
13. J. Zhao, Z.C. Wu, J.Y. Chen, *Hydrometallurgy*, **46**, 3632 (1997).
14. E. Guerra, D.B. Dreisinger, *Hydrometallurgy*, **51**, 1552 (1999).
15. P.L. Breuer, M.I. Jeffrey, *Minerals Engineering*, **13**, 1071 (2000).

Study on the effect of diesel blended with n-butanol on particulate matter state characteristics of a small agricultural diesel engine

L. Chen [1,2*], Z. Wang [1], S. Liu [1]

[1]School of Automotive and Traffic Engineering, Jiangsu University, Zhenjiang, China
[2] CATARC Yancheng Automotive Proving Ground Ltd. Yancheng, China

This work studied the effect of diesel blended with n-butanol on particulate matter (PM) state characteristics of a small agricultural diesel engine which revealed the mechanism of n-butanol reducing PM emissions in diesel engine. The microstructure, oxidation characteristics, components and surface functional groups of PM with N5 (5% n-butanol and 95% diesel fuel in quality basis), N10 and diesel fuel were measured. The results indicated that n-butanol/diesel PM displayed cluster structure. With the increase in n-butanol content, the average diameter of PM gradually decreased while aggregation degree increased. Pyrolysis of PM in the air was divided into two stages - soluble organic matter evolution stage and soot combustion stage. With the increase in n-butanol content, the initial combustion temperature of soot decreased, the temperature corresponding to the mass change rate peak of weightlessness with PM dropped, soluble organic matter and soot content in particulate fractions increased, while metal and inorganic salt content decreased. The equivalent peak height ratio (IC-H-IC=C)/IC=C of aliphatic functional C-H on particulate surface increased and its relative content gradually increased.

Key words: Particulate matter, n-Butanol, Microstructure, Diesel engine

INTRODUCTION

Particulate matter (PM) is the main pollutant of diesel engine; it discharges into the atmosphere environment and suspends in the atmosphere for a long time. Besides, PM from diesel engine can involve in the formation of haze, and affect the human physical and mental health. [1-4] As alternative fuels, oxygenated fuels include alcohols, esters and ethers that are widely used in diesel engine for today's applications and effectively control the diesel PM emissions.

Many scholars have carried out studies on the characteristics of PM formed by the mixing of oxygenated fuels for diesel engine. Chen [5] has studied the particle size distribution of diesel engine with ethanol/methyl ester/diesel combustion PM. The results showed that in the oxygenated fuel, PM were essentially unchanged with a size greater than 0.5 μm, the number of PM decreased when the size was between 0.2~0.5 μm, and the number increased when the size was less than 0.2 μm. Carbon cores formed by burning of oxygenated fuels are less in comparison with diesel fuel. Tsolakis' studies showed that biodiesel PM coagulated and aggregated to spherical fundamental particulates. The PM were arranged closely in grape-like state and clusters, while the structure of the diesel PM was loose in a state of chain [6].

As a kind of alcohol fuel, N-butanol is one of the best additives for diesel engines due to its features such as high oxygen content and intersolubility with diesel. It is widely used in the blending of methanol and diesel fuel. The physical and chemical properties of n-butanol are close to diesel fuel and cause little corrosions without needing to rebuild the structure of the original fuel supply control systems. This is the particular reason for directly applying a low ratio of n-butanol blending to diesel in the diesel engine [7-9].

Great progress has been made in this field; however the effect of diesel blended with n-butanol on PM state characteristics has not been fully characterized. Compared with vehicle diesel engine, the moving range of off-road diesel engine such as the agricultural machinery, engineering machinery and so on is small, which leads to high PM emission [10-12]. In view of this, the study takes off-road diesel engine 186F as the research object which is widely applied in pump and diesel engine power generator units. n-Butanol/diesel blended fuel was studied with the aid of scanning electron microscopy, thermogravimetric analysis, and infrared spectroscopy. The studies covered various aspects of microstructure, oxidation characteristics, components and distribution of surface functional groups of n-butanol/diesel combustion particulates. The study investigates the effects of n-butanol on the state characteristics of diesel engine particulates which provide a theoretical basis for revealing the mechanism of n-butanol reducing particulate emission of diesel engine, as well as the promotion

*To whom all correspondence should be sent:
E-mail: chenlin@catarc.ac.cn

of n-butanol substituted fuel for off-road diesel engine.

EXPERIMENTAL

Test for diesel engine and fuels

The experimental work was conducted on 186F diesel engine, and the main technical parameters are shown in Table 1.

Table 1. Main parameters of 186F diesel engine

Project	Parameter
Engine type	Single-cylinder, direct injection, air cooling
Bore	86 mm
Stroke	70 mm
Rated power	5.7 kW
Rated speed	3000 rpm
Compression ratio	19
Link length	117.5 mm
Displacement	0.406 L
Supply advance angle	12°CA

Test materials for the experiment were diesel and anhydrous n-butanol, from which three kinds of fuel on the basis of diesel were prepared: diesel fuel, N5 w (5% n-butanol and 95% diesel fuel on quality basis), N10 w (10% n-butanol and 90% diesel fuel on quality basis).

The cetane number of n-butanol is less than that of diesel fuel. The mass fraction of oxygen was about 21.6% which effectively improved the oxygen concentration of the blended fuel and perfected the fuel combustion process. The calorific value of n-butanol was lower by 77% than that of diesel fuel, and the calorific value of the blended fuel slightly decreased on blending with a small amount of n-butanol.

Test scheme

The bench test was carried out on the premise of unchanged supply advance angle and structural parameters of the diesel engine. The schematic diagram of the test system is shown in Figure 1.
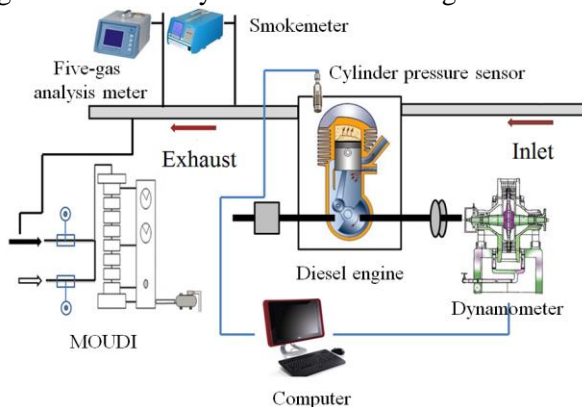

Fig. 1. Schematic diagram of the test system

For sampling, aluminum foil filter paper was used whose microporous diameter was 47 nm, the sampling rate was 6 L/min, and the sampling time lasted 30 min. The collected samples were characterized by scanning electron microscopy, thermogravimetric analysis and infrared spectra to discuss the effects of n-butanol on PM state characteristics.

RESULTS AND DISCUSSION

Soot emission

The change law of smoke intensity value with different loads at a speed of the diesel engine of 1800 rpm and 3000 rpm is shown in Figure 2.
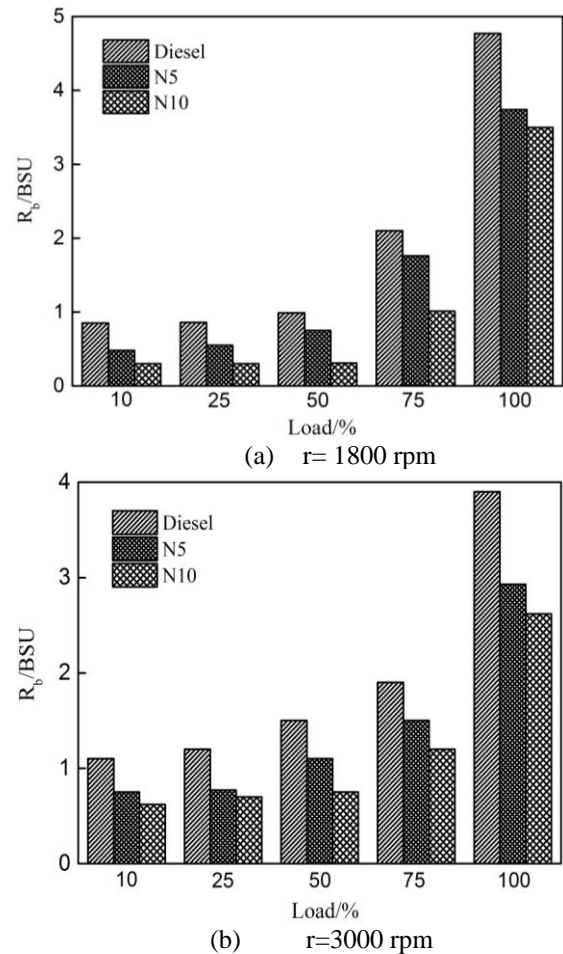

(a)   r= 1800 rpm

(b)   r=3000 rpm

Fig.2. Effects of different n-butanol blends on soot emission

As shown in Figure 2, the trends of soot emission with the three tested fuels were basically the same. The fuel burnt completely and the possibility of soot generation was small at the low load. The smoke value obviously increased with the load increase at medium-to-high load. At the high load, the superfluous air coefficient decreased, air mixed unevenly in the combustion chamber, which resulted in a low air-to-fuel ratio in some areas, incomplete combustion of fuel and generation of a

lot of soot. The smoke intensity value sharply increased. Under the same conditions, smoke intensity value gradually decreased with the increase in n-butanol content. Compared with diesel fuel, smoke intensity value of N10 obviously decreased and was reduced by 26.7% and 32.8% at the speed of 1800 rpm and 3000 rpm, respectively, with full load. Diesel blended with n-butanol could reduce soot emissions for the main factors: Compared with diesel fuel, the vaporization heat of n-butanol is high. By blending with n-butanol, the vaporization heat of the blended fuel increased which resulted in the addition of heat absorption. The time of physical and chemical reaction was prolonged and the ignition delay period was extended.

Microstructure

The PM microstructure of the three tested fuels was recorded by scanning electron microscopy (8×10^4 magnification). The results are shown in Figure 3.

(a) PM microstructure of diesel

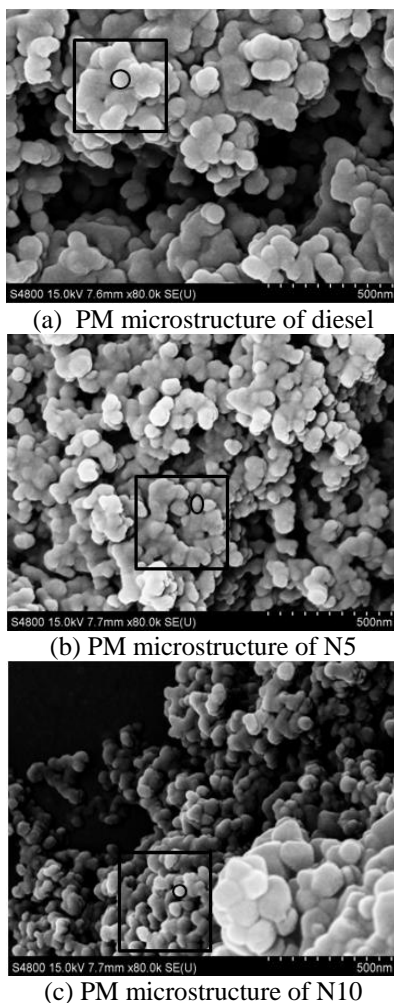(b) PM microstructure of N5

(c) PM microstructure of N10

Fig. 3. SEM images of n-butanol/ diesel combustion PM

Under the action of adhesive forces such as van der Waals force, electrostatic force, liquid bridge force and so on, the PM showed clusters as a whole and accumulated by hundreds of unequigranular spherical basic accumulations of carbon particulates which formed different density of PM. Average diameter of PM was calculated by the number of per unit area by scanning electron microscopy. The average diameters of PM with diesel, N5 and N10 were 1.43, 0.85, 0.52 μm, respectively. The average size of the PM decreased with the increase in n-butanol content. The reasons why blending n-butanol could decrease the size were as follows: (1) n-butanol could reduce the concentration of polycyclic aromatic hydrocarbons in the precursor of soot; decrease the formation of nuclear particulates; reduce the polymerization ability of carbon nuclei, and decrease the size of formed particulates [13]; (2) as an oxygenated additive fuel, n-butanol improved the combustion process and promoted the transformation of PM in the diesel engine; (3) at high temperature, n-butanol easily cracked into longer-living radicals which could oxidize PM and reduce the diameter of the carbon nuclei in the process of PM formation.

The SEM images of diesel engine PM revealed typical fractal structure, and the growth mechanism of PM determined its fractal structure characteristics. The agglomeration morphology of PM was mainly divided into settlement by gravity, diffusion of PM in the process of turbulence and irregular Brown motion [14]. For further analyzing the geometric structure characteristics of PM, the density of pellet geometry structure was quantitatively studied. At bigger fractal dimensions there was a higher degree of overlap between the primary carbon particulates and higher compactness of the PM which consisted of fundamental carbon particulates and *vice versa* [15]. Fractal characteristics of PM with different n-butanol/diesel blends were studied in this article by self-similar fractal dimension which is known as the box-counting dimension. The algorithm of box-counting dimension could be expressed as described in [16].

By calculating the box-counting dimension of the SEM image of PM in the diesel engine, the threshold binarization and the relationship lgN(r)-lgr of diesel PM were obtained. After fitting curve, the results are shown in Figure 4. It can be seen that the linear regression coefficient of the fitting curve is 0.9981, and the box-counting dimension of diesel PM is 1.942. Calculating box-counting dimensions of PM (N5, N10) used the same method. The results are shown in Table 3.

It can be seen that the linear regression coefficient of lg$N(r)$-lg$r$ fitting curve of PM is higher than 0.99 which signifies a good fitting. The calculated box-dimensions were 1.975 and 1.995, respectively. With the increase in n-butanol content, the box-dimension of the PM gradually increased which indicated that the agglomeration degree of PM gradually increased, and the structure arrangement was more compact.

Table 3. Box dimensions of n-butanol/diesel combustion PM

Test sample	Fitting line	R^2	D_B
Diesel	y=-1.942+13.647	0.9981	1.942
N5	y=-1.975+13.781	0.9987	1.975
N10	y=-1.995+12.058	0.9947	1.995

With the increase in w (n-butanol) content, the proportion of the single molecule decomposition reaction in n-butanol gradually increased, generating more propyl (-C_3H_7), hydroxymethyl (-CH_2OH) and other active radicals which accelerated the chain propagation reaction rate. In addition, O and C formed stable C-O bonds in the molecular structure of n-butanol which promoted PM oxidation and reduced the produced quantity of polycyclic aromatic hydrocarbon material in the soot precursor [17]. Each carbon and hydroxyl of the n-butanol molecules easily participated in dehydrogenation and non-bridging agglomeration reactions, which generated trace amounts of water molecules; promoted the attraction by the van der Waals force between PM, and made the reunion more compact.

Thermogravimetric analysis

Thermogravimetric analysis studied a series of physical and chemical changes such as volatility, pyrolysis, oxidation, combustion and other physical and chemical changes of PM samples by controlling the temperature. It measured the quality of PM with the temperature change in the thermogravimetric curve (TG curve). The derivative TG curve reflected the derivative thermogravimetric curve of PM samples mass rate (DTG curve). Through the combination of TG curve and DTG curve, the relative content of soluble organic matter, soot, metals, inorganic salts, etc. in the particulates was determined [18]..

Figure 4 shows the TG-DTG curves of PM fuelled with n-butanol/diesel.

As can be seen from the TG curve, with the rise of temperature, the mass of PM gradually decreased. When the temperature reached around 640°C, the mass of PM no longer changed. What could be seen from the DTG curve was that each
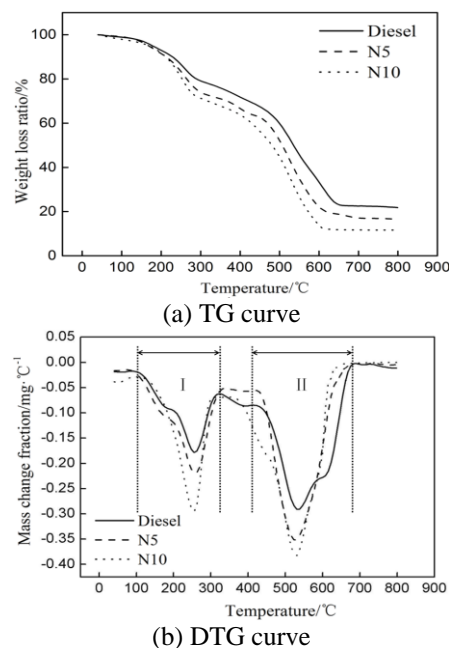

(a) TG curve

(b) DTG curve

Fig. 4. Effects of w (n-butanol) on TG-DTG of PM

curve had two peaks which could be considered as the two main reaction stages corresponding to the temperature range. The first stage was the low-temperature zone. The temperatures of the mass change rate peak of weightlessness of the PM samples (diesel, N5, N10) were 254℃, 250℃ and 247 °C, respectively. The main reaction in this section was the evolution of soluble organic matter. At the initial heating stage, the moisture in PM and low boiling point components of HC volatilized with the increase in temperature. When the temperature gradually reached the boiling point of HC, evaporation and oxidation reaction with oxygen occurred in the air. When the moisture of PM and HC basically volatilized and completely oxidized, the weight loss ratio was equal to the content of soluble organic matter in the PM. With the increase in n-butanol content, the initial combustion temperature TSOF decreased. As a small molecular oxygenated fuel, the carbon chain length of n-butanol was short; more oxygen groups were adsorbed on the particulate surface after burning which resulted in soluble organic matters oxidizing and burning easily in air atmosphere. The second stage was the high-temperature zone; main reactions in this stage were the oxidation and combustion of soot. When the temperature increased and there was no change in PM mass, the remaining components were mainly metal and inorganic salt groups. With the increase in the n-butanol content, the temperature corresponding to the mass change rate peak of weightlessness decreased which indicated that the weight loss curve of PM was shifted to the low temperatures.

CONCLUSIONS

1. At the same speed, with the increase in load, the smoke intensity value gradually increased, slowly under small and medium loads and sharply under medium and high load. Under the same conditions, the formation of soot gradually decreased with the increase in n-butanol content. When the speed of the diesel engine was 1800 rpm and 3000 rpm with full load, the smoke intensity value of N10 was reduced by 26.7% and 32.8% respectively, compared with the diesel fuel.

2. The microstructure of the n-butanol/diesel PM appeared as irregular clusters, and the average diameters of the PM were 1.43, 0.85, 0.52 μm. The PM size decreased and the aggregation degree gradually increased with the increase in the n-butanol content.

3. The pyrolysis process of PM in air was divided into two stages: (i) soluble organic matter evolution stage, (ii) soot oxidation and combustion stage. With the increase in n-butanol content, the initial combustion temperature of PM decreased; the temperature corresponding to the mass change rate peak of weightlessness of PM decreased; the weightlessness curve moved toward low temperatures. The content of soluble organic matter and soot components increased, but the content of nonvolatile and nonflammable materials such as metals, inorganic salts and other decreased.

REFERENCES

1. Z. H. Zhang, R. Balasubramanian, J. *Hazard. Mater.*, **264**, 395 (2014).
2. O.B. Popovicheva, E.D. Kireeva, N.K. Shonija, M. Vojtisek-Lom, J. Schwarz, *Environ. Sci. Pollut.* R., **22**, 4534 (2015).
3. L. Zhu, W. Zhang, W. Liu, Z. Huang, *Sci. Total. Environ.*, **408**, 1050 (2010).
4. Z. Liu, B. Hu, L. Wang, F. Wu, W. Gao, Y. Wang, *Environ. Sci. Pollut*. R., **22**, 627 (2014).
5. H. Chen, W. M. Chen, J. X. Wang, S. Shuai, *Transactions of CSICE*, **25**, 47 (2007).
6. A. Tsolakis, *Energy Fuels*, **20**, 1418(2006).
7. B. Choi, X. Jiang, *Fuel*, **154**, 188 (2015).
8. B. Choi, X. Jiang, Y. K. Kim, G. Jung, C. Lee, I. Choi, C. S. Song, *Appl Energ.*, **146**, 20 (2015).
9. S. S. Merola, C. Tornatore, S. E. Iannuzzi, L. Marchitto, G. Valentino, *Renew. Energ.*, **64**, 225(2011).
10. B. F. Yin, T. Guan, J. G. He, Y. Xu, *Applied Mechanics Materials*, **43**, 476 (2010).
11. M. Pietikäinen, A. Väliheikki, K. Oravisjärvi, T. Kollia, M. Huuhtanena, S. Niemib, S. Virtanenc, T. Karhuc, R. L. Keiskia, *Renew. Energ.*, **77**, 377 (2015).
12. A. Chung, A.A. Lall, S.E. Paulson, *Atmos. Environ.*, **42**, 2129 (2008).
13. H. Huang, Q. Liu, R. Yang, T. Zhu, Y. Wang, *Energy Convers. Manage.*, **106**, 748 (2015).
14. S.K. Friedlander, C.S. Wang, *Politics Policy*, **22**, 126 (1996).
15. J. Park, J. Yoon, S. Song, K.M. Chun, *J. Aerosol Sci.*, **41**, 531 (2010).
16. P. Bouboulis, L. Dalla, V. Drakopoulos, *J Approx Theory*, **141**, 99 (2006).
17. S.M. Sarathy, M.J. Thomson, C. Togbé, P. Dagaut, F. Halter, C. Mounaim-Rousselle, *Combust Flame*, **157**, 852 (2009).
18. M. M. Conceição, R. A. Candeia, F. C. Silva, A. F. Bezerrab, J. F. J. Valter, G. Antonio, *Renew. Sust. Energ. Rev.*, **11**, 964 (2007).

Research on acetylation and antioxidant activity of *Russula alutacea* Fr. water-soluble polysaccharides

Y. Zhao[1], X.N. Li[1], T. Chen[1], Q.Y. Tang[1], Q.P. Duan[1], B.J. Wang[1*], Q.S. Yang[2*]

[1] *College of Science, Yunnan Agricultural University, Kunming, Yunnan, China*
[2] *School of Ethnic Medicine, Yunnan Minzu University, Kunming, Yunnan, China*

There is a large amount of alkali-soluble polysaccharides in *Russula alutacea* Fr., but insolubility in water limits its development. Chemical modification can improve the solubility of natural polysaccharides limiting their activities, and enlarge their application range. Water-soluble polysaccharide was extracted by water and precipitated with alcohol in this study. It was further modified by acetylation, thus improving its water solubility. The scavenging activity of water-soluble polysaccharide, acetylated polysaccharide and vitamin C on the hydroxyl radical (OH•), 2,2-diphenyl-1-picrylhydrazyl (DPPH), superoxide anion(O_2^-•) was analysed and compared. The results showed that water-soluble polysaccharide, acetylated modified polysaccharide and vitamin C have a strong scavenging effect on O_2^-• which increases with the increase with mass concentration in the range of 0.34 ~ 1.7 mg/mL of mass concentration. The yield of water-soluble polysaccharide was 1.75%. The mass concentration of acetic acid was 0.63 mg/ml, the degree of substitution (DS) was 0.44%. According to its EC50 value, it can be concluded that the order of OH• scavenging ability was: VC>acetylated polysaccharide>water-soluble polysaccharide; the order of DPPH scavenging ability was: acetylated polysaccharide>VC>water-soluble polysaccharide; the order of O_2^-• scavenging ability was: VC>acetylated polysaccharide>water-soluble polysaccharide.

Key words: *Russula alutacea* Fr., Acetylation, Hydroxyl radical (OH•), 2,2-Diphenyl-1-picrylhydrazyl (DPPH), Superoxide anion (O_2^-•).

INTRODUCTION

Russula alutacea Fr. is a kind of ectomycorrhizal fungi with forest tree symbiosis [1,2]. It has an important economic value. It can be used not only for food but also for medicine purposes. When eated, it is rich in nutrition and delicious; it has blood enriching, nourishing Yin, cooling, detoxificating, cholesterol lowering, liver protecting, anticancer effects [3]. The polysaccharide structure modification is an important branch of polysaccharides pharmacology. To improve the biological activity of polysaccharides, molecular modification and structural modification of polysaccharides are of great significance, and acetylation of polysaccharides is one of the most important methods for their chemical modification. Acetylation can change the stretch of sugar chain, make hydroxyl (OH•) exposed, increase solubility in water.

It regulates the body's immune function mainly through the reticuloendothelial system (RES), macrophages (MO), lymphocytes and so on, and improves the immune capacity of the body. More and more polysaccharide preparations have been widely used in clinical practice, and have achieved encouraging results in autoimmune diseases,

immune dysfunction, cancer treatment, etc. Among them, the polysaccharide extracted from traditional Chinese edible and medicinal fungi is the most important one [4]. The anti-tumor effect of fungal polysaccharides is the most important biological activity, and also the most active part of the study. Pharmacological and clinical trials have found that 178 kinds of extract from the 50 genus of higher fungi have biological effects of inhibiting the cell growth of mouse sarcoma and Ehrlich Ascites tumor [5]. Polysaccharide Krestin (PSK) and *Grifola Frondosa* polysaccharide have been used as clinical antitumor drugs, have showed a broad spectrum of anti-tumor effects, and are quite remarkable anticancer drugs in recent years [6]. Modern research shows that *Russula alutacea* Fr. contains 5 kinds of polysaccharides. The polysaccharide content is about 2.47%, among them, monosaccharides and oligosaccharides account for 33.9% of total sugars; it contains anti-cancer polysaccharide substances, is conducive to blood circulation, reduces the cholesterol in the blood, suppresses metastasis of cancer cells, improves immunity, fights off viruses, also has certain curative effect in the treatment of acute spinal optic neuropathy. At present, the research is mainly focused on *Russulavinosa* in *Russula*, but studies on *Russula alutacea* Fr. of Yunnan Province are rarely reported [7]. However, a lot of polysaccharides extracted with alkali solution from

---

*To whom all correspondence should be sent:
E-mail: yangqskm@163.com;
wangbaijuan123@126.com

the fruiting body and mycelium are of interest because of their water solubility. Therefore, its water solubility should be increased by chemical modification, which will significantly improve the biological activity of the polysaccharides and extend its application range. At present, the extracting methods of polysaccharides are mainly using water extraction and ethanol precipitation, alkali extraction, and enzymatic hydrolysis [8,9]. The reaction of alkali extraction is intense, the extraction fluid needs to be neutralized, which could destroy the structure of the polysaccharide, decrease the molecular weight of *Russula alutacea* Fr. *Velutipes* polysaccharide, lead to a decline in its medicinal value [10]. Although the reaction time is short, the enzymatic hydrolysis method can greatly increase the extraction rate of polysaccharide, but the price of enzyme is higher. Although the extraction time of traditional water extraction is long, the extraction effect is better, and easily available materials are used. In this paper, the extraction of *Russula alutacea* Fr. polysaccharide, the antioxidant activity of the polysaccharide, the preparation of water-soluble polysaccharide by acetylation, its structural characterization, activity, etc. were studied. The scavenging ability of water-soluble polysaccharide, acetyl polysaccharide and vitamin C towards OH•, 2,2-diphenyl-1-picrylhydrazyl (DPPH) and superoxide anion (O_2^-•) was compared and valuable information on the modification/structure activity relationship of *Russula alutacea* Fr. polysaccharide was accumulated.

EXPERIMENTAL

Materials

Analytical methods

Fresh *Russula alutacea* Fr. fruiting bodies were purchased from a local market in Jinggu County, Yunnan. The fresh bodies were air-dried and shattered with mini plant sample grinder (DFT-100, Beijing KeSi Jia Technology Co., Ltd.)*,* and then the powder was sieved with a 100-mesh screen.

Preparation of of Russula alutacea Fr. water-soluble polysaccharide

Russula alutacea Fr. samples (40 g) were weighed and extracted three times with water at a solid-to-liquid ratio of 1:20 at 80℃ for 2 h. The combined extracts were centrifuged and the residue was discarded. 1% (w/v) activated carbon was added to the water-soluble crude polysaccharide in the last step, the mixture was shaken at 75 ℃ for 2.5 h, centrifuged and the precipitate was discarded.

Add 5 times sevage solution (n-butyl alcohol to chloroform, 1:5) into the decolorized supernatant, shake for 20~30 min, centrifuge the obtained supernatant then add 4 times absolute alcohol into it, place in the refrigerator (4℃) for 4 h. After centrifugation and drying of the precipitate pure *Russula alutacea* Fr. water-soluble polysaccharide was obtained.

The content of crude polysaccharide was determined by the phenol-sulfuric acid method [11]. The polysaccharide content in the extract was determined by the absorption values at OD490 which was the maximum absorption wavelength of the polysaccharide.

Acetylation modification of Russula alutacea Fr. polysaccharide

Acetylation modification was used [12]. The acetylation substitution degree was determined [13]. The content of total carbohydrates was determined using a phenol-sulfuric acid colorimetric method with glucose as a standard [14].

FT-IR analysis

For IR spectroscopy, polysaccharide powders were mixed with KBr, grinded, and pressed into 1 mm pellets. Then scanning measurement was performed in the range from 4000 to 400 cm^{-1}.

In vitro analysis of the antioxidant activity

Reducing power was evaluated with a slight modification of the published method [15]. The scavenging effect of superoxide anion (O_2^-•) was determined by the pyrogallol autooxidation method [16]. The scavenging rate of DPPH was determined according to [17]. The scavenging ability of hydroxyl free radical (OH•) was determined according to [18].

RESULTS AND DISCUSSION

The standard curve of *Russula alutacea* Fr. polysaccharide content was obtained by the phenol-sulfuric acid method in the range of 40.00-200.00 µg/ml, the regression equation is y=7.8436x+0.0138 (R^2=0.9993) and has good linear relationship. The polysaccharide rate was 1.75%. The regression equation of the standard curve of acetyl using a standard sample of acetylcholine chloride was y=0.4575x-0.0007 (R^2=0.9997), and has good linear relationship within the determination range. According to the regression equation the calculated acetyl concentration of the acetylated polysaccharide was 0.63 mg/ml, and the substitution degree was 0.44%. 1 mg of dry sample

and 150 mg of KBr were pressed onto a pellet, then scanning measurement was performed in the range of 4000-400 cm^{-1}.The modified polysaccharides exhibited a strong stretching vibration characteristic absorption peak of O-H and a bending vibration absorption peak of C-O at 3400 cm^{-1} and 1105 cm^{-1}, respectively, with typical absorption characteristics of polysaccharides. Acetylation products, in addition to retaining the characteristic absorption of the original polysaccharide, also remarkably enhanced the C=O stretching vibration characteristic absorption peak of the ester group at 1731 to 1743 cm^{-1} and the C-O stretching vibration absorption characteristic peak of the ester group at about 1246 cm^{-1}. The above results showed that the polysaccharide was successfully modified by acetylation (Figs. 1 and 2).
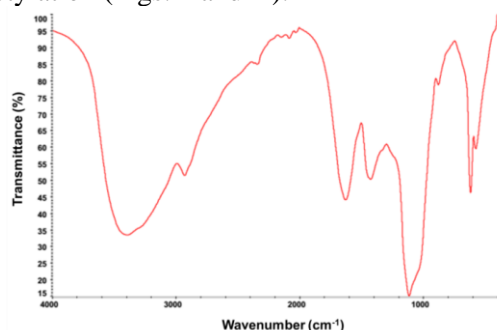

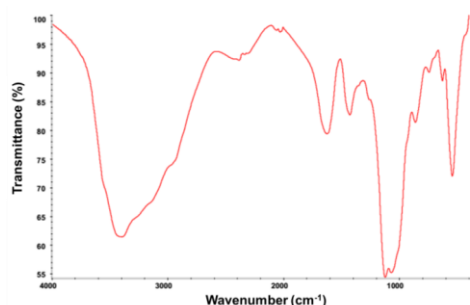**Fig.1.** Infrared spectrum of unmodified polysaccharides

Fig.2. Infrared spectrum of modified polysaccharides

Reducing force is one of the indices to evaluate the antioxidant activity of the material. The antioxidant mechanism is: material with reducing force can react with free radicals to stabilize free radicals, for interrupting the lipid peroxidation of the chain reaction.

From table 1 it is seen that before and after acetylation modification, the *Russula alutacea* Fr. polysaccharide concentration and ascorbic acid were positively correlated with reducing ability.

Table 2 shows that water-soluble polysaccharide, acetylation-modified polysaccharide and vitamin C have strong scavenging effect on $O_2^-\bullet$, which increases with the increase in mass concentration in the range of 0.34 ~ 1.7 mg/mL.

Table 1. Effect of acetylation cation on reducing power

Sample	Concentration (mg/mL)	Absorbance
Polysaccharides	0.34	0.151
	0.68	0.403
	1.02	0.55
	1.36	0.733
	1.70	0.87
Acetylated polysaccharides	0.34	0.196
	0.68	0.681
	1.02	0.857
	1.36	0.979
	1.70	1.218
Ascorbic acid (vitamin C)	0.34	0.295
	0.68	0.631
	1.02	1.02
	1.36	1.454
	1.70	1.839

Table 2. Scavenging effect on superoxide anions

Sample	Concentration (mg/mL)	Scavenging activity (%)	EC$_{50}$ (mg/ml)
Polysaccharides	0.34	2.2	
	0.68	19.9	
	1.02	27.9	1.4725
	1.36	48.2	
	1.70	58.3	
Acetylated polysaccharides	0.34	29.1	
	0.68	58.9	
	1.02	68.8	0.6621
	1.36	76.3	
	1.70	86.8	
Ascorbic acid (vitamin C)	0.34	7.3	
	0.68	24.8	
	1.02	35.6	1.3701
	1.36	51.6	
	1.70	61.3	

Table 3. Scavenging effect on DPPH free radicals

Sample	Concentration (mg/mL)	Scavenging activity (%)	EC$_{50}$ (mg/ml)
Polysaccharides	0.34	19.6	
	0.68	24.6	
	1.02	30.5	1.2543
	1.36	58.4	
	1.70	70.3	
Acetylated polysaccharides	0.34	30.7	
	0.68	42.8	
	1.02	61.9	0.8498
	1.36	66.5	
	1.70	77.4	
Ascorbic acid (vitamin C)	0.34	37.8	
	0.68	54.6	
	1.02	76.9	0.5473
	1.36	92.9	
	1.70	97.7	

In the range of 0.34~1.7 mg/mL of mass concentration, the scavenging ability of acetylation-modified polysaccharide on $O_2^-\bullet$ is greater compared with water-soluble polysaccharide and

vitamin C, and the scavenging ability of vitamin C $O_2^-\bullet$ is greater than that of water-soluble polysaccharide.

As can be seen from table 2, the highest scavenging rates of water-soluble polysaccharide, acetylation-modified polysaccharide and vitamin C are: 86.8%, 58.3%, 61.3%, respectively. According to the value of EC50 the scavenging ability on $O_2^-\bullet$ is: acetylation-modified polysaccharide>vitamin C>water-soluble polysaccharide. After acetylation modification, the activity of water-soluble polysaccharide is enhanced.

From table 3 it can be seen that water-soluble polysaccharide, acetylation- modified polysaccharide and vitamin C have a strong scavenging effect on DPPH which increases with the increase in mass concentration in the range of 0.34 ~ 0.7 mg/mL. In this range, the scavenging ability of vitamin C on DPPH is greater compared to water-soluble polysaccharide and acetylation-modified polysaccharide, and the scavenging ability of acetylation-modified polysaccharide on DPPH is greater than that of water-soluble polysaccharide. As can be seen from table 3, the highest scavenging rates of water-soluble polysaccharide, acetylation-modified polysaccharide, vitamin C are 70.3%, 77.4%, 97.7%, respectively. According to the value of the scavenging ability on DPPH is: vitamin C > acetylation- modified polysaccharide>water-soluble polysaccharide. After acetylation modification, the activity of the water-soluble polysaccharide is enhanced.

Table 4. Scavenging effect on hydroxyl free radicals

Sample	Concentration (mg/mL)	Scavenging activity (%)	EC_{50} (mg/ml)
Polysaccharides	0.34	5.6	
	0.68	24.9	
	1.02	36.2	1.3072
	1.36	56.2	
	1.70	64.3	
Acetylated polysaccharides	0.34	14.9	
	0.68	31.1	
	1.02	48.7	1.1152
	1.36	61.4	
	1.70	73.3	
Ascorbic acid (vitamin C)	0.34	25.4	
	0.68	44.2	
	1.02	56.2	0.8948
	1.36	64.5	
	1.70	85.6	

From table 4 it can be seen that water-soluble polysaccharide, acetylated polysaccharide and vitamin C have strong scavenging effect on OH• which increases with the increase in mass concentration in the range of 0.34 ~ 1.7 mg/mL. In this range, the scavenging ability of vitamin C on OH• is greater in comparison with water-soluble polysaccharide and acetylated polysaccharide, and the scavenging ability of acetylated polysaccharide on OH • is greater than that of water-soluble polysaccharide.

As can be seen from table 4, the highest scavenging rates of water-soluble polysaccharide, acetylation modified polysaccharide, vitamin C are 64.3%, 73.3%, 85.6%, respectively. According to the value of EC50 the scavenging ability on OH• is: vitamin C> acetylated polysaccharide>water-soluble polysaccharide. After acetylation modification, the activity of water-soluble polysaccharide is enhanced.

CONCLUSION

In this paper, *Russula alutacea* Fr. water-soluble polysaccharides were extracted. Acetylation technology was applied to the study of *Russula alutacea* Fr. polysaccharide. Acetic anhydride was used as an acylation reagent to perform the acetylation modification of *Russula alutacea* Fr. polysaccharide, Then the antioxidant activity of *Russula alutacea* Fr. polysaccharide and its acetylated products was studied by *in vitro* test method to investigate the effect of acetylation on the biological activity of *Russula alutacea* Fr. polysaccharide. *Russula alutacea* Fr. processed by water extraction and ethanol precipitation yielded water-soluble polysaccharide and acetylation-modified polysaccharide. They have a good scavenging effect on OH•, $O_2^-\bullet$ and DPPH. According to the EC50 value, the scavenging ability on superoxide anion was: acetylation-modified polysaccharide > vitamin C> water-soluble polysaccharide; the scavenging ability on DPPH was: vitamin C > acetylation-modified polysaccharide > water-soluble polysaccharide; the scavenging ability on OH• was: vitamin C> acetylation-modified polysaccharide>water-soluble polysaccharide. After acetylation modification, the scavenging ability of water-soluble polysaccharide on OH•, $O_2^-\bullet$ and DPPH were enhanced.

Acetylation is one of the most important methods in the study of the antioxidant activity of polysaccharides. Jiao *et al.* [19] studied the molecular modification and biological activity of jujube polysaccharide. On the basis of extraction and purification of jujube polysaccharide, in this paper, molecular modification techniques were applied to the study of jujube polysaccharide. By ultrasonic treatment, hydrochloric acid degradation and sulfatation, carboxyl methylation and

acetylation modification, its molecule was further modified, and then the antioxidant activities, hypoglycemic activity and inhibitory effect on hyaluronic acid enzyme of jujube polysaccharide and its molecular modification products were studied by *in vitro* test method. It confirmed that jujube polysaccharides have inhibitory effect on α-amylase, α-glucosidase, hyaluronidase and nonenzymatic glucosylation reaction.

Molecular modification can significantly change the biological activity of jujube polysaccharide, and this change is more related to the change of the advanced structure of jujube polysaccharide caused by molecular modification. Jujube polysaccharide conformational changes caused by molecular modification are more important for its biological activity effect than physical and chemical changes. To maintain a certain length and space conformation is the key to keep its activity. Xie [20] studied the molecular modification and biological activity of *Cyclocarya paliurus* (Batal) Iljinskaja polysaccharide. The study of molecular modification, including sulfatization, hydroxyl methylation, phosphorylation, and so on, has gradually become one of the hot topics in the study of polysaccharides. Among them, because of its good antioxidant and antiviral activity, sulfated polysaccharides have been widely concerned by researchers. Wang *et al.* [21] studied the preparation and antioxidant activity of acetylated fucoidan from *Laminaria japonica* and determined the scavenging ability on OH• and O_2^-•, DPPH and reduction ability of acetylation derivatives under different conditions. The results showed that the acylating agent dosage and reaction temperature have significant effects on fucoidan acetylation ($P<0.05$). The scavenging activities on OH• and O_2^-•, DPPH and reduction ability of acetyl derivatives were different. It was concluded that NBS as a catalyst for acetylation of Fucoidan from *Laminaria japonica* is feasible, could replace the traditional strong toxicity of pyridine fucoidan from *Laminaria japonica* by acetylation of hydroxyl. The antioxidant activity of the polysaccharide was obviously enhanced after acetylation. It is of great significance to carry out further research on it.

REFERENCES

1. G. J Li., H. A. Wen, *Mycosystema*, **28**(2), 303 (2009).
2. S. G. Du, T. L. Zhao, X. M. Xi, Q. Y. Xue. *Edible Fungi*, **03**, 7 (2015).
3. N. L. Huang, Z. B. Lin, G. L. Chen, Edible and Medicinal Mycology of China, Shanghai Science& Technical Publishers, Shanghai, 2010.
4. W. Y. Tao, Z. H. Ao, H. Y. Xu, Biological Technology of Edible Fungi, Chemical Industry Press, Beijing, 2007.
5. K. H. Zeng, J. Ming, K. F. Zeng, *Food Sci. Tech.*, **04**, 65 (2011).
6. S. W. Zhou, C. F. Xu. *Chin. J. Biochem. Pharm.*, **15**(2), 143 (1994).
7. P. Yu, Y. R. Liu, X. i. Lin, *Nat. Prod. Res. Devel.*, **18**(04), 30 (2006).
8. F. Wang, Q. Ren, Q. Li, Y. M. Dong, Y.Y Zhao, *Edible Fungi*, **05**, 58 (2008).
9. X. D. Li, J. H. Rong, M. C. Wu, *Acta Edulis Fungi*, **9**(04), 50 (2002).
10. D. Liu, J. Y. Qian, *Edible Fungi*, **02**, 43 (2003).
11. Q. Liu, M. Zhu, X. Geng, H. Wang, T. B. Ng.. *Molecules*, **22**(2), 234 (2017).
12. L. Zhang, L. Xiong, Q. J. Sun, *J Chin Inst Food Sci Tech*, **11**(08), 53 (2011).
13. Y.H. Li, F.S. Wang, Y.L. He. *Chin. J. Biochem. Pharm.*, **28**(01), 43 (2007).
14. M. Dubois, K. A. Gilles, J. K. Hamilton, P. A. Rebers, F. Smith. *Anal. Chem.* **28**, 350 (1956).
15. L. Estevinho, A. P. Pereira, L. Moreira, L. G. Dias, E. Pereira, *Food Chem. Toxicol.* **46**, 3774 (2008).
16. K. B. Jeddou, F. Chaari, S. Maktouf, Q. Nouri-Ellouz, C. Boisset Helbert, R. Ellouz Ghorbel, *Food Chem.*, **205**, 97 (2016).
17. L. Sun, J. Sun, Y. Meng X. B. Yang, G. Y. Guo, *International Journal of Food Engineering*, **13**(3), (2017).
18. J. Q. Jia, W. J. Le, M. Han, Z. Z. Gui, Q. Y. Wu, H. Yan, *Food Sci. Tech.*, **36**(03), 70 (2011).
19. R. Zhang, H. Wei, M. Zhen, C. Man, C Zhao, *Life Sci. Instrum.*, **10**, 37 (2012).
20. J. H. Xie, M. Y. Shen, S. P. Nie, *Carbohydrate Polym.*, **84**(1), 255 (2011).
21. F. Wang, Q. Ren, Q. Li, Y. M. Dong, *Edible Fungi*, **05**, 58 (2008).

Kinetic analysis of biogas produced from kitchen waste conducted using population growth and first order analytical models

L. Feng[1], T.Y. Gao[1], S.Y. Gu[2*], W. Kou[3], P. Gao[2], X.Y. Dong[3], M.L. Yu[3], D.L. Zhang[3], J.Z. Wang[4]

[1]Liaoning Province Clean Energy Key Laboratory, Shenyang Aerospace University, Shenyang, China
[2]Shenyang Agricultural University,China
[3]Liaoning Institute of Energy Resources, Yingkou,China
[4]Liaoning haosheng biogas power generation co. LTD, Liaozhong, ,China

Sequencing batch anaerobic digestion (AD) of kitchen waste at 37 °C was studied. The classic population growth equations and the first-order biogas production were used to analyze the characteristics of biogas production in kitchen waste anaerobic digestion process under the condition of initial total solids (TS) = 4, 5, 6 and 7 wt %. Logistic equation was better fitted to the experimental data for kitchen waste of initial TS=7 wt % comparing with the modified Gompertz equation. For kitchen waste (AD) process at other TS concentrations in this research to the Modified Gompertz equation was preferred. No lag phase time appeared in the experiment, k of kitchen waste of initial TS= 4, 5, 6 and 7 wt % were 0.2179, 0.1430, 0.1170, and 0.0954, respectively. The kitchen waste of initial TS=4 wt % gave the highest biogas production, followed by initial TS=6 wt % and initial TS=5 wt %. The kitchen waste of initial TS=7 wt % displayed the worst characteristics of biogas production.

Key words: Kitchen waste; Population growth equation; First order model; Kinetics

INTRODUCTION

Undesirable kitchen waste accounts for 30%–50% of municipal solid waste [1]. In China, the production of kitchen waste reached 110 million t in 2012 [2]. Traditionally, kitchen waste can not only be used for feeding pigs [3,4] but also be disposed by landfill or composting with other wastes. The landfill or composting occupies a lot of valuable land and pollutes the surroundings [5-7]. Kitchen waste is composed of starch, proteins, fibers, fat and other organic substances and contains a large amount of moisture and organic matter, rendering it subject to acidification [8]. Based on these characteristics of kitchen waste, anaerobic digestion technique has advantages. Anaerobic digestion technique can dispose solid organic wastes and produce biogas as a source of clean energy [9-12]. After anaerobic digestion, the biogas residue is rich in nitrogen, phosphorus and other elements, the emissions of which will cause eutrophication of waters, and hence the residue can serve as a fertilizer for agricultural production [13,14]. Moreover, the residue can also be utilized to cultivate microalgae to produce biodiesel [15].

In a typical sequencing batch anaerobic digestion process, biogas production has a certain relationship with the growth of microorganisms. The logistic equation and the revised Gompertz equation are classic and prevalent models for the description of population growth in the anaerobic digestion for

biogas production. Pommier, Brullmann, Gao *et al.* [16-18] used the revised Gompertz equation to model the process of anaerobic digestion for biogas production. Yusuf *et al.* [19-21] modeled the process of anaerobic digestion for biogas production with the Gompertz equation. In addition, the first-order hydrolysis model is the simplest model for the hydrolysis of complex organic compounds, assuming that the substrate is a limit, and the rate of hydrolysis is proportional to the concentration of unhydrolyzed organic matter. This model fits well with the actual hydrolysis behavior of particulate organic matter. In this paper, a first-order biogas production model was obtained on the basis of the first-order hydrolysis model. By combining the classic population growth model with the first-order gas production model, the behavior and characteristics of biogas production were analyzed using kitchen waste with different concentrations of total solid (TS) to find out under which initial TS kitchen waste can produce the highest biogas amount. This study is meaningful for industrial applications of the anaerobic digestion of kitchen waste and gives practical guidance for the actual operation.

EXPERIMENTAL

Experiments

The kitchen waste was derived from the Canteen of Shenyang Aerospace University in China, and cut into particulates with a diameter of 10 mm. The inoculated sludge which was domesticated at a temperature of 37°C was obtained from a waste water treatment plant in north Shenyang. The initial kitchen

*To whom all correspondence should be sent:
E-mail: fl_iceee@163.com

waste weight and the inoculated sludge volume are shown in table 1. Water was added to the reactor to a level of 1L. Mass fractions of TS and volatile solids (VS) in the kitchen waste were 23.31 and 92.84 wt %, respectively. Mass fractions of TS and VS in the inoculated sludge were 11.95 and 78.05 wt %, respectively. The C/N ratio of the raw material was 21.38. VS was calculated on the base of TS.

Table 1. Initial kitchen waste weight and inoculated sludge volume

Initial TS weight content (wt %)	Initial kitchen waste weight (g)	Inoculated sludge volume (mL)
4	17.8	300
5	60.7	300
6	103.6	300
7	146.5	300

Experimental apparatus and method

A self-designed anaerobic fermentation reactor was used. Two wide-mouthed 1L bottles acted as a gas collecting bottle and a water collecting bottle. Total volume of the reactor was 1.1 L. The bottleneck was sealed with a rubber stopper and sealant. The apparatus was placed in airtight and anaerobic environment.

The fermentation reactor was heated with a thermostated water bath. In this study, the initial mass fraction of TS was separately set as 4, 5, 6, and 7 wt%. Triple experiments were performed with the same initial mass of 17.8 g, 60.7 g, 103.6 g, and 146.5 g of kitchen waste and 300 mL of inoculated sludge was aslo added into the reactor as the inoculum. Water was added to the fermentation reactor to a level of 1L, then the bottles were sealed and cultured at 37 ºC for 30 days in the water bath.

The fermentation liquor was withdrawn with a syringe and the pH was measured with a digital pH meter once a day before adding new kitchen waste during the experimental peroid. The fermentation liquor was then returned into the reactor. When the pH was less than 6.8, pH was adjusted to 7.0 with the addition of $NaHCO_3$ at about 5 pm. Stirring was performed 2 times per day by hand shaking during 5 min each time. pH of the $NaHCO_3$ solution was 9. During the anaerobic process, the pH of the fermenting liquid was below 7. The ideal value pH of the fermenting liquid was 7. Volume of $NaHCO_3$ solution injected was calculated and added according to the rule above. The production of biogas was determined once per day, and the volume of water in the water-collecting bottle was that of produced biogas. Biogas production of the sequencing batch reactor was further revised with the production of control group where only inoculum was added without any substrates. TS and VS were determined by using the drying method at 103–105 ºC and 600 ºC, respectively.

Models

Population Growth Model: The logistic equation can be described as follows:

$$P = \frac{P_{max}}{1 + \exp[\frac{4R_{max}(\lambda - t)}{P_{max}} + 2]} \qquad (1)$$

where P is the cumulative biogas production ($mL \cdot g^{-1}$ VS) at time t. P_{max} is the maximum biogas production ($mL \cdot g^{-1}$ VS). R_{max} is the maximum biogas production rate ($mL \cdot g^{-1}VS \cdot d^{-1}$). t represents reaction time (d). Lag-phase time is denoted by λ.

The Gompertz equation is given by:

$$M = P \times \exp\{-\exp[\frac{R_m \times e}{P}(\lambda - t) + 1]\} \quad (2)$$

where M is the cumulative biogas production ($mL \cdot g^{-1}$ VS) at time t. P is the maximum biogas production ($mL \cdot g^{-1}$ VS). Rm is the maximum biogas production rate ($mL \cdot g^{-1}VS \cdot d^{-1}$). t represents reaction time (d). Lag-phase time is denoted by λ.

Evidently, P, P_{max}, and R_{max} in the logistic equation correspond to the counterparts of M, P, and Rm in the revised Gompertz equation. Kinetic parameters of the logistic equation and the revised Gompertz equation were fitted and analyzed with nonlinear regression by using an Origin8.0 software, whose producer is OriginLab company.

First-order biogas production model: A first-order biogas production model proposed by Lei Feng et al. [23] was used herein and expressed as follows:

$$\frac{1}{t}\ln(\frac{dy_t}{dt}) = \frac{1}{t}(\ln(y_m) + \ln k) - k \qquad (3)$$

where y_m represents the maximum biogas production per gram of volatile substances ($mL \cdot g^{-1}$ VS); y_t represents the biogas production per gram of volatile substances at time t ($mL \cdot g^{-1}$ VS); t represents reaction time (d) and k is the hydrolysis constant (d^{-1}).

The experimental data were analyzed based on the above equation with an Origin8.0 software, which gave the values of $\ln y_m + \ln k$ and k of relevant organics.

RESULTS AND DISCUSSION

Data analysis based on the logistic equation and revised Gompertz equation

Under optimal conditions such as temperature, pH, amount of inoculum, etc., the experimental data in an anaerobic digestion process were nonlinearly fitted

with the Origin software (Figure 1). The fitting parameters of anaerobic digestion of different materials based on the logistic equation and revised Gompertz equation are tabulated in Tables 2 and 3.
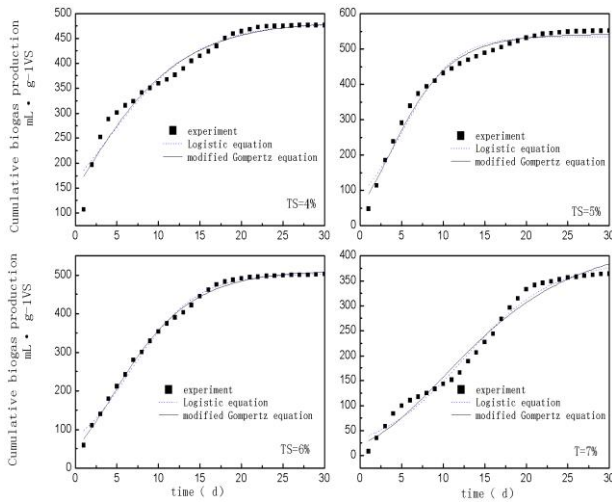

Fig. 1. Cumulative biogas production of logistic equation and modified Gompertz equation

Table 2. Model of parameters of logistic equation

Initial TS concertration (wt %)	P_{max} (mL g^{-1}VS)	R_{max} (mL g^{-1}VS·d^{-1})	λ (d)	R^2
4	480.60	21.91	-7.42	0.95125
5	534.81	42.48	-1.18	0.97202
6	503.78	32.24	-1.17	0.99414
7	389.82	18.35	1.92	0.98458

Table 3. Model of parameters of modified Gompertz equation

Initial TS concentration (wt %)	P (mL g^{-1}VS)	R_{max} (mL g^{-1}VS d^{-1})	λ (d)	R^2
4	485.10	26.52	-5.53	0.95981
5	540.94	32.18	-4.95	0.98597
6	513.09	23.67	-6.34	0.99595
7	429.87	11.70	-8.32	0.97951

The R^2 values in Tables 2 and 3 range from 0.95 to 1, indicating that the anaerobic digestion of kitchen waste with low solid concentrations for biogas generation agrees well with the population growth equation. Specifically, a good fit was obtained when the logistic equation was used for the fit of the anaerobic digestion of kitchen waste with 7 wt % of TS. In contrast, the revised Gompertz equation fitted well with the anaerobic digestion of kitchen waste with 4 wt %, 5 wt %, and 6 wt % of TS. The potential biogas production of kitchen waste with 5 wt % of TS reached a maximum of 540.94 mL·g^{-1} VS, followed by 513.09 and 485.10 mL·g^{-1} VS at 6 wt % and 4 wt % of TS respectively. The potential biogas production of kitchen waste with 7 wt % of TS had a minimum of 389.82 mL·g^{-1} VS. Except that the delay time of the anaerobic digestion of kitchen waste with 7 wt % of TS was 2 days, no delay phenomenon was observed at other contents of TS. This is because the kitchen waste contained large amounts of decomposable rice, bread and other starches as well as certain amounts of lean meat, eggs and other protein-bearing organics, resulting in a favorable C/N ratio to the anaerobic digestion. Consequently, the hydrolysis reaction was accelerated and the growth and reproduction of microorganisms was ensured to promote the progress of the reaction. The delay time at 7 wt % of TS was probably ascribed to the relatively low inoculation ratio at the beginning of the reaction, and hence the micro-organisms did not have enough time to reproduce for the production of biogas.

Analysis of results based on first-order biogas production model

First of all, considering that the anaerobic digestion process in the first-order gas production model does not involve delay time, the experimental data in the first two days were ignored at 7 wt % of TS due to it was relative short to the whole period, otherwise it can not be neglected, and the rest data were shifted to an earlier date accordingly. The experimental data were fitted with equation 8 and plotted in Figure 2, in which the linear fits of (1/t)*ln(dyt/dt) against 1/t at 4 wt %, 5 wt %, 6 wt % and 7 wt % of TS were respectively illustrated.
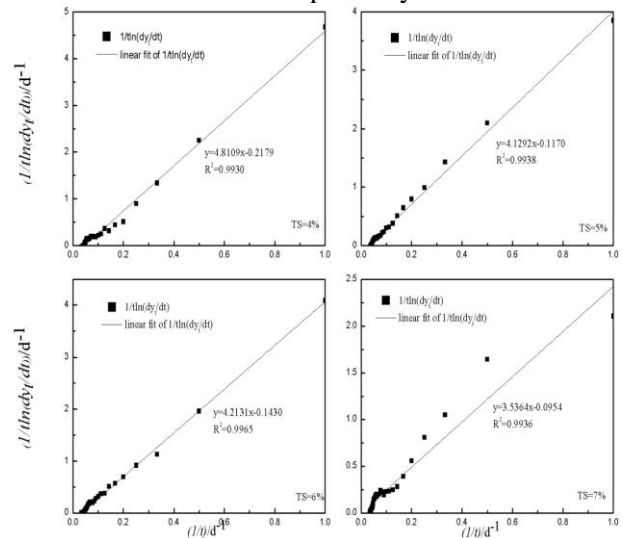

Fig. 2. Plot of 1/t(ln(dyt/dt) against 1/t for kitchen waste anaerobic digestion of different initial TS

All the coefficients of determination (R^2) were greater than 0.99, indicating that this model agreed well with the biogas production behavior of the anaerobic digestion of kitchen waste with low solid concentrations and can be used for theoretical analysis of experiments. Additionally, the values of k and lny_m + lnk of the anaerobic digestion of kitchen waste with varied TS concentrations are depicted in Table 4.

Table 4. Parameter values obtained under the condition of the model for kitchen waste anaerobic digestion of different TS concentration

Initial TS concentration (wt %)	ln(y_m)+lnk	K (d⁻¹)	R²
4	4.8109	0.2179	0.9930
5	4.1292	0.1170	0.9938
6	4.2131	0.1430	0.9965
7	3.5364	0.0954	0.9936

Where, k represents the removal efficiency of degradable substrates. A higher k value indicates a higher reaction speed. It was calculated that the hydrolysis constants of kitchen waste with a TS content of 4 wt %, 6 wt %, 5 wt %, and 7 wt % were 0.2179, 0.1430, 0.1170, and 0.0954 d^{-1}, respectively.

The item lny_m + lnk represents the exploitability of biodegradable substrates and is also a com prehensive index of biogas production rate and biogas production. Therefore, we could evaluate the biogas production capacity of a substrate according to the index, and a higher value indicates a greater gas production capacity of a substrate. The derived k values reflect the conversion rates of a variety of large organic molecules into small molecules, while the item lny_m + lnk size indicates both the biogas production rate and biogas production of various large organic molecules. The values of R^2 in the first-order hydrolysis model of kitchen waste at each TS concentration are greater than those in the population growth model. Therefore, the first-order hydrolysis model is better in the fit. The value of lny_m + lnk at TS concentration of 4 wt % reached a maximum of 4.8109, indicating that its biogas production capacity was the highest. Namely, both the hydrolysis rate and biogas production were high. The values of lny_m + lnk at a initial TS mass fraction of 6 wt %, 5 wt %, and 7 wt % were 4.2131, 4.1292, and 3.5364 respectively. He conducted a sequencing batch anaerobic digestion experiment using garbage of leafy vegetables, which demonstrated that under conditions of 3% of solids and an inoculation ratio of 3.5, the average and maximum daily biogas production rate were the highest with the shortest delay time. Moreover, at the inoculation ratio of 3.5, the biogas production rate was decreased and delay time was extended with the increase of solids percentage. In contrast, the k values in our experiments were independent on the concentrations of TS. This may be attributed to the difference between the raw materials and intermediates in the anaerobic digestion processes of different studies. The values of lny_m + lnk at TS mass fractions of 4 wt %, 6 wt %, 5 wt %, and 7 wt % were not in accordance with the conclusion of potential biogas production drawn from the Logistic equation

and Revised Gompertz Equation. The reason may be the fitting error of the Logistic equation and Revised Gompertz Equation, which was reflected by the much lower coefficients of determination (R^2) of the Logistic equation and Revised Gompertz Equation than those of the first-order biogas production model. The dependences of the TS concentrations on k and lny_m + lnk agree with each other. In detail, the hydrolysis rate and biogas production capacity of the anaerobic digestion of kitchen waste were the highest at an initial TS concentration of 4 wt %, followed by those at initial TS concentrations of 6 wt %, 5wt %, and 7 wt %. The maximum of k was higher than the minimum by 128.41%, and the maximum of lny_m + lnk was 36.04% higher than the maximum. Hence, the initial TS content could be 4 wt % for the kinetic study of the anaerobic digestion of kitchen waste with low concentrations of solids. Other factors such as reaction temperature or pH should be adjusted afterwards in the experiment.

CONCLUSION

(1) At appropriate inoculation ratios, the anaerobic digestion process of kitchen waste with a small amount of solids almost does not have delay time. The change of k value along with TS concentrations accords with the variation of lny_m + lnk along with TS concentrations.

(2) The hydrolysis constants of kitchen waste at TS mass fractions of 4, 5, 6 and 7 wt % were 0.2179, 0.1430, 0.1170 and 0.0954 d^{-1}, respectively, corresponding to decreasing hydrolysis rates. The maximum of k values was higher than the minimum by 128.41%.

(3) At a TS content of 4 wt %, the biogas production capacity of anaerobic digestion of kitchen waste was the highest, followed by the capacities at TS contents of 6,5, and 7 wt %. The maximum of ln y_m+lnk values was 36.04% higher than the minimum.

(4) Both of maximum of k values and the biogas production capacity occurred when initial TS was 4% among the four, which help researchers choose the initial TS concentration of experiment. The first-order biogas production model can be used to calculate the biogas production capacity of single component such as protein, starch, cellucose and fat. On the basic of this, the biogas production capacity of mixed organic waste can be improved by adjust the content of some organics such as adding some kind of orgaics.

REFERENCES

1. Y. P. Xie, Y. J. Liang, *Environ Sanitat Eng.*, **16**,2(2008).
2. Yin. C. H, Liang. Y. J, *Food Sci. Biotechnol.*, **22**, 1(2013).
3. S. Ribbens, J. Dewulf, F. Koenen, *Prev Veterin Med.*, **5**, 83, (2008).
4. S. Y. Yang, K. S. Ji, Y. H. Baik, *Bioresour. Technol.*, **97**, 15 (2006).
5. S. Manfredi, R. Pant, *Inter J. Life Cycle Assess.,* **18**, 1 (2013).
6. A. Hanc, J. Szakva, P. Svehla, *Bioresour. Technol.*, **126**, 85(2012).
7. D. B. Emilia, D. B. Jan, J. Jadwiga, *Waste Manage. Res.*, **30**, 8, (2012).
8. R.T. Romano, R. Zhang, *Bioresour. Technol.*, **99**, 18 (2008).
9. D.J. Batstone, J. Keller, I. Angelidaki, *Water Sci. Technol.*, **45**, 19 (2002).
10. S. M. Ismail, I. M. Ginia, O. Rozita, *Applied Microbial. Biotechnol.*, **95**, 2, (2012).
11. L. Feng, H. L. Kou, X. D. Zhang, R. D. Li, *J. Res. Sci. Technol.*, **12**, 4(2015).
12. M. Recktenwald, E. S. Dey, O. Norrlow, *J. Res. Sci. Technol.*, **12**, 4(2015).
13. A. J. Wang, W. W. Li, H. Q. Yu, *Adv. Biochem. Eng. Biotechnol.,* **34***, 128 (2012).
14. C. H. Song, Z. M. Wei, B. D. Xi, *J. Safe Environ.*, **13**, 2 (2013).
15. Z. Q. Liu, *Zhejiang Univ. Technol.,*(2012).
16. S. Pommier, D. Chenu, *M. Quintard, Biotechnol. Bioeng.*, **97**, 3 (2007).
17. D. D. Brüllmann, A. M. Sachs, *Oral Surg. Oral Med. Oral Pathol. Oral Radiol.*, **115**, 3 (2013)
18. S. M. Gao, M. X. Zhao, Z. Y. Xu, *J. Safe. Environ.*, **15**, 1 (2015).
19. N. Annop, C. P. Pratap, P. C. William, *Waste Manage.*, **8**, 27(2007).
20. N. Ali, M. Saleem, K. Shahzad, S. Hussain, A. Chughtai, *Polish J. Chem. Technol.*, **18**, 88 (2016).
21. M. S. Rao, S. P. Singh, *Bioresour. Technol.*, **95**, 8 (2004).

High-solid hydrolytic kinetic model of kitchen waste anaerobic digestion

L. Feng[1], N. Wang[1], S.Y. Gu[2*], W. Kou[3], P. Gao[2], X.Y. Dong[3], M.L. Yu[3], D.L. Zhang[3], J.Z. Wang[4]

[1]*Liaoning Province Clean Energy Key Laboratory, Shenyang Aerospace University, Shenyang 110136, China*
[2]*Shenyang Agricultural University, China*
[3]*Liaoning Institute of Energy Resources, Yingkou, China*
[4]*Liaoning Haosheng Biogas Power Generation Co. LTD, Liaozhong, China*

The high-solid kitchen waste fermentation process can be divided into four phases: adaptation (0~13 d), start-up (14~34 d), inhibition (35~72 d), and recovery and stabilization (72~120 d). In dry kitchen waste fermentation, the reaction rate constant k was found to be 0.133 d^{-1} depending on the hydraulic retention time (HRT), organic loading rate (OLR), and maximum gas production rate of kitchen waste at the different fermentation phases. The formula for the relationship between the cumulative gas production (L) and time (d) was: $y = 0.1139x^2 - 5.0447x + 77.737$. The cumulative gas (L) y and the reaction time relationship (d) x obeyed the corresponding linear relationships in each period.

Keywords: Hydrolytic, Kitchen waste, High-solid, Anaerobic digestion, Kinetic model

INTRODUCTION

Waste management and resolving the energy crisis are two significant problems in the modern world. The quest to find alternative fuel sources led to the discovery and use of biogas, which reduces nitrogen and odor from manure management, and intensifies nutrient recycling in agriculture in the form of bio-fertilizers [1]. Currently, kitchen waste production per person per day is 0.15 kg; in 2011, China's cumulative kitchen waste production was over 30 million tons. According to relevant statistics, the proportion of kitchen waste production by region area was as follows: Beijing 40%, Guangzhou 63%, Chongqing 40%, Shanghai 70%, Tianjin 50%, Shenyang 62%, and Shenzhen 57% [2,3], an annual gradual growth rate of 10% to 15%.

Kitchen waste is mainly a mix of organic ingredients, along with a small amount of inorganic constituents. Its properties are as follows [1]:

1. It has a complex composition with poor homogeneity. Sources of kitchen waste are very broad, including restaurants, hotels, flats, student fast kitchen shops, hotels, and catering [4].

2. It has high moisture content. Kitchen waste water content is higher than 70%, resulting in high kitchen waste mobility and easy output leachate leakage. It is therefore difficult to transport [4].

3. It possesses high organic matter content. Dehydrated kitchen waste organic components account for more than 85% of the dry matter. Microbial biodegradation can be used as base material transformation because it contains protein, starch, fat, cellulose, and hemicellulose [4-6].

4. It is digestible. Organic matter can be digested at normal temperatures [5].

5. Kitchen waste has high fat and salt content, which can lead to accumulations of these materials [6-8].

Anaerobic digestion (AD) is a biochemical process that produces energy in the form of biogas [9]. Biogas comprises methane (CH_4) and carbon dioxide (CO_2); biogas is renewable and can replace fossil fuels as an energy source. Anaerobic digestion positively influences waste management, energy production, and fertilizer production [10].

There are several models to assess organic waste anaerobic digestion kinetics [11-13]. The first-order model can compare the AD's performance under practical conditions [14]. Several models and reactor configurations have been developed in recent years, which make it possible to predict a real process response to specific conditions [15-23]. Some authors have also predicted biogas production potential using a modified version of the Gompertz model [24]. Wu and Zhang [25] proposed a segmented hydrolysis kinetic model. In this model, the first segment corresponds to the diffusion of large organic particulates; the second segment corresponds to the reaction rate with small organic particulates. It is believed that hydrolysis is basically unrestricted from diffusion for kitchen waste that is 10 mm in size. Vavilin proposed a hydrolysis rate equation for particulates with different shapes [25]. This equation is consistent with the corrected first-order model proposed by other researchers [24]. The present research aims to simulate the continuous high-solid AD process of kitchen waste with an established model, to prove

---

*To whom all correspondence should be sent:
E-mail: fl_iceee@163.com

the efficacy of simulation, and to provide a theoretical guidance for continuous high-solid kitchen waste anaerobic digestion.

MATERIALS AND METHODS

Table 1 details the initial characteristics of the experimental kitchen waste; these characteristics are also compared with previous studies and their results.

Table 1. Initial mixed kitchen waste characteristics

No.	Parameter	This study	Dupade (2013)	Zhang (2007)
1	pH	7	4-7.1	7.57
2	COD (g/L)	-	5-25	-
3	TS (g/L)	218.1	80-110	309
4	TVS (g/L)	202.83	68- 93	263
5	Moisture content (%)	78.2	30-70	70

Effective volume of the reactor was 20 L. High-solid kitchen waste AD was monitored; more than 23% of TS was achieved, and a kinetic model of gas production was developed. Table 2 shows the devices used in the continuous kitchen waste AD experiment. The set temperature of the AD reactor was 37 °C, and the stirring speed was 120 r.p.m. The pH value was increased to 7.0 with the addition of NaOH at about 5 pm. Stirring were performed 2 times per day. One was after the pH adjustment, the other was at about 9 am.

RESULTS AND DISCUSSION

According to the conservation of materials, input materials equal the sum of the reaction part of the material and the remaining reactors. According to the establishment of a CSTR reactor and an anaerobic fermentation kinetic model [28,29], it is the case that:

$$V_R \left(\frac{dC}{dt} \right) = m_0 C_0 - m_0 C \qquad (1)$$

where, V_R: reactor volume, L; m_0: dosing of the amount of material, L/d; C_0: reactor feed concentration, gVS/L; C: substrate concentration in reactor, gVS / L.

The effective volume of the reactor (VR) remained unchanged; in a completely mixed anaerobic digestion reactor, a solid system of residence time (SRT) is equal to the hydraulic retention time (HRT). In the steady state HRT = C_0 / OLR, you can get:

$$HRT = \frac{1}{k} \left(\frac{C_0}{C} - 1 \right) \qquad (2)$$

In AD reaction, there is a relationship between the substrate concentration and the gas production rate, as shown in Fig. 1.
and,

$$\frac{C_0 - C}{C_0} = \frac{y}{y_m} \qquad (3)$$

From equations (2) and (3) we obtain:

$$HRT = \frac{1}{k} \frac{y}{y_m - y} \qquad (4)$$

$$\frac{y}{y_m - y} = \frac{C_0 k}{OLR} \qquad (5)$$

and also:

$$r_{vs} = \frac{y}{y_m} = \frac{kHRT}{1 + kHRT} \qquad (6)$$

$$y = \frac{kHRT y_m}{1 + kHRT} \qquad (7)$$

where, C_0: reactor feed concentration, gVS / L; C: substrate concentration in reactor, gVS / L; y: t time gas production rate, ml / gVS; y_m: maximum gas production rate, ml / gVS; r_{vs}: organic matter degradation rate, %; OLR: organic loading rate, gVS / (L·d); k: hydrolysis constant, d^{-1}.
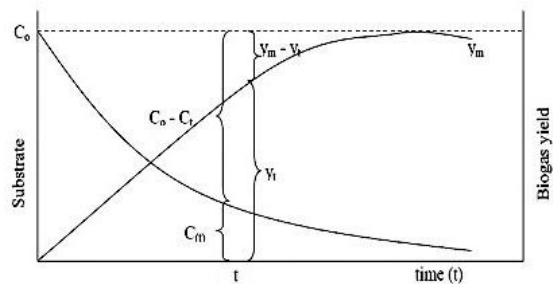

Fig. 1. Changes of substrate concentration and rate of gas production

Table 2. Experimental devices

Name	Analysis	Device	Model
Moisture content (MS)	Dry weight under 105 ℃	Ovens	CJ/T 3039-1995
Volatile solids (VS)	Weight loss on ignition at 600 ℃	Muffle furnace	CJ/T 3039-1995
VFAs	Volatile fatty acids	LC	
pH	Glass electrode method	PHS-3CType pH Meter	CJ/T 99-1999
NH4-N	HACH reagents	Spectrophotometer	
Biogas composition	Gas chromatography	GC	

Equations (6) and (7) present the single-phase continuous AD reactor gas production and biodegradation kinetic models.

Model assumptions: The initial assumptions were as follows: constant temperature; constant volume of digester; perfect mixing; ideal bacterial condition, meaning full digestion; input waste consists only of C, H, and O; products of reaction only include biogas; no ash accumulation.

In this study, continuous mixed kitchen waste AD was carried out according to the different stages of the anaerobic digestion of organic load (OLR), the hydraulic retention time (HRT), and the maximum gas production rate of kitchen waste. Software can be used to simulate the least squares method, which can give the reaction rate constant. Y_m stands for substrate maximum gas production rate, we can understand it as biogas production potential for kitchen waste, which consists of starch, fat, protein, cellucose. We can get biogas production potential for each component according to the Buswell equation. Y_m can be obtained by the sum of the product of the methane production potential and its mass fraction in the kitchen waste. Here, $C_0 = 203$ gVS/L, $y_m = 918$ mL/gVS, OLR in the four different reaction phases, each 1.015 gVS/(L·d), 5.075 gVS/(L·d), 2.5375 gVS/(L·d), 10.15 gVS/(L·d), which were known. After calculation it was obtained that k was $0.133 d^{-1}$. HRT and gas kinetic equation are as follows:

$$y = \frac{122.094 HRT}{1 + 0.133 HRT} \quad (8)$$

$$r_{VS} = \frac{0.133 HRT}{1 + 0.133 HRT} \quad (9)$$

Fig. 2 shows HRT's impact on the gas production rate. Fig. 3 shows HRT's impact on organic matter degradation rates, VS, which is a fitting curve.
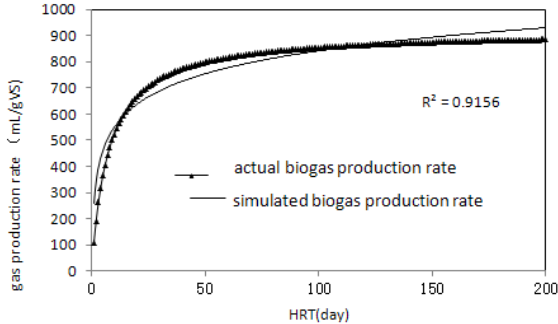

Fig. 2. Hydraulic retention time of organic matter gas production rates
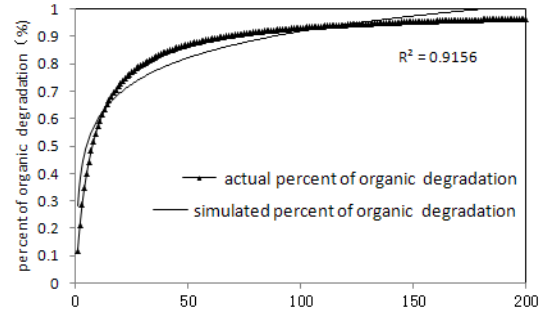

Fig. 3. HRT effects on VS degradation rate

The process is as follows:

Known: Maximum gas production potential rate $y_m = 918$ mL/gVS, the first order reaction constant $k = 0.133$ d^{-1}, then the 70%, 80%, 90% and 99% of the maximum rate of gas production were 642.6 ml/gVS, 734.4 ml/gVS, 826.2 ml/gVS and 908.82 ml/gVS, respectively. HRT were 16 days, 30 days, 68 days and 74 days.

HRT varies depending on other factors, such as the nature of the fermentation substrate, OLR, and temperature. In this experiment, the continuous digestion process and feed concentration $C_o = 203$ gVS/L. This experiment was divided into four phases: adaptive, start-up, inhibition, and recovery phase. They were 200 days, 40 days, 80 days, and 20 days, respectively. The HRT was calculated; at 200 days, the gas production rate can reach 96.38% of the maximum gas production rate.

Volatile fatty acid (VFA) is an intermediate AD product; HRT generates VFA, which has a significant impact. When HRT is large, organic matter degradation efficiency improves, especially in favor of the degradation of biodegradable substances, such as lignin and cellulose. High degradation efficiency and gas production increase, but the reactor's processing capacity will be reduced.

As shown in Fig. 4, the start-up and inhibition phases are marked by a small pH suppression coefficient, low cumulative gas production growth, a slow growth phase to the recovery, and steadily increasing cumulative gas production stability.
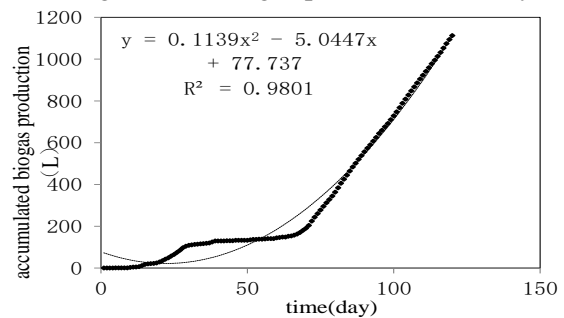

Fig. 4. Comparison of accumulated biogas production and model curve

71

As can be seen from Fig. 4, in the entire 120-day response period, the cumulative gas production growth trend quadratic function and cumulative gas production fits the following formula: $y=0.1139x^2 - 5.0447x + 77.737$; daily gas production for $dy/dx = 0.2278x-5.0447$. Biogas production was not higher than zero until the reaction time $x\geq22$, which is obviously not consistent with the experimental data.

We can also vary gas production models depending on the different phases. This experiment was divided into four phases: adaptive, start-up, inhibition, and recovery phase. They occurred at (0-13th day), (14-34th day), (34-72nd day), and (72-120th day), respectively. Cumulative gas production data during the whole period (120 days) can be divided into three mathematical forms: quadratic function gas phase (1-30 days), complex function gas phase (31 to 65 days), and linear gas phase (66 to 120 days).

From Fig. 5 it can be seen that the adaptation and start-up phases increase gas production. Daily gas production for $dy/dx=0.3554x-1.7517$, indicating that as time increases, the daily gas production increases linearly. $X\geq5$, but only when the reaction time and the daily gas production y were greater than zero. This means that the first four days produced little to no gas. As can be seen from Fig. 5, this agrees with the experimental data.
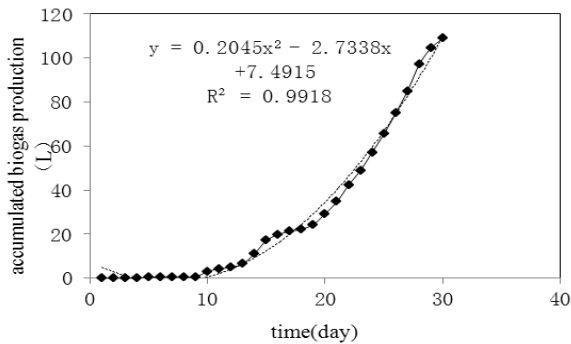

Fig. 5 Adaptation and start-up phase of accumulated gas production and quadratic model curve

From Fig. 6 it can be seen that the cumulative biogas production growth trends have three functions: power, quadratic, and linear. The power function model for daily gas production is $dy/dx = 11.696x-0.6232$, indicating that as time increases, the daily gas production shows negative growth trend compared to the power function when x = 31, when $dy/dx=1.376$; x=65 when $dy/dx = 0.867$. The quadratic model of daily gas production is $dy/dx=-0.0142x+1.7404$, indicating that as time increases linearly, daily gas production displays a negative growth trend when assuming x= 31, $dy/dx=1.300$ was obtained, assuming x= 65, $dy/dx=0.8174$ was obtained. The model's linear function is 1.0565

72

daily gas production, indicating that daily gas production does not change over time.

As can be seen from the figure's three function models, R^2 is about 0.95, indicating that this mathematical function model can accurately reflect the actual experiment conditions, but the R^2 (power function)=0.9521 is greater than R^2 (quadratic function) and R^2 (linear function). So, as the time increases from 31 to 65 days, the daily biogas production displayed a trend of negative growth power function.
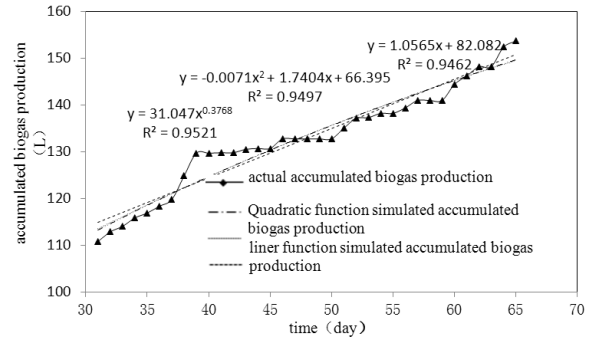

Fig. 6. Inhibition of the late stages of cumulative biogas production before mid 7-12 start-up phase and three function curve fitting

From Fig. 7 it can be seen that at the late recovery and stable phases, with the increase in reaction time, cumulative biogas yield linearly increases. The linear function model for daily gas production is 18.209 L, indicating that as time increases, daily gas production remains unchanged.
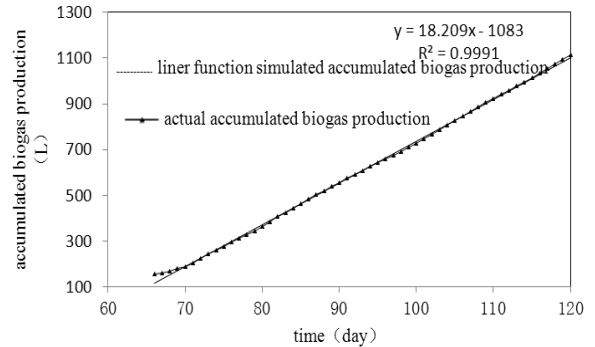

Fig. 7. Recovery and stabilization phase of the accumulative gas yield and linear model curve

CONCLUSIONS

For high-solid kitchen waste AD experiments, depending on the anaerobic digestion stage, the HRT and maximum gas production rate were obtained and the reaction rate constant K was derived (0.133 d^{-1}).

Different HRT organics resulted in different gas kinetic models:

$$y=\frac{122.094HRT}{1+0.133HRT} \quad (10)$$

Anaerobic degradation of VS matter kinetic model for different HRT:

$$r_{vs} = \frac{0.133HRT}{1+0.133HRT} \qquad (11)$$

With the increase in HRT, the gas production rate and organic matter degradation rate showed a logarithmic increment; when the gas production rate was 70%, 80%, 90% and 99% of the maximum gas production rate, the hydro HRT was respectively 16, 30, 68, and 744 days. HRT was calculated for the 200-day adaptation period; the gas production rate can reach 96.38% of the maximum gas production rate.

The obtained cumulative gas (L) and the reaction time relationship y (d)/x form the following model: y = 0.1139x^2 - 5.0447x + 77.737. The phased cumulative gas (L) y and the reaction time relationship (d)/x is as follows: in the adaptation phase, y = 0.2045x^2 - 2.7338x + 7.4915; in the start-up and inhibition phase, y= 31.047x0.3768 or y =-0.0071x^2+1.7404x + 66.395, or y=1.0565x+82.082; in the recovery and stabilization phase, y = 18.209x - 1083.

REFERENCES

1. D.Y. Wang, A.J. Gong, Z.X. Zhang, *Environ. Sanitat. Eng*., **18**, 1 (2010).
2. Y. Chen, J.J. Cheng, *Bioresour. Technol*., **99**, 10 (2008).
3. J. Horiuchi, T. Shimizu, K. Tada, *Bioresour. Technol*., **82**, 35 (2002).
4. A. Hanc, J. Szakva, P. Svehla, *Bioresour. Technol*., **126**, 6 (2012).
5. D. F. Yan, *Environ Sci.Technol*., **23**, 02 (2011).
6. N. Ali, M. Saleem, K. Shahzad, S. Hussain, A. Chughtai, *Polish J. Chem. Technol*., **18**, 88 (2016).
7. X. Guo, E. Trably, E. Latrille, *Hydrocarbon Energy*, **35**, 19 (2010).
8. R.T. Romano, R. Zhang, *Bioresour. Technol*., **99**, 18 (2008).
9. M.S. Rao, S. P. Singh, *Bioresour. Technol*., **95**, 8 (2004).
10. Y.R. Chen, Agric Waste, **8**, 6 (2004)
11. M.S. Rao, S. P. Singh, *Bioresour. Technol*., **95**, 3 (2004).
12. C. Wandrey, A. Aivasidis, *Ann. New York Acad. Sci*., **413**, 48 (1983).
13. R. Moletta, D. Verrier, *Water Res*., **20**, 15 (1986).
14. J.P. Bolte, D. T. Hill, *Waste Manage*., **31**, 18 (1990).
15. S.G. Pavlostathis, G.E. Gomez, *Crit. Rev. Env. Control*, **21**, 4 (1991).
16. D.J. Batstone, J. Keller, I. Angelidaki, *Water Sci. Technol*., **45**, 19 (2002).
17. G. N. Demirer, S. Chen, *Chem. Technol. Biotechnol*., **79**, 13 (2004).
18. E. Sanchez, R. Boria, L. Travieso, *Bioresour. Technol*., **96**, 33 (2005).
19. A. J. Wang, W. W. Li, H. Q. Yu, *Adv Biochem. Eng. Biotechnol,* **34**, 128(2012).
20. C. H. Song, Z. M. Wei, B. D. Xi, *J. Safe. Environ.*, **13**, 2 (2013).
21. A. Nopharatana, P.C. Pullammanappallil, *Waste Manage*., **27**, 5 (2007).
22. S. Pommier, D. Chenu, M. Quintard, *Biotechnol. Bioeng.*, **97**, 3 (2007).
23. D.D. Brüllmann, A. M. Sachs, *Oral Surg. Oral Med. Oral Pathol. Oral Radiol.*, **115**, 3 (2013)
24. S.M. Gao, M.X. Zhao, Z.Y. Xu, *J. Safe Environ.*, **15**, 1 (2015).

Helicopter transient electromagnetic combined waveform transmitting technology for metal exploration

B. Guo[*], Y. M. Zhang, J. L. Zhang, X. H. Wang, J. Z. Ding, J. X. Gao

Faculty of Information Technology, Beijing University of Technology, Beijing, China

Aiming at the technical requirements to a Helicopter Transient ElectroMagnetic (HTEM) transmitter for metal ore exploration, a novel multi-pulse transmitter circuit based on LC resonance principle is proposed. Based on the full control characteristics of the IGBT device and the energy four-quadrant operation technology of the bridge circuit, a combined multi-pulse transmission circuit was realized, and precise driving timing was generated by the DSP module. The power control circuit transmits a multi-pulse waveform consisting of half-sine and trapezoidal wave to realize reuse of the same set of circuits. The principle and the circuit design method of multi-pulse emission were discussed in detail. The dynamic process and the circuit parameters of energy conversion in the half-sine and the trapezoidal wave were analysed. A bipolar multi-pulse transmitter prototype circuit with main pulse of 500A and trapezoidal wave of 50A was developed and verified by test experiments. The test results showed that the emission control method proposed in this paper achieves high-pulse current emission and small-pulse emission along the steep edge, the small-pulse edge is linearly turned off and the pulse duration is controllable. The validity of the proposed circuit topology was verified and the capability of HTEM transmitting system was improved.

Key words: Helicopter transient electromagnetic, Broadband, Combination waveform, LC resonance.

INTRODUCTION

Airborne electromagnetism is an effective method for prospecting in areas with complex topography such as deserts, swamps and forests because of its fast speed, efficiency and no need for surface personnel in prospection [1,2]. Because of its low cost, high resolution and good trafficability, the HTEM system has gradually become an important technical means in the field of airborne electromagnetic exploration [3-6]. The principle is that a primary magnetic field signal is transmitted through an aerial transmitting coil, a second magnetic field generated by induced eddy currents in an underground ore body is detected by a receiving coil, and underground electrical structure is estimated according to a second magnetic field signal [7] (Figure 1).

With the development of helicopter transient electromagnetic systems, it becomes more and more important to acquire detailed shallow area information while improving the system's depth sounding [2-8]. Simultaneous acquisition of deep and shallow area information in a flight requires that transmitters have wide-band excitation signal transmission capabilities as not only strong low-frequency signals are needed for deep information, but also abundant high-frequency information is needed for fine delineation of shallow geological structure [9,10]. SkyTEM achieves low-frequency

large magnetic moments (30 Hz, 1 million Am^2) and high-frequency small magnetic moments (270 Hz, 0.4 million Am^2) by using different transmitting coils [11]. The two transmit modes require cooperation of transmitting coils with a specific number of turns and need two flights along the same survey line to obtain deep and shallow area information, so the field construction efficiency is low. Canadian Geotech's VTEM system makes the transmit waveform approximate square waves to provide large magnetic moments and rich high-frequency information by increasing current peaks and off-time of transmit waveform [12]. Since the transmitting coil has high perceptual characteristics, quick turn-off under high emission current will cause a very large turn-off voltage stress. Improvement in turn-off time and enhancement of transmitted magnetic moment are a paradox. It is difficult to greatly increase emission current while keeping rapid turn-off at the same time, so the transmitted magnetic moment is limited. The company's VTEM-Max system achieves a peak magnetic moment of 1.3 million Am^2 by increasing the area of transmitting coil. However, the increased area of transmitting coil leads to increased difficulty in flight control. The system can only fly in flat area with flat terrain, so its practical application is limited. The CHTEM-I system developed by Chen *et al*. [13] under the support of "863" program adopts trapezoidal wave approximate to square wave with a transmitted magnetic moment of 0.25 million Am^2. By

---
[*] To whom all correspondence should be sent:
E-mail: guobing2014 @emails.bjut.edu.cn

increasing the current turn-off speed, the system effectively increases high frequency components of the system transmit signals, but the transmitted magnetic moment is low, so it is difficult to achieve large depth in exploration. Yu *et al*. [14] achieved transmitted magnetic moment of 0.5 million Am^2 by using half-sine transmit waveforms, but still failed to solve the problem of low resolution of shallow area due to the use of half-sine waveform.

Considering the high inductive characteristics of transmitting coil and skin effect of signal propagating in the strata, the half-sine wave with strong electromagnetic field diffusion ability and easy realization of large current and rectangular wave or trapezoidal wave containing abundant frequency information are combined to transmit half-sine wave with a large magnetic moment and one or more trapezoidal waves with small magnetic moments in one transmit cycle [10]. Half-sine waves with large magnetic moment are transmitted to achieve deep exploration. The fast turn-off of small magnetic moment trapezoidal wave enables high-resolution shallow geological information. The transmitted waveform realizes deep sounding and high resolution at shallow area probing.

In recent years, based on the exploration and application of mineral resources and the needs of national energy strategy, the technology and methods of transient electromagnetic transmitted waveform control are developing rapidly. Fu *et al*. [15] realized a shaping circuit to speed up current shut-off. Li *et al*. [16] proposed a flat-topped half-sine waveform transmitting circuit for a fixed-wing transient electromagnetic system. Liu *et al*. [17] proposed an active clamp to achieve linear control of waveform edges. Yu Shengbao *et al.* [14] proposed a series resonant half-sine generation circuit based on a semi-controlled device. However, there is still no effective solution to multi-pulse combined emission. Although high current and high power pulse power supply have been widely used in other fields, for example, there are related studies and applications in the fields of laser power sources [18], photon sources [19] and particle accelerators [20], these impulse sources are generally bulky and heavy with low repetition frequency and only single pulse waveform can be transmitted, which are very difficult to be directly applied to an HTEM system.

In order to improve the exploration capability of the HTEM electromagnetic system and realize wideband emission current waveform, targeting at transmission of multi-pulse combination waveform, a multi-pulse transmitting circuit and control method suitable for the HTEM transmitter system was proposed in this paper. Based on full control

characteristics of IGBT device and energy four-quadrant operation technology of bridge circuit, multi-pulse combination waveform transmitting circuit was developed. The precise drive timing was generated by DSP. The multi-pulse combination waveform composed of half-sine and trapezoidal wave enabled reuse of the same set of circuit, thus offering advantages of simple structure and high reliability.
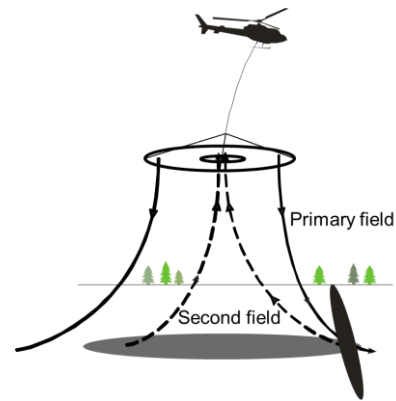

Fig. 1. HTEM operation principle.

COMBINED WAVE TRANSMITTER ARCHITECTURE

The operating principle of multi-pulse HTEM system transmitter is shown in Figure 2. The system mainly includes four parts of high-power main circuit, control unit, power management and operation interface. The high-power main circuit consists of power supply, charging circuit, resonant circuit, signal detection and drive circuit. The control unit is mainly composed of DSP control module, synchronization circuit and remote control logic. The operation interface provides user control information input, transmitter status output, synchronization signal access and transmitter remote control connection.

The functions of each part of the system are as follows: DSP control unit and the master control system have real-time data exchange to generate synchronized timing logic control signals; signal detection unit provides voltage detection and current waveform recording, temperature detection and small trapezoidal wave turn-off detection for real-time monitoring of transmitter status; driver circuit converts PWM control signal generated by DSP to IGBT gate drive signal with a certain driving ability, and fully controls opening and shutoff of IGBT; IGBT transmitting bridge is for power conversion that controls capacitor bank charging and LC resonant circuit sub-combination. The power management converts high voltage

power into voltages required for functional circuits, and safely isolates strong and weak power.
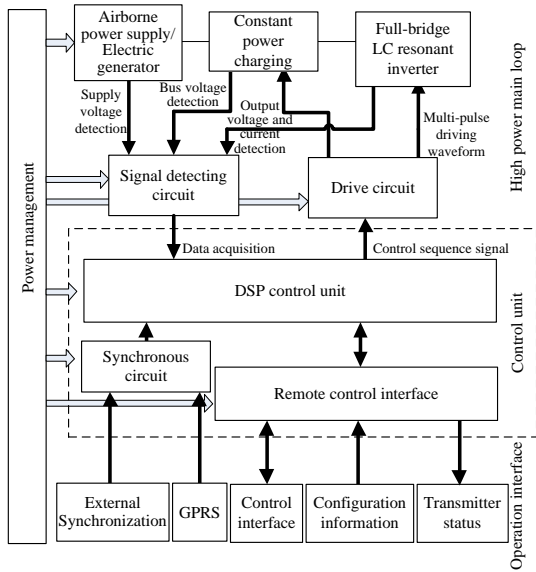

Fig. 2. Diagram of time domain multi-pulse airborne electromagnetic transmitter.

COMBINED MULTI-PULSE TRANSMITTER PRINCIPLE

It is because the shorter the turn-off delay time, the richer is the high-frequency information contained in the corresponding frequency spectrum, and the higher is the capacity of high-frequency signal, which can effectively improve system exploration ability in shallow area. As can be known from skin effect of signal, high-frequency signal decays rapidly during the propagation in strata, while low-frequency signal can penetrate the strata and reach deeper. Hence, deep exploration requires emission of low-frequency pulse with a large magnetic moment and long current duration as much as possible. It is because of the longer duration, stronger energy is sensed in subterranean medium, and the corresponding late observation signal is stronger [21].

The multi-pulse transmission control method proposed in this paper consists of a transmitting coil, a capacitor bank and an IGBT bridge circuit. The four-quadrant operation mechanism of pulse energy was used to realize multi-pulse transmission, residual energy recovery of the transmitting coil and voltage clamping on the edge of the trapezoidal wave.

The proposed multi-pulse transmitting circuit structure is shown in Figure 3, which consists of three parts: DC/DC capacitor charging circuit, storage capacitor bank C_{bank} and LC resonant bridge inverter circuit. Multi-pulse transmission waveform is shown in Figure 4, which includes half-sine main

76

pulse and sub-waveform small trapezoidal wave. A cycle is divided into two parts of positive half cycle and negative half cycle. A cycle consists of 10 control intervals (Figure 5). Positive and negative polarity pulse have similar control mode. The following is a detailed description of the transmission process of positive-polarity wave under steady state conditions.
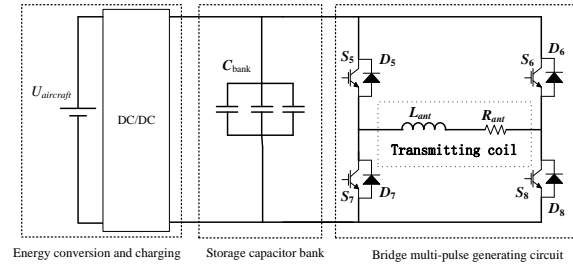

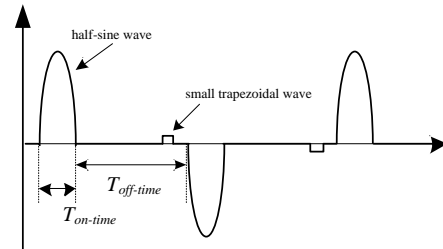**Fig. 3.** Transmitter circuit topology.

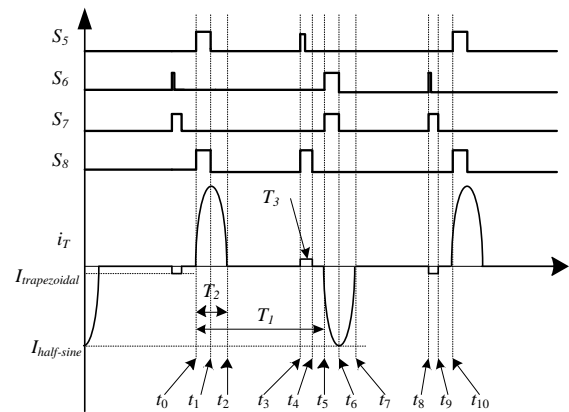**Fig. 4.** Multi-pulse transmitting waveform.

Fig. 5. Multi-pulse current generation waveform.

Before time t_0, C_{bank} is charged to voltage U_C and the charging circuit is disconnected. S_5 and S_8 are turned on at time t_0, as shown in Figure 6(a). C_{bank} and transmitting coil then form a loop, transmitting half-sine rising current waveform as shown in time period t_0 to t_1 in Figure 5. At time t_1, S_5, S_8 are closed, then transmitting coil L_{ant} constitutes a resonant circuit through D_6, D_7 and C_{bank}, and the equivalent circuit is shown in Figure 6(b) below. Half-sine drop-out current is transmitted in time period t_1 to t_2 (Figure 5). Half-sine main waveform

output is completed at time t_2. At time t_2, S_5-S_8, D_5-D_8 are turned off, charging circuit is started, so that U_{charge} charges C_{bank}, and the equivalent circuit is shown in Fig. 6(c). At time t_3, S_5, S_8 are turned on, the rising edge of the small trapezoidal wave is transmitted by the resonance of the transmitting coil and the storage inductor as shown in Figure 6(d). When the output current reaches I_2, S_5 is turned off, and a freewheeling circuit is formed through D_7, S_8, resulting in a flat top part of the small trapezoidal wave, as shown in Figure 6(e).
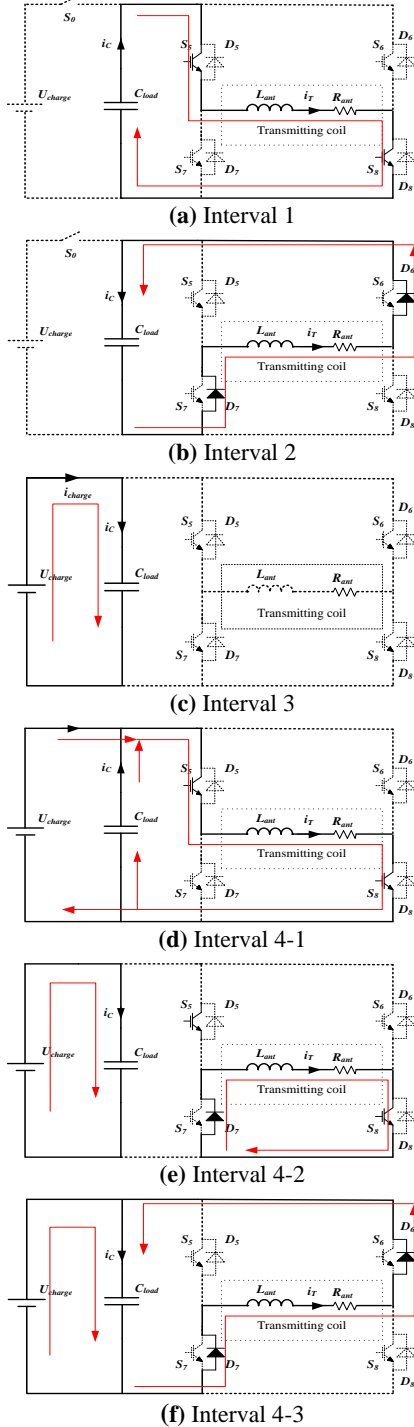

(a) Interval 1

(b) Interval 2

(c) Interval 3

(d) Interval 4-1

(e) Interval 4-2

(f) Interval 4-3

Fig. 6. Multi-pulse generation process equivalent circuit.

At time t_4, S_8 is turned off, L_{ant} and C_{bank} form a resonant circuit, resulting in falling edge of small trapezoidal wave and completing transmission of small trapezoidal wave, as shown in Figure 6(f).

During [t_4, t_5], U_{charge} continues to charge C_{bank}. At time t_5, voltage on both ends of C_{bank} reaches the present value U_C, and the charging circuit is turned off. Thus, positive polarity waveform transmission of the first half cycle is completed and preparation for the negative polarity half cycle is done.

EXPERIMENTAL

Experiments

According to the theoretical analysis of a multi-pulse transmission process, the experimental parameters were been deduced without considering the coupling between the transmitting coil and the earth target. Equations (1)~(3) refer to multi-pulse base frequency, duty cycle and sine wave frequency, respectively, where, T_1 is the duration of a single half-sine waveform and T_2 is the duration of a half-cycle.

$$f_{base} = 1/(2T_1) \tag{1}$$
$$D = T_2/T_1 \tag{2}$$
$$f_{\sin} = 2f_{base}/D \tag{3}$$

When S_5 and S_8 are closed, the resonant circuit equivalent circuit is shown in Figure 7. It can be drawn from the law of Huff voltage that:

$$L_{ant}C_{bank}\frac{d^2i_T(t)}{dt^2} + R_{ant}C_{bank}\frac{di_T(t)}{dt} + i_T(t) = 0 \tag{4}$$

$$R_{ant} < 2\sqrt{L_{ant}/C_{bank}} \tag{5}$$

$$\begin{cases} L_{ant}\dfrac{di_T(t)}{dt}\bigg|_{t=0} = -U_C \\ \quad i_T(0) = 0 \end{cases} \tag{6}$$
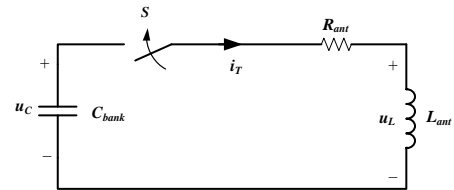

Fig. 7. Equivalent circuit at beginning resonance.

The transmitting coil is generally made of conductor with high conductivity and can easily satisfy the condition (5). According to the initial condition (6), the expression of half-sine transmitting current can be obtained:

$$i_T(t) = \frac{1}{\omega L_{ant}} U_C e^{-\delta t} \sin \omega t \qquad (7)$$

where,

$$\begin{cases} \delta = \dfrac{R_{ant}}{2L_{ant}} \\[3mm] \omega = \sqrt{\dfrac{1}{L_{ant}C_{bank}} - \left(\dfrac{R_{ant}}{2L_{ant}}\right)^2} \end{cases} \qquad (8)$$

When $\omega t = \pi / 2$, the electric field energy stored in the capacitor can be completely converted into magnetic field energy in the transmitting coil. The peak value of the transmitting current is:

$$I_{half-sine} = \frac{U_C}{\omega L_{ant}} e^{-\delta \frac{\pi}{2\omega}} \qquad (9)$$

When the loss in the loop freewheeling process is not considered, the rising and falling edge time of the small trapezoidal wave is:

$$t = \frac{1}{\omega} \arcsin \frac{I_{trapezoidal}}{I_{half-sine}} \qquad (10)$$

Edge slope of the trapezoidal wave can be obtained according to the resonant current equation (9):

$$K = \frac{R_{ant}}{2L_{ant}^2} U_C \qquad (11)$$

Small trapezoidal wave duration is short, and U_C descends according to the cosine curve, U_C is approximately regarded as unchanged at the initial moment of resonance, then the edge slope of the trapezoidal wave is in linear relationship with U_C.

Raw material

The detailed input and output parameters of the prototype are shown in Table 1. Precise timing control was achieved by DSP operation. The transmission of large half-sine magnetic wave was achieved by full energy exchange, and small trapezoidal waves were transmitted by voltage clamping of storage capacitor and fast switching of IGBT, and the same transmitting circuit was reused. US Tektronics oscilloscope and the corresponding high-precision current and voltage detection probes were used to measure the actual transmitted current and voltage waveform.

Table 1. Transmitter I/O

Parameter	Value
Half-sine peak current ($I_{half-sine}$)	500 A
Small trapezoidal current ($I_{trapezoidal}$)	50 A
Transmission base frequency(f_{base})	25 Hz
Main pulse duty cycle (D)	0.4
Transmitting coil radius	10 m
Transmitting coil turns	6
Transmitting coil inductance	1.98 mH

RESULTS AND DISCUSSION

According to the above multi-pulse transmission circuit principle and control method, a set of principle prototype circuit was completed, and its experimental testing and verification were done.

Figure 8 shows the current and voltage waveforms of charging and discharging of storage capacitor. Due to the large capacity of the storage capacitor bank and the use of low ESR dedicated storage capacitors, charging and discharging of current are stable, and there is no current distortion.
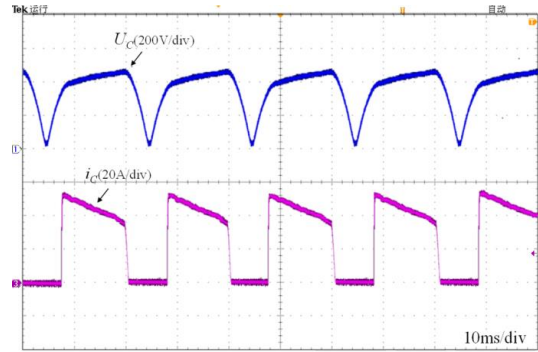

Fig. 8. C_{bank} charging current and voltage

Figure 9 shows the waveform of multi-pulse current i_T, the waveform of transmitting voltage U_T and the voltage of the storage capacitor U_C. It can be seen from the figure that during the non-transmission period $T_{off-time}$, the storage capacitor voltage is charged by the charging circuit to the preset voltage value, so that repetitive transmission at base frequency 25Hz can be well realized. Also, half-sine main waveform duty cycle can reach 0.4, half-sine main waveform peak current reaches 500A. After the transmission current reaches the peak, by controlling the IGBT switch combination, the remaining energy in the inductance of the transmitting coil is guided back to the storage capacitor.
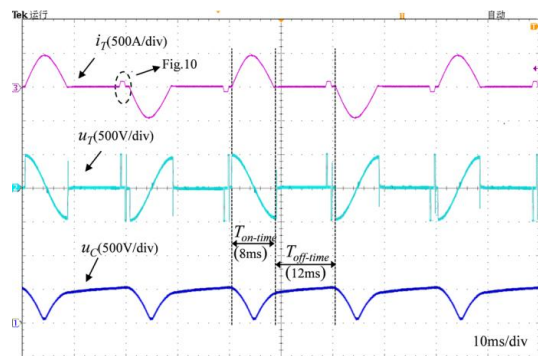

Fig. 9. Multi-pulse current and voltage.

Figure 10 shows an enlarged view of the small trapezoidal wave. Based on the experimental test

waveforms, it can be seen that the rising and trailing edge time of the small trapezoidal wave is approximately 200 μS, which is approximately linearly transformed and consistent with the theoretical analysis. During the transition between resonance and freewheeling mode, smooth current transition can be ensured without current overshoot and oscillation. The flat top current reaches 50 A, which can be effectively adjusted by controlling the time of LC resonance at the rising edge.
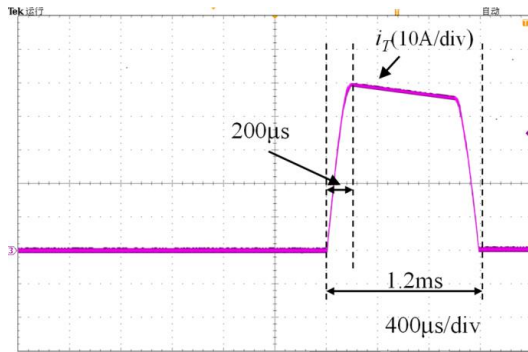

Fig. 10. Zoom-in view of the small pulse.

CONCLUSION

In order to solve the problem of wideband primary field signal transmission by a time-domain airborne electromagnetic system, a novel multi-pulse combined waveform transmission control method and circuit was proposed in this paper. Based on LC resonance and IGBT combined control technology, fast buffer and efficient recovery of transmitting coil energy was realized. More high-frequency signal components were provided under the premise of ensuring large emission current. Experimental results showed that the proposed control circuit can transmit high-quality bipolar multi-pulse waveform. Also, transmitter reliability was improved by reuse of the transmitting circuit.

REFERENCES

1. D. Fountain, *Exploration Geophysics*, **29**, 1 (1998).
2. C.C. Yin, B. Zhang, Y.H. Liu, *Chinese J. Geophysics*, **58**, 2637 (2015).
3. W.P. Wang, Y.Y. Fang, C.P. Wu, *Chinese Journal of Engineering Geophysics*, **6**, 411 (2009).
4. S.J. Liang, L.K. Zhang, X.F. Cao, Q.K. Liu, *Geology and Exploration*, **50**, 735 (2014).
5. V. Sapia, G.A. Oldenborger, A. Viezzoli, M. Marchetti, *Journal of Applied Geophysics*, **104**, 35 (2014).
6. D. D. Massa, G. Florio, A. Viezzoli, *Journal of Applied Geophysics*, **125**, 45 (2016).
7. Y.F. Pei, C.C. Yin, Y.H. Liu, *Progress in Geophysics*, **29**, 2191 (2014).
8. J. Macnae, *Fifth Decennial International Conference on Mineral Exploration*, **387**, 1 (2007).
9. C.C. Yin, X.Y. Ren, Y.H. Liu, *Chinese J. Geophysics*, **58**, 3370 (2015).
10. T. Chen, G. Hodges, P. Miles, *Exploration Geophysics*, **46**, 49 (2015).
11. J. Reid, N. Christensen, K. Godber, *ASEG*, 2012, 1 (2012).
12. K. Tan, N. Symington, K. Lawrie, N. B. Christensen, *ASEG*, 2016, 1062 (2016).
13. B. Chen, L. F. Mao, G. D. Liu, *Chinese J. Geophys.*, **57**, 303 (2014).
14. S. Yu, Z. Han, C. Sun, Z. Zhu, J. Jiang, *Journal of Central South University (Science and Technology)* 2017, 729 (2017).
15. Z.H. Fu, J.L. Zhao, L.W. Zhou, *Chinese Journal of Scientific Instrument*, **29**, 933 (2008).
16. J.F. Li, W.J. Li, J.J. Liu, *Geophysical and Geochemical Exploration*, **38**, 1186 (2014).
17. L.H. Liu, K. Wu, Z. Geng, *Progress in Geophysics*, **31**, 0449 (2016).
18. C.K. Chana, C.C. Changa, C.L. Chena, C.S. Yanga, K.H. Hsua, Y.T. Huanga, C.K. Kuana, H.P. Hsueha, S.N. Hsua, P.J. Choua, G.Y. Hsiunga, J.R. Chenab, *Nuclear Instruments and Methods in Physics Research*, **709**, 56 (2013).
19. S.D. Jarvis, J. Mukherjee, M. Perren, S. J. Sweeney, *IET Optoelectronics*, **8**, 64 (2014).
20. K. Yoshinori, *IEEE Trans. Appl. Supercond.*, **26**, 1 (2016).
21. C.C. Yin, C.K. Qiu, Y.H. Liu, J. Cai, *Chinese J. Geophys.*, **59**, 3079 (2016).

Experimental study on permeability improvement of different rank coal samples by acidification

M. K. Luo [1,3], S. Li [1,2,3*], C. J. Fan [1,3], Z. H. Yang [1,3], H. Z. Yang [1,3]

[1] College of Mining, Liaoning Technical University, Fuxin, Liaoning, 123000, China

[2] State Key Laboratory of Coal Resources and Safe Mining, China University of Mining and Technology, Xuzhou, Jiangsu 221116, China

[3] Resrach Center of Coal Resources Safe Mining and Clean Utilization, Liaoning Technical University, Fuxin, Liaoning, 123000, China

In view of the fact that the coal seam is blocked by filling material, the permeability in the coal seam is low. Therefore, a new method was put forward to enhance the permeability of coal seam by acid injection. The permeability increase effect *via* acid injection in different-rank coal reservoirs was studied. The characteristic changes of surface structure, pore structure, mineral content and permeability of coal samples were analyzed by SEM, ASAP, XRF and permeability measurements. Experimental results showed that: After acidification, the surface crack profile of the coal sample was clearer, the number and width of the cracks increased, the porosity-fracture network connectivity was enhanced, but the dissolution effects of high-rank coal were relatively poor. The specific surface area of coal samples decreased, the pore volume increased, and the changes were mainly concentrated at the pore width of 2~10 nm. Ca, Mg and other mineral content obviously decreased. Acidification did not cause damage to the organic matter of coal. The permeability of coal samples generally increased, the lower the coal rank, the higher were the initial permeability and the carbonate mineral content, the more obvious was the permeability increment. Coal injection technology can effectively improve the pore structure of coal, enhance the diversion capacity, and increase the permeability of coal reservoir, which leads to the improvement of gas drainage rate and gas resource exploitation.

Key words: Coal bed acidification, Chemical permeability improvement, ASAP, XRF.

INTRODUCTION

The permeability of the coal seam can affect the coal bed methane (CBM) recovery factor and gas extraction rate. The permeability of the coal seam in China is generally by 2~ 3 orders of magnitude lower than that in America due to the special geological conditions [1,2], causing difficulty of gas flow in the coal seam and low productivity of CBM. Moreover, with the increase in mining depth, gas content will increase and coal seam permeability will further decrease [3].

A lot of studies have been done for the permeability improvement in low gas permeability coal seams. The hydraulic fracturing technology was improved by using high-voltage pulse pressure [4,5]. On the basis of hydraulic fracturing technology, chlorine dioxide was used as a gel breaker to increase the permeability of coal seam [6]. Based on the fracture mechanics and seepage mechanics theory, the parameters between hydraulic slotting and hydraulic fracturing were optimized [7,8]. The liquid CO_2 blasting technology was used to improve coal seam permeability [9,10]. The coexistence of coal seam permeability improvement and stability of surrounding rock

through controlled crack evolution direction was studied by directional blasting technology [11]. Ultrasonic technology has also been used for low coal seam permeability enhancement [12,13]. Through the acidification experiment of No. 3 coal reservoir in Jincheng mining area, it was proved that hydrochloric acid can effectively enhance the rich calcite coal seam [14]. The effect of microorganisms on enhancing the permeability of different-rank coals was also studied [15]. At present, the permeability of coal reservoir is mainly improved by physical methods, such as hydraulic fracturing, hydraulic slotting, deep hole blasting; there are also several chemical and biological methods, gradually showing a trend of diversification.

The pore-fracture system of the coal reservoir is the channel of material exchange in the coal seam; the development degree and the connectivity of coal seam influence the permeability of the coal reservoir. In the long geological time, a lot of the coal reservoir pore-fracture has been blocked by minerals such as calcite, dolomite, hematite, pyrite, and other impurities. For example, the coal reservoir fractures in North China Permo-Carboniferous coal and Henan Jiaozuo area are mainly filled with calcite [16,17]. For this kind of low permeability coal seams, it is undoubtedly one

of the better choices to use a chemical method to increase permeability by acid injection in the coal seams.

THEORY

The permeability improvement of coal reservoirs by acid injection is a method which can improve the conductivity of the coal reservoir by injecting one or several kinds of acid into the coal seam. Through the dissolution and corrosion of the acid to the cement and blockage in the coal reservoir pore–fracture system, the permeability of the coal seam is increased [18,19]), as Figure 1 shows.
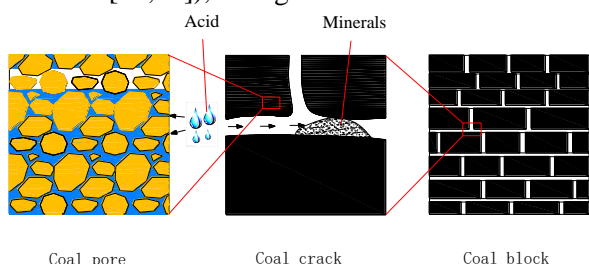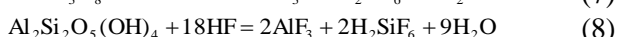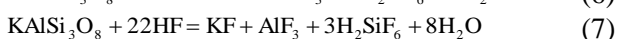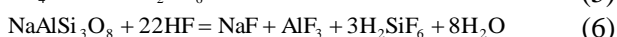

Fig. 1. Principle of coal bed acidification

Chemical reactions

The chemical principles of reactions between different minerals and acids in coal seams are different. According to the common components of minerals in coal seams, the main reaction equations are as follows:

$$CaCO_3 + 2HCl = CaCl_2 + CO_2 \uparrow + H_2O \quad (1)$$
$$CaMg(CO_3)_2 + 4HCl = CaCl_2 + MgCl_2 + 2CO_2 \uparrow + 2H_2O \quad (2)$$
$$Fe_2O_3 + 6HCl = 2FeCl_3 + 3H_2O \quad (3)$$
$$SiO_2 + 4HF = SiF_4 + 2H_2O \quad (4)$$
$$SiF_4 + 2HF = H_2SiF_6 \quad (5)$$
$$NaAlSi_3O_8 + 22HF = NaF + AlF_3 + 3H_2SiF_6 + 8H_2O \quad (6)$$
$$KAlSi_3O_8 + 22HF = KF + AlF_3 + 3H_2SiF_6 + 8H_2O \quad (7)$$
$$Al_2Si_2O_5(OH)_4 + 18HF = 2AlF_3 + 2H_2SiF_6 + 9H_2O \quad (8)$$
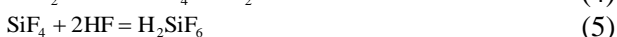
Erosion

When acid is injected into coal seam, the chemical reaction will occur. At the same time, the acid will corrode the coal matrix touched by the acid. Some colloid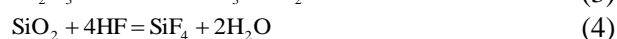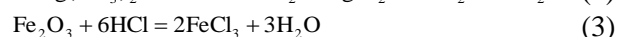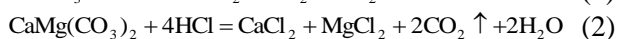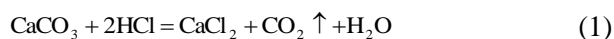s and blockages in the coal matrix are eroded and dissolved under the action of acid. With the process of acid flowback, the dissolved substance is brought out of the coal body, thus increasing the porosity and connectivity of coal. The basic condition for acid to produce corrosion of coal is that the acid liquid can be fully contacted with coal. The more the coal contacts with the acid solution, the more H+ is transferred, the reaction rate is faster and the degree of dissolution is higher.

EXPERIMENTAL

Acid system

According to the principle of increasing permeability by injecting acid into the coal seam, in this experiment, the "HCl+HF" mixed acid was chosen to do the acidification experiment. In order to avoid damage of coal seam due to the secondary reaction with HF in acidification process, high concentration of HCl is needed to restrain that. Therefore, the mass fractions of HCl prepared in this experiment were 9%, 12% and 15%, and the mass fraction of HF was 3%. At the same time, it was considered that the non-crystalline kaolinite and other minerals in the fissures of the coal reservoir expanding and blocking the channel during the acidification process, on the contrary, reduce the permeability of the coal seam. So, 2% NH_4Cl (commonly used in petroleum field) was added as an antiswelling agent [20,21]. So, three kinds of acid systems of this experiment were constituted: 9%HCl+3%HF+2%NH_4Cl (Acid Ⅰ), 12%HCl+3%HF+2%NH_4Cl (Acid Ⅱ) and 15%HCl+3%HF+2%NH_4Cl (Acid Ⅲ). Both the acid container and the acidification site were inert plastic bottles.

Experimental program

The experimental coal samples were collected from Xinzhouyao mine of Datong in Shanxi province, Qianjiaying mine of Tangshan in Hebei province and Jiangjiahe mine of Xianyang in Shaaxi province, the coal ranks of which are coking coal, fat coal, non-caking coal. Basic characteristic parameters of the initial coal samples are shown in Table 1. In order to study the permeability increase effect *via* acid injection in different-rank coal reservoirs, four series of experiments, A, B, C and D, were carried out.

Series A was a scanning electron microscope (SEM) observation experiment. First of all, parts of the coal samples in each mine were acidified with acid II for 24 h, and then dried for 3 h. All coal samples were prepared from thin coal of about 1 cm². The surface structure characteristics of different-rank coal samples before and after acidification were comparatively analyzed by a Q45 tungsten filament SEM system.

Series B was a low-temperature nitrogen adsorption experiment. First of all, parts of the coal samples in each mine were acidified with acid II for 24 h, and then dried for 3 h.

Table 1. Characteristic parameters of coal samples

Sample source	Coal seam	M_{ad} / %	A_{ad} / %	V_{daf} / %	$R_{o,max}$ / %	Porosity/%	Coal rank
Xinzhouyao mine	11-2#	2.04	8.62	25.29	1.32	6.94	Coking coal
Qianjiaying mine	12#	1.70	14.11	28.36	1.08	7.23	Fat coal
Jiangjiahe mine	4#	5.03	7.54	30.56	0.87	6.58	Non-caking coal

The coal samples before and after acidification were prepared into 60 ~ 80 mesh, then the surface area and pore structure characteristics of coal samples were measured by a Micromeritics ASAP 2020 physisorption instrument. The experimental procedure is as follows: put about 2 g of the pulverized coal into the sample tube and after degassing, quality test and sample analysis were carried out for each sample. At a correlation coefficient greater than 99.9%, the test results were believed to be reliable.

Series C was a mineral content measuring experiment. Parts of the coal samples in each mine were acidified with acid II for 24 h, and then dried for 3 h. The coal samples before and after acidification were prepared into 200 mesh. The mineral content of coal samples before and after acidification was measured by a XRD6100 test system on a S8 TIGER X-ray fluorescence spectrometer. The test angle range of XRD was 2°~120°.

Series D was a permeability test. In this experiment, the permeability of the coal samples was measured by a self-made coal and rock permeability measurement system (Figure 2) mainly composed of high-pressure gas source, sealing device, pressure chamber, pressure device, pressure stabilizer, gas collecting device and other parts. Assuming that experimental coal sample is a continuous incompressible medium, on the basis of the one-dimensional theory of a single-phase flow, gas state equation and Darcy's law, the formula of coal and rock permeability can be obtained [22]:

$$K = \frac{2\mu P_0 QL}{A\left(P_1^2 - P_2^2\right)} \qquad (9)$$

where K is permeability, mD; μ is viscosity coefficient of methane, mPa·s; P_0 is standard atmospheric pressure, Mpa; P_1 and P_2 are the gas pressures of pressure chamber inlet and outlet, MPa, respectively; Q is the gas flow under standard conditions, cm³/s; L is the length of coal sample, cm; A is the cross section area of coal sample, cm².

The coal samples were made into standard specimens of size ϕ 50mm × 100mm by a core drilling machine and cutting machine. The permeability of the standard specimens was tested by soaking the specimens in acid I, II, III for 6, 12, 18, 24, 30 and 36 h. The specimens must be dried at 60 ℃ for 3 hours before testing, to avoid the effect of moisture content on the permeability test. During the test, the confining pressure was 2 MPa, the axial pressure was 1 MPa and the experimental temperature was 25 ℃.
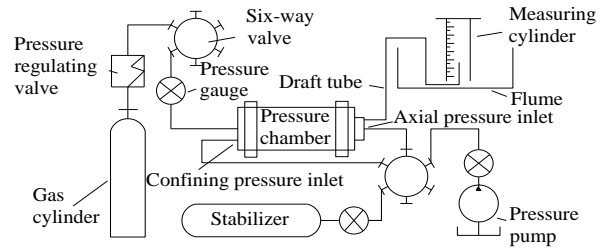

Fig. 2. Coal permeability measurement system

RESULTS AND DISCUSSION

Surface structure characteristics

The surface structures of coal samples before and after acidification are shown in Fig. 3. In the initial state, Xinzhouyao and Qianjiaying coal sample porosity degrees were better in comparison with Jiangjiahe. Some fillings can be observed in the pores and fissures of each coal sample. Among them, scattered minerals (Figure 3e) can be observed in the coal samples of Jiangjiahe. After the acidification, the fillings (such as minerals and colloids) were eroded, the outline of pores was clearer, the length, width and number of cracks increased, and the connectivity of pore-fracture system was remarkably improved, especially, the coal samples of Jiangjiahe.

The results show that the acidification corrosion of the low rank coal samples of Jiangjiahe is obviously better than that of the high-rank coal samples of Xinzhouyao and Qianjiaying under the same conditions. First reason, there are differences in the content of minerals contained in each coal sample. Jiangjiahe coal sample contains more minerals, its acidizing effect is better. Another reason is that high-rank coal has a high degree of aromatic ring polymerization, and less side chains reacting with the acid, so it can greatly resist acid corrosion.

At a larger specific surface area, the higher degree of coal body tortuosity inside leads to higher conductivity to gas storage in the coal seam. However, this is not good for gas storage.
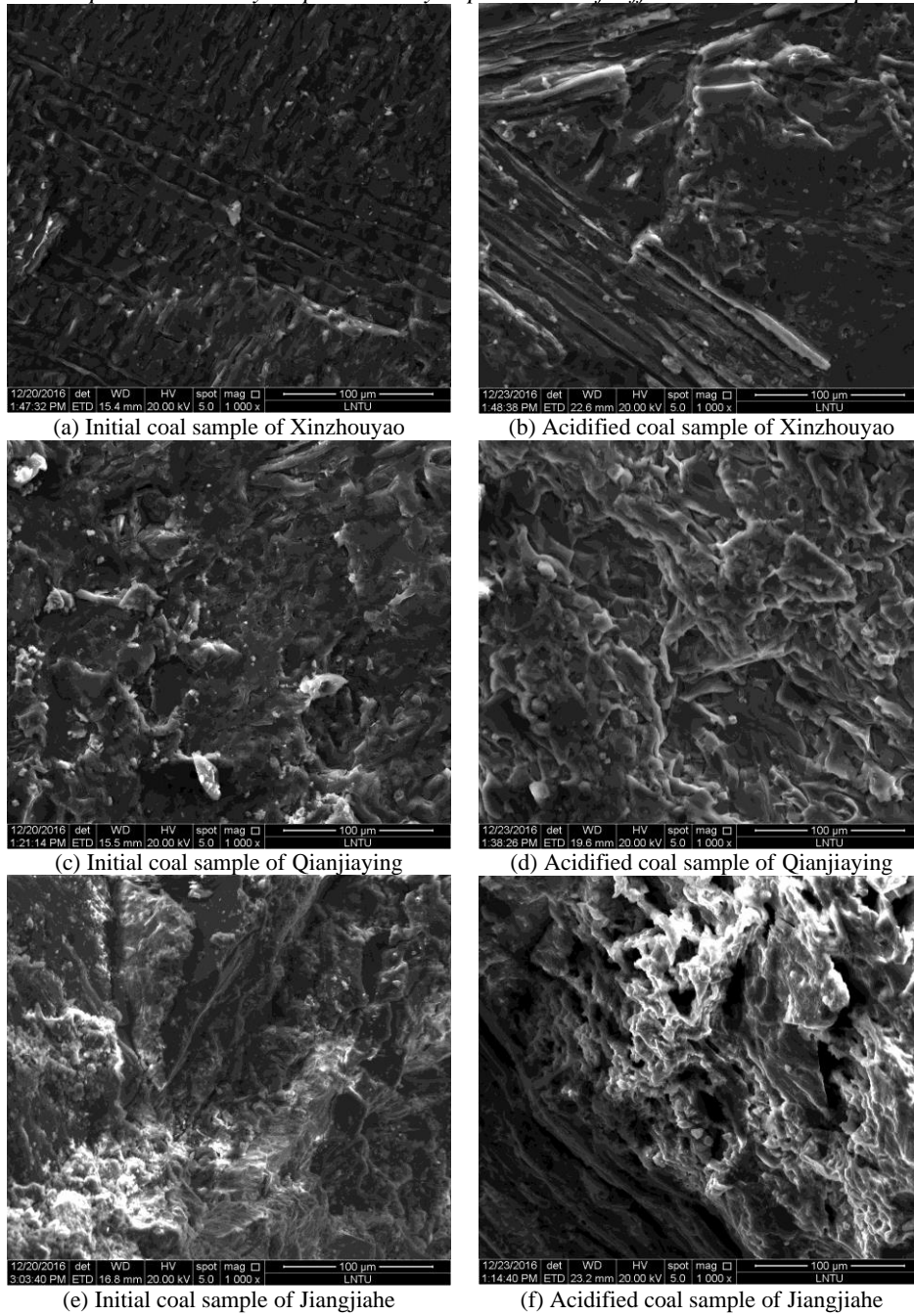
(a) Initial coal sample of Xinzhouyao

(b) Acidified coal sample of Xinzhouyao

(c) Initial coal sample of Qianjiaying

(d) Acidified coal sample of Qianjiaying

(e) Initial coal sample of Jiangjiahe

(f) Acidified coal sample of Jiangjiahe

Fig. 3. The surface structure before and after acidification . Magnification 1000×

The greater the pore volume of coal, the higher is the connectivity of coal anf the conducivity to fluid migration in the coal seam. The test results of this experiment are shown in Table 2 and Figures 4 and 5.

According to Table 2, before coal sample acidification, the pore structure of coal increases with the increase in coal rank. After the acidification of coal samples, the specific surface area of coal decreased, indicating that the acidification process makes the internal structure of coal become simpler, and reduces the gas adsorption sites which are conducive to gas desorption. With the development of acidification, the internal space of coal increases, and the total pore volume increases. Whether in specific surface area or pore volume, Jiangjiahe coal samples changes were the most obvious while Xinzhouyao coal samples changes the least obvious. This shows that the effect of acidizing decreases with the increase in coal rank.

Table 2. Comparison of specific surface area and pore volume before and after acidification

Sample source	Initial specific surface area /m²/g	Specific surface area after acidification/m²/g	Decrease percentage /%	Initial total pore volume /cm³/g	Total pore volume after acidification /cm³/g	Increase percentage /%	Coal rank
Xinzhouyao mine	8.1609	7.7085	5.54	0.017018	0.018211	7.01	Coking coal
Qianjiaying mine	6.4111	5.1739	19.30	0.005918	0.011032	86.42	Fat coal
Jiangjiahe mine	4.3567	2.2170	49.11	0.003186	0.007991	150.82	Non-caking coal

(a) Xinzhouyao mine

(b) Qianjiaying mine

(c) Jiangjiahe mine

Fig. 4. Relationship between specific surface area and pore width before and after acidification

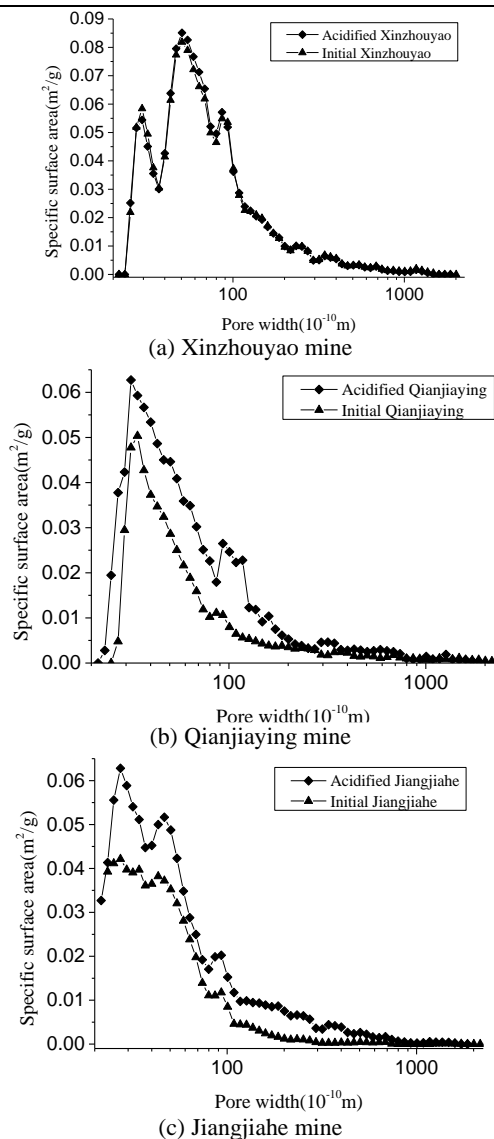(a) Xinzhouyao mine

(b) Qianjiaying mine

(c) Jiangjiahe mine

Fig.5. Relationship between pore volume and pore width before and after acidification

Figures 4 and 5 show that the specific surface area and pore volume of the coal samples are mainly distributed in the pore width range of 10 nm or less, which indicates that the micropores in the coal are well developed. After acidification, the specific surface area of the coal samples obviously increases within the pore width of 2~10 nm (except Xinzhouyao).

Its distribution regularity is consistent with that of initial coal samples. It indicates that the acid also has a good corrosion effect on the micropores of coal samples.

The change in pore volume obeys the same law. Moreover, the pore volumes of the coal samples from Qianjiaying and Jiangjiahe mine also obviously increased in the range of 10~100 nm, which indicates that the pores in the scale are filled with more fillers and the fillers are sufficiently corroded, so that the connectivity between the pores is effectively enhanced.

Mineral content

The types and contents of the fillings in the coal samples directly affect its permeability. XRD experiment was mainly intended to determine the composition of minerals in the coal samples.

(a) Initial coal sample of Xinzhouyao

(b) Acidified coal sample of Xinzhouyao

(c) Initial coal sample of Qianjiaying

(d) Acidified coal sample of Qianjiaying
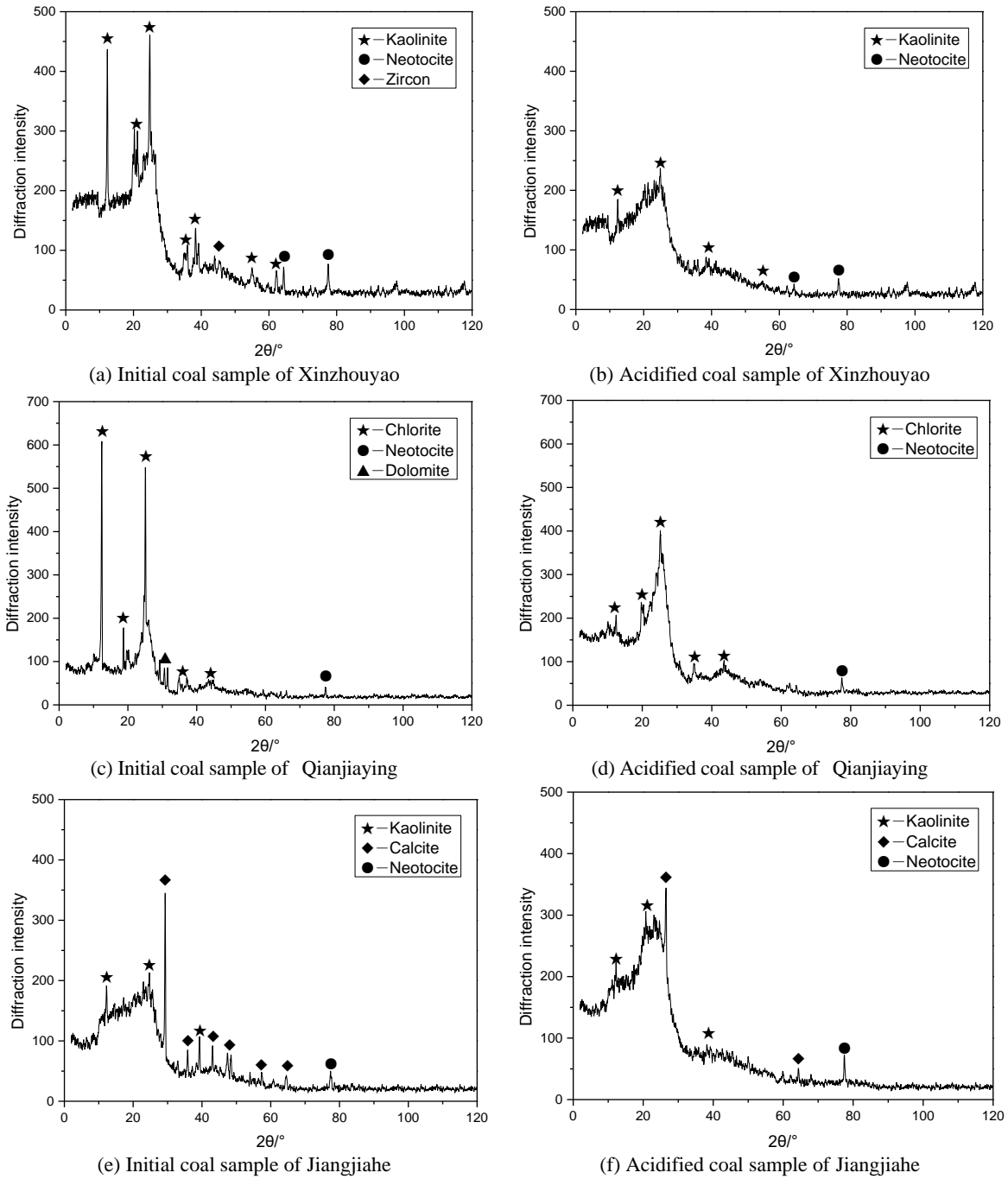
(e) Initial coal sample of Jiangjiahe

(f) Acidified coal sample of Jiangjiahe

Fig.6. XRD spectra of coal samples before and after acidification

XRD test

After the test, MDI Jade5.0 post-processing software was used for peak search, smooth, integral and other processing, and finally draw the scanning range and the diffraction intensity curve (Figure 6).

As shown in Figure 6, after acidification, the diffraction intensity of dolomite, calcite, kaolinite, chlorite, zircon in each coal sample is reduced, and some diffraction peaks of these minerals have disappeared, but the diffraction peak of neotocite is almost not changed. It can be inferred that the minerals whose diffraction peak is reduced or disappeared, are effectively dissolved, and the effect of acidification on bannisterite is not obvious.

Organic speciation analysis

Because the acid solution is very corrosive to metals, people are bound to doubt whether the coal sample acidification process affects the coal quality. The organic matter in coal consists of two parts: amorphous and microcrystalline component (Figure 7) [23]. The amorphous component has no fixed structure and cannot form an X-ray diffraction peak; but the diffraction peak of the microcrystalline structure is basically consistent with the 002 and 100 diffraction peaks of the graphite crystal [24,25].
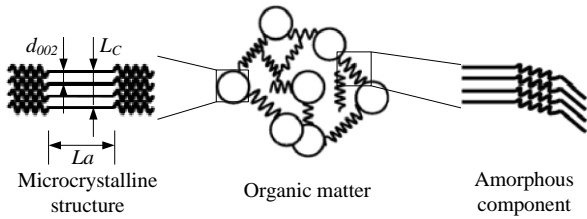
Fig.7. Organic structure of coal

According to the Prague method, the morphology of crystallites in coal can be characterized by the spacing of aromatic carbon layers, the diameter of nucleation lamellae, the height of lamellae and the number of lamellae, equations (10)~(13) [23, 26]. If the above parameters are greatly different before and after acidification, this proves that the acid solution has greater harm to the coal quality; otherwise, the damage is less or not harmful.

$$d_{002} = \frac{\lambda}{2\sin\theta_{002}} \qquad (10)$$

$$L_c = K_1 \frac{\lambda}{\beta_{002}\cos\theta_{002}} \qquad (11)$$

$$L_a = K_2 \frac{\lambda}{\beta_{100}\cos\theta_{100}} \qquad (12)$$

$$N_c = \frac{L_c}{d_{002}} + 1 \qquad (13)$$

where d_{002} is aromatic carbon film spacing, 10^{-10} m; λ is wavelength of X rays, 1.5406×10^{-10} m; θ_{002}, θ_{100} are 002 and 100 peak positions, °; L_c is aromatic carbon crystal height, 10^{-10} m; L_a is aromatic carbon nucleus laminar diameter, 10^{-10} m; K_1 and K_2 are shape factors, K_1=0.94, K_2=1.84; β_{002} and β_{100} are the half heights of 002 and 100 peaks,

10^{-10} m; N_c is aromatic carbon nucleus laminar number.

According to the XRD test results before and after acidification of each coal sample, the diffraction angle and half width of 002 peaks and 100 peaks of each coal sample were extracted, then the microcrystalline structure parameters of each coal sample were calculated. The calculation results are shown in Table 3.

From the table above, it is seen that the microcrystalline structure parameters of coal samples before and after acidizing are basically unchanged, which indicates that the acidification process does not cause obvious damage to the organic matter in coal. In addition, the acid system is inorganic. According to the principle of similarity and compatibility, the solubility of organic matter in coal is very limited.

XRF test

The final test results of XRF are expressed as oxide contents. The test results of this experiment are shown in Table 4.

Table 4 shows that the composition and content of minerals in coal samples are related to the depositional environment. The coal samples of Qianjiaying are mainly composed of Si and Al minerals, the coal samples of Jiangjiahe are dominated by Ca mineral, and the mineral content of coal samples from Xinzhouyao is low.

The mineral content of the coal samples after acidification was greatly reduced, and the acidizing effect was obvious. Among them, the percentage of CaO in Jiangjiahe coal sample decreased from 14.61% to 0.32%, which is the reason why the coal sample produced a large number of bubbles during the acidification reaction.

Table 3. Microcrystalline structure parameters of coal samples

Sample source	Type	(°) $2\theta_{002}$	(°) $2\theta_{100}$	(Å) d_{002}	(Å) L_c	(Å) L_a	(Å) N_c
Xinzhouyao mine	Initial	24.87	43.68	3.56	8.21	6.62	3.31
	Acidized	24.65	43.75	3.59	8.20	6.87	3.28
Qianjiaying mine	Initial	23.91	43.02	3.73	14.82	6.08	4.97
	Acidized	23.42	42.51	3.74	14.79	6.07	4.95
Jiangjiahe mine	Initial	25.67	43.80	3.47	4.16	5.38	2.20
	Acidized	25.49	43.69	3.50	4.14	5.40	2.18

Table 4. Content of mineral before and after acidification

Sample name	SiO$_2$%	Al$_2$O$_3$%	TFe%	CaO%	MgO%
Initial coal sample of Xinzhouyao	2.17	0.82	0.11	0.088	0.066
Acidified coal sample of Xinzhouyao	0.66	0.32	0.07	0.042	0.012
Initial coal sample of Qianjiaying	5.71	5.37	1.47	1.25	0.39
Acidified coal sample of Qianjiaying	1.93	1.83	0.79	0.28	0.10
Initial coal sample of Jiangjiahe	2.32	1.65	1.07	14.61	1.30
Acidified coal sample of Jiangjiahe	0.78	0.56	0.57	0.32	0.16

Compared with the dissolution of different minerals, the contents of Ca and Mg minerals are larger than those of Si, Al and Fe minerals. This is because the former mainly exist as carbonates, relatively easy to react with acid solution, the latter mainly exist as oxides, the reaction rate is relatively slow, and the reaction conditions are relatively harsh. Therefore, the greater the content of Ca and Mg minerals in the coal seam, the more conducive is the latter to the acidification reaction and the better is the acidizing effect, for example, the Jiangjiahe coal mine.

Permeability

The test results of the permeability changes of coal samples in different acids after different acidification times are shown in Table 5 and Figure 8. From the test results, the permeability characteristics of different acidified coal samples can be obtained:
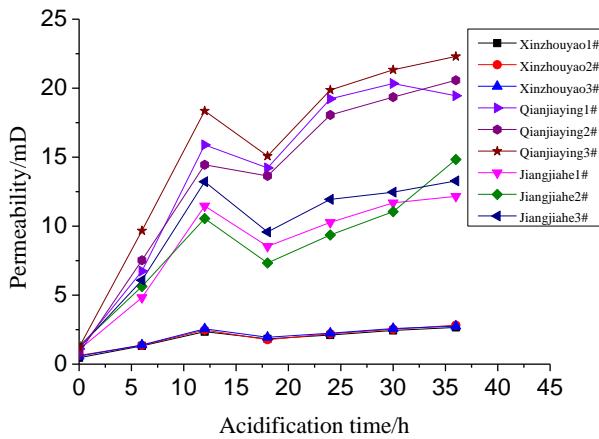

Fig. 8. Relationship between coal sample permeability and acidification time

1) At the beginning of acidification, the permeability of coal samples increased rapidly, but after acidification for 12 h, the permeability slightly decreased. The reason is that the coal sample contains clay minerals. After a period of immersion, the clay minerals expand and plug the pore-fracture channel, which leads to a decrease in permeability. However, due to the limited content of clay in the coal sample and the anti-swelling effect of ammonium chloride, the permeability slightly decreased. The extent and depth of the corrosion are larger with the acidification proceeding. The permeability gradually increases and eventually reaches a stable value. With the continuation of acidification, the extent and depth of corrosion increase, the permeability gradually increases, and finally tends to be stable.

2) The permeability increase effect *via* acid injection in Xinzhouyao coal samples with high-rank coal is obviously inferior to that of low-rank coal samples. The contents of Ca and Mg minerals and the initial permeability in Jiangjiahe and Qianjiaying coal samples are high, which provided more reactants and reaction conditions for the acidification reaction. More pores and fissures were connected and the permeability was greatly increased.

3) In the same acidification time, the higher the acid concentration, the faster increased the permeability. However, due to the excess acid in the experiment, the filler in the coal sample pores can be fully corroded, thus the final permeability improvements of different acid systems are not very different.

DISCUSSION

According to the four series of experiments, the effect of permeability increase of coal seam by acid injection was analyzed from different emphases. Under the same conditions, the coal samples of Xinzhouyao showed the worst effect on permeability improvement by acid injection, and Jiangjiahe and Qianjiaying were gradually weakened.

Table 5. Permeability changes of coal sample before and after acidification

Sample name	Acid system	Permeability /mD						
		Acidified 0 h	Acidified 6 h	Acidified 12 h	Acidified 18 h	Acidified 24 h	Acidified 30 h	Acidified 36 h
Xinzhouyao 1#	I	0.46	1.32	2.35	1.83	2.11	2.44	2.66
Xinzhouyao 2#	II	0.63	1.36	2.47	1.77	2.20	2.53	2.82
Xinzhouyao 3#	III	0.58	1.39	2.56	1.95	2.24	2.58	2.75
Qianjiaying 1#	I	1.05	4.82	11.46	8.54	10.27	11.69	12.16
Qianjiaying 2#	II	1.32	5.63	10.55	7.33	9.36	11.05	14.83
Qianjiaying 3#	III	1.18	6.08	13.22	9.58	11.94	12.46	13.28
Jiangjiahe 1#	I	1.10	6.74	15.89	14.22	19.23	20.34	19.45
Jiangjiahe 2#	II	0.82	7.53	14.45	13.64	18.06	19.35	20.57
Jiangjiahe 3#	III	1.23	9.67	18.35	15.08	19.87	21.33	22.30

The distribution of the permeability improvement was the same as the distribution of mineral content in the coal sample, that is, the amount of the mineral component and the content of the coal sample are the keys to the permeability increase of coal seam by acid injection. Moreover, the initial permeability of Qianjiaying coal sample was higher than that of Xinzhouyao, the higher initial permeability is favorable for the acid to seep into the coal seam and promote acidification. In addition, the results of microscopic observation and low-temperature nitrogen adsorption test showed that the corrosion of acid for the medium-rank coal samples of Jiangjiahe and Qianjiaying is better than for the high-rank coal samples of Xinzhouyao. It can be seen that under the same acid system, the permeability increase of coal samples by acid injection is influenced by the mineral content, initial permeability, coal rank and other factors.

CONCLUSIONS

1) A lot of pore channels are blocked in the coal seam, which leads to the difficulty of gas migration and the low permeability of the coal seam. Therefore, a chemical method for increasing permeability of coal seam by acid injection was put forward. After acidification, the filling materials such as minerals and colloid were corroded, and the fracture connectivity of the coal sample surface was obviously improved. The lower the coal rank, the lower was the degree of polymerization of the aromatic ring, the more easily it was corroded.

2) After acidification, the specific surface area and the total pore volume increased, and the specific surface area and total pore volume mainly increased within pore widths of 2 ~ 10 nm. The porosity parameters of middle- and low-rank coal samples were larger than those of high-rank coal samples, which were corroded easily.

3) Acidification does not cause damage to the organic matter of coal. After acidification, the contents of Si, Al, Fe, Ca, Mg and other minerals in the coal samples all decreased, especially Ca and Mg minerals, indicating that the higher the content of these minerals, the better is the permeability of coal seam by acid injection.

4) The permeability of coal samples increased after acidification. The higher the initial permeability of coal samples, the higher were the mineral contents of Ca and Mg, and the better was the permeability of the coal seam by acid injection. The higher the concentration of acid, the greater was the rate of increase in permeability.

5) It is a good method to increase the permeability of the coal body by using acid solution to dissolve and corrode the fillings in the pores and fractures of the coal seam. However, how to control the concentration and dosage of acid in different coal seams needs to be solved in the further research.

REFERENCES

1. Q. Zhang, S.L. Feng, X.L. Yang, *J. Chin. Coal Soc.*, **26**, 230 (2001).
2. L.B. Colmenares, M.D. Zoback, *Terra Nova*, **91**, 51 (2007).
3. C.J. Fan, S. Li, M.K. Luo, Z.H. Yang, H.H. Zhang, *J. Chin. Coal Soc.*, **41**, 3076 (2016).
4. Q. Li, B. Lin, C. Zhai, *J. Nat. Gas Sci. Eng.*, **21**, 296 (2014).
5. C. Di, X.Z. Li, Q.G. Li, *J. Chin. Coal Soc.*, **36**, 1996 (2011).
6. H.Y. Guo, X.B. Su, J.H. Chen, H.F. Wang, Q. Si, *J. Chin. Coal Soc.*, **38**,633 (2013).
7. F. Yan, C. Zhu, C. Guo, Q. Zou, S.Qiao, *J. Chin. Coal Soc.*, **40**,823 (2015).
8. F. Yan, B. Lin, C. Zhu, C. Shen, Q. Zou, C. Guo, T. Liu, *J. Nat. Gas Sci. Eng.*, **22**, 571 (2015).
9. X.H. Zhou, J.L. Men, D.P. Song, H.B. Zhao, *Chin. Saf. Sci. J.*, **25**, 60 (2015).
10. M. Bilz, E. Uhlmann, *Adv. Mater. Res.*, **1018**,115 (2014).
11. C.M. Mu, H.L. Wang, W.Y. Huang, C.J. Kuang, *Rock and Soil Mech.*, **34**, 2496 (2013).
12. S. Chaki, M. Takarli, W.P. Agbodjan, *Constr. Build. Mater.*, **22**,1456 (2008).
13. X.C. Xiao, Y.S. Pan, X.F. Lv, X.L. Yang, *Chin. J. Geophys.*, **56**, 1726 (2013).
14. R. Li, K. Wang, Y.J. Wang, *J. Chin. Coal Soc.*, **39**, 913 (2014).
15. H.Y. Guo, Y. Luo, J.Q. Ma, T.P. Xia, C.J. Ji, *J. Chin. Coal Soc.*, **39**, 1886 (2014).
16. X.B. Su, Y.Y. Tang, *J. Jiao-zuo Inst. Technol.*, **17**, 406 (1998).
17. L.X. Duan, S.W. Wang, M. Zhang, *Coal Geol. & Explor.*, **27**,33 (1996).
18. Z.Y. Han, *Dong ying: Chin. Univ. of Pet., Chin.*, (2009).

19. W.X. Zhao, R. Li, *Chin. Coalbed Methane*, **9**, 10 (2012).
20. D.N. Hopkins, E.S. Snavely, *Arlingtontx Usdallastx Us*, (1985).
21. F.L. Zhao, *Dong ying: Pet. Univ. Press, Chin.*, (1997).
22. B.Q. Lin, S.N. Zhou, *J. Chin. Univ. Min. & Technol.*, **17**, 21 (1987).
23. Q.Z. Li., *Jiaozuo: Henan Polytech. Univ., Chin.*, (2014).
24. Y. Zhao, J. Zhang, *J. Appl. Crystallogr.*, **41**, 1095 (2008).
25. Q.F. Zheng, Z.M. Wang, B.G. Chen, G.F. Liu, J. Zhao, *Spectrosc. & Spectral Anal.*, (2016).
26. R.A. Wickham, A.C. Shi, Z.G. Wang, *J. Chem. Phys.*, **118**, 10293 (2003).

Comprehensive evaluation and case study of urban underground space development under multiple constraints

C.A. Zhou[1]*, H. Ren[1], G. Liu[2], C. Chen[3]

[1]School of Construction Management and Real Estate, Chongqing University, Chongqing 400045, China;
[2]School of Civil Engineering, Chongqing University, Chongqing 400045, China）
[3]CMCU Engineering Corporation, Chongqing 400039, China)

This paper presents a research on the evaluation and case analysis of urban underground space development under several constrains such as geological, technical and economic factors. To solve the problem of incomplete information, correlation and ambiguity in the multi-restrictive environment factors were comprehensively evaluated. First of all, six main factors which restrict the urban underground space sustainable development were selected; secondly, the degree of the restrictive factors and their frequency were discussed, the restrictive factors which occupied more than 95% were determined by expert advice, the evaluation index was quantified by the Likert scale, the evaluation index system of urban underground space sustainable development and utilization was constructed. Moreover, Analytic Hierarchy Process (AHP) and Fuzzy Comprehensive Evaluation Method (FCE) were used to construct the fuzzy comprehensive evaluation model of multi-level constraints, the weight vector for consistency check was calculated, and the fuzzy evaluation membership matrix was computed. Finally, Jiangbei District, Hechuan District and Qianjiang District in Chongqing City were chosen as representatives of urban function core district, city development district, and southeast ecological reserve district in Chongqing City. The urban underground space sustainable development in the chosen districts was analyzed by the multi-factors fuzzy comprehensive evaluation model, and the evaluation results were verified by multi-level grey assessment. The case study results showed that applying AHP and FCE method for multi-constraint factors comprehensive evaluation of urban underground space sustainable development has high viability and effectiveness for the beneficial exploration and comprehensive evaluation of multi-restrictive environment factors.

Key words: Urban underground space, Multi-constraints environments, Sustainable development, Index system, Fuzzy comprehensive evaluation

INTRODUCTION

Rational development of urban underground space can effectively alleviate the shortage of city land, and effectively deal with environmental pollution, ecological deterioration and urban traffic congestion problems [1], and contribute to the intensive use of urban land resource and urban sustainable development [2]. Compared with the exploitation of ocean space resource, universe space resource and so on, the development of underground space resource is more direct, economic and secure. Compared with the urban ground space resources, potential urban underground spaces for urban development are relatively large, which are the products of general area multiplied by the depth of development 40% [3]. As a "potential and abundant natural resource" [4] urban underground space has been widely used in transportation, warehousing, air defense, environmental protection, energy, housing, commerce, culture, entertainment, sports and other

fields in the developed countries, for example, stone mined-out areas were used as tombs, churches, wine cellars, drains, etc in Paris in the 12th century [5]; the world's first underground railway was built in London, England, in 1863 [6], after that, the underground railways were promoted rapidly by New York, the United States, Tokyo, Japan and other international cities [7]. The stage of development of urban underground space can be divided in urban subway early utilization, the Second World war, the urban Renaissance, the oil crisis impact, environmental protection demands [8], and it is now moving in the sustainable development stage [9]. In recent years, China's urban underground space development also got rapid development [10], but the overall level is still in the primary, dot, shallow stage of development [11], such as urban underground space waste, unreasonable layout and resource development sequence confusion [12]; there are also a series of restrictive factors for sustainable development of urban underground space [13].

*To whom all correspondence should be sent:

E-mail: 329822472@qq.com

EXPERIMENTAL

Research ideas

The research idea of this article is to establish the index system, which is the basis framework of comprehensive evaluation, and then establish a multi-restriction-factors fuzzy comprehensive evaluation model of sustainable development of urban underground space, to analyze and demonstrate the urban underground space sustainable development.

The coordinated development of resources, environment, economics and society is emphasized in urban sustainable development [41]. Urban underground space is the downward extension of urban space resource, and the urban underground space sustainable development should include but is not limited to these four aspects. Theoretically speaking, the development of urban underground space is almost infinite. But considering the feasibility, security, economics, sustainability of development of urban underground space, there are not only problems such as long construction period, large investment, complex technology, high risk, difficult in disaster relief etc., but also many unfavorable environments such as geotechnical stability, hydro-geological conditions [42], construction technology, economic level, environmental benefits [43].

Through investigation and analysis of the frequency statistics and control degree of the restrictive factors, the indices which have higher frequency or larger control degree were chosen to compose of the preselected evaluation indices set. Then the characteristics of the preselected indices were analyzed, according to the frequency and the degree of restriction. Finally, the fewer indices, which have the most important restrictive effects on the urban underground space sustainable development were chosen to compose the index system.

Therefore, four items of work were carried out in this paper as follows: Firstly, the main constraint environments which influence the urban underground space sustainable development were analyzed from the perspective of engineering geology, environment consciousness, regional economics, technical standards, laws and regulations, etc. Secondly, through consultations, statistics, analysis of expert opinions, the main constraint factors were classified and quantified to layer, the weight of each index was calculated by using software. Thirdly, the evaluation index system and fuzzy comprehensive evaluation model of multi-level constraint factors were established by

using the fuzzy mathematics theory. Fourthly, by consulting experts, taking the administrative area of urban underground space as the evaluation unit, representative urban underground space administrative districts were chosen for empirical analysis, to verify the reliability and validity of the method.

Establishing a fuzzy comprehensive evaluation index system of sustainable development of urban underground space

Selection of evaluation index. Firstly, a preselected evaluation index needs to be set. The primary evaluation index system was divided into two levels, the fist level is criterion layer and the second level is index layer. In the criterion layer there are 5 first-level control indices, which contain engineering geology, environmental consciousness, regional economy, technical standards, laws and regulations. There are 4 second-level restriction indices belonging to engineering geology index, which include geological uncertainty, bad geological susceptibility, regional instability, rock and soil corrosivity, to reflect the restriction conditions of regional characteristics and geological availability on the development of urban underground space. There are 4 second-level restriction indices belonging to environmental consciousness index, which include ideas, knowledge level, environmental conditions. Connection systems reflect the constraints conditions of interactive impact on the environment of exploitation of urban underground space. There are 4 second-level restriction indices belonging to regional economy index, which include *per capita* GDP, project cost, input-output ratio, return on investment cycle, to reflect the restriction conditions of urban social economic conditions or comprehensive benefit of the underground project on the urban underground space sustainable development. There are 4 second-level indices belonging to technical standards index, which include standard specification, technical research, construction difficulty, safety risk, to reflect the restriction conditions of technology level and risk control ability on sustainable development of urban underground space; There are 4 second-level restriction indices belonging to laws and regulations index, which include management regulations, laws and regulations and management function, land use right, overall planning, to reflect the restriction conditions of the administrative ability and comprehensive evaluation ability, corresponding laws and regulations and public participation in the process of development of urban underground space.

Secondly, the pre-selected evaluation indices were screened out by using expert consultation method, which is confirmed through some expert opinions and scored the indices respectively. Expert opinion consultation table was designed in two parts: the first part was designed for asking experts' opinions on the evaluation index and experts can add, delete and adjust the pre-selected indices; the second part was designed for asking experts score the indices by using Likert scales, the score of each index was divided into five levels such as: very important, important, generally important, less important and not important and given 5, 4, 3, 2, 1 score. Average arithmetic score values were thought to represent expert opinions concentration, and the coefficient of variation was used to represent the opinion coordination degree. The less the coefficient of variation, the higher is the degree of coordinated expert opinion targets. The screening standard was set to when the arithmetic mean value is greater than 3.5 and the coefficient of variation is less than 0.25.

In order to obtain the basic data, 30 experts accepted the surveys of design, management, research, questionnaire, and who were from Chongqing Survey Institute, Chongqing city rail transit (Group) Co. Ltd., Chongqing Design Institute, Chongqing municipal engineering design and Research Co Ltd, Chongqing City Planning Bureau, Chongqing Jiao tong University and other 10 units engaged in design and construction of underground space resource in city. All experts agreed that the evaluation index system can be divided into criterion layer and index layer, and there was no objection to the criterion layer index's composition, but there were some adjustment advices on the composition of index layer by 11 experts. At the same time, experts scored all the first-level control indices of the criterion layer and second-level control indexes of the index layer separately.

Finally, statistical analysis was carried out on the data obtained from the expert opinion consultation table with the above method, the opinion concentration degree and the opinion coordination degree of each index were calculated, and finally 5 first-level indices concerning regional economy and 20 second-level indices concerning *per capita* GDP were set to compose the indices set for decision-making system of the urban underground space sustainable development and utilization, $U=\{U_1, U_2,..., U_5\}=\{U_{11}, U_{12},..., U_{54}\}$, as shown in Table 1. The 20 specific indices were the most important and the most critical factors, accounting for more than 95% of all factors, and were enough to reflect the restriction condition of the urban underground space sustainable development and utilization.

Calculation of decision weight index

The weight coefficient of each evaluation index was determined through analytic hierarchy process (AHP) method, which can make the index and its

Table 1. Evaluation index system and weights of the indices for evaluation of the urban underground space sustainable development and utilization

Criterion layer	Weight of criterion layer(A_i)	Index layer	Weight of index layer(A_{ij})
Regional economy (U_1)	0.2719	Per capita GDP (U_{11})	0.1709
		Engineering cost (U_{12})	0.4227
		Input-output ratio (U_{13})	0.2165
		Investment return period (U_{14})	0.1899
Technical standards (U_2)	0.1974	Standard specification(U_{21})	0.2220
		Technology research (U_{22})	0.1306
		Construction difficulty(U_{23})	0.2774
		Safety risk (U_{24})	0.3700
Laws and regulations (U_3)	0.1720	Management regulations (U_{31})	0.2239
		Management functions (U_{32})	0.0829
		Land use rights (U_{33})	0.3733
		Overall planning (U_{34})	0.3199
Engineering geology (U_4)	0.2290	Geological uncertainty (U_{41})	0.1479
		Bad geological susceptibility (U_{42})	0.1740
		Regional instability (U_{43})	0.6429
		Rock and soil corrosion (U_{44})	0.0352
Environmental awareness (U_5)	0.1297	Ideas (U_{51})	0.2460
		Understanding level (U_{52})	0.0869
		Environmental status (U_{53})	0.3000
		Connection system (U_{54})	0.3671

Note: this table is comprehensive expert advice, which is analyzed, sorted and calculated.

weight more reasonable, more practical and easily quantitatively represented. 1–9 scaling law was used by the experts to compare with the relative importance of the two-two factors of evaluation index of the multiple constraint factors of development of urban underground space. In view of different views on the relative importance of evaluation indices by the experts, the final index calibration value can be obtained by twice feedback evaluation, then the judgment matrix of each hierarchy can be constructed, and weight vector calculation and consistency check were applied by calculation software.

Here, the evaluation index in the criterion layer was taken as an example to illustrate the weight computational process. The judgment matrix of the evaluation index in the criterion layer is listed in Table 2. The maximum feature vector value can be obtained λ_{max}=5.003, when the judgment matrix is input to the software, the corresponding eigenvector is: A=(0.2719, 0.1974, 0.1720, 0.2290, 0.1297), the coincidence index is:

$$CI = \frac{\lambda_{max} - n}{n-1} = (5.0030\text{-}5)/(5\text{-}1) = 0.00075 \qquad (1)$$

the mean random consistency index is:

$$CR = \frac{CI}{RI} = 0.00075/1.12 = 0.000625 < 0.1 \qquad (2)$$

RI is the mean random consistency index of the judgment matrix, which can be obtained from Table 3. It can be seen that the judgment of the weight value of the criterion layer is reliable. Otherwise, the values in the judge matrix need to be adjusted. Thus, the criterion layer evaluation index weight coefficient A=(0.2719, 0.1974, 0.1720, 0.2290, 0.1297).

The judgment matrix of the evaluation index in the second-level index layer is listed in Table 4. Meanwhile, the weight coefficients A_{ij} of each evaluation index can be obtained, the evaluation index weight coefficient in the second-level index

layer A_{1i} = (0.1709, 0.4227, 0.2165, 0.1899),
A_{2i} = (0.2220, 0.1306, 0.2775, 0.3700),
A_{3i} = (0.2239, 0.0829, 0.3732, 0.3199),
A_{4i} = (0.1479, 0.1740, 0.6429, 0.0352),
A_{5i} = (0.2460, 0.0869, 0.3000, 0.3671) and can be passed through the consistency test, the results are shown in Table 1.

Multi-level fuzzy evaluation model of sustainable development for urban underground space

Five indices in the first-level criterion layer and 20 indices in the second-level index layer of sustainable development of urban underground space affect and restrict each other, and show a nonlinear relationship, which makes the prediction and evaluation fuzzy and subjective. Considering that it is difficult to put all the restricting factors of sustainable development of urban underground space into the evaluation index system, and based on the limited cognitive level and decision information, using fuzzy comprehensive evaluation method (FCE) is a way to solve these problems. It can be well combined with the qualitative evaluation and quantitative evaluation, and be able to better control man-made interference factors, and the decision result is as close as possible and can reflect the real situation. According to the established evaluation index system, using the theory of fuzzy mathematics, the main steps are to establish the multi-level fuzzy comprehensive evaluation model of sustainable development of urban underground space as follows:

First step: the given factors set U={U₁, U₂,…, Uₙ} is divided into subset S in accordance with certain attributes:

$$U_i = \{U_{i1}, U_{i2}, \cdots, U_{in}\} i=1,2,3\cdots,S, \qquad (3)$$

The conditions as follows:

(a) $n_1+n_2+\cdots+n_s=n$;

(b) $U_1 \cup U_2 \cup \cdots \cup U_s = U$;

(c) $U_i \cap U_j = \Phi, i \neq j$.

Table 2. The judge matrix of the evaluation index in the criterion layer

Index	U_1	U_2	U_3	U_4	U_5
U_1	1	9/7	9/6	9/8	9/4
U_2	7/9	1	9/8	8/9	9/6
U_3	6/9	8/9	1	7/9	9/7
U_4	8/9	9/8	9/7	1	9/5
U_5	4/9	6/9	7/9	5/9	1

Table 3. Mean random consistency index RI

Order of matrix (*n*)	1	2	3	4	5	6	7	8	9	10
Mean random consistency index (RI)	0	0	0.58	0.9	1.12	1.24	1.32	1.41	1.45	1.49

Table 4. Judge matrix of the evaluation index in the second-level index layer

Index	U_{11}	U_{12}	U_{13}	U_{14}
U_{11}	1	0.4	0.75	0.9
U_{12}	1/0.4	1	0.75/0.4	0.9/0.4
U_{13}	1/0.75	0.4/0.75	1	0.9/0.75
U_{14}	1/0.9	0.4/0.9	0.75/0.9	1

Index	U_{21}	U_{22}	U_{23}	U_{24}
U_{21}	1	1.7	0.8	0.6
U_{22}	1/1.7	1	0.8/1.7	0.6/1.7
U_{23}	1/0.8	1.7/0.8	1	0.6/0.8
U_{24}	1/0.6	1.7/0.6	0.8/0.6	1

Index	U_{31}	U_{32}	U_{33}	U_{34}
U_{31}	1	2.7	0.6	0.7
U_{32}	1/2.7	1	0.6/2.7	0.7/2.7
U_{33}	1/0.6	2.7/0.6	1	0.7/0.6
U_{34}	1/0.7	2.7/0.7	0.6/0.7	1

Index	U_{41}	U_{42}	U_{43}	U_{44}
U_{41}	1	0.85	0.23	4.2
U_{42}	1/0.85	1	0.23/0.85	4.2/0.85
U_{43}	1/0.23	0.85/0.23	1	4.2/0.23
U_{44}	1/4.2	0.85/4.2	0.23/4.2	1

Index	U_{51}	U_{52}	U_{53}	U_{54}
U_{51}	1	2.83	0.82	0.67
U_{52}	1/2.83	1	0.82/2.83	0.67/2.83
U_{53}	1/0.82	2.83/0.82	1	0.67/0.82
U_{54}	1/0.67	2.83/0.67	0.82/0.67	1

Second step: for each factor set U_i, which is respectively to make comprehensive evaluation, and to let $V=\{V_1, V_2, \ldots V_m\}$ is supposed to the evaluation set, the weight distribution of the various factors in U_i which is relation to V is: $A_i=\{a_{i1}, a_{i2}, \ldots, a_{in}\}$, where $a_{i1}+a_{i2}+\ldots+a_{in}=1$. R_i is the single factor evaluation matrix, then the one-level evaluation vector can be obtained:

$$B_i=A_i \cdot R_i=\{b_{i1}, b_{i2}, \cdots, b_{im}\}, i=1,2,3,\cdots,S. \qquad (4)$$

Third step: each U_i is regarded as a factor of U, $U=\{U_1, U_2, \ldots, Us\}$, and then U is a set of factors, single factor evaluation matrix of U is:

$$R=\begin{bmatrix} B_1 \\ B_2 \\ \vdots \\ B_s \end{bmatrix}=\begin{bmatrix} b_{11} & b_{12} & \cdots & b_{1m} \\ b_{21} & b_{22} & \ldots & b_{2m} \\ \ldots & \ldots & \ldots & \ldots \\ b_{s1} & b_{s2} & \ldots & b_{sm} \end{bmatrix} \qquad (5)$$

where U_i is a portion of U, which reflects certain attributes, the weight distribution can be relying on the importance of them: $A=\{a_1, a_2, \ldots a_s\}$, and then the second stage evaluation vector can be obtained:

$$B_i=A \cdot R=\{b_1, b_2, \cdots, b_m\} \qquad (6)$$

Fourth step: the second-level evaluation vector is uneven, and the evaluation set is divided into 5 grades, with 5 points for each evaluation set. Each index is evaluated respectively: $V=(V_1, V_2, V_3, V_4, V_5)=(5,4,3,2,1)$ = (restriction influence is very large, restriction influence is larger, restriction influence is general, restriction influence is smaller, restriction influence is very small), then use the weighted average method to evaluate score and the sustainable exploitation of urban underground space.

Finally, according to the different evaluation results, the paper put forward strategies of the urban underground space sustainable development and utilization, and the multi-level gray evaluation method was applied to evaluation the results.

Case study

Chongqing city is the largest area resource of municipality directly under the central government of China. There are five functional areas of strategic deployment in Chongqing city's space utilization from the perspective of sustainable development of urban space resource, based on the resources and environment bearing capacity, existing development density and development potential factors. The overall positioning of the city space resource development direction, development timing and strength of the overall positioning of the different parts has been put forward. Therefore, taking administrative district as basic assessment unit,3 administrative districts of Jiangbei, Hechuan, Qianjiang in Chongqing City has been selected as representative districts, and fuzzy comprehensive evaluation on the multiple constraint factors of sustainable development of urban underground space of Jiangbei District, Hechuan District, Qianjiang District has being done, respectively.

Calculation of the evaluation membership matrix

Experts are invited respectively to score the evaluation index of the multiple constraint factors of sustainable development of urban underground space of Jiangbei District, Hechuan District, Qianjiang District, then, the evaluation matrix of the multiple constraint factors of sustainable development of urban underground space of Jiangbei District, Hechuan District, Qianjiang District are made up.

Here, Hechuan District is taken as an example, firstly the evaluation matrix of the multiple constraint factors of sustainable development of urban underground space of Hechuan District is structured, and then the fuzzy evaluation

membership matrix R_1, R_2, R_3, R_4 and R_5 are calculated.

$$R_1 = \frac{1}{30} \times \begin{bmatrix} 6 & 12 & 11 & 8 & 3 \\ 11 & 10 & 6 & 7 & 6 \\ 8 & 9 & 9 & 7 & 7 \\ 7 & 10 & 9 & 9 & 5 \end{bmatrix} R_2 = \frac{1}{30} \times \begin{bmatrix} 7 & 6 & 8 & 10 & 9 \\ 4 & 7 & 6 & 10 & 13 \\ 8 & 7 & 8 & 9 & 8 \\ 10 & 9 & 7 & 7 & 7 \end{bmatrix}$$

$$R_3 = \frac{1}{30} \times \begin{bmatrix} 9 & 8 & 8 & 8 & 7 \\ 3 & 5 & 7 & 13 & 12 \\ 10 & 9 & 8 & 7 & 6 \\ 9 & 9 & 8 & 7 & 7 \end{bmatrix} R_4 = \frac{1}{30} \times \begin{bmatrix} 6 & 7 & 8 & 9 & 10 \\ 7 & 8 & 9 & 10 & 6 \\ 12 & 10 & 9 & 5 & 4 \\ 3 & 5 & 6 & 15 & 11 \end{bmatrix}$$

$$R_5 = \frac{1}{30} \times \begin{bmatrix} 7 & 8 & 9 & 10 & 6 \\ 3 & 4 & 5 & 15 & 13 \\ 8 & 9 & 10 & 7 & 6 \\ 9 & 10 & 11 & 6 & 4 \end{bmatrix} \qquad (7)$$

Fuzzy comprehensive evaluation

Using the weight of the evaluation index A_1 and fuzzy evaluation membership matrix R_1, B_1 was used by the software:

$$B_1 = A_1 \wedge R_1 = (0.2164, 0.2508, 0.1999, 0.1870, 0.1460) \qquad (8)$$

Simultaneously, B2, B3, B4 and B5 can be obtained:

$$B_2 = A_2 \wedge R_2 = (0.1999, 0.1879, 0.1842, 0.2153, 0.2126) \qquad (9)$$

$$B_3 = A_3 \wedge R_3 = (0.2219, 0.2111, 0.1979, 0.1930, 0.1760) \qquad (10)$$

$$B_4 = A_4 \wedge R_4 = (0.2481, 0.2258, 0.2187, 0.1703, 0.1370) \qquad (11)$$

$$B_5 = A_5 \wedge R_5 = (0.1922, 0.2172, 0.2422, 0.2017, 0.1469) \qquad (12)$$

R and B can be obtained:

$$R = \begin{bmatrix} B_1 \\ B_2 \\ B_3 \\ B_4 \\ B_5 \end{bmatrix} = \begin{bmatrix} 0.2164 & 0.2508 & 0.1999 & 0.1870 & 0.1460 \\ 0.1999 & 0.1879 & 0.1842 & 0.2153 & 0.2126 \\ 0.2219 & 0.2111 & 0.1979 & 0.1930 & 0.1760 \\ 0.2481 & 0.2258 & 0.2187 & 0.1703 & 0.1370 \\ 0.1922 & 0.2172 & 0.2422 & 0.2017 & 0.1469 \end{bmatrix} \qquad (13)$$

$$B = A \wedge R = (0.2182, 0.2215, 0.2062, 0.1917, 0.1624) \qquad (14)$$

RESULTS AND DISCUSSION

Analysis of the evaluation results

The fuzzy vector is uneven, and each evaluation grade of the evaluation on the domain was assigned to $V_1 = 5, V_2 = 4, V_3 = 3, V_4 = 2, V_5 = 1$. The score of the multiple constraint factors of sustainable development of urban underground space of Hechuan District was obtained by using the weighted average method:

$$W_1 = (0.2182 \times 5 + 0.2215 \times 4 + 0.2062 \times 3 + 0.1917 \times 2 + 0.1624 \times 1)/(0$$

$$.2182 + 0.2215 + 0.2062 + 0.1917 + 0.1624) = 3.1414 \qquad (15)$$

Similarly, the scores of the multiple constraint factors of sustainable development of urban underground space of Jiangbei District and

Qianjiang District can be obtained. Respectively, $W_2 = 2.2817$, $W_3 = 4.4055$.

Then the fuzzy comprehensive evaluation scores of these three districts, Jiangbei District, Hechuan District and Qianjiang District, multi-constraint factors of urban underground space sustainable development were in the order: $W_2 < W_1 < W_3$.

According to the principle of maximum membership degree and the comparative analysis of the above fuzzy comprehensive evaluation, conclusions can be drawn about the Jiangbei District, Hechuan District and Qianjiang District of sustainable development of urban underground space constraints decision: because the regional economy of Jiangbei District is better and the engineering geological conditions of Jiangbei District are more stable, the influence on the multiple constraint factors of urban underground space sustainable development of Jiangbei District is between influence normal and influence smaller, and closer to influence smaller, the development of urban underground space of the Jiangbei District is in a strong sustainable stage and can be vigorously promoted.

Because the regional economy of Hechuan District is average and the engineering geological conditions of Hechuan District are suitable, etc, the influence on the multi-constraint factors of urban underground space sustainable development of Hechuan District is between influence general and restriction influence larger, closer to influence general, the development of urban underground space of the Hechuan District is in the basic stage of sustainabilitye and can be gradually developed.

Because the regional economy of Qianjiang District is relatively poor and the engineering geological conditions of Qianjiang District are more complex, the influence on the multiple constraint factors of urban underground space sustainable development of Qianjiang District is between influence very large and influence larger, but closer to influence larger, the development of urban underground space of the Qianjiang District is in a weak sustainable stage and can be gradually developed with cautions.

Validation of evaluation results

In order to verify the reliability of the multiple constraint factors for comprehensive evaluation of sustainable development of urban underground space based on AHP and FCE, the multiple level grey evaluation method was used to re-evaluate and the results were used as a comparison. The experts were asked to evaluate and sort on the multiple

constraint factors of sustainable development of urban underground space of Jiangbei District, Hechuan District and Qianjiang District. The conclusions from the multiple level grey evaluation method were consistent with the results of the multiple constraint factors comprehensive evaluation. This shows that the multiple constraint factors comprehensive evaluation method of sustainable development of urban underground space has certain reliability and validity, and it can be in line with the actual situation of sustainable development of urban underground space, and achieve the expected goals.

CONCLUSIONS

The multiple constraint factors on the urban underground space sustainable development were comprehensively evaluated. It would be inconsistent with the real situation if the factors were considered separately from the effects of various restrictive factors neglecting the correlation between them. Simultaneously, it is difficult to take all the constraint factors which affect urban underground space sustainable development into the evaluation index system, and there are some ambiguities in the comprehensive evaluation information. AHP and FCE were used in this paper to construct the evaluation index system, which consists of 5 one-level criterion level indices and 20 two-level indices for urban underground space sustainable development, and the comprehensive evaluation model of urban underground space sustainable development was constructed based on AHP and FCE.

Case evaluation results showed that the comprehensive evaluation model of urban underground space sustainable development based on AHP and FCE can contribute to solve fuzziness and uncertainty problems of the evaluation process, whose comprehensive evaluation and the corresponding evaluation index system are feasible, credible, and it may be a new way which is beneficial for scientific and standardized comprehensive evaluation of urban underground space sustainable development and provides a reference for other fields.

REFERENCES

1. J.P. Godard, R.L. Sterling, *Tunnelling and Underground Space Technology*, **3**, 287 (1995)
2. J.J. Cano-Hurtado, J. Canto-Perello, *Tunnelling and Underground Space Technology*, **3**, 335 (1999)
3. D.G. Joseph, *Tunnelling and Underground Space Technology*, **1**, 3 (1996)
4. P. Pascal, B.Pascal, M.L. Lepage, M.A. Mayer, Olivier, *Cities*, **28**, 567 (2011)
5. R. Madlener, Y. Sunak, *Sustainable Cities and Society*, **1**, 45 (2011)
6. S. Michael, *Progress in Planning*, **68**, 97 (2007)
7. B. Pierre, *Tunnelling and Underground Space Technology*, **3**, 272 (2007)
8. S. B. Alvaro, *Culture and Society*, **12**, 1 (2013)
9. United Nations Statistics Division, New York, United Nation, 117, 2000.
10. China Statistical Yearbook, <http://esa.un. org/unup> 17.04.13 (2012).
11. L.X. Tong, China Building Industry Press, Bei Jing, China, 35, 2005.
12. C. Zhang, Z.L. Chen, X.L. Yang, *Procedia Engineering*, **21**, 16 (2011).
13. L.X. Kong, R.F. Shen, *Journal of Natural Disasters*, **16**, 122 (2007).
14. M.A.V. Claudia, R.W.A.L. Wouter, Adriaan, R. M. Huub, *Conservation and Recycling*, **64**, 3 (2012).
15. K.J. Maja, C. Katarzyna, United Nation Press, New York, United Nation, 14, 2014.
16. K. James, B.S. Niels, *Energy Policy*, **38**, 4870 (2010).
17. M.S. Patrick, B.C. Ralph, *Sustainable Cities and Society*, **11**, 31 (2014).
18. Z.P. Zhao, X.Z. Li, *Chinese Journal of Underground Space and Engineering*, **6**, 1538 (2010).
19. I.M. Voskamp, F.H.M. Van de Ven, *Building and Environment*, **83**, 159 (2015).
20. H. Bossel, International Institute for Sustainable Development Winnipeg Publication, Toronto, Canada, 121, 999.
21. United Nations, World urbanization prospects Publication, Washington, United Nations, 113, 2012.
22. M. Wackernagel, W.E. Rees, *Ecological Economics*, **20**, 3 (1997).
23. OECD. OECD Environmental Outlook Publication, France, Paris, 327, 2001.
24. Q. H. Qian, *Underground Space*, **18**, 69 (1998).
25. J. L. Jia, X.L. Li, *Municipal Engineering Technology*, **22**, 56 (2004).
26. W. Z. Xie, *Undergound Space*, **12**, 110 (1992).
27. F. H. Li, *Undergound Space*, **20**, 206 (2000).
28. X. Wang0, L.D. Yang, Y. Shu, *Tongji University Journal*, **6**, 105(1995).
29. W.M. Feng, *Cities and Towns Construction in Guangxi*, **6**, 105(1995).
30. H. Li, *Journal of Jianghan University*, **28**, 55 (2011).

31. J. Kong, C.Y. Lv, *Journal of Shangdong Architectural and Civil Engineering Institute*, **11**, 27 (1996).

32. Y.H. Shao, Z.H. Zhou, *Chinese Journal of Underground Space and Engineering*, **2**, 182 (2006).

33. H. Li, C. Feng, *Journal of Hubei University of Economics*, **8**, 25 (2011).

34. B.M. Chen, *Journal of Natural Resources*, **16**, 197 (2001).

35. J.Y. Zhou, X.L. Zhang, L.Y. Shen, *Cities*, **46**, 8(2015).

36. X. F. Zhang, L.H. Lv, Y.Q. Bai, G. Bai, *Chinese Journal of Underground Space and Engineering*, **8**, 8 (2012).

37. X. Wang, X.J. Huang, J. Tang, *Journal of Bei Jing University of Technology*, **36**, 213 (2010).

38. Y.M. Li, G.Z. Wang, L.P. Liu, Y. Yang, *Journal of Hehai University*, **39**, 285 (2011).

39. L.H. Li, Sustainable Development Index System and Evaluation Publication, Chengdu, China, 33, 2002.

40. Y.R. Chen, *Journal of Business Research*, **8**, 9 (2012).

41. N. Dempsey, C. Brown, G. Bramley, *Progress in Planning*, **77**, 89 (2012).

42. L. Zhou, *Journal of Shanghai Jiaotong University*, **12**, 16 (2008).

43. M. Alberti, J.M. Marzluff, *Urban Ecosystems*, **7**, 241 (2004).

Social network analysis of innovation of industry-university-research cooperation in chemical industry (based on China patent licensing data)

H.Y. Yan, X.Z. Bao [*], Q. He

Management College，Beijing Union University, Beijing, China

Industry-university-research cooperation is one of the main ways for an enterprise to gain a competitive advantage. Based on the research perspective of social networks, this paper uses patent licensing announcement in the chemical industry among universities, research institutes and enterprises in 2010-2013 as the data source, and draws a map of innovation network of industry-university-research cooperation in the chemical industry using the software of Pajek and Gephi, and makes an analysis on trend and innovative subject analysis as well as the characteristics of innovation network of industry-university-research cooperation in the chemical industry. The results show that innovation network of industry-university-research cooperation in the chemical industry is a complex network system as a whole with more nodes and uneven distribution, showing scale-free and small-world properties. Chemical enterprises should actively participate in the industry-university-research cooperation and play the role of innovative subject in the industry. They need to establish a stable and effective incentive mechanism for innovation network environment, information and resource sharing, and promote interaction among network actors to enhance innovation ability of all parties.

Key words: Chemical industry, Industry-university-research innovation network, Network structure

INTRODUCTION

With the continuous development of the economy, various dividends have disappeared and the economic growth has declined. Innovation-driven social and economic development has become an inevitable approach. However, innovation requires an appropriate system and environment. To this end, China has proposed that universities, research institutes, enterprises and other organizations jointly establish industry-university-research projects and promote innovation through creating an industry-university-research (IUR) cooperative innovation network [1]. The paradigm of innovation is experiencing a shift from a linear structure to a networked paradigm. In the process of IUR cooperative innovation, all innovation subjects spontaneously form an informal cooperation network and make full use of the communication function and collision effect of the cooperation network to stimulate innovation。At present, domestic and foreign scholars carry out various research and discussion on the relevant contents of IUR cooperative innovation network. Lavie and Drori(2012) think that the cooperation model between enterprises and universities or research institutes is mainly exploratory, while the cooperation between enterprises and enterprises focuses on exploitative innovation[2]; Guan and Zhao. (2013) find that small-world structure has parabolical effect on patent value at firm-level [3]. Hemmert *et al.*, studied trust formation in university–industry research collaborations (UICs) and analyzed survey data on UICs in the US, Japan and South Korea [4]. Laurens and Noelle unraveled the interaction between champions and what this entails in terms of role complementarities and conflicts as regards innovation network orchestration [5]. Hong and Su found that the central Ministries and local governments are two sources of institutional force that could impose or encourage university–industry collaborations without considering the geographic distance between them[6].The university industry collaboration network in the emerging and rapidly evolving interdisciplinary field are examined at firm-level [7].Yoon found that university-industry collaboration is the strongest within the triplehelix in recent years, followed by industry-government relations and then UIG relations[8].Throughout the above studies, we find that there are few researches on the IUR cooperation network in the chemical industry. In the existing empirical study, most cooperative networks are built on the basis of national, provincial and industrial levels. However, given the availability of data, there are fewer cooperation networks based on the level of enterprises, universities and research institutes. Scholars mainly use the co-authored sci-tech papers and patent data to construct IUR cooperative innovation network, which is confined to the research output stage of innovation, and short of production stage brought by exploitation of patent

To whom all correspondence should be sent:
E-mail: yanhy819@126.com

and empirical research on the micro-level of IUR cooperative innovation network subjects. This paper includes following parts: The first part builds the IUR cooperative innovation network in the chemical industry; the second part analyses the main body of the IUR cooperative innovation network in the chemical industry; the third part analyzes the characteristics of IUR cooperative innovation network; and the fourth part offers proposals based on the findings of the study.

EXPERIMENTAL

IUR cooperative innovation network is a network system established among innovative subjects of enterprises, universities and scientific research institutes. Its purpose is to provide a better platform for resources interexchange among innovation subjects to better meet the market demand and achieve higher economic benefits. Regarding the establishment of IUR cooperative innovation network, most scholars mainly use co-authored scientific papers and jointly applied patents, and most of which are utility patents. Patent licensing data not only reflects the cooperation among network subjects, but also reflects innovation. This paper uses patent licensing data as the data source of IUR cooperative innovation network in the chemical industry to study the impact of network structure on the innovation output of IUR cooperation network members in the chemical industry.

The patent licensing data studied in this paper comes from the State Intellectual Property Office (SIPO) and the patent service information platform. According to the purpose of this article, the innovation network has a few search conditions: Chinese invention patents; the application date is from 2010 to 2013; applicants of patent include enterprises, universities, colleges or research institutes, or their combinations, such as "enterprises % universities", "enterprises % research institutes", "colleges % enterprises" and "enterprises % enterprises". By analyzing status quo of the industry-university-research cooperation on innovative technology in the chemical industry, it is found that the cooperation among industry, universities and research institutes in the chemical industry is frequent and the intricate network system is formed. Innovative products have been fully introduced with a large number of innovative outputs to enhance the level of economic development in the chemical industry. Therefore, this article builds IUR cooperative innovation network based on the patent licensing data in the chemical industry. Enterprises, universities and

research institutes in the chemical industry participating in the industry-university-research cooperation from 2010 to 2013 represent nodes in the IUR cooperative innovation network, and IUR cooperative innovation network represents a collection of cooperative relationships among innovation subjects. After data screening, 1313 valid nodes were found in the innovation network, which mainly include enterprises, universities and research institutes. This paper uses Pajek to build an innovation network and draws the IUR cooperative innovation network for chemical industry during 2010-2013 and universities, research institutes and enterprises respectively. When building an innovation network, the size of each node is adjusted according to the centrality of the innovation subjects, that is, the larger the network node, the more prominent central position in the network is. The thickness of the line represents the weight of the edge where the node is located.

RESULTS AND DISCUSSION

Subjects of IUR cooperative innovation network in the chemical industry

Fig.1. shows the network structure diagram based on the patent licensing data in the chemical industry from 2009 to 2013. Wherein, the network with high centrality (the larger node) has fewer network subjects, and the centrality degree 1 (green) has the closest cooperative relationships.
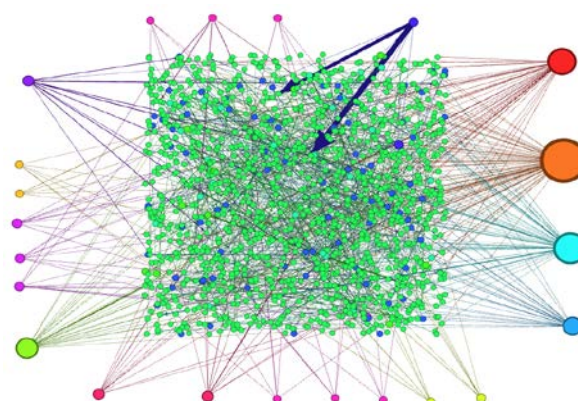

Fig. 1. IUR cooperation network structure diagram in the chemical industry

In this study, the main body of IUR cooperative innovation network in the chemical industry is divided into colleges and universities, research institutes and enterprises. Innovation network size refers to the total number of participants involved in the innovation network, that is, the number of nodes in the network. Table 1. Shows that the larger the size of an innovation

network, the more complex its network structure is, and the more likely it is that the network structure will affect the network main body. The innovation network size of enterprises plays the greatest role.

Table 1. Distribution list of IUR cooperation scale in the chemical industry

Time	Organization type	Network size	Percentage
2010	Colleges universities	88	16.57%
	Research institutes	82	15.44%
	Enterprises	361	67.99%
	Total	531	100%
2011	Colleges universities	130	19.94%
	Research institutes	126	19.33%
	Enterprises	396	60.73%
	Total	652	100%
2012	Colleges, universities	71	8.39%
	Research	211	24.94%
	Enterprises	536	63.36%
	Personal	28	3.31%
	Total	846	100%
2013	Colleges, universities	62	10.18%
	Research institutes	106	17.41%
	Enterprises	385	63.21%
	Personal	56	9.20%
	Total	609	100%

Due to the incomplete patent licensing data after 2012, and taking into account that there is little change in the structure of innovation network from 2010 to 2013, the innovation output after the patent licensing lags in terms of time points, and it is unclear how many years of hysteresis, so this article studies innovation network of four years, which will not only have little effect on the results of the study, but also offset the hysteretic nature of patents. The different types of network subjects have different positions in the IUR cooperative innovation network of chemical industry, and network densities vary in different years. It can be seen that the centrality of universities and research institutes is larger and the number of central nodes is smaller, and the proportion of one-to-many cooperation is larger than the cooperation network of enterprises. Enterprises' innovative network structure is most similar to the overall network structure. A few nodes are at the core status and establish a patent licensing relationship with a large number of enterprises and public institutions. They have frequent internal exchanges and more opportunities to obtain innovative achievements with a stronger competitive edge. Most of the enterprises are at the edge of the innovation network, and only establish cooperation relations with a small number of enterprises and public institutions. In addition, there are more one-to-many partnerships between universities and research institutes in the chemical industry, while

the cooperative relationships among enterprises are relatively fragmented, mainly on a one-on-one basis.

Scaleless property of IUR innovation network

Scale-free networks are complex networks whose degree distribution satisfies the power-law distribution, in which the connection status of each node is not evenly distributed and has serious heterogeneity.

Table 2 shows the calculation of the centrality of nodes in the innovation network. In terms of the overall network, the relevance of each subject (mean value of the centrality) is 2.91546, which means that on average, each subject has about 3 relationships with other subjects. The variance of the network centrality is 55.84891, and the maximum centrality (159) is larger, while the overall network density (0.001) is smaller, which indicates that the network connections are unevenly distributed in the innovation network. The centrality of the nodes in the IUR cooperative innovation network of chemical industry is calculated according to the frequency of appearances, and the frequency distribution of each node's centrality can be obtained. The probability distribution of the centrality of the nodes is plotted in the double logarithmic coordinate system.The centrality of network nodes is extremely uneven in the network. Most of the nodes have a low degree of centrality while fewer nodes have a larger centrality, which follows the power-law distribution, thus the innovation network is a scale-free network.

Small-work property of IUR innovation network

A small-world network is a kind of mathematical graph based network, most of the nodes are not directly connected, but can be connected by any other nodes in a few steps. In the industry-university-research innovation network, the small-world phenomenon mainly affects the length of path that various nodes need to communicate with each other.

Table 2. Statistics of IUR cooperative innovation network node centrality in the chemical industry

Index	Centrality
Mean value	2.915
Std. Dev.	7.473
Variance	55.848
Total degree	3828.000
Maximum	159.000
Minimum	1.000
Network average degree	0.694
Network density	0.001
Network average weighted	1.458

The shorter the node path of innovation network is, the shorter the path of information exchange among enterprises, colleges and universities and scientific research institutions in the innovation network, and the shorter the characteristic path length of innovation network, the higher transmission efficiency of information in innovation network. The lower the degree of information distortion is, the higher the clustering coefficient in the innovation networks.

The higher the probability of coincidence among innovative subjects in the innovation network, the higher the possibility of establishing cooperative relationships, indicating that such innovation networks have high development potential.

According to the statistical analysis of node data in IUR cooperative innovation network in the chemical industry from 2010 to 2013 shown in Table 3, the average path length of chemical industry IUR cooperative innovation network is 1.994 and the average clustering coefficient is 0.001, which indicate that any two of the 1313 cooperating parties of the IUR cooperative innovation network can establish relationship through 2-3 intermediaries on average.

Table 3. Statistics of innovation network

Distance	Value
Average characteristic path length	1.994
Average clustering coefficient	0.001

The characteristic path length of the IUR cooperative innovation network is small, the speed of information exchange among innovation subjects is high, the clustering coefficient is large, and the innovation subjects are more likely to establish cooperative relationships, indicating that the IUR cooperative innovation network in the chemical industry is a small-world network with great development potential.

Centrality of IUR innovation network

The eigenvector centrality of the network refers to the ratio of the number of eigenvectors of a connected node to the total number of other eigenvectors connected to the node, which can be used to measure the centrality of the network.

By calculating and comparing the centrality of network eigenvectors, we can observe the nodes at the core of the network. The higher the centrality of nodes in the network, the better the development prospect of the network. In the IUR cooperative innovation network, cooperative partners at the core position have greater potential for innovation and more access to innovative resources, which is more conducive to the innovation output of enterprises.

By calculating the eigenvector centrality of the network, we get the statistical table of eigenvectors of IUR cooperative innovation network, as shown in Table 4.

Table 4. Eigenvector centrality of integrated network

Items	Eigenvector centrality (digraph)	Eigenvector centrality (undigraph)
Mean value	0.0417710	0.0151951
Std. Dev.	0.0831275	0.0416054
Variance	0.0069102	0.0017310
Total	54.8452610	19.9511565
Maximum	1.0000000	1.0000000
Minimum	0.0000000	0.0016465
Number of nodes	1313.0000000	1313.000000

The organizations with larger centrality have a special network location and easier access to the resources needed for innovation output, making other agencies are more willing to cooperate with them to further promote inter-agency cooperation and social development. The more subjects at central position of the innovation network, the higher the innovation level of the network and the greater the competitive advantage. According to the study, the nodes that connect with the organization will affect the content or quality of the information acquired by the organization, thereby affecting the innovation potential of the organization in the central network.

Density of IUR innovation network

Network density refers to the degree of closeness among nodes in the network, reflecting the rate and range of network information diffusion. When there is no link between nodes, the density is 0, and when any two nodes are directly connected, the density is 1. The range of network density is [0,1]. According to Gephi software analysis, the density of IUR cooperative innovation network in the chemical industry is 0.001.

Proposals for development of industry-university-research cooperation in the chemical industry

IUR cooperative innovation network is a relatively stable network, which mainly refers to the network cooperation established by innovation entities such as enterprises, colleges and universities or research institutes in some region. At present, industry-university-research cooperation has good potential for development in the chemical industry. However, there are also some factors that constrain long-term development, mainly due to the large environmental differences and the low

conversion rate of scientific and technological achievements. In order to further promote the development of industry-university-research in the chemical industry, this paper combines the results of social network research and views of domestic and foreign scholars, and puts forward the following suggestions for industry-university-research cooperation in the chemical industry.

From the research results, we can see that in the industry-university-research innovation network of chemical industry, colleges and universities, research institutes and enterprises in the process of industry-university-research cooperation should fully understand their respective advantages and characteristics, put them in the right position and give full play to their own advantages. As training bases for talents, colleges and universities can increase the scope of cooperation with enterprises and research institutes through talent transfer and scientific research cooperation to increase the number of nodes, their centrality and their structural holes. Enterprises and research institutes can boost innovation output, and the innovation output of the entire IUR cooperative innovation network will also be greatly improved. Enterprises are located at the key point of the IUR cooperative innovation network, and play an important role in the transformation of innovative achievements and also the biggest interest recipient in innovation cooperation. Although enterprises of different sizes have different degrees of resource allocation, capital and technology in the network, they should effectively combine their own advantages and develop better under the industry-university-research development system. Enterprises can take advantage of the network location and resource advantages, expand the industrial chain according to the development direction of the market, promote innovation within the network, and then promote the optimization and integration of the innovation elements within the network. They can also make full use of relevant preferential policies and actively participate in the industry-university-research cooperation to play the role of innovative subject in the industry.

The positive impact of structural holes and centrality on innovation output is based on the assumption that subjects that span structural holes can efficiently access and receive information and resources, and that structural holes do not enclose their own information and resources on both sides. Structural holes in industry-university-research innovation networks have a negative impact on the innovation output of research institutes and enterprises, which is most likely due to the existence of social competition mechanisms that lead to the reluctance of sharing resources and information, resulting in the main body of structural holes or subject with high betweenness centrality cannot give full play to their advantages, access to information and resources, and decline in innovation output. Therefore, in the process of promoting industry-university-research cooperation, we need to establish a reasonable incentive mechanism for sharing information and resources so as to promote prompt access to information among network subjects.

A stable and effective innovation network environment is conducive to the exchange of information and cooperation between members of the network. The construction of overall network can promote the creation and development of all small networks, and the steady development of small networks will in turn promote the development of the whole network and promote the innovation output of all network members. Therefore, in order to promote the influence of IUR cooperative innovation network on the innovation output of network members, not only the innovation network needs to be built on the whole, but also the development of each small network needs to be considered.

CONCLUSIONS

Based on the research perspective of social networks, this paper uses patent licensing data in the chemical industry among universities, research institutes and enterprises in 2010-2013 as the data source, and draws a map of innovation network of industry-university-research cooperation in the chemical industry using the software of Pajek and Gephi, and makes an analysis on trend and innovative subject analysis as well as the characteristics of innovation network of industry-university-research cooperation in the chemical industry. The results show that innovation network of industry-university-research cooperation in the chemical industry is a complex network system as a whole with more nodes and uneven distribution, showing scale-free and small-world properties.

As SIPO has changed the way of announcing the patent licensing data since 2013, the researcher cannot obtain sufficient patent licensing data, which affects the timeliness of the research in this article. In the next step, we need to further update the data to explore the influence of network characteristics such as centrality and structural holes on the innovation output of network members.

REFERENCES

1. J. f. Yuan, Z. Xu, C. Zhai, *Science and Management* of *S.&.T.* **2**, 115 (2017).
2. D. Lavie, I. Drori, *Organization Science*, **23**, 704 (2012).
3. J.C. Guan, Q.J. Zhao, *Technological Forecasting & Social Change*, **7**, 1271(2013).
4. M. Hemmert, L. Bstieler, H. Okamuro, *Technovation*, **34**, 605 (2014).
5. K. Laurens, A. Noelle, *Technovation*, **6**, 193 (2013).
6. W. Hong, Y.S. Su, *Research Policy*, **42**, 454 (2013).
7. J. Guan, Q. Zhao, *Technological Forecasting and Social Change*, **80**(7), 1271 (2013).
8. J. Yoon, T*Scientometrics*, **104**, 265 (2015).

Biodegradation of di-n-butyl phthalate ester by newly isolated *Raoultella* sp. ZJY

T. F. Liu, H. Y. Zhang, J. Y. Chu, L. Q. Qiu [*]

College of Biotechnology and Bioengineering, Zhejiang University of Technology, Hangzhou, 310032, China

A bacterial strain ZJY that could degrade di-n-butyl phthalate was isolated from sludge of river of Hangzhou city, and identified as *Raoultella* sp. by morphological, physiological characteristics and the analysis of 16S rRNA gene sequence. The results of DBP-degrading characteristics showed that the optimal temperature and pH for dibutyl phthalate biodegradation was 30 °C and 7.0, respectively. The degradation was best fitted by first-order kinetic equation and the half-life was 40.81 h at 418 mg/L dibutyl phthalate of initial concentration. GC-MS analysis of the metabolites revealed that initial step of dibutyl phthalate was degradation was transesterification. To our knowledge, this is the first report on the biodegradation characteristics of DBP by a member of the *Raoultella* genus.

Key words: *Raoultella* sp; Di-n-butyl phthalate; Biodegradation; Phthalic acid esters

INTRODUCTION

Phthalic acid esters (PAEs) are major industrial products used as plasticizers in the industrial production of plastics. In recent years, phthalic acid diesters have appeared as important pollutants in environmental samples as endocrine disrupting chemicals which influence the genitals. Among rats and adult men, phthalate exposure resulted in decreased testicular weight, seminiferous tubular atrophy and increased DNA damage in sperm [1, 2]. Some of the PAEs including dimethyl phthalate (DMP), di-n-butyl phthalate (DBP), and di-n-octyl phthalate (DOP) have been listed as priority pollutants by the China National Environmental Monitoring Center [3] and the US Environmental Protection Agency [4].

Since the rates of photolysis and chemical hydrolysis of phthalate esters are very slow, metabolic breakdown by microorganisms is considered to be one of the major routes for the environmental degradation of these widely spread pollutants in aquatic and terrestrial systems. In recent years, various microorganisms are mainly responsible for the degradation of phthalic acid esters [5], these include *Gordonia* sp. [6], *Sphingomonsa* sp. [7], *Arthrobacter* sp. [8], *Rhodococcus* sp. [9], *Acinetobacter* sp. [10]. Numerous studies have demonstrated the microbial bio-degradation pathways of phthalate esters. The metabolism of phthalate esters is initiated in bacteria by their hydrolysis to mono-phthalate esters, which are further degraded by ester-hydrolysis to phthalate. Phthalate is further metabolized in aerobic bacteria by two different dioxygenase-initiated pathways through the common intermediate, protocatechuate (3,4-dihydroxybenzoate). Protocatechuate is further degraded into organic acids through either ortho- or meta-cleavage pathway by ring cleavage enzymes, which eventually converted them to CO_2 and H_2O through Krebs cycle [11-15]. In this paper, the aerobic degradation of selected phthalate esters by a pure culture of *Raoultella* sp. ZJY isolated from river sludge, was studied. To our knowledge, there is no report that *Raoultella* strains have the capacity to mineralize PAEs. In addition, we investigated the effects of temperature, pH, DBP concentration and the biochemical degradation pathway on the biodegradation performance of the strain ZJY. These results allow for a better understanding of the mechanism of PAEs degradation of the genus *Raoultella*.

EXPERIMENTAL

Chemicals

DMP, Diethyl phthalate (DEP), DBP, di(2-ethylhexyl)phthalate (DEHP), mono-butyl phthalate (MBP) and mono-methyl phthalate (MMP) were purchased from Sinopharm Chemical Reagent Co.,Ltd, all were >98% pure. HPLC-grade methanol was purchased from Tianjin Siyou Fine Chemicals Co., Ltd. (Tianjin, China). Other chemicals were of analytical-reagent grade, and were purchased locally.

Enrichment culture, isolation and identification of bacteria

The sludge samples were collected from sludge of the river of Hangzhou city. 1 g sample was mixed with 100 ml of a basic inorganic salt medium (BSM) ($K_2HPO_4 \cdot 3H_2O$ 1.0 g, NaCl 1.0 g, $(NH_4)_2SO_4$ 0.5 g, $MgSO_4 \cdot 7H_2O$ 0.4 g, $CaCl_2$ 0.0755 g, $FeCl_3 \cdot 6H_2O$ 0.0143 g in 1 L of distilled water, the pH of the medium was adjusted to 7.0), and supplemented with DBP (DBP dissolved in methanol) to 125 mg l^{-1} of final concentration as the sole carbon and energy source. After

acclimation for 7 days, the enriched medium was used to inoculate nutrient agar plates under aseptic conditions. The plates were incubated at 30 °C, and colonies were observed after 72 h. The colonies were then transferred to fresh plates, and the incubation process was repeated until pure cultures were obtained.

The identification of bacteria was based on their morphology, biochemical characteristics and analysis of the 16S rRNA gene. Cell morphology was observed by a transmission electron microscope (JEOL JEM-1230, Japan). The 16S rRNA gene was amplified from genomic DNA using universal bacterial primers F27 (5'-AGA GTT TGA TCC TGG CTC AG-3') and R1492 (5'-GGT TAC CTT GTT ACG ACT T-3') [16]. The PCR products were cloned into the pGEM-T Easy vector (Sangon, Shanghai, China) and sequenced. The sequence data of the closest relatives NCBI GenBank (http://www.ncbi.nlm.nih gov./BLAST) were aligned by ClustalX. A phylogenetic tree was then constructed using the neighbor-joining method with MEGA 7.0 software.

Substrate utilization tests

The isolated strain was inoculated into MSM containing 125 mg l^{-1} of one of the following substrates: DMP, DEP, DBP, DEHP, MBP, MMP, phthalic acid (PA), catechol and phenol as the carbon source to examine the ability of the strain to utilize these compounds. Substrate utilization was based on microbial growth as indicated by an increase in biomass ascertained by OD_{600} measurements.

Environmental factors effect on DBP biodegradation

The effect of different initial pH on DBP degradation was studied at initial pH values of 5.0, 6.0, 7.0, 8.0, and 9.0. Meanwhile, the degradation of DBP at different temperatures was studied at different temperatures: 25, 30, 37, and 42 °C. The degradation efficiency was determined by HPLC.

Based on the optimal pH and temperature established above, the DBP degradation kinetics of strain was studied. The effect of initial DBP concentrations on the degradation was investigated between 62.7 and 627 mg l^{-1} and the degradation efficiency was determined by HPLC.

Degradation of mixed PAEs

To study the degradation ability of mixed PAEs, the isolated strains and PAEs (a mixture of DMP, DEP, DBP and DEHP (each at 125 mg l^{-1}) were incubated aerobically at 30 °C and 180 rpm on a rotary shaker for 48 h. As a control, medium inoculated with heat-killed cells was maintained at the same conditions. The degradation efficiency was determined by HPLC.

Analysis of DBP and its metabolites

The concentration of DBP was analyzed by HPLC (Agilent 1100 series, USA) equipped with a Diamonsil-C18 column (4.6 mm×250 mm×5 µm; Dikma Technologies Inc, China). A mixture of methanol and H_2O (90:10 by volume) was used as the mobile phase at a flow rate of 1.0 ml min^{-1}. The UV detector wavelength was 235 nm and the sampling quantity was 20 µl.

DBP degradation metabolites were identified using a Hewlett Packard 6890N gas chromatograph (Hewlett Packard, USA) equipped with an Agilent 5975C mass selective detector (Agilent, USA). The column used was a HP-5MS（30m×250 m×0.25 m）capillary column. The temperature program consisted of 1 min hold at 60 °C, an increase to 220 °C at 30 °C min^{-1}, and 2 min hold, an increase to 250 °C at 5 °C min^{-1}, and 2 min hold, an increase to 280 °C at 5 °C min^{-1}, and 3 min hold. The injection volume was 1 µl and the carrier gas was helium (1.0 ml min^{-1}). The mass spectrometer was operated at an electron ionization energy of 70 eV. Instrumental library searches, comparison with available authentic compounds, and mass fragmentation pattern were used to identify the metabolites.

Statistical analysis methodology

Each treatment in the experiment was performed in triplicate. Software Origin 8.0 was used to draw the figures with error bars.

RESULTS AND DISCUSSION

Identification and characteristics of strain ZJY capable of DBP degradation

A bacterial strain ZJY that could degrade DBP was isolated from river sludge of Hangzhou city. The strain had a short-rod shape, a size of (0.8-1.2) µm × (0.4-0.7) µm. It was a Gram-negative, non-sporulating, and non-pigmented bacterium without flagella. The morphological features of strain ZJY are shown in Fig. 1.
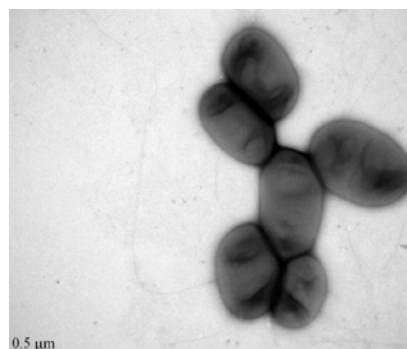

Fig. 1. Transmission electron micrograph of strain ZJY

Based on 16S rRNA gene sequence similarity, it was identified as a member of the genus *Raoultella* (GenBank accession no. KY317922.1). The phylogenetic relationship of strain ZJY with its close relatives is shown in Fig. 2.

Substrate utilization tests

The substrate utilization tests indicated that the strain ZJY was able to use PA, DMP, DEP, DBP, MBP and MMP as the sole carbon sources while no growth was observed in the presence of DEHP, catechol, phenol (Table 1). Members of the genus *Raoultella* are widespread in the nature and can be obtained from various sources such as plants, soil, and water. Although studies have shown that *Raoultella* species can degrade a variety of pollutants such as dimethoate, trinitrotoluene and petroleum [17,18], none prior to the present study have shown that *Raoultella* sp. degrades PAEs

Effects of pH and temperature on DBP biodegradation

The effect of pH on DBP degradation by *Raoultella* sp.ZJY is shown in Fig. 3A. The DBP degradation rate was the highest (about 95.7%) when pH was 7.0 after incubation for 48 h. When the pH was 5.0 and 9.0, the degradation rate was 9.8% and 54%, respectively, after incubation for 48 h. The highest DBP degradation rate was achieved at 30 °C (about 98%) after incubation for 48 h (Fig. 3B). When the temperature was 37 °C, 25 °C and 42 °C, the degradation rate was 81.8%, 49.8% and 6.7%, respectively, after incubation for 72 h.

Therefore, pH 7.0 and 30 °C were chosen for all subsequent experiments as the optimal conditions for DBP degradation by the strain ZJY.

Effect of the initial DBP concentration on DBP biodegradation

The degradation of DBP by *Raoultella* sp. ZJY was investigated at different initial concentrations (from 62.7 to 627 mg/l) (Fig. 4). DBP biodegradation by *Raoultella* sp. ZJY was assumed to fit the Monod first-order kinetic equation as follows: $\ln C = -Kt + A$ (where C is DBP concentration, t expresses time, K is the first-order rate constant and A is a constant). Table 2 shows the DBP degradation kinetic equations at different initial DBP concentrations. The results showed that when the initial DBP concentration was <627 mg l^{-1}, DBP biodegradation reaction fitted well with first-order kinetics. When the initial DBP concentration was 418 mg l^{-1}, the half-life of DBP was 40.81 h.
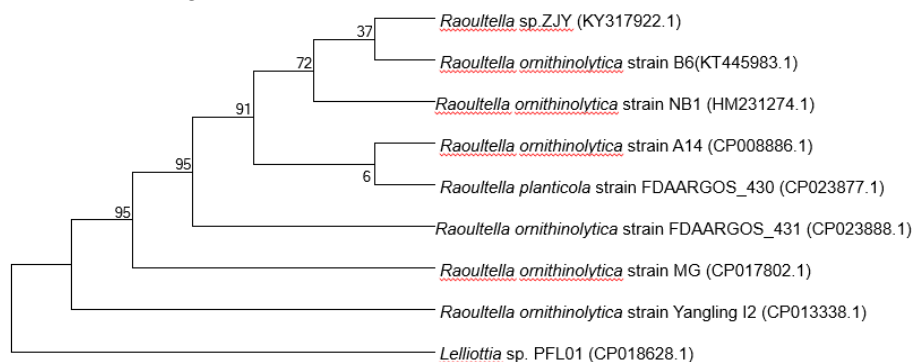

Fig. 2. Phylogenetic tree of *Raoultella* sp. ZJY.

Note: Distances were calculated using neighbor-joining method. The numbers at the branch nodes are bootstrap values (%). Accession numbers of the bacterial isolates are shown in brackets.

Table 1. Substrate utilization tests by *Raoultella* sp. ZJY

Substrates	DMP	DEP	DBP	DEHP	PA	MBP	MMP	Catechol	Phenol
Growth	+	++	++	-	+	+	+	-	-

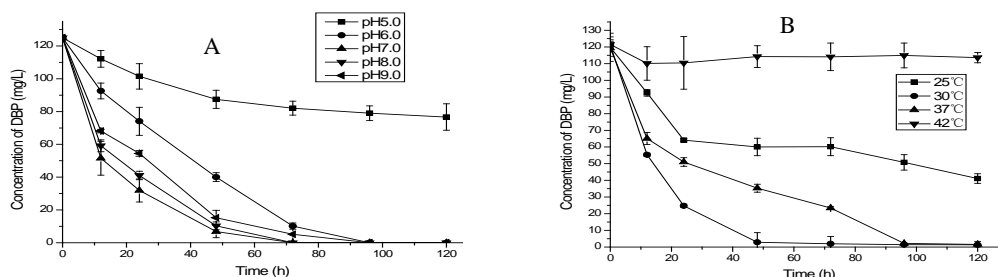++：means vigorous growth; +：means growth; −：means no growth

Fig.3. Effect of pH (A) and temperature (B) on degradation of DBP by *Raoultella* sp. ZJY.
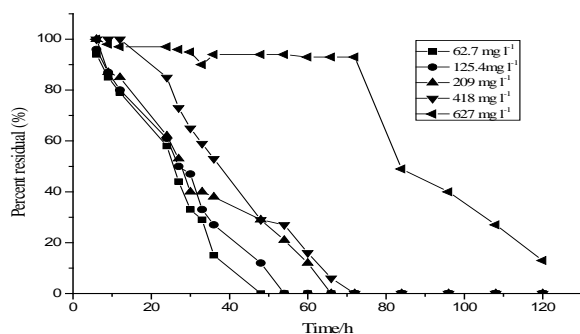
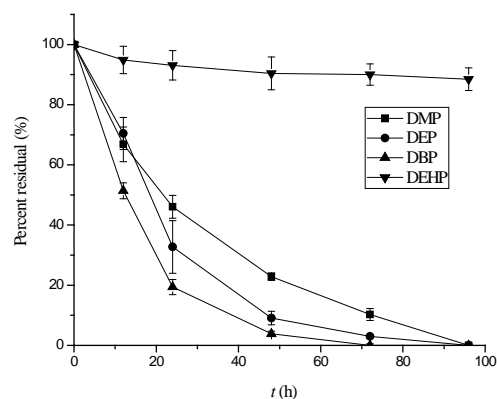**Fig. 4.** Effect of different initial DBP concentrations on degradation by *Raoultella* sp. ZJY.

Table 2. Kinetics of aerobic DBP degradation by *Raoultella* sp. ZJY

Initial concentration /mg l^{-1}	Kinetic equations	$t_{1/2}$ /h
62.7	lnC =4.9264 -0.1413 t	22.13
125.4	lnC=5.0156-0.1203 t	24.25
209	lnC=5.0782-0.0862 t	27.02
418	lnC=5.2115-0.0634 t	40.81

Degradation of mixed PAEs

The degradation of a PAEs mixture consisting of DMP, DEP, DBP and DEHP (125 mg/l respectively) was performed (Fig. 5). The results showed that DBP was degraded very quickly, with more than 98.5% removed in 72 h. The degradation rate of DEP and DMP was 96% and 89%, respectively, after incubation for 72 h. This results indicated that PAEs with longer alkyl chains are easily degraded, while PAEs with shorter alkyl chains are harder to degrade. Previous studies have reported similar findings [19].

In the substrate utilization tests, no growth of strain ZJY was observed in the presence of DEHP as the sole carbon source. However in PAEs mixture, the degradation rate of DEHP was 10% after incubation for 72 h. This result might be due to the adsorption of microbial cells.

Fig.5. Degradation of mixed PAEs by *Raoultella* sp. ZJY

Biochemical degradation pathway

To explore the metabolic pathways for DBP degradation by *Raoultella* sp. ZJY, metabolites of DBP were identified by GC-MS. Four major metabolites besides the parent compound DBP (Fig. 6A), butyl-methyl phthalate (Fig. 6B), DMP (Fig. 6C) and PA (Fig. 6D) were identified. GC-MS analysis of the metabolites revealed that the initial step of dibutyl phthalate degradation was transesterification in the presence of CH$_3$OH. In the first step, butyl-methyl phthalate was formed by the first transesterification, and DMP was formed by the second transesterification, then followed hydrolysis of DMP to PA. The above results are similar to those previously reported [20]. Based on the above results, a conjectural metabolic pathway for the degradation of DBP by *Raoultella* sp. ZJY may be proposed (Fig. 7).
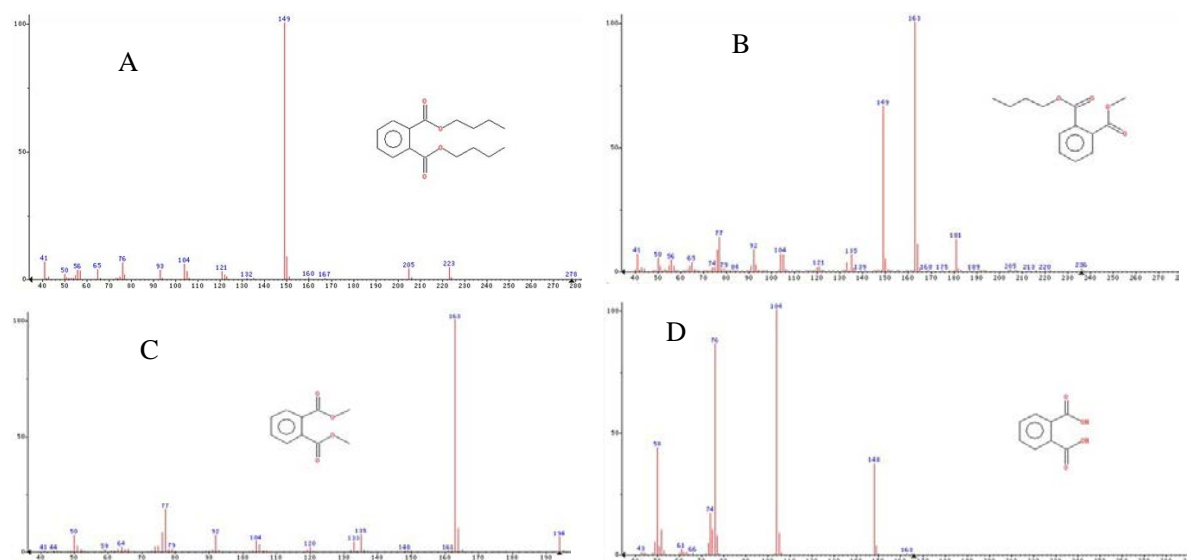

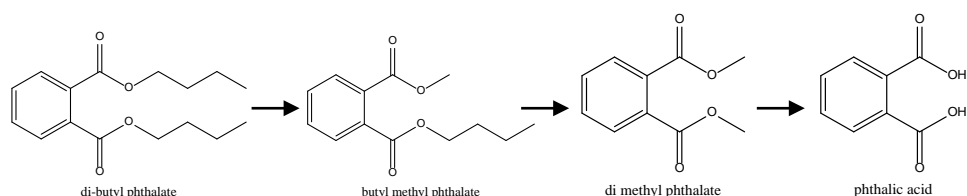**Fig. 6.** GC-MS analysis during the degradation of DBP by *Raoultella* sp. ZJY

di-butyl phthalate   butyl methyl phthalate   di methyl phthalate   phthalic acid

Fig. 7. The degradation pathway of DBP by *Raoultella* sp. ZJY

CONCLUSIONS

A bacterial strain ZJY that could degrade di-n-butyl phthalate was isolated from sludge of the river of Hangzhou city. Strain ZJY was identified as *Raoultella* sp. based on the analyses of morphological, physiological characteristics and 16S rRNA gene sequence. To our knowledge, this is the first report on the biodegradation characteristics of DBP by a member of the *Raoultella* genus. The optimal temperature and pH for dibutyl phthalate biodegradation were 30 °C and 7.0, respectively. The strain ZJY was able to use PA, DMP, DEP, DBP, MBP and MMP as the sole carbon sources. GC-MS analysis of the metabolites revealed that the initial step of dibutyl phthalate degradation was transesterification.

REFERENCES

1. O. S. Fatoki, A. O. Ogunfowokan, *Environ. Int.*, **19**, 619 (1993).
2. Y. Y. Wang, Y. Z. Fan, J. D. Gu, *Int. Biodeter. Biodegr.*, **53**, 93 (2004).
3. J. L. Wang, P. Liu, Y. Qian, *Chemosphere*, **31**, 4051 (1995).
4. US EPA, Code of Federal Regulation, 40 CFR Part 136 (1992).
5. S. M. Duty, N. P. Singh, M. J. Silva, D. B. Barr, J. W. Brock, L. Ryan, R. F. Herrick, D. C. Christiani, R. Hauser, *Environ. Health Perspect.*, **111**,1164 (2003).
6. D. Jin, Z. Bai, D. Chang, D. Hoefel, B. Jin, P. Wang, D. Wei, G. Zhuang, *Journal of Hazardous Materials*, **221-222**, 80 (2012).
7. W. Wirongrong, S. Pareenart, N. Monnapa, T. Sirinthra, M. Skorn, L. Suvit, *International Biodeterioration & Biodegradation,* **99**, 45 (2015).
8. Y. Wang, B. Miao, D. Hou, X. Wu, B. Peng, *Process Biochemistr*y, **47**, 936 (2012).
9. D. Jin, R. Liang, Q. Dai, R. Zhang, X. Wu, W. Chao, *J. Microbiol. Biotechnol*., **20**,1440 (2010).
10. J. Wu, X. Liao, F. Yu, Z. Wei, L. Yang, *Appl. Microbiol. Biotechnol.*, **97**, 2483 (2013)
11. S.W. Mary, M.E. Stephanie, S.B. Gertrud, X. Ye, J. S. Manori, C. Zhu, W. James, M. C. Antonia, *Environ. Health Perspect.*, **116**,1092 (2008).
12. R.W. Eaton, *J. Bacteriol.*, **183**, 3689 (2001).
13. R. L. Stingley, B. Brezna, A. A.Khan, C. E. Cerniglia, *Microbiology*, **150**, 2749 (2004).
14. P. Keyser, B. G. Pujar, R. W. Eaton, *Environ. Health Persp.*, **18**, 159 (1976).
15. S. E. Williams, E. M. Woolridge, S. C. Ransom, J. A. Landro, P. C. Babbitt, J. W. Kozarich, *Biochemistry*, **31**, 9768 (1992).
16. C. R. Fang, J. Yao, Y. G. Zheng, C. J. Jiang, L. F. Hu, *International Biodeterioration & Biodegradation*, **64**,442(2010)
17. Y. Liang, FH. Zeng, GZ. Qiu, XY. Lu, XD. Liu, *Biodegradation*, **20**, 363 (2009).
18. H. Claus, T. Bausinger, I. Lehmler, N. Perret, G. Fels, U. Dehner, J. Preuss, H. König, *Biodegradation*, **18**, 27 (2007).
19. B. V. Chang, C. M. Yang, C. H. Cheng, S. Y. Yuan, *Chemosphere*, **55**, 533 (2004).
20. Y. Okamoto, C. Toda, K. Ueda, K. Hashizume, N. Kojima, *Journal of Health Science*, **57**, 293 (2011).

Methods for modeling spatial variability of soil organic carbon under different land use in middle reaches of the Heihe river basin, northwestern China

J.H. Zhang, G.D. Li [*], C.l. Lu, Y.H. Liu, Y.P. Ding

[1] *College of Environment and Planning, Collaborative Innovation Center on Yellow River Civilization of Henan Province, Henan University, Kaifeng 475004, Henan, China*

The aim of this paper is to identify the influence of land uses on soil organic carbon (SOC) distribution in the middle of Heihe, China. Geostatistical methods including ordinary kriging (OK), spline (SPLIN), inverse distance weight (IDW) and local polynomial interpolation (LP) were compared. It is noteworthy that OK engenders smaller prediction errors than SPLIN, IDW, and LP. We selected the OK method to estimate SOC distribution. Results show that spatial distribution of SOC has an obvious gradual decreasing trend from high to low sections at different layers in the depth of the 100 cm soil profile. Most notable is that SOC content of cultivated land is higher than that of desert, sandlot, saline-alkali and naked fields. From a spatial perspective, paddy fields with a long history of cultivation are distributed on the two sides of Heihe river, while land with a shorter history of cultivation is located at a greater distance from the river. Land use change will increase or decrease SOC content. The extension of cultivated land with desert, naked land, sandlot, saline-alkali fields and middle density grassland with low SOC content will enhance the content of SOC in soil profile by a carbon fixation process, although sandy desertification is a reverse process. The results show that cultivation is an important process of increasing SOC content.

Key words: Distribution, SOC storage, Land use, Cultivation, Heihe river basin

INTRODUCTION

Global warming and the climate change including warming temperature, changing precipitation and rising sea levels are some of the most serious environmental problems in the world confronting the international community [1]. The essential issue is the increasing level of CO_2 in the air because the rate of anthropogenic emissions exceeds the rate of absorption by natural carbon sinks (terrestrial biosphere and oceans). The Intergovernmental Panel on Climate Change reports that more than 95% in 2014 are being caused by anthropogenic activities. However, we still cannot balance the global C budget and predict its change because of a number of unknowns [2]. At present, SOC pool in soil is twice that of the atmosphere [3], with estimated value at about 1550 Pg in the world [4,5]. Change here may be the source or sink of carbon in CO_2 [6-10]. If more carbon is stored in the soil and transformed to soil organic carbon (SOC), it will reduce or decrease the amount present in the atmosphere, and help ease the problem of global warming and climate change. Therefore, it is very important to comprehend the dynamic change of SOC, as well as its role in bringing about food security [11] and cutting carbon emissions down to air from the terrestrial ecosystem [12].

Content and storage of SOC and its composition are the foundation of the mechanism of organic carbon changes in different regions [13-15]. Methods for modeling spatial distributions of SOC can be realized by using GIS (Geographic information systems) models integrated with image data using remote sensing methods in regional scale, to select the appropriate model to improve the simulation accuracy. Geostatistics provides a superior tool to quantify the spatial variations of SOC and to perform spatial interpolation. It can calculate and visualize the spatial differences between SOC distribution and its influencing factors.

Arid regions are one of the highest sensitivity zones for global changes. The oasis is one of main productive bases in arid regions. Although their area amounts to only 3.3% of the arid regions in China, they support over 90% of the population and create over 95% production values of industry and agriculture. The study area is situated in the middle of Heihe River Basin. Land use and farming have modified SOC content and the related properties. In this study, the objectives were to investigate (1) the spatial variation characteristics of SOC under different land uses, and (2) to evaluate the methods including OK, SPLIN, IDW, LP. and to search for the best one to simulate the spatial variability of soil organic carbon.

To whom all correspondence should be sent:
E-mail: oklgd@163.com

EXPERIMENTAL

Study area

The study area is situated in the northwest of China between 37°45′-42°40′ N and 97°05′-102°00′ E (Figure 1). Because of the position in the inner Eurasia, it belongs to a kind of dry climate with high temperature and evaporation rates. Yearly rainfall average ranges between 110 mm and 130 mm, and annual evaporation average is 2341 mm. Evaporation surpasses precipitation, so irrigation is a typical means for increasing crop production. However, water resources including surface water and groundwater from the melting ice and snow from the Oilian Mountains are unevenly temporal-spatial distributed. It brings cropland to mostly occupy both sides of the Heihe River. From south to north of the study area. The soil is mainly formed under drought conditions, there are respectively the types of chesnut soil, sierozem, gray desert soil, gray-brown desert soil, aeolian sand soil and dry saline soil. Away from village or small town area to desert, the soils are respectively deep dark horsebean, irrigated aeolian sand soil and aeolian sand soil. Horsebean and fluvo-aquic soil are the two main agricultural soils occupying abundant area.
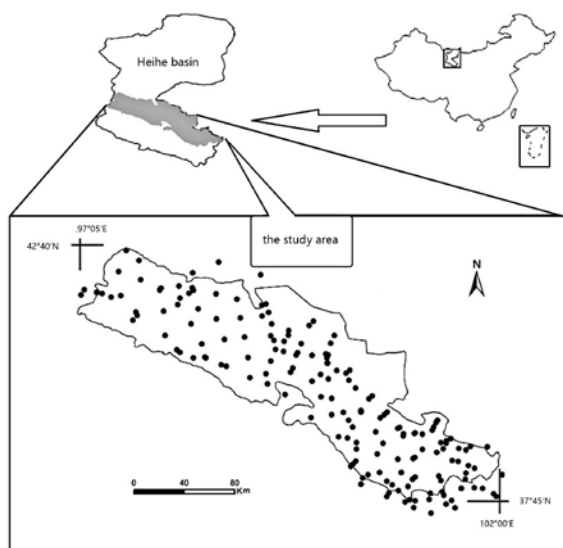
Fig. 1. Location of field sampling points

Data Collection

Field sampling was carried out using a grid with 12 km×12 km cells. 195 soil sampling points were chosen and the locations were measured with a GPS instrument (global positioning system) (Figure 1). It was divided into five layers in 100 cm depth of the soil profile, with an interval of 20 cm. The fresh soil was collected and then moved to the laboratory for further air-dried disposal process. After removal of visible roots, the soil sample was

110

passed successively through 2 mm and 0.15 mm sieves. SOC content was measured by the method of acid dichromate digestion and $FeSO_4$ titration [16].

Introduction of application models

Previous studies have used geostatistical analysis methods for soil organic carbon content interpolation at spacial scale based points' data [17-19]. Four classical interpolation models, IDW, OK, SPLINE and LP were tested to estimate different layers distribution of SOC. IDW obtained the value at unsampled region using a weighted average from exsting adjacent points, and the weight designated to each adjacent point diminshed the adjacent point increase at the distance [20]. The IDW model can be given as Eq.1.

$$Z(i) = \frac{\sum_{j=1}^{n} z(j)/D_{ij}^{r}}{\sum_{j=1}^{n} 1/D_{ij}^{r}} \tag{1}$$

where $Z(i)$ is the value at location i, $Z(j)$ is the value at sampled location j, $D_{i,j}$ is the distance between i and j, n is the quantity of sampled points; and r is the power of inverse-distance weight.

OK is the most commonly and extensively used Kriging method. It supposes that the distance or direction between spatial points reflects a spatial correlation that can be used to interpret changes in the surface. OK model is given as Eq.2.

$$Z(x_0) = \sum_{i=1}^{n} \lambda_i Z(x_i) \tag{2}$$

where $Z(x_i)$ is the monitoring value at point x_i, $Z(x_0)$ is the predicted value at the unexpected point, λ_i is the kriging weight.

SPLINE estimates values using a mathematical function that minimizes over surface curvature. It forms a smooth surface relying on the input points or the given point. It is based on modeling the measurements $Z(S_i)$ where $S_i = (x_i, y_i)$ is a point of coordinates x_i, y_i (Eq.3).

$$Z(S_i) = f(S_i) + \varepsilon(S_i), \ i = 1,......, n \tag{3}$$

where n is the number of measurement points or controlling points; f is an unknown deterministic smooth function, and $\varepsilon(S_i)$ are random errors. The function can be estimated by minimizing:

$$\Sigma[Z(S_i) - f(S_i)]^2 + \lambda J_2(f) \tag{4}$$

where $J_2(f)$ is a measure of smoothness of f computed by the following double integral (Eq.5)

$$J_2(f) = \int_{-\infty}^{\infty} \int_{-\infty}^{\infty} \left\{ \left(\delta^2 f / \delta x^2 \right)^2 + 2\left(\delta^2 f / \delta x \delta y \right)^2 + \left(\delta^2 f / \delta y^2 \right)^2 \right\} dxdy \tag{5}$$

λ is the smoothing parameter which regulates the trade off between the closeness of the function to the data and the smoothness of the function.

LP method suits numerous polynomials to the whole surface, each within specified overlapping neighborhoods. It fits the specified order polynomial based known points only in the range of the defined neighborhood. The neighborhoods overlap, and the predicted value of each point is the value of the fitted polynomial at the center of the neighborhood.

Statistical parameters including ME (mean error) and RMSE (root mean square error) were used as evaluation criteria for IDW, OK, SPLINE and LP models (Eq. 6).

$$ME = \frac{1}{n}\sum_{i=1}^{n}(\overset{\wedge}{z_i} - z_i)$$

$$RMSE = \sqrt{\frac{\sum_{i=1}^{n}(\overset{\wedge}{z_i} - z_i)^2}{n}}$$

(6)

where z is the value at point i, $\overset{\wedge}{z_i}$ is the predicted value, and n is the number of data points.

RESULTS AND DISCUSSION

Model tests

In order to obtain the best simulation results, all data were divided into two parts: analog part set and validation part set. Simulations of the positions of the validation points and experimental value at spatial position were compared by ME and RMSE (Figure 2).

By comparing simulated results of the four models, it was found that ME error is relatively low for OK and SPLINE models, and is generally the lowest on for OK model in the soil profile. OK method gives the lowest RMSE, IDW gives poor performance in the whole profile. In addition, there is similar variation in error in the soil profile, the highest value is in 0-40 cm and the lowest in 80-100 cm, which probably reflects the greater regional SOC differences in the surface layer.

Prediction errors with the worst results were produced by LP and IDW. Spatial result of IDW method has a higher error and is prone to appear "buphthalmos" for uneven sampling points. LP method must be considered spatially trendy ignoring the local variations, as a result of which the simulation is not consistent with the actual situation. SPLINE needs data with little change without extreme values. OK method considers the points' distance, azimuth and irregular changes of spatial continuity, it can give appropriate

description using a random surface. It is proved that OK model does the best job and is the best choice to perform the trend prediction in the study.
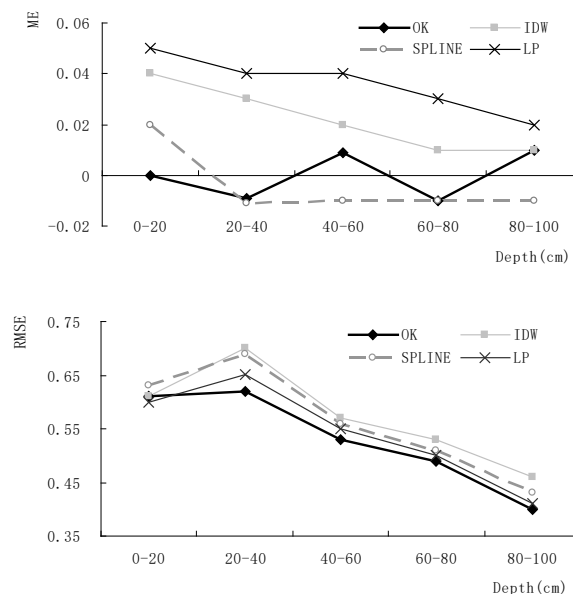

Fig. 2. Validation of ME and RMSE for the four interpolation methods in 0-100 cm depth

Spatial distribution of different land use

Land use map in the region was obtained from the website (http://heihe.westgis.ac.cn). Figure 3 shows the spatial distribution of the land use.
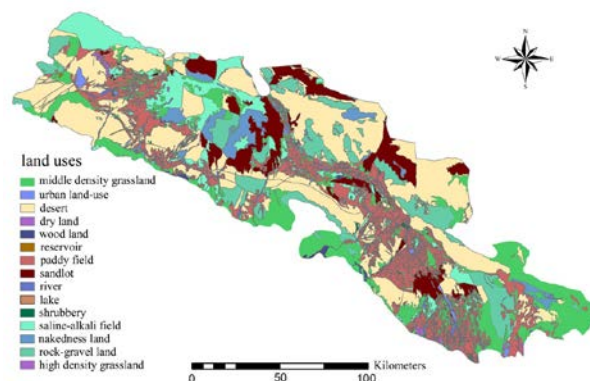

Fig. 3. Distribution of different land use in the area

There are 15 types of land use in middle Heihe river basin: desert, paddy field, middle-density grassland, rock-gravel land, saline-alkali field and sandlot. Each covers a relative large portion of the region, whereas, lake, reservoir, dry land, high-density grassland, shrub land, woodland, river, urban land-use, and bare land each cover a relatively small portion. The cultivated land including dry land and paddy field is about 17.09% of the total. From a spatial perspective, paddy field and urban land-use are mainly located along the two sides of the Heihe River, and the middle-density grassland is close to the paddy field and dry

111

land. Desert, sandlot, saline-alkali field, bare land, and rock-gravel land are more distant from the river.

Spatial distribution of SOC in soil profile

Spatial distribution between SOC and land use displays a homologous trend in each layer of soil profile (Figure 4). There are two high-value areas, the one is situated in the southeast of the study area near to Qilian Mountain, affected by factors including climate, plants and soil animals. For the reason of high precipitation and low temperature, vegetation species and coverage are rich, litter and falling matter have adequate sources. This will enhance the SOC content in the surface layer (0-20 cm), and further increase the content in the deep layer (20-100 cm). The other high section is the paddy field near to the suburb of Jiuquan city. It is found that irrigation from domestic sewage is the main reason. From surface layer (0-20 cm) to deep layer (80-100 cm) in 0-100 cm, SOC content gradually decreased at the same land use, the reduced amplitude is smaller. From high to low section at different layers in the depth of 100 cm soil profile, it is an obvious gradually decreasing trend.

In the oasis region of the study area, the most notable character is that SOC content of cultivated plots is higher than those of the desert, sandlot, saline-alkali field, and naked land at each layer. This trend is most obvious in the surface 0-20 cm and 20-40 cm. From a spatial perspective, paddy fields with a long history of cultivation are located at both sides of the river, while land with a shorter history of cultivation is located at a greater distance from the river. This reflects the trend in cultivation to spread from the river border to the outer wilderness. Previous studies showed that the cultivation activites cause SOC content reduction and loss, such as plough, fertilization, etc. On the other hand, some measures can enhance SOC content under the effect of the straw organic matter returning, crop rotation and organic fertilizer increasing. At the study area, SOC content is low compared with the land use of desert, sandlot, saline-alkali field, naked land and rock-gravel. These lands distribute the oasis inward and show an inlaid distribution pattern with the cultivated plots. For the low vegetation coverage and few plant species, it will cause a little litter and falling matter and low organic matter return. Under the effect of high temperature and low precipitation conditions, the amount of SOC decomposition and transformation is less. So, if these land uses with low SOC are changed into cultivated plots, it will increase the content of SOC. Land uses such as

rock-gravel land, high density grassland, woodland and shrub land are unsuitable for cultivation.
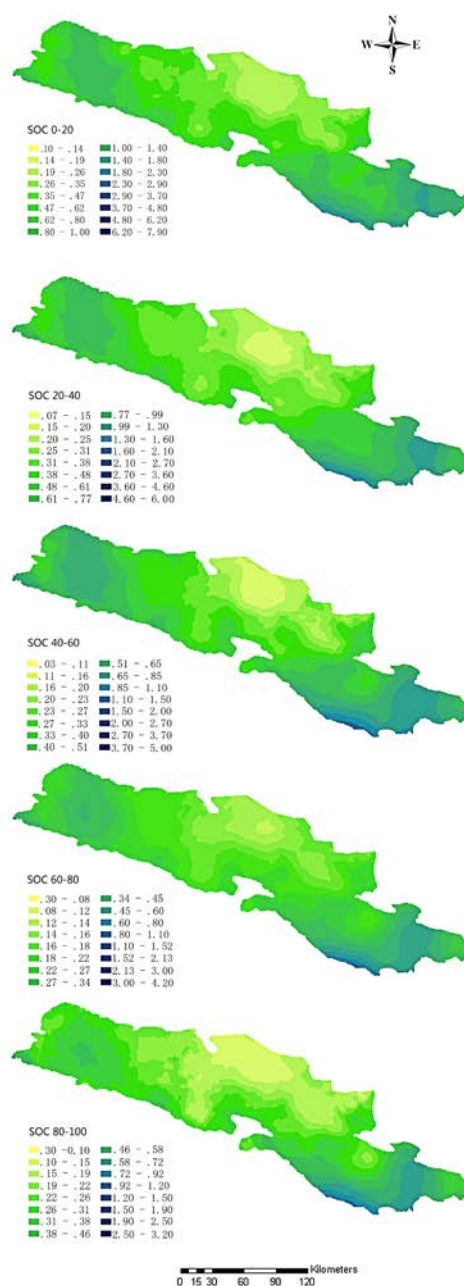

Fig. 4. Spatial distribution of soil organic carbon in 0-100 cm (%)

Rock-gravel land is located at the foreland of the Heli-longshou Mountains which are far away from water sources and are not covered with any vegetation. High-density grassland and woodland occupy the transitional zone between the middle Heihe River Basin and the low-temperature section of the Qilian Mountains. Shrubbery land provides ecological protection but covers only small areas at scattered locations.

DISCUSSION

SOC is an important matter in soil, and also the basis of soil fertility. How to improve soil organic carbon content in the region has become the core issue of climate change and food production. Usually, the results of experiments are constrained to points or the region where the experiments are involved, the forecasts of soil organic carbon at regional scale are scarce for their spatial variability for lack of amounts of experimental data. Spatial variability based on GIS methods at spatial scale is more advantageous than the studies at points or regions where the experiments are carried out for resource utilization and rational allocation.

Comparing OK, SPLINE, IDW and LP models, the simulated results showed that OK model provides minimum error with higher spatial resolution. Spatial distribution between SOC and land use is a homologous trend in each layer of soil profile.

There are significant spatial differences of SOC content under different land use types in 0-100 cm. The transitions or conversions of different land uses drive the SOC content changes. Land use change will increase or decrease SOC content. Numerous studies have shown that the expansion of cultivated plots, sandy desertification and urban land-use are the primary factors driving land use change in oasis regions, resulting in the shrinkage of middle-density grassland and water area [21-27]. The extension of cultivated land, by which low SOC content uses such as desert, naked land, sandlot, saline-alkali field and middle-density grassland are changed to dry land and paddy field, will enhance the content of SOC in the soil profile, is a carbon fixation process, although sandy desertification is a reverse process. Many studies have also proven that cultivation and soil desertification have an important influence on SOC content and pools for oasis farmland, and that oasis soil can act as a carbon sink [28-32].

CONCLUSION

It is very important to build better models at a regional scale because it is the level at which management and decision making are carried out. By comparing four interpolation models (OK, IDW, SPLINE and LP), the prediction errors indicate that OK model does the best job and is the best choice to perform the trend prediction in the study.

Spatial distributions of SOC are an obvious gradually decreasing trend from high to low section at different layers of soil profile, the high sections located at the southeast of the study area near to Qilian Mountain and the paddy field near to the suburb of Jiuquan city.

In the oasis region of the study area, the most notable character is that SOC content of cultivated plots is higher than those of desert, sandlot, saline-alkali field and naked land. From a spatial perspective, paddy fields with a long history of cultivation are distributed on both sides of Heihe river, while land with a shorter history of cultivation is located at a greater distance from the river. The transitions of different land uses drive the SOC content changes, the extension of cultivated land, by which low SOC content such as desert, nakedness land, sandlot, saline-alkali field and middle density grassland are changed to dry land and paddy field will enhance the content of SOC in the soil profile. It is a carbon fixation process, although sandy desertification is a reverse process. These should attribute to deserts and desertification land uses initially having a low SOC content because of the effect of scarce water resources. Reasonable cultivation is an important process of increasing SOC content.

REFERENCES

1. R.A. Houghton Cambridge, Univ. Press, Cambridge, 2004.
2. D. Schimel, I. G. Enting, M. Heimann, T. Wigley, D. Raynaud, D. Alves, U. Siegenthaler, Cambridge Uni. Press, Cambridge ,1995.
3. W.H. Schlesinger, *Ann. Rev. Ecol. Syst.*, **8**, 51 (1977).
4. N.H. Batjes, *Eur. J. Soil Sci.*, **47**,151 (1996).
5. R. Lal, *Progr. Environ. Sci.*, **1**, 307-326 (1999).
6. R. C. Dalal, R.J. Mayer *Aust. J. of Soil Res.*, **24**, 265(1986).
7. R.A., Houghton, J.L. Hackler, *Global Biogeochem.*
8. Q.S. Ge, J.H. Dai, F.N. He, Y. Pan, M.M. Wang, *Sci. China Earth Sci.*, **38**,197 (2008).
9. B. Han, X.K. Wang, F. Lu, X.N. Duan, Z.Y. Ouyang, *Acta Ecol. Sin.*, **28**, 612 (2008).
10. Z.C. Qin, Y. Huang, *Sci. China Life Sci*, **53**, 868 (2010).
11. R. Lal, *Geoderma*, **123**, 1(2004).
12. Z.Y. Su, Y.M. Xiong, J.Y. Zhu, Y.C. Ye, M. Ye, *Pedosphere*, 16 , 10 (2006).
13. X.M. Yang, M.W. Michelle, *Soil Till. Res.*, **52**, 1(1999).
14. X. Fang, Z.J. Xue, B.C. Li, S.S. An, *Catena*, **88**, 6(2012).

15. J.P. Neal, R. Matthew, K.W. Bruce, *Geoderma*, **230-231**, 79(2014).

16. Q.X. Wen, 1984. *Agr. Press*, Beijing (1984).

17. X.F. Cheng, X.Z. Shi, D.S. Yu, X.Z. Pan, H.J. Wang, W.X. Sun, *Pedosphere,* **14**, 425 (2004).

18. D. Mcgrath, C. Zhang, *Appl. Geochem.*, **18**, 1629 (2003).

19. D.W. Liu, Z.M. Wang, B. Zhang, K.S. Song, X.Y. Li, J.P. Li, F. Li, H.T. Duan, *Agr. Ecosyst. Environ.*, **13**, 73 (2006).

20. C.D. Lloyd, *J. Hydrol.*, **308**, 128(2005).

21. Y. Zhuang, G.M. Liu, H.Y. Ma, G.X. Wang, *J. of Glaciol. and Geocryol.*, **26**, 740(2004).

22. B. H. Zheng, Z. Q. Tian , Z. C. Li, *J. of Arid Land Resour. & Environ.*, **19**, 62(2005).

23. J. J. Meng ,X. Q. Wu , Z. G. Li, *Acta Sci. Nat.Univ. Pekinesis*, **40**, 922(2004).

24. G. X.Wang, G. D. Chen, *J. Desert Res.*, **19**, 368(1999).

25. S.Z. Qi, T. Wang, F. Luo, J.L. Ding, *J. Mtn. Res.*, **23**, 153(2005).

26. J. Zhou, X. Li, G.X. Wang, J. Zhao, *J. Nat. Resour.*, **24**, 498 (2009).

27. C.Z. Li, F.L. Yu, J. Li, D.H. Yan, T. Zhou, *J. Nat. Resour.*, **26**, 353(2011).

28. W.Q. Xu, G.P. Luo, X. Chen, L.X. Xiao *Geogr. Res.*, **25**, 1013 (2006).

29. W.L. Xu, G.M. Tang, J. D. Sheng, Z. Liang, B. Zhou, M. Zhu, *Acta Ecol. Sin.*, **30**, 1773 (2010).

30. Y.Z. Su, R. Yang, W.J. Liu, X.F. Wang, *Soil Sci.*, **175**, 246 (2010).

31. F. Wang, H.L. Xiao, Y.Z. Su, G.P. Fang, *J. Desert Res.*, **31**, 723 (2011).

32. J.H. Zhang, G.D. Li, Z.R. Nan, H.L. Xiao, *Geogr. Res.*, **31**, 608 (2012).

Characterization of a glycoprotein from the silk of caddisfly *Stenopsyche marmorata*

Q. Lin[1#], H. Wang[2#], H. Chen[1], Y. Peng[1], B. Kwan[1], M. Nakagaki[3], Y. Wang[1*]

[1] Guangxi Key Laboratory of Beibu Gulf Marine Biodiversity Conservation, Ocean College, Qinzhou University, Qinzhou-535011, China
[2] College of Humanities, Qinzhou University, Qinzhou-535011, China
[3] Department of Applied Biology, Faculty of Textile Science and Technology, Shinshu University, Ueda-386-8567, Japan

By sequencing the N-termini of the luminal proteins and screening the silk gland cDNA library of the caddisfly *Stenopsyche marmorata (S. marmorata)*, a major silk component (Smsp-12k) which proved to be a glycoprotein, was identified in this suborder. The primary structure of Smsp-12k consists of three degenerate repeats with Gly (29.7%), Trp (18.7%) and Ser (13.2%) present as the most abundant amino acids. The SXSXSXSX and GGX motifs were repeatedly found in Smsp-12k and are also present in the repetitive region of the heavy chain fibroin (H-fibroin) of *S. marmorata*. The SXSXSXSX and GGX motifs confer toughness and elasticity to the caddisfly silk, respectively. The abundant expression and structural resemblance of Smsp-12k to the repetitive region of H-fibroin indicates that this protein may play an important role in contributing to the physical properties of the aqueous silk.

Keywords: Caddisfly, Silk, *Stenopsyche marmorata*, Glycoprotein

INTRODUCTION

Silk, generally defined as fibrous proteins, is produced by many groups of terrestrial arthropods including spider and insect. Silk production in spider, generally used for prey capture, is secreted from spinnerets at the tip of the abdomen. The domestic silkworm *Bombyx mori* has served as a primary model for *Lepidoptera* insect silk. Silk fibroin is secreted in the lumen of posterior silk gland (PSG) and consists of three main protein components: heavy chain fibroin (H-fibroin; about 350 kDa), light chain fibroin (L-fibroin; 26 kDa) and fibrohexamerin (p25; about 30 kDa) proteins with a molar ratio of 6:6:1 [1]. It was presumed that these three components in the silk of Lepidopteran have been conserved over 150 million years, although the fibroin of *Saturnidae* species was secreted as dimer of H-chain [2]. H-chain and L-chain are linked by a single disulfide bond between Cys-172 of L-chain and Cys-c20 (twentieth residue from the C terminus) of H-chain [3]. It was suggested that in *Lepidoptera* the disulfide linkage of H-fibroin and L-fibroin is not an absolute requirement for secretion of fibroin [1]. But the H-L linkage is essential for the secretion of a vast amount of fibroin, because evidence showed that fibroin is retained in endoplasmic reticulum in the absence of disulfide linkage between the H-and L-chains [4]. P25 is a glycoprotein containing Asn-linked oligosaccharide chains and is associated with the H-L complex by noncovalent interactions, i.e. mainly by hydrophobic interactions with the H-chain moiety [5].

Special attention has been focused on the *Trichoptera* silk for decades due to its stable properties even under long exposure to water. Most caddisfly (*trichoptera*) spin a fine silk-catching net that is anchored to a substrate in fresh water habitats [6,7]. Tensile strain research has shown that the net silk of the caddisfly is a group III silk, with high extensibility and low breaking stress [8]. The physical properties of the silk mainly depend on the molecular design of the proteins which constitute the silk filament. The larvae of *S. marmorata* spin hiding tubes and catching nets (Fig. 1).
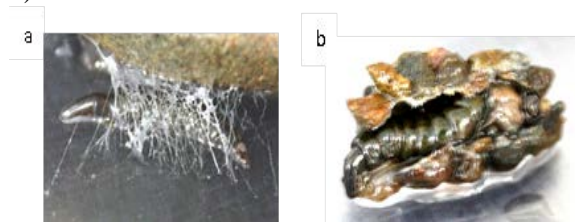

Fig. 1. A catching net (a) and hiding retreat (b) spun by the larva of *S. marmorata*

In a previous study, two filamentous constituents in the caddisfly *S. marmorata* were identified which termed the heavy chain fibroin (H-fibroin) and light chain fibroin (L-fibroin) [9]. Both proteins have counterparts in *lepidoptera*. The H-fibroin of *S. marmorata* has a high molecular weight of >400 kDa and is composed of four blocks (SA, SB, SC and SD) arranged in an order. Each

block is distinguished by unique motifs such as the SXSXSX(SX), GPXG(X)$_{1-3}$ or the triplet GGX sequence. The 24 kDa L-fibroin is similar to its counterpart found in lepidopteran silk. Characteristics found to be similar include molecular weight, charged residues and hydrophobicity, and presumably Cys-links to the H-fibroin to form the H/L-fibroin dimer in the lumen of the silk gland. The homologues of H-fibroin and L-fibroin have also been reported in other caddisfly species [10-11]. A 37 kDa Net forming protein (Nf-1) from one *Hydropsyche* species was assumed to be an essential component of the silk filament [12].

Both the proteins extracted from silk gland and the silk screen of *S. marmorata* were analyzed through SDS-PAGE. Unexpectedly, the results showed that a 16 kDa protein, rather than H-fibroin or L-fibroin, is the most abundant constituent in the lumen or fiber. Identification of the primary sequence of this 16 kDa protein would further contribute to our understanding of the caddisfly silk. In the present study, the protein was cloned and named Smsp-12k. The primary sequence characteristics of Smsp-12k suggest that this protein is an important component of *S. marmorata* silk.

EXPERIMENTAL

Insect care and sample preparation

Fully grown larvae of *S. marmorata* (*Annulipalpia* suborder, *stenopsychidae* family) were gathered from under the stones of the Chikuma River shallow area, Ueda, Japan. For most collected larvae, their silk glands were dissected immediately for total RNA isolation and lumen proteins collection. The freshly dissected silk glands were ruptured in cold distilled water (60 μl per pair of glands), incubated overnight at 4 °C and the luminal proteins that are released from the glands were collected for protein analysis. The remaining larvae were cultivated in a fish jar at room temperature to allow the *S. marmorata* to produce nests. Silk fiber proteins were extracted in 8 M urea and heated for 12 min in a water bath.

Silk protein analysis and cDNA library construction

The lumen proteins of silk glands and fibers were dissolved in a buffer solution containing 2% SDS and 5% β-mercaptoethanol. Denatured electrophoresis was performed by using an 8% polyacrylamide gel under reducing conditions. Part of the gels were stained with Coomassie brilliant blue R-250, Gel Code Glycoprotein Staining Kit (Pierce Biotechnology, Inc., USA), the other were

electronically transferred onto a PVDF membrane (polyvinyl fluoride) for the purpose of protein sequencing. The steps of RNA isolation and cDNA library construction were based on the method described by Wang *et al.* (2010) [9].

Northern blotting

About 6 μg of the total RNA were collected from the silk glands of 20 insects. By utilizing the standard procedures of the DIG nucleic acid detection kit (Boehringer Mannheim), total RNA and RNA markers were electrophoresed on a 1% agarose gel (1× MOPS, 0.66 M formaldehyde) and subsequently blotted, as described by Wang *et al.,* (2010) [9]. The forward primer Sm12-FW: 5'-GCGTCAGTTGGGAACAT-3' (corresponding to the Smsp-12k nucleotides 109 to 126) and the reverse primer Sm12-RV: 5'-TCGCACTGTGACT AGCTGA-3' (corresponding to the Smsp-12k nucleotides 330 to 349) were used to amplify the Smsp-12k probe.

RESULTS AND DISCUSSION

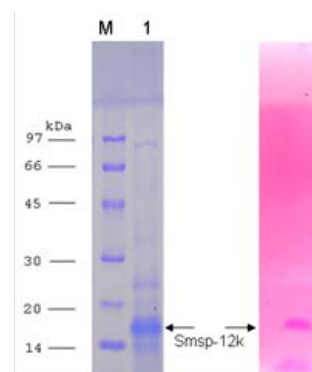The 16 kDa protein separated by SDS-PAGE showed the strongest band (Fig. 2).

Fig. 2. Silk proteins of *S. marmorata* separated by SDS-PAGE from the silk fibers used to construct webs for food collection (lane 1) and from dope collected from the silk gland lumen (lane 3). Lane 2 shows the molecular mass standards (Bio-Rad) and the numbers on the left represent the molecular masses of the protein bands. The protein band at ~16 kDa (indicated by an arrow) was N-terminally sequenced and corresponds to the mature sequence of Smsp-12k.

According to sequencing results, the 11 amino acids of its N-terminus were read as HVGGYWPXGXG, in which the X amino acid was unidentified. An EST library was constructed from the silk glands of the final instar larvae of *S. marmorata*. Using the EST library, a gene encoding a protein with an N-terminal sequence of HVGGYWPXGXG was identified. Of the 260 ESTs analyzed, 18 fell into one cluster which was represented by the clone TBS2D11. TBS1A02

clone displayed a complete open reading frame (ORF) by sequence analyzing. Residues 22-32 of the ORF had the sequence HVGGYWPVGRG, which closely matched the N-terminal sequencing result for the unknown 16 kDa protein. Furthermore, the molecular weight of the protein deduced from TBS2D11 was approximately14 kDa, and the first 20 residues were predicted to be a signal peptide (Fig. 2). Consequently, taking into account the signal peptide, the gene from TBS2D11 was coded for a 12 kDa mature protein. The similar molecular weight and matching sequence revealed that the 16 kDa protein was encoded by the gene present in the TBS2D11 clone. The gene was named Smsp-12k for the gene encoded a 12 kDa silk protein of *S. marmorata*. However, the molecular weight of Smsp-12k observed in the SDS-PAGE analysis was larger than that determined from the gene sequence. Therefore, Smsp-12k may be a glycosylated protein. The sugar moiety of Smsp-12k was proved to be a glycosylated protein by using a glycoprotein staining kit (Fig. 2).

Such glycosylation has been found in particular *Chironmous* (midge) silk proteins which are also secreted underwater [13,14]. Northern blot analysis revealed that Smsp-12k is expressed specifically in the silk gland (Fig. 3).
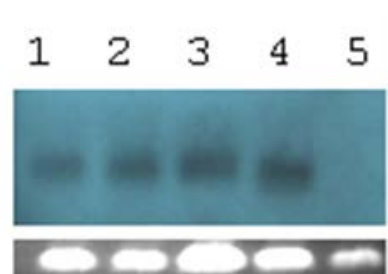
Fig. 3. Identification of Smsp-12k mRNAs on a Northern blot of total RNA (5 µg) prepared from the MSG-1, MSG-2, MSG-3 and PSG sections and the whole larva that were removed from the silk glands (lanes 1, 2, 3, 4 and 5, respectively). RNA was fractioned by electrophoresis and blotted onto Hybond N+ membranes (Amersham Bioscience). The probes were amplified from the appropriate cDNA clone (TBS2D11) using the special primers Sm12-FW and Sm12-RV, and isolated with a QIAquick gel extraction kit. Probes were labeled with the DIG-HIGH-primer reagent. As an internal control, ribosomal RNA was stained with ethidium bromide as presented at the bottom of the photo.

The Smsp-12k gene had an ORF of 396 base-pairs and was predicted to translate to a premature protein of 132 residues. The sequence of Smsp-12k is shown in Figure 3. Amino acid analysis shows that, like most silk proteins, Gly (29.7%) is the predominant amino acid present in the sequence. Trp (18.7%) and Ser (13.2%), unexpectedly, were the second and third most abundant amino acid, respectively. The aromatic residue Trp was an energy rich, probably essential amino acid for insects [15]. But the residue could be supplied by the larva's main food resource, such as algae which contain energy rich amino acids (for example Arg, Leu, His and Trp). Comparison of the Smsp-12k and H-fibroin protein sequences showed that both sequences contained the same motifs (Fig. 4).

Fig. 4. Comparison of the primary sequences of (A) Smsp-12k with (B) the SA1, SA2 and SA3 blocks from the H-fibroin of *S. marmorata*. The core region of Smsp-12k is loosely divided into three repeats based on the alignments of the motifs. The first 21 residues (italics) were proved to be a signal peptide. Two major motifs SXSXSXSX (highlighted in light gray) and GGX (highlighted in heavy gray) were conserved in Smsp-12k and H-fibroin. The cysteines in Smsp-12k which likely form intermolecular or intramolecular disulfide bonds are printed in bold.

Four blocks (SA, SB, SC and SD), tandemly repeated many times, represent the large repetitive regions of *S. marmorata* H-fibroin. The three degenerate SA blocks SA1, SA2 and SA3 which are located at the N-terminus of H-fibroin contain motifs such as SXSXSXSXE and GGX which are motifs present in Smsp-12k. The Ser-rich motifs $(SX)n$ are likely to form a β-sheet and three-dimensional crystallites that reinforce the silk filaments, whereas the GGX triplet provides a stable spiral conformation conferring elasticity to the protein polymer [16-18]. However, DNA analysis revealed that codon bias for the abundant amino acids in Smsp-12k and the three degenerate SA blocks in H-fibroin were different (Table 1), indicating that the genes of Smsp-12k and H-fibroin were not evolutionary related. The research about caddisfly silk gene was very limited. However, the rapid development of science and technology as well as the discovery of caddisfly silk applications has enhanced our understanding of silk protein and its properties.

Yonemura *et al.* (2006) [10] firstly reported two important silk fibroins from Czech caddisfly silk,

Table 1: Codon bias for the three most abundant amino acids in Smap-12k and the SA$_1$, SA$_2$ and SA$_3$ blocks from the H-fibroin of *S. marmorata**

	Smsp-12k		SA$_1$ + SA$_2$ + SA$_3$	
	Occurrence (%)	Codon (%)	Occurrence (%)	Codon (%)
Gly	29.7%	gga/40.8% ggc/22.2% ggg/3.7% ggt/33.3%	33.3%	gga/63.3% ggc/6.7% ggt/30%
Ser	13.2%	agc/25% agt/50% tca/8.3% tcg/8.3% tct/8.3%	14.4%	agc/23.1% agt/30.6% tca/23.1% tcc/15.4% tct/7.7%
Pro	4.4%	cca/50% cct/50%	8.9%	cca/100%

*The three blocks of SA$_1$, SA$_2$ and SA$_3$ are regarded as a whole in this analysis and their sequences are presented in Fig.1.

namely caddisfly fibroin heavy chain (Fib-H), a heavy chain protein with a molecular weight greater than 300 kDa, and caddisfly fibroin light chain (Fib-L), a light chain protein with a molecular weight about 25 kDa. As the main components of caddisfly silk, both protein molecules are homologous proteins of fibroin protein of *Bombyx mori* [11]. Nevertheless, the silkworm protein P25 and sericin homologous protein of the caddisfly silk have not been found. For the caddisfly silk protein with small molecular weight, only three novel silk fiber components were determined, in which two of them are active enzyme proteins in the silk, and another is a small molecule structural protein. The two enzyme proteins, which distributed in silk fibroin and peripheral layers of sticky protein, are associated with the cohesive function of the caddisfly silk [19]. The structural protein is a kind of protein rich in proline, similar to the muscle group (titin) PEVK in the field of protein structure, and is specifically distributed in the fibroin layer [19]. All these small molecular weight proteins were identified through the silk gland transcriptome and proteomics; however, their concentrations in the caddisfly silk are very low. In the analysis of SDS-PAGE of caddisfly silk, we found that the amount of Smsp-12 k protein is richer than the light chain protein, after the caddis heavy chain protein, demonstrating the importance of this protein.

The expression of Smsp-12K varied seasonally. It tends to be higher in summer than in winter, suggesting that the protein plays more critical roles in summer. As the caddisfly larvae are more active and spin more silk fibers in summer, it suggests that efficient silk production may be related to the Smsp-12K.

Compared with the silkworm silk (*Bombyx mori*) or spider silk (*Araneida*), the caddisfly silk has many unique properties. Keeping high viscosity in torrent water is the most remarkable feature of caddisfly silk [20-22]. Apart from that, caddisfly silk has excellent physical and mechanical properties. Though caddisfly silk is soft, it remains with high tensile strength and breaking elongation in the water. The fracture strength of some caddisfly silk species can be five times that of the steel. Its breaking elongation is 150% - 200%, which is much higher compared to the silkworm silk [23-25]. Caddisfly silk also has the feature of high-temperature resistance and heavy metal ions adsorption. The maximum decomposition temperature of caddisfly silk is 242 °C, which is higher than that of the silkworm silk (220 °C) and of most spider silk (230 °C) [24]. The highly efficient adsorption feature of caddisfly silk on heavy metal ions, especially Cd, Pb, and Zn, has been confirmed several years ago [26]. In addition to the above-mentioned properties, the caddisfly silk has considerable antibacterial activity and cell growth promotion. After the sterilization process (121°C, 115 kPa, 20 min), the antibacterial property of caddisfly silk was maintained without affecting its physical properties [24].

It is generally believed that the Fib-H protein is the decisive protein which determines the specific properties of the silk [25, 27]. There is a high homology of the N and C terminals of Fib-H protein between caddisfly and *Bombyx mori*, but their sequence of the repeat region of the silk varied.

The repeat regions of Fib-H protein were connected with four blocks, SA, SB, SC and SD. species. Each repeat consists of at least one (pSX)n motif (pS = phosphoserine, X = arginine or aliphatic amino acid, n =2–6).

The unique structure of SA repeats is believed to be closely related to the properties of silk. It contains two (pSX)4 motifs and 11 residues in between of the two motifs. This is easy to form β-sheet structure [20]. It is believed that the structure forms the molecular basis of the featured mechanical property of the silk in water.

A large number of SA-like structures was found in Smsp-12k. We speculate that the serines in the SA unit were also highly phosphorylated, and form complexes with metal ions such as Ca^{2+} and Mg^{2+}. Together with Fib-H, Smsp-12k plays a key role in the excellent performance of the caddisfly silk.

As observed for H-fibroin, hydrophilicity also prevailed in Smsp-12k (Fig. 5). Smsp-12k most likely forms intermolecular disulfide bonds through the cysteines present in the sequence and such features of Smsp-12k provide protein stability and

insolubility in an aqueous environment. The H-fibroin and L-fibroin, examined in *S. marmorata* have additional cysteines in contrast to the counterpart proteins present in *Lepidoptera* [1, 10].
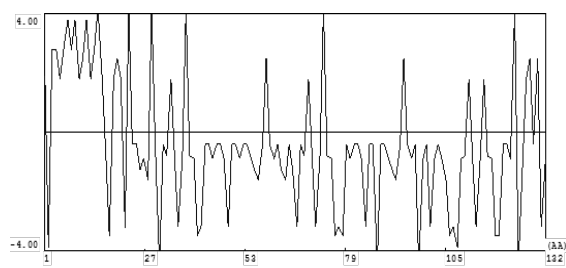

Fig. 5. Kyte-Doolittle hydropathy plots for the determined amino acid sequence of Smsp-12k. The scale bar depicts the number of amino acid residues. The numbers on the axis above the plots indicate amino acid position. The residues above the abscissa indicate hydrophobicity, while those below the abscissa indicate hydrophilicity. Smsp-12k is largely hydrophobic and the total average hydropathicity value is 0.44.

It is generally accepted that the order *Lepidoptera* and its sister order *Trichoptera* diverged from the common ancestor *Amphiesmenoptera* and it was presumed that the polymer components of H-fibroin, L-fibroin and p25 have been conserved over 150 million years in the silk of *Lepidoptera* [2], however, the homologue p25 was not found by studying the filament of caddisfly suborder of *H. angustipennis* and *L. decipiens* [10]. In *S. marmorata*, the homologue of p25 also was not found; this confirmed the suggestion that the lack of p25 is a general feature of *Trichoptera* [10]. On the contrary, Smsp-12k homologue was found in all reported suborders of caddisfly species, and was a major component in their spinning silk. It was hypothesized that the net-spinning caddisfly produce silk-like protein and adhesive protein simultaneously [10]. But no adhesive protein was reported to date.

Considering the glycosylated property of Smsp-12k and its high expressing, we infer that Smsp-12k may be playing an important role in making caddisfly silk sticky underwater. Consequently, Smsp-12k most likely links with the H-fibroin or L-fibroin by formation of disulfide bridges to form an insoluble filament polymer in the lumen of *S. marmorata* silk glands.

CONCLUSION

In summary, data in this study revealed that Smsp-12k is one of the most abundant proteins in the silk of *S. marmorata*. The repeat sequence regions of this protein are mainly composed of two motifs ((SX)n and GGX) which are also present in the H-fibroin of *S. marmorata*.

The (SX)n motif is the only sequence that has the potential to form a crystalline structure in the H-fibroin, raising the intensity of the silk. The combination of the (SX)n and GGX motifs within the Smsp-12k sequence contribute significantly to the physical properties of the *S. marmorata* silk.

REFERENCES

1. S. Inoue, K. Tanaka, F. Arisaka, S. Kimura, K. Ohtomo, S. Mizuno, *J. Biol. Chem.*, **275**, 40517 (2000).
2. N. Yonemura, F. Sehnal, *J. Mol. EVol.,* **63**, 42 (2006).
3. K. Tanaka, N. Kajiyama, K. Ishikura, S. Waga, A. Kikuchi, K. Ohtomo, T. Takagi, S. Mizuno, *Biochim. Biophys. Acta*, **1432**, 92 (1999).
4. M.L. Casem, L.P. Tran, A.M. Moore, *Tissue Cell.*, **34**, 427 (2002).
5. K. Mori, K. Tanaka, Y. Kikuchi, M. Waga, S. Waga, S. Mizuno, *J. Mol. Biol.*, **251**, 217 (1995).
6. P.S. Giller, B. Malmqvist, *The biology of rivers and streams*, Oxford University Press, 119, 1998.
7. R.W. Holzenthal, R.J. Blahnik, A.P. Prather, *Zootaxa*, **1668**, 639 (2007).
8. S.A. Brown, D.R. Graeme, H. Stuart, *J. N. Am. Benthol. Soc.*, **23**, 771 (2004).
9. Y.J. Wang, K. Sanai, H.X. Wen, T.F. Zhao, M. Nakagaki, *Mol. Biol. Rep.*, **37**, 2885 (2010).
10. N. Yonemura, F. Sehnal, K. Mita, T. Tamura, *Biomacromolecules*, **7**, 3370 (2006).
11. N. Yonemura, T. Tamura, K. Mita, F. Sehnal, *J. Mov. Evol.*, **68**, 641 (2009).
12. J.H. Eum, S.M. Yoe, Y.R. Seo, S.W. Kang, S.S. Han, *Insect. Biochem. Mol. Biol.*, **35**, 435 (2005).
13. S.E. Wellman, S.T. Case, *J. Biol. Chem.*, **264**, 10978 (1989).
14. S.V. Smith, J.J. Correia, S.T .Case, *Protein Sci.*, **4**, 945 (1995).
15. R. Fedic, M. Zurovec, F.J. Sehnal, *J. Biol. Chem.*, **278**, 35255 (2003).
16. E. Bini, D.P. Knight, D.L. Kaplan, *J. Mol. Biol.*, **335**, 27 (2004).
17. J. Ashida, K. Ohgo, K. Komatsu, A .Kubota, T Asakura, *J. Biomol. NMR.*, **25**, 91 (2003).
18. R. Fedic, M. Zurovec, F. Sehnal, *J. Insect Biotech. Sericol.*, **71**, 1 (2002).

19. N. Ashton, R. Stewart, D. Ferré, A. Amaré, G. Prendergast, E. Ziff, S. Burley, *Soft Matter*, **11**, 1667 (2015).
20. R. Stewart, C. Wang, *Biomacromolecules*, **11**, 969 (2010).
21. C. Wang, N. Ashton, R. Weiss, R. Stewart, *Insect Biochem. Mol. Biol.*, **54**, 69 (2014).
22. C. Wang, H. Pan, G. Weerasekare, R. Stewart, *Journal of The Royal Society Interface*, **12**, 112 (2015).
23. S. Brown, G. Ruxton, S. Humphries, *J.N. Am. Benthol.Soc.*, **23**, 771 (2004).
24. M. Tszydel, A. Zabłotni, D. Wojciechowska, *J. Mech. Behav. Biomed. Mater.*, **45**, 142 (2015).
25. L. Albertson, M. Daniels, *Freshwater Biology*, **61**, 670 (2016).
26. M. Tsukada, M.M. Khan, E. Inoue, G. Kimura, J.Y. Hun, M. Mishima, K. Hirabayashi, *Int. J. Biol. Macromol.*, **46**, 54 (2010).
27. Y. Wang, K. Sanai, M. Nakagaki, *Adv. Mater. Res.*, **79**, 1631 (2009).

Effect of maize irrigation on water use efficiency in the Semiarid region of Northeast China

H.X. Zhao, S.F. Bian*, L.C. Wang, X.Q. Fang, G.B. Tan, L.H. Zhang, W.P. Yan,
N. Sun, X.M. Meng

Jilin Academy of Agricultural Sciences, Changchun 130033, China

In order to popularize and apply technology of the corn regulated deficit irrigation in Northeast Semi-arid Region and achieve efficient use of water resources, the test was carried out to deal with different degrees of water deficit processing of corn in different growth stage, and studied the effects of Regulated Deficit Irrigation on maize's water consumption, yield and water use efficiency (WUE). The results showed that: in terms of the regulated deficit irrigation of each growth stage, the heavy drought will affect the yield greatly during tasseling periods, while the water deficit had little effect on the yield in seedling stage. It showed a downward opening parabola relationship between the yield and water consumption, and if the maize is short of water in the jointing stage, the yield would be significantly decreased. It needs to be dealt with water deficit of maize appropriately, and the best irrigation treatment mode is the moderate water deficit in the seedling stage (the upper limit of water control was 60%).

Keywords: Regulated deficit irrigation, Water saving irrigation, Water use efficiency, Semiarid area of Northeast China

INTRODUCTION

A serious state of imbalance, the efficiency of water use is not high, so that the distribution of water resources and the distribution of productive forces are not matched. There are large reserves of water resources in our country, but due to the large population base, so there is a relatively small amount in per capita use of water, China is one of the world's 13 water-poor countries [1]. Water is the lifeblood of the agricultural production; it has been the basic norms and ethics in our daily life to save water in production and life. Irrigation water use in the country's total water use can reach 73.4%, it can be said that the water consumption is very large, but the irrigation water use efficiency in agriculture is only about 43% of the developed countries [2]. With the accelerated process of urbanization in China, population and economic prosperity involves food problem of basic necessities of life, the most eye-catching is water use and water saving in agriculture. The drought conditions in recent years force us to take water-saving measures and technology to reduce water loss with the maximum extent and improve water use efficiency.

The irrigation system can improve the water use efficiency without reducing the yield, and it is an effective way to solve the problem of water resources irrigation in agriculture in China, which is in line with the current sustainable development strategy.

Northeast region is the most important commodity grain production base in China[3]. The west of Northeast China has a temperate semi humid continental monsoon climate perennially. Due to the monsoon, and it is often windy and the rain is low in spring, the spring drought often occurs in this region, resulting in people's economic burden, waste people's both energy and money, so it constrains social development and brings great influence on agricultural production to some extent. Maize is an important cereal crop, not only can be taken as health food to human and animal feed with rich nutrient, but also has a high industrial value; its straw and maize ear was processed into fuel, to provide raw materials for further solving the energy problem. It is obvious that maize plays a significant role in the grain crop cultivation and production in the world. In recent years, it has been stimulating the cultivation of maize due to its rising prices, the planting area is increasing year by year. In 2011, China's total production of corn continued to rise, accounting for about 24.5% of the world [4]. Especially in recent years, China has increased support for agriculture, the planting area is gradually expanded in the northeast area, and the yield is increased, so there has been a general uptrend in the yield with promising results. As one of the important factors of maize yield, how to maximize the efficiency of water use is extremely important. It will affect corn yield if the irrigation stage is inappropriate and choice is unreasonable, it will make farmers' harvest years into a bad crop years.

In terms of regulated deficit irrigation and its effects on the quality and physiological indexes of crops, domestic and foreign scholars have carried out a lot of research. The research of relationship between irrigation water and grape growth, yield and wine quality by Intrigliolo[5]. indicated that it does not affect the yield and wine quality under the regulated deficit irrigation conditions. In Liu Xianzhao's study[6] of apple showed that root partition irrigation can effectively improve the water use efficiency and fruit quality. The above studies were focused on the effects of water content in the root zone of the plant or irrigation water on the growth of fruit trees, water use efficiency and fruit yield, quality and so on. Although regulated deficit irrigation technology made a large number of research results in the field of fruit trees, but there are still some problems, first, some of the test results stay in the pot, greenhouse and simulation stage; second, there is a few research of crop, and systematic research is rarer. Especially, there lacks of the study of maize system in the Northeast Semiarid Region, especially in the different stages of fruit development, the different irrigation methods on its water consumption, growth, yield and quality are rarely reported.

In this paper, the effects of water deficit treatment on the growth of maize were obtained through experimental study, so as to select a reasonable crop regulated deficit irrigation growth stage and regulated deficit level. According to the different stages of maize in the black soil region and different regulated deficit irrigation, the water consumption of maize was discussed.

EXPERIMENTAL

Test Conditions

Test area is a comprehensive test base in the west of Jilin Province, its total area is 55 km^2; it has a temperate continental monsoon climate, the annual average temperature is 4.9℃, and frost free period lasts 157 days. The range of average annual rainfall is approximately 400 mm , and June to August is the multiple period of rainfall, it accounts for about 70% of the total rainfall throughout the year. And the multi-year average evaporation is about 796 mm.

The content of nitrogen (N) in soil is 154.4 milligram per kilogram, the content of phosphorus (P$_2$O$_5$) and potassium (K$_2$O) are 40.1 milligram per kilogram and 37.68 milligram per kilogram respectively, the soil pH value is 7.27. The average field water holding rate in the 50cm soil layer is 28.57%, and the soil bulk density is 1.14 gram per cubic centimeter.

Experiments

The pot experiment is used in the test, and variety of maize is Demeiya No. 1, it is carried out in the mobile canopy. The design of the experiment is to set up 16 treatments, and repeat 3 times under the same test condition. Plastic bucket size: the height is 33 cm, and the diameter is 29 cm. Soil needs to be dried, and the soil particles will put into the plastic bucket after the sieve to ensure that the weight of soil in each basin is the same, they are all 15kg. There are 5 grains to be planted in each pot, and keep a full stand of seedlings in the trefoil stage. Using electronic balance to weigh the water content in the basin and record their change. The time to weigh is at 17:00 in the afternoon, and using dosage cup to and water to the standard control until the crop is mature. Through observation and record biological traits of Maize under different water treatment, analyzing the relationship between biological traits and yield of maize under different water treatment and law of water consumption and water use efficiency of Maize under different deficit irrigation.

The test design is based on the growth stage of Maize in the upper limit of different soil moisture, and the maize's growth and development period and yield are studied for the purpose, it will be divided into four growth stages, that is seedling, jointing, tasseling periods and grain filling stage, and there are 4 water level to be designed in each growth stage (to account for the percentage of field water capacity).

Phenological period

Record the growing period of different treatments and the growth situation of each treatment and the control of diseases and insect pests.

Soil moisture

Using the soil drilling method for the determination of drying.

Agronomic traits

①plant height: using meter rule to measure, the starting point of height is from the base of the plant to tassel top; ② the stem diameter: using vernier caliper to measure, the position to be measured is the first section of the above the root of maize plants; ③ root weight: after harvest of maize, removed the root out of the basin, washed them with water, and dried them, then put them into the bag respectively, into oven, drying them at 105℃ for 8 hours, take out to weigh them until the quality does not change, and record the corresponding root weight; ④ the dry weight of aboveground part: after harvest of maize, dry the aboveground part, put it into the bag respectively, then into the oven,

and drying them at 105°Cfor 8 hours, then take out to weigh them until a constant weight, record the corresponding weight of the aboveground part; ⑤ the calculation of water use efficiency of maize: Water utilization efficiency of Maize = yield / water consumption.

Yield

10 ears were selected randomly before harvest of maize from per plot, and test their ear length, bald tip length, ear diameter, ear rows number, grain number, 100 kernel qualities, the yield is the measured results of acquiring harvesting alone and threshing alone.

Statistical analysis method

The test data were analyzed by SPSS22.0, and the 3 repeated values of different treatments was analyzed by the variance. If the difference was significant (P < 0.05), multiple comparisons were performed. The average value of each process and the drawing of the graph are processed by Excel 2007.

RESULTS AND DISCUSSION

The effect of irrigation on plant height
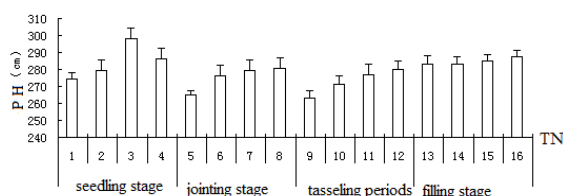
Fig. 1. Plant height in different irrigation levels

It can be seen from the Figure 1, the deficit irrigation in the various growth stages, the measured plant height changes a lot in the seedling stage. The plant height difference is 24.2 cm after deficit irrigation in seedling stage, 15.9 cm in jointing stage, 16.9 cm in tasseling periods, and 4.7 cm in filling stage. The maximum plant height difference reached 35.1 cm in each growing stage of 16 treatments. Except for seedling stage, the plant height showed ladder trend in other growth stages for processing, namely, the height is gradually increasing with the increasing of deficit degree, so it explained that deficit irrigation plays a certain role in promoting the growth stage of the maize in seedling period. In the early stage of seedling, deficient water can promote root growth, and then promote the growth of plant height in the late stage. The plant height of treatment 5 and 9 water deficit degree of 40% in jointing, and tasseling stage was significantly lower than the plant height in other growth stages under the different water deficit treatment (P < 0.05). It is not

suitable for severe deficit in jointing stage and tasseling stage, otherwise it will affect maize normal growth. The growth stage of maize plant is mainly concentrated in the early time, late time is the formation of maize grain, and so during the grain filling period, the deficit irrigation has little effect on plant height. The above chart shows that the plant height after regulated deficit irrigation in filling stage changes a little (P > 0.05). Research shows that water and fertilizer is the main factor affecting the yield of maize, in certain irrigation condition, the yield will be increased with the increase of fertilizer, but reached a certain amount of fertilizer, the yield did not increase or even reduce; also in certain fertilization level, the yield will increase with the increase of irrigation amount, but to achieve a certain amount of irrigation, the yield did not increase or even reduce, thus making reasonable irrigation and fertilization system on maize yield, saving water, improve water and fertilizer utilization rate is very important.
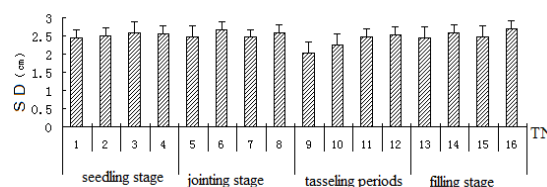
The effect of irrigation on stem diameter

Fig. 2. Stem diameter in different irrigation levels

It can be seen from the Figure 2, after regulated deficit irrigation in the various stages, the measured stem diameter changes a lot in tasseling periods, and it showed a ladder upward trend with the increase of the degree of regulated deficit irrigation. In tasseling stage, the stem diameter of treatment 12 is more 0.5 cm than that of treatment 9, the difference was significant (P < 0.05), while in seedling, jointing stage, filling stage grew respectively 5.7%, 8.9% and 9.8%, the whole stem diameter is about 2.45 cm. It can be seen that regulated deficit irrigation on corn stalk diameter impact is relatively large in tasseling stage. Tasseling stage is the key stage of corn growth, is also the accumulation process of the aboveground part, by straw cannot transport nutrients needed for maize growth by absorbing more water, resulting in straw lack of nutrition and contraction, stem diameter is decreased, and therefore there appeared the phenomenon. So under the suitable soil moisture conditions, the growth of stem diameter contributes to improving the lodging resistance and good foundation for improving the yield of Maize in the late.
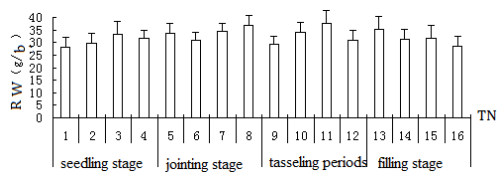
The effect of irrigation on root weight

Fig. 3. Root weight in different irrigation levels

It can be seen from the Figure 3, after water deficit treatment in the seedling stage, the root weight of treatment 11 reached 37.6g per basin, followed by the treatment of 8, the root weight is 36.9 g per basin. Overall, all treatments did not follow the law, and the differences between the treatments were not significant ($P > 0.05$), in treatment at seedling stage, root weight of treatment 3 is the largest, is 33.4 g per pot, the jointing stage is treatment 8, tasseling stage is treatment 11, the filling stage is treatment 13, the average root weight is 35.3 g per pot. Water deficit in seedling, water stress will affect the physiological metabolism. During the seed germination, seed vigor and germination rate will be reduced, resulting in their own material conversion rate being decreased. Maize seedlings will absorb enough growth required nutrients under water stress in order to ensure normal growth and development of roots, its root needs to be extended to more distant, and then form larger absorption area to adapt to the arid environment. During the filling stage, the root system has been basically formed, so the treatment of 13, 14, 15, 16 of the root weight is relatively small.

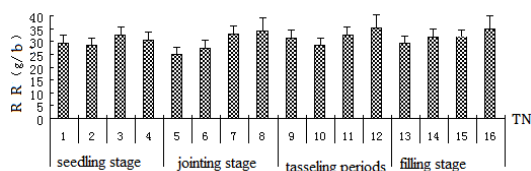*The effects of irrigation on root ratio*

Fig. 4. Root ratio in different irrigation levels

It can be seen from Figure 4, the root ratio changed a little after the water deficit in the seedling stage, the root ratio of treatment 5 after severe water loss in jointing stage was 23.67%, it is significantly higher than that of the treatment for the rest in the jointing stage（P＜0.05）, the root ratio after deficit water treatment in tasseling stage is larger, its maximum of root ratio is 26.9% than that of treatment 11 after moderate water deficit and root cap after deficit water treatment in grain filling stage exhibits that it will be decreased with the decreased water deficit than the overall, because the water supply is adequate, root ratio of treatment 16 is the minimum of 15.25%. In the growth process of maize, a certain degree of water deficit

processing can increase the root ratio of corn plant. To control the assigned amount between the underground part and the aboveground part so that the root system can obtain enough assimilates through their own transformation and inhibit growth of aboveground part and the dry mass increased a little, and the process of maize growth need draw nutrition by root from the soil, use of the internal structure of straw to deliver nutrients to grain, then promote its growth.

The effect of water deficit treatment on water consumption in seedling stage
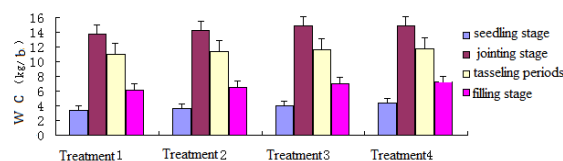

Fig. 5. Water consumption of water deficit treatment in seedling stage

It can be seen from Figure 5, water deficit treatments in seedling, the average water consumption of each treatment in the seedling stage is 3.86kg per basin. As a whole, water consumption of corn seedling has no big difference, but for the late jointing stage, tasseling periods and grain filling stage had little change. After deficient water treatment, the total water consumption of the treatments 1, 3, 4, and 2 were 34.28 kg per basin, 35.78 kg per basin, 37.49 kg per basin, 38.28 kg per basin, respectively. It can be seen from the above chart that water consumption in jointing stage was significantly higher than other stages ($P < 0.05$), followed by tasseling and filling period, and the water consumption in seedling stage was significantly lower than that of other stages ($P < 0.05$), because the seedling stage is the growth stage, the water demand is not so large. A small amount of water on the irrigation and Han Zhanjiang can not only meet the water requirement of crop metabolism, improving the resistance of plants, and because of the characteristics of induced plant compensation of water, the water use efficiency increased significantly, is theoretically consistent.

The effect of water deficit treatment on water consumption in jointing stage
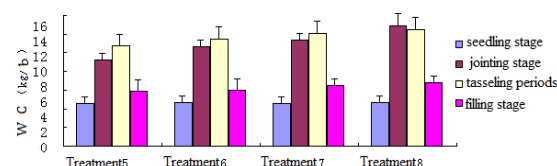

Fig. 6. Water consumption of water deficit treatment in jointing stage

It can be seen from Figure 6, after the water deficit treatment at jointing stage, treatment 8 changes greatly, its water consumption reached the maximum in jointing stage, but water consumption of treatments 5, 6, 7 reached the maximum in tasseling stage, indicating that if the deficit water is serious in jointing stage, it will increase the water consumption in tasseling stage to provide the required amount of water for corn growth in the later stage. The water consumption was small if it has normal irrigation during the seedling stage, and the water consumption treatment 8 is 3.59kg per basin more than treatment 5 in the jointing stage, which was enough to prove that the water requirement of Maize at the jointing stage was large. Water deficit at jointing stage, with the increase of the degree of loss, the amount of water consumption is also an upward trend, so there is a close relationship between the jointing stage and the tasseling stage. In contrast, the water consumption in the grain filling stage showed stable, there is no big difference（P＞0.05）.

The effect of water deficit treatment on water consumption in tasseling periods
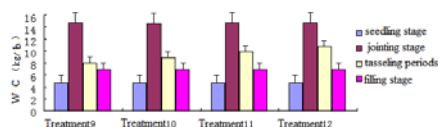

Fig. 7. Water consumption of water deficit treatment in tasseling period

It can be seen from Figure 7, due to normal irrigation treatment in the seedling stage and jointing stage, the water consumption of each treatment changed little. Treatment 9 is to adjust the deficit under 40% of field water capacity, the difference of the water consumption between the jointing stage and tasseling stage can reach the 6.59kg per basin, the minimum difference is 3.95kg per basin, water consumption is significant difference. In the tasseling stage, the water consumption and growth were seriously affected by water deficit treatment. However, the difference of water consumption was not significant when the normal irrigation was resumed at the grain filling stage. The average water consumption between different treatments was 35.55kg per basin. As can be seen, the overall difference of the total water consumption was not significant, but the water consumption difference of the four treatments in the jointing stage and tasseling stage was significant（P＜0.05）.

The effect of water deficit treatment on water consumption in filling stage
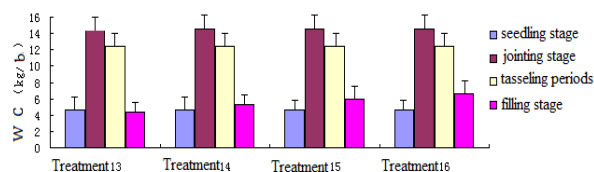

Fig. 8. Water consumption of water deficit treatment in filling stage

It can be seen from Figure 8, due to normal irrigation in seedling, jointing and tasseling stage, little differences are shown in the figure, the overall level is also smooth, so it has not prominent features, and water consumption in jointing stage is still the largest（P＜0.05）. During the filling stage, the water consumption of the treatment 16 is more than 2.16kg per basin to treatment 13. The grain filling stage is formation stage of corn grain, it needs more water to transport sufficient nutrients needed by it, so it is helpful to prevent plant senescence by keeping soil moist state appropriately, also can prolongs the duration of grain filling, improve the degree of filling, and increase grain weight.

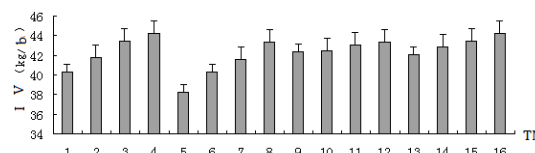*The effect of water deficit treatment on water consumption in filling stage*

Fig. 9. The effect of irrigation volume in different growth stages

As can be seen from Figure 9, the irrigation amount of each treatment during the growth period showed a stepwise rise, the irrigation amount in the seedling stage and the jointing stage had a larger change, but changed slightly in tasseling stage and filling stage. The irrigation amount of treatment 5 is the minimum in jointing stage under degree of 40% field capacity. In its whole growth period of irrigation, the irrigation amount is 38.27kg per basin, it is significantly less than other treatments (P < 0.05), the difference between treatment 5 and 8 is 5.07kg per basin. After regulated deficit treatment in the seedling stage, the difference of irrigation amount between treatment 1 and treatment 4 is 3.98 kg per pot. After regulated deficit treatment in the tasseling stage, irrigation amount difference between treatment 9 and 12 is 1.01 kg per basin. After regulated deficit treatment in the tasseling stage, irrigation amount difference between treatment 13 and 16 is 2.18kg per basin.

After deficient water treatment of maize plants in seedling stage and jointing stage, the water requirement of maize plants changed greatly, which was consistent with the natural growth of the plants.

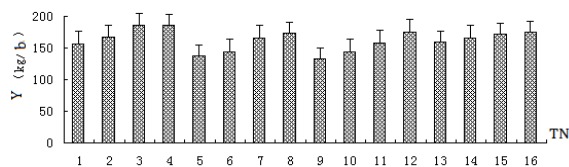*Yield of water deficit treatment in different growth stages*

Fig. 10. Yield of water deficit treatment in different growth stages

The output of each treatment present stepped changes. production of treatment 3 is the largest after deficient water treatment in the seedling stage, its output is 186.45g per basin, increased 29.65g per pot than treatment 1（$P <0.05$）, the yield of treatment 4 was less than 1.1 g per pot to the treatment 3（$P >0.05$）, the yield of treatment 5 and 9 are 13.76 g / pot and 132.2 g / pot respectively, the two treatments had the lowest yield in 16 treatments（$P <0.05$）. The average output of treatments 5, 6, 7, 8 in jointing stage is 15.53 g / pot, The average output of treatments 9, 10, 11, 12 is 152.39 g / pot in tasseling stage, and yield average of treatment 1, 2, 3, 4 in seedling is 173.78 g / pot, yield average of treatment 13, 14, 15, 16 in filling stage is 167.68 g / pot. Based on the above analysis, the water deficit treatment in jointing and tasseling stage will affect the yield greatly. Compared to water deficit treatment and in seedling stage and filling stage, the yield difference is 16 g / pot. According to the above shows, the water deficit treatment in the jointing stage and tasseling stage leads to heavy drought of the corn plant; it will have a serious impact on the grain maturing rate and yield of maize in latter time. The moderate water deficit in maize seedling has significant effect on the yield, so moderate drought in the seedling stage can improve crop yield, severe water deficit in tasseling stage increases the corn ear barren tip length, it will has adverse effects on the final yield of corn. Tan Hua[7] thought that water deficit treatment of corn in tasseling stage will lead to bad effect on maize pollination, and the reduction of the seed rate, and even lead to tasseling difficulties and other issues, which is what people often say "card neck drought". Therefore, it needs sufficient irrigation in the tasseling stage, otherwise it will seriously affect production. Fan [8]believed that due to the reduction of the leaf area in the grain filling period, the daily water consumption is decreased, but due to a longer period of time, the stage of water consumption is still more. Water deficit treatment in filling still can

maintain a high yield, is because the growth stage before the grain filling stage has not been influenced by water deficit.

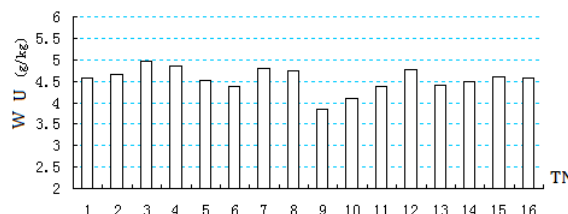*The effect of irrigation level on the water use of Maize*

Fig.11 Water utilization efficiency of water deficit treatment in different growth stages

Table 1. Effect of irrigation level on water use of Maize

Treatment number	Water consumption（kg/basin）	Yield（kg/basin）	WUE (g/kg)
1	34.29±6.14	156.8±12.9	4.57±1.13
2	35.78±6.27	166.5±12.5	4.65±1.52
3	37.49±6.56	186.4±12.3	4.97±1.11
4	38.27±6.12	185.3±13.5	4.84±1.12
5	30.47±6.11	137.6±12.8	4.52±1.25
6	32.77±6.25	143.7±12.6	4.38±1.19
7	34.57±6.68	165.8±12.8	4.80±1.28
8	36.84±6.42	174.2±12.4	4.73±1.14
9	34.32±6.32	132.2±11.2	3.85±0.92
10	34.91±5.21	143.2±12.8	4.09±0.89
11	36.72±5.12	158.4±12.9	4.39±1.19
12	36.82±5.58	175.7±12.5	4.77±1.26
13	36.07±6.56	158.6±12.8	4.40±0.93
14	36.91±6.91	165.3±12.5	4.48±1.42
15	37.47±6.45	172.0±12.7	4.59±1.12
16	38.25±6.25	174.8±12.5	4.57±1.14

It can be seen from Table 1 and Figure 11, the degree of water deficit is 60% of the field water holding capacity in the seedling stage, the maximum of water use efficiency of the treatment 3 is 4.97g per kg per basin, it is significantly higher than other treatments (P < 0.05). The average value of water utilization efficiency of treatment 1, 2, 3, and 4 after water deficit in seedling is 4.75 g / (kg / basin), it is the maximum value for regulated deficit in four stages, water use efficiency is the highest, so it shows that water deficit treatment in the seedling stage can improve water use efficiency. The water use efficiency in jointing period is 460 g / (kg / basin), water utilization efficiency of treatment 5, 6, 7, 8 float up and down at this value, changes is obvious in tasseling stage, the difference between treatment 9 and 12 is 0.92g/ (kg / basin)（P＜0.05）and water use efficiency in this growth stages changes a lot after regulated deficit irrigation. The regulated deficit degree in tasseling stage is 40% of field water holding capacity, water use efficiency of treatment 9, is 3.85 g / (kg / basin) in minimum, regulated deficit in the period will make soil moisture supply relatively insufficient, and maize plant growth will be affected, so it cannot manufacture organic matter and transport smoothly to the grain plant, it is easily to lead reduction. the water use efficiency value of treatment 13, 14, 15,

16 in filling stage shows smooth in the overall, they have not much difference, water use efficiency value float up and down in 4.51 g/ (kg / basin), change a little. Comprehensively, regulated deficit in seedling stage and jointing stage will have high water use efficiency while regulated water deficit in tasseling stage, its water use efficiency was affected most, and regulated water deficit in filling stage, its water use efficiency was affected least, it is stable.

It can be seen from Figure 12: it showed a downward opening parabola relationship between the yield and water consumption, this is consistent with the conclusion of Kang S Z [9]; when water consumption is 134.0kg / basin, yield is 465.62g / basin, the parabolic value reached the maximum, namely the water utilization efficiency is 3.47g/kg at this moment. When the water consumption is lower than 134kg/ basin, the yield will be decreased with the decrease of water consumption, and the water consumption is higher than 134 kg/ basin, the yield will be increased with the decrease of water consumption. This shows that excessive water deficit will lead to a decline in maize production; moderate water deficit can not only reduce the consumption of water, but also improve the yield of corn, and achieve the effect that save water and increase grain. Corn is a dry crop, the demand for water is not very large, only in the individual growth stage, and water requirement is large. The experimental study showed that moderate water deficit in seedling stage was favorable to the growth of root system and the formation of grain in the later stage. This is the reason why farmers often restrain the growth of seedlings (for root development) in the seedling stage.
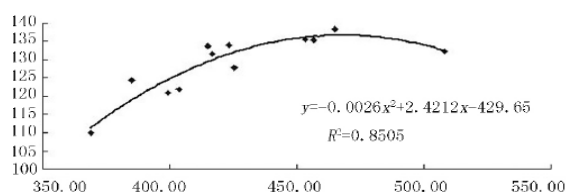

Fig. 12: Relationship between maize yield and water consumption

Through the regression analysis of water consumption and yield in each growth stage, the relationship between the two is drawn, and obtains the corresponding relation type:
$y = -0.0026x^2 + 2.4212x429.65$ ($R^2 = 0.8505$)

CONCLUSION

This experiment carried out a pot experiment of maize regulated deficit irrigation, which is aimed at the problem of lack of water resources and the lower crop yield and water use efficiency in the semiarid region of Northeast China. Experiments were used to study the biological characteristics, water consumption and water use efficiency of

maize under different regulated deficit period and different water deficit degree. The preliminary results of the study are summarized as follows:

1. After water deficit in each growth stage has normal irrigation, the plant height increase higher under the high level of regulated deficit treatment than under the low level of the regulated deficit treatment, but the effect of regulated deficit treatment in grain filling stage on the plant height was not high.

2. The difference of the water requirement of maize is relatively large in different growth stages.

3. Water deficit in the jointing stage and tasseling stage has great effect on the yield of maize, the yield was decreased obviously.

4. Sufficient irrigation increases water consumption of plant growth, but inhibits the growth of the dry matter on aboveground, and waste water resources, regulated deficit treatment in seedling can increase water use efficiency of maize.

REFERENCES

1. M.W.R, China water resources bulletin. Beijing: Ministry of Water Resources of China, (2005)
2. X.N. Zhang, Q.P. Guo, X.X. Shen, S.W. Yu, Y. Qiu, *Journal of Integretive Agriculture*, **14**, 2365 (2015).
3. X. Chen, F. Chen , Y. Chen , Q. Gao, L. Yang, F. Zhang, G. Mi, *Glob Chang Biology*, **19**, 923 (2013).
4. H.L. Feng, *China rural water and hydropower*, **2**, 10 (2016).
5. D.S. Intrigliolo, J. R. Castel, *Agricultural Water Management*, **96**, 282 (2009).
6. X.Z. Liu, Q. Su, H.Y. Sun, *Acta Ecologica Sinica*, **30**, 4881 (2010).
7. H.Tan, D.B. Zheng, C.L. Zou, X.X. Wei, A.H. Huang, Y.S. Wu. W.P. Jiang, H. Wei, R.X. Mo, K.J. Huang, *Agricultual Research in the Arid Areas*, **33**, 18 (2015).
8. Y.J. Fan, Z.Y. Lu, D.L. Tian, K.Z. Guo, B. Xu, J.J. Li, *Agricultual Research in the Arid Areas*, **33**, 123 (2015).
9. S.Z. Kang, T.S. Du, J.S. Sun, R.S. Ding, *Shuili Xuebao*, **38**, 661 (2007).

Optimization of pepsin-assisted extraction of polysaccharides from *Cynomorium songaricum*

H. Fan[1,2], Y. Su[1], L. Wang[1], G. Chen[1,*]

[1] School of Life Sciences, The Good Agriculture Practice Engineering Technology Research Center of Chinese and Mongolian Medicine, Inner Mongolia University, Hohhot, China
[2] College of Chemistry and Chemical Engineering, Inner Mongolia University, Hohhot, China

In this paper, the pepsin-assisted extraction of *Cynomorium songaricum* polysaccharides was investigated. The study comprised a single factor experiment design and an optimization response surface methodology using Box-Behnken design providing the optimal extraction conditions as pH of 1.5, liquid-to-solid ratio of 108:1, and proteolysis temperature of 40 °C. Under these conditions, the highest *C. songaricum* polysaccharides yield reached 23.63 ± 0.21%, which represented an increase of 233% compared to the conventional hot-water extraction. Their structures were determined *via* chemical analysis, ultraviolet spectra, Fourier-transform infrared spectra, scanning electron microscopy, and atomic force microscopy. These findings may provide a theoretical basis for further systematic research and utilization of *C. songaricum* polysaccharides resources.

Key words: Pepsin, Extraction, *Cynomorium songaricum*, Polysaccharide

INTRODUCTION

Cynomorium songaricum, is a wild perennial plant mainly parasitizing on the roots of the genera *Nitraria* which widely is distributed across the deserts of Northwestern China, Central Asia, Iran, and Mongolia [1]. In traditional Chinese medicine, *C. songaricum* is generally prescribed for reinforcing the immune system, treating lumbar weakness and enhancing sexual ability [2]. Modern chemical research revealed that polysaccharides from *C. songaricum* displayed a range of biological effects, including anti-fatigue, anti-oxidation, and hypoglycemic activity [3-5], rendering it an ideal candidate for treating senile diseases without side effects [2]. Because there were only few reports [5-7] during last decades, the development of efficient extraction and purification methods is essential to meet the increasing demand for high-quality and multi-functional *C. songaricum* polysaccharides (CSPs).

The main factor affecting the extraction yield of polysaccharides is the extraction process used. Many technologies have been discovered, including hot water extraction (HWE), microwave-assisted extraction, and bio-enzymatic method [7-9]. Among them, enzyme-assisted extraction attracted much attention due to its high efficiency and environmental compatibility overcoming the shortcomings of conventional procedures [10].

Up to now, extraction of polysaccharides from *C. songaricum* using pepsin-assisted extraction (PAE) technology has not been reported. The objective of this study was to investigate the main variables and optimize the PAE conditions using single factor experimental design and Box-Behnken design (BBD) [11,12]. Moreover, the characteristics of CSPs-PAE and CSPs-HWE were determined by chemical composition analysis, UV, FT-IR, SEM and AFM analysis. These data will lay a foundation for future pharmacological and biochemical studies of CSPs.

EXPERIMENTAL

Materials and chemicals

Fresh *C. songaricum* stems were collected in a marginal zone of Hobq Desert, Inner Mongolia, China. The voucher specimen was kept in the Herbarium of Inner Mongolia University. Pepsin (≥1200.0 U/g) was obtained from Sinopharm Chemical Reagent Co., Ltd. All other reagents were of analytical grade.

PAE procedure

C. songaricum powder (100 g) was infused in triplicate by dichloromethane:methanol (2:1) at room temperature for 12 h to remove lipids and colored materials. After the defatted powder was hydrolyzed in a thermostatic oscillator vibrator (Electron 420, Thermo Co., USA) using pepsin at certain conditions, the sample was rapidly heated in boiling water and refluxed for a designated time. The mixture was centrifuged, and the supernatant was deproteinated using the Sevag reagent. Then, it was concentrated, precipitated and lyophilized to obtain

crude polysaccharides, labelled as CSPs-PAE. The CSPs yield (%) resulting from the extraction was calculated using the equation below:

$$CSPs\ yield(\%) = \frac{weight\ of\ dried\ crude\ CSPs(g)}{weight\ of\ samples(g)} \times 100\% \qquad (1)$$

Hot water extraction (HWE) of CSPs was performed as a control experiment.

Single factor experimental design

The ranges of proteolysis pH (pH), proteolysis temperature (PTe), proteolysis time (PTi), extraction time (ET), pepsin concentration (PC) and liquid-to-solid ratio (LS) were studied using a single factor design. The levels of each factor are given in Table 1. One factor was changed with the other factors remaining constant in each experiment. The effect of each factor was evaluated by the resulting CSPs yield.

Table 1. The levels of each factor used in the single factor experimental design.

Level	Factors					
	pH	PTe(^{o}C)	PTi(h)	ET(min)	PC(%)	LS(V/w)
1	1.0	30	3	10	0.5	30:1
2	1.5	35	4	30	1.0	50:1
3	2.0	40	5	60	1.5	70:1
4	2.5	45	6	90	2.5	100:1
5	3.0	50	7	120	4.0	140:1

Box-Behnken design (BBD)

Based on the preliminary study, a three-factor and three-level BBD (Design-Expert software, version 8.0.6.1, USA) was used to determine the optimal conditions for PAE of CSPs. The levels of each factor and the design matrix are given in Table 2. The extraction yield was taken as the response. The low, middle, and high levels of each variable were coded as -1, 0, and 1, respectively.

Chemical composition analysis

The polysaccharide content of the CSPs was evaluated using the phenol-sulfuric acid method with glucose as the standard [13]. Protein content was measured by the Bradford method [14] with bovine serum albumin as the standard.

Ultraviolet spectra (UV) and Fourier-transform infrared spectra (FT-IR)

The samples (CSPs-PAE and CSPs-HWE) were dissolved and diluted to a proper concentration and scanned from 200 to 400 nm with the UV-vis spectrophotometer (TU-1901, Purkinje General Instrument, China). The FT-IR spectrum was detected on a Nicolet 6700 spectrometer (Thermo

Co., USA) using KBr disk method in the frequency range of 400 - 4000 cm^{-1} [15].

Atomic force microscopy analysis (AFM)

The polysaccharides were dissolved in deionized water at 100 μg/mL. 10 μL of the solution was deposited onto a freshly cleaved mica surface and allowed to dry at room temperature. Meanwhile, a filter paper was placed at the end of the mica to remove excessive solution [16]. Atomic force microscopy (AFM) was performed in intermittent contact mode with a scanning probe microscope (CSPM5500, Benyuan Nano Co., China).

Scanning electron microscopy analysis (SEM)

The sample particles were coated with a thin layer of gold under reduced pressure. The shape and surface characteristics were determined using field-emission SEM (FESEM, S-4800, Hitachi, Japan).

RESULTS AND DISCUSSION

Single factor analysis of PAE

Plant cell wall consists of a rigid skeleton of cellulose and glycoprotein. Pepsin treatment was able to cleave specifically at the telopeptide region of glycoprotein from the cell wall [17]. The effects of several parameters were proven to be critical to the yield of the PAE procedure, such as pepsin activity, extraction time and liquid-to-solid ratio. Hence, we designed a five-level single factor analysis to assess their optimum scope and the results are summarized in Figure 1.
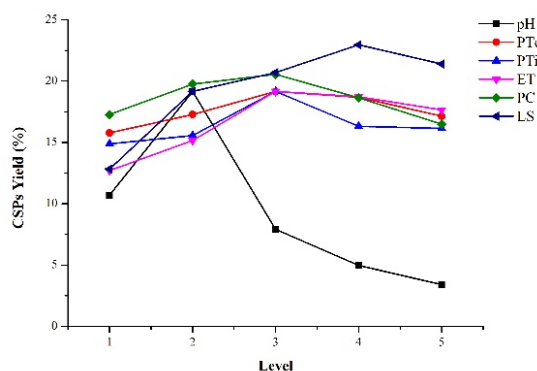

Fig. 1. Effect of pH, PTe, PTi, ET, PC and LS on the yield of CSPs. PTe, proteolysis temperature; PTi, proteolysis time; ET, extraction time; PC, pepsin concentration; LS, liquid-to-solid ratio.

In the single factor experiments, maximum CSPs yield was obtained with the following levels: pH level 2; proteolysis temperature level 3; proteolysis time level 3; extraction time level 3; pepsin concentration level 3; and liquid-solid ratio level 4.

129

In other words, the optimum conditions were as follows: pH, 1.5; proteolysis temperature, 40 °C; proteolysis time, 5 h; extraction time, 60 min; pepsin concentration, 1.5%; and liquid-to-solid ratio, 100:1.

Box-Behnken design and analysis for model fitting

A 17-run BBD was utilized to optimize the three independent variables (X_1: proteolysis pH, X_2: liquid-solid ratio, and X_3: proteolysis temperature). Table 2 shows the layout and the corresponding results obtained with each run. Based on the analysis of multiple regressions, the resulting quadratic polynomial equation was as follows:

$$Y = 22.82 + 1.84X_1 + 0.30X_2 + 0.74X_3 - 0.20X_1X_2 \\ - 0.13X_1X_3 + 0.47X_2X_3 - 3.53X_1^2 - 0.96X_2^2 - 0.037X_3^2 \quad (2)$$

Analysis of variance (ANOVA) study was used to evaluate the impact and significance of each term (linear terms, squared terms and interactions) in the regression equation, and results are summarized in Table 3. The *F*-value of 173.65 suggested that the model is highly significant at $P < 0.0001$. The adjusted determination coefficient (Adj-R^2) of 0.9898 confirmed that the model was significant. A low coefficient of variation (CV) of 1.17% clearly indicated a high degree of precision and good reliability of the experimental values. In this research, the lack of fit *F*-value and *P*-value were found to be 2.78 and 0.1741, respectively, which indicated that the model was sufficiently accurate for predicting the relevant response.

Additionally, the two linear coefficients (X_1 and X_3), two quadratic coefficients (X_1^2 and X_2^2), and one interactive coefficient (X_2X_3) have extremely high significance ($P < 0.01$) to explain the individual effects of proteolysis pH and temperature and the

Table 2. Design and results for BBD.

Run	Coded variable levels			CSPs yield (%)	
	pH (X_1)	LS (X_2, V/m)	PTe (X_3, °C)	Experimental	Predicted
1	(1.4) 0	(80:1) -1	(40) 1	21.90	21.80
2	(1.0) -1	(100:1) 0	1	18.26	18.28
3	0	(120:1) 1	(30) -1	20.81	20.91
4	(1.8) 1	-1	(35) 0	19.83	20.07
5	1	1	0	20.34	20.26
6	0	1	1	23.12	23.34
7	1	0	1	21.84	21.70
8	-1	1	0	17.23	16.99
9	0	-1	-1	21.47	21.25
10	-1	0	-1	16.41	16.55
11	1	0	-1	20.49	20.47
12	-1	-1	0	15.91	15.99
13	0	0	0	23.01	22.82
14	0	0	0	22.83	22.82
15	0	0	0	22.95	22.82
16	0	0	0	22.54	22.82
17	0	0	0	22.78	22.82

Table 3. Analysis of the variance (ANOVA) for the fitted quadratic polynomial model.

Source	Sum of squares	d*f*	Mean square	*F*-value	*P*-value	Significance
Model	91.71	9	10.19	173.65	<0.0001	**
X_1	26.97	1	26.97	459.69	<0.0001	**
X_2	0.71	1	0.71	12.17	0.0102	*
X_3	4.41	1	4.41	75.16	<0.0001	**
X_1X_2	0.16	1	0.16	2.80	0.1385	
X_1X_3	0.063	1	0.063	1.07	0.3364	
X_2X_3	0.88	1	0.88	15.06	0.0060	**
X_1^2	52.61	1	52.61	896.54	<0.0001	**
X_2^2	3.88	1	3.88	66.09	<0.0001	**
X_3^2	5.842E-3	1	5.842E-3	0.100	0.7616	
Residual	0.41	7	0.059			
Lack of fit	0.28	3	0.093	2.78	0.1741	
Pure error	0.13	4	0.033			
Cor. Total	92.12	16				
	$R^2 = 0.9955$		Adj-$R^2 = 0.9898$		CV% = 1.17	

*Significant at $P < 0.05$, **Significant at $P < 0.01$.

interaction effect of liquid-to-solid ratio and proteolysis temperature on the extraction yield of CSPs. The linear coefficient (X_2) was significant ($P < 0.05$), which means that the liquid-to-solid ratio was also an important independent variable. The other term coefficients were insignificant ($P > 0.05$).

Optimization of the procedure

The 3D response surfaces and 2D contour plots were generated based on the regression equation 2, providing a visual interpretation of the interactions between variables, as well as the relationships between CSPs yields and the experimental levels of each variable, as presented in Figure 2. An elliptical or saddle contour plot indicates significant interactions between the corresponding variables while a circular contour plot implies otherwise. In this work, the mutual interactions between the three independent variables (proteolysis pH, proteolysis temperature, liquid-to-solid ratio) were all significant.

Figures 2A and 2D, which fixed the proteolysis temperature at level 0, show that the CSPs yield increased with increasing proteolysis pH (X_1) and liquid-to-solid ratio (X_2) from 1 to 1.5 and 80:1 to 108:1, respectively. At this fixed temperature (0 level), the maximal CSP yield was 23.01%. The plots based on varying pH (X_1) and temperature (X_3) are shown in Figures 2B and 2E, while liquid-to-solid ratio was kept constant at the central point of design. Figures 2C and 2F present that the

CSPs yield increased with liquid-to-solid ratio from 80:1 to 108:1. When the pH was fixed at 1.5, a medium liquid-to-solid ratio and moderate proteolysis temperature were good for the CSPs yield.

Verification of predictive model

The predicted optimum values of the tested variables were 1.5 for proteolysis pH, 108:1 for liquid-to-solid ratio, and 40 °C for proteolysis temperature. This set of conditions was used to experimentally validate and predict the values of the responses using the model equation. Under the optimal conditions, the extraction yield of CSPs was $23.63 \pm 0.21\%$ (N = 3), which was not significantly different ($P > 0.05$) from the predicted value of 23.86%. This indicated that the model designed in this study was adequate for the extraction process.

Comparison of HWE and PAE

The CSPs yields obtained using HWE and PAE were $7.10 \pm 1.23\%$ and $23.63 \pm 0.21\%$, respectively. Thus, the application of PAE positively affected the CSPs yield. Under the optimal conditions for PAE, the CSPs yield increased by 233% compared to the conventional HWE method.

Chemical composition analysis

The crude CSPs were preliminarily characterized using chemical analysis. The contents of
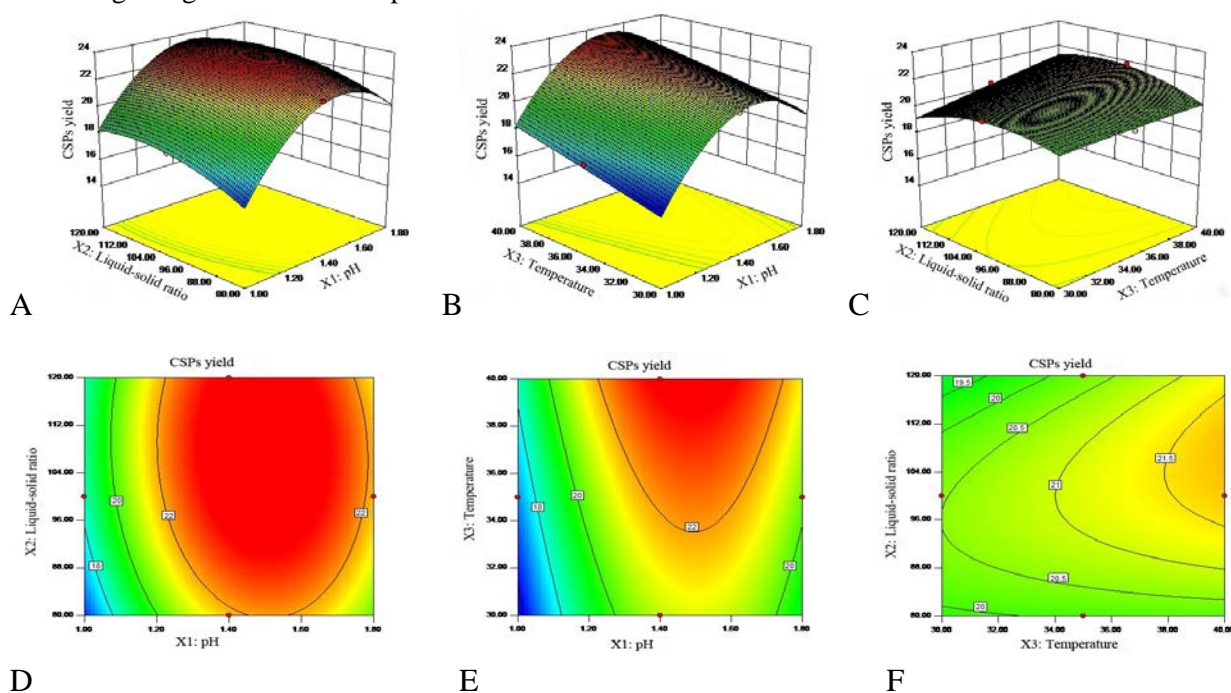

Fig. 2. Response surface plots (A, B, and C) and contour plots (D, E, and F) showing the effects of the interaction of proteolysis pH, liquid-solid ratio, and proteolysis temperature on the response of CSPs yield.

polysaccharide and protein in CSPs-PAE were 90.63 ± 0.77% and 1.07 ± 0.19%, respectively. In the control (HWE), the corresponding contents of CSPs were 71.73 ± 0.64% and 7.57 ±0.28%.

UV and FT-IR analysis

The UV spectra of CSPs-HWE showed strong absorbance at about 200 nm and medium absorbance at 280 nm, indicating the involvement of protein which is consistent with the relatively higher protein contents obtained by chemical analysis. No apparent UV absorption peak was observed around 280 nm in the spectrum of CSPs-PAE, suggesting that the protein content of the sample was negligible.

The FT-IR spectra of CSPs-PAE and CSPs-HWE are shown in Figure 3, which displays a similar trend but differentiates in details.
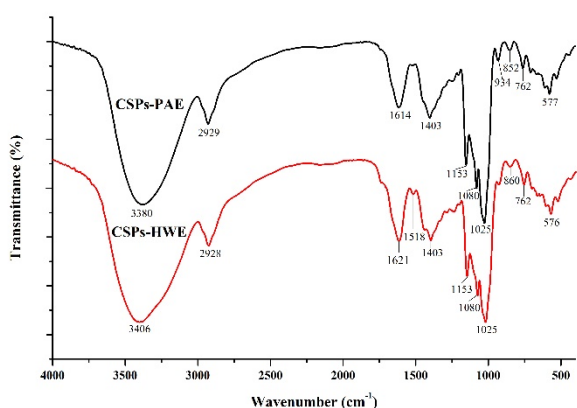

Fig. 3. UV (A) and FT-IR (B) spectra of CSPs-HWE and CSPs-PAE.

Both CSPs-HWE and CSPs-PAE exhibited absorption bands of O-H at 3400 - 3500 cm^{-1}, C-H at 2900 - 3000 cm^{-1}, C-O and C-O-C at 1000 - 1200 cm^{-1}. Three peaks at 1153, 1080, 1025 cm^{-1} in the 1200-1000 cm^{-1} region indicated pyranose rings in these two samples.

In the spectrum of CSPs-HWE, the absorption band at 1518 cm^{-1} was the characteristic peak of CO-NH bending vibration [18], which was not observed in CSPs-PAE. This result further explained the lower protein content in CSPs-PAE (1.07 ± 0.19%). The peak at 852 cm^{-1} was the absorption of α- pyranose ring [19] in CSPs-PAE. However, in the spectrum of CSPs-HWE, the peak was found at 860 cm^{-1} proving the existence of β-configuration.

AFM and SEM analysis

The surface morphology of CSPs obtained from different process and the residues after extraction were elucidated by AFM and SEM.

AFM was exploited to directly observe the chain conformation of the polysaccharides. An AFM image of CSPs-HWE (Figure 4A) shows polysaccharide chains tangling with each other and emerging as large condensed clusters. Figure 4B shows two long stretches where no clustering happens and regions where there is a clear presence of aggregation in CSPs-PAE. Some of the polysaccharide chains were nicely spread out and measured to be longer than 500 nm. The highest single polysaccharide chain can reach 6.5 nm. Compared to CSPs-HWE, CSPs-PAE was associated with lower molecular aggregation and an extended polysaccharide chain, increasing the flexibility of the molecule.
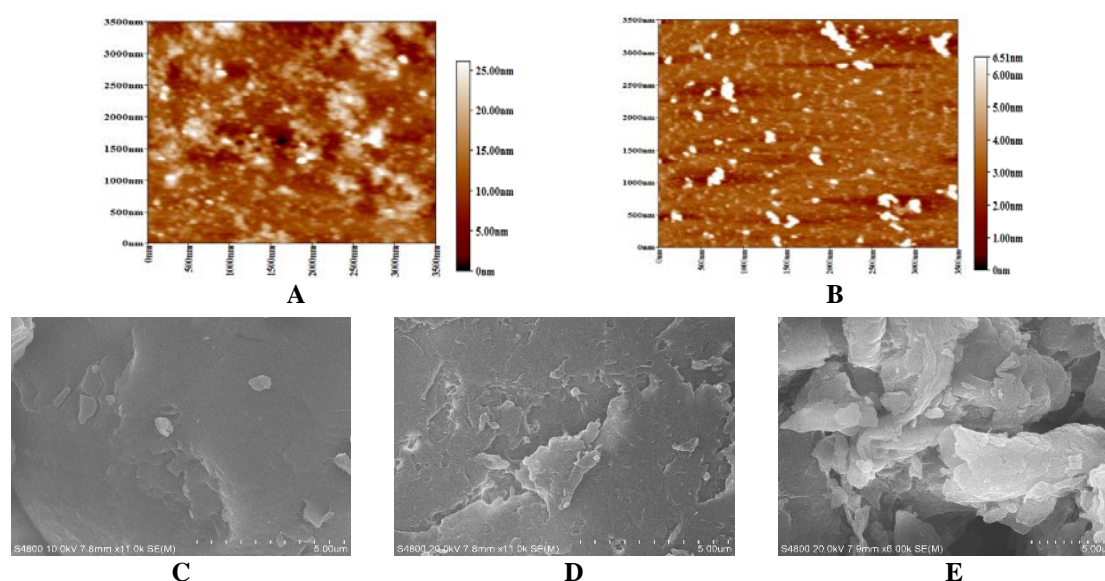

Fig. 4. Atomic force microscopy (AFM) images of CSPs obtained by HWE (A) and PAE (B). and scanning electron microscope (SEM) photographs of the raw material (C), residues after extraction by HWE (D) and PAE (E)

Figures 4C-E present the micrographs of the raw material (C), residues after extraction by HWE (D) and PAE (E), respectively. After a HWE process, little destruction of the residues microstructure occurred, while the residues resulting from PAE had large lamellae on their surfaces. This significant change is probably due to the degrading ability of pepsin rendering the intracellular materials more accessible for extraction, which contributed to the higher efficiency of polysaccharide extraction. Therefore, in the PAE process, the plant tissues were remarkably destructed, and the CSPs can be released more easily into the extraction solution than by the HWE process.

CONCLUSION

A pepsin-assisted extraction to acquire CSPs from the stem of *Cynomorium songaricum* was optimized by a 17-run BBD with response surface methodology based on single factor experiments. The second-order polynomial model gave a satisfactory description of the experimental data giving the optimum conditions as pH of 1.5, liquid-solid ratio of 108:1, and proteolysis temperature of 40 °C. Under these conditions, the highest CSPs yield was 23.63 ± 0.21% in accordance with the predicted value of 23.86% and represented 233% of that obtained by the traditional HWE method. Compared to CSPs-HWE, CSPs-PAE provided higher contents of polysaccharide (90.63 ± 0.77%), as well as lower contents of protein (1.07 ± 0.19%). Moreover, the CSPs were characterized by UV, FT-IR, SEM, and AFM which showed that CSPs-PAE differentiated from CSPs-HWE in functional groups and surface morphology leading to their distinct properties. The precise chemical structures and the unique biological functions of CSPs-PAE are currently under investigations.

REFERENCES

1. S. Jin, Eerdunbayaer, A. Doi, T. Kuroda, G. Zhang, T. Hatano, G. Chen, *J. Agric. Food Chem.*, **60**, 7297 (2012).
2. Q. Chu, X. Tian, M. Lin, J. Ye, *J. Agric. Food Chem.*, **54**, 7979 (2006).
3. Z. Xiong, X. Ma, Y. Sun, C. Yao, A. Chi, W. Wang, L. Zheng, L. Li, J. Ma, M. Zhang, *J. Shaanxi Norm. Univ.*, **39**, 103(2011).
4. F. Wang, Q. Liu, W. Wang, X. Li, J. Zhang, *Int. J. Biol. Macromol.*, **87**, 222 (2016).
5. J. Wang, J. Zhang, B. Zhao, Y. Wu, C. Wang, Y. Wang, *Food Chem.*, 120, 443 (2010).
6. G. Shi, W. Jiang, L. Cai, G. Sui, *Int. J. Biol. Macromol.*, **48**, 788 (2011).
7. F. Wang, W. Wang, Y. Huang, Z. Liu, J. Zhang, *Food Hydrocolloid.*, **47**, 79 (2015).
8. K. Zhong, W. Lin, Q. Wang, S. Zhou, *Int. J. Biol. Macromol.*, **51**, 612 (2012).
9. M. Puri, D. Sharma, C.J. Barrow, *Trends Biotechnol.*, **30**, 37 (2012).
10. H. Chen, X. Zhou, J. Zhang, *Carbohyd. Polym.*, **111**, 567 (2014).
11. A. Zhang, X. Li, C. Xing, J. Yang, P. Sun, *Int. J. Biol. Macromol.*, **65**, 28 (2014).
12. Y. Xu, F. Cai, Z. Yu, L. Zhang, X. Li, Y. Yang, G. Liu, *Food Chem.*, **194**, 650 (2016).
13. M. Dubois, K.A. Gilles, J.K. Hamilton, P.A. Rebers, F. Smith, *Anal. Chem.*, **28**, 350 (1956).
14. M.M. Bradford, *Anal. Biochem.*, **72**, 248 (1976).
15. Q. Xiong, X. Li, R. Zhou, H. Hao, S. Li, Y. Jing, C. Zhu, Q. Zhang, Y. Shi, *Carbohyd. Polym.*, **108**, 247 (2014).
16. I. Austarheim, B.E. Christensen, I.K. Hegna, B.O. Petersen, J.O. Duus, D. Diallo, M. Inngjerdingen, B.S. Paulsen, *Carbohyd. Polym.*, **89**, 259 (2012).
17. R. Mohammadi, M.A. Mohammadifar, A.M. Mortazavian, M. Rouhi, J.B. Ghasemi, Z. Delshadian, *Food Chem.*, **190**, 186 (2016).
18. B.E. Abdelmalek, J. Gómez-Estaca, A. Sila, O. Martinez-Alvarez, M.C. Gómez-Guillén, S. Chaabouni-Ellouz, M.A. Ayadi, A. Bougatef, *LWT - Food Sci. Technol.*, **65**, 924 (2016).
19. H. Zhang, J.Q. Wang, S.P. Nie, Y.X. Wang, S.W. Cui, M.Y. Xie, *Int. J. Biol. Macromol.*, **79**, 248 (2015).

Research on health assessment of main forest vegetation in Kuankuoshui nature reserve

C.W. Zhou [1,2], L.B. Yan [1,2], L.F. Yu [1,2,*], C.H. Zhong [1], G.P.Chen[3], C. Zhou [1], F.J. Pi [1]

[1] Life Science College of Guizhou University, Guiyang, Guizhou,China
[2] Collaborative Innovation Center for Mountain Ecology & Agro-Bioengineering (CICEAB), College of Life Sciences and Institute of Agro-Bioengineering, Guizhou University, Guiyang ,Guizhou,China
[3]Kuankuoshui National Nature Reserve Authority, Suiyang, Zunyi, Guizhou,China

The main forest vegetation health evaluation studies in nature reserves provide scientific basis for their operation and management and are of significance for the sustainable development of forest vegetation in nature reserves and the further improvement of the nature reserves construction. This study of the Kuankuoshui national nature reserve of Suiyang county as the research object, combined with Kuankuoshui nature reserve forest resources "second subcompartment survey" in 2031 subcompartments samples and 80 000 data, applying sensitivity analysis, etc. to screen indicators, adopting an analytical hierarchy process to determine the weight of each index, set up the main forest vegetation health evaluation model of the broad water nature reserve. To assess the broad water nature reserve, evaluation analysis of the main forest vegetation health was performed. The main results were as follows: The nature reserve is in a relatively healthy grade as a whole，the forest subcompartments evaluated as unhealthy are composed by ≥25° slope farmland, shrub wood, unformed man-made forest, barren hills and wasteland suited for forestry.

Keywords: Forest health assessment, Small яubcompartment, Nature зreserve, Kuankuoshui of Guizhou Province

INTRODUCTION

The forest vegetation ecosystem is a natural ecological system with the largest area [1], the most complex composition structure, the richest biological resources and relatively perfect functions on the terrestrial ecosystem [2]. The forest vegetation plays ь significant role in protecting the diversity of species and avoiding ecosystem unbalance [3].

The forest vegetation resources in China are relatively tense, with a forest vegetation coverage rate and average holding volume for the forest vegetation resources lower than the world's average level [4]. However, with the rocketing development of economy and the improvement in people's living standards, under various pressures, the forest vegetation is damaged in large quantity, destroying forest resources and greatly damaging the diversity of species and forest vegetation. Therefore, the research on the forest vegetation health evaluation plays significant a role in improving the ecological environment and protecting the diversity of species. Guo *et al*. [5] in their research on the health status of the typical natural secondary forest ecosystem in the Tushi mountainous area in Northern China, employed the Comprehensive value method for the evaluation indicators to calculate the specific values

for each indicator at subcompartment level, categorizing the health degree of the forest vegetation into 5 grades. Tan [6] in his research on health evaluation of the complex network-based forest vegetation, also categorized the health degree of the forest vegetation into 5 grades by calculating the specific health indices for each landscape patch of the subcompartment network in the treatment of the subcompartment network with even distribution of areas. Wang, in the research on the health evaluation and health operation technology of the man-made forest in Hebei Mulan Paddock [7], established a hierarchical analysis structure model to categorize the health status of the forest vegetation into 4 grades as high-quality, healthy, sub-healthy and unhealthy with the principles of equivalence and the nearest rounding. Liu *et al.*, in the research on the establishment of a health evaluation system for the man-made locust forest, established an evaluation system model for the man-made locust forest with the combination of the cluster analysis method and hierarchical analysis method, categorizing the health status of the locust forests in different ages into 3 grades as healthy forest, sub-healthy forest and unhealthy forest by calculating the health evaluation indices for different sample fields [8].

Nowadays there is a diversity of studies [9,10], systems and methods for health evaluation of forests. Having referred to the relevant literature, on the basis of the theoretical studies made by a number of experts and scholars, this paper tried to explore the research methods applicable to the vegetation health

evaluation for the main forest in the Kuankuoshui nature reserve. The research theoretical system for health evaluation of forests was developed and enriched.

There is a significant difference between this study and the studies made by the experts and scholars, which is well explained by the difference of evaluation targets. Their target is of forest type, while this paper deals with a nature reserve, a virgin forest reserve with major trees of forest arbors, which is divided into three functional areas as core area, buffer area and experimental area. The vegetation here is more diversified and more complex.

EXPERIMENTAL

General introduction of the studied area

The Kuankuoshui nature reserve, located in the northwest part of Suiyang County of Guizhou Province, is part of the Dalou Mountains. Its altitude is between 651 and 1766 m, and the highest peak is located on the Sun Mountain with an altitude of 1766 m. Its geographical location is east longitude of 107°02′22″ ～ 107°14′08″ and north latitude of 28°06′24″～28°19′26″. It stretches 19 km from the east to the west and 25 km from the north to the south [11].

The Kuankuoshui nature reserve, with the greatest geographical environment and diversified habitat types, maintains 1,300 hectares of *cyclobalanopsis glauca* forest with a high natural disposition, the best preservation and the more representative concentration, and a variety of state first-level protected animals – the *Trachypithecus francoisi* and the bird with the most characteristics of Kuoshui named golden pheasant.

Data sources

The second-type inventory data for the forest resources of Kuankuoshui nature reserve obtained in 2010 as the data source, the forest form map as the base map and GIS constructed the nature reserve forest vegetation resources database with the basic unit of subcompartment level. The database covers almost 80 indicators and recorded over 80,000 of forest vegetation resources data including cadastral information, forest land-related information, forest vegetation-related information, site environment and some other relevant information.

The second-type inventory data for the forest resources in the Kuankuoshui nature reserve can be categorized into 2031 subcompartment fields, in which there are 636 core subcompartments, 461 buffer zones and 934 experimental zones. The nature reserve is composed of several kinds of fields as ≥25° slope farmland, unformed man-made forest land, pure forest, shrub forest, mixed forest, barren hills and wasteland suitable for forestry.

Evaluation index system

The layer of principles: which reflect the behaviors and abilities of the forest vegetation in the nature reserve included the vigor, the organizational structure and recovery ability of the forest vegetation. The health indicators on the various layers of principles can be calculated with weights.

This research carried out health evaluations of the vegetation of the nature reserve by employing the comprehensive indicators evaluation method. Its HI calculation equation (1) is:

$$HI=\omega_1 V+\omega_2 O+\omega_3 R \quad (1)$$

In the equation, HI refers to the HI for the forest vegetation, V refers to the vigor evaluation index of the forest vegetation, O refers to the organizational evaluation index for the forest vegetation and R refers to the recovery evaluation index for the forest vegetation.

The relevant evaluation measure for the health evaluation indicators of the forest vegetation can be measured with specific values measured. For those whose index measure values cannot be determined or are inconvenient to measure, the Degree categorization method in the qualitative research is employed for the quantitative description studies, categorizing into three grades (with the natural endowments of 1, 3 and 5, respectively) with the standard of the influence level for the specific indices on the health of forest vegetation. Some evaluation indices cannot only be measured with specific values, but could also be determined by the grades categorization with the qualitative method based on the specific situations. For the relevant condition of the natural endowment and the specific grades categorization for the various indicators, please refer to Table 1.

RESULTS AND DISCUSSION

Based on the health evaluation model established above for the main forest vegetation in the Kuankuoshui nature reserve, and with the employment of the data obtained, its health status results are calculated as follows:

Table 1 Grades categorization for the health evaluation indices in the 'Second Survey' data

	Grade and Scores		
	1	3	5
Field type	Barren hills and wasteland suited for forestry ≥25 Slope farmland	Shrub forest Unformed man-made forest	Pure forest, mixed forest and bamboo forest
Advantageous trees	Pyracantha and shrub wood	Evergreen coniferous forest	Broad-leaved evergreen forests and mixed forest
Degree of naturalness	Forest type which almost maintains the primitive status with little man-made influences	Forest type with a certain disturbance by human. The top tree types can be obviously seen or expected	The forest type with a significant disturbance by human or the zonal forest type which has been almost destroyed. In the late period of retrograde succession
Slope (°)	Slope ≥36	Slope 16～35	Slope 0～16
Altitude (M)	>130	1000～1300	<1000
DBH (cm)	＜10	＞65 or [10, 20)	[20, 65]
Type of soil	Cultivated soil		Yellow soil, red-yellow soil and yellow-brown soil Lime soil, purple soil
Age group	Young-aged forest, Over-mature forest	Almost mature forest, Mature forest	Middle-aged forest
Degree of forest disasters	Tree crown damage ≥50% Number of damaged trees ≥50%，taking the main form of the dying wood and the dead wood	Tree crown damage 20～49%, Degree of damaged trees 20～49%, a few trees have died	No disasters have happened, tree crown damage ＜20%
Crown density (%)	Low level 0.20～0.39	High level ≥0.70	Medium level 0.4～0.69
Depth of soil (cm）	＜40	40～79	≥80
Bedrock bare rate (%）	≥70	50～69	0～49
Degree of natural renewal	III	II	I

Table 2 HI of the Kuankuoshui nature reserve

Functional zone	Organizational structure	Vigor	Recovery ability	HI
Core zone	0.728	0.318	0.482	0.509
Buffer zone	0.612	0.279	0.461	0.451
Functional zone	0.623	0.301	0.490	0.472
Total	0.654	0.302	0.481	0.479

It can be seen from Table 2 that its HI is 0.479, which falls between 0.319 and 0.634. Combined with Table 3, it is of relatively healthy grade. That means, main forest vegetation in the Kuankuoshui nature reserve is in relatively healthy status in general. In the meantime, the experimental zone, the buffer zone and the core zone are in a relatively healthy grade. The HI status for each functional zone is: core zone (I=0.510 ＞ experimental zone (HI=0.471) ＞ buffer zone (HI=0.451). All sub-indices for the core zone, the buffer zone and the experimental zone are: organizational index ＞ recovery index＞vigor index (Fig. 1.).

Looking from the entire nature zone, there are 447 subcompartments in the main forest vegetation in the Kuankuoshui nature reserve that are healthy in general, taking 47.12% of the total subcompartment number. With an area of 5,766 hectares, they take 24% of the total area of the nature reserve. 957 subcompartments are in a relatively healthy status, taking 47% of the total subcompartment number. With an area of 12,736 hectares, they take 23% of the total area of the nature reserve. Looking in the different functional zones for healthy subcompartments, there are 147 blocks in the core zone, 103 blocks in the buffer zone and 197 in the experimental zone. As for the quantitative proportion, the core zone takes the largest part (23.1%), followed by the buffer zone (22.3%), and the experimental zone (21.1%), with areas of 2,101.46 hectares, 1,491.81 hectares and 2,172.61
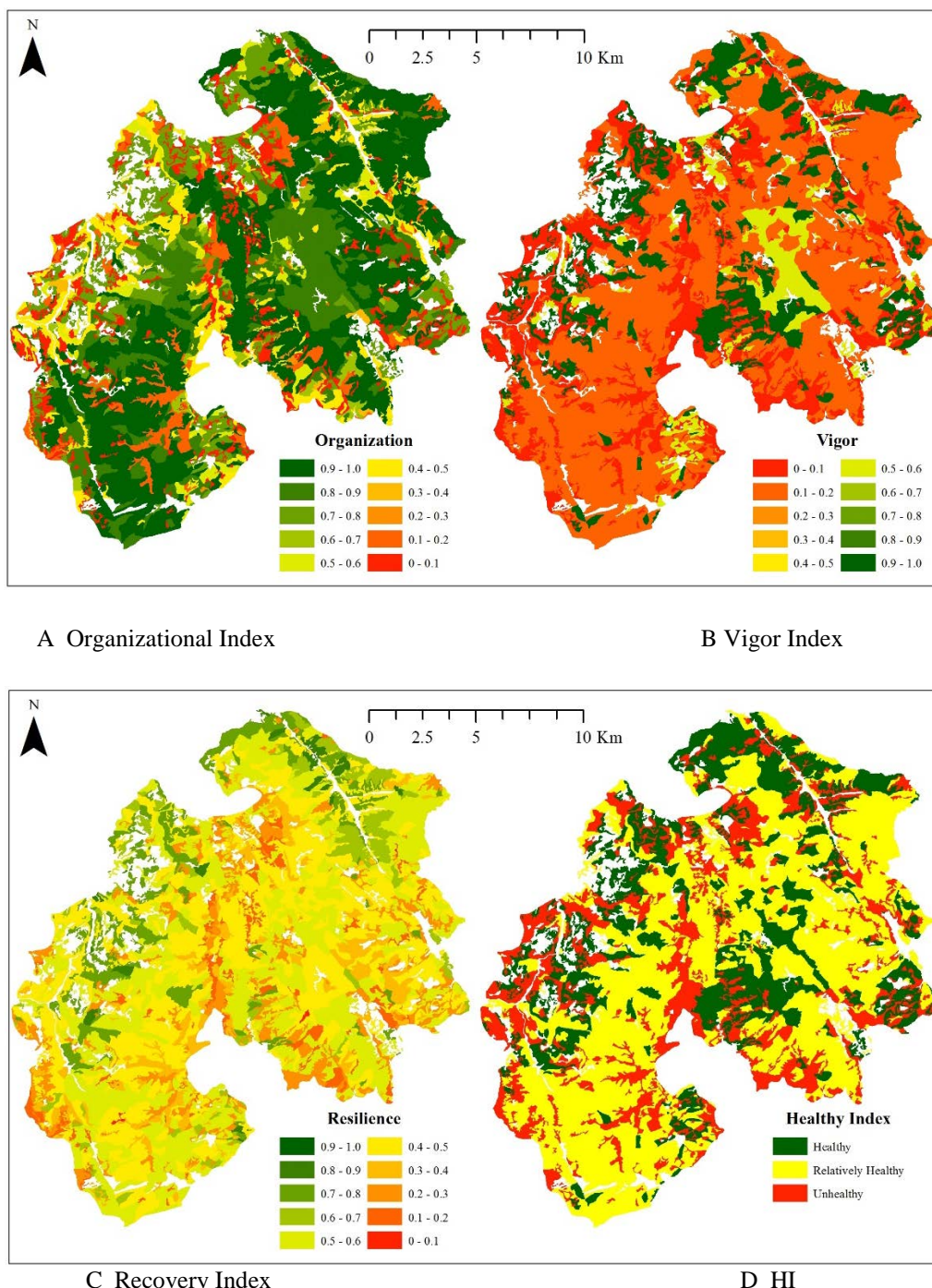
A Organizational Index   B Vigor Index

C Recovery Index   D HI

Fig. 1. Health status evaluation for the forest vegetation subcompartment level in the nature reserve (A-D)

hectares, respectively, taking 36.45%, 25.87% and 37.68% of the total area of the healthy subcompartment, respectively.

There are 342 blocks of relatively healthy subcompartments in the core zone, 183 blocks in the buffer zone and 432 in the experimental zone, with areas of 5327.26 hectares, 2482.71 hectares, 4925.83 hectares and 12735.8 hectares respectively, taking

41.83%, 19.49% and 38.68% of the total area of the relatively healthy subcompartments, respectively.

There are 147 unhealthy subcompartments in the core zone, 175 in the buffer zone and 3.5 in the experimental zone, with areas of 1,325.46 hectares, 1,623.51 hectares and 2,595.46 hectares respectively, taking 23.91%, 29.28% and 46.81% of the total area of the unhealthy subcompartments, respectively (Table 3, Figure 2).

Table 3. The general health condition evaluation for the Kuankuoshui nature reserve

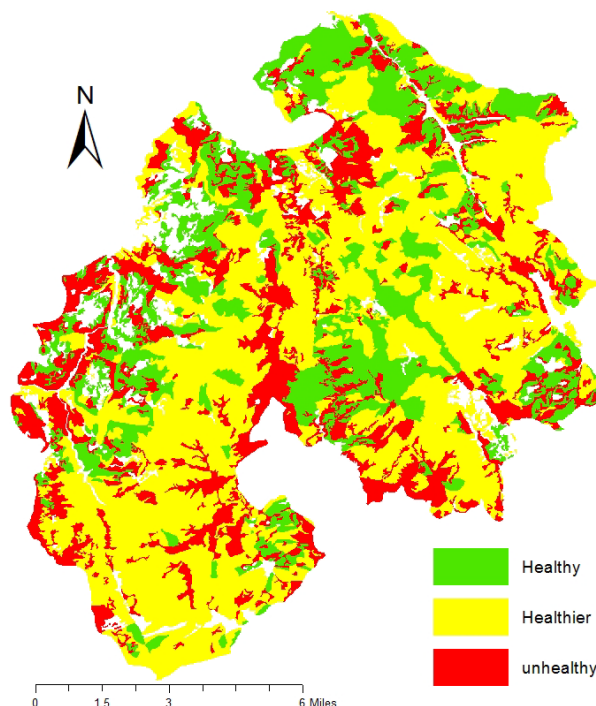|	Healthy	Relatively healthy	Unhealthy	Total
Number of subcompartments	447（22.01%）	957（47.12%）	627（30.87%）	2031
Area of subcompartments (hectares)	57656（23.98%）	12736（52.96%）	5544（23.06%）	24046

Fig.2. Distribution map of Forest health in Kuankuoshui nature reserve

The field types in the forest vegetation of the Kuankuoshui nature reserve that fall into the relatively healthy and healthy categories are mixed forest, taking 80.3% and 56.8%, respectively.

The unhealthy field types include ≥25°slope farmland (36.7%), unformed man-made forest (25.0%), barren hills and wasteland suited for forestry (19.5%) and shrub wood (18.8%). But there are in fact infant trees in the unformed man-made forest which could reach a healthy grade with a certain time of growth. Besides, according to the regulations of the state, the shrub wood field type is already stable on the mountain top and the cliffs. Therefore, these two field types should not be unhealthy factors in the health evaluation for the Kuankuoshui forest vegetation.

Considering the different health status of the forest vegetation of the different field types, it follows that: the mixed forest has the most significant contributions to the health of forest with a proportion of 72.79%. The ≥25° slope, with a proportion of 38.10%, and the barren hills and wasteland suited for forestry, with a proportion of 21.77%, are the two major unhealthy field types affecting the health of the forest in the core zone. Therefore, converting farmland to forest and

planting trees are the major measures to recover the vegetation health of the forest in the core zone.

CONCLUSIONS

1. Carrying out calculations for the 2,031 subcompartments data in the second subcompartment survey for the forest resources in the Kuankuoshui nature reserve based on the forest vegetation health evaluation model it is found that the forest vegetation HI is 0.479. The nature reserve is in a relatively healthy grade as a whole, among which the core zone (HI=0.510)＞experimental zone (HI=0.471)＞buffer zone (HI=0.451).

2. As for the subcompartment level, there are 1,404 subcompartments above the relatively healthy level, taking 60.1% of the total subcompartments, among which there are 489 in the core zone, 629 in the experimental zone and 286 in the buffer zone, and the proportions taken in the various functional zones are 76.9%, 62.0% and 67.3% respectively. In the healthy subcompartments proportion, the core zone takes the largest proportion (23.1%), followed by the buffer zone (22.3%), and the experimental zone (21.1%).

3. The forest subcompartments evaluated as unhealthy are composed of ≥25° slope farmland,

shrub wood, unformed man-made forest and barren hills and wasteland suited for forestry (the total of these subcompartments takes above 90% of the total amount). But there are in fact the infant trees in the unformed man-made forest which could reach a healthy grade with a certain time of growth. Besides, according to the regulations of the state, the shrub wood field type is already stable on the mountain top and the cliffs. Therefore, these two field types should not be unhealthy factors in the health evaluation of the Kuankuoshui forest vegetation.

4. As for the major factors affecting the health status of the various functional zones, it is the≥25° slope farmland (38.10%)for the core zone, the ≥25° slope farmland (31.43%) for the buffer zone, and the ≥25° slope farmland (39.02%) and the barren hills and wasteland suited for forestry (19.02%) for the experimental zone.

REFERENCES

1. W.X. Chen, Central South University of Forestry and Technology, Chengdu, China, 2012.
2. J.K. Gao, Beijing Forestry University, Beijing, China, 2007.
3. F.J. Xiao, H. O.Yang , J.H. Sun, *Forestry Resources Management*, **1**, 27 (2004).
4. F.J. Xiao, H.O. Yang, B.j. Fu, *Geographical Journal,* **58**, 803 (2003).
5. J.Zhang, Central South University of Forestry and Technology, Changsha, China, 2014.
6. G.Q. Zhang, *Sichuan Forestry Technology*, **29**, 77 (2008).
7. H.Zhang, Beijing Forestry Univeristy, Beijing, China, 2010.
8. H. Yang, H.T. Dai, D. Liu, *Modern Agricultural Technology,* **10**, 187 (2010).
9. J.X. Fan, Sichuan Agricultural University, Chengdu, China, 2013.
10. Y.Wang, Northwest Normal University, Xian, 2012.
11. L.F. Yu, S.X. Xie, T.L. Wu, Guizhou Science and Technology Publishing House Co.,Ltd., Guiyang, China, 2004.

Study on functional division optimizing of Kuankuoshui national nature reserve based on resistance surface analysis

L.B Yan[2,3], L.F. Yu[2,3], C.W Zhou[2,3], R. Yang[1,3*]

1 College of Forestry, Guizhou University, Huaxi District, Guiyang, Guizhou 550025, China

2 College of Life Sciences, Guizhou University, Huaxi District, Guiyang, Guizhou 550025, China

3Collaborative Innovation Center for Mountain Ecology & Agro-Bioengineering(CICEAB), College of Life Sciences and Institute of Agro-Bioengineering, Guizhou University, Guiyang 550025, China

Functional division of nature reserve is the region set for the protected object. For optimizing and adjusting it, we selected Kuankuoshui national nature reserve as research area. This research utilized 5 ecological sources as research objects, which included 4 types of animals (*Phasianidae, Cervidae, Felidae* and Primate) and *Fagus lucida* woods, and the used resistance factors containing altitude, slope, landscape type and rock bare rate defined the distribution pattern of the resistance surface. The complex strategic points were identified by combining the statistics and superposition of the ecological corridors. The results showed that the resistance surface model gives excellent simulation of the potential biodistribution; classical function zoning may protect the ecological source and strategic points at saddle points except for strategic points at intersections, multiple strategic points at intersections and multiple ecological corridors. On the basis of the research results suggestions are put forward for the functional division adjustment, three-dimensional ecological corridor construction measures and management measures on time.

Key words: Nature reserve, Ecological source, Division into districts, Ecological corridor, Strategic points

INTRODUCTION

With the development of society, the human interference ability is gradually strengthened, which has resulted in the gradually increased degree of fragmentation of natural habitat. Habitat segregation leads to faster extinction and increased loss of biodiversity [1]. As a sanctuary for endangered species, the importance of the function of biodiversity protection has been brought into play, and the nature reserve has come into being. The circle structure of nature reserve – functional zoning is the basis for the implementation of management and protection, for scientific and rational functional zoning can effectively protect and utilize all kinds of resources in nature reserves. In the current way of development, construction of roads, farmland cultivation and tourism activities exist in protected areas, which will to some extent affect the function of protected areas, the formation of linear gallery landscape types, cutting and interference of roads to some biological habitats. For different kinds of living things, habitat suitability evaluation as a potential biological distribution area is necessary. Including it in a higher-level reserve area is beneficial to biodiversity protection and achieves the purpose of establishment of protected areas. Ecological corridors for biological diffusion of different types of organisms can help reasonable planning and construction of protected areas, so as to break the restrictions on biological habitats. The core problem of corridor protection is to control or maintain the ecological process on the surface through some location or part of the space, this location / part is the landscape strategic point [2], and the establishment of the resistance zone of biological migration / diffusion in the region can better identify corridors between birth sources.

The natural function zoning districts are usually divided based on simple data statistics, human experience, and existing habitat for protected objects, while there is less consideration of potential distribution, suitability, biological diffusion corridors and complex problems [3-6]. With the development of landscape ecology theory and the development of GIS technology, there is a new way of studying and dividing the functional zoning [7]. This paper intends to carry out multiple analysis on diffusion, resistance and ecological corridors of 5 types of ecological sources, current functional zoning in Kuankuoshui nature reserve, so as to find out the insufficiency of functional zoning, and provide a scientific basis for the construction of rational functional zoning.

To whom all correspondence should be sent:
E-mail: yr553017@163.com

EXPERIMENTAL

Research area overview

Kuankuoshui nature reserve is located in north Suiyang County of Zunyi city of Guizhou Province, the geographic coordinates are: east longitude of 107°02′42″-107°13′26″, north latitude of 28°08′23″-28°19′10″; it extends about 19 km from east to west and has a depth of about 20 km in the north and south. It belongs to the humid subtropical monsoon climate. The mountains belonging to the protected area are undulating, and the annual temperature on the raised upland is relatively low. The cloud cover time is long and the sunshine time is short, which has the characteristics of low-altitude mountain humid climate, the annual average temperature is 11.7-15.2 °C, annual precipitation is 1300-1350 mm. There are over 200 days with rainfall≥0.1mm, and the annual average relative humidity is high (more than 82%). It is the only remaining evergreen deciduous broad-leaved mixed forest in the eastern section of the Da Lou mountain range in Guizhou province, including the ancient plants remaining from the Tertiary period – primary forest, secondary forest, artificial forest, bamboo forest and shrub forest based on *Fagus lucida* forest. Furong River and its main streams, Qingxi River, Yangyan River, Chiwei stream and other river valleys form a steep ravine valley; there are typical landscapes such as primeval forests and karst caves on karst landform. There are favorable water and heat conditions, geological soil conditions and forest ecosystems in the reserve area, which provide a favorable habitat for the growth and breeding of wild animals and plants of forest, therefore, rich biodiversity has been formed in the reserve.

Research method

Research data were used to establish a 2.5 m resolution digital elevation model (DEM) by using vectorization 1:1 topographic map, and slope data were obtained based on DEM calculations. The 2015 remote sensing image (GF-1, China) was used to interpret land use type as landscape type data; what is more, rock bare rate data in the second type forest resources survey database of 2015 were used. We built up 4 resistance layers where the slope division was: 0-5°, 5-15°, 15-25°, 25-35°, 35-45° and >45°, divided in 6 grades of slope in total. The altitude division was: <700m, 700-800m, 800-900m, 900-1000m, 1000-1100m, 1100-1200m, 1200-1300m, 1300-1400m, 1400-1500m and >1500m, a total of 10 altitude classes. The rock bare rate data division

was: 0-10%, 10-20%, 20-30%, 30-40%, 40-50%, 50-60% and >60%, a total of 7 levels. The landscape types were divided into 9 types including residential areas, farmland, evergreen coniferous forests, deciduous broad-leaved forests, evergreen shrubs, evergreen broad-leaved forests, deciduous shrubs, water bodies and roads. The study selected 5 biological groups of more accurate and comprehensive distribution of animals that contain *Phasianidae* (*Syrmaticus ellioti*, *Tragopan satyra*, *Chrysolophus pictus* and *Phasianus colchicus*), *Cervidae* (*Muntiacus reevesi*, *Elaphodus cephalophus*), *Felidae* (*Prionailurus bengalensis*, *Viverra zibetha*), Primate (*Trachypithecus francoisi*), and *Fagus lucida* in the nature reserve as ecological source. The resistance surfaces of Kuangkuoshui nature reserve were established and analyzed according to the grade division, and the ecological sources of the different biological groups investigated in the reserve were counted and superimposed to identify compound strategic points. Based on the types and quantities of interchange corridors, a more important strategic point of interchange was explored, and multiple corridors in some areas were combined to form compound corridor. All calculations, analyses and drawings in this study were conducted with ArcGIS 10.2.

RESULTS ANALYSIS

Distribution pattern of different resistance surfaces

According to the classification factors of different resistance layers, the distribution pattern of different resistance levels in the Kuankuoshui nature reserve was constructed (Figure 1). In elevation resistance surface distribution, the altitude range is between 649.2-1758.9m, the protection area is mainly at 1200-1600m, 1600-1800m high altitude mainly distributes in the middle of the reserve, 600-1000m's low elevation mainly distributes in the edge of the reserve; In slope resistance surface distribution, in the west, there are deep karst peak clusters with the tributary of the Tang River and its right bank ("V" type valley and gorge), in the east, there are watershed, and northwest to southeast of the karst valley, and in the middle, there are three ridges, Daping ridge, Jinlin Mountain – Tianping ridge, and Pijiapo ridge, relatively flat areas are between the high altitude ridges, and inside human settlements. The resistance surface distribution of landscape types is based on evergreen broad-leaved forest, followed by evergreen coniferous forest, deciduous broad-leaved forest, and large farmland area; while in rock detachment rate resistance surface distribution, the rock cover rate is very low on the whole, and high distribution areas of exposed rock distribute on both sides of canyon and valley, and the karst geomorphic area in the West.
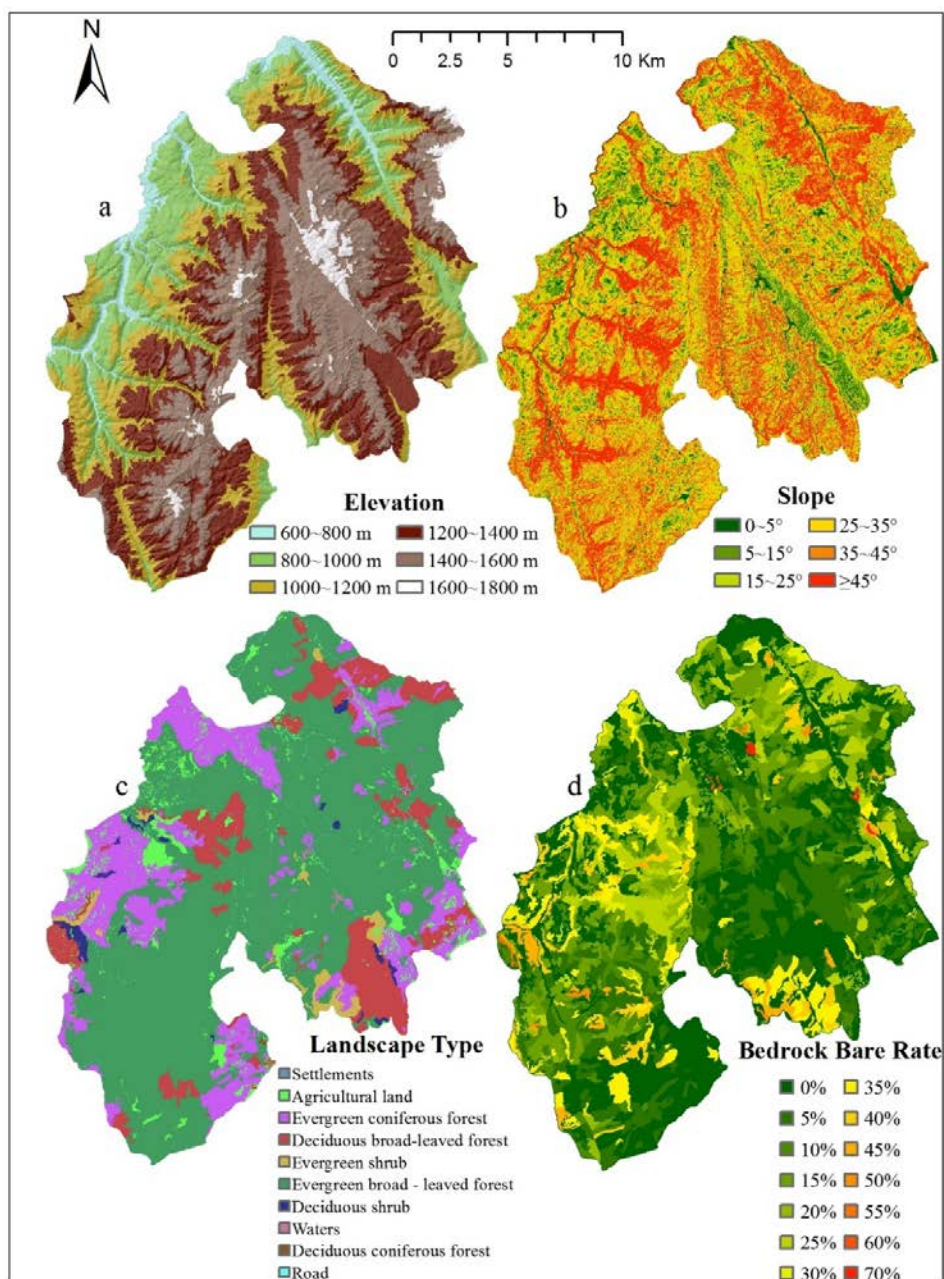
Fig. 1. Distribution pattern of different resistance surface in Kuankuoshui nature reserve

Different ecological source areas of Kuankuoshui Nature Reserve survey were recorded; combining with the analysis of bio-diffusion ecological corridor, we identified the strategic points of structure type of the landscape ecology [2]. The identified strategic points were superimposed on different functional partitions of the Kuankuoshui nature reserve, statistical results (Table 1) indicated that: in quantitative distribution of ecological sources, the core area > experimentation area > buffer zone, the proportion of the core area was 42.3%; in quantitative distribution of saddle strategy points, core area > buffer area > experimentation area, and the proportion of the core area was 56.9%.

Table 1 Status of protected strategic points.

Functional areas	Ecological source		Saddle strategy points		Interchange strategic points		Total	
	Quantity	Proportion	Quantity	Proportion	Quantity	Proportion	Quantity	Proportion
Core area	19	42.3%	29	56.9%	15	48.4%	44	53.7%
Buffer area	13	25.0%	12	23.5%	6	19.4%	18	22.0%
Experimental Area	17	32.7%	10	19.6%	10	32.3%	20	24.4%
Total	52	-	41	-	31	-	82	-

The proportion of buffer and experimentation area was relatively low; while in quantitative distribution of strategic points at interchange, core area > experimentation area > buffer zone, the core area accounted for more than 50%, the proportion of experimentation area in the buffer zone was very small. On the whole, half of the strategic points were in the core area, and compared to the conservation status of ecological resources, the proportion of strategic points falling in the core functional areas was higher; according to the types of strategic points, the proportion of strategic points at the core area of the interchange was lower than that of the saddle strategy points, the proportion in experimentation area was relatively high (32.3%), that is, in the present functional zoning, the saddle strategy points could get better protection than the intersection strategy points, and the convergence strategic points had not been well protected.

CONCLUSION AND RECOMMENDATIONS

In view of the 5 biological groups of more accurate and comprehensive distribution of rare and endangered animals pheasants (Elliots pheasant, tragopan temminckii, Chrysolo phuspictus and necked pheasant) in the nature reserve, Felidae (leopard cat, zibet), Primates (Francois monkey) and *Fagus lucida* under protection in the Kuankuoshui reserve, the distribution patterns of resistance levels of 4 factors of elevation, slope, landscape type and bare bedrock were used for analysis, and combined with functional zoning of protected areas. It was found that all kinds of ecological resources and landscape strategic points in the reserve had not been optimally protected, and relative to the source and the saddle ecological strategy points, the strategic points in junction, the strategic points in compound interchange and compound ecological corridors had not been better protected.

According to the protection status of the reserved area, suggestions on improving the protection efficiency were put forward from two aspects of the protection function zone adjustment and the artificial biological corridor construction. The function zoning of the south of the core area of the reserve can be adjusted, so that more landscape strategic points, compound junction strategic points and compound corridors can be included in the buffer zone, so as to achieve a higher level of protection. Planning and construction of important corridors of compound forest corridor landscape could help isolated island habitats to link together, so as to reduce wildlife dispersal resistance and increase wildlife activity and dispersal surfaces.

We should abandon the idea of plain planning and build a three-dimensional functional area, and build complex artificial passages on important strategic points and corridors. Taking into account the barrier and interference of roads to the landscape, ecological highway tunnels and ecological bridges and biological channels can be built in the important terrain, so that people and creatures make their way separately, which can reduce the interference of human activities. Meanwhile, scientific studies of long-term succession of plant communities, location observation, monitoring of animal migration and channel selection can be conducted in the passageway.

REFERENCES

1. W. D. Zhai, N. X. Ma, *China Environmental Science*, **20**, 337 (2000).
2. K. J. Yu, *Acta Geographica Sinica*, **53**, 11 (1998).
3. C. G. Wu, Z. X. Zhou, P. C. Wang, W. F. Xiao, M. J. Teng, L. Peng, *Chinese Journal of Applied Ecology*, **20**, 2042 (2009).
4. S. Q. Zhou. *Sichuan forestry exploration and design*, **3**, 37 (1997).
5. W. D. Zhai, N X Ma, *Journal of Northwest University (Natural Science Edition).*, **29**, 429 (1999).
6. X. Liu, *Journal of Guizhou Normal University (Natural Science).*, **17**, 69 (1999).
7. J. H. Li, X. H. Liu, *Journal of Natural Resources*, **21**, 217 (2006).

Research on the ecology spatial pattern of basic farmland guided by the concept of "negative planning"

X. Lan*, Z. Q. Wang, C. Wei, L. G. Zhang

School of Public Management, China University of Geosciences (CUG), No.388 Lumo Road, Wuhan 430074, China

After the 19th National Congress of the Communist Party of China had been launched successfully, the Chinese government showed confidence by improving the ecological environment of the whole country in changing the traditional planning method which considers the social and economic benefits rather than the ecological one. In this paper, the simulation experiment tries to delimit an area of ecological infrastructure with the guidance of the "security pattern" and "negative planning" concept which has a more favorable index of ecological environment than the traditional way in the spatial pattern planning of basic farmland. The results show that the new planning provides more high-quality and less fragmentary cultivated land than the traditional one, and the cultivated land is more adaptable in biodiversity and producing activity, which is in line with the development of environmental policies of the Chinese government and the global sustainable development.

INTRODUCTION

As a core part of Chinese "keep farmland in 1.8 billion mu (approximately 120 million hectares)" policy, the protection of basic farmland should be attended to with great importance, whether in laws and regulations or planning and coordination. However, due to the accelerated rate of urbanization, the construction land is in short supply and as a result, certain farmlands with high yield and quality of grain production are occupied. In the land planning (i.e. basic farmland planning), in order to meet the largest investment and the best urban development, some local governments will customize certain preferential policies for the targeted investors, and at the same time, in order to achieve the quantitative index on basic farmland asked by the upper governments, they often stick to the principle of "label the bad lands instead of the good ones; label the far away lands instead of the closer ones" [1], which leads to a drop of land quality. Also, some of the construction projects and land usages may cut the farmland into pieces, which not only affects the continuity of basic farmland, but also destroys the ecological environment. Due to this, the function of arable land cannot be played fully.

Since the 1980s, the overseas scholars have improved the recognition on arable land protection from social and economic benefits to the ecological function [2], and have gradually moved the focus to the improvement of environmental damage caused by the deagriculturalization of arable land, protection of ecology and innovation of criteria of farmland division [3-6]. In China, some scholars have proposed that when protecting arable land, we should pay more attention to its multifunctionality, specify the reasonable direction of usage and carry out the practical plans for usage, enhancing the mobility of protecting the cultivated land [7-9]. Since 2002, Professor Yu Kongjian has proposed the term "anti-planning" and has combined it with urban planning [10-12]. Many other experts and scholars have also begun to study the integration of "anti-planning" and planning on land and urban areas, such as making new, comprehensive plans with ecological security, grain security and rational use of construction as their core, protecting the land from being polluted and optimizing the overall land pattern through negative planning [13,14].

On the basis of "negative planning", this paper sticks to the principle of protecting the regional ecology and ensuring the sustainable development. Combining the regional agricultural land classification, this paper studies the spatial pattern of basic farmland protection in Baokang county, in order to set a comprehensive evaluation system which can maximize the fundamental and derivational functions of arable land. According to the study, on the one hand, protection of farmland, ecology and landscape can be achieved; on the other hand, the avoidance of destruction and waste of high-quality arable land can be met to improve the sustainability of arable land on the aspects of its multifunctionality.

Introduction of the study area, data resources and research methods

Baokang county is located in the northwest mountainous area of Hubei province, and southwest of Xiangyang city, with a longitude of 110°45′—

To whom all correspondence should be sent:
E-mail: lanxi_cug@163.com

111°33´, and a latitude of 31°21´—32°06´. It is the only mountainous county in Xiangyang city, east to Nanzhang county, west to Shennongjia area, south to Yuan'an, Yiling and Xingshan, and north to Gucheng and Fang counties. In 2010, the total land area of the county was 322152.57 hectares, agricultural land of which was 309460.51 hectares, accounting for 96.06% of the total area; and construction land was 8376.41 hectares, accounting for 2.6% of the total area; the rest was 4315.65 hectares, accounting for 1.34% of the total area.

The basic data come from the "county-level overall plan of land utilization in Baokang county (2006-2020)", farmland classification report of Baokang county and base information of "The second land survey data and updating data of Baokang county". The geological hazard data are in the "Prevented and cured plan of geological disasters from 2006 to 2020". The socioeconomic data come out of the "Statistical yearbook of Hubei province in 2005 to 2010" and "Statistical yearbook of Xiangfan city".

The research is based on the comprehensive productivity of agricultural land gradation evaluation of cultivated land, determination of the spatial distribution of cultivated land, delimitation of an area of ecological infrastructure (or EI zone) with the guidance of "security pattern" and "negative planning" concept. The spatial distribution of cultivated land and EI zone was analyzed by GIS software, and the spatial distribution of cultivated land which is inside or outside the EI zone was finally obtained and a new pattern of farmland protection was established (Fig.1).

EXPERIMENTAL

Research analysis and calculation

Comprehensive productivity index of cultivated land can be figured out from the theoretical and actual unit area yield of cultivated land in agricultural land gradation evaluation. The particular formula is expressed as:

$$Q_{1i} = \frac{c_i}{c_q} \qquad (1)$$

$$Q_{2i} = \frac{t_i}{t_q} \qquad (2)$$

$$Q_i = \sqrt[2]{Q_{1i} \times Q_{2i}} \qquad (3)$$

where Q_{1i} is the actual productivity advantage index of the ith unit; C_i and C_q represent the actual unit area yield of cultivated land of of the ith unit and the average actual unit area yield of cultivated land of the whole county, respectively; Q_{2i} represents the theoretical productivity advantage index while t_i and t_q represent the theoretical unit area yield of cultivated land of of the ith unit and the average actual unit area yield of cultivated land of the whole county, respectively; Q_i means the comprehensive productivity index of cultivated land of the ith unit.

Q_i value is greater than 1, which shows that the comprehensive productivity of this unit is higher than the average level of the county. The higher the Q_i value, the higher is the comprehensive productivity of the unit area, also meaning that the comprehensive quality of the cultivated land is better. Q_i value is less than 1, which shows that the comprehensive production capacity of this unit is lower than the county average.

With cultivated land comprehensive productivity advantage index, the comprehensive productivity of cultivated land in Baokang county and the comprehensive quality of cultivated land can be evaluated. The research divides cultivated land comprehensive productivity advantage index into five levels using ArcGIS. The first level is the highest quality of cultivated land, and the fifth level is the relatively poor quality of cultivated land.
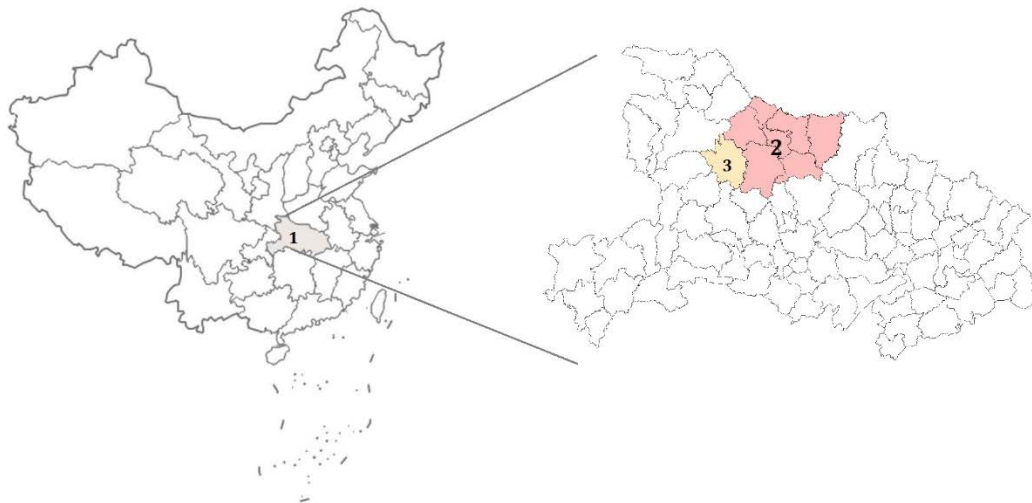

Fig.1. Location of study area. The administrative divisions are: 1: Hubei Province, 2: Xiangyang City, 3: Baokang County.

Figure 2 shows that the distribution of basic farmland should be planned from the high-quality level to the low-quality level according to the spatial distribution of cultivated land quality grade and the spatial distribution of the EI zone.
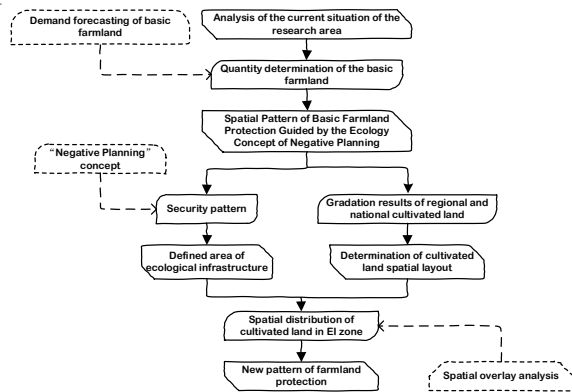

Fig. 2. Research approach

The overall planning of the EI zone

The overall planning of regional EI analysis includes three kinds of process in Baokang county (including the soil and water conservation, biological conservation, cultural and recreation) using the method of landscape security pattern with natural characteristics, biological characteristics and cultural characteristics of Baokang county and the establishment of ecological security pattern. Finally, results of landscape safe pattern will be superimposed and analyzed, then, the comprehensive ecological infrastructure area under different security levels can be obtained, which provides guidance for the ecological service function of the basic farmland protecting area.

Security patterns of water and soil conservation

Considering comprehensively the influence degree of soil erosion in terms of the characteristics of natural factors in Baokang county (such as complex geological structure, soil erosion, etc.), selecting vegetation cover, slope, river reservoir waters and geological disasters to classify the grade of slope and vegetation, then buffer analyzing the area of river and reservoir in different range. The results of three factorial analyses are compared with considering the map of geologic hazards and the security patterns of water and soil conservation are obtained. They can be divided into high, medium and low security patterns at three levels: high level security pattern of soil erosion is slight, which should maintain the current situation and prevent human destructing activities; at the medium level of security the pattern is sort of heavier, it should be classified as a secondary protected area; and the low level of security pattern, which should be a key protected area is in the pattern of serious soil erosion with a fragile environment (Table 1).

Table 1. Classification assessment of conservation of water and soil in Baokang county

Level	Slope (°)	Forest land types	River and reservoir (m)	Hazardous geological area
1	> 25	Woodland	0-150	High occurrence area
2	15~25	Shrubland	150-450	Medium occurrence area
3	0~15	Others	450-600	Low occurrence area

Security patterns of biological conservation

Wildlife in Baokang county is abundant, while the forest coverage rate of the total land area is 79%. But due to the infrastructure construction (such as large transport and water conservancy) and the development of the industrial park, those series of human activities make the destruction of habitat increasingly serious. The biosecurity of Baokang county suffered serious interference shown as narrowing home range of wildlife and biodiversity decrease. In order to determine the impact of these human factors on biosecurity, the security patterns of biological conservation in this research should be analyzed based on the resistance surface model which can be established with the minimum cumulative resistance (MCR) model [15]:

$$MCR = f_{min} \sum_{j=n}^{i=m} D_{ij} \times R_i \quad (4)$$

In the model, D_{ij} presents the distance from the source point I to the target point J to which the species move, R_i means the resistance coefficient of the target point J to the species, and $\sum$ represents the distance and resistance accumulation from the source point I to the target point J.

Minimum cumulative resistance model analysis should first determine the origin of species. Based on the wild animals and plants characteristics of Baokang county, in the research *Syrmaticus reevesii* was selected which is a species of first class national protected animals in China as representative animal, and determined the source type shrub distributed in the west, south and southeast of Baokang county; after the first step, using the Delphi method and literature methods to formulate the resistance coefficient of each element and limit it between 0 to 300 to establish the species resistance surface. Finally, using conversion tool in GIS to rasterize the current situation map of the resistance coefficient and source point figure of biological protection pattern, the MCR model was constructed using the "cost distance" of spatial analysis faculty in GIS,

setting up the space motion resistance side of biological species resistance in Baokang county, and ultimately determining the security patterns of biological conservation in Baokang county (Table 2).

Table 2. Security pattern of biological conservation in Baokang county

Factor	Classification	Resistance Coefficient
Land coverage pattern	Shrubland	0
	Others Forestland	10
	Woodlands	20
	Garden Land	30
	Cultivated Land	50
	Unutilized Land	100
	Rural Residential Land	200
	Organic Town	300

Security patterns of cultural recreation

Topography, landscape, scenic spots and nature reserves all have a great influence on the recreation pattern. Baokang County is bordering Shennongjia area, which is rich in forest resources, and the natural landscape has a very high value of appreciation.

The analysis and simulation method of security patterns of cultural recreation is equal to the security patterns of biological conservation by using the MCR model.

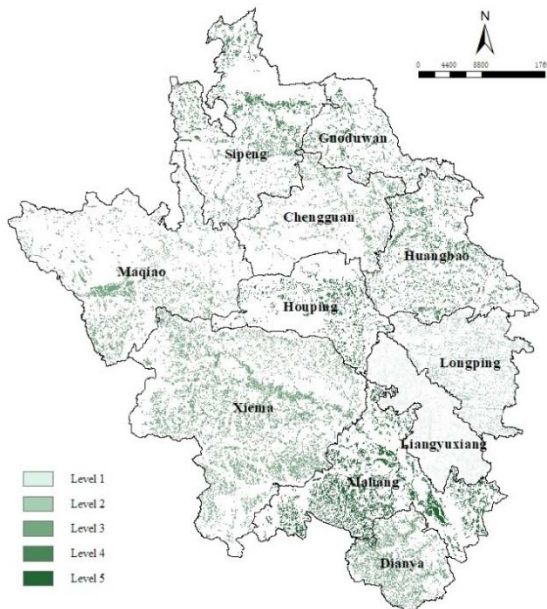### Comprehensive ecological security pattern analysis

Fig. 3. Distribution pattern of comprehensive quality of cultivated land of Baokang County

The (a) part in figure 3 shows that problems of soil and water conservation in Baokang county are serious and the ecological environment is relatively fragile due to the larger area of the medium level pattern in security patterns of water and soil conservation than the high level pattern. In the (b)

and (c) parts which show the security patterns the local authority should also preserve and keep the original natural ecology and human customs and habits in order to avoid human-caused destruction.

Table 3. Security pattern of cultural recreation in Baokang county

Factor	Classification	Resistance Coefficient
Land coverage pattern	Shrubland	0
	Others Forestland	0
	Woodlands	10
	River and Reservoir	20
	Scenic and Recreation Facilities Land	30
	Garden Land	40
	Cultivated Land	100
	Unutilized Land	200
	Other Construction Land (except for Scenic and Recreation Facilities Land)	300

Three comprehensive security patterns, based on the analysis of Baokang County Soil and water conservation, biodiversity conservation and local culture and recreation system, finally formed the regional ecological infrastructure in Baokang county. In this paper, the statistical method of setting weights was used to calculate the safety level of ecosystem facilities. Compared with biological conservation and rural recreation, soil and water conservation has more important influence on its ecological security pattern in two aspects in Baokang county by reason of its peculiarity of being a county in a mountain area, so the security patterns of water and soil conservation have a weight of 0.4, while the security patterns of biological conservation and rural recreation are all 0.3. Quality distribution of cultivated land under different EI grades can be achieved by overall analyzing the figures of security patterns of ecological infrastructure and the distribution pattern of comprehensive quality of cultivated land. Table 4 shows that the amount of cultivated land at the middle, high and low levels of EI accounts for 53.89%, 38.44% and 7.67% of the total cultivated land area. The cultivated land in the EI zone mainly consists of cultivated land of level 1 to level 4, and the areas of levels 2 and 4 are larger than of the levels 1, 3 and 5, while the area of level 5 is the smallest one, which is just 0.43%, 1.71% and 5.06 % of the total area.

Calculation of the number of basic farmlands

So far, the traditional way to determine the amount of basic farmland is the superior departments of land management to evaluate comprehensively the number of basic farmlands by collecting and analyzing the natural characteristics of regional

Table 4. The cultivated land on statistics in different grades of EI zone

Level of Cultivated land	Grade of EI zone					
	EI-Low		EI-Medium		EI-High	
	Area (hectare)	Percent (%)	Area (hecrare)	Percent (%)	Area (hectare)	Percent (%)
1	138.66	2.64%	2959.31	6.87%	4075.60	9.46%
2	601.02	1.40%	4744.24	11.02%	6423.43	14.91%
3	790.03	1.83%	2511.30	5.83%	3477.44	8.07%
4	587.06	1.36%	5601.96	13.01%	7056.25	16.38%
5	186.25	0.43%	737.29	1.71%	2178.22	5.06%
Subtotal	3303.01	7.67%	16554.09	38.44%	23210.95	53.89%
Total of Cultivated Land	43068.04	100%	43068.04	100%	43068.04	100%

social and economic conditions based on land management departments of the county to report the amount of cultivated land, then transmit the policy indicators to the department of the county..Although this method facilitates the administration of the land management department and enables the targets to be completed on time, the grain production capacity of the basic farmland is still not guaranteed and is only a formalism.

The purpose of protection of basic farmland is actually to protect the safety of food production, to balance the relationship between supply and demand of population growth and food production; quantity index is representative of the regional farmland production capacity, rather than just an area. Therefore, after the primary consideration to determine the amount of basic farmland is the basic farmland demand (S) combined with the policy indicators, transmitted to the superior land management departments, the final decision on the production capacity can be ensuring the quantity standard of basic farmland at the same time.

$$S = \begin{cases} S_1, & When\ S_1 < S_2 \\ S_2, & When\ S_1 \geq S_2 \end{cases} \quad (5)$$

S_1 and S_2 represent the predicted area of basic farmland and the policy indicated target of basic farmland. When S_1 is greater than S_2, it means that the actual protected area is equal to the area of prediction; on the other hand, when S_1 is smaller than S_2, the actual protected area should be equal to the policy indicated target in order to meet the amount of protected basic farmland.

The predictor formula is:

$$DAC = \frac{DTG \times SUP}{IMC \times OPG \times GPAP} \quad (6)$$

$$DTG = PEO \times PER \quad (7)$$

In the formula, DAC means the quantity demand of basic farmland, DTG and SUP mean quantity demand and self-sufficiency rate of grain, respectively; IMC represents the multiple crop index while OPG and GPAP present the ratio of sown area

of grain crops to total sown area of crops and the single yield of sown area of grain crops, respectively; PEO and PER represent population size and grain demand *per capita*.

According to the formula above, the protected area of basic farmland of Baokang county in 2020 will be 34299.96 hectares.

Determination of spatial pattern of basic farmland

In order to enable multiple functions of cultivated land to develop limitless, the traditional single producing function of cultivated land should be changed including ecological protection, cultural and regional sustainable development functions. According to the regional situation in Baokang county and the basic farmland distribution inside and outside of the EI zone, this research will select the high level of security as the optimal scheme and program of the layout of basic farmland.

When the area of high quality cultivated land is larger than the area of basic farmland, the basic farmland in the EI zone should be included from high to low according to the comprehensive quality; otherwise the superior quality of basic farmland will be included first, then the high quality cultivated land can be brought into based on the farmland grades (from high grade to low grade) and the area size.

According to different safety levels in the EI zone and the statistics of cultivated area in Baokang county in the actual situation, the research superimposed the high level of security pattern in the EI zone and the distribution pattern of comprehensive quality of cultivated land as the basic map of basic farmland spatial planning, at the same time to ensure that the amount of basic farmland is not lower than the basic farmland protecting goals, the high quality of cultivated land which are near the edge of EI zone but not in the zone will be selected as the basic farmland. At last, the spatial pattern of basic farmland protection was achieved by combining and analyzing the pattern figures of basic farmland inside and outside the EI zone (Fig. 4).
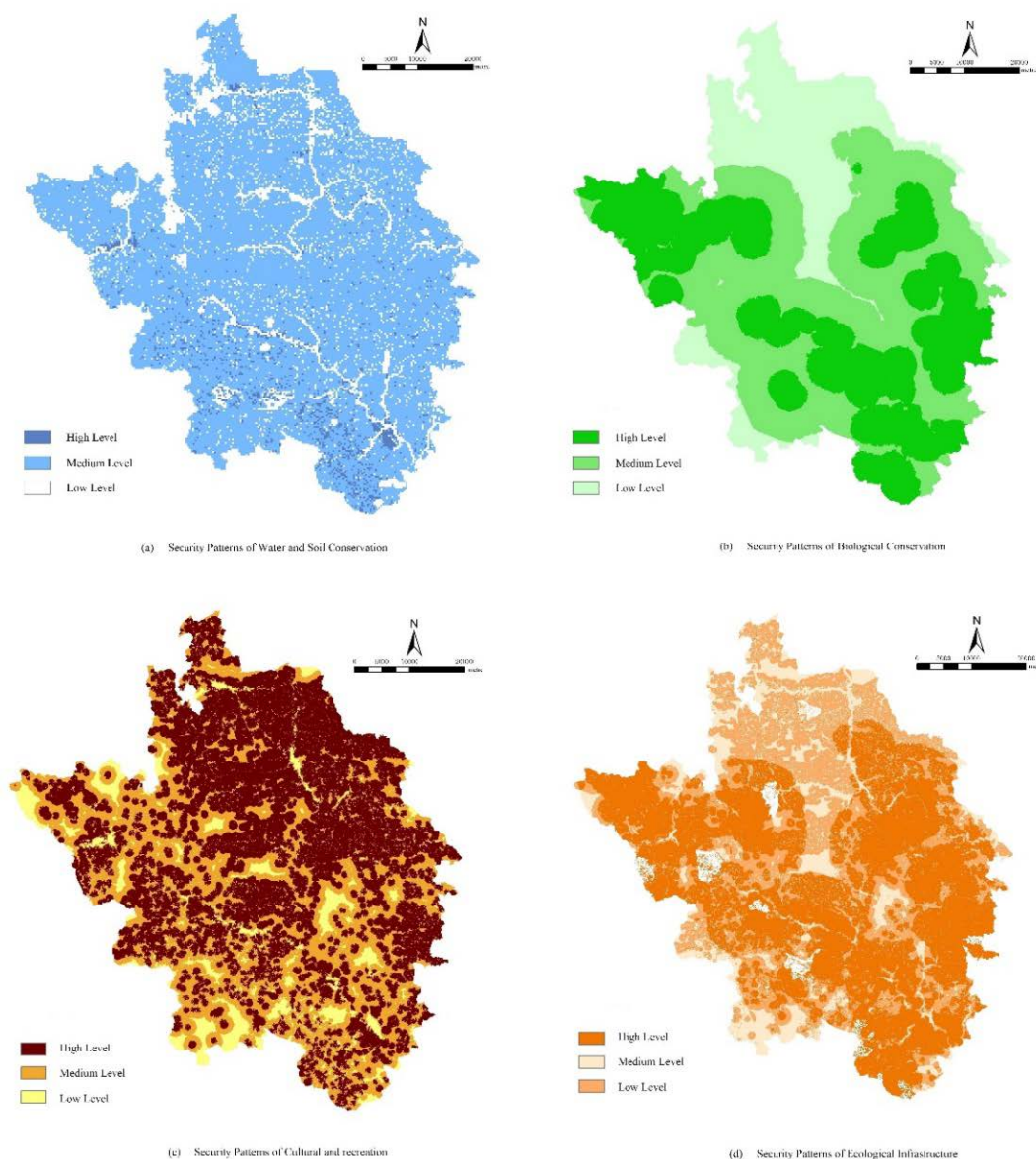
Fig. 4. Research process of the ecological Infrastructure security patterns of Baokang county

RESULTS AND DISCUSSION

Experimental results

Quantitative structure comparison. In the research, the planned area of basic farmland was 36849.52 hectares, by 1423.63 hectares more than the current situation, and by 5024.15 hectares more than the quantity issued by Xiangyang city, which is 31825.37 hectares.

Qualitative comparison. By superimposing and analyzing the current situation figure of basic farmland and the one which is new planned with "negative planning" concept, the picture below (Fig.5) shows that after planning, the fifth grade was not included in the basic farmland, and the proportion of the fourth grade dropped from 56.99% to 34.35%, while the proportion of the first and third grade of cultivated land greatly increased, while the occupancy of the second grade was flat.
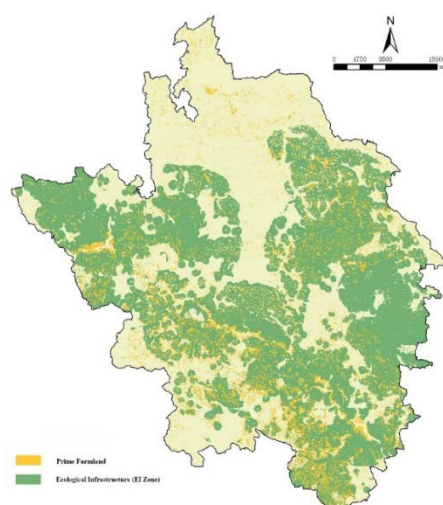
Fig. 5. Distribution pattern of basic farmland protection of Baokang county in 2020

Distribution comparison

Compared with 66.44% of the basic farmland distribution in EI zone which is planned renewal in this paper, the basic farmland of current situation figure distributed in the EI zone is 60.56% (Fig.6).
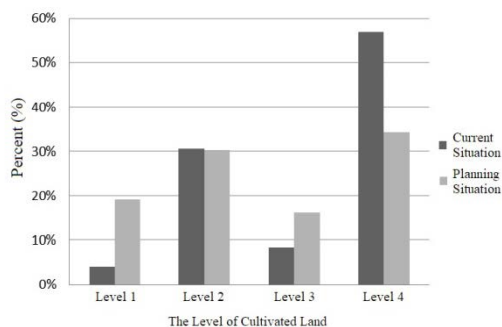

Fig. 6. Qualitative comparison of basic farmland of Baokang county

DISCUSSION

The number of cultivated lands in the current situation of Baokang county is less and scattered. The high-quality cultivated land is fewer and discontinuous, and the ecological environment is fragile. Therefore, the influence factors to classify

the basic farmland in Baokang county are more complex. Only the use of quantitative and qualitative comparison to classify the basic farmland cannot safeguard the sustainable development of cultivated land in Baokang county.

The research simulates and marks off a reasonable security pattern of basic farmland by building the ecological infrastructure and distribution pattern of comprehensive quality of cultivated land with the "negative planning" concept. The two aspects of ecological protection and landscaping are promoted to the same height as the quantity and quality, which can not only realize the sustainable development of the basic farmland, but also maximize the derivative function of the basic farmland. At the same time, comparing with the current situation pattern of basic farmland, the new plan considers more the ecological, production and sustainable development in constructing the pattern of basic farmland in Baokang county.The comprehensive quality of the basic farmland was been improved while the basic functions and derivative functions also were fully developed. At the same time the indices of basic farmland protection Xiangyang city were formulated.
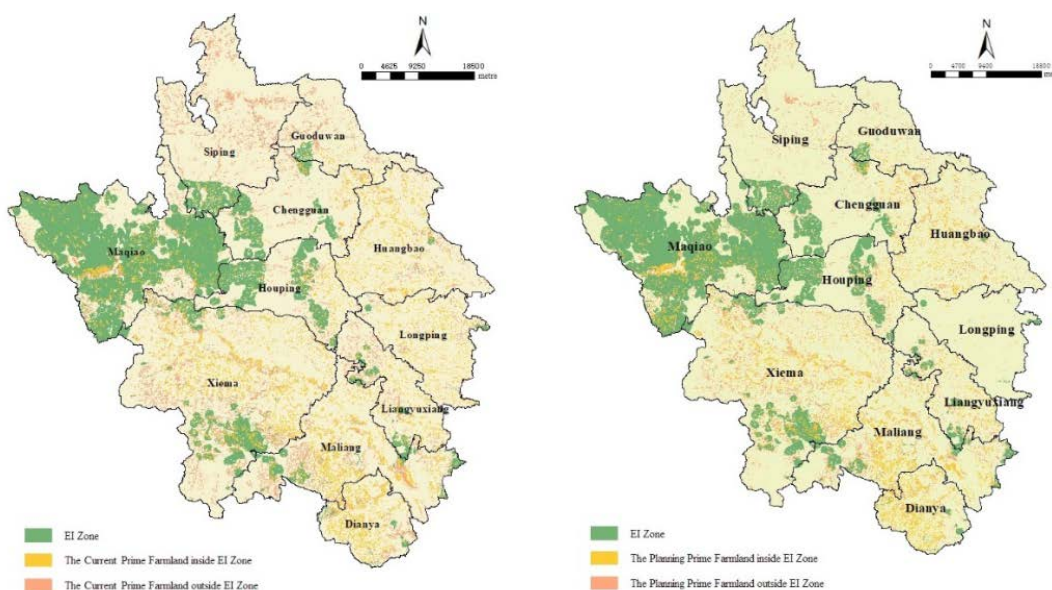

Fig. 7. Comparison of cultivated land comprehensive quality between actually graph and program graph of basic farmland in Baokang county

REFERENCES

1. F.K. Qian, Q.B. Wang, Z.X. Bian, X.R. Dong, *Chinese Journal of Agricultural Resources and Regional Planning*, **34**, 22 (2013).
2. B.D. Gardner, *American Journal of Agricultural Economics*, **59**, 1027 (1977).
3. C. Perrings, L. Jackson, K. Bawa, L. Brussaard, S. Brush, T. Gavin, R. Papa, U. Pascual, P. De Ruiter, *Conservation Biology*, **20**, 263 (2006).
4. G.V. Kooten, Land resource economics and sustainable development: economic policies and the

common good, University of British Columbia Press, Vancouver, 1993.
5. D.W. Bromley, Handbook of environmental economics, Wiley-Blackwell, New Jersey, 1995.
6. C.J. Nickerson, H. Daniel, *Agricultural & Resource Economics Review*, **32**, 129 (2003).
7. G.H. Jiang, F. R. Zhang, X. B. Kong, H. F. Zhao, D. Y. Zhou, *China Land Science*, **25**, 42 (2011).
8. X. Song, Z. Ouyang, *Progress in Geography*, **31**, 859 (2012).
9. B. Fang, C. F. Wu, J. Lü, *Journal of Soil and Water*

Conservation, **20**, 177 (2006).

10. K.J. Yu, D.H. Li, *Proceedings of 2002 CAST Annual Meeting*, **22**, 12 (2002).

11. K.J. Yu, Q. Qiao, H. Yuan, B. Yan, D.H. Li, K. Liu, *China Land Science*, **23**, 24 (2009).

12. K.J. Yu, H.L. Li, D.H. Li, *Journal of Natural Resouces*, **23**, 937 (2008).

13. Y. Pan, Y.H. Liu, J. Wang, Z.R. Yu, *Acta Ecologica Sinica*, **31**, 529 (2011).

14. L. Wang, W. J. Li, *Chinese Journal of Agricultural Resources and Regional Planning*, **33**, 73 (2012).

15. J.P. Knaapen, M. Scheffer, B. Harms, *Landscape & Urban Planning*, **23**, 1 (1992).

Efficiency analysis of cross-season high-temperature energy storing in cold areas based on FLUENT simulation

K. R. Ma, M. H. Cui[*], Ch. M. Ni, R. J. Yu, X. D. Xian

College of Architecture Engineering, Hebei University of Science and Technology, Shijiazhuang, Hebei 050018, China

In this paper, by applying FLUENT simulation, a heat-storing and heat-removing system in cold areas was simulated, based on the interaction between the solar energy and the buried pipes. In spring, summer, and autumn, the soil is heated by the hot water produced from the solar energy, so the temperature of the soil is accordingly risen. This is the heat-storing stage. In winter, the cold water within the buried pipes is heated by the high-temperature soil, which can provide heat for the building. This is the heat-removing stage. According to this simulation process, the geometrical and mathematical models were established, the data when the system reaches balance were analyzed, the optimal distance for placing the buried pipes was obtained, and reference for actual projects was eventually provided.

Keywords: solar energy, buried pipe, heat-transfer simulation, heat storing, heat removing, heat providing

INTRODUCTION

Through combining with a heat-storing technology, the solar energy can be used more efficiently [1,2]. By virtue of certain storing media (such as heat storing based on hot water, heat storing based on gravel and water, heat storing based on soil with buried pipes, heat storing based on aquifer, etc.), Central Solar Heating Plants with Seasonal Storage (referred to as CSHPSS) can store solar energy (heat storing) in case of different demands for solar radiation and heat in different seasons. Through this process, the above-mentioned goal can be realized using solar energy more efficiently [3]. In this paper, among the various models of heat storing systems based on solar energy and buried pipes, the heat transfer model based on soil with buried pipes was chosen, taking the climate environment and soil environment of Shijiazhuang as an example, to simulate the long-term heat-storing and heat-removing process and analyze its energy efficiency.

In non-heating seasons, heat transfer between the water in the cold water tank and the hot water produced by the solar collectors will be conducted through the plate. When the water temperature rises, it will enter the hot water tank. When the water temperature of the hot water tank is higher, transfer between the hot water and the soil will take place.

The low-temperature water that flows out from those pipes will enter the cold water tank again, will be heated through the plate and will enter the hot water tank again. This process will circulate again and again.

EXPERIMENTAL

As shown in Figure 1, the main heat source of the whole heat providing system is the solar energy. The system can be divided into three parts [4-6]: (1) collector part, which mainly produces hot water, which is used to lift the temperature of the water tank through plate one; (2) the buried pipes part of the water tank, which is used to lift the temperature of the soil through the buried pipes; (3) the terminal of the heat users, which transfers the hot water heated by a variety of ways to the final heat users and provides heat for the building. In addition, the system is also equipped with an auxiliary heat source, pressurization through water refilling, and other devices [7].

At present, some technologies related to solar energy collectors are relatively mature, so in this paper, a simulation study on heat storing and heat removing of the soil, was conducted and its energy efficiency was analyzed.

Establishment of the geometrical model

The geometrical model consists of the following four parts: fluid (water), pipe wall, borehole backfill and ordinary soil [8,9]. In the FLUENT software, if a model is symmetrical, the symmetrical central plane can be set as a symmetrical plane, simplifying the calculation [10,11]. Because, in this paper, the buried pipes of the whole system take a cross form, so they are symmetrical in every direction. In order to reduce the time for calculation, a model based on a quarter of the whole one was established [12,13].

To whom all correspondence should be sent:
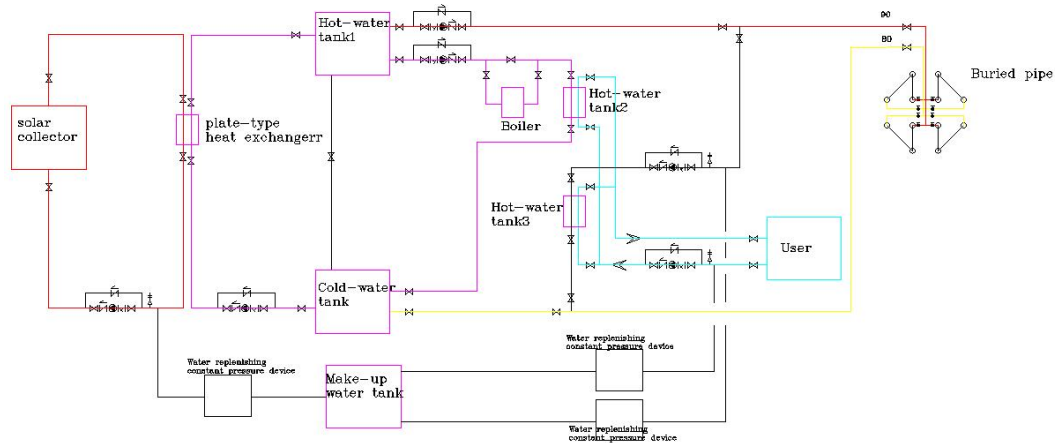E-mail: cuiminghui666@163.com

Fig. 1. System diagram on cross-season solar energy storage

The depth of the buried pipes is 20 m, which are composed of three U-pipes in a series. The outside diameter of the pipes is 25 mm. The three U-pipes are distributed in right-angle form. The size of the borehole is 150 mm. The structure is shown in Figure 2.
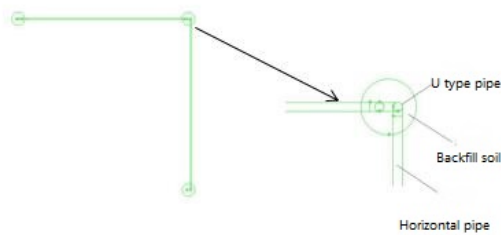

Fig. 2. Geometrical model of U-pipes and borehole backfill

In this model, the depth of the buried pipe is 20m. The distance from the farthest boundary of the soil to the outermost U-pipe is 20 m and it is divided into two parts. In the first part, the distance to the outermost pipe wall is 5m, while in the second part, the distance to the first part soil is 15 m, as shown in Fig. 3
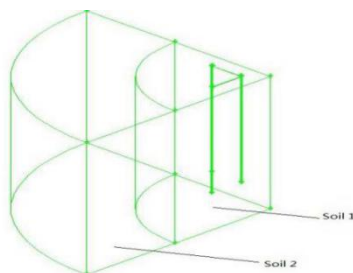

Fig. 3. Overall soil model

When the number of the drilling wells is determined, the interval among drilling wells has a great influence on heat storing and heat removing. In order to get the optimal interval, based on the above model, other specifications were left intact and only the interval among pipes was changed, establishing three models with different intervals (2m, 3m, 4m) to make comparison.

FLUENT numerical simulation

Heat transfer between the heat exchanger made by buried pipes consisting of U-pipes and the surrounding soil consisting of six processes
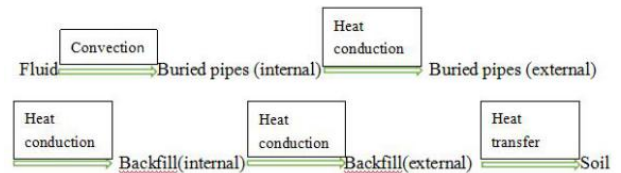
Boundary conditions and physical parameters: The soil temperature at the initial stage was set at 15°C. Insulation layer was set at the upper surface, thus, taking it as the ideal situation, the upper surface was set as the insulation surface [14]. During heat storing, the inlet temperature was set at 90 °C and the two right-angle surfaces were set as symmetrical surfaces.

RESULTS AND DISCUSSION

Determination of the thermal efficiency

For all models, during the heat storing process, the inlet temperature was 90 °C; the flow velocity was 0.5 m/s; the time for heat storing was 5880 h (245 days); and the time for heat removing was 2880 h (120 days). Then, according to the different conditions related with the heat removing process, their influence on the results was analyzed. The specific types of heat removing are listed in Table 1.

Table. 1. Experimental models of different conditions

Material	Density	Specific heat	Thermal conductivity	Viscosity
Water	998.2	4182	0.6	0.001
Backfill	2082	837	0.8	
Soil	2082	837	0.8	

Because there are several models and the simulation time is relatively long, so, in order to reduce the time for simulation, two models with 3-4-meter intervals, respectively, were first chosen,

and the inlet temperature during heat removing was set at 35℃ to conduct long-term simulation. The results from the preliminary simulation are shown in Figure 4.
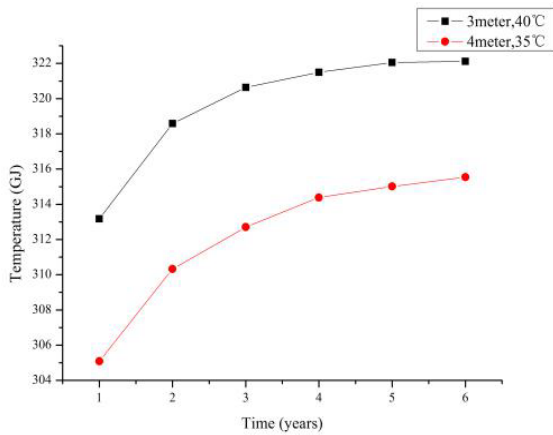

Fig. 4. Results of heat storage of soil under different conditions

According to the curve of soil temperature over time, it follows that 4 years later, when the heat storing ends, the change of the soil temperature tends to be smooth, and, at that time, the heat transfer rate reaches the highest level. So, the time for the system to reach balance is four years. Given it, each model can only simulate four years' time.

Efficiency of heat utilization under different conditions

Efficiency of heat utilization: it refers to the ratio between the heat removed from soil and the heat stored in it each year. Comparison of efficiencies of heat utilization over different intervals is shown in Figures 5-7. As can be seen, in the first year, the efficiency of heat utilization is generally low. The reason is that the soil temperature then is relatively low, so the heat stored in the soil is largely used to heat it. With the rise of the soil temperature, the efficiency of heat utilization also gradually increases. Among those models, the efficiency of heat utilization of the model with 2-meter interval begins to stabilize in the third year, with about 85% efficiency of heat utilization. However, the time for reaching stability for models with 3- and 4-meter interval was relatively long. In the actual situation, it is useless. So, from the view of practical application, the model with 2-meter interval is the best.
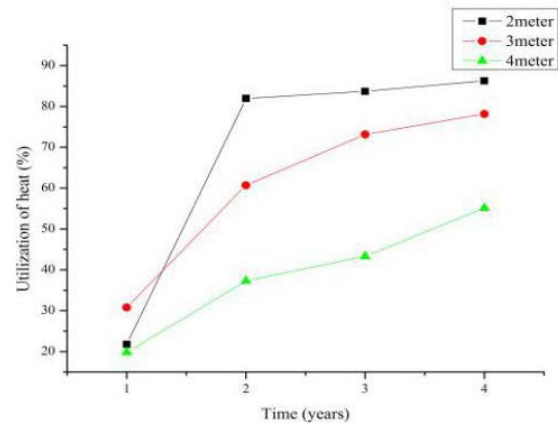

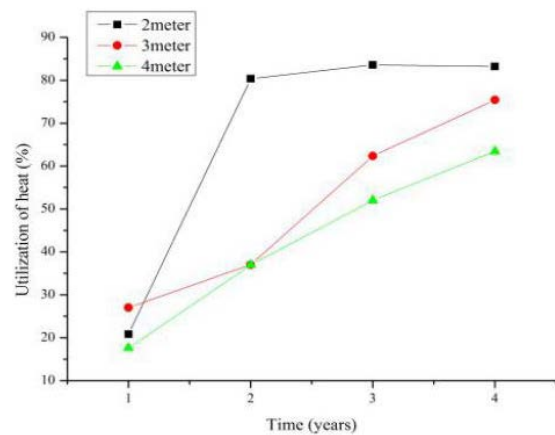**Fig. 5.** Temperature of the return water during the heat removal process is 30 ℃

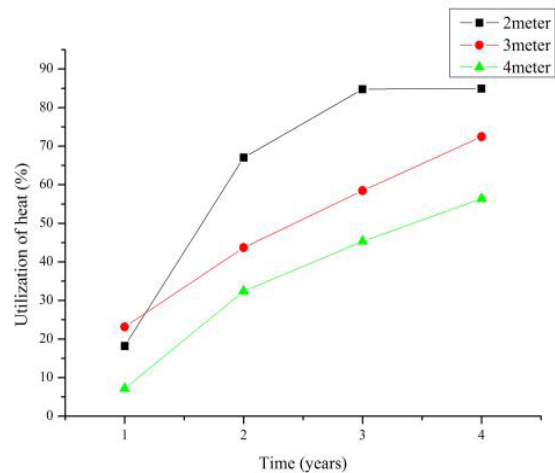**Fig. 6.** Temperature of the return water during the heat removing process is 35 ℃

Fig. 7. Temperature of the return water during the heat removing process is 35 ℃

Calculation of the heat removing amount

The change of heat removing amount of the soil over time under different conditions is shown in Figures 8-10.
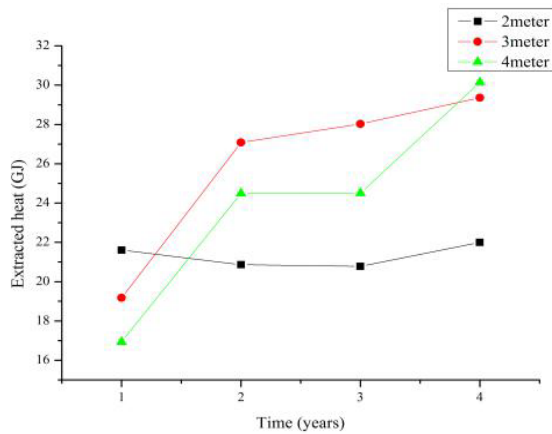
Fig. 8. Temperature of the return water during the heat removing process is 30 °C
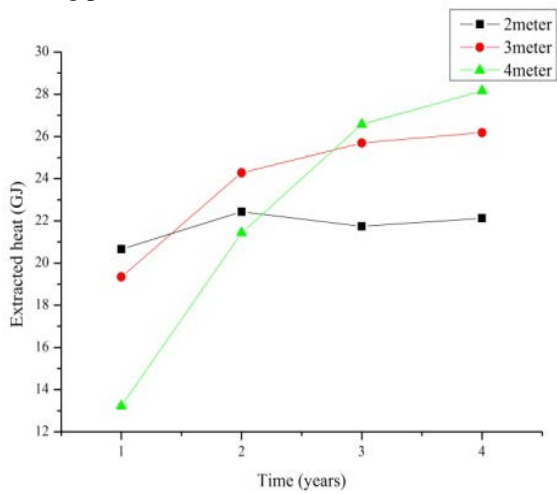

Fig. 9. Temperature of the return water during the heat removing process is 35 °C
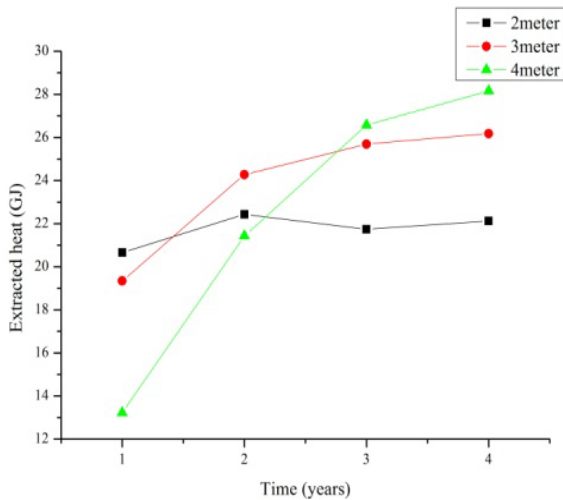

Fig. 10. Temperature of the return water during the heat removing process is 40 °C

According to the data above, when the temperature of the return water is 30 °C, the final heat removing amount under 3-meter interval is almost the same as that under 4-meter interval; when the temperature of the return water is 35 °C, based on the same condition, the removing amount under 3-meter interval is by 2.2GJ lower than that under 4-meter interval; when the temperature of the return water is 40 °C, the final heat removing amount under 3-meter interval is by 0.48GJ higher than that under 4-meter interval. After comprehensive analysis, the 3-meter interval among buried pipes was considered as the best choice.

CONCLUSION

This paper simulates the cross-season energy storing of the solar energy with regard to the heat storing and heat removing of the soil. It was concluded that for Shijiazhuang, the heat storing and heat removing can reach balance after four years, and, at the same time, the ratio between the heat removing amount and the heat storing amount tends to be stable. After considering the efficiency of heat removing and the heat removing amount, the 3-meter interval was considered as most suitable for the actual project.

Table. 2. Specific values of the heat removing amount under different conditions

Values of the heat removing amount under different conditions in the fourth year (GJ)		
Temperature of the return water		
30 °C	35 °C	40 °C
2 m	21.99	22.12	20.48
3 m	29.44	26.17	23.2
4 m	30.18	28.37	22.72

REFERENCES

1. M.Z. Zhou, *Acta Energiae Solaris Sinica*, **04**, page? (1984).
2. C. Liu, *Southwest University of Science and Technology*, **TK253**, 2012.
3. X.B. Zeng, *Chongqing University*, **F224,** 2 (2007).
4. K.F. Li, J.L. Ren, *Wireless Interconnect Technology*, **165**, 11 (2013).
5. J.J. Chen, *Energy Policy*, **39**, 5076 (2011).
6. H.L. Zhang, *Jilin University*, **F426.2,** 2014.
7. Z.R. Liu, *Municipal Technology,* **1**, 99, (2010).
8. B.B. Chen, Chongqing University, TU312.1, 2014.
9. J. Qian, Zhejiang University, S157.1 (2014).
10. Y. Li, A. Delsante, Building and Environment, 36, 59-71, (2001).
11. F.J. Wang, Tsinghua University press, TK124, 2004.
12. H. Chen, Huazhong University of Science and Technology, TK172, 2014.
13. H. Zhong, N. L. Hu, G. Q. Li, Journal of Safety and Environment,66, 1 (2017).
14. Z.Z. Han, J. Wang, X.P. Lan, Beijing Institute of Technology Press, 39, 8 (2014).

A study method of risk evaluation for children's toys

G.Z. Huang, A.W. Zhou[*], S.H. Sun, N. Wang

College of Civil and Resource Engineering, University of Science and Technology Beijing, Beijing, China

China is an important toy production and export country in the world. The injury incidents caused by Children's toys have become increasingly prominent, and the recall of toys also led to a large number of economic losses. Therefore, in this paper, the fuzzy comprehensive evaluation method is proposed for the children's toys risk evaluation. Firstly, the ETA method is used to determine the index and establish the index system of risk evaluation for children's toys. To determine the index weight, AHP method is adopted to calculate the weight of each index. Then make the fuzzy comprehensive evaluation model for the risk evaluation of children's toys. Finally, the feasibility and effectiveness of method were illustrated by an example. Result shows that it provides a new perspective and tool for the risk evaluation of children's toys.

Key words: ETA, Risk evaluation, Children's toys, Fuzzy comprehensive evaluation

INTRODUCTION

With the development of China's economy and the improvement of people's living standards, more and more children want to have their own toys, and parents are willing to spend money for their children to buy all kinds of toys with little security concerns.

China is an important toy production and export country in the world. Every year, the toy industry offers an annual product income in excess of 80 billion RMB and invests almost 6 billion dollars in the export of Chinese products [1]. Toys made in China occupy a substantial part of the international market, for example, 65% of imported toys in America and 80% of those in Australia originate from China [2]. However, the fact that toys made in China make up a large proportion in terms of recall times and recalled products indicates that toys made in China pose a threat in respect of potential safety hazards [3]. Table 1 shows the amount and the proportion of toy injury cases during the period from January to July 2014. In this duration, the product injury surveillance system of China cited 246 injury cases relating to toys from 11 different cities, accounting for 45.06% of the total amount of injury cases pertaining to children's toys and supplies injury cases.

Currently, the risk evaluation for children's toys is still far from satisfactory, therefore the majority of countries worldwide continue merely using the quality inspection according to national standards, such as the Chinese Safety for Toys criteria (GB 6675-86) and the American Safety for Toys (ASTM-F963), required by the American Society for Testing and Materials [4]. A product which is tested according to these regulations, however, does not necessarily entail having zero risk, and cannot

explicitly display this safety grading. In the view of the injury model, a simple and effective model of children's toys risk evaluation is put forward based on the method of Fuzzy-AHP. The evaluation conclusions obtained through the model and calculation are advantageous in identifying hidden dangers, thus reducing potential hazards, and ultimately preventing accidents.
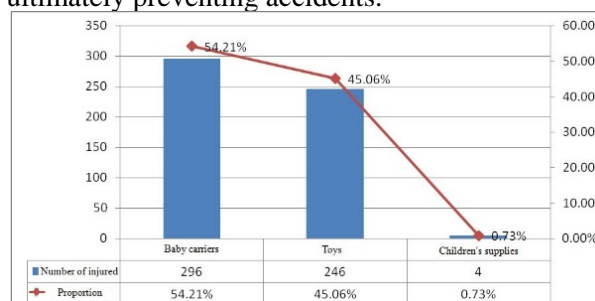

Fig. 1. The amount and proportion of children's toys and supplies injury cases

BUILDING THE INDEX SYSTEM

There are some qualitative factors necessary in the process of evaluating toys, which involve definite intension and indefinite extension, two methods which are difficult to be described in numerical form. The evaluation of these factors depends on the experience. However, if factors without measurement are impossible to be given a valuation, it would make gathering the basic data an impossible task. In this eventuality further research would not be feasible.

Some common factors have been identified in the manufacture of toys which can lead to the occurrence of potential injuries, however, the relationship between them is complex. A single-factor evaluation merely gives one factor's degree of

---

[*] To whom all correspondence should be sent:
E-mail: 1561199878@qq.com

safety from a different perspective, and is ineffective in pinpointing potential problems owing to a toy's complex manufacturing system and the fact that the influence of factors leading to injuries is so diverse. Therefore a method which can determine the weights of factors and which can carry out a comprehensive evaluation is of paramount importance.

According to the statistics on toy recall reports provided by the Consumer Product Safety Commission (CPSC) and Rapid Alert System for non-food Consumer Products (RAPEX), five types of injury models are summarized: physical wounds, chemical wounds, burns and scald wounds, those caused by suffocation and so on, and the causes are analyzed based on the theory of Event Tree Analysis (ETA). ETA is commonly used to identify the consequences which result from the occurrence of a potentially hazardous event. The system was first applied in risk assessment for the nuclear industry, but nowadays it is also used in other industries. Figure 2 shows the causes analysis of the process of physical wounds. The specific injury forms of physical wounding include compression, crash and impact, stab wounds and cut wounds, friction and so on, and the causes leading to these injuries are classified into unqualified materials, sharp pointed edges, invalid fixing devices and so on.
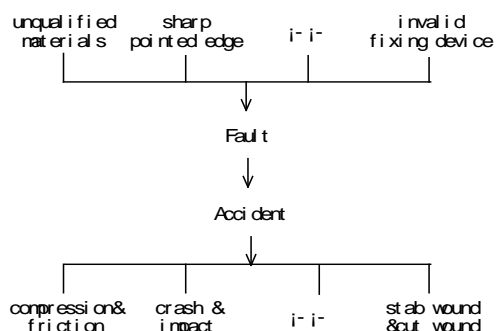

Fig. 2. The cause analysis of the process of mechanical wound based on ETA

Based upon the analysis outlined above and related literature [5], four types of toy injury causes which are used as evaluation factors for children's toys, are categorized as follows:

(a) Physical properties, including a toy's physical index, structure, strength, etc.;

(b) Flammable properties, including the material's flammability, combustibility, burning rate and so on;

(c) Chemical properties, including the content of harmful heavy metals used in the manufacturing process along with other toxic and harmful substances;

(d) Electrical properties, including overheating of batteries, explosion and burning caused by batteries, leakage of battery liquid and dangers imposed by congestion of the cell.

Table 1. Index system of risk evaluation for children's toys

Assessment object	Primary Index	Grade Two Index
Risk Evaluation for Children's Toys U	Physical properties U1	Structural stability
		Product material
		Parts Fastener
		Component strength
		Gap and opening
		Surface roughness, sharp edges, sharp tips
		Ejection kinetic energy
		Folding mechanism clearance and its reliability
	Flammable properties U2	Flame retardant properties of non metallic materials
		Flame retardant properties of textile materials
		Shell protection defect
		Parts installation problem
		Component structure and dimensions
		Battery overcharging / overdischarging
	Chemical properties U3	Content and concentration of toxic and harmful substances
		Volatile and odor of toxic and harmful substances
		Shell tightness and sealing property
		Parts installation problem
		Component structure and dimensions
		Creepage distance and clearance
		Moisture resistance
		Double insulation structure

DETERMINING THE INDEX WEIGHT

The Fuzzy Analytic Hierarchy Process entails a combination of Analytic hierarchy process (AHP) and Fuzzy mathematics [6,7]. It is one of the most effective approaches used to address uncertainty and ambiguity from a subjective perception and involves the experience of humans in its decision-making process. F-AHP combines the advantages of both the AHP and fuzzy comprehensive evaluation method, in a fuzzy environment, to consider numerous

factors, and thus uses fuzzy membership theory to adequately quantify the qualitative indicators [8,9]. The Fuzzy-AHP method is useful in providing an attribution as to which indicators significantly affect the results, the degree of membership, it confirms the factors' weight, and then carries out a comprehensive evaluation through the fuzzy transformation principle [10,11]. The traditional AHP uses a two-two and more judgment matrix which is called the 1-9 scale method. This method entails using integers from 1 to 9 to represent the comparison of results of different aspects' relative importance degree, displayed in Table 2.

Table 2. Scale method

Scale	Meaning
1	Factor A_i and factor A_j, are the same importance
3	Factor A_i is slightly more important than factor A_j
5	Factor A_i is obviously more important than factor A_j
7	Factor A_i is significantly more important than factor A_j
9	Factor A_i is extremely more important than factor A_j
2,4, 6,8	The mid-value of these two adjacent judgment values
Reciprocal	Compare A_i to A_j, get a_{ij}, so compare A_i to A_j get $a_{ij}=1/a_i$

Although each discrete number shown in the table is clear, this Scale method does not reflect the ambiguity of human judgment. Owing to this shortcoming, the Dutch mathematician Van Laarhoven, used triangular fuzzy number taken from the branch of fuzzy mathematics to carry out the transition from traditional AHP to Fuzzy-AHP. Its basic concept is to use triangular fuzzy number to replace traditional AHP's 1-9 scale and uses this to show the result of the comparison. According to this method, a fuzzy judgment matrix can be obtained from the triangular fuzzy number. A hierarchical analysis of the fuzzy environment can then be achieved. Figure 3 shows the basic steps of Fuzzy Hierarchical Analysis.

The basic steps of Fuzzy-AHP are described below

1. One must find the basic influential factors in the problems which are being studied.

2. Analyse the relation and interrelation between aspects to create an orderly hierarchical structure.

3. Make a comparison between different aspects of factors on the same level, to build a judgment matrix.

4. Based on the judgment matrix, a calculation can be made relating to weight problems, for example comparative factors' corresponding standards, and then carry out a consistency examination.

158

5. Calculate the weight of every level's relative total system and place in hierarchical order.
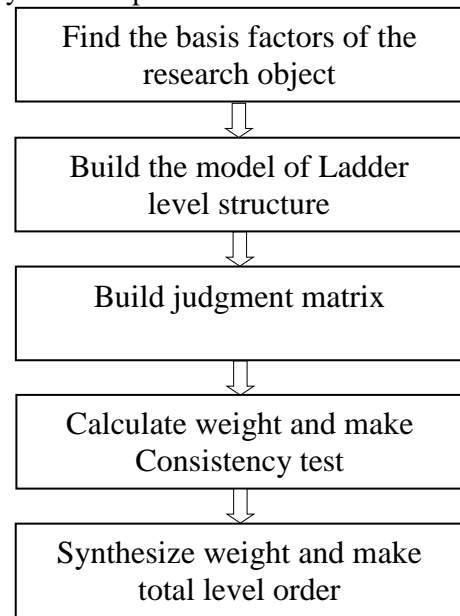

Figure 3. Basic steps of Fuzzy Hierarchical Analysis

To calculate the evaluation factors' weight, the process based on AHP is shown as follows [12]:

(a) Compare each pair of factors with the method of 1-9 scale method and form judgment matrix A, where a_{ij} indicates the relative importance degree of factor i compared with factor j. In the Fuzzy-AHP, building the judgment matrix is a crucial step. To obtain the judgment elements of the upper layer in the judgment matrix, to evaluate the relative importance degree among every set of related elements is very important, the form is shown below:

$$A = \begin{bmatrix} a_{11} & a_{12} & \cdots & a_{1n} \\ a_{21} & a_{22} & \cdots & a_{2n} \\ a_{m1} & a_{m2} & \cdots & a_{mn} \end{bmatrix} \quad (1)$$

Or A= [a_{ij}], i, j=1,2….n

(b) Calculate the products M_i of the elements in the same line of judgment matrix A;

(c) Calculate W_i, then the root of M_i, obtaining the weight W_i^0, and then form the weight set:

$$W = \begin{bmatrix} W_1^0 & W_2^0 & \cdots & W_n^0 \end{bmatrix}^T \quad (2)$$

where $W_i^0 = \dfrac{W_i}{\sum_{j=1}^{n} W_j}$ (3)

(d) Calculate the maximum feature root λ of the judgment matrix A, where

$$\lambda_{max} = \sum_{i=1}^{n} \frac{(AW)_i}{nW_i^0} \quad (4)$$

(e) Check the consistency of judgment matrix A.

Calculate consistency index CI and consistency rate CR. A number of experts note the importance of n indicators on the same layer by using the Delphi

method, then establish the judgment matrix, and finally check the consistency. If CR is less than 0.1, the judgment matrix A meets the requirements of the consistency and the weight set W can be adopted. Otherwise, the judgment matrix A can be adjusted. The CI and CR are described as follows:

$$CI = \frac{\lambda_{max} - n}{n - 1} \qquad (5)$$

and, $CR = \frac{CI}{RI}$ (6)

where, RI is the mean random consistency index shown in Table 3.

Table 3. The values of RI

n	1	2	3	4	5
RI	0.00	0.00	0.58	0.90	1.12
N	6	7	8	9	10
RI	1.26	1.36	1.41	1.46	1.49

FUZZY COMPREHENSIVE ASSESSMENT METHOD

The fuzzy comprehensive evaluation method [13] is a kind of comprehensive evaluation method for complex systems with multiple levels and multiple factors, based on fuzzy mathematics and applied the principle of fuzzy relation synthesis to quantify the unclear boundary factors. Because the assessment is concerned with many factors, the multi-level fuzzy evaluation method was used in this paper. Based on the fuzzy mathematics theory [9], fuzzy comprehensive evaluation for children's toys was carried out.

Evaluation factors

According to the index system of emergency capability assessment, determine the evaluation factors set: $U = \{U_1, U_2, ..., U_4\}$, $U_1 = \{U_{11}, U_{12}, U_{13}, ..., U_{18}\}$, $U_2 = \{U_{21}, U_{22}, U_{23}, ..., U_{26}\}$, $U_3 = \{U_{31}, U_{32}, U_{33}\}$, $U_4 = \{U_{41}, U_{42}, ..., U_{46}\}$

Comment sets

Comment set is a set of evaluation results of the evaluation object. According to the fuzzy characteristic of children's toys risk evaluation index, 5 grades of reviews (i.e., excellent, good, moderate, qualified and unqualified) were used as the evaluation sets to evaluate emergency capability assessment of port coal storage base, marked $V = \{v_1, v_2, v_3, v_4, v_5\}$. In order to more directly reflect the evaluation results, assign the 5 comment sets a value from 0-1, shown in table 4.

Table 4. The score of each level

Level	Value
Excellent	100-80
Good	80-60
Moderate	60-40
Qualified	40-20
Unqualified	20-0

Degree of membership

Because the risk is difficult to be quantified, the fuzzy statistical method was used to determine the degree of membership. The expert graded the indicators according to the given set of V, and then registered the statistics of the frequency of each target. The membership degree of index uij is a ratio between the frequency and the total number of experts.

$$r_{ijl} = {n_{ijl}}/{N} \qquad (7)$$

By determining the membership degree, the fuzzy evaluation matrix is obtained.

$$R_i = \begin{bmatrix} r_{i11} & \cdots & r_{i15} \\ \vdots & \ddots & \vdots \\ r_{im1} & \cdots & r_{im5} \end{bmatrix} \qquad (8)$$

Assessment of Primary Index

According to the weight matrix ω_i and evaluation matrix R_i, carry on the grade two index and primary index evaluation calculation.

$$R = B_i = \omega_i R_i = \begin{bmatrix} \omega_1 R_1 \\ \omega_2 R_2 \\ \omega_3 R_3 \\ ... & ... \\ \omega_4 R_4 \end{bmatrix} \qquad (9)$$

Fuzzy comprehensive assessment

After each evaluation index of the index layer is evaluated, the evaluation matrix C is obtained by fuzzy comprehensive evaluation of the criteria layer index U_i.

$$C = W^T R = [c_1, c_2, c_3, c_4, c_5] \qquad (10)$$

The comprehensive evaluation matrix C is characterized by the form of membership degree, but the result is not very intuitive. So select the median value of the value of the critical value of the evaluation grade, $D = (90, 70, 50, 30, 10)$, as the rank weighted vector of the evaluation set:

$$E = CD^T \qquad (11)$$

According to the E value, determine the risk level of children's toys. This method has been widely used in the field of environmental quality [14-15], for example building [16] and petrochemicals [17] and receives satisfactory feedback, although it is seldom used in toy risk evaluation.

APPLICATION EXAMPLE

A kitchen model was taken as the application example in this article. The toy was assembled employing the models of water tank, cupboard and refrigerator, and some components can be dismantled. Prior to the recall date, the manufacturer has received 48 complaints, one of which is a serious accident in which a child became asphyxiated from

159

swallowing a component and subsequently recovered following removal of the object.

Calculate the index weights of evaluation factors

According to the AHP method to calculate the weight of each layer index，taking U1—U4, 4 primary indices were taken as the criteria layer indices, as an example.

Employing the 1-9 scale method, the judgment matrix A was formed by some senior experts according to their experience.

$$A = \begin{pmatrix} 1 & 4 & 2 & 5 \\ 1/4 & 1 & 3 & 3 \\ 1/2 & 1/3 & 1 & 4 \\ 1/5 & 1/3 & 1/4 & 1 \end{pmatrix}$$

After M_i, the products of the elements in the same line of judgment matrix A and W_i, then the root of M_i were calculated, the weight W_i^0 was obtained and the weight set W was formed.

$$W = \begin{bmatrix} 0.503 & 0.245 & 0.180 & 0.072 \end{bmatrix}^T$$

It is known that the maximum feature root λ is 3.016, the consistency index CI is -0.328 and the consistency rate is -0.36 following the calculation. As CR was less than 0.1, the judgment matrix A meets the requirements and the weight set W is identified.

Forming the membership matrix R

Table 5 shows ten senior experts' evaluation levels for each evaluation factor, based on their experience.

Table 5. Experts' evaluation table

	V1	V2	V3	V4	V5
U1	0	1	3	5	1
U2	1	4	3	2	0
U3	2	5	2	1	0
U4	5	4	1	0	0

The membership matrix R formed according to the data in Table 5 was processed using the method of normalization.

$$R = \begin{pmatrix} 0 & 0.1 & 0.3 & 0.5 & 0.1 \\ 0.1 & 0.4 & 0.3 & 0.2 & 0 \\ 0.2 & 0.5 & 0.2 & 0.1 & 0 \\ 0.5 & 0.4 & 0.1 & 0 & 0 \end{pmatrix}$$

Fuzzy comprehensive assessment

Using fuzzy comprehensive evaluation to determine the risk level:

$$C = W^T R =$$
$$[0.0965 \quad 0.2671 \quad 0.2676 \quad 0.3185 \quad 0.0503]$$
$$E = CD^T = 50.82$$

Therefore, the comprehensive evaluation of the kitchen toy was 50.84, between 60 and 40. The level is general, need to moderate.

CONCLUSIONS

1. In this article, only four evaluation factors were considered. However, as awareness of safety and environmental protection is raised, environment protection and biosafety will be considered as other important evaluation factors.

2. As the score of evaluation level, the degree of membership and the weight all depend considerably on the experts' experience; it is the senior experts who will be invited to participate in the practical operation.

3. According to the application example, it is explained how the model of children's toys risk evaluation based on Fuzzy-AHP is calculated and that the process is deemed simple enough to change the qualitative description into a quantitative analysis.

4. The weights of the evaluation factors based on the model are in accordance with conclusions from corresponding reports and the application example.

5. Collection of more extensive data, test of the accuracy of the evaluation theory and relevant improvements will be needed in further study through empirical research. The operating model needs continuous analysis and research to adapt to the changes and adjustments in the market, which will certainly promote the overall development and safety in the toy industry.

REFERENCES

1. J.J. Shi, *China Quality Supervision*, **6**,14 (2005).
2. X.L. Yin, *Safety & Health at Work*, **6**, 16 (2001).
3. Y.S. Wang, L. Feng, Standard Science, **5**, 47 (2009).
4. N. Liu, J.H. Zhang, W. Xu. *IEEE Transactions on Power Delivery*, **2,** 876 (2011).
5. T.S. Wang, J. Li, *Inspection and Quarantine Science*, **5**, 71 (2008).
6. L.A. Zadeh, *Information and Control*, **3**, 338 (1965).
7. T.L. Saaty, *Fundamentals of Decision Making and Priority Theory With the Analytic Hierarchy Process*, **1**, 478 (2000)
8. X. Zheng, Z.M. Zhao, J. Xu, *Technology & Economy in Areas of Communications*, **6**, 41 (2010)
9. G.N. Xu, F. Jiang, *Journal of Safety and Environment*, **2**, 196 (2010).
10. M. Chen, X.P. Jiang, Z.S Xu, *China Safety Science Journal*, **8**, 119 (2008).
11. J.D. Song, Z.H. Tian, *Construction Safety*, **9**, 17 (2008).
12. L.F. Wang, S.B. Xu, *Analytic Hierarchy Process Introduction*, **1**, 87 (1990).

13. R.P. Tong. *The Application of Common Safety Evaluation Method*, **1**, 200 (2010).
14. H. Liu, H.B. Zhang, *The Chinese Journal of Geological Hazard and Control*, **4**, 82 (2007).
15. X. Chen. *Computer Engineering and Design*, **10**, 1847 (2004).
16. Z.B. Wei, G.R. Zhu, N. Ma, *Journal of Safety Science and Technology*, **6**, 55 (2005).
17. D.Y. Xia, Q.C. Kang, D.D. Jia, X. H. Cheng, J. Liu, X. Deng, *China Safety Science Journal*, **8**, 80 (2008).

Research of *Morinda officinalis How's* oligosaccharide extraction and antidepressant effects

X.J. Li[2], S.Y. Ma[1], D. Cheng[1], H.S. Chang[2], L.L. Li[2], Y. Lu[1*]

[1]*School of Traditional Chinese Medicine, Beijing University of Chinese Medicine, Beijing 100029, China*

[2] *School of College of Traditional Chinese Medicine, Beijing University of Chinese Medicine Beijing 100102, China*

Morinda officinalis How, as a traditional Chinese medicine aiming at nourishing kidney yang, not only can remove wind-dampness effects and strengthen muscles and bones, but, according to modern research, has also antidepression effect, enhances immunity and other functions. These functions are related to its complex chemical composition. *Morinda officinalis How*'s polysaccharide has been widely used in food, health care products and other fields. At present, in the field of medicine, oligosaccharides from *Morinda officinalis How* gain more attention. A number of experiments show that *Morinda officinalis How*'s oligosaccharides have a good antidepressant effect with less toxic side effects compared with Western medicines. However, the physical and chemical properties of oligosaccharide monomers are similar, so oligosaccharide monomers are hard to be separated and detected. This paper organized literature related to the chemical composition and pharmacological effects of *Morinda officinalis How* at home and abroad, and summarized the extraction method and antidepressant effect of *Morinda officinalis How*'s oligosaccharides. In addition, it provided scientific basis for further development of *Morinda officinalis How* medicine, and tried to improve the utilization of *Morinda officinalis How*.

Keywords: *Morinda officinalis How*, Oligosaccharides, Antidepressant effect, Extraction

INTRODUCTION

Morinda officinalis How, as dry roots of the *rubiaceae* family, is classified as a top grade in *Shennong's Classic of Materia Medica*. Together with bitter cardamon, fructus amomi and betel nut, they are known as *four southern medicines. Morinda officinalis How* is effective on nourishing kidney yang, removing wind-dampness effects and strengthening muscles and bones, so it is clinically used to treat impotence and emission, uterine cold with infertility, irregular menstruation, cold pain of the lower abdomen, arthralgia due to wind and dampness and limp wilting sinews and bones [1]. Research in recent years has found that *Morinda officinalis How* contains 11 compounds and 24 inorganic elements such as iridoids, inorganic acids, saccharides and anthraquinones [2]. *Morinda officinalis How* is clinically used to treat anti-depression, regulate immune and thyroid functions, enhance memory, and fight with tumor and other diseases [3,4]. The physical and chemical properties of oligosaccharide monomers are similar, so oligosaccharide monomers are hard to be separated and detected.

Morinda officinalis How has many saccharides which have similar chemical properties, so there are some difficulties in the processes of extraction, separation and examination. Optimizing the extraction method of chemical constituents of *Morinda officinalis* and exploring its biological activity are the hotspots of the present research.

EXPERIMENTAL

Studies on chemical compounds of Morinda officinalis How

Anthraquinone compounds. The anthraquinone compounds are effective ingredients showing the bioactivity of *Morinda officinalis How*. According to reports from home and abroad, the number of anthraquinone compounds which are extracted from the *Morinda officinalis How* is 34, with 7 groups of isomers [5]. Among them, 14 anthraquinone compounds are isolated from the root of *Morinda officinalis How* and their chemical structure is identified (Table 1).

Iridoids. The iridoids are widely distributed in *Morinda officinalis How* and have multiple biological activities [12]. 7 iridoids have been extracted and identified from *Morinda officinalis How* [5] (Table 1).The main features of iridoids in *Morinda officinalis How* are that in C_1 positions are mostly active –OH groups (occasionally keto appear), and iridoids mostly combine with D-glucose to form glycosides [13].

Saccharides. Saccharides account for a large part of the proportion of active ingredients in *Morinda officinalis How*. Shen [14] measured the content of several important components in *Morinda officinalis How*. The total content of water-soluble saccharides

*To whom all correspondence should be sent:
E-mail: luyi@bucm.edu.cn

is 69.12%. therefore, water-soluble saccharides are the most active ingredients of *Morinda officinalis How* and have certain research and development value. Saccharides in *Morinda officinalis How* include monosaccharides, polysaccharides and oligosaccharides, the latter being also called inulin-type oligosaccharides.

Cui *et al.* [15] extracted four water-soluble oligosaccharide monomers from the roots of *Morinda officinalis How*. Feng *et al.* [16], using spectroscopy and chromatography with activated carbon and silica gel, isolated and identified 6 oligosaccharides from *Morinda officinalis How*. Three of the compounds were isolated from *Morinda officinalis How* for the first time.

According to *Chinese Pharmacopoeia* 2015, *Morinda officinalis How* should be calculated on the anhydrous substance, and nystose ($C_{24}H_{42}O_{21}$) should not be less than 2.0%. Today, research at home and abroad pays lots of attention to the anti-depressive effect of oligosaccharides in *Morinda officinalis How*. How to optimize the extraction and isolation method of *Morinda officinalis How* oligosaccharides and find a high- efficient, rapid and accurate method for structural analysis is of significant interest to research.

Organic acids. Zhou *et al.* [17] isolated palmitic acid, while Cui *et al.* [15] isolated succinic acid from *Morinda officinalis How*.

Amino acids. Li *et al.* [18] isolated 11 kinds of free amino acids and 17 hydrolytic amino acids from the root of *Morinda officinalis How*, 7 of which are essential amino acids (Table 1).

Inorganic elements. Morinda officinalis How contains a vast number of inorganic elements, 11 of which are essential trace elements for humans [2]. It has been suggested that the biological activity of *Morinda officinalis How* may be the result of its chemical composition and content of inorganic elements, but this viewpoint needs to be proved.

It is well to be reminded that due to different origin, texture and processing methods of *Morinda officinalis How*, there are some variations in the chemical composition and element content of *Morinda officinalis How*.

Extraction and separation process of Morinda officinalis How's oligosaccharides

The chemical composition and pharmacological effects of *Morinda officinalis How* have been well studied, but there are few reports on the extraction and separation of active ingredients from *Morinda officinalis How*, especially for the *Morinda officinalis How*'s oligosaccharides. Natural oligosaccharides are generally extracted by traditional methods such as ethyl alcohol reflux. However, there are many uncertain factors like high extraction temperature, long time and solvent, which

result in reducing the extract amount and affect clinical efficacy [19]. In addition, biochemical technology and enzyme reaction can also be used with starch and disaccharides (such as sucrose, etc.) to synthesize oligosaccharides. The isolation and purification of oligosaccharides are key steps in the study of oligosaccharide monomers, and silica gel column chromatography, ion exchange chromatography and other methods are commonly applied. This paper summarizes the various methods of extraction and isolation of oligosaccharides from *Morinda officinalis How*, and lays the foundation for finding a new effective, efficient and fast extraction method.

Extraction

Organic solvent methods. Oligosaccharides are often formed by 2-10 monosaccharides connected with glycosidic linkages. They are polyhydroxy, with a certain degree of hydrophilicity. According to the similarity-intermiscibility theory, many polar organic solvents can be used (such as ethanol, methanol, acetone, etc.) for extraction. Ethanol is most recommended, and oligosaccharides are generally insoluble in more than 90% ethanol.

Zhou *et al.* [20] chose 95% ethanol solution as the extracting solution, 8:1 liquid ratio, and extracted 3 times by reversed flow under heating, for 30 min each time. They got cinnamon oligosaccharides with 90.29% extraction rate, which was significantly higher than that of water extraction. Xin *et al.* [21] chose ethanol-methanol and ethanol to observe their effect on the extraction rate, and determined the optimum extraction conditions. The extraction rate of oligosaccharides was up to 3.6% by the phenol-sulfuric acid method.

Oligosaccharide extraction method mostly used in experiments was water solution and alcohol sedimentation method. 80% ethanol extracted polysaccharide precipitate in order to reduce the interference and be suitable to further purifying.

Ultrasonic extraction method. Ultrasonic extraction method mainly uses ultrasonic cavitation to destroy cell membranes, which contributes to the dissolution and release of active ingredients, reduces the extraction time, allowing to extract the maximum amount of ingredients in the shortest time. Ultrasonic extraction method has the advantages of high extraction speed, short time, high yield, no heating, etc. It has become an important means of many Chinese medicine composition analysis processes.

Microwave extraction method. Microwave extraction is a new technology that uses microwave to improve the extraction rate. Microwave-assisted extraction studies [22] have show that microwave irradiation-induced extraction has the characteristics of high selectivity, short operating time, low solvent consumption and high yield of active ingredients. In

the process of extraction, the medicine is nor agglomerated or gelatinized, which overcomes the characteristics of hot water extraction. Wang *et al.* [23] not only significantly increased the soybean oligosaccharide content, but made it easier to desalt through 500W microwave.

Biological methods

Traditional Chinese medicine enzymatic extraction is the main method of extracting the active ingredients in Chinese herbal medicine by biotechnology. Enzyme reactions with high specialization and other features are used to destroy the cell wall structure, so that the active ingredients can be fully exposed, which leads to improved extraction rate of the active ingredients. Shao [24] used *paenibacillus* WL strains with agarase to ferment and to find the optimum technology for oligosaccharides through agar enzyme degrading agar.

Isolation and purification

Absorbent activated carbon isolation method. Activated carbon is a non-polar adsorbent, and has a strong affinity for non-polar components. It is mainly used to separate water-soluble ingredients, such as glycosides, saccharides and amino acids in Chinese medicine. It is suitable for industrial large-scale preparation and separation because of its easy preparation and cheap price. Che *et al.* [25] used this method to separate *Crossostephium chinense* oligosaccharides and got oligosaccharides with different molecular weights.

Gel column chromatography. Gel chromatography is a separation and analysis technique developed in the 1960s with molecular sieve properties for the separation and purification of proteins and saccharides. Gels that are commonly used are Sephadex G and Sephadex LH-20. Harry *et al.* [26] got a kind of xylooligosaccharide with arabinosyl by Bio-Gel P-2 gel separation.

High performance liquid chromatography (HPLC). HPLC is a new type of rapid separation and analysis method developed on the basis of classical conventional chromatography. The principles include distribution chromatography, ion exchange chromatography and other methods. Nowadays the combination of HPLC-MS is commonly applied to qualitatively and quantitatively analyze high-purity samples.

Wang *et al.* [27] analyzed monosaccharides and oligosaccharides qualitatively and quantitatively with HPLC-MS in tea, such as rhamnose, arabinose, mannose, raffinose and others. The results show that rhamnose, xylose, arabinose and mannose were not detected in all tea samples.

PROGRESS IN PHARMACOLOGICAL EFFECTS OF *MORINDA OFFICINALIS HOW'S* OLIGOSACCHARIDES

Morinda officinalis How is a top grade in *Shennong's Classic of Materia Medica,* and a preferred medicine for tonifying the kidney Yang. There is an archaism, *Morinda officinalis How is a medicine for blood tier on kidney meridian.* As people enjoy improved living conditions with faster and faster pace of life, people's mental and psychological pressure are also virtually increased, and mental illness-patients tend to be younger than before. Domestic survey data show [28] that the suicide rate of depression patients is about 20 times higher than that of the average population. By 2020, depression is predicted to be the second major disability factor only to cancer. The commonly current clinical medicines for depression are TCAs, SNRIs, SSRIs and others. However, these drugs are only effective for a part of the depression patients, and may bring about delay in efficacy, adverse reactions and other issues [29]. Therefore, there is a great demand for the development of antidepressant drugs that have faster and effective features. In recent years, it has been found that oligosaccharides in *Morinda officinalis How* have an obvious therapeutic effect as antidepressants with little side effects, which is worth to be researched. This point of view provides foundation for the development of new antidepressant drug based on *Morinda officinalis How's* oligosaccharides.

Antidepressant effect of oligosaccharides in Morinda officinalis How

Cui *et al.* [15] were the first to extract oligosaccharides from *Morinda officinalis How*, and gave the initial determination of oligosaccharides in *Morinda officinalis How* with antidepressant effect, which opened the door to the new world for scholars to study antidepressants.

Cai *et al.* [30] reported that oligosaccharides isolated from *Morinda officinalis How* could significantly shorten the immobility time of mouse tail suspension test without affecting the spontaneous activity of mice, demonstrating that oligosaccharides had certain antidepressant effect.

In Xu *et al.* [31] experiment, the depression male SD rats model was induced by chronic unpredictable stress methods. The behavioral changes of rats were observed by sugar-water preference test and forced swimming test with *Morinda officinalis How's* oligosaccharides and fluoxetine as the reference substance. It was found that *Morinda officinalis How's* oligosaccharides could increase the preference of rats for sugar and significantly reduce the time of forced swimming, indicating that oligosaccharides in *Morinda officinalis How* had antidepressant effect.

Zhang *et al.* [32] used rat lDRL 72s method and rats and mice forced swimming method [33,34]. The antidepressant effect of the alcohol extract of *Morinda officinalis How* was tested with ip desipramine as control. The results showed that the alcohol extract of *Morinda officinalis How* could significantly shorten the immobility time of the rats and mice, and greatly increased the number of rats intensified, with a dose-dependent manner. However, the alcohol extract did not affect the number of reaction rates and the effect ratio, indicating that *Morinda officinalis How*'s alcohol extract also had antidepressant effect.

Antidepressant mechanism of Morinda officinalis How's oligosaccharides

The main active ingredients in *Morinda officinalis How* are oligosaccharides, polysaccharides, DFM and so on. The antidepressant mechanism may consist in reduction of the oxidative damage of the brain tissue and neuronal damage in the hippocampus, increase in the expression of BD-NF, direct increase in the expression of 5-HT neurotransmitter, regulation of the hippocampal neural plasticity, etc. [35].

Cai *et al.* [30] induced mouse head-twitches test and other experiments with 5-HTP to determine the *Morinda officinalis How*'s oligosaccharides pharmacokinetic behavior. The results showed that the number of head twitches was increased in mice, and the contents of 5-HT and its metabolite 5-HIAA in the brain were significantly increased, but the ratio of 5-HT to 5-HIAA did not obviously change, indicating that *Morinda officinalis How* antidepressant effect may be related to increased 5-HT activity, but does not exclude the possibility of other neurotransmitter receptors.

With Western blot, Xu *et al.* [31] found that *Morinda officinalis How*'s oligosaccharides could significantly improve the expression of BDNF, GSK-3β and synapse proteins of hippocampus in depression male SD rat models, suggesting that the antidepressant effect of *Morinda officinalis How*'s oligosaccharides may be related to the regulation of key nodes in the neurotrophic pathway.

Li *et al*. [36] did further research with the RT-PCR method. In their study, *Morinda officinalis How*'s oligosaccharides (100 mg/kg) and desipramine (10 mg/kg) were chronically administrated in 21 d, which resulted in increasing expression of BDNF and BDNF mRNA in rat NGF. It demonstrates that the mechanism of *Morinda officinalis How*'s oligosaccharides in the treatment of depression may be related to the protection of corticosterone- induced injured neurons.

The current research shows that the mechanism of the antidepressant effect of *Morinda officinalis How*'s oligosaccharides is still not clear. It is just preliminarily proved, and needs further study to be confirmed.

Clinical applications of antidepressant effect of Morinda officinalis How's oligosaccharides

Liu *et al.* [37] observed 42 cases of kidney deficiency in depression patients, and treated them with *Morinda officinalis How*'s oligosaccharide capsules. They found that *Morinda officinalis How*'s oligosaccharide capsules were effective on mild to moderate depression.

The traditional Chinese medicine kidney deficiency scale [38] showed that the effectiveness of *Morinda officinalis How*'s oligosaccharide capsules was higher than that of the placebo control group. Within the therapeutic dose, comparing with fluoxetine hydrochloride, which was the control, the adverse reactions of *Morinda officinalis How*'s oligosaccharide capsules were lighter with better safety. This provides a basis for the promotion of clinical treatment of depression with *Morinda officinalis How*'s oligosaccharide capsules.

The study found that most depression patients had emotional depression, decreased interest in things, memory loss and other symptoms, which belong to "Yang deficiency" in traditional Chinese medicine. Warming kidney-yang can be considered to help with psychological disorders in depression patients, further treat depression [39]. Ren [40] found the effective rate of *Morinda officinalis How*'s oligosaccharide capsules for many symptoms in depression patients with kidney-yang deficiency was 85%, including depression mood, insomnia, fatigue, tinnitus, forgetfulness and slow statement. The results show that *Morinda officinalis How*'s oligosaccharides have a certain therapeutic effect for depression patients with kidney-yang deficiency.

RESULTS AND DISCUSSION

Morinda officinalis How contains complex chemical compounds and has a wide range of biological activities (Table 1), with no-hereditary little side effects. In clinical aspect it is effective and safe, therefore it has great research and development potential in the fields of diet, medical treatment and health care.

In recent years, the proportion of mental illness-patients is larger, with more and more young generation, but the mechanism of mental illness is still not clear. Most clinical medicines do not have notable curative effect but obvious side effects. The present study found that saccharide components accounted for more than half of the active ingredients in *Morinda officinalis How*, and *Morinda officinalis How*'s oligosaccharides had significant antidepressant effect.

Table 1. *Morinda officinalis Ho*w's compound names and pharmacological effects

Morinda officinalis How's compound name	Compound Name	Molecular formula	Pharmacological effects
Anthraquinones	l-Hydroxy-anthraquinone	$C_{14}H_{10}O_3$	Resists mutation and tumor
	1-Hydroxy-2-methylanthraquinone	$C_{15}H_{10}O_3$	
	1,6-Dihydroxy-2,4-dimethoxy-anthraquinone	$C_{16}H_{12}O_6$	
	1,6-Dihydroxy-2-methoxy-anthraquinone	$C_{15}H_{10}O_5$	
	1-Hydroxy-2-methoxy-anthraquinone	$C_{15}H_{10}O_4$	
	Physcion [6]	$C_{16}H_{12}O_5$	
	Rubiadin	$C_{14}H_6O_3$	
	Ruhiadin-1-methylether [7]	$C_{16}H_{12}O_4$	
	2-Hydroxy-3-hydroxymethyl-anthraquinone [8]	$C_{15}H_{10}O_4$	
	Tectoquinone [9]	$C_{15}H_{10}O_2$	
	3-Hydroxy-methoxy-2-methylanthraquinone	$C_{16}H_{12}O_4$	
	3-Hydroxy-1,2-dimethoxy-anthraquinone [10]	$C_{16}H_{12}O_3$	
	1,3,6-Trihydroxy-2-methoxy-anthraquinone	$C_{15}H_{10}O_6$	
	1,4-dihydroxy-2-methoxy-7-methylanthraquinone [11]	$C_{16}H_{13}O_5$	
Iridoids	Monotropein	$C_{16}H_{22}O_{11}$	Neuroprotective, antiinflammatory and analgesic
	Desacetylasperulosic acid		
	Asperuloside	$C_{18}H_{22}O_{11}$	
	Asperulosic acid	$C_{18}H_{24}O_{12}$	
	Asperuloside tetraacetate	$C_{26}H_{31}O_{15}$	
	Morindolide	$C_9H_{12}O_3$	
	Morofficinaloside	$C_{17}H_{26}O_{11}$	
Oligosaccharides	Nystose	$C_{24}H_{42}O_{21}$	A variety of biological activities (antidepressant, anti-stress)
	1F-Fructofuranosyl-nystose	$C_{30}H_{52}O_{26}$	
	Inulin-type hexasaccharide	$C_{36}H_{62}O_{31}$	
	Inulin-type heptasaccharide	$C_{42}H_{72}O_{36}$	
Polysaccharides	MOHP-I, MOHP-II, MOHP-III, MOHP-IV		Immune regulation, anti-osteoporosis
Organic acids	Palmitic acid	$C_{16}H_{32}O_2$	Antibiosis
	Succinic acid	$C_4H_6O_4$	
Amino acids	Isoleucine	$C_6H_{13}NO_2$	Ensures the normal operation of the body
	Methionine	$C_5H_{11}O_2NS$	
	Leucine	$C_6H_{13}NO_2$	
	Phenylalanine	$C_9H_{11}NO_2$	
	Valine	$C_5H_{11}NO_2$	
	Lysine	$C_6H_{14}N_2O_2$	
	Cystine	$C_6H_{12}N_2O_4S_2$	
Micro elements	Fe, Mn, Cu, Zn, Cr, Sn, Ni, Mo, Co, V, Sr		Tonify the kidney Yang, bone-invigorating

Therefore, the research and development of *Morinda officinalis How*'s oligosaccharides have a certain value for the treatment of modern depression. However, the commonly current extraction method of *Morinda officinalis How*'s oligosaccharides is water solution and alcohol sedimentation. The technology for isolation and determination of *Morinda officinalis How*'s oligosaccharides monomer is still not perfect. Besides, the understanding of *Morinda officinalis How*'s oligosaccharides is limited, and needs to be studied and improved at a higher level.

REFERENCES

1. Chinese Pharmacopoeia, *China Medical Science and Technology Press*, **1**, 75 (2015)

2. W.P. Wang, *Li Shi Zhen Medicine and Materia Medica Research*, **11(7)**, 665 (2000).

3. Z.B. Wang, Q.Y. Lu, H.Y. Lu, W.M. Liao, Z.P. Wu, G.Z. Kuang, *International Journal of the Physical Sciences*, **6(1)**, 112 (2011).

4. M.Y. Zhu, C.J. Wang, X. Wang, S.H. Chen, H. Zhu, H.M. Zhu, *Carbohydrate Polymers,* **85(1)**, 23 (2011).

5. Z.Z. Huang, *Guangzhou University of Chinese Medicine,* (2013).

6. Y.J. Yang, H.Y. Zheng, Z.D. He, *Acta Pharmaceutica Sinica*, **27(5)**, 358 (1992).

7. H.L. Zhang, Q.W. Zhang, X.Q. Zhang, Y.E. Wen-Cai, *Chinese Journal of Natural Medicines*, **8(3)**, 192 (2010).

8. F.X. Zhou, *Chinese Pharmaceutical Journal*, **11(9)**, 554 (1986).

9. S. Li, Q. Ouyang, X. Tan, S. Shi, Z. Yao, H. Xiao, *China Journal of Chinese Materia Medica*, **16(11)**, (1991).

10. A.D. Pawlus, B.N. Su, W.J. Keller, A.D.Kinghorn. *Journal of Natural Products*, **68(12)**, 1720 (2005).

11. S.W. Kim, B.K. Jo, J.H. Jeong, S.U. Choi, Y.I. Hwang, *Journal of Medicinal Food*, **8(4)**, 552 (2005).

12. J. Liu, J.Y. Liang, T. Xie, *Strait Pharmaceutical Journal*, **16(1)**, 14 (2004).

13. J.Y. Xu, T.L. Chu, P. Ding, *Journal of Guangzhou University of Traditional Chinese Medicine*, **23(3)**, 268 (2006).

14. Y.C. Shen, *Nanjing Forestry University*, (2008).

15. C.B. Cui, *China Journal of Chinese Materia Medica*, **20(1)**, 36 (1995).

16. F. Feng, L.L. Wang, X.P. Lai, Y.B. Li, Z.M. Cao, Y.J. Zhou, *Journal of Chinese Medicinal Materials*, **35(8)**, 1259 (2012).

17. F.X. Zhou, *China Journal of Chinese Materia Medica*, **11(9)**, 554 (1986).

18. S. Li, *Chinese Traditional Patent Medicine*, **10**, 33 (1988).

19. X.W. Wu, H. Li, Y.H. Shao, P. Ding, *Chinese Pharmaceutical Journal*, **49(2)**, 102 (2014).

20. F.J. Zhou, M. Huang, X.J. Peng, X.M. Bai, C.L. Qiao, S.Y. Li, *West China Journal of Pharmaceutical Sciences*, **32(1)**, 63 (2017).

21. W.P. Xin, *Cereals and Oils Processing*, **12**, 178 (2009).

22. R.B. Shi, Y.Y. Jiang, Z.Wang, Y.Y. Wang, *Journal of Beijing University of Traditional Chinese Medicine*, **35(3)**, 153 (2012).

23. Z.C. Wang, W.D. Liu, S.F. Wang, *Chinese Agricultural Science Bulletin*, **22(6)**, 102 (2006).

24. J.T. Shao, *Zhejiang University of Technology*, (2011).

25. J.Z. Che, D.X. Fu, F. Ouyang, *Natural Product Research and Development*, **16(5)**, 458 (2004).

26. H. Gruppen, R. A. Hoffmaann, F. J. M. Kormelink, A. G. J. Voragen, J. P. Kamerlin, J. F. G. Vliegenthar, *Carbohydr. Res*., **233(2)**, 45 (1992).

27. C. P. Wang, L. Zhu, X. Liu, Y. B. Zhang, S. J. Zhou, *Food Science*, **23(12)**, 1776 (2014).

28. Y.H. Li, L.F. Zhang, *Chinese Journal of Information on Traditional Chinese Medicine*, **13(10)**, 1 (2006).

29. L.Y. Zou, H.Y. Zhang, *Chinese Journal of New Drugs*, **16**, 1889 (2012).

30. B. Cai, C.B. Cui, Y. Chen, Y. Xu, Z. Luo, M. Yang, *Chinese Journal of Pharmacology & Toxicology*, **10(2)**, 109 (1996).

31. D.F. Xu, W.F. Mi, S.Z. Zhang, L.Z. Li, H.Y. Zhang, *The Chinese Journal of Clinical Pharmacology*, **15**, 1539 (2015).

32. Z.Q. Zhang, L. Yuan, N. Zhao, *Chinese Pharmaceutical Journal*, **35(11)**, 739 (2000).

33. R.D. Porsolt, A. Bertin, M. Jalfre, *Archives Internationales de Pharmacodynamie et de Therapie*, **229(2)**, 327 (1977).

34. H. Nishimura, Y. Ida, A. Tsuda, M. Tanaka, *Pharmacology Biochemistry & Behavior*, **33(1)**, 227 (1989).

35. J.Y. Wei, G.X. Yue, *Traditional Chinese Medicine Journal*, **2**, 67 (2017).

36. Y.F. Li, M. Yang, *China Journal of Chinese Materia Medica*, **25(9)**, 551 (2000).

37. F.H. Liu, J.G. Shi, X.H. Zhang, Y. Zhang, B.J. Li, Y. Li, *Shaanxi Journal of Traditional Chinese Medicine*, **33(2)**, 165 (2012).

38. Q.M. Kong, L. Shu, H.Y. Zhang, F.Y. Jiao, Z.C. Han, J. Wang, *The Chinese Journal of Clinical Pharmacology*, **27(3)**, 170 (2011).

39. N.N. Huang, X. Pu, X.J. He, M.R. Ye, *Traditional Chinese Medicinal Research*, **8**, 25 (2014).

40. F. Ren, *Journal of Shanxi College of Traditional Chinese Medicine*, (2015).

Bibliometric analysis of integrated complementary medicine research articles included in Science Citation Index

J. Zhu[1#], X. Zhai[1#], Y. Chang[2], J. Liu[1], X. Sun[1], K. Liu[1], F. Guo[1], Y. Huang[1], X. Li[1], X. Cao[1], B. Wen[3], X. Xu[1], Z. Guo[1*], X. Ma[1*]

[1]Beijing University of Chinese Medicine, 11 Bei San Huan Dong Lu, Chaoyang District, Beijing, 100029, China
[2]Beijing Municipal Science & Technology Commission
[3]Beijing University of Chinese Medicine, Dongfang Hospital, Beijing, China

More and more new concepts and methods are surfacing thanks to integrated complementary medicine research. As many laws and new discoveries have been covered in the sea of existing literature, understanding research progress and following its direction has become difficult for researchers. This study investigates the global development of integrated complementary medicine research over the past ten years through bibliometric analysis to provide reference to researchers for future work. Searched and selected were articles in 22 integrated complementary medicine journals published globally in the Web of Science database. Analysis of the articles was based on changes of publication years, geographical distribution, research institutes, research fields and so on with multiple bibliometric analysis methods. Generally, the total amount of integrated complementary medicine research articles has increased. However, there was a slight decrease in the last two years. Research in China, US and South Korea has taken the dominant position. Integrated complementary medicine is the inevitable trend of the development of Chinese medicine and even world medicine. Traditional Chinese medicine should take in achievements of modern technology to make breakthroughs. Although research in the last two years declined compared with the peak time of 2013, integrated complementary medicine research will still flourish. There will be more and more research institutes and researchers involved in the near future.

Keywords: Integrated complementary medicine; Science Citation Index (SCI); Development; Bibliometrics

INTRODUCTION

Integrated complementary medicine is a recently developed medical discipline with Chinese characteristics. It combines the essence of traditional Chinese medicine (TCM) and modern medicine in an attempt to develop medical science by applying modern science, including modern medical theories and methods, to studying the fundamental theories and clinical practice of TCM [1]. At present, it has become an indispensable part of the Chinese medical and health system. In recent years, with the rapid development and infiltration of molecular biology and computer science, integrated complementary medicine research has been greatly improved. The discovery of new concepts and methods has promoted this research, and the amount of related articles and reports has been increasing [2]. The features of the development of medical literature rapidly increase, including duplication, scattered contents, and quick updates. All these features create difficulties for researchers in immediate, correct and comprehensive understanding of literature. Therefore, it is necessary to analyze and study literature with scientific methods. Bibliometrics, which is applied in medical literature research, has provided an effective method. [3]

Bibliometrics is a cross-discipline quantitative analysis of information repositories. It has been widely used in medical research including HIV [4], tuberculosis [5], Parkinson's [6], Alzheimer's diseases [7], TCM [8] and acupuncture [9]. This study statistically analyzed articles from 22 Science Citation Index (SCI) journals related with 'general medicine and complementary medicine' in the area of Chinese Academy of Sciences in 2013. The changes in publication years, geographical distribution, research institutes, research highlights and keywords were studied to understand the current situation and the trends of development to provide reference for future research.

MATERIALS AND METHODS

The literature data we analyzed were collected from the Web of Science database by the Information Sciences Institute (ISI). Search terms included 22 general medicine and complementary medicine SCI journal names selected according to 2012 Journal Citation Reports (JCR), 2013 JCR Journal Categories Index by China Academy of Sciences (*Alternative Medicine Review, Phytomedicine, Journal of Ethnopharmacology, Integrative Cancer Therapies, American Journal of*

---

*To whom all correspondence should be sent:
E-mail: maxueling@bucm.edu.cn
　　　guozhiling@bucm.edu.cn
#These authors contributed equally to this work.

Chinese Medicine, Complementary Therapies in Medicine, BMC Complementary and Alternative Medicine, Evidence-based Complementary and Alternative Medicine, Journal of Manipulative and Physiological Therapeutics, Journal of Alternative and Complementary Medicine, Alternative Therapies in Health and Medicine, Chinese Journal of Integrative Medicine ,Acupuncture in Medicine, Explore-the journal of Science and Healing, Homeopathy, Acupuncture & Electro-Therapeutic Research, Journal of Traditional Chinese Medicine, European Journal of Integrative Medicine, African Journal of Traditional, Complementary and Alternative Medicines, Holistic Nursing Practice, Journal of the Australian Traditional-Medicine Society Chinese Medicine) and 'integrative complementary medicine'. As the earliest literature accessed was in 2004, the years in our study were limited from 2004 to 2016. All literature sources searched were downloaded and imported to EndNote with 'Full Record'. The information regarding title, abstract, keywords, publication year, authors, and research institutes was statistically analyzed with Excel 2010. RefViz software was used to study the keywords and research highlights. The search of the literature was completed on September 6th, 2017. Final data were included in the database on the day.

The statistics of core country/region publishing relative articles were determined with Bradford law. Journals were permutated in descending order with the amount of published articles under one theme. Consequently, journals were distinguished into a group with the highest rate of published articles and other groups with equal rate of published articles [10].

In 2005, J. E. Hirsch, physicist from US, published an article entitled 'An Index to Quantify an Individual's Scientific Research Output' in *Proceedings of the National Academy of Sciences of the United States of America* [11]. Articles of one researcher in one database were permutated in descending order with cited frequency until the order number of one article was bigger than the cited frequency of this article. The h-index was generated by the order number of this article minus one. [11] This study attempted to analyze the features and impact factors of countries or regions and institutes by the h-indices of articles. The graph analyzing co-author networks between countries was constructed by Gephi software in this study [12].

Refviz is a tool of visualized text analysis and data mining [13]. It is able to do cluster analysis by title and abstract, and present the results in graphs to users. The graph can be altered according to the adjustments between major and minor topics made by users to achieve accurate results and results that meet the professional information requirements of users [14]. This study analyzed literature related to integrated complementary medicine using Endnote and Refviz. The research highlights were concluded to provide reference for further research.

RESULTS

According to the selection methods 31 963 articles were included in the study. There were 14 categories of articles, in which 'original article' was the top with 26 175 results, followed by reviews (2439), editorial material (1773) and letters (693).

Article numbers in years

As shown in Table 1, the amount of integrated complementary medicine research articles has increased from 2004 to 2016. After 2012, there were more than 3000 articles every year. This indicated that the discipline has come to a mature period of development.

Table 1. Yearly amount of published articles related to integrated complementary medicine

No.	Year	Amount in the year	Amount accumulated by year
1	2004	989	989
2	2005	1329	2318
3	2006	1376	3694
4	2007	1744	5438
5	2008	1697	7135
6	2009	1955	9090
7	2010	1968	11058
8	2011	2971	14029
9	2012	3278	17307
10	2013	3885	21192
11	2014	3551	24743
12	2015	3673	28416
13	2016	3547	31963

Geographical distribution

Regions were determined by the geographical location of the organization or institute extracted from the literature. According to statistics, integrated complementary medicine research has already covered 148 countries. The top ten countries with most related research articles are China (8368), USA (5306), Southkorea (2583), India (1767), Taiwan (1682), Brazil (1525), Germany (1354), England (1306), Japan (1028), Australia (980).
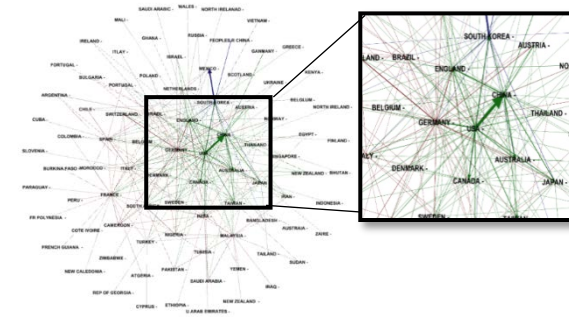

Fig. 1. Inter-country co-author networks graph

The co-authorship between countries is presented in Figure 1. Each node represented one country in the co-authorship while the connection between nodes represented the co-authorship between two countries.

Research institutes

The research institutes (different departments, renamed or merged organizations were regarded as the same one) was determined based on the organizations extracted from literature. According to statistics, 31 963 articles were from 5058 research institutes. Top ten institutes with most publishing articles were China Academy of Chinese Medical Sciences (865), Kyung Hee
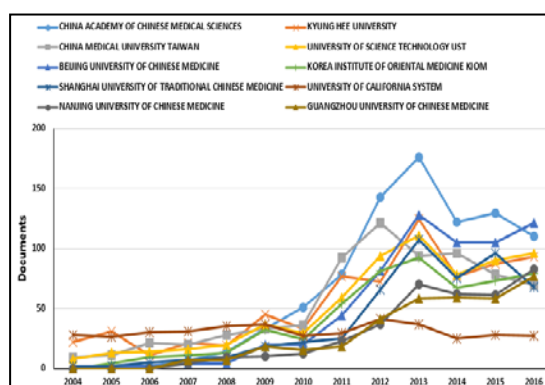
Fig. 2. Top ten institutes with the most published articles by year

University (712), China Medical University Taiwan (708), University of Science Technology (665), Beijing University of Chinese Medicine (636), Korea Institute of Oriental Medicine Kiom (539), Shanghai University of Traditional Chinese Medicine (500), University of California System (401), Nanjing University of Chinese Medicine (371), Guangzhou University of Chinese Medicine (351).

The total amount of published articles from these institutes was 5432, making up 16.99% of the general amount. The increasing trends by year of the top ten institutes are shown in Figure 2. The numbers increased gradually before reaching a peak in 2013. The numbers decreased slightly after 2013, but the number of articles published by some institutes presents an increasing trend after 2015.

Inter-organization co-author networks are shown in Figure 3. As demonstrated, cooperation between the main organizations and others is divided into several categories (differentiated by color), which also indicates that there are several big research groups. The local picture describes the main research institutes cooperating with Beijing University of Chinese Medicine (BUCM). The institutes that have closer cooperation with BUCM were China Academy of Chinese Medical Sciences,

China-Japan Friendship Hospital, Peking University, Hong Kong Baptism University, Tianjin University of TCM, Shandong University of Traditional Chinese Medicine, and Peking Union Medical College Hospital.
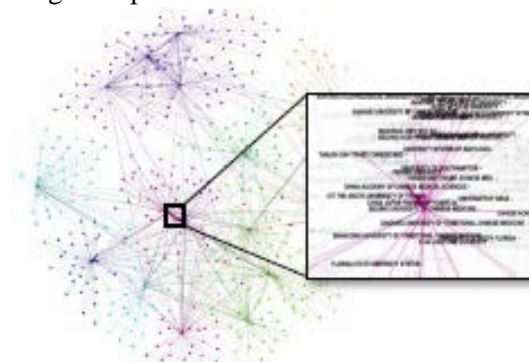

Fig. 3. Inter-organization co-author networks graph and main institutes cooperating with Beijing University of Chinese Medicine

KEYWORDS ANALYZED

Keywords analyzed by time period

Keywords in scientific essays refer to words or phrases selected from the title, abstract and main body, which reflect the topic of the article. Chiu and Ho [15] were the first to use keywords in bibliometrics to track the direction and breakthrough points of scientific development. The distribution of keywords revealed current common research themes and methods.

We divided major topics mined by Revfviz from 2004 to 2016 into two periods (2004-2010 and 2011-2016) to compare. Key words such as db, mutans, venom, etc. were found to be frequently seen by comparing the frequency of key words in these two periods, which indicates that problems with these words were the research focus in recent ten years. However, some words were only popular in a certain period, for instance, cancer, needling, polysaccharide, etc. These words were frequently seen in the first period. But they were not as frequently seen in the second one. It indicated that problems presented by these words were no more a research focus in the second period as some of problems were better resolved in the first period or the words were changed in the latter period. Research questions with the keywords of massage, resveratrol, emodin, etc. were the focuses in recent years.

Keywords cluster analysis

Figure 4 is the keywords dendrogram of integrated complementary medicine literature from 2004 to 2016 created using Refiviz. Icons represent a group of literature. The size of the icons demonstrates the number of works in the group while the space between the icons shows the

correlation of each work. In other words, the bigger the icon, the greater is the number of articles in the group. The closer the icons are together, the stronger is the correlation. We numbered each icon and extracted the keywords and related literature represented by the icon. We divided them into two concentrated areas according to the space between icons.
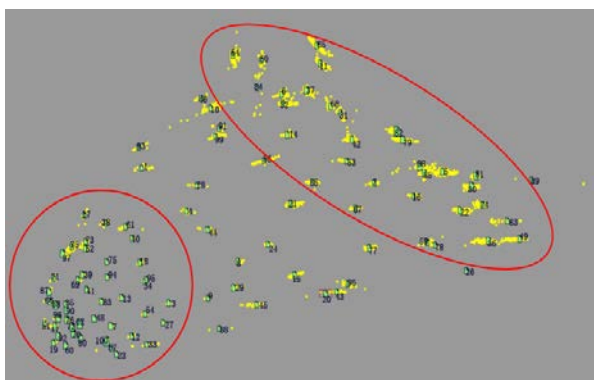

Fig. 4. Keywords dendrogram from 2004 to 2016

CONCLUSION

By studying integrated complementary medicine articles from 22 journals, we found a general increase in the number of articles and established core research area, core research institutes and core research highlights in this field.

From the amount of published articles every year, the development of research and application related to integrated complementary medicine can be divided into three periods. The first period is 2004 – 2010, which is the period of stable increase. The second one is 2010 – 2013, which is the period of rapid increase. In the third period, 2014 – 2015, the number of articles has slightly decreased.

In the analysis of geographical distribution, we found that Asia was the area that published the most papers while the region with the lowest amount of papers published was Oceania. From the statistics of countries participating in publication in every continent, although North America had fewer countries involved in co-author work, the general amount of articles was similar to that of Europe. China had the most published articles followed by the US, Korea and India.

From the study of the institutes that published more than 200 articles, half of the research was from institutes in Mainland China with high h-indices. This revealed that China has taken the leading position in this field in quantity and quality. As integrated complementary medicine has become a new discipline, more and more organizations and universities have become involved in research work, such as California University, Kyung Hee University, Seoul National University, Zhejiang University, Fudan University, National Taiwan University, and

Hong Kong University.

With the keywords extracted from the literature we found that research in this field is mainly focused on recovery, oncology, healthcare, nursing, acupuncture and neurosciences. Modern technology, such as multi-discipline and multi-indices, is applied in research methods to do in-depth study in subjects including *zheng hou*, five phases theory and four diagnostic methods. Research on chemical analysis of Chinese medicines has made great progress. Besides, there are some specific studies drawing international attention, for example, acupuncture anesthesia, integrated complementary treatment in leukemia, viral hepatitis, etc.

In the keywords cluster analysis, combined with the code and keywords, the highlights were as follows:

a. *Pharmacomolecular research*: Keywords scattered in Area 1 showed research on *materia medica*, especially focused on the pharmacomolecular research. The research on active ingredients in Chinese herbs is an important part of modernization of *materia medica*. In the treatment of cancer, active ingredients in Chinese herbs extractives such as curcumin, sophocarpidine, and tea polyphenol have achieved good effects on treating malignant tumors by inducing apoptosis of cancer cells and antioxidants. Therefore, it has become a research highlight in recent years.

b. *Acupuncture research*: Acupuncture is one of many unique diagnostic and treatment methods in TCM. It has been used in the treatment and prevention of diseases. As visible from the dendrogram, modern research on acupuncture has increased in the ten years surveyed. Research on the mechanism and molecular material basis of acupuncture for treating diseases has also become a highlight. People are increasingly willing to understand these mechanisms to find better solutions for patients.

c. *Diseases and mechanism*: According to the results of data mining, research on molecular mechanism of diseases has become a research highlight in recent years as well. For example, in the study of diabetes, people found one-third of diabetes patients deteriorate to diabetic nephropathy. [16] During the process, albuminuria is the main clinical symptom. The occurrence of albuminuria is closely related with sertoli cells. Advanced glycation end products (AGEs) are important products in the patient's body. The combination of AGEs and receptors can reduce the expression of sertoli cells connecting protein and induce the damage of sertoli cells to affect the occurrence of albuminuria. [17]

d. *Others*: The tongue as a place of manifestation of changes in disease and body constitution effects on diseases have become highlights in integrated complementary medicine. As syndrome

differentiation is the essence of TCM diagnosis and treatment, tongue manifestation and body constitution reflect this idea well. Correct syndrome differentiation is the premise of guaranteeing the effect of TCM.

Considering the results of data mining, keyword cluster analysis has provided a new path for us to study integrated complementary medicine. It helps us to understand the current clinical application and research situation of this discipline. However, we also found some limitations during our research. For instance, there were some keywords analyzed that were not in accordance with integrated complementary medicine. It may be because the keywords in the original articles could not appropriately reflect the contents of the articles. As a result, we should use the logical combination of keywords to present the ideas and contents of articles to access required literature rapidly, correctly and comprehensively.

In short, an increase in research on integrated complementary medicine is the inevitable trajectory of medical development. Traditional Chinese medicine should combine with modern technology to become more powerful. The direction of the development of integrated complementary medicine should be an open, dynamic, sustainably developed scientific system [18]. Although research in recent two years has slightly decreased compared with the peak in 2013, it can be foreseen that research in this field will be flourishing in certain time. There will be more domestic and overseas institutes and research dedicated to this topic. Integrated complementary medicine research will develop in multi-discipline, multi-level and comprehensive directions. New medical achievements will further promote the combination of theory and practice.

REFERENCES

1. Ci Hai Editorial Board, Shanghai Ci Hai Press, Shanghai, 2227, 2002.
2. S.K. Chen, *Chin. J. Pract. Chin. with Modern Med.*, 13, bottom cover (2000).
3. J.G. Lu, Guangzhou University of Chinese Medicine, Guangzhou, 2007.
4. C.A. Macias-Chapula, *Bull. Med. Libr. Assoc.*, **88**, 56 (2000).
5. J.M. Ramos, S. Ramos, M. Masiá, F. Gutierrez, *Int. J. Tuberc. Lung. Dis.*, **12**, 1461 (2008).
6. T. Li, Y.S. Ho, C.Y. Li, *Neurosci. Lett.*, **441**, 248 (2008).
7. A.A. Sorensen, *J. Alzheimers. Dis.*, **16**, 451–465 2009.
8. S. Leung, K. Chan, L. Song, *Cat. Health Info. Libr. J.*, **23**, 13 (2006).
9. J.S. Han, Y.S. Ho, *Neurosci. Biobehav. Rev.*, **35,** 680 (2011).
10. J.P. Jing, F.C. Ma, X.X. Zhang, *Intelligence Science Theory*, Science Press, Beijing, 56, 2009.
11. J.E. Hirsch, *Proc. Natl. Acad. Sci. U S A*, **102**, 16569 (2005).
12. D.J. Price, D.D. Beaver, *Am. Psychol.*, **21**, 1011 (1966).
13. Y. Wang, W.H. Rong, *Chin. J. Med. Lib. Info. Sci.*, **15**, 61 (2006).
14. D. Li, J. Wu, *Application of medical literature analysis and management software*, People's military medical press, Beijing, 62, 2007.
15. W.T. Chiu, Y.S. Ho, *Scientometrics*, **73**, 3 (2007).
16. Y.M. Farag, J.S. Al Wakeel, *Clin. Pract.*, **119**, c317 (2011).
17. C.L. Cheng, Z.D. Zheng, C.G. Shi, Z.C. Ye, X. Liu, T.Q. Lou, *J. Third Military Med. Uni.*, 35, 1779 (2013).
18. S.K. Chen, K.J. Chen, *Forum For Advancement*, **3**, 29 (2003).

Research on plasma metabolomics of hypertensive rats with liver–fire hyperactivity syndrome

J. Zhu[1#], J. Liu[1#]，X. Li[1#] , Zh. Li[2] , X. Zhai[1], T. Wang[1], X. Xue[3], Y. Li[4], Sh. Guo[1], H. Zhao[1],

W. Wang[1*], X. Ma[1*]

[1] Beijing University of Chinese Medicine, China
[2] Department of Chemistry, Capital Normal University, China
[3] Chinese PLA General Hospital, China
[4] China Academy of Chinese Medical Sciences, China

This paper reports a study of plasma metabolites in hypertensive rats with syndrome of liver-fire hyperactivity in order to elucidate the biological basis of hypertension with syndrome of liver-fire hyperactivity. ^{1}H-NMR method was used to identify and compare the small-molecule endogenous metabolites in the plasma of spontaneous hypertensive rats with liver-fire hyperactivity syndrome and normal rats. The results of ^{1}H-NMR pattern recognition showed that hypertensive rats with liver-fire hyperactivity were significantly different from those of the control group. The results of ^{1}H-NMR analysis indicated that there are close relationships between plasma metabolites and TCM syndromes, which is expected to be an objective diagnostic indicator in the further studies.

INDRODUCTION

The high incidence, high mortality and high morbidity of hypertension have great influence on human health [1-3]. Hypertension is the leading cause of cardiovascular disease and premature death worldwide [4]. More than 60% of the risk factors for hypertension are associated with metabolic disturbances. Metabolic abnormalities increase the risk for hypertension and cause high blood pressure. Improving metabolic disturbances is beneficial for hypertension treatment [5]. Therefore research on relationship of clinical classification of hypertension and the metabolic abnormalities become very important since traditional chinese medicine lies primarily in "treatment based on syndromes differentiation of the patients" [6]. Although recent research indicated that the pathogenesis of hypertension is closely related to biochemical and metabolic disorders, the pathogenesis and mechanism of hypertension are still unclear [7]. Liver-fire hyperactivity is one of the most common syndromes of hypertension. On the basis of our previous study we found that spontaneous hypertensive 14-18 weeks old rats mainly manifested the liver-fire hyperactivity syndrome [8, 9]. Therefore, in this study ^{1}H nuclear magnetic resonance (^{1}H-NMR) technology [10-11] was used

to comprehensively identify and analyze the differences of small endogenous molecule metabolites in plasma of hypertensive rats with liver-fire hyperactivity syndrome, to find the metabolic markers and provide a basis for its objective diagnosis and treatment.

EXPERIMENTAL

Instruments and reagents

Japan's Softron BP-98A rat noninvasive tail vein arterial pressure meter; open field reaction box; animal behavior record analysis system (EthoVision 3.1, Noldus Netherlands); colorimetric card: Casmtch Color Card (BEAR Medic Japan). CNU-VNMRS 600MHz superconducting Fourier transform nuclear magnetic resonance spectrometer (Varian, USA), superconducting magnet with a field strength of 14.1T (600MHz), equipped with a 1H/13C/31P/19F quad core probe, gradient inversion probe (109Ag-31P) (Thermo Revo Value Plus ULT-2586-4-V, Thermo Corporation, USA), and a small high-speed refrigerated centrifuge (Sigma-15PK, SIGMA, Germany). Reagent: 98% heavy water solution (D_2O) purchased from Beijing Jingju Chemical Industry & Trade Co., Ltd.

General experimental procedure

A total of 20 rats, 10 spontaneously hypertensive rats (SHR), 13 weeks old, male; and 10 Kyoto Wistar rats, 13 weeks old, male, clean grade (all purchased from Beijing Weitong Lihua Experimental Animal Technology Co., Ltd.) were used. The rats were kept

---

*To whom all correspondence should be sent:
E-mail: maxueling@bucm.edu.cn
        Wangwei@bucm.edu.cn
#These authors contributed equally to this work.

in the animal room of the Research Center of Beijing University of Traditional Chinese Medicine at ambient temperature (20-25 ℃). Light rhythm was 12L: 12D (6:00-18:00) with conventional food feeding. Preliminary experiments were performed in our group [8,9], through comprehensive and dynamic collection of spontaneous hypertensive rats macroscopic characterization and behavioral tests (open-field test, irritability score, rotation tolerance time determination). About 2 ml blood samples were *in vitro* collected, centrifuged at 4 ℃, and stored at - 80 ℃.

1H-NMR data acquisition and processing

The supernatant was centrifuged at 4 °C for 10 min and 200 μl of the supernatant was added to a 1.5-ml EP tube. To the EP tube, 400 μl of a heavy water solution was added and the mixture was centrifuged at 4 ℃, 14000 r/min speed for 10 min; 550 μl of the mixture were transferred to the nuclear magnetic tube. Plasma samples were analyzed using a Varian VNMRS 600M superconducting Fourier transform nuclear magnetic resonance spectrometer to observe the relaxation of small molecule signal (CPMG) pulse sequences. The saturation time was 2 s, the mixing time was 0.15 s, the spectral width was 8012.8 Hz, the number of sampling points was 32 k, the number of accumulation was 64, and the pre-saturation frequency and center frequency were all in the water peak position. The free induction decay (FID) signal was converted to a one-dimensional 1H-NMR spectrum by 32-k Fourier transform. The 1H-NMR spectra were processed using MestReNova software. (4.7 to 5.2 ppm); automatic adjustment of the phase and baseline; lactic acid as the chemical shift reference peak, set to 1.33 ppm; 0.5-5.5 ppm (CPMG experiment) range of sub-integral, each 0.001 ppm. The integral was normalized by the total integral intensity of each spectrum and scaled by the median method, the resulting data output was saved in Excel format.

1H-NMR data analysis

The data were processed in SIMCA-P 12.0 software (Umetrics, Umea, Sweden). PCA was used to calculate the principal components (PC), and the plasma metabolic components were analyzed by orthogonal partial least-squares discriminant analysis (PC-PCA) using PC. The data were analyzed by Pareto scale (PCA) OPLS-DA) to obtain the OPLS-DA scatter plot and loading plot of the corresponding plasma samples. The data of the metabolites of each group of blood samples were visually displayed and the characteristic difference metabolites were identified. OPLS-DA is a newly developed data analysis method. Orthogonal signal correction (OSC) and partial least squares (PLS) can be combined to modify PLS. In the metabonomics

study. The color linear load map was drawn by MATLAB software, and the different metabolites of each group were visually expressed. The difference was statistically significant (P <0.05).

RESULTS AND DISCUSSION

Spontaneously hypertensive 14-18 weeks old rats manifesting liver-fire hyperactivity syndrome

Spontaneously hypertensive 14-18 weeks old rats have the following characteristics: significantly increased irritability score, shortened rotation tolerance, increased number of small vessels in ear and claw, increased image R-value of tongue and claw, dry tongue, dry and hard stool, difficult and prolonged defecation, significantly increased total activity distance and increased grid crossing times in open field test. SHR rats at the age of 14-18 weeks manifested liver-fire hyperactivity according to the diagnostic criteria of hypertension with liver-fire hyperactivity syndrome [9].

Plasma 1H-NMR spectrum metabolite analysis of hypertensive Wistar rats and normal rats with syndrome of liver-fire hyperactivity

The endogenous differences in the 1H-NMR spectra of hypertensive rats with liver-fire hyperactivity were compared with those of the normal control group. The t-test/non-parametric test was used for statistical analysis after normalized treatment of the integral values of the small molecule substances. There are 21 substances, including tryptophan, sarcosine, glycerol, choline, urea, formic acid, isoleucine, leucine, methionine, β-hydroxybutyric acid, β-glucose, α-glucose, β-hydroxyisobutyric acid, glycoprotein, glutamine and carnitine (see Table 1).

Results of PLS-DA analysis of spontaneously hypertensive rats with liver-fire hyperactivity

The OPLS / O2PLS-DA integral matrix and the PLS-DA integral matrix of the plasma CPMG metabolites in spontaneously hypertensive 18 weeks old rats with liver-fire hyperactivity syndrome and in the normal group were measured. The results are shown in Figures 1 and 2. Spontaneously hypertensive rats with liver-fire hyperactivity and normal rats were completely separated along the t (1) axis of the first principal component, with no obvious cross or overlap. Corresponding load matrix diagram (Figure 3) and colored linear load map (Figure 4) intuitively expressed the different metabolic substances in the plasma of spontaneously hypertensive rats with liver-fire hyperactivity and normal rats, such as tryptophan, thiazine, leucine, histidine, proline, α-glucose, β-glucose, β-hydroxyisobutyrate, glutamate.

Table 1. Comparison of plasma metabolites of spontaneously hypertensive rats with liver-fire hyperactivity syndrome

Metabolites	Ascription	δ(1H)	Multiplicity	p
Tyrosine	CH2	3.20	ABX	0.003
Trimethylamine-N-oxide	N(CH3)3	3.27	S	0.012
Myo-Inositol	H5	3.28	T	0.009
Tryptophan	CH2	3.49	ABX	0.034
Sarcosine	CH2	3.61	S	0.012
Glycerol	CH2	3.65	ABX	0.038
Choline	OCH2	4.07	M	0.011
Urea	NH2	5.78	S	0.019
Formate	CH	8.46	S	0.000
Isoleucine	δ-CH3 , γ-CH2 , α-CH	0.94,1.26,3.68	t , m , d	0.009
Leucine	δ-CH3 , α-CH	0.96,0.97,3.73	T	0.012
Methionine	S- CH3 , α-CH	2.14 , 3.86	s	0.006
Acetoacetate	CH3 , CH2	2.29 , 3.45	s	0.003
β-Hydroxybutyrate	CH	2.31 , 4.16	ABX	0.000
Phenylalanine	b-CH2	3.13 , 3.28	m	0.013
β-Glucose	C-H4 , C-H3 ,	3.4 ,3.47 ,3.49	t , ddd	0.030
α-Glucose	C-H2 ,C-H6 ,C-H5 ,CH1	3.53,3.84,5.23	ddm , ddd , d	0.011
β-Hydroxyisobutyrate	CH3	1.20	d	0.000
Glycoproteins	CH3	2.05	s	0.006
Glutamine	b-CH2	2.142	m	0.004
Carnitine	CH2(COO)	2.44	dd	0.045
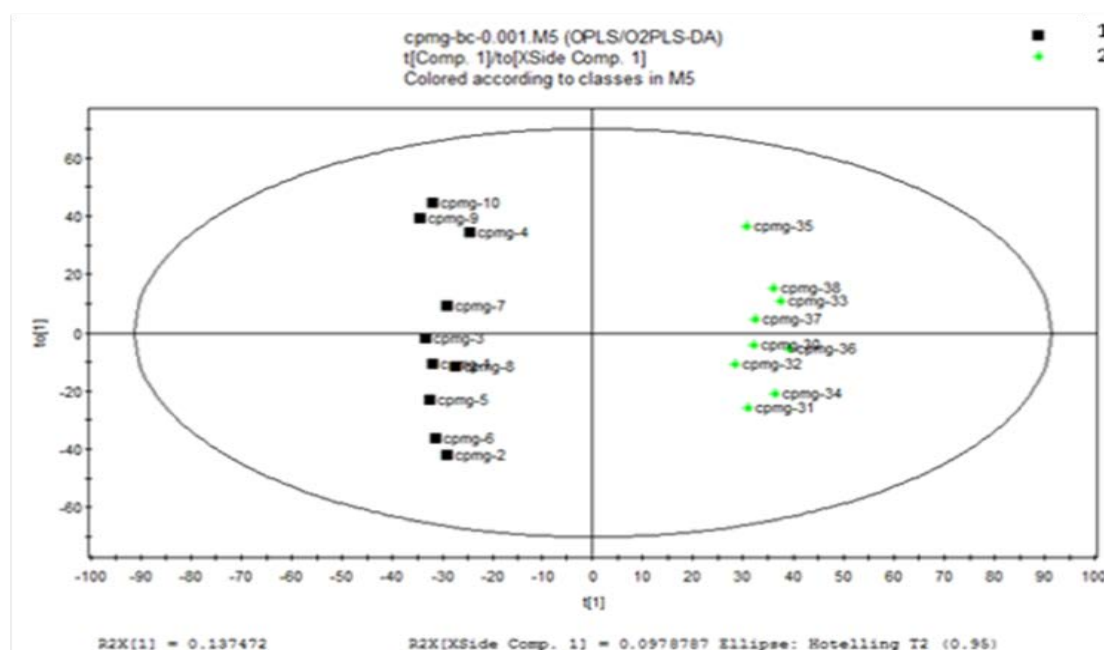
Fig. 1. OPLS/O2PLS-DA score graph of plasma samples of spontaneously hypertensive rats with liver-fire hyperactivity and normal rats. Note: 1= group of spontaneously hypertensive rats with liver-fire hyperactivity , 2= normal group, Wistar rats

At present, metabolomics-based technique has been demonstrated in the process of TCM syndrome research [12], which showed significant advantages compared to other techniques in the past. Although there are few works applying metabolic methods in the study of hypertension, with the development of metabolomics, the combination of metabolomics and TCM as a whole system thinking will provide more efficient techniques and methods for standardization of TCM syndrome differentiation, diagnosis and basic research of syndrome biology. In this study, metabolomics techniques were used to explore the differential metabolites of plasma in spontaneously hypertensive rats with liver-fire hyperactivity and normal rats, and to further explore the biological basis of liver-fire hyperactivity.
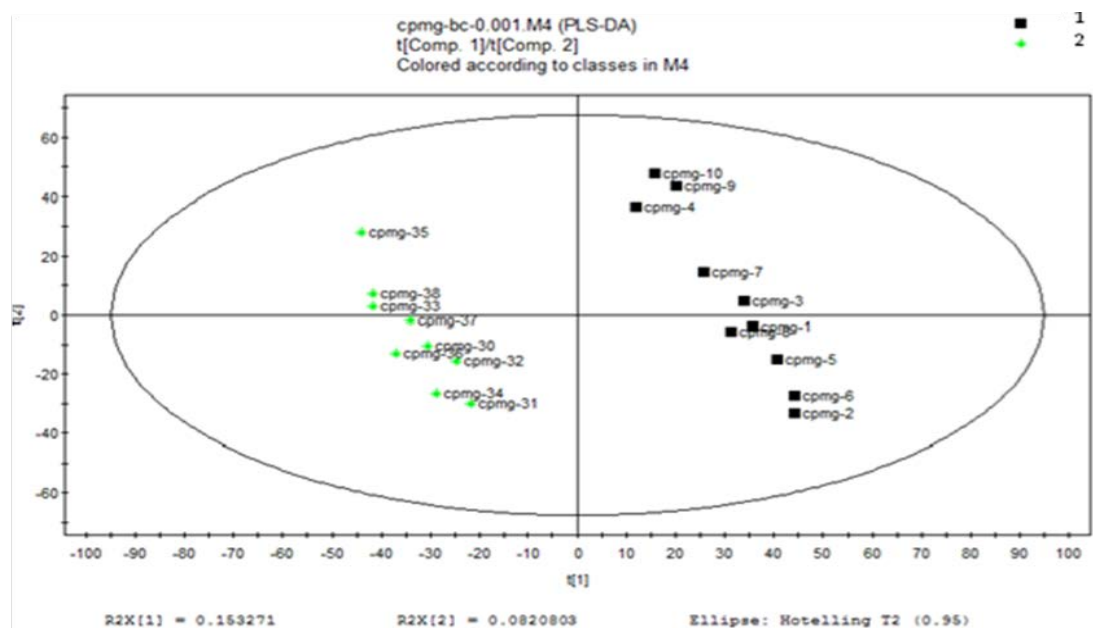
Fig. 2. PLS-DA score graph of plasma samples of spontaneously hypertensive rats with liver-fire hyperactivity and normal rats.
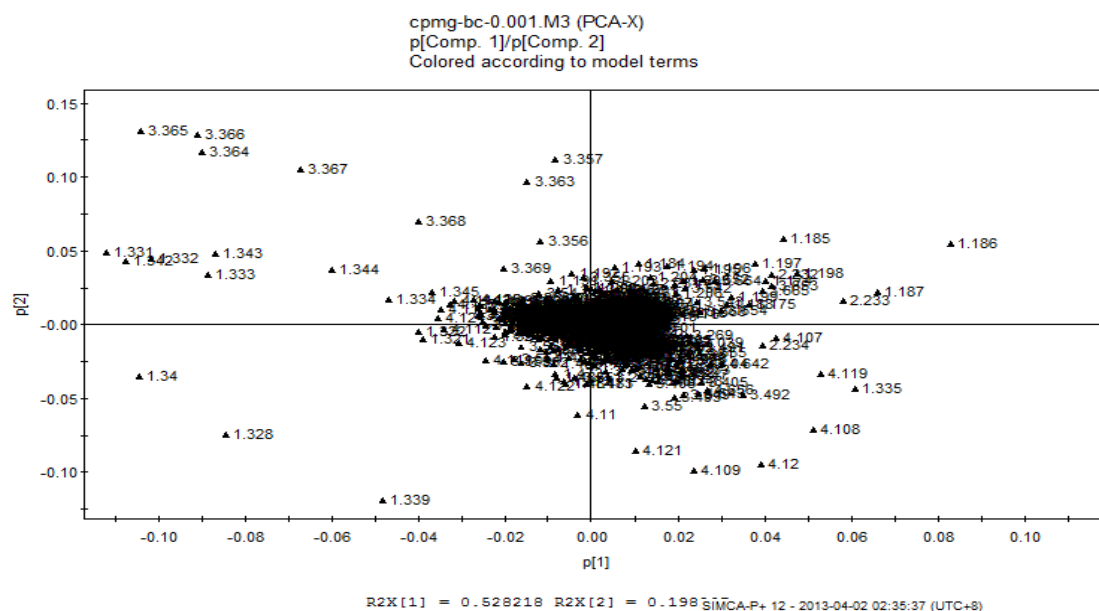

Fig. 3. Corresponding load matrix diagram of plasma samples of spontaneously hypertensive rats with liver-fire hyperactivity and normal rats.
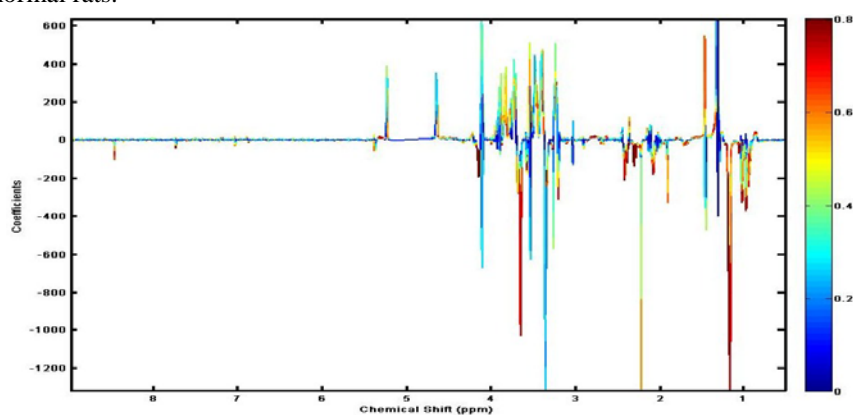

Fig. 4. Color linear load diagram of the metabolites of spontaneously hypertensive rats with liver-fire hyperactivity and normal rats.

The results of this study suggested that the different metabolites in the plasma of spontaneously hypertensive rats with liver-fire hyperactivity are tryptophan, tyrosine, leucine, histidine, proline, α-glucose, β-glucose, glutamic acid. Peripheral tryptophan exists in two forms in circulating blood, one is bound, TRP relaxation and albumin in the blood binding, fatty acid, FA can be competitive with albumin; the second is free type that is not bound to albumin, which can be transported through the blood-brain barrier. To penetrate the blood-brain barrier f-TRP must rely on a special carrier, which in turn can be combined with other neutral amino acids, especially branched-chain amino acids (BCAA), including leucine, isoleucine and valine. Therefore, the concentration of f-TRP in the brain depends on the concentrations of f-TRP and BCAA in the plasma and their ratio, that is, the increase of 5-HT synthesis in the brain is closely related to the increase in f-TRP in the blood [13]. Central 5-HT is the most potent vasoconstrictor in the brain circulation. It is formed by the hydroxylation of L-tryptophan through mitochondrial tryptophan hydroxylase (TPH) to form 5-hydroxytryptophan (5-HTP) [14],

5-hydroxytryptophan is transported through the cytoplasm of L-aromatic amino decarboxylase (ADD) decarboxylation to produce 5-HT. In addition, being recovered in the synaptic cleft, 5-HT is also oxidized by monoamine oxidase to dehydroxylate and form 5-oxindole acetaldehyde, which is then inactivated by aldehyde dehydrogenase oxidation to 5-hydroxyindole acetic acid (5-HIAA) [15]. The concentration of 5-HT in the brain affects the activity of tryptophan hydroxylase, and thus plays a feedback self-regulatory role in 5-HT. In this study, the results of 1H-NMR analysis showed that the content of tryptophan increased, and the increase in plasma tyrosine level in spontaneously hypertensive rats with liver-fire hyperactivity may be a substitute for their irritability indicators of increased irritability score. Open-field activity increased, because tyrosine is one of the precursors of neurotransmitters, which can increase the body fluid neurotransmitters, especially dopamine and norepinephrine content. Emotional impact is mainly reflected in the high stress of the crowd [16], while the literature reported dopaminergic hyperactivity, the animal will quickly explore the activities of a substantial increase in exercise.

Due to the limitation of current metabolomics techniques, still many metabolites cannot be identified, although some have significantly different content of compounds. However, it is certain that there must be some relationship between these specific different metabolic groups and syndromes, which can be expected to become indicators of objective diagnosis of syndromes, some of which may be eventually determined as candidate biomarkers.

REFERENCES

1. S. F. Qi, B. Zhang, H. J. Wang, J. Yan, Y. J. Mi, D. W. Liu, Q. B. Tian, *J. Epidemiol. Community Health,* **70**, 444 (2016).
2. G. Tocci, G. Nati, C. Cricelli, D. Parratti, F. Lapi, A. Ferrucci, C. Borghi, M. Volpe, *High Blood Press , Cardiovasc. Prev.* **23**, 387 (2016).
3. A. Camara, N. M. Baldé, M. Diakité, D. Sylla, E. H. Baldé, A. P. Kengne, M. Baldé, J. Hum. Hypertens., 30, 237 (2016).
4. V. E. Irazola, L. Gutierrez, G. Bloomfield, R. Carrillo, P. Dorairaj, T. Gaziano, N. Levitt, J. J. Miranda, A. Bernabe-Ortiz, K. Steyn, Y. F. Wu, D. Xavier, L. L. Yan, J. He, A. Rubinstein, *Glob Heart*, **11**,47 (2016).
5. Z. Zhu, P. Wang, S. Ma, *Front Med.*, **7**, 201 (2013).
6. G. Li, Z. He, F. Shao, A. Ou, X. Lin, *BMC Med Genomics*, **8**, S4 (2015)**.**
7. J. T. Brindle, H. Anti, E. Holmes, G. Tranter, J. K. Nicholson, H. W. L. Bethell, S. C. Clarke, P. M. Schofield, E. Mckilligin, D. Mosedale, D. Grainger, *Nat. Med.*, **8**,1439 (2002).
8. X. Xue, Y. Li, H. Lian, J. Li, J. Yan, X. Ma, W. Wang, W. Wang, *Chinese Journal of Experimental Traditional Medical Formulae*, **21**, 97 (2015). (in Chinese)
9. X. Ma, Y. Li, J. Chen , S. Guo, Y. Ouyang, W. Zhang, Z. Wu, W. Wang, H. Zhao, W. Wang, *World Chinese Medicine*, **8**,134 (2013). (in Chinese)
10. S. K. Hekmatyar, M. Wilson, N. Jerome, R. Salek, J. L. Griffin, A. Peet, R. A. Kauppinen, *Br. J. Cancer*, **103**, 1297 (2010).
11. M. Kyriakides, N. Rama, J. Sidhu, H. Gabra, H. C. Keun, M. EI-Bahrawy, *Oncotarget*., **7**,7216 (2016).
12. H. Zhao, J. Chen, Q. Shi, X. Ma, Y. Yang, L. Luo, S. Guo, Y. Wang, J. Han, W. Wang, *Evid. Based Complement. Alternat. Med.,* 638723 (2012).
13. M. Muscaritoli, P. Peverini, A. Cascino, C. Cangiano, F. Fanfarillo, M. Russo, *Adv Exp Med Biol*., **467**, 275 (1999).
14. C. A. Browne, G. Clarke, T. G. Dinan, J. F. Cryan, *Neuropharmacol.*, **60**, 683 (2011).
15. S. Pfeiffer , J. Boyle , S. Daly , E. Dowd, J. Haase, D. McLaughlin, *Stem Cells Dev. ,* **20**, 341 (2011).
16. H. G. Ruhé, N. S. Mason, A. H. Schene, *Mol. Psychiatry*, **12**, 331 (2007).

ERK/MAPK-mediated alleviation in cognitive dysfunction in chronically stressed mice treated with ethyl acetate extracts of *Cynomorium Songaricum*

S.Y. Ma[1#], H.S. Chang[2#], D. Cheng[1], J. C. Zheng[1], F.Z. Tian[1], L.L. Li[2], X.J. Li[2], Y. Lu[1*]

[1] School of Traditional Chinese Medicine, Beijing University of Chinese Medicine, Beijing 100029, China
[2] College of Traditional Chinese Medicine, Beijing University of Chinese Medicine Beijing 100102, China

This study explored the neuroprotective mechanism of ethyl acetate extracts of *Cynomorium Songaricum* Rup (ECS) in improving the cognitive dysfunction in chronically stressed mice. We tested the spatial learning and memory ability through water maze, the expression level of phosphorylated extracellular signal regulated kinase 1/2(P-Erk1/2) and phosphorylated cAMP response element protein (P-CREB) of mitogen-activated protein kinase (MAPK) signal pathway in the hippocampus. Besides, the expression of synaptophysin (Syn) and postsynaptic density protein 95 (PSD-95) was assessed. We also detected the long-term potentiation (LTP) by neurotic electrophysiology, observing the morphological change of hippocampal neurons by HE staining. The results showed that ECS could improve the learning and memory disorders caused by chronic stress in mice. This may be related to the raise in the expression of Syn and PSD-95 by activating the expression of P-Erk1/2 and P-CREB in MAPK signaling pathway.

Keywords: Ethyl acetate, *Cynomorium songaricum* (ECS), Cognitive function, Chronic stress, LTP, MAPK, Synaptic plasticity

INTRODUCTION

It has been reported that chronic stress has an influence on cognition, particularly on spatial memory and learning ability [1, 2]. Some studies revealed that this reaction might be correlated to hippocampal morphology and function [3]. Interestingly, this morphologic and functional change differs sexually: When ovarian hormones are removed by ovariectomy (OVX), chronic stress produces robust dendritic retraction in CA3 neurons, as the dendritic pruning extends beyond the traditional apical region found in males, and can be detected in the basal arbors of some of the CA3 neuronal subtypes [4]. Estrogen probably plays an important role in these distinct responses. One of the ways through which estrogen works in the central nerve system involves G-coupled protein estrogen receptor, GPER, which mediates the rapid signaling pathways of estrogen, including ERK/MAPK pathway. ERK/MAPK pathway activation leads to synaptic plasticity change that accordingly induces cognition variation [5, 6].

Cynomorium Songaricum Rup. is a well-know Chinese herb medicine which is used for treating aging and weakness syndrome. In our previous study we found that ethyl acetate extract of *Cynomorium Songaricum* (ECS) can protect the SK-N-SH cells from cytotoxicity induced by amyloid β (Abeta or Aβ) 25-35. Moreover, it shows antioxidant effect *in vitro*. By *in vivo* test it was found that the extract can improve spatial cognition in aging rats through estrogen-like effect [7,8]. Whether ECS can improve the cognition induced by chronic stress and its probable mechanism needs to be explored.

In this study, the effect of ECS on cognition was assessed *in vivo*. Besides, we also tested the key protein expression that is correlated to synapse plasticity and the probable pathway, which will give us clues to explain how ECS works in cognitive disorder induced by chronic stress.

EXPERIMENTAL

Drugs and reagents

The sources of various drugs and reagents are given here: P-Erk1/2 antibody (ABCAM), P-creb (CST), Synaptophysin antibody (ABCAM), PSD-95 (ABCAM), β-actin (COMBIN), RIPA lysate (BEYOTIME), PMSF (BEYOTIME), protease inhibitors (ROCHE), BCA protein quantification kits (THERMO), prestained protein markers (THERMO). NaCl (SIGMA, Lot No. SLBJ9883V); KCl (SIGMA, Lot No. SLBH5524V); $MgSO_4$ (SIGMA, Lot No. 091M02151V); D-glucose (SIGMA, Lot No. SLBD 9496V); $CaCl_2$ (SIGMA, Lot No. SLBK 9976V); $NaHCO_3$ (SIGMA, Lot No. SLBF3956V); NaH_2PO_4 (SIGMA, Lot No. 20140409); HEPES (SIGMA, Lot No. I1114).

Extraction method

Accurately weighed 20 kg of *Cynomorium songaricum* decoction pieces bought from Anguo Chinese herbal medicine market, Hebei province, China were used for extraction. Each time, 160 kg of

*To whom all correspondence should be sent:
E-mail: maxueling@bucm.edu.cn
      Wangwei@bucm.edu.cn
[#] These authors contributed equally to this work and share first authorship.

70% ethanol solution was added to the decoction pieces, then heated and refluxed three times, for 1.5 h each time. The solution was recycled and concentrated under reduced pressure till no alcohol taste. Then petroleum ether and ethyl acetate were used for extraction. The solution was recycled and the ethyl acetate polar part was extracted.

Animals

For this study, 30 ICR female mice in SPF level having an age of 56-62 days were offered by Beijing Vital River Laboratory Animal Technology, Beijing, China (Permit No: SCXK 2012－0001). This study was approved by the University Ethical Committee on Research Practice at Beijing University of Chinese Medicines and performed in accordance with approved standards of laboratory animal care and use in experiments.

Animal grouping and drug administration

The experimental animals were randomly divided into control group, model group and ECS group. Each group consisted of 7 rats. After a week of adaptive feeding, 0.06 mL/10 g of 7% chloral hydrate was used for anesthesia and bilateral ovaries were removed. After 7 days, drug administration was started. Seven kinds of methods were used to stimulate model group and ECS group, they were tail clamp, day and night reversed, restraint, cold stimulation, heat stimulation, water deprivation for 24 h, fasting for 24 h. ECS group was fed with 0.47 mg/ml of drug, and the dosage was 0.1 ml/10 g, 10 times of the adult oral dose. The drug was dissolved in distilled water under ultrasound.

Index detection

Morris water maze test. This spatial learning and memory test involved pre-experiment for 1 day, place navigation test for 5 days, and space exploration experiment for 1 day. The platform was located in the southwest quadrant. In the place navigation test, the southeast, northeast, and northwest quadrants were the entry points into the water. The time of searching platform, also called escape latent period, was recorded. For example, if mice did not find the platform within 60 s, they would be led to the platform by the experimenter, and the escape latent period was recorded as 60 s. Space exploration experiment withdrew platform on the 6th day, while the water entry point was on the opposite side of the platform, and the number of crossings across the original platform was recorded.

Western Blot. The hippocampal tissue protein of mice was extracted for protein quantification, 12% separation gel and 5% concentrated gel was prepared.

Wet turning method was used, with 80 V 0.5 h, and 100 V 1 h electrophoresis. Transmembrane conditions comprised 75 V constant voltage for 1.5 h, and 0.45 μm PVDF membrane. The closure of the primary antibody was incubated for one night. On next day, the membrane was washed and the second antibody was incubated. Finally, the gel imaging system was exposed.

Neurotic electrophysiology. The brain slice was prepared by using the hippocampus of two mice in each group for neurotic electrophysiology LTP test.

Hematoxylin and eosin (HE) staining. Rats were randomly selected from each group for morphometric analysis, anesthetized with 7% chloral hydrate, perfused with PBS (phosphate buffer saline, 0.1 M, 4°C) and again perfused with 4 % paraformaldehyde through the ascending aorta, until stiffening of tail and limbs. Afterwards, the brains were divided into two parts: One part was stored with 4% paraformaldehyde for 7 days and other part was with 2.5% glutaraldehyde. Former part was sliced into coronal sections of 4 μm thickness for hematoxylin-eosin (H & E) staining, while the latter one was used for electron microscope study.

Statistical method

The results of the behavior test were statistically analyzed by SPSS version 20.0 software. The experimental data were expressed as x ± s, and single-factor analysis of variance was performed. LSD was used for multiple comparisons. If $P < 0.05$, the difference was statistically significant.

RESULTS

Morris water maze test

The results from the orientation navigation experiment showed that the escape latency of each group was gradually shortened, and there was non-significant ($P > 0.05$) difference in escape latency during 1-4 days for each group. On the 5th day of the experiment, compared with the female control group, the incubation period of the female model group was significantly ($P < 0.05$) longer. Compared with the female model group, the escape latency of female ECS mice group was significantly ($P < 0.05$) shorter. Space exploration experiment results showed that compared with the female control group, the times of crossing platform in the female model group was decreased, and the difference was statistically significant ($P < 0.01$). Compared with the female model group, the times of crossing platform in the female ECS mice group increased, and the difference was statistically significant ($P < 0.01$) (Table 1).

Table 1. Comparison of learning and memory behavior of all groups ($n = 7$, $\overline{x} \pm s$)

Group	Latency to platform (s)					In Quadrants Southwest Frequency
	Day 1	Day 2	Day 3	Day 4	Day 5	
Control	26.0 ± 12.7	20.7 ± 7.9	18.3 ± 7.2	11.0 ± 4.3	10.0 ± 4.1	8.3 ± 0.82
Model	36.7 ± 14.7	26.0 ± 12.6	25.6 ± 11.4	18.0 ± 12.9	22.0 ± 7.8*	4.8 ± 2.0**
ECS	33.9 ± 15.3	24.4 ± 8.4	20.3 ± 9.7	15.3 ± 7.9	13.0 ± 6.8#	7.2 ± 0.4##

Note: Compared with control, *$P < 0.05$; **$P < 0.01$; Compared with model, #$P < 0.05$; ##$P < 0.01$.

Western Blot

The results showed that the Syn protein expression of female model group was significantly ($P < 0.01$) lower than that of the female control group, and the Syn protein expression of the female ECS mice group was significantly ($P < 0.05$) higher than that of female model group. Besides, the PSD-95 protein expression of female model group was significantly ($P < 0.05$) lower than that of female control group, and the PSD-95 protein expression of the female ECS mice group was significantly ($P < 0.05$) higher than that of female model group (Figure 1 and Table 2). P-Erk1/2 protein expression in female model group was significantly ($P < 0.01$) lower than that in female control group, and the content of P-Erk1/2 protein expression in the female ECS mice group was significantly ($P < 0.01$) higher than that of female model group. In addition, P-creb protein expression in female model group was significantly ($P < 0.05$) lower than that in female control group, and the P-creb protein expression of the female ECS mice group was significantly ($P < 0.05$) higher than that of female model group (Figure 2 and Table 2).
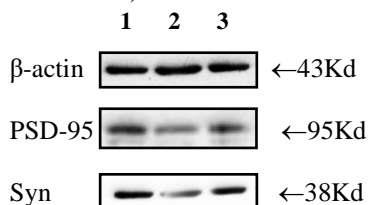
Fig.1. Expression of PSD-95 and Syn in hippocampus (1-control; 2-model; 3-ECS)

Neurophysiological results

The results showed that the slope percentage of a field excitatory postsynaptic potential (fEPSP) in the model group was significantly ($P < 0.01$) lower than that in the control group, suggesting that the learning and memory function of the model group mice may be defective.

Table 2. Comparison of proteins expression of all groups ($n = 4$, $\overline{x} \pm s$)

Group	Syn	PSD-95	P-Erk1/2	P-creb
Control	0.9± 0.2	0.9 ± 0.2	1.3 ± 0.2	1.1 ± 0.3
Model	0.4± 0.2**	0.5 ± 0.1*	0.4 ± 0.1**	0.7 ± 0.1*
ECS	0.8 ±0 .1#	0.9 ±0 .3#	1.3 ± 0.3##	1.1 ± 0.3#

Note: Compared with control, *$P < 0.05$; **$P < 0.01$; Compared with model, #$P < 0.05$; ##$P < 0.01$.
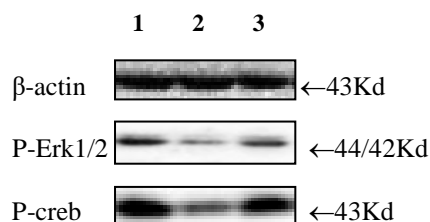

Fig.2. Expression of P-Erk1/2 and P-creb in hippocampus (1-control; 2-model; 3-ECS)

The slope percentage of fEPSP in the female ECS mice group was significantly ($P < 0.01$) higher than that in the model group, arguing that ECS can improve the cognitive dysfunction in chronically stressed mice after castration (Table 3, Figure 3).

HE staining

The results showed that the pyramidal cells in the hippocampal CA1 region of the model group were disordered, sparse, the cell volume was reduced, the nucleus was fixed and the cytoplasm was deep stained. The pyramidal cell morphology of the hippocampal CA1 region of the ECS group was normal, arranged balanced and neatly, with clear structures (Figure 4).
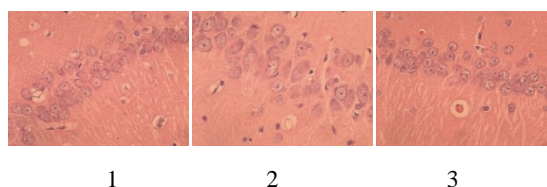

Fig.4. Neurological form of pyramidal cells in hippocampus from control group (1), model group (2), ECS group (3) HE staining, X40.

DISCUSSION

Cynomorium songaricum is the main herb for nourishing kidney and enriching essence. Recent studies have shown that *Cynomorium songaricum* can promote cell regeneration and differentiation, and help synaptic growth and memory function improvement, with significant antiaging effect [9, 10]. ECS is a mixture of various antioxidant ingredients [11], and was used as the research medicine in this experiment. Estrogen plays an important role in learning and memory, neuroprotection, emotional cognition and other aspects [12]. Thus, this study involved the removal of bilateral ovary of mice to simulate the rapid

withdrawal effect of estrogen, then combined with chronic stress to create cognitive dysfunction model, and to study estrogen-mediated signaling pathways, such as MAPK pathway.
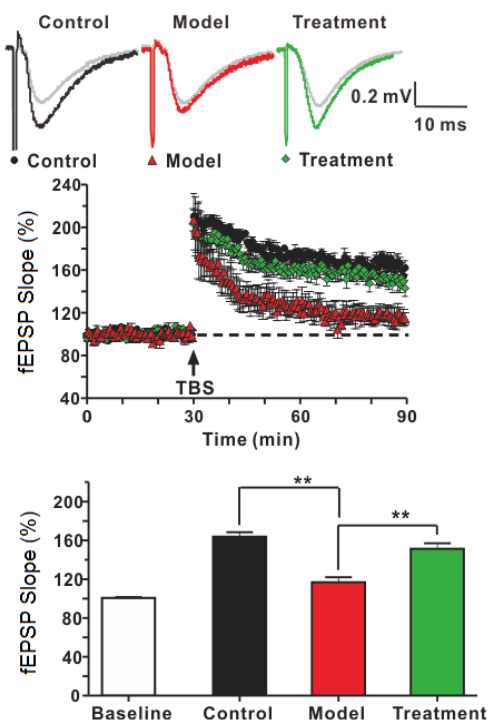

Fig.3. LTP in all groups

Table 3. Comparison of LTP of all groups

Group	Control (n = 6)	Model (n = 5)	ECS (n = 6)
Before	100.1 ± 1.2	99.7 ± 1.8	102.1± 1.4
After TBS	163.9 ± 4.5	116.8 ± 5.1[**]	151.3 ± 5.8[##]

Note: Compared with control, [*] $P < 0.05$; [**] $P < 0.01$; Compared with model, [#] $P < 0.05$; [##] $P < 0.01$.

The synaptic plasticity of the central nervous system is closely related to the learning and memory, so the number and density of dendrites in the nerve cells are very sensitive to changes in estrogen concentration, and hippocampal neurons can produce new dendrites and synapses when estrogen level is increased [13]. This experiment was intended to detect the functional plasticity and structural plasticity of synapse, and explore the neuroprotective effect of ECS in hippocampus histomorphology.

MAPK pathway is involved in cell growth, proliferation, apoptosis and other physiological processes, and affects synaptic plasticity. After its signal cascade, Erk1/2 is phosphorylated, forming P-Erk1/2. It induces the phosphorylation of nuclear transcription factor, creb, and triggers the biological change to play a biological effect [14].

Synaptic plasticity refers to the dynamic changes in the information transfer efficiency of synapses with the changes in neuronal activity, including synaptic structural plasticity and synaptic functional plasticity. Functional plasticity directly affects life activities, and structural plasticity is the

morphological basis of functional plasticity. The structural plasticity is mainly manifested as the growth and the increase of density. The main manifestation of synaptic functional plasticity is neurophysiological LTP [8]. A large number of experimental studies [15, 16] have proved that changes in synaptic plasticity can affect learning and memory.

Erk1/2 is one of the main members of the MAPK family, and is involved in the body's stress response [17]. P-Erk1/2 is the product of phosphorylated Erk1/2. ERK, after phosphorylation, can transfer a variety of extracellular signals step by step to the nucleus, and activate a variety of nuclear transcription factors. It is also involved in cell growth, development, division, differentiation and other processes [18]. When p-Erk1/2 enters the nucleus, and acts on the transcription factor, it can phosphorylate nuclear transcription factor creb, other protein kinases and other substrates. It regulates the transcription of related genes, and participates in many physiological processes such as cell growth, development, division and cell function synchronization [19]. Studies have shown that P-Erk1/2 has neuroprotective effects [20], and ERK signal transduction pathways may be involved in the process of learning and memory [21].

CAMP response element binding (CREB) protein is a target protein for phosphorylation in the MAPK signaling pathway [4]. This transcription factor exists in the nucleus and can be activated by P-Erk1/2 (i.e., P-CREB). It is widely expressed in the nerve cells. The regulation and transcription functions are closely related to the level of phosphorylation itself, and exist in non-phosphorylated form in the nucleus, with no transcriptional activity. When the mitogen-activated protein kinase (MAPK) is activated, the CREB site can be identified to activate the phosphorylation level reaction and activate the transcriptional activity [4]. CREB plays an important role in the axon growth [22], which is also important in synaptic plasticity, learning and long-term memory [23-25].

Syn is a kind of sugar-containing transmembrane structural protein on synaptic vesicle membrane. It participates in synaptic vesicle exocytosis and the fusion process of synaptic vesicles and the anterior membrane of synapses, and is closely related to the release of neurotransmitters [26]. At the same time, Syn also participates in synaptic formation, and is closely related to the plasticity of synapses [27,28]. In embryonic development, the expression of Syn is consistent with the formation of synapses, and is a sign of synaptogenesis in which the number and distribution density can indirectly reflect the density of synapses. Its expression can be used as a specific marker for presynaptic terminals to reflect the density and distribution of synapses [29].

PSD-95 is a scaffolding protein with a molecular

weight of 90 to 95 kDa found in the synaptic dense region of glutamate synapses. As a postsynaptic membrane marker [30, 31], it is the main protein involved in NMDA receptor-mediated long-term potentiation (LTP) formation and learning and memory maintenance [32]. LTP is the main form of synaptic plasticity, and the biological basis of learning and memory [33]. The studies have shown that PSD-95 plays an important role in synaptic development, stabilization, and plasticity [32]. The removal of PSD-95 gene can cause changes in mouse synaptic LTP and learning and memory dysfunctions [34].

The behavior results of the experimental water maze test showed that the number of crossings across platform in the ECS group was significantly ($P < 0.01$) increased. In the animal behavior index, ECS showed alleviated spatial memory impairment in chronically stressed mice after emasculation. The results of the Western blot test showed that the expression of p-Erk1/2 ($P < 0.01$) and p-creb ($P < 0.05$) was increased in the ECS group. In the signal pathway cascade reaction ECS showed activation of the MAPK pathway and exhibited estrogen protection. The expression of Syn ($P < 0.05$) and PSD-95 ($P < 0.05$) was also increased. In the synaptic plasticity-related proteins, the extract of ECS showed an increase in the expression of cognitive related synaptophysin. Nerve electrophysiological LTP results showed that the slope percentage of fEPSP in ECS group was significantly ($P < 0.01$) higher. In addition, ECS showed a function of improving spatial memory impairment in chronically stressed mice after emasculation. The results of HE staining showed that the pyramidal cell morphology of hippocampal CA1 region in ECS group was normally arranged, balanced, neatly and structurally clear, which reduced the neuronal damage in hippocampus and had neuroprotective effect.

CONCLUSION

The extract of ECS, by activating MARK pathway, may increase the expression of p-Erk1/2 and its downstream signal factor p-creb, and the expression of synaptic plasticity-related proteins Syn and PSD-95, and improving the synaptic structural and functional plasticity, protect the hippocampal pyramidal cell morphology, play a neuroprotective effect, and finally improve the cognitive dysfunction in chronically stressed mice after emasculation.

REFERENCES

1. P. S. Coburn-Litvak, K. Pothakos, D. A. Tata, D. P. McCloskey, B. J. Anderson, *Neurobiol. Learn. Mem.*, **80**,11 (2003).
2. D. J. F. de Quervain, B. Roozendaal, J. L. MeGaugh *Nature.*, **394**, 787 (1998).
3. Q. P. Xian, MSc Thesis, FMMU, China, 2014.
4. Y.M. Hou, MSc Thesis, CDUTCM, China, 2015.
5. F. Li, Y. Huang, W.D. Tong, B.H. Liu. *Chongqing Med. J.*, **38**, 1354 (2009).
6. E.R. Prossnitz, M. Barton, *Prostaglandins Other Lipid Mediat.*, **89**,89 (2009).
7. Y. Lu , Q. Wang , M.F. Melzig , K. Jenett-Siems, *Phytother. Res.*, **23**, 257 (2009).
8. Y. Lu, X. Wang, K .Jenett-Siems, Q. Wang. *Planta Med.*, **74**, PA200 (2008).
9. K. Liu, J.J. Wu, *TCMR.*, **5**, 24 (2010).
10. Y.Q. Zhao, Z.W. Wang, Y.H. Jing, *CJCR.*, **8**, 2220 (2002).
11. Y. Lu, F.F. Cheng, X.Q. Wang, *J. Anhui Tradit. Chin. Med. Coll.*, **31**, 57 (2012).
12. H. Liu, Y. Hu, Y.D. Zhu, *J. Nanjing Med. Univ.*, **35**, 992 (2015).
13. P. Luo, F.K. Xing, Z.X.Wu, *Chongqing Med. J.*, **40**, 2384 (2011).
14. J. Lu, X.Y. Yang, Q. Hua. *Sheng Li Ke Xue Jin Zhan.*, **39**, 371 (2008).
15. P. R. Gordon-Weeks, *J. Neurobiol.*, **58**, 70 (2004).
16. T. Yoshimura , N. Arimura, K. Kaibuchi, *Ann. N. Y. Acad. Sci.*, **1086**, 116 (2006).
17. Q.Y. Ren. MSc Thesis, SXTCM, China, 2015.
18. M. Karin, *J. Biol. Chem.*, **270**, 16483 (1995).
19. Y.J. Gu, C.F. Bao, J. Wei, J. Liang, Z.A. Gao. *Chin. J. Histochem. Cytochem.*, **3**, 328 (2009).
20. Q. Y. Wang, F. Liu, F.J. Wu, J.L. Li. *Chin . J . Integr. Tradit . West Med .*, **2**, 229 (2013).
21. X.J. Cao, C.Y. Geng, W. Dong, C.L. Zhang, S. Liu, Q.J. Li. *Zhong guo Bi JiaoYi Xue Za Zhi.*, **23**,40 (2013).
22. C.H. Bailey, D. Bartsch, E.R.Kandel, *Proc. Natl. Acad. Sci.*, **93**, 13445 (1996).
23. S. Finkbeiner, S.F. Tavazoie, A. Maloratsky, K.M. Jacobs, *Neuron.*, **19**, 1031 (1997).
24. T.D. Palmer, J. Takahashi, F.H..Gage, *Mol. Cell. Neuro. Sci.*, **8**, 389 (1997).
25. D.Y. Zhu, L. Lau, S.H. Liu, J.S. Wei, Y.M. Lu, *Proc. Natl. Acad. Sci.*, **101**, 9453 (2004).
26. C.P. Arthur, M.H. Stowell, *Structure*, **15**, 707 (2007).
27. F. Valtorta, M. Pennuto, D. Bonanomi, F. Benfenati, *Bioessays*, **26**,445 (2004).
28. W.G. Honer, P. Falkai, C. Chen, V. Arango, J.J. Mann, A.J. Dwork, *Neuroscience.*, **91**, 1247 (1999).
29. C. LaVecchia *Maturitas.*, **47**, 265 (2004).
30. M. Takeuchi, K. Hirao, A. Toyoda, M. Irie, Y. Takal, *J. Biol. Chem.,* **272**,11943 (1997).
31. Q. Liu, J. Trotter, M.M. Peters, H. Cheng, J. Bao, X.

Han, E.J. Weeber, G. Bu, *J. Neurosci.,* **30**, 17068 (2010).

32. El-Husseini AE, Schnell E, Chetkovich DM, Nicoll RA, D. S. Bredt, *Science,* **290**, 1364 (2000).

33. T. C. Sacktor, *Prog. Brain Res.,* **169***, 27 (2008).

34. M. Migaud, P. Charlesworth, M. Dempster, L.C. Webster, A.M. Watabe, M. Makhinson, Y. He, M.F. Ramsay, R.G. Morris, J.H. Morrison, T.J. O'Dell, S.G. Grant, *Nature*, **396**, 433 (1998).

Mechanical properties and microstructure of hot rolled NM360/Q345R composite interface analysis

J. Li[13], L.Ma[123]*, G. Zhao[123], Q. Huang[23], X. Yang[123], M. Cheng[123]

[1.]*Taiyuan University of Science and Technology, Taiyuan 030024,Shanxi,China*
[2.]*Shanxi Provincial Key Laboratory of Metallurgical Device Design Theory and Technology,*
[3.]*The Coordinative Innovation Center of Taiyuan Heavy Machinery Equipment*

The rolling reduction rate is one of the important factors that affect the bonded interface of a composite plate. In this paper, the mechanical properties and microstructure of the interface were studied for 30%, 50% and 70% rolling reduction rates. The NM360/Q345R composite plates were analyzed by a universal tensile testing machine, OM, SEM and EDS. As the rolling reduction rate increased, both the tensile strength and the elongation increased. When the reduction rates were 30% and 50%, the bonding interface was poor and apparent cracks could be observed after the tensile tests. When the reduction rate reached 70%, no voids or cracks existed, the breaking interface was smooth and neat and the bonding interface formed a common structure. Significant decarbonization of NM360 occurred at the bonding interface. When the reduction rates were 30% and 50%, long strips or black dots of particles appeared near the interface. The black particles were Mn and Si oxides, which could have a negative effect on the bonding interface.

Keywords:NM360/Q345R, Mechanical properties, Bonded interface, Microstructure.

INTRODUCTION

The wear-resistant composite steel plate is a new anti-wear composite material manufactured by a cladding technology, which could not only fully utilize the advantage of anti-wear alloys and base materials, but it could also make up for the corresponding shortcomings. Owing to their perfect performance not displayed by other single metals or alloys, the wear-resistant composite steel plates are widely utilized in various industrial fields [1-8].

The wear-resistant composite steel plates are often fabricated by an overlaying technology [9]. During overlaying, the base steel plate is unevenly heated; therefore the gradient of temperature fields is high. This could easily lead to high welding residual stress and deformation. Moreover, the overlaying leads to significant roughness of the overlaying surface, which could cause issues to further machining.

In hot roll bonding [10-12] rolling mills are utilized in the production of composite plates. As a result of the strong force of the rolling mill in combination with the thermal effect, two surfaces of compound metals are pressed together and plastic deformation occurs over the entire metallic cross-section [13].

Until recently, there have been only a few studies on wear-resistant hot rolled bonding plates has been significantly rare. Qiu [4] studied the effects of rolling and heat-treatment on the structure and properties of the NM450D/ Q235B clad plate [14]. Gong studied the cladding rolling technology of the wear-resistant steel/carbon steel [15].

In this paper, the mechanical properties, the metallographic structure and microstructure of the wear-resistant steel 360 (NM360) - carbon steel Q345R composite plate after vacuum hot rolling were analyzed.

EXPERIMENTAL PROCEDURE

Fabrication of hot-rolled two-layered NM360/Q345R composite

In this study, the two-layered NM360/Q345R composite was roll-bonded, Q345R, being the base layer and NM360 the cladding layer. The chemical composition of Q345R and NM360 is presented in Table 1.

Firstly, the NM360 and Q345R steels were prepared and underwent surface treatment. The composite surface had to be cleaned and smoothly ground, which allowed the two types of metal atoms to mutually diffuse and reach a metallurgical bonding.

Table 1. Main chemical composition of NM360 and Q345R materials (mass fraction %)

	C	Si	Mn	P	S	Cr	Ni	Mo	B
NM360	≤0.25	≤0.70	≤1.30	≤0.025	≤0.010	≤1.40	≤1.00	≤0.50	≤0.004
Q345R	0.15	0.35	1.40	0.013	0.004	—	—	—	—

By a wire brush machine the surfaces were polished until the "sand surface" effect was observed, though the surface roughness increase led to the subsequent rolled bonding of the composite.Subsequently, the polished surfaces were cleaned with absolute ethanol for surface adhesion and oil removal. The surfaces were blown-dried. Secondly, the NM360 and Q345R steels were batched and welded with the clean surfaces facing each other. The composite slab was sealed by argon arc welding and the vacuum evacuating nozzle was welded. Finally, a two-stage diffusion vacuum pump was utilized for the slab to be pumped to the high vacuum state of 1.0×10^{-3}Pa and the suction nozzle was sealed at a high temperature by hot pressure.

The NM360 thickness was 3 mm and the Q345R thickness was 10 mm. The NM360/Q345R composite slabs were preheated at 1200ºC and held at this temperature for 10 min. Consequently, hot rolling experiments were performed at 0.2 m/s, the stacks were roll bonded with reduction rates of 30%, 50% and 70%, respectively and cooled down in the air, subsequently to rolling. The sizes of the stacks and the rolling conditions of hot rolled composite are presented in Table 2.

Microstructure analysis and mechanical tests

In order to evaluate the rolling reduction effects of the NM360/Q345R composites on the tensile strength, the rolled composites were prepared according to the Chinese Standard GB/T 6396-2008, along the rolling direction. For the tensile fracture type study, the tensile fracture surfaces were observed by a scanning electron microscope (SEM).

The NM360/Q345R composites were polished and etched in a solution of 4% nitric acid and 96%

ethyl alcohol. The RD-ND plane microstructure was observed by ultra-deep microscope (OM), scanning electron microscope (SEM) (ZEISS SIGMA FE-SEM) and EDS.

RESULTS AND DISCUSSION

Mechanical properties of NM360/Q345R composite plate

Fig.1 demonstrates the tensile strength data of the NM360/Q345R composites with various rolling reduction rates. The yield and tensile strength increased along with the elongation, as the rolling reduction rate increased. Regarding the NM360/Q345R composite at 70% rolling reduction rate, the yield and tensile strength reached the maximum of 396.12 MPa and 514.84 MPa respectively, whereas the elongation was the longest, 39.95%. The tensile strength revealed that coherent and well-bonded layers could support each other; this had a direct effect on both the tensile strength and the elongation [16]. The best performance was observed when the reduction rate was 70%.
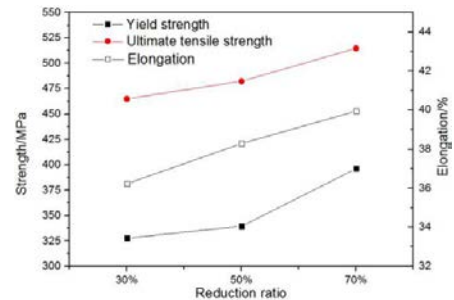

Fig.1. Comparison of mechanical properties of NM360/Q345R composite

Tensile fractography

Fig. 2 a/b presents the fractography at 30% and 50% reduction rate, respectively.

Table 2. Various base layer thicknesses of rolling compound crafts

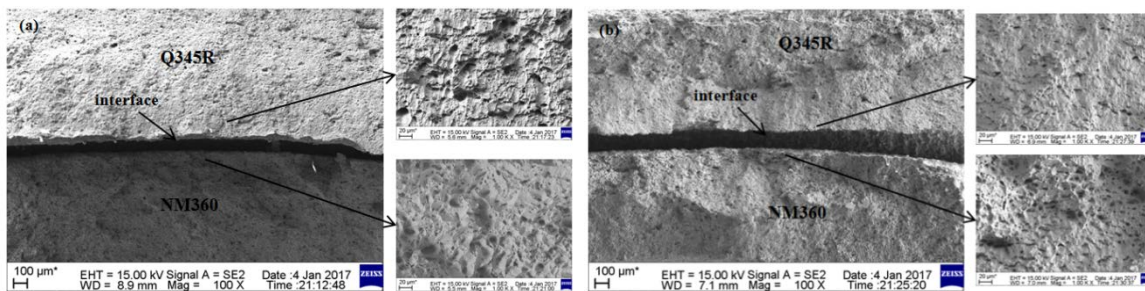|	Plate length +width	NM360	Q345	Rolling temperature	Rolling reduction rate
1	200×100	3mm	9mm	1150℃	30%
2	200×100	3mm	9mm	1150℃	50%
3	200×100	3mm	9mm	1150℃	70%

Fig. 2. Interface and fracture morphology of NM360/Q345R composite: (a) 30% reduction rate; (b) 50% reduction rate
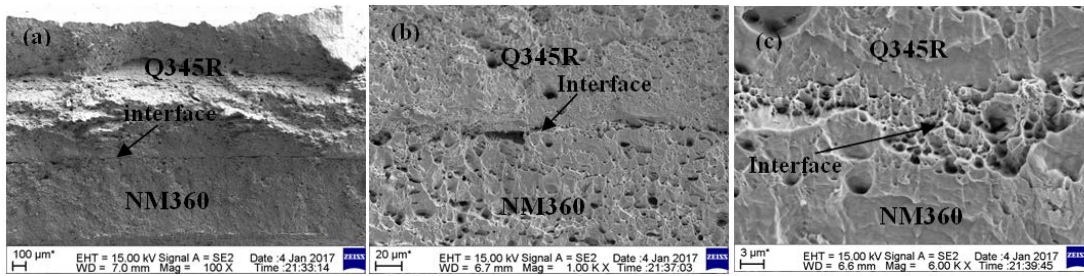
Fig. 3. Interface and fracture morphology for NM360/Q345R composite at 70% reduction rate

Subsequently to tensile failure, an apparent delamination could be observed from the low-magnification picture (100×) in these two conditions, which could be attributed to low bonded strength and poor compatibility of deformation. In NM360 and Q345R a high number of dimples existed, therefore it could be proved that the fracture type of the substrates was ductile. As the reduction rate increased, an increasing number of dimples on the substrates occurred and became increasingly low-sized. It could be observed that the toughness of every single layer was improved as the reduction rate increased, which could also be proved from the tensile mechanical properties.

Fig. 3 presents the tensile fracture morphology at 70% reduction rate. The bonding interface was quite straight and neat, no visible cracks and high-sized pores appeared which proved that the bonding performance was good, as shown in Fig. 3a/b. When the reduction rate increased to 70%, the interface was well-bonded and no delamination could be observed at the interface.Therefore, the bonding strength was high. Through further observation of the fracture morphology (Fig. 3b/c), it could be seen that the substrates near the interface displayed a number of dimples that were the typical ductile fracture feature, demonstrating that a ductile fracture occurred on the substrate. Compared to Q345R or te NM360, the dimples on the interface were quite close and the overall interface was well combined. From the aforementioned discussion, only at a reduction rate of 70%, good bonding between NM360 and Q345R could be obtained under the tested conditions.

Microstructure analysis of interface

The microstructure morphology and grain size under various reduction rates were analyzed by OM. It could be observed that the bonding interface was straight and the NM360 grain size exceeded the Q345R grain size. Defects such as holes in the composite interface were not observed and the grain distribution was uniform, which indicated that a bonded interface could be formed under the experimental conditions. The Q345R side formed a high amount of pearlites that are displayed as black bands in Fig. 4. Also, as the rolling pressure increased, the pearlites changed from coarse to fine.

A degree of decarburization existed on the side of NM360. This was due to the fact that the mass fraction of NM360 exceeded that of Q345R and the carbon atoms of the NM360 side spread to the Q345R side. It was observed that the carbon steel side decarburizing layer width decreased as the reduction rate increased. Although the high temperature could beneficiate carbon atoms diffusion, the deformation effect on the decarburization layer was higher compared to the temperature effect. Therefore, the decarburization layer became thin when the rolling pressure gradually increased. In addition, the grain size became increasingly lower as the reduction rate increased, which was due to the occurrence of total recrystallization in the grains. This recrystallization could make the grains fine and improve the mechanical behavior of the composite plate.
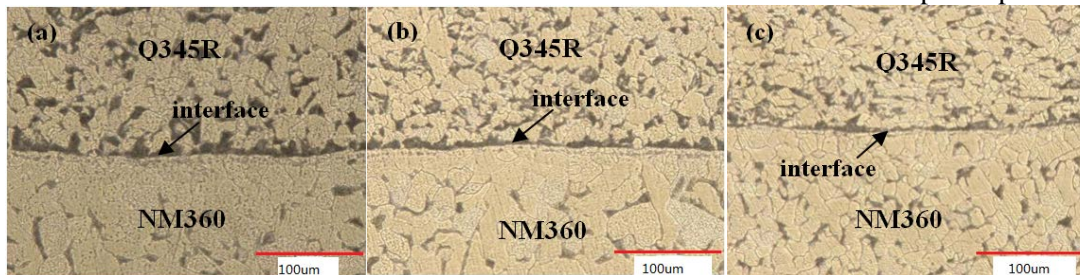

Figure.4. OM of NM360/Q345R composite (a) 30% reduction rate; (b) 50% reduction rate; (b) 70% reduction rate
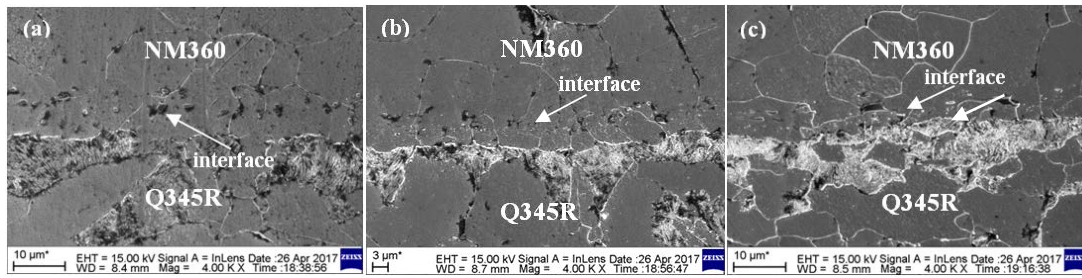
Fig.5. SEM of NM360/Q345R composite: (a) 30% reduction rate; (b) 50% reduction rate; (b) 70% reduction rate

The SEM micrographs of the NM360/Q345R are presented in Fig. 5a/c. The material interfaces were bonded without pores or voids, which indicated a successful fabrication of NM360/Q345R sheets by hot-roll-bonding. Thin elongated pearlites were located along the interface. The NM360/Q345R composite plate structures were mainly ferrite and pearlite. The mechanical performance was defined by the pearlite spacing and the pearlite mass diameter, because fracture usually occurred on the surfaces of pearlite and ferrite when the lamellar pearlite was being stretched by external forces. When the pearlite spacing and mass diameter became low, the phase interface increased and the dislocation motion inhibition was high. This led to an increase in the deformation resistance and possibly contributed to the strength, hardness and plasticity improvement. Moreover, the lamellar pearlite spacing decreased. When the carburizing layer was significantly thin, it could slide under external force, possibly producing plastic deformation and also be bent. As the rolling reduction rate increased, both the spacing and the diameter of pearlite in the NM360/Q345R composite interface decreased, which could improve the mechanical properties. When the reduction rate reached up to 70%, lowest pearlite spacing and pearlite mass spacing diameter were observed. This ensured that the composite interface was well combined and was not stratified during stretching (as shown in Fig. 6).

The transformation of pearlite included an incubation period, the carbide nucleus grew along with the iron grain core growth. During pearlite transformation, the strong carbide forming elements titanium, niobium and vanadium formed alloy carbides, while the weak carbide forming element manganese formed rich manganese alloy cementite. Therefore, the nucleation and growth of carbides depended on the diffusion and enrichment of the elements. The atomic diffusion coefficient of the carbide forming element in austenite was by 10^5 orders of magnitude slower than the atomic diffusion coefficient of the carbon atom, which could slow down the nucleation and growth of the alloy carbide or cementite and lead to an increase in the pearlite transformation period, whereas the pearlite spacing decreased [17]. Significantly low amounts of manganese existed at the interface, which means that the micro-alloy addition to steel could not only have an effect on the refined grain and precipitation strengthening. Also, the carbide formed by the micro-alloy elements could refine the pearlite lamellar spacing and further improve the strengthening effect. As the reduction rate increased, the NM360/Q345R recrystallization well refined the austenitic grains. Moreover, elements such as Mn and Si, dispersed in the interface, provided conditions for a high amount of pearlite to be formed. The composite plate thermal deformation temperature decreased as the rate increased, which could reduce the carbide forming elements atomic diffusion coefficient in austenite, further leading to a significant slow down of nucleation and growth of the alloy carbide or alloying cementite. This phenomenon increased the incubation period of pearlitic transformation and decreased the pearlite spacing.
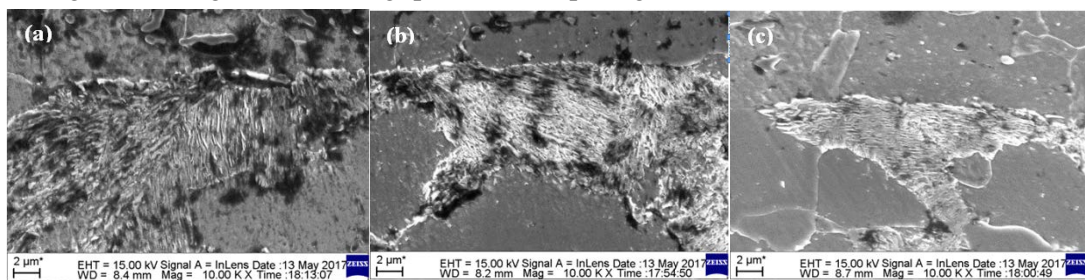

Fig. 6. SEM of pearlite at the interface of NM360/Q345R composite: (a) 30% reduction rate; (b) 50% reduction rate; (b) 70% reduction rate
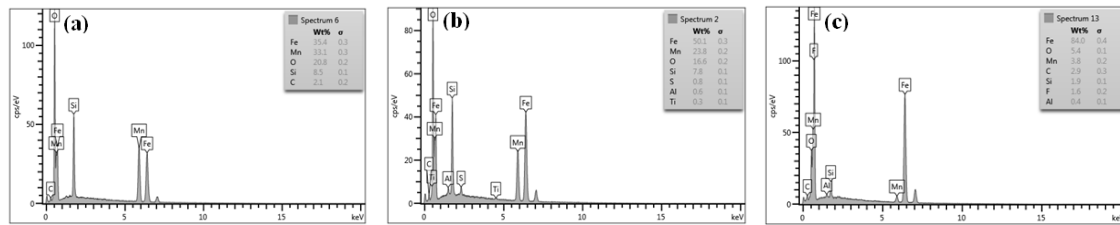
Fig.7. EDS of particles at interface of NM360/Q345R composite: (a) 30% reduction rate; (b) 50% reduction rate; (b) 70% reduction rate

Through further observation, the interface had a continuous dense distribution of dotted black particles or black long strips, when the reduction rate was low. The interface had a high amount of oxygen by point scanning (Fig. 7), even if the NM360/Q345R slab was vacuumed. Since the surface to be bonded was rough, a high amount of oxygen was still attached to the surface. Except oxygen, there were also Fe, Mn and Si. Fe is an inherent element in both NM360 and Q345R, whereas Mn and Si were elements in NM360 and Q345R that were diffused around the interface. It was found that the black objects at the interface were Mn and Si oxides and these oxides had an effect on the bonding strength. Also, similar studies demonstrated that both black impurities and oxides formed at the interface. Nomura *et al*. [18] discovered that a steel surface containing Si and Mn was easy to produce Si-Mn oxide formations [18]. Peng *et al*. [19] reported that the breakdown oxide led both sides of the interface to reach a solid metallurgical combination during rolling[19] . The higher the amount of fine oxides, the easier was the interface bonding. Jing *et al*. [20] reported that a 5 μm wide black strip inclusion existed at the interface of the steel/carbon steel composite, which was caused by both oxidation and diffusion [20].

Therefore, when the reduction was 30% and 50%, the mechanical properties of the composite were poor and cracks occurred through stretching. As presented in Fig. 8, the long strips of particles became lower-sized and distributed in the interface, which occurred because the oxide was crushed under the high positive pressure. When the reduction rate increased to 70%, no black particles existed. The crushed oxide was dissolved in the structure of the bonding interface and subsequently dispersed in the interface, leading to low impact on the interface. Therefore, at a higher roll reduction rate, the interface was significantly improved.

CONCLUSIONS

In this paper, the effects of rolling reduction rates on the mechanical properties, metallographic interface and microstructure of the NM360/Q345R composite were studied.

1) As the rolling reduction rate increased, both the tensile strength and the elongation increased. The best comprehensive performance occurred when the reduction rate was 70%.

2) At a reduction rate of 30% and 50%, the bonding interface was poor and apparent cracks could be observed subsequently to the tensile tests. When the reduction rate reached up to 70%, no voids or cracks existed and the breaking interface was smooth and neat. Also, the bonding interface formed a common structure.

3) It could be observed by the ultra-deep microscope that the bonding interface was straight. Significant decarbonization of NM360 occurred. When the reduction rate was 30% and 50%, long strips or black dotted particles appeared near the interface. These black particles were Mn and Si oxides, which could have a negative effect on the bonding interface.

REFERENCES

1. Z. Yang, Z. Meng, *Metallurgical Equipment*, **6** (3), 55 (1997).
2. R.C. Schrama, *Lubrication Engineering*, **50** (6), 438 (1994).
3. X.Wen, X. Wang, X. Yuan, P. Wwn, Q. Yang, *Heat Treatmen*t, **26** (3), 56 (2011).
4. X.W. Qiu, Y.P. Zhang, G.L. Chun, *Applied Mechanics and Materials*, **121-126**, 3551-3554(2012).
5. F.C. Li, *Shandong University of Science and Technology* (2011).
6. L.G. Zhang, *Cement Engineering*, (3),50-53(2012)
7. Yuan Jinsheng, *China Building Material Equipment,* (3), 26-27(1996).
8. P. Zhang, Y.H. Zhang, Q.M. Chang, *Foundry Equipment and Technology*, **2**(1),53-55 (2012)

9. L. Li, M.Y. Chen, *Wide and heavy plate*, **22**(2),38-43 (2016)

10. J.Y. Kang, J.G. Kim, S.K. Kim, K.G. Chin, S. Lee, H.S. Kim. *Scripta Materialia*, **123**,122-125 (2016)

11. J. Park, M. Kang, S. S. Sohn, J. S. Kim, H. S. Kim, W. T. Cho, *Materials Science & Engineering A*, **686**,160-167, (2017).

12. J. Park, J.S. Kim, M. Kang, S.S. Sohn, W.T. Cho, H.S. Kim, *Scientific Reports*, **7**:40231,(2017).

13. G. Zhao, Q. Huang, C. Zhou, Z. Zhang, L. Ma, X. Wang, *Revista De Metalurgia ,* **52**(2), e069, (2016).

14. J. Qiu, X.R. Cheng, K. Lan, D. Lei, D.J. Huang, *Special Steel*, (2),56-59(2017)

15. C.W. Gong, *Wuhan University of Science and Technology* (2015).

16. R. Abedi, A. Akbarzadeh, *Materials & Design*, **88**, 880-888 (2015).

17. C. Yang, *Kunming University of Science and Technology* (2011).

18. M. Nomura, I. Hashimoto, S. Kozuma, M. Kamura, Y. Omiya, *Tetsu-to-Hagane*, **92**(6), 378-384(2006)

19. X.K. Peng, R. Wuhrer, G. Heness, W.Y. Yeung, *Journal of Materials Science,* **35**(17),4357-4363 (2000)

20. C. Jing, J. Tong, Beijing, *Journal of University of Science & Technology Beijing,* **29**(10), 985-988.(2007)

Benzothiazole-based ionic liquids (BIL)-induced acute toxicity attributed to damage to antioxidant enzyme system in zebrafish (*Danio rerio*)

Y. Luo[1], H. Song[1]*, Y. Chen[1], G. Li[1], M. Zhu[2],

[1]*Department of Pharmaceutical and Biological Engineering, Sichuan University, Chengdu, China*
[2] *Chengdu University of Traditional Chinese Medicine, Chengdu, China*

Ionic liquids (ILs), considered to be green solvents, are widely distributed in the environment and thus exposure to these chemicals has attracted attention due to the potential adverse consequences on organisms and ecosystems. The aim of this study was to investigate the influence of benzothiazole-based IL (BIL) on zebrafish survival and determine whether oxidation was responsible for mortality. Zebrafish (*Danio rerio*) were exposed to 5 different concentrations of 4 acidic and one neutral IL solutions for 24 h and the 50% lethal concentrations (LC50) for each benzothiazole-based IL were determined and compared. Hepatopancreas samples were taken at the 6th, 12th, 18th and 24th h after exposure. Catalase (CAT) and glutathione peroxidase (GSH-Px) activity, as well as levels of reactive oxygen species (ROS) and malondialdehyde (MDA) were measured. Data demonstrated that BIL could significantly decrease hepatopancreas CAT and GSH-Px activity accompanied by an increase in the levels of reactive oxygen species ROS and MDA. It was also found that the toxicity of acidic ionic liquids was higher than that of neutral ionic liquids.

Keywords: Ionic liquids, Oxidative stress, Reactive oxygen species, Catalase, Malondialdehyde; Glutathione peroxidase

INTRODUCTION

Ionic liquids (ILs) are organic salts consisting of organic cation and organic or inorganic anion, such as Br-, BF_4^-, PF_6^-, or $-CH_3SO_3^-$ and are considered to be green solvents [1,2]. They are extensively used in catalysis, electrochemistry, extraction separation due to specific physical and chemical properties, such as low melting points (<100ºC), negligible vapor pressure, high thermal stability and good conductivity [3-7]. It is found that IL are more effective than traditional solvents and are considered to be relatively "green" because of their good recyclability [7-9]. In recent years, a series of benzothiazole-based ionic liquids (BIL) were developed which demonstrated potential applications in catalysis and extraction separation [10,11]. It is an unavoidable problem that traces of IL are released in the environment during large-scale use. At present most of toxicity tests concentrated on imidazole-based IL but data regarding BIL are rare.

Zebrafish are sensitive to environmental chemical-induced effects [12-16] and have characteristics such as small size, water quality tolerance and low cost and thus are widely used as a model to test the effects of ultraviolet rays, heavy metal salts, pesticides, sewage and also to assess water quality [14-18].

Recent studies have found that some ILs are potentially toxic because of the raw organic material used in synthetic processes. The chemical stability of ILs may result in environmental accumulation and lead to certain damage to organisms and ecosystems [19,20]. The effect of IL-mediated toxicity on aquatic organisms has attracted significant attention [21-23]. Thus, this study concentrated on the acute toxicity due to exposure of fish to ILs. Moreover, it was found the SOD of zebrafish decreased after exposure to ILs, which induced oxidative stress in zebrafish [24]. This study selected five BILs including 4 acidic ILs ([HB][CH₃SO₃], [HB][ρ-TSA], [HB][BF₄], [HB][Br]) and one neutral IL ([C₄B][Br]) to examine acute toxicity in aquatic environment and to recognize the influence of different cations (or anions) on the toxicity. Finally, the underlying mechanisms of the toxicity wereexplored.

The study on the acute toxicity of pollutants to zebrafish can throw light on the possible impact of the tested chemicals on the aquatic organisms and the short-term exposure effect [25,26]. Some important bio-chemical indices such as reactive oxygen species (ROS) content, antioxidant enzyme (GSH-Px and CAT) activity and malondialdehyde (MDA) content of zebrafish could provide more detailed information on the toxicity [27-30]. Therefore, in this study, zebrafish were used as indicator organisms to study the acute toxicity and the indices above were determined. Based on the results, the toxicity of different ILs on zebrafish was evaluated and compared, which could provide the basis for the study of the effect of the change of cation or anion on the ionic liquid toxicity.

To whom all correspondence should be sent:
E-mail: hangsong@vip.sina.com

EXPERIMENTAL

Materials and methods

Chemicals and reagents

The ILs were prepared as previously described [31] and purities were more than 98% as measured by high performance liquid chromatography (HPLC) following recrystallization. Analytical grade chemicals for IL synthesis were purchased from Kelong (Chengdu, China). BCA protein assay kit, reactive oxygen species (ROS) assay kit, glutathione peroxidase (GSH-Px) assay kit, catalase (CAT) assay kit and malondialdehyde (MDA) assay kit were purchased from Jiancheng Bioengineering Institute (Nanjing, China). The IL solutions were made fresh by dissolving the IL in distilled water and diluting to the desired concentrations. The UV–Vis spectra were recorded on a UV-2800 spectrophotometer (Hengping Scientific Instrument, China) in methanol. The fluorescence intensity was recorded on a microplate reader (Molecular Devices, USA). The concentrations of the products were determined by HPLC using an LC-20AT HPLC instrument (SHIMADZU international trade, China) with a C18 column (3.9 mm×150 mm, 5 µm) with an internal standard.

Experimental fish

Zebrafish, purchased from Chengdu Aquarium Fishery (China), displayed body length of 30 ± 5 mm and weighed 0.3 ± 0.1 g with normal appearance, without visible deformity and were considered healthy. Each batch was raised in a 20 L fish tank for 1 week and mortality rate was below 10% under the lab conditions of pH = 7.4 ± 0.2 and temperature of $28 \pm 1°C$. The water was maintained in aerated state and was replaced with fresh water once a day to ensure clean conditions for the fish. During this period, fish were fed every two days, on a 12 h light/dark cycle [32]. Finally, fish were fasted for 24 h before test.

Preliminary acute toxicity test

Preliminary experiments were conducted according to procedure [33] with modification [34] to acquire 50% lethal concentration (LC50) after 24 hour exposure.

Index determination

All index determinations were carried out according to standard procedures. For example, ROS was measured by the DCFH-DA incineration method [35] and protein content was determined

with BSA as the standard protein [36]. CAT activity was measured by the rate of ultraviolet absorption decrease (Ultraviolet spectrophotometer instrument TU - 1810，Beijing Purkinje General Instrument，Beijing China) [37]. Glutathione peroxidise (GSH-Px) was determined according to the reported method [28]. The content of MDA in zebrafish was determined by the method of thiobarbituric acid (TBA) colorimetry [38]

RESULTS AND DISCUSSION

Effect of ILs in acute toxicity test

According to the test method of Fish Acute Toxicity for Dangerous Chemical Products (GB/T 21281-2007) and International Organization for Standardization (ISO), a substance is considered to be super virulent when the LC50 of sample solution < 50 mg·L^{-1} and hypotoxic when LC50 of sample solution was beyond 100 mg·L^{-1}. Therefore. it was necessary for the LC50 test to consider zebrafish's lethal data in the range from 10 mg·L^{-1} to 300 mg·L^{-1} of 5 kinds of BILs. The acute toxicity was measured in ILs solutions of pH $\approx$ 7. The test results are shown in Table 1. The results showed that the acid ILs had a more significant impact on the growth behavior of zebrafish than the neutral ILs.

Table 1 LC50 of 5 types of BILs on acute toxicity of zebrafish

ILs	LC$_{50}$/24 h	Toxicity grade
Deionized water	2L	none
[HBth][CH$_3$SO$_3$]	20.6±1.2 mg·L^{-1}	high
[HBth][ρ-TSA]	26.4±0.4 mg·L^{-1}	high
[HBth][BF$_4$]	18.21±0.8 mg·L^{-1}	high
[HBth][Br]	31.3±1.2 mg·L^{-1}	medium
[C$_4$Bth][Br]	166.7±17.8mg·L^{-1}	low

The results of Table 1 suggested that the toxicity of acidic BILs was higher than that of neutral BILs. BILs with the same cation [HB] all caused corrosion to zebrafish. The toxicity grade of the acidic ILs ranged from highly to medium, while that of the neutral [C$_4$B][Br] was of low toxicity grade. This indicated that the safety of neutral ILs [C$_4$B][Br] was much better than that of some reported acid ILs [39].

ROS index

ROS detection could be used in toxicology studies to evaluate the toxic effect of contaminants and to explore to a certain extent the mechanism of toxic effects on organisms. The ROS level of the five groups (four tested groups and one control group) was measured for various time periods of each IL.

All ILs increased the ROS content of liver cells in zebrafish with time. In general, the ROS content of zebrafish liver cells treated with the 5 kinds of ionic liquids was significantly higher than that of the control group.

The ROS content of zebrafish liver cells treated with acidic ionic liquids was significantly higher than that of neutral ionic liquids. The analysis results are shown in Fig.1.
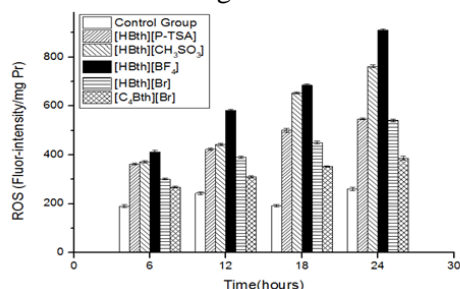

Fig. 1. Reactive oxygen species (ROS) in the hepatopancreas of zebrafish at different kinds of ionic liquids. Each bar is the mean of three replicates. The error bars represent standard deviation (SD).

The liver is an important organ that regulates the mechanism of redox reaction and is also the main detoxification organ. Some key enzymes such as Most of the antioxidant enzymes are present in the liver and these enzymes can be used to remove excess ROS. Under normal circumstances, the metabolism of living oxygen free radicals is in equilibrium, however, when the body is destroyed after contamination, ROS free radical metabolism in the liver cells may be abnormal, resulting in excessive production of ROS, which induced cell oxidative stress. In this experiment, the ROS content of all the treated groups was higher than that of the control group and the ROS content in the zebrafish treated by the acidic ionic liquid was significantly higher than that of the neutral ionic liquid. The ionic liquid induces the ROS content of zebrafish and increases its accumulation over time. With the accumulation of time, the ROS content of each concentration group exceeded the control group, indicating that time accumulation is also a reason for the increase of ROS content. The exposure time has a certain effect on the toxicity accumulation of ionic liquids.

Enzyme index

The CAT and GSH-Px levels of the five groups (four test groups and a control group) were measured at various time intervals for each IL. The analysis results are shown in Figs.2 and 3. It is seen that after exposure to the five BILs for different time intervals, the CAT and GSH-Px activities were remarkably reduced. In particular, the CAT and GSH-Px levels of the acidic ILs were lower than

that of the neutral IL with time.

CAT belongs to the antioxidative system which plays the role of indirectly clearing hydroxide radicals. It follows from Fig. 2 that after exposure to the five BILs for different times, the CAT activities were remarkably reduced. The CAT activity significantly dropped after 6 h for all tested acidic ILs [HB][p-TSA], [HB][CH$_3$SO$_3$], [HB][BF$_4$] and [HB][Br], while it gradually decreased for the neutral IL [C4B][Br]. However, after 12-h exposure, the activity of acid ILs apparently increased. This phenomenon might occur through an internal regulation mechanism which is similar to the feedback regulation of fish. CAT activity rapidly decreased during the first 6 h. Due to the zebrafish suffering from the ILs solution, the internal system of fish would produce corresponding hormones or steroids to steadily adjust internal environment, and it was raised during the second 6 h [40,41]. When exposed longer than 12 h, the CAT activity decreased because the internal system was out of balance and could not take any available adjustment reaction. These results proved that the acidic ILs could significantly impact on the enzyme regulation mechanism of zebrafish but the monotonously decrease of CAT activity demonstrates that the neutral ILs [C$_4$B][Br] has a weak effect on the regulating ability.

GSH-Px belongs to antioxidant enzymes which present in the liver. GSH-Px can remove viable intracellular peroxides and play a key role in protecting cells from free radical damage. Intracellular lipids easily react with free radicals to produce lipid peroxides. GSH-Px can use GSH to reduce lipid peroxides, thereby eliminating the toxic effects of free radicals.
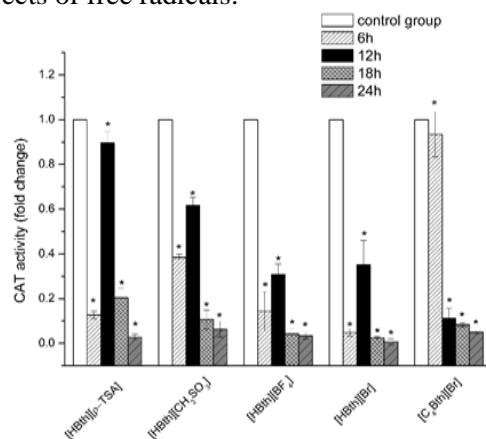

Fig. 2. Catalase (CAT) activity (multiple numerals) in hepatopancreas of zebrafish at different time intervals. Each bar is the mean of three replicates. The error bars represent standard deviation (SD). The asterisk denotes a response that is significantly different from the control (*p<0.05)

Fig. 3 demonstrates decrease in the antioxidant enzyme activity. In particular, the GSH-Px level of acidic ILs was lower than that of neutral ILs and with time, GSH-Px activity in the body gradually decreased. This is due to the accumulation of ionic liquids in the body to destroy the antioxidant activity of the organism.
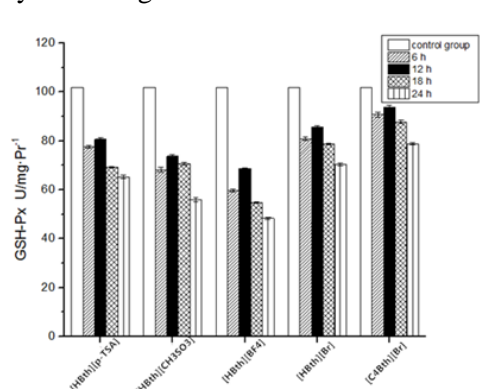

Fig.3. Glutathione peroxidase (GSH-Px) activity (multiple numerals) of zebrafish at different time intervals. Each bar is the mean of three replicates. The error bars represent standard deviation (SD).

The test on SOD [24] showed that the zebrafish took in ionic liquids into the body, and the liver metabolism had an impact on the reduction of SOD activity which on its turn reduced the ability to eliminate oxygen free radicals producing toxic effects on zebrafish.

The MDA levels of the five groups (four tested groups and one control group) were measured in various time periods for each IL. The results are shown in Fig.4 which demonstrates that the MDA contents of all test groups notably increased.
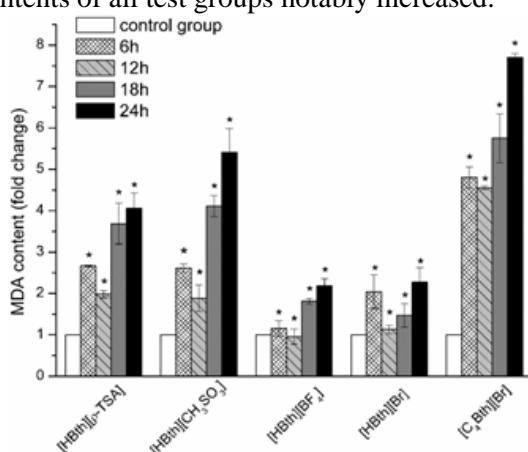

Fig.4. MDA activity (multiple numerals) of zebra fish at different time intervals. Each bar is the mean of three replicates. The error bars represent standard deviation (SD). The asterisk denotes a response that is significantly different from the control (*p<0.05)

Lipid peroxidation is a series of reactions caused by free radicals, which have an important relationship with the active oxygen content in the

organism. MDA is the product of lipid peroxidation. The change in MDA content reflects the degree of lipid peroxidation and indirectly reflects the degree of oxidative damage. The MDA contents of all test groups notably increased. The acidic ILs groups decreased a little at 12 h, which could be attributed to feedback regulation. The MDA contents of all ILs tended to rise up during the whole experiment, which proved that the damage of the cells by the ILs solutions was gradually accumulated.

CONCLUSIONS

The ROS in zebrafish increased and inhibited the activity of antioxidant enzymes under the experimental conditions. It was deduced that if the experimental time was prolonged, with the reactive oxygen species accumulation and damage of the anti-oxidation system, the reactive oxygen species caused tissue damage - at high concentrations of the treatment group zebrafish sick or even death phenomenon was likely to appear. The benzothiazole-based ILs, especially those with acidic anion, exhibited toxicity to zebrafish at a certain lethal concentration. The toxicity test indicates that the acidic ILs are more corrosive than the neutral ILs to superficial and internal organs of aquatic life. The CAT, GSH-Px and SOD activity of fish exposed to acidic or neutral ILs solution decreased. The MDA level of fish increased significantly for all ILs and exhibited a higher level for the neutral ILs. These results suggest that acidic ILs have higher lethal toxicity while neutral ILs have a more serious impact on internal enzyme activity. This research could provide basic toxicological data and reference indicators of enzyme activity for benzothiazole-based ILs and be supposed to be beneficial for further study of the toxicity of ILs.

REFERENCES

1. R. A. Sheldon, F. Van Rantwijk, *Green Chem.*, **7**, 267 (2005).
2. Y.R. Luo, S.H. Wang, M.X. Yun, X.Y. Li, J.J. Wang, Z.J. Sun, *Chemosphere.*, **77**, 313 (2009).
3. K.M Docherty, *Green Chem.*, **7,** 185 (2005)
4. J. Ranke, S. Stolte, R. Stoermann, J. Arning, B. Jastorff, *Chem.Rev.*, **107**, 2183 (2007).
5. A. Romero, A. Santos, J. Tojo, A. Rodriguez, *J Hazard Mater.*, **151**, 268 (2008).
6. D. Ajloo, M. Sangian, M. Ghadamgahi, M. Evini, A.A Saboury, *Int. J. Biol. Macromol.*, **55**, 47 (2013).
7. T. Liu, L.S. Zhu, H. Xie, J. Wang, F. Sun, F. Wang, *Environ. Sci. Pollut. Res.*, **21**, 3936 (2013).
8. J.D. Holbrey, R.D. Rogers, *Industrial Applications for*

9. *Green Chemistry*, 446 (2001).
10. M. Petkovic, K.R. Seddon, L.P.N. Rebelo, C.S.Pereira, *Chem.Soc.Rev.*, **40**, 1383 (2011).
11. W.F. Luo, S. Yao, J.B. Liu, X.S. Zhou, H. Song, *West China Journal of Pharmaceutical Sciences,* **27**,61 (2012).
12. S.S. Dong, S.S. Dong, D.D. Zhou, X. Zhou, D.M. Ma, Y.L. Du, *Applied. Chem, Ind.,* **43**, 2343 (2015).
13. Z.P. Liu, S.L. Zhang, J.H. Yang, R. Tang, B.J. Li, *Environ. Sci. Technol.,* (2011).
14. J. Pérez, I. Domingues, M. Monteiro, AMVM. Soares, S. Loureiro, *Environ. Sci. Pollut., R.,* **20**, 4671 (2013).
15. D. Lima, L.F. Castro, I. Coelho, R. Lacerda, M. Gesto, J. Soares, A. Andre, R. Capela, T. Torres, A.P. Carvalho, M.M. Santos, *Journal of Toxicology and Environmental Health A.*,**78**, 747 (2015).
16. J.L. Lyche, I.M. Grzes, C. Karlsson, R. Nourizadeh-Lillabadi, P. Alestrom, E. Ropstad, *Journal of Toxicology and Environmental Health A,* **79**, 602 (2016).
17. J.G.S.D Rosa, G Koakoski, A.L Piato, M.R Bogo, C.D Bonan, L.J.G Barcellos, *Journal of Toxicology and Environmental Health A ,* **79**, 1 (2016) .
18. C. Pretti, C. Chiappe, D. Pieraccini, M. Gregori, F. Abramo, G. Monni, L. Intorre, *Green Chem.*, **8**, 238 (2006).
19. H.J. Jeon, Y.H. Lee, M.J. Kim, S.D. Choi, B. J. Park, S. E. Lee, *Environ. Toxicol. Pharm.,* **43**, 166 (2016).
20. R.D. Rogers, K.R. Seddon, *Acs Symposium.,* 1568 (2002).
21. A. Latała, P. Stepnowski, M. Nedzi, W. Mrozi, *Aquat. Toxicol.*, **73**, 91 (2005).
22. S.H. Wang, P.P. Huang, X.Y. Li, C.Y. Wang, Zhang, W.H.Wang, *Environ.Toxicol.*, **25**, 243 (2010).
23. X.Y. Li, X.Q. Miao, L.F. Zhang, J.J. Wang, *Ecotoxicol. Environ. Saf.*, **75**, 180 (2012).
24. M. Dong, L. Zhu, S. Zhu, J. Wang, J. Wang, H. Xie, Z. Du, *Chemosphere,* **91**, 1107 (2013).
25. C. Yanwen, L. Yingjie, Y. Xiaoxue, Y. Shun, S. Hang, *Chemical Industry and Engineering Progress,* 1000 (2016).
26. D. Xiong, T. Fang, L. Yu, X. Sima, W. Zhu, *Science of the Total Environment*, **409,** 1444 (2010).
27. L.N Clements, R Lemus, A.D Butler, K. Heim, M. R. Rebstock, C. Venezia, M. Pardus, *Arch. Environ. Contam. Toxicol.,* **63**, 391 (2012).
28. A.A. Horton, *Crit. Rev. Toxicol.*, **18 (1)**, 27 (1987).
29. F.V. Breusegem, E.Vranová, J.F. Dat, D. Inzé, *Plant.,* **161**, 405 (2001).
30. V.B Djordjevic, *Int. Rev. Cytol.*, **237**, 57 (2004)
31. V.I. Lushchak, *Comp Biochem Phys C.*, **153**, 175 (2011).
32. Q. Peng, Y.W. Zhang, X.M. Wang, Z.D. Wang, S. Yao, H. Song, *Chinese Journal of Synthetic Chemistry,* (2012).
33. M Diekmann, P Waldmann, A Schnurstein, T. Grummt, T. Braunbeck, R. Nagel, *Aquat .Toxicol.*, **68,** 27 (2004).
34. X.Y. Li, S.H. Zeng, W.H. Zhang, L. Liu, S. Ma, J.J. Wang, *Environ. Toxicol.,* **28**, 207 (2013) .
35. X. Zhang, Y.G. Liu, Beijing Medical University China Xiehe Medical University Press: Beijing. 211, 2007.
36. J.M. Lawler, W. Song, S.R. Demaree, *Free Radic. Biol. Med.*, **35**, 9 (2003).
37. M.M Bradford, *Anal. Biochem.*, **72**, 248-254 (1976).
38. S.B. Song, Y. Xu, B.S. Zhou, *Chemosphere*, **65**, 699 (2006).
39. Q.M. Zhang, L.S. Zhu, J. Wang, H. Xie, J. H. Wang, Y.N. Han, *Environ. Sci. Pollut. Res.*, **20**, 201 (2012).
40. J. Ranke, K. Mölter, F. Stock, U. Bottin-Webera, J. Poczobutta, J. Hoffmannb, B. Ondruschkab, J. Filsera, B. Jastorffa, *Ecotoxicol. Environ, Saf.,* **58**, 396 (2004).
41. A. Romero, I. Cakir, C. A. Vaslet, R. C. Stuart, O. Lansari, H. A. Lucero, *Journal of Biological Chemistry.*, **283**, 31438 (2008).
42. M. Perello, R. Stuart, E.A. Nillni, *Journal of Bio Chem.*, **283**, 19936 (2008)

Large eddy simulation of multiphase flow in button - type micro channels

Zh. He, J. Liu, X.-Y. Sun *, X. Gu

*College of Aerospace and Civil Engineering, Harbin Engineering University, Harbin
150001 China*

The reduction of the micro channel scale creates surface tension, wettability cannot be ignored, the capillary action and the friction between the fluid and the wall also play an important role, which makes difficult the direct observation. In this paper, various structure-micro channels with cross-sectional area of 200 μm × 200 μm were taken as the research object. Numerical simulation based on Smagorinsky model and VOF model (for dealing with multiphase flow interface problems) was used as research method to study the mixing effect of fluids in the micro channel. The results showed that the distance between the two button nodes, the node diameter, the distribution position, and the channel entrance angle have a certain effect on the mixing effect in the micro channel.

AIMS AND BACKGROUND

The flow characteristics of the fluid in a micro channel are very different from those in a general pipeline. Micro channels are widely used in the fields of electronics, aerospace and biotechnology because of their fast reaction rate and simple structure. With the development of computer technology, numerical simulation has been used to study micro channel problems and obvious results have been achieved. The numerical simulation can be a simple and economical method to respond to some phenomena in the micro channel, which is of great significance for the study of the mixing effect in the micro channel.

Yagmur *et al.* [1] used the large eddy simulation (LES) turbulence model in ANSYS-Fluent software to simulate the flow around a triangular column. The separation point of the flow and the Carmen vortex formed in the wake region were simulated. This shows that the large eddy simulation can well simulate the flow phenomenon.

Zhang *et al.* [2] used the dynamic model of the LES model to simulate the 60 ° inclined jet with a bottom impact, and compared the simulation results of the dynamic model and the k-ε model. When simulated by the k-ε model, the change of the reaction concentration is stable, and no local accumulation at the impact point was observed. The dynamic model could be used to observe the phenomenon, which indicated that the simulation results were more accurate.

Hu *et al.* [3] carried out large eddy simulation of the axial flow of a cylinder with different inclination angles. The LES turbulence model was used and the results showed that a turbulence vortex was formed on the rear side of the cylinder, which improved the efficiency of the washing. The larger the inclination angle, the better was the cleaning effect.

EXPERIMENTAL

Theory

The large eddy simulation (LES) builds on the turbulence statistical theory and the understanding of the Quasi-ordered structure overcomes the defects of the traditional turbulence model in time averaged processing and universality, which core is the simulation of sub-grid (small-scale movement) Reynolds stress [2]. At present, the commonly used sub-grid scale model is the Smagorinsky model, dynamic model, structure function model and so on.

Mass fraction equation and momentum equation were used to describe the VOF model [4]:

$$\frac{\alpha_q^{n+1}\rho_q^{n+1} - \alpha_q^n\ \rho_q^n}{\Delta t}V + \sum_f(\rho_q^{n+1}U_f^{n+1}\alpha_{q,f}^{n+1}) = \left[S_{\alpha_q} + \sum_{p=1}^n \dot{m}_{pq} - \dot{m}_{qp}\right] \quad (1)$$

where:

$n+1$ = index for current time step;
n = index for previous time step;
α_q^{n+1} = cell value of volume fraction at time step n+1;
α_q^n = cell value of volume fraction at time step n;
$\alpha_{q,f}^{n+1}$ = face value of the qth volume fraction at time step n+1;
U_f^{n+1} = volume flux through the face at time step n+1;
V = cell volume;

$$\frac{\partial}{\partial t}(\rho\vec{v}) + \nabla \cdot (\rho\vec{v}\vec{v}) = -\nabla\rho + \nabla \cdot [\mu(\nabla\vec{v} + \nabla\vec{v}^T)] + \rho\vec{g} + \vec{F} \quad （2）$$

In this paper, a button-type micro channel with a cross-sectional area of 200 μm × 200 μm was taken as the research object. Channel length is 6 mm, lengths of three entry sections are 0.9 mm, distance between the first button-type node to the inlet 3 is 2 mm, basic phase is water, second phase is air. Water flows from inlet 1 and inlet 2 into the channel, air flows from inlet 3 into the channel, the flow rate is

0.1m/s, the three inlets are velocity inlets, the outlet is a pressure outlet, the pressure is the standard atmospheric pressure. Using pressure-velocity couple algorithm, the pressure difference program selected PRESTO! algorithm, the time dispersion method is Bounded second order implicit format, and the momentum equation discrete mode is Bounded central differencing format, the time step is 0.0001 s, Courant number, sub-relaxation iterative factor and other parameters were selected according to the stability and convergence of calculation. The calculation model is shown in Fig. 1.

Fig. 1. Calculation model

As the size of the micro channel and the macro pipe varies widely, resulting in a large difference in boundary conditions, according to the different Knudsen number, several intervals can be distinguished [5]:

1）$Kn \to 0$ （$Re = 0$）

Ignores the diffusion term, satisfies the Euler equation;

2) $Kn \ll 10^{-3}$

Satisfies the N-S equation, suitable for non-slip boundary condition;

3）$10^{-3} \ll Kn \ll 10^{-1}$

Satisfies the N-S equation, not suitable for non-slip boundary condition;

4）$10^{-1} \ll Kn \ll 10$

Transition zone;

5）$Kn > 10$

Belongs to a free molecular flow.

Where $Kn=l/L$，l is the molecular free path, L is the characteristic size of the micro device. In the standard state, the effective diameter of the air molecule is 3.5×10^{-10} m, the average molecular weight is 29. Using the above formula the calculated average free path is $= 6.9 \times 10^{-8}$m. In this paper, the characteristic size of the model is L=2×10^{-4}m, and Kn=1.75×10^{-6} - much less than 10^{-3}, so it is suitable for non-slip boundary conditions.

The channels are segmented using a regular hexahedral mesh. In order to eliminate the effect of grid density on the simulation results, a grid independence test is performed. The change in the section air fraction with the number of grids is shown in Fig. 2.

It can be seen from Fig. 2 that when the number of grids is greater than 1200000, the section air fraction almost no longer changes, the number of grids increases from 1200000 to 2000000, the section air fraction is reduced by 1.32%. It can be assumed that the numerical simulation of the number

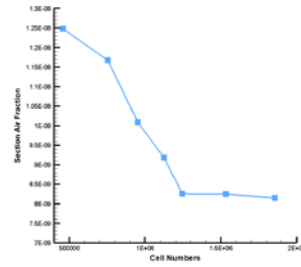of grids is 1200000 as a grid independent solution.

Fig. 2. Grid-independent validation

To study the effect of two button-type spacing and nodal diameter on the mixing effect in the channel, two button-type spacing of 500μm, 800μm, 1200μm, and node diameters of 200μm and 400μm, respectively, were taken. The water distribution cloud of the vertical section at 0.0028 m from the outlet and the cross section at 0.000175 m from the upper surface of the channel are shown in Figs. 3 and 4, respectively.
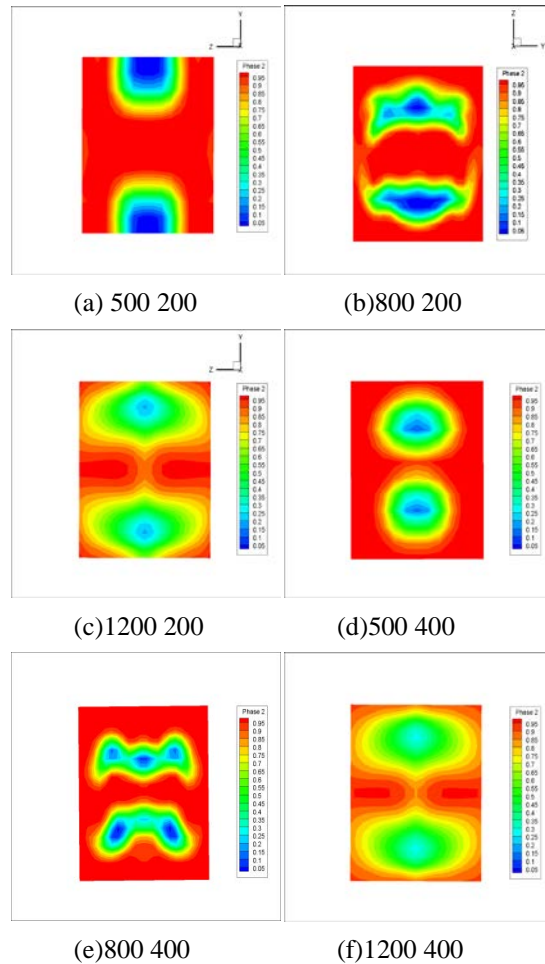

(a) 500 200   (b)800 200

(c)1200 200   (d)500 400

(e)800 400   (f)1200 400

Fig. 3. The water distribution cloud of the vertical section

(a) 500 200   (b)800 200

(c)1200 200   (d)500 400
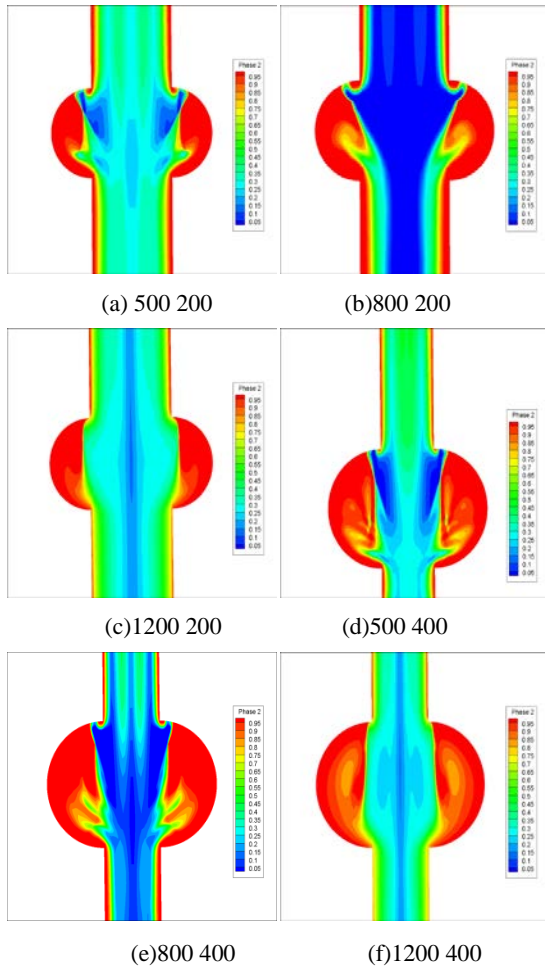
(e)800 400   (f)1200 400

Fig. 4. The water distribution cloud of the cross section

In order to study the effect of the nodal distribution position on the mixing effect in the channel when the channel entrance angle is 90 °, the nodes were placed on the same plane as the channel entrance, perpendicular to the channel entrance plane. The water distribution cloud of the vertical cross section at a distance from the outlet section of 0.0028 m is shown in Fig. 5.

To investigate the effect of the nodal distribution position on the mixing effect in the channel when the channel entrance angle is 45 °, the nodes were placed on the same plane as the channel entrance perpendicular to the channel entrance plane. The water distribution cloud of the vertical cross section at distance from the outlet section of 0.0028 m is shown in Fig. 6.

To investigate the effect of channel entrance angle on the mixing effect in the channel, the inlet angle was taken as 45° or 90°. The water distribution cloud of the vertical section at 0.0028 m from the outlet section and the cross section at 0.000175 m from the upper surface of the channel are shown in Figs. 7 and 8.

In order to compare the accuracy of the distribution of the cloud, the section air fraction of the vertical section at 0.0028 m from the outlet
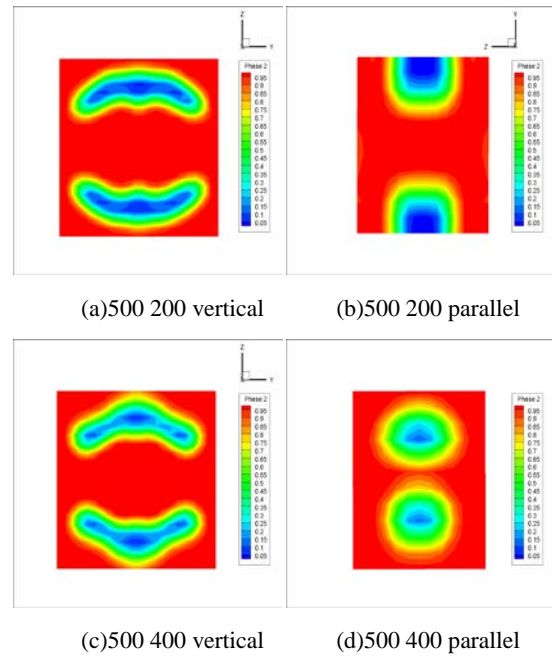
section was calculated. The results are shown in Table 1.

(a)500 200 vertical   (b)500 200 parallel

(c)500 400 vertical   (d)500 400 parallel

Fig. 5. The water distribution cloud of the vertical section

(a)500 200 vertical   (b)500 200 parallel

(c)500 400 vertical   (d)500 400 parallel

Fig. 6. The water distribution cloud of the vertical section

（a）500 200 45°　　　　（b）500 200 90°

（c）500 400 45°　　　　（d）500 400 90°

Fig. 7. The water distribution cloud of the vertical section

(a)　500 200 45°　　　　(b) 500 200 90°

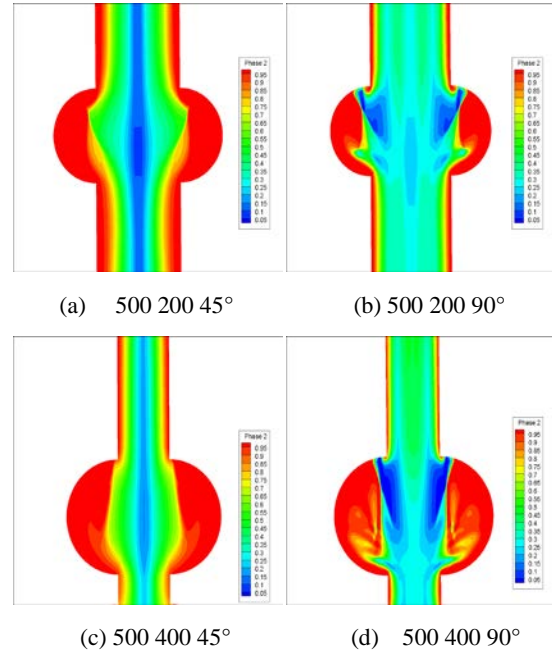(c) 500 400 45°　　　　(d)　500 400 90°
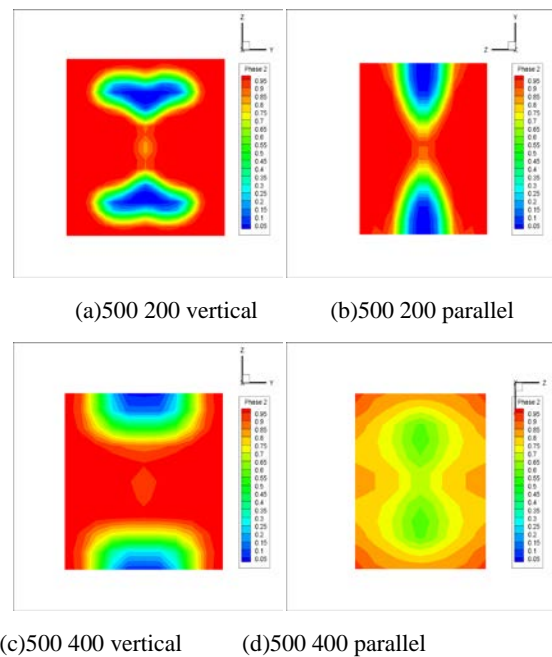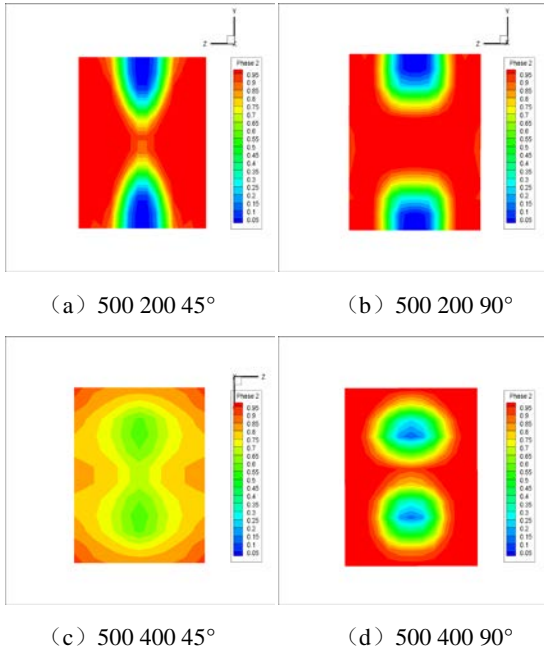
Fig. 8. The water distribution cloud of the cross section

Table1. Section air fraction

Nodal spacing (μm)	Nodal diameter (μm)	Position distribution of the nodes	Entrance angle (°)	Air phase area (m²)	Distance from the outlet section	Time	Air fraction
12000	200	parallel	90	1.1282280E-08			28.21%
800	200	parallel	90	8.9983620E-09			22.50%
500	200	parallel	90	8.2554070E-09			20.64%
500	400	parallel	90	7.3176700E-09			18.29%
800	400	parallel	90	7.8148170E-09			19.54%
1200	400	parallel	90	1.0916560E-08			27.29%
500	200	Vertical	90	9.0497850E-09	0.0028m	0.05s	22.62%
500	400	Vertical	90	8.6280130E-09			21.57%
500	200	parallel	45	7.9874200E-09			19.97%
500	200	Vertical	45	7.7125440E-09			19.28%
500	400	parallel	45	9.9487690E-09			24.87%
500	400	Vertical	45	8.4233990E-09			21.06%

RESULTS AND DISCUSSION

It can be seen from Fig. 3 that when the nodal diameter is 200μm, with the larger nodal spacing, air distribution is more and more uniform. The data in Table 1 show that the section air fraction increases from 20.64% to 28.21% when the nodal spacing increases from 500μm to 1200μm. This is so because as the nodal spacing becomes larger, the decrease in the amount of air remaining in the channel leads to a greater increase in the section air fraction. The air distribution is more uniform when the nodal spacing is 500μm, the section air fraction decreases from 20.64% to 18.29% when the nodal diameter increases from 200μm to 400μm, The air distribution is more concentrated. It can be seen from Fig. 4 that at constant nodal diameter, as the space of the nodal

198

becomes larger, the vortices at the node are significantly reduced, the mixing effect at the nodule decreases and the air fraction becomes larger (see Figure 3). When the space is constant and the diameter of the node changes from 200μm to 400μm, the vortices at the node increase, indicating that the mixing effect in the micro channel is better when the nodal diameter is 400μm. The above description shows that when the node diameter is constant, with the increase in nodal spacing the air fraction of the section becomes larger. When the space is constant, with the increase in nodal spacing the air fraction of the section becomes smaller. The gas distribution is more concentrated.

It can be seen from Fig. 5 that if the channel entrance angle is 90 ° and the nodal diameter is 200 μm, when the button structure changes from vertical

distribution to parallel distribution, the section air fraction decreases from 22.62% to 20.64%. When the nodal diameter is 400 μm, the above air fraction is also reduced from 21.57% to 18.29%. Note that when the button type node and the channel entrance are on the same plane, the air distribution is more concentrated with a better mixing effect.

It can be seen from Fig. 6 that at a channel entrance angle of 45 ° and nodal diameter of 200 μm, when the button structure changes from vertical distribution to parallel distribution, the section air fraction increases from 19.28% to 19.97%. When the nodal diameter is 400 μm, the above air fraction also increases from 21.06% to 24.87%. Note that when the button type node is vertical to the channel entrance plane, the air distribution is more concentrated with a better mixing effect.

It can be seen from Fig. 7 that for a nodal spacing of 500μm and nodal diameter of 200μm, when the inlet angle is from 45 ° to 90 ° and the section air fraction from 19.97% to 20.64%, the change is not obvious. For a nodal spacing of 500μm and nodal diameter of 400μm, when the inlet angle is from 45 ° to 90 ° and the section air fraction is from 24.87% to 18.29%，Fig. 8 shows that when the entrance angle is 90 °, the vortices at the button-type node increase and the air stays at the nodules, resulting in smaller air fraction. It is shown that the effect of the angle change on the section air fraction is small when the diameter of the node is small, and the effect of the angle change on the section air fraction increases as the diameter of the node becomes larger. For a channel entrance angle of 45 °, when the node diameter is from 200μm to 400μm, the section air fraction increases from 19.97% to 20.64%. For a channel entrance angle of 90 °, when the node diameter is from 200μm to 400μm, the section air fraction increases from 24.87% to 18.29%. Note that for an inlet angle of 45°, if the diameter of the node is increased, the air fraction also increases. For an inlet angle of 90 °, if the diameter of the node is increased, the air fraction decreases.

CONCLUSIONS

When the inlet angle is 90 °, with the increase in the node space, the section air fraction becomes larger and the gas distribution more uniform. With the increase in the node diameter, the section air fraction becomes smaller and the gas distribution more focused.

When the inlet angle is 45 °, the mixing effect of the vertical distribution is better than that of the parallel distribution. The larger the node diameter, the worse is the mixing effect. When the inlet angle is 90 °, the parallel distribution of the button type node is better than the vertical distribution; the greater the diameter of the node, the better is the mixing effect.

As the diameter of the nodal increases, the effect of the angle change on the section air fraction increases.

REFERENCES

1. S. Yagmur, S. Dogan, M. H. Aksoy, I. Goktepeli, M. Ozgoren, *Flow Measurement and Instrumentation*, **55**, 23 (2017).
2. Sh Zhang, A W.-K. Law, M. Jiang, *Journal of Hydro-environment Research*, **15**, 54 (2017).
3. G. Hu, K.T. Tse, K.C.S. Kwok, Y. Zhang, **146,** 172 (2015).
4. S.S. Lafmejani, A.C. Olesen, S.K. Kær, *International Journal of Hydrogen Energy*, **42** (26), 16333 (2017).
5. D.M. Bond, V. Wheatley, M. Goldsworthy, *International Journal of Heat and Mass Transfer*, **76,** 1 (2014).

Ecological response to land use change: a case study from the Chaohu lake basin, China

B. Wang[1,2], L. Chen[1*], L. Li[1,3], H. Xie[4], Y. Zhang[1]

[1] School of Environment Science and Spatial Informatics, China University of Mining and Technology, Xuzhou 221116, China
[2] Anhui Province Institute of Land Surveying and Planning, Hefei 230631, China;
[3] Department of Geography, Earth System Science, Vrije Universiteit Brussel, Brussels 1050, Belgium
[4] School of Environment and Energy Engineering, Anhui Jianzhu University, Hefei, 230601, China

Land use change (LUC) has been considered as a major cause of global environmental change. Characterizing LUC and its impact on the eco-environment can contribute to the sustainability of regional development. In order to accurately assess the ecological response to LUC, this study proposed a land use change and ecological response (LUCER) framework by means of remote sensing, incorporating the land use transition matrix, remote sensing ecological index (RSEI), and spatial regression methods. The LUCER framework was tested on the Chaohu lake basin. Results showed that the LUC intensity of the study area increased significantly, but RSEI decreased by a large margin, and the change trend showed a U shape. Moreover, LUC was the Granger cause of RSEI and their correlation remained negative. The LUCER framework performed well in measuring the LUC and RSEI changes. Our research suggests that the LUCER framework could effectively explain the dynamic process and functioning mechanisms of LUC and RSEI changes and quantitatively evaluate the LUC ecological response. From an ecological environment protection perspective, the results of this study can provide an insight into land use decision-making for policy makers.

Key words: Land use change; Remote sensing ecological index; Ecological response

INTRODUCTION

As a physical basis of various ecosystems, land serves as the most direct link between humans and nature. Land use change (LUC) has been closely connected with global environmental change and development sustainability [1]. By changing the structure and functions of an ecosystem, LUC can further impact its services [2]. The ecological impact of LUC, which is important to human wellbeing, has escalated in recent years. In general, LUC can be divided into two types, namely, implicit change and explicit change. The former refers to structural change, such as the change in the quantitative scale and spatial structure, whereas the latter, which is dependent on the former, reflects the change in quality, function, input, output, and so on. Economic growth is one of the main drivers of LUC and the overall impact of LUC on the eco-environment is negative. From 1978 to 2016, the urbanization rate in China rose from 17.9% to 57.4%, with an annual growth rate of 1.04%. However, China's ecologically vulnerable areas accounted for more than 60% of its total territory in 2014. As such, the Chinese government is committed to the construction of ecological civilization. In response to the central government's call, the research scope of LUC should be further expanded, for example, to cover the changes in land ecosystems.

To date, LUC and ecological changes have been long investigated but researchers have mainly focused on the characteristics and effects of LUC and ecological index changes. LUC or ecological change data are often extracted from remote sensing or simulated by CLUE-S and CA-Markov models [3,4]. From the perspective of biological habitats and resource distribution, Fu *et al*. [5] concluded that land use pattern can impact ecosystem services. Meanwhile, LUC is also considered responsible for soil erosion [6,7], frequent flooding [8], and urban heat island [9]. In addition, ecological indices, which can directly reflect eco-environmental quality, have been increasingly used to study ecological quality change. Xu [10] developed the remote sensing ecological index (RSEI) for evaluating the ecological quality of Chinese cities and suggested its wide application. Most of the abovementioned research described the correlation between LUC and ecological change while they did not reveal the impact of LUC on ecosystems in a systematical manner. Additionally, these studies mainly used remote sensing image data of two different years, which is insufficient to provide an accurate assessment and an overview understanding of the ecological quality change.

This study therefore presents a framework of land use change and ecological response (LUCER) to evaluate the impact of the LUC on regional

ecological changes. Remote sensing image data acquired in four different years (2000, 2005, 2010 and 2015) were used for deriving land use cover maps and RSEI. LUC and RSEI change were then characterized through the land use transition matrix and statistical measures and then their relationships were modeled by linear regression.

EXPERIMENTAL

Materials

Drainage basins are usually densely populated areas with highly intensive land use and the Chaohu Lake Basin is one of the examples. The Chaohu Lake is located in the center of the eastern Chinese province of Anhui (Fig. 1) and profiled as one of the five fresh water lakes in China. The Chaohu Lake Basin consists of 14 districts/counties among which nine belong to the provincial capital city of Hefei – one of the centers in the Yangtze River delta mega-city region. In 2016, the Chaohu Lake Basin registered 11.37 million permanent residents, with an urbanization rate of 65.97%. The basin covers a geographical area of 1.97×10^4 km^2, 3.8% of which is the water surface of the Chaohu Lake. Lying on the Yangtze River-Huai River hilly belt, the basin is characterized by elevations in the west and lowland in the east (Fig. 1c). The subtropical moist monsoon climate has resulted in the formation of 33 rivers of different lengths. Due to increasing human activity, water blooms have rapidly spread in these rivers. It was estimated in 2016 that water blooms affected 31.99% (237.6 km^2) of the total lake surface.
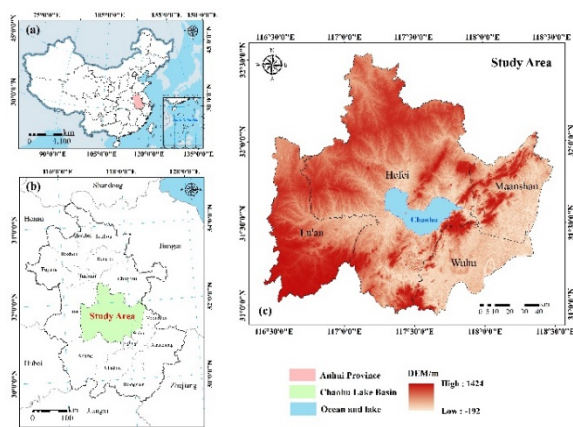

Fig. 1. Location of the study area: (a) Anhui province in China; (b) Chaohu lake basin in Anhui province; (c) elevation map of the study area with the Chaohu lake highlighted in blue. The study area covers part of four Anhui cities, namely Hefei, Maanshan, Wuhu, and Lu'an.

Data used in this study include remote sensing images and DEM data. They were used to interpret land use cover maps and derive RSEI. Table 1 shows the details of the four remote sensing images (i.e. 2000, 2005, 2010 and 2015).

Table 1. Remote sensing image data of the study area used for deriving RSEI

Date	Scene	Acquisition date	Path/Row
2000	Landsat 5 TM	10 October 2000	120/38; 121/38
2005	Landsat 5 TM	24 October 2005	120/38; 121/38
2010	HJ-1B-CCD	31 October 2010	452/76; 452/80; 457/76; 457/80
2015	HJ-1B-1RS	18 October 2015	455/70
	HJ-1B-CCD		454/76
	HJ-1B-1RS		456/77

The Landsat 5 TM data were downloaded from the Geospatial data cloud (http://www.gscloud.cn/) and the HJ-1B data were from the China Center for resources satellite data and application (http://www.cresda.com/). Landsat 5 TM and HJ-1B sensors have identical spatial resolutions (i.e. 30 m) with basically consistent spectral ranges, which allows their data to substitute each other [11]. All these cloud-free images were acquired in October, guaranteeing that vegetation was at nearly the same growth stage. Pre-processing of the Landsat 5 TM and HJ-1B image data such as clipping, radiation correction, and geometric correction was performed in ENVI 5.1. The DEM covering of the study area was produced by mosaicking 30-m-resolution DEM datasets from the ASTER GDEM V2 (N30E116; N31E116; N31E117; N31E118; N32E116; N32E117; N32E118) in ArcGIS 10.2. Based on the *Codes for the Current Land Use Classification in China (GB/T21010-2007),* the remote sensing data were classified using a SVM (support vector machine) and land use was divided into six Level-1 types: arable land, forest land, grass land, waters, land for urban and rural construction, and other land. Among them, arable land was further divided into two Level-2 types (paddy field and unirrigated field), and land for urban and rural construction into three Level-2 types (urban residential land, rural residential land, and industry-traffic land). The accuracy assessment results showed that the Kappa indexes for each time period for arable land, forest land and waters, etc. were larger than 0.8, and the Kappa index for grass land was 0.75. The accuracy of classification conformed to the requirement of the study.

Analytical methods

Land use transition matrix

The land use transition matrix was used to represent the transition between different land use types (Table 2). The row represents the land use type A_i at time T_1, while the column represents the land

201

use type A_j at time T_2. The matrix element C_{ii} represents the constant area of land use type i from T_1 to T_2 while the matrix element C_{ij} represents the area of land use type i, which is transitioned into land use type j from T_1 to T_2, and P_{ij} denotes the percentage of the transition.

Table 2. Land use transition matrix

T_1	T_2					
	A_1	A_2	$\cdots$	A_j	$\cdots$	A_n
A_1	C_{11}	C_{12}	$\cdots$	C_{1j}	$\cdots$	C_{1n}
	P_{11}	P_{12}	$\cdots$	P_{1j}	$\cdots$	P_{1n}
A_2	C_{21}	C_{22}	$\cdots$	C_{2j}	$\cdots$	C_{2n}
	P_{21}	P_{22}	$\cdots$	P_{2j}	$\cdots$	P_{2n}
$\vdots$	$\vdots$	$\vdots$	$\vdots$	$\vdots$	$\vdots$	$\vdots$
A_i	C_{i1}	C_{i2}	$\cdots$	C_{ij}	$\cdots$	C_{in}
	P_{i1}	P_{i2}	$\cdots$	P_{ij}	$\cdots$	P_{in}
$\vdots$	$\vdots$	$\vdots$	$\vdots$	$\vdots$	$\vdots$	$\vdots$
A_n	C_{n1}	C_{n2}	$\cdots$	C_{nj}	$\cdots$	C_{nn}
	P_{n1}	P_{n2}	$\cdots$	P_{nj}	$\cdots$	P_{nn}

In order to investigate how much a land use type (i) was transitioned into another land use type (j), we proposed a measure termed transition rate (TR_j):

$$TR_j = \frac{GA_j}{LA_i} \tag{1}$$

where LA_i is the total lost area of land use type i over the period, GA_j is the area of land use type j that is gained through transition from land use type i.

Remote sensing ecological index

The RSEI is a function of greenness, wetness, heat and dryness that human beings can directly feel in the environment. The four components can be represented by different remote sensing based measures, namely the normalized difference vegetation index (NDVI), wet index (WI), land surface temperature (LST), and normalized different built-up soil index (NDBSI). Therefore, the function can be expressed by:

$$RSEI = f(NDVI, WI, LST, NDBSI) \tag{2}$$

The four components in the function are given as follows:

(1) The NDVI is a vegetation index that provides vegetation biomass information can be calculated by [12]:

$$NDVI = \frac{\rho_{NIR} - \rho_{red}}{\rho_{NIR} + \rho_{red}} \tag{3}$$

where ρ_{NIR} and ρ_{red} are reflectance in the near infrared and red bands of Landsat 5 TM (or HJ-1B)

202

data. Variables such as ρ_{green}, ρ_{blue}, ρ_{LWIR} and ρ_{SWIR} in the following equations have similar meaning.

(2) The WI is a humidity component obtained through a tasseled-cap transform. Calculation of WI varies with sensor type.

For Landsat 5 TM data, WI can be obtained by [13]:

$$WI = 0.03\rho_{blue} + 0.20\rho_{green} + 0.31\rho_{red} + 0.16\rho_{NIR} - 0.68\rho_{SWIR1} - 0.61\rho_{SWIR2} \tag{4}$$

For HJ-1B data, it can be obtained by [14]:

$$WI = -0.14\rho_{blue} + 0.004\rho_{green} + 0.73\rho_{red} - 0.67\rho_{NIR} \tag{5}$$

(3) LST can be derived from remote sensing imagery through the method presented in the study of Nichol [15]. However, it was substituted by brightness temperature (BT) for simplicity in this study because BT approximates it [16] and accurate calculation of land surface temperature is not the main target. BT was computed by [17]:

$$BT = \frac{K_2}{\ln\left(1 + \frac{K_1}{\rho_{LWIR}}\right)} \tag{6}$$

where $K_1 = 607.76$ $W/(m^2 \cdot sr \cdot \mu m)$ and $K_2 = 1260.56$ K for Landsat 5 TM data [17], and $K_1 = 579.20$ $W/(m^2 \cdot sr \cdot \mu m)$ and $K_2 = 1245.58$ K for HJ-1B data [18].

(4) The normalized different building-soil index (NDBSI) is the average of the built-up index (BI) and the soil index (SI) [19]:

$$NDBSI = \frac{SI + IBI}{2} \tag{7}$$

where SI and BI can be computed by [19], respectively:

$$SI = \frac{(\rho_{SWIR1} + \rho_{red}) - (\rho_{blue} + \rho_{NIR})}{(\rho_{SWIR1} + \rho_{red}) + (\rho_{blue} + \rho_{NIR})} \tag{8}$$

$$IBI = \frac{2\rho_{SWIR1}/(\rho_{SWIR1} + \rho_{NIR}) - \left[\rho_{NIR}/(\rho_{NIR} + \rho_{red}) + \rho_{green}/(\rho_{green} + \rho_{SWIR1})\right]}{2\rho_{SWIR1}/(\rho_{SWIR1} + \rho_{NIR}) + \left[\rho_{NIR}/(\rho_{NIR} + \rho_{red}) + \rho_{green}/(\rho_{green} + \rho_{SWIR1})\right]} \tag{9}$$

Because our focus was on the area around the Chaohu Lake and water affects the calculation of the four components, surface water was masked out [10]. In addition, the four components varied in units and range of values, they were normalized to the 0-1 range. Here we applied Eq. (10) to the NDVI and WI and applied Eq. (11) to LST and NDBSI:

$$Y_i = \frac{X_i - Min_i}{Max_i - Min_i} \tag{10}$$

$$Y_i = \frac{Max_i - X_i}{Max_i - Min_i} \tag{11}$$

where X_i and Y_i are the original and normalized values of the four components, respectively; Max_i and Min_i are the maximum and minimum values of the four components, respectively. It is noted that greenness and wetness have positive effects on the environment while heat and dryness have negative effects on the environment.

To exclude the impact of artificially introduced weights on RSEI estimation, Xu [10] reported that their weights can be obtained through their principal component analysis (PCA). Through PCA, most of the normalized measures were explained by the first principal component (PC1):

$$PC1 = a \times Normalized\ NDVI + b \times Normalized\ WI + c \times Normalized\ LST + d \times Normalized\ NDBSI \quad (12)$$

where a, b, c, and d are the coefficients of the normalized measures, which could be used as their corresponding weights for calculating the RSEI. In this case, the PC1 was actually the RSEI.

However, such coefficients vary from imagery to imagery, which suggests that the RSEI of the study area in different years would be obtained from different functions. This does not allow a direct comparison of the RSEI of different years. To solve this problem, we proposed a new simple method to determine the weights by averaging their values of different years, e.g. $a = \left(a_{2000} + a_{2005} + a_{2010} + a_{2015}\right)/4$. Finally, the RSEI was also normalized to the 0-1 range for zoning and comparison. After normalization, a higher RSEI value indicates a better ecological quality and *vice versa*.

Spatial multiple regression based on geographical grid

In order to identify LUC hot spots, and analyze the percentage of LUC and the corresponding RSEI change values, we built a geographical grid for the study area. For a more effective ecological quality evaluation, the size of the grid unit is recommended to be 2 to 3 times larger than the average patch area of the study area [20]. As the average patch area of the study area was 4.23 km², the size of the grid unit was set at 3 km × 3 km – the study area was covered by a total of 2,400 grid units. A simple regression model of RSEI was constructed with the percentage of LUC area in a grid unit. These variables were computed within the grid unit if it was completely within the study area.

LUCER framework

By integrating all the above-mentioned measures and methods, we proposed a LUCER framework to evaluate the impact of the LUC on regional ecological changes. This framework consists of two parts: the first part was to derive LUC and RSEI from remote sensing image data, through land use classification and remote sensing based measures (NDVI, WI, LST, and NDBSI), respectively. The second part was to identify hotspots of LUC and RSEI changes. The Granger analysis and the spatial regression analysis based on the geographical grid were combined to examine the interaction between LUC and RSEI change. Through this model, the mechanism of ecological response to LUC was revealed.
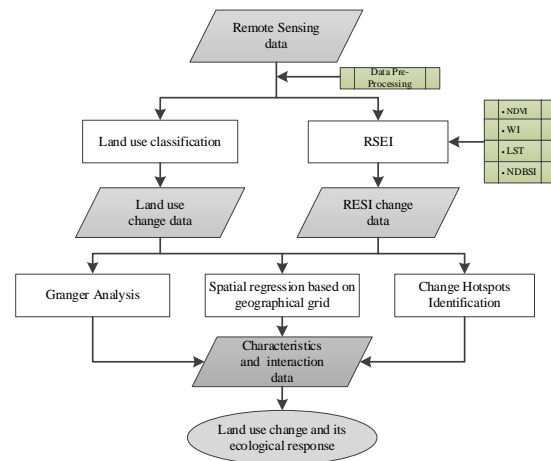
Fig. 2. Structure of LUCER framework presented in this study

RESULTS AND DISCUSSION

Characterizing land use change

From land use cover maps for 2000, 2005, 2010 and 2015 (Fig. 3) it was clear that arable land was the major land use type, accounting for 68.19%, 67.64%, 65.87%, and 63.66% of the total area for the four years, respectively.
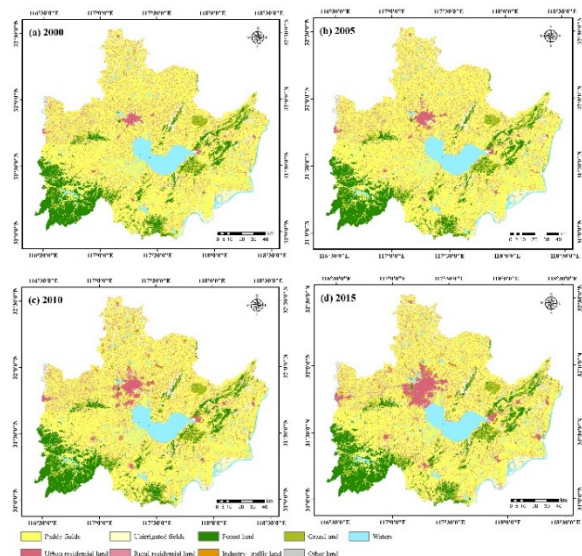
Fig. 3. Land use cover maps

However, the arable land continuously shrank while land for urban and rural construction increased steadily, with a growth rate of 41.30%. The increase in the area of land use for urban and rural construction was 91.66% of the decrease in the area of arable land. This suggests that the expansion of land for urban and rural construction was a major cause of arable land decrease for the period from 2000 and 2015.

Table 3 shows that paddy field, unirrigated field, rural residential land and industry-traffic land were the main land use types that experienced significant changes from 2000 to 2015, all their change rates being higher than 5%. It illustrates that:

(1) Urban residential land was a hotspot of land use transition. From 2005 to 2010, the transition of industry-traffic land was among the most dramatic ones – 4.99 km^2 (21.36%) were transitioned into urban residential land. This can be explained by the fact that industrial parks were mainly in suburbs, which were later incorporated into cities as a result of urban expansion.

(2) Most arable land was transitioned into land for urban and rural construction. From 2000 to 2005, the transition rate of unirrigated field transitioned into urban residential land was 85.50%. From 2010 to 2015, part of arable land was transitioned into waters. This change was made mainly in response to the policy for protection of the wetland and return farmlands to lakes.

(3) The land use transition of urban residential land was diversified. From 2000 to 2005 and from 2005 to 2010, the urban residential land was mainly reclaimed into paddy fields, and the transition rates were 77.65%, 50.14%, respectively. However, from 2010 to 2015, urban residential land started to transform into grass land and waters in accordance with eco-environment requirements.

Characterizing the RSEI change

Mean values of the normalized NDVI, WI, LST, NDBSI, and the RSEI of the study area were calculated for each year. The normalized NDVI was highest (0.57) in 2000 and fell in the following 10 years before rising to 0.53 in 2015. This suggested that the influence of afforestation projects in the study area from 2010 to 2015 was obvious. The normalized WI increased from 2005 to 2010 and decreased afterwards, with a highest value (0.63) in 2005. The normalized LST and NDBSI changed little over the 15 years. The RSEI changed in a similar way to the normalized NDVI.

The eigenvalue contributions of the first principal component (PC1) were all higher than 94%. This suggests that the first PC explains most of the variability of input normalized measures. However, the PC1 coefficients of the four normalized measures varied significantly. The differences between the maximum and minimum PC1 coefficients of normalized NDVI, WI, LST, and NDBSI were 28.95%, 18.60%, 43.14%, and 38.89%, respectively. Through averaging, the weight values of the

Table 3. Land use transition matrix of the study area from 2000 to 2015 (km^2, %)

	Paddy fields	Unirrigated field	Forest land	Grass land	Waters	Urban residential land	Rural residential land	Industry - traffic land	Other land
Paddy field	12013.14	16.43	12.68	13.95	95.04	385.08	305.45	104.86	4.37
	—	0.13	0.10	0.11	0.73	2.97	2.36	0.81	0.03
Unirrigated field	4.86	766.69	0.65	0.75	6.71	35.98	16.10	2.85	0.67
	0.58	—	0.08	0.09	0.80	4.31	1.93	0.34	0.08
Forest land	8.72	0.47	2136.46	3.85	2.50	0.65	6.12	4.54	0.39
	0.40	0.02	—	0.18	0.12	0.03	0.28	0.21	0.02
Grass land	2.64	0.20	3.37	747.73	1.25	0.02	7.86	7.68	0.01
	0.34	0.03	0.44	—	0.16	0	1.02	1.00	0
Waters	16.46	2.48	0.17	0.60	1436.14	3.65	1.37	1.03	0.00
	1.13	0.17	0.01	0.04	—	0.25	0.09	0.07	0
Urban residential land	0.26	0.06	0.00	0.00	0.49	193.05	0.03	0.01	0.00
	0.13	0.03	0	0	0.25	—	0.02	0.01	0
Rural residential land	31.15	5.94	0.28	1.21	3.13	52.99	1710.64	10.16	0.45
	1.72	0.33	0.02	0.07	0.17	2.92	—	0.56	0.02
Industry-traffic land	0.42	0.04	0.02	0.01	0.00	4.99	0.07	17.81	0.00
	1.80	0.17	0.09	0.04	0	21.36	0.30	—	0
Other land	0.01	0.00	0.01	0.01	0.00	0.00	0.00	0.00	0.93
	1.04	0	1.04	1.04	0	0	0	0	—

different measures were obtained, which were 0.22, 0.24, 0.32, and 0.22, respectively. Using the natural breaks method, the RSEI images were classified into five levels, namely, worst (0-0.2), worse (0.2-0.4), medium (0.4-0.6), better (0.6-0.8), and best (0.8-1) (Fig. 4.).
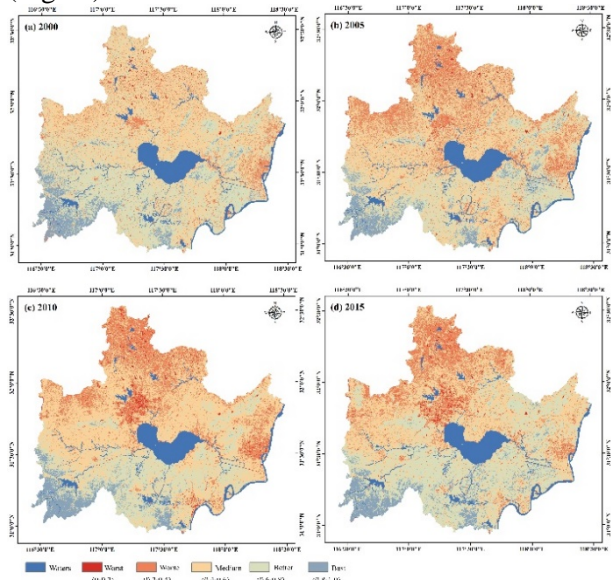
Fig. 4. The RSEI maps of the study area in 2000, 2005, 2010, and 2015

The percentages of the medium level and above were 90.11%, 78.96%, 80.09%, and 82.49% in 2000, 2005, 2010 and 2015, respectively. As such, the RSEI showed a U-shaped trend with a rapid drop in the 2000-2005 period and a slow increase in the 2005-2015 period. This suggested that the ecological quality was seriously worsened before gradual improvement. It was also noted that the medium level remained the largest one over the 15 years, accounting for at least 40%.

A comparative difference analysis was conducted on the RSEI classification maps. In the analysis, numbers from 1 to 5 were assigned to the levels from the worst to the best for differencing. Differencing result ranging from -1 to -4 was considered as worsening (indicated in red in Fig. 5.), and differencing result ranging from 1 to 4 was considered as improvement (green), while the 0 value was considered as consistency (white).

From 2000 to 2015, the worsening area was 5,854 km² (29.72% of the total RSEI area) while the improvement area was 3,900.10 km² (19.80%). From 2005 to 2010, the worsening trend was alleviated as the worsening area was only 1.18 times larger than the improvement area. From 2010 to 2015, the worsening area was however reduced to only half of the improvement area – the ecological quality was significantly improved during this period. The contrasting change over the 15 years was

consistent with our knowledge of the study area: the eco-environment of the Chaohu lake basin was first partly damaged and then recovered.
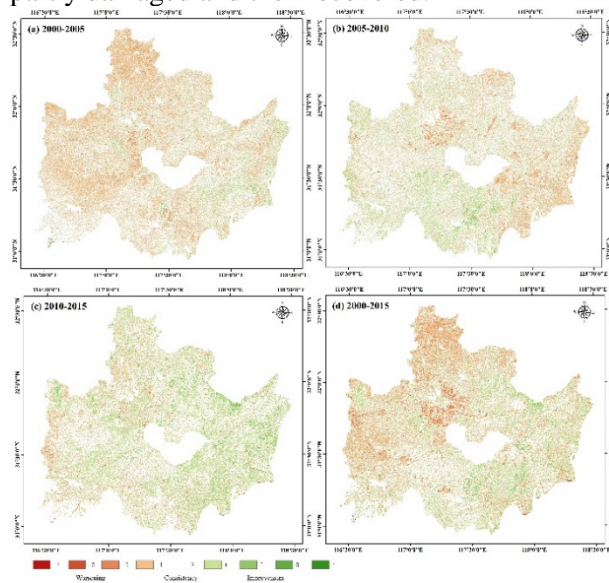
Fig. 5. The RSEI differencing

Modeling the interaction between land use change and RSEI change

The LUC types with a transition rate higher than 5% were treated as LUC hotspots, including paddy into urban land (32.25%), paddy into rural residential land (25.58%), and paddy into industry-traffic land (8.78%). Thus, the overall land use transition rate was 66.61%. The change process exerted a similar influence on the ecological quality. For example, the underlying surface conditions changed and the surface runoff increased, which led to changes in ecological system structure and services, decline of biological diversity maintenance, and weakening of adjustment capability. Therefore, the above change can be explained by the transition of paddy into land for urban and rural construction. The scatter plot of the percentage of the land use transition in the grid against the RSEI change value on the grid reveals their negative correlation ($R^2 = 0.82$) (Fig. 6.).

The Granger test showed that, at the significance level of 5%, X was the Granger cause of Y (F = 70.52, P < 0.05). This means that the transition of paddy into land for urban and rural construction was a major cause of the declining RSEI. The regression model meant that the increase in the transition of paddy into land for urban and rural construction in the geographical grid by 1% (0.09 km²) would lead to a decrease in the overall RSEI by 12.91 in the geographical grid. The ecological quality decline was obvious.
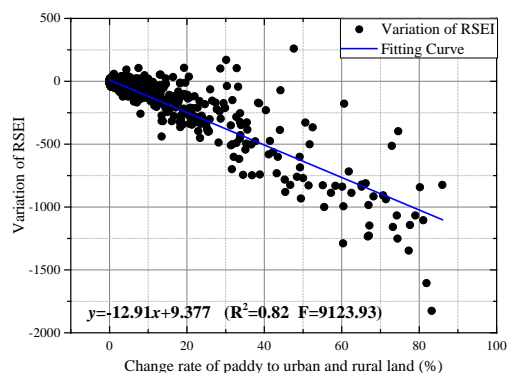
Fig. 6. Scatter plot of variation of RSEI against change rate of paddy to urban and rural residential land ($R^2 = 0.82$).

CONCLUSIONS

To achieve an accurate assessment of the ecological response to LUC, we used Landsat 5 TM and HJ-1B remote sensing imagery to build the land use change and ecological response (LUCER) framework and tested it on the Chaohu Lake Basin. Through the results, we have concluded that:

(1) The land use change analysis shows an increasingly dramatic LUC in the study area from 2000 to 2015. The change hot spots were reflected as quality arable land transitioned into land for urban and rural construction. During the 15 years, the RSEI dropped significantly, and the change trend presented a U shape. This was consistent with the true facts.

(2) The Granger test and the regression model based quantitative analysis indicated that LUC was the Granger cause of the RSEI change. LUC and RSEI change were negatively correlated. The government should monitor the LUC to control the land development and utilization of the area nearby.

(3) The LUCER framework can effectively explain the dynamic change process of land use and RSEI, reflect the interaction between the LUC and the RSEI change, predict the trend of LUC and RSEI change, and provide technical support for land management decision-making.

The LUCER framework can facilitate the analysis of the regional land use ecological response mechanism and characteristics, and improve the comprehensive effectiveness of regional land use management and ecosystem protection both in

theory and in practice. However, LUC is not the only factor that triggers ecological change. Land utilization also has a potential influence on ecological change. It is recommended that further research should focus on the combined influence of LUC and land utilization on ecological quality to reveal the LUCER mechanism in depth.

REFERENCES

1. E. Lambin, A. Veldkamp, *Glob. Chang. Newsl.*, **2**, 147 (2005).
2. T. Hasegawa, S. Fujimori, A. Ito, K. Takahashi, T. Masui, *Sci. Total Environ.*, **580**, 787 (2017).
3. T. Xia, W. Wu, Q. Zhou, P. H. Verburg, Q. Yu, P. Yang, L. Ye, *J. Geogr. Sci.*, **26**, 173 (2016).
4. B. Abuelaish, M.T.C. Olmedo, *Arab J. Geosci.*, **9**, 274 (2016).
5. B. Fu, S. Wang, C. Su, M. Forsius, *Curr. Opin. Environ. Sustain.*, **5**, 10 (2013).
6. V. Simonneaux, A. Cheggour, C. Deschamps, F. Mouillot, O. Cerdan, Y.L. Bissonnais, *J. Arid. Environ.*, **122**, 73 (2015).
7. M. Zare, T. Panagopoulos, L. Loures, *Land Use Policy*, **67**, 568 (2017).
8. J. Liu, Z. Shi, *Land Use Policy*, **65**, 206 (2017).
9. X. Du, Z. Huang, *Ecol. Indic.*, **81**, 243 (2017).
10. H. Xu, *China Environ. Sci.*, **33**, 891 (2013).
11. J. Luo, J. Zhang, W. Huang, G. Yang, X. Gu, H. Yang, *Spectroscopy Spectr. Anal.*, **30**, 3287 (2010).
12. J.W. Rouse, R.H. Hass, J.A. Schell, D.W. Deering, *Third Earth Resour. Technol. Satell. Symp.*, **1**, 310 (1974).
13. E. P. Crist, *Remote Sens. Environ.*, **17**, 303 (1985).
14. P. Cui, D. Li, C. Ma, *J. Taiyuan Univ. Technol.*, **47**, 316 (2016).
15. J. Nichol, *Photogramm. Eng. Remote Sens.*, **71**, 613 (2005).
16. Y. Zhang, L. Chen, Y. Wang, L. Chen, F. Yao, P. Wu, B. Wang, Y. Li, T. Zhou, T. Zhang, *Remote Sens.*, **7**, 10740 (2015).
17. Z. Qin, A. Karnieli, P. Berliner, *Int. J. Remote Sens.*, **22**, 3719 (2001).
18. S. Zhao, Q. Qin, F. Zhang, Q. Wang, Y. Yao, L. You, H. Jiang, R. Cui, Y. Yao, *Spectroscopy Spectr. Anal.*, **31**, 1553 (2011).
19. H. Xu, *Int. J. Remote Sens.*, **29**, 4269 (2008).
20. W. Zuo, G. Zhang, B. Wan, S. Li, Q. Wang, *Acta Geod. Cart. Sin.*, **32**, 269 (2003)

Instructions about Preparation of Manuscripts

General remarks: Manuscripts are submitted in English by e-mail The text must be typed on A4 format paper using Times New Roman font size 11, normal character spacing. The manuscript should not exceed 15 pages (about 3500 words), including photographs, tables, drawings, formulae, etc. Authors are requested to use margins of 2 cm on all sides

Manuscripts should be subdivided into labelled sections, e.g. **Introduction, Experimental, Results and Discussion**, *etc*. **The title page** comprises headline, author's names and affiliations, abstract and key words. Attention is drawn to the following:

a) **The title** of the manuscript should reflect concisely the purpose and findings of the work. Abbreviations, symbols, chemical formulas, references and footnotes should be avoided. If indispensable, abbreviations and formulas should be givenin parentheses immediately after the respective full form.

b) **The author**'s first and middle name initials and family name in full should be given, followedby the address (or addresses) of the contributing laboratory (laboratories). **The affiliation** of the author(s) should be listed in detail by numers (no abbreviations!). The author to whom correspondence and/or inquiries should be sent should be indicated by asterisk (*) with e-mail address.

The abstract should be self-explanatory and intelligible without any references to the text andcontaining not more than 250 words. It should be followed by key words (not more than six).

References should be numbered sequentially in the order, in which they are cited in the text. The numbers in the text should be enclosed in brackets [2], [5, 6], [9–12], etc., set on the text line. References are to be listed in numerical order on a separate sheet. All references are to be given in Latin letters. The names of the authors are given without inversion. Titles of journals must be abbreviated according to Chemical Abstracts and given in italics, the volume is typed in bold, the initial page is given and the year in parentheses. Attention is drawn to the following conventions:a) The names of all authors of a certainpublications should be given. The use of "*et al.*" inthe list of references is not acceptable.b) Only the initials of the first and middle names should be given. In the manuscripts, the reference to author(s) of cited works should be made without giving initials, e.g. "Bush and Smith [7] pioneered...". If the reference carries the names of three or more authors it should be quoted as "Bush *et al*. [7]", if Bush is the first author, or as "Bush and co-workers [7]", if Bush is the senior author.

Footnotes should be reduced to a minimum. Each footnote should be typed double-spaced at thebottom of the page, on which its subject is first mentioned.**Tables** are numbered with Arabic numerals on the left-hand top. Each table should be referred to inthe text. Column headings should be as short as possible but they must define units unambiguously.The units are to be separated from the preceding symbols by a comma or brackets. Note: The following format should be used when figures, equations, *etc*. are referred to the text (followed by the respective numbers): Fig., Eqns., Table, Scheme.

Schemes and figures. Each manuscript should contain or be accompanied by the respective illustrative material as well as by the respective figure captions in a separate file (sheet).As far as presentation of units is concerned, SI units are to be used. However, some non-SI units are also acceptable, such as °C, ml, l, etc.The author(s) name(s), the title of the manuscript, the number of drawings, photographs, diagrams, etc., should be written in black pencil on the back of the illustrative material (hard copies) inaccordance with the list enclosed. Avoid using more than 6 (12 for reviews, respectively) figures in the manuscript. Since most of the illustrative materials are to be presented as 8-cm wide pictures, attention should be paid that all axis titles, numerals, legend(s) and texts are legible.

The authors are required to submit the text with a list of three individuals and their e-mail addresses that can be considered by the Editors as potential reviewers. Please, note that the reviewers should be outside the authors' own institution or organization. The Editorial Board of the journal is not obliged to accept these proposals. The authors are asked to submit **the final text** (after the manuscript has been accepted for publication) in electronic form by e-mail. The main text, list of references, tables and figure captions should be saved in separate files (as *.rtf or *.doc) with clearly identifiable file names. It is essential that the name and version of the word-processing program and the format of the text files is clearly indicated. It is recommended that the pictures are presented in *.tif, *.jpg, *.cdr or *.bmp format.

The equations are written using "Equation Editor" and chemical reaction schemes are written using ISIS Draw or ChemDraw programme.

EXAMPLES FOR PRESENTATION OF REFERENCES

REFERENCES

1. D. S. Newsome, *Catal. Rev.–Sci. Eng*., **21**, 275 (1980).

2. C.-H. Lin, C.-Y. Hsu, *J. Chem. Soc. Chem. Commun*., 1479 (1992).

3. R. G. Parr, W. Yang, Density Functional Theory of Atoms and Molecules, Oxford Univ. Press, New York, 1989.

4. V. Ponec, G. C. Bond, Catalysis by Metals and Alloys (Stud. Surf. Sci. Catal., vol. 95), Elsevier, Amsterdam, 1995.

5. G. Kadinov, S. Todorova, A. Palazov, in: New Frontiers in Catalysis (Proc. 10th Int. Congr. Catal., Budapest,(1992), L. Guczi, F. Solymosi, P. Tetenyi (eds.), Akademiai Kiado, Budapest, 1993, Part C, p. 2817.

6. G. L. C. Maire, F. Garin, in: Catalysis. Science and Technology, J. R. Anderson, M. Boudart (eds), vol. 6, SpringerVerlag, Berlin, 1984, p. 161.

7. D. Pocknell, *GB Patent* 2 207 355 (1949).

8. G. Angelov, PhD Thesis, UCTM, Sofia, 2001, pp. 121-126.

9 JCPDS International Center for Diffraction Data, Power Diffraction File, Swarthmore, PA, 1991.

10. CA **127**, 184 762q (1998).

11. P. Hou, H. Wise, *J. Catal.*, in press.

12. M. Sinev, private communication.

13. http://www.chemweb.com/alchem/articles/1051611477211.html.

Texts with references which do not match these requirements will not be considered for publication!!!

CONTENTS